Université du Québec
Institut National de la Recherche Scientifique
Centre Eau Terre Environnement

# MODÉLISATION HYDRODYNAMIQUE DE L'ESTUAIRE FLUVIAL DU SAINT-LAURENT

Par

Pascal MATTE

Thèse présentée pour l'obtention du grade de
*Philosophiæ Doctor* (Ph.D.) en sciences de l'eau

**Jury d'évaluation**

| | |
|---|---|
| Examinateurs externes | Stephen G. Monismith<br>Department of Civil and Environmental Engineering<br>Stanford University |
| | Daniel Bourgault<br>Institut des sciences de la mer,<br>Université du Québec à Rimouski |
| Examinateur interne | Alain Mailhot<br>Centre Eau Terre Environnement,<br>Institut national de la recherche scientifique |
| Codirecteur de recherche | Jean Morin<br>Section Hydrologie et Écohydraulique,<br>Environnement Canada |
| Directeur de recherche | Yves Secretan<br>Centre Eau Terre Environnement,<br>Institut national de la recherche scientifique |

**À Catherine et Félixe**

*L'imagination est plus importante que le savoir*

– Albert Einstein

# REMERCIEMENTS

Ces remerciements s'adressent à tous ceux qui ont contribué, souvent dans l'ombre, au succès de cette thèse. Je pense à mes superviseurs, à mes collègues, à mes collaborateurs, et aussi à mes proches, qui ont laissé leur marque dans ma vie d'une façon particulière. L'écriture de cette section marque la fin d'un long périple, non sans embuches, qu'a été la réalisation de cette thèse. Elle vient en quelque sorte sceller une partie de ma vie, intense mais riche en interactions, en créativité et en émotions…

Je tiens, dans un premier temps, à remercier mon directeur de thèse, Yves Secretan. Merci d'abord de t'être laissé convaincre par mon idée de projet au Mexique, un peu broche-à-foin au début, mais qui nous a tout de même valu un voyage là-bas, subventionné en plus! Tu as semblé voir un certain potentiel (non certain!) en moi et tu as cru bon y investir du temps et de l'énergie, en me proposant un stage, puis une maîtrise, suivie d'un passage au doctorat. Je suis tranquillement entré dans le monde Secretan (!), un monde de logique et de rigueur sans compromis. Nul besoin de dire que ce fut très formateur! L'estime personnelle en a pris un coup au début, pour revenir un peu plus tard dans le processus… Tu as toujours maintenu la barre haute, en exigeant le meilleur de moi, mais en me donnant les moyens pour y arriver. J'ai bénéficié de ton solide appui dans tous mes projets et d'une énorme liberté. Tu as témoigné une grande confiance dans mon travail, en me laissant m'approprier pleinement mon sujet, tout en sachant calmer mes élans ou mieux les orienter. Tu as fait preuve d'une disponibilité sans bornes – mais à condition d'arriver préparé dans ton bureau! Tu n'as jamais eu peur de dire les choses telles qu'elles sont – quand c'est mauvais, c'est mauvais! (et inversement) – d'une manière directe mais toujours constructive. Et par-dessus-tout, tes raclettes annuelles et nos nombreuses « grosses soupes thaïes, poulet et crevettes, moyennement épicées » ont facilité, non pas ma digestion, mais la traversée de mes longues années de doctorat! Tu as été un mentor pour moi et je te remercie d'avoir pris ce rôle au sérieux. J'espère suivre tes traces et continuer de te côtoyer, que ce soit dans un cadre professionnel ou autre. Merci pour ce legs!

Merci également à Jean Morin, mon co-directeur. Ta contribution et ton input ont toujours été très pertinents. J'ai été inspiré par ton expérience en modélisation, l'originalité de tes idées et ton ambition. Je crois que tu m'as transmis à ta façon l'héritage que tu as toi-même reçu de Michel

Leclerc, dont nous sommes tous des produits dérivés! Toujours prêt à rendre visite à nos deux Hervé lyonnais, j'ai eu la chance de t'y accompagner. Avec comme objectif louable de modéliser le Rhône, j'ai pu mettre la main à la pâte avec toi et passer à travers le processus de modélisation, un verre de Côtes du Rhône à la main (après les heures de bureau bien sûr… c'est-à-dire en après-midi). J'ai beaucoup appris! Merci de ta confiance et de ton support tout au long de mon doctorat. Tu as créé maintes opportunités pour moi, au-delà même du cadre académique, et je t'en remercie. On risque fortement de se recroiser…!

Je tiens à remercier les autres membres de mon jury d'évaluation de thèse, qui ont fait preuve d'un grand intérêt pour mon sujet et d'une analyse rigoureuse et approfondie de mon travail. Alain Mailhot, c'est toujours un plaisir d'échanger avec toi. Ton esprit critique et d'analyse ont mené à des discussions très constructives. La prochaine fois, je tenterai d'ajouter plus de fautes « d'inattention », pour diminuer ta frustration…! Thank you Stephen Monismith for being part of this evaluation; your contribution and your comments were very much appreciated. I hope we will meet in person next time! Merci Daniel Bourgault pour ta contribution, pour avoir posé des questions qui nous ont poussés à revenir un cran en arrière et à repenser certaines hypothèses de départ. Nos discussions ont été très stimulantes.

David Jay, thank you for offering me this opportunity to work in your lab at PSU. The teaching that I received is invaluable. Our many discussions fueled my thoughts and shaped a large part of my thesis. This 6-month stay in Portland has not only opened my eyes to the complex world of river tides, but also to the astounding amount of micro-breweries and hipsters cafes, a perfect distraction to escape the gloomy and rainy winter! A research collaboration was born out of this project, which I hope will continue long.

Merci aux étudiants, stagiaires et professionnels de recherche qui sont passés dans l'équipe et qui ont apporté une contribution significative à mon projet, en débroussaillant certains aspects non explorés et en faisant du « travail de bras » indispensable au développement du modèle. Merci Lucie, Dikra, Matthieu, Simon, Benoit, Charles et Jimmy. Un grand merci à toute l'équipe d'Environnement Canada de Québec qui m'a suivi depuis le début et qui s'est impliquée directement dans mon projet. Merci Guy pour ta bonne humeur! Douze heures sur un bateau à traverser le fleuve au même endroit, c'est long, très long, surtout pendant douze jours… Merci Olivier et Patrice pour votre aide sur le terrain et pour votre support à la modélisation. Merci

Jean-François et André d'avoir fourni les moyens financiers et techniques pour réaliser ce projet et, surtout, d'avoir vaincu l'adversité administrative à maintes reprises; vos efforts n'ont pas été vains! Et merci à tous les autres pour votre aide ponctuelle mais indispensable.

Merci à toutes les personnes qui ont croisé mon chemin durant mon doctorat. Merci Val pour ces discussions existentielles et tes nombreux conseils qui ont souvent dépassé le domaine académique. Selim, nos longues jases ont été très stimulantes. Muluneh, Tinbite and Abi, thank you for all the coffee breaks and for your friendship. Matt and Lisa, Tim and Janeen, Jonathan and Annalyn (and the kids!), Hamed and Reza, Uncle Bob and Aunt Roberta, you all made a difference during our stay in Portland, each in your own way, and your friendship has been precious. Armando y Mechie, gracias por su cálida bienvenida, los paseos en lancha, los ceviches y la comida increíble. Gracias a mis hermanitos Quique, Tony y Adrian por las guerras de popotes improvisadas (¡Canadá ganó!). Merci à la gang du mardi, vous vous reconnaissez; nos échanges ont réellement été enrichissants, j'ai beaucoup appris et cheminé à vos côtés. Marie, Mumu, Mitch, un seul mot : Edmonton.

Merci Charles Tisseyre pour votre bon programme! Je vous suis avec assiduité depuis mon adolescence et je vous dois en partie mon intérêt pour la science (exaequo avec Les Débrouillards). J'aurais voulu vous dédier ma thèse, mais la place pour cette dédicace était déjà prise. Je ne dis pas si j'avais déjà passé à Découverte, mais la réalité est tout autre… Il n'en demeure pas moins que j'accepterais probablement l'invitation!

Merci à mes amis qui ont contribué indirectement au succès de cette thèse par leur présence et leur influence dans ma vie : Joël, tu as laissé ta marque. Tu as été un exemple de patience, de courage et de persévérance dans la maladie; jusqu'à la fin, tu t'es tenu debout. Repose en paix…

Francis, malgré ton choix de renier ta patrie et de nous quitter pour une femme de Winnipeg (!), tu occuperas toujours une place particulière, bien qu'ambigüe, dans ma vie. Nous avons le mérite d'être les deux seuls Canadiens à avoir cherché du travail en Grèce, en hiver; d'avoir courageusement (?!) posé le pied en Tunisie aux lendemains du 11 septembre, à Noël; d'avoir goûté à la perfection suisse (clin d'œil à mon directeur!), en ponçant le *chni* sur les murs, peignant par-dessus, re-ponçant le *chni* qu'on venait de faire, repeignant le tout, et ainsi de suite pendant deux mois. Puisque, avec les années, la mémoire fait tranquillement défaut, je tenais à immortaliser dans cette thèse ces quelques moments qui nous ont marqués, façonnés et préparés à affronter le

monde. Malheureusement pour toi, je ne pourrais non plus passer sous silence ton amour inconditionnel des Canadiens de Montréal (qui vacille toutefois devant les Jets). Défaite après défaite, déception par-dessus déception, tu restes fidèle, dans l'espoir (vain) de voir un jour ton équipe (perdante) porter à nouveau la Coupe à bout de bras (ramollis). Ta conviction (désolante) suscite mon admiration (éphémère), mais surtout a su, pour ma part, ponctuer mes journées moins productives d'un grain d'humour. En attendant que le futur (lointain) se charge de renverser le sort du tricolore, je te remercie pour ces moments de moquerie et d'ironie qui ont agrémenté ces années, malgré la distance qui nous sépare aujourd'hui. Au-delà de nos expériences et des souvenirs qu'elles nous ont laissés, je ressors enrichi par notre amitié.

David, mon cher et seul ami mexicain digne de ce nom, fils d'une mère chilienne et d'un père beauceron, que dire de plus sinon que l'absurdité de notre relation apporte une légèreté qui fait du bien (et j'inclus Julie et Élodie ici!). Mais derrière nos discussions codées, destinées à confondre les espions (et les zombies), se cache une profondeur inattendue. Tu as été un ami (lire « une ligne ouverte 24h ») qui a compté réellement à des moments cruciaux dans ma vie, depuis le secondaire jusqu'à ce qu'on devienne des adultes responsables, ou plutôt qui ont des responsabilités! J'apprends beaucoup en te côtoyant, en partie parce que, secrètement, je tente de copier ta vie. J'essaie par contre de laisser passer un peu de temps pour éviter que ça ne paraisse… Nos voyages de pêche, le Maine et nos déjeuners de gars ont été salutaires pendant ma thèse. Ils m'ont permis de garder le cap et de me recentrer sur l'essentiel. Vos innombrables conseils et fous rires à toi et à Julie ont toujours été très rafraichissants, même si on colle longtemps quand on débarque. Merci à vous deux pour votre simplicité et votre amitié sincère!

Merci Philippe pour ta fontaine de connaissances, alimentée par tes nombreuses passions, et qui, telle des effluves qui émanent de ta personne, ne cesse de m'épater. Meggie (comme dans « mes guitares ») parle d'aveuglement, mais je ne peux me résoudre à faire ce constat. Ton esprit compétitif et ton goût pour le jeu sont exemplaires, mais surtout ta détermination à ne pas perdre parce qu'on joue mal! Tu es l'un des seuls qui comprends les jokes de Sheldon et avec qui je peux parler de physique sans me faire dévisager. Ça m'a aidé à purger et à résoudre mes bogues de code et de cerveau. Merci de m'avoir toujours supporté dans mon amour pour Découverte, d'avoir sacrifié vos soirées du dimanche soir pour moi, sous la menace de vous exclure de ma famille. Vous avez réussi à infiltrer notre gang du secondaire, ce qui est un exploit en soi, puis tranquillement notre quartier (jadis), nos bières du mardi et ses ramifications, et nos soirées

familiales avec Charles, à un point tel que j'ai l'impression que vous nous épiez. Vous êtes des amis vrais et plein de vie. Nous sommes bénis de vous avoir dans notre cercle sélect (!) et de vous voir grandir dans vos relations. Il va falloir qu'on fasse notre Iron Chef Pont-Rouge version Veggie une bonne fois pour toute! J'ai fini mon doc, j'ai plein de temps maintenant…

Merci Richard pour nos nombreuses jases autour d'une bière, pour m'avoir enseigné les vertus du travail, des relations, et pour tes paroles de sagesse appuyées par de nombreux textes de l'un des sages de ce monde… Avec ton authenticité qui fait parfois peur et qui nous confronte, tu as su ébranler nos bases et nous aider à construire sur du solide. Après plus de 10 ans passés à tes côtés, tu commences à déteindre sur nous; mon souhait c'est de transmettre à mon tour l'héritage que tu nous as laissé. Sans l'ombre d'un doute, tes talents de pêcheur nous portent malheur, puisque tu balances ton matériel par-dessus bord! Mais ta présence est plus importante que l'idée de pêcher la prise de notre vie. D'autres, moins subtils, obnubilés par l'appât du gain, choisissent simplement une autre chaloupe… Pour reprendre une de tes phrases fétiches : « Les concombres ne sont pas tous dans le vinaigre », et je suis content de faire partie de ta gang de concombres! Je dois une partie du succès de cette thèse à toi (et à Sylvie, si on en croit le dicton!).

Merci à mon père d'avoir toujours cru en moi, un peu aveuglément; merci pour ta fierté de papa et ta sensibilité, malgré ton air un peu perplexe de me voir étudier pendant aussi longtemps. Ton humour m'a souvent décoiffé et m'enseigne à accueillir les difficultés du moment avec un peu de légèreté. Merci à ma mère qui s'est donnée corps et âme pour moi; merci pour ton soutien et tes encouragements. Tu m'as toujours écouté parler de mon projet avec l'intérêt sincère d'une mère. Tu t'es réellement acharné à tenter de comprendre mon sujet, en prenant des notes pour t'aider, mais vraisemblablement tu as souvent perdu tes notes! Tu verras, tout deviendra clair lorsque Charles Tisseyre vulgarisera mon travail… (je ne lâcherai pas le morceau!). Merci Denis de m'avoir soutenu par divers moyens durant ce périple. J'ai toujours senti ta fierté et ta joie devant mes réalisations, quelles qu'elles soient. Merci à mes beaux-parents Jeff et Josée, qui apportent une odeur particulière à ma vie…! Jeff, j'admire ton V. Tes compliments sans bornes me rendent mal à l'aise, mais j'avoue que j'y prends goût! Josée, tu me surprendras toujours par ta détermination à te surpasser jour après jour; tu fais sortir le meilleur de moi! Merci à mes autres beaux-parents, Rick (as in "Rick and Wayne") et Céline. Merci pour le rock'n roll, pour les festins et les Chocolats Favoris! Vous êtes généreux de vous-mêmes. Sans oublier notre chère Eileen, accueillante, aimante et ricaneuse, vous avez été une deuxième grand-mère pour moi; votre

souvenir nous est cher… Merci à mes belles-sœurs Véro et Raph; vous êtes les petites sœurs que je n'ai jamais eues, un peu immatures par contre!

Chère Catherine, tu es mon inspiration et ma motivation. Sans toi, rien de tout cela ne serait arrivé. Tu m'as aimé, épaulé, soutenu et encouragé, tu m'as enduré, tu as gardé le fort. Nous avons ri et pleuré ensemble et nous avons évolué côte-à-côte en donnant le meilleur (et parfois le pire!) de nous-mêmes. Merci de ta patience, de ta dévotion et de ton brin de folie. Merci aussi pour tes relectures et pour ton aide indispensable sur le terrain; les RTK n'ont plus de secrets pour toi! Tu arrives à expliquer les marées dans le fleuve d'une manière qui m'émeut; tu m'écoutais vraiment quand je te racontais mes histoires! Merci d'être là, comme une complice, toujours présente et, surtout, merci de nous avoir concocté le plus beau trésor… Chère petite Félixe, l'anticipation de ton arrivée m'a aidé à me lever chaque matin (pas toujours de bonne heure!) et à terminer ce projet avant que le temps et le sommeil ne me manquent trop. Malgré nos cernes, tu apportes une joie sans bornes à nos vies, tu es la plus belle (j'ai vérifié!) et nous apprenons à te connaître avec excitation. Tu étais dans le ventre de ta mère lors de ma soutenance, mais j'espère que tu as retenu l'essentiel… Je te ferai le topo lorsque tu seras en âge de parler. Finalement merci Léo, joueur et niais par excellence! Ta bonne humeur de chien met du piquant dans notre quotidien et nos jeux de balle ont si souvent changé le mal de place!

Pour terminer, j'aimerais remercier Environnement Canada (encore!), le SHC, Pêches et Océans Canada (notamment Denis Lefaivre et Alain D'Astous de l'IML), le MDDEFP (maintenant MDDELCC) et le MTQ pour avoir fourni les données et/ou le soutien financier indispensable à la réalisation de ce projet. Je remercie finalement les différents organismes subventionnaires qui m'ont supporté à travers de substantielles bourses : le CRSNG, le FQRNT, Hydro-Québec (via la FUQ), la Société de Météorologie de Québec, la RBC Banque Royale (via la FUQ), le Ministère de l'Éducation du Québec (via l'INRS), l'Association Canadienne des Ressources Hydriques et l'Association Québécoise pour l'Évaluation d'Impacts. À défaut de me répéter, merci!

# RÉSUMÉ

Le système Saint-Laurent – Grands Lacs forme la plus grande voie navigable intérieure au monde. Il abrite un écosystème unique et représente une source d'eau potable pour près de la moitié des Québécois. Toutefois, l'aménagement et l'utilisation du chenal de navigation, la disparition de grandes superficies de milieux humides sous les remblais et l'empiètement, la contamination des sédiments près des aménagements portuaires et les industries du secteur sont autant de facteurs qui modifient l'hydrodynamique, détériorent la qualité des eaux, restreignent les activités récréatives et affectent les ressources halieutiques de la région.

La modélisation numérique s'avère l'outil technologique idéal pour comprendre et analyser les liens entre la physique et le milieu naturel. Complémentée par des mesures de terrain, elle fait le pont entre les différents processus, à diverses échelles spatiales et temporelles. Alors que la portion fluviale du Saint-Laurent (de Cornwall à Trois-Rivières) est bien documentée, tant par des études numériques que par des mesures de terrain, très peu d'études ont été réalisées dans sa portion fluvio-estuarienne (de Trois-Rivières à Québec). Composé d'eau douce, l'estuaire fluvial est soumis à l'influence grandissante d'une marée semi-diurne, responsable de fortes inversions de courant, du mélange des masses d'eau et de la présence de larges estrans. Il se caractérise par une topographie complexe et par une forte hétérogénéité des substrats, auxquels s'ajoutent des débits fluviaux et des conditions météorologiques variables.

La présente recherche vise à fournir une description détaillée de l'hydrodynamique de l'estuaire fluvial du Saint-Laurent au moyen de la modélisation numérique et de mesures de terrain, afin d'en améliorer la compréhension physique, d'identifier l'importance respective des facteurs qui en contrôlent la dynamique et d'en prédire l'évolution. Cet objectif est poursuivi suivant trois axes, soit : 1) acquérir des données détaillées permettant de quantifier la variabilité spatiale et temporelle des niveaux d'eau et des vitesses; 2) développer un modèle 1D de propagation de la marée afin d'exprimer les variations spatiales et temporelles du contenu fréquentiel de la marée en fonction des conditions non-stationnaires de forçages fluvial et océanique; et 3) fournir une description intégrée du système via une modélisation hydrodynamique 2D à haute résolution.

Une campagne de terrain a été réalisée, divisée en deux volets visant, d'une part, à densifier le réseau de marégraphes en place par l'installation de sondes de pression et, d'autre part, à mesurer

les variations intratidales des niveaux d'eau et des vitesses sur des sections contrastées, en combinant les technologies du RTK GPS (« Real-Time Kinematic Global Positioning System ») et de l'ADCP (« Acoustic Doppler Current Profiler »). Une procédure pour la reconstruction de champs latéraux continus et synoptiques a été développée, validée par l'entremise de mesures indépendantes, permettant ainsi d'établir un niveau de confiance élevé dans les données et leurs sous-produits. Ces dernières constituent le jeu le plus complet et détaillé à ce jour, qui documente l'hydrodynamique du système. Elles ont rendu possible une validation serrée des modèles développés et une évaluation précise de l'erreur associée à cette modélisation.

Un modèle 1D de propagation de la marée a été développé, s'appuyant sur une spatialisation des coefficients de régression issus d'analyses harmoniques non-stationnaires de la marée. Il permet de prédire les niveaux d'eau moyens et les propriétés de la marée en fonction des conditions de débit fluvial et de marée océanique. Le modèle a été validé aux stations marégraphiques et par comparaison avec le modèle ONE-D, opérationnel sur le fleuve. Une précision inférieure à 30 cm en niveaux d'eau, comparable à ONE-D, a été obtenue sur l'ensemble du système. Les résultats font ressortir les effets de la friction et du débit fluvial sur l'asymétrie du signal et sur l'amplitude et la phase des composantes harmoniques de la marée. Une extension du modèle a également permis d'estimer les débits tidaux, par intégration de l'équation de continuité.

Un modèle hydrodynamique 2D a été développé, reposant sur une discrétisation par éléments finis des équations de Saint-Venant. Il a été élaboré à partir de données de terrain à haute densité, issues de sondages bathymétriques multifaisceaux et LIDAR pour la topographie des berges et des estrans. L'étalonnage du modèle a permis d'atteindre des standards de qualité élevés avec, notamment, des erreurs quadratiques moyennes inférieures à 5% du marnage local aux stations aval et inférieures à 6 cm aux stations amont. Le modèle reproduit adéquatement les propriétés de la marée et la variabilité spatiale et temporelle des niveaux d'eau et des vitesses. La répartition des débits autour de l'île d'Orléans est également reproduite conformément aux mesures.

Les données mesurées et les modèles développés fournissent des moyens pour décrire l'hydrodynamique de ce tronçon où les connaissances sont extrêmement limitées. Ils permettront, notamment via un couplage de modèles, de prédire les impacts potentiels de divers scénarios de changements anthropiques ou climatiques sur l'écologie, sur la qualité de l'eau et sur les activités socio-économiques qui dépendent du Saint-Laurent.

# ABSTRACT

The Great Lakes/St. Lawrence Seaway System is the world's largest inland waterway. It has a unique ecosystem and is a source of drinking water for nearly half of the Quebecers. However, the development and use of the navigation channel, the loss of large areas of wetlands under the embankment and encroachment, sediment contamination near the port facilities, and industries are all factors that alter the hydrodynamics, deteriorate water quality, limit recreational activities and affect fishery resources in the region.

Numerical modeling is the perfect technological tool to understand and analyze the links between the physical and natural environment. Complemented by field measurements, it bridges the various processes at different spatial and temporal scales. While the fluvial section of the St. Lawrence (from Cornwall to Trois-Rivières) is well documented, both by numerical studies and field campaigns, very few studies have been conducted in the fluvial estuary (from Trois-Rivières to Québec). Composed of freshwater, the fluvial estuary is subject to the growing influence of a semidiurnal tide, responsible for strong current reversals, the mixing of water masses and the presence of large tidal flats. It is characterized by complex topography and highly heterogeneous substrates, adding to the variable river flows and weather conditions.

This research aims to provide a detailed description of the hydrodynamics of the St. Lawrence fluvial estuary by means of numerical modeling and field measurements, in order to improve physical understanding of the system, identify the relative importance of factors controlling its dynamics and predict its evolution. This objective is pursued along three axes: 1) acquire detailed data to quantify the spatial and temporal variability of water levels and velocities; 2) develop a 1D tidal propagation model that expresses the spatial and temporal variations in the frequency content of the tides as a function of nonstationary river and oceanic forcing variables; and 3) provide an integrated and synoptic description of the system via the development of a 2D high-resolution hydrodynamic model.

A field campaign was conducted, divided into two parts aiming, firstly, at densifying the network of tide gauges currently in place by installing pressure sensors and, secondly, at measuring the intratidal changes in water levels and velocities along contrasting river sections, by combining the RTK GPS ("Real-Time Kinematic Global Positioning System") and ADCP ("Acoustic

Doppler Current Profiler") technologies. A procedure for the reconstruction of continuous and synoptic lateral fields was developed, validated using independent measurements, thereby establishing a high level of confidence in the data and their by-products. They constitute the most complete and detailed dataset to date, which documents the hydrodynamics of the system. They allowed a tight validation of the models developed and an accurate assessment of their error.

A 1D tidal propagation model was developed, based on a spatialization of the regression coefficients obtained from nonstationary tidal harmonic analyses. The model allows the prediction of mean water levels and tidal properties as a function of river flow and ocean tide conditions. It was validated using a densified network of tide stations and by comparison with the ONE-D operational model. Errors less than 30 cm in water levels were obtained for the entire system, which is comparable to ONE-D. The results bring out the effects of friction and river flow on tidal asymmetry as well as on the amplitude and phase of the tidal constituents. An extension of the model was developed for the estimation of tidal discharges, by integrating the continuity equation.

A 2D hydrodynamic model, based on a finite-element discretization of the Saint-Venant equations, was developed using high-density field data arising from multibeam bathymetry and LIDAR topography of the banks and foreshores. Calibration of the model allowed meeting high quality standards, with root-mean-square errors less than 5% of the local tidal range at downstream stations and less than 6 cm at upstream stations. The model adequately reproduces tidal properties and the spatial and temporal variability of water levels and velocities in the system. The flow distribution around the Orleans Island is also reproduced in accordance with the observations.

The measured data and developed models provide a means to describe the hydrodynamics of this region of the St. Lawrence where knowledge is extremely limited. They will allow, in particular through model coupling, to predict the potential impacts of various scenarios of anthropogenic or climate changes on the ecology, water quality and socio-economic activities that rely on the St. Lawrence.

# TABLE DES MATIÈRES

# LISTE DES TABLES

# LISTE DES FIGURES

# CHAPITRE 1 : SYNTHÈSE

## 1.1 Introduction

Les estuaires marquent la transition entre fleuves et océans. Leurs écosystèmes comptent parmi les plus productifs et diversifiés au monde, alors que les contraintes anthropiques et climatiques qui pèsent sur eux sont grandissantes. Devant le développement des villes et des industries, l'augmentation du transport maritime, et la dégradation des côtes, les systèmes fluvio-estuariens se trouvent de plus en plus vulnérables aux changements géomorphologiques et hydroclimatiques auxquels ils font face. Par conséquent, la qualité de l'eau et des habitats aquatiques s'en trouve réduite (Prandle, 2009, U.S. EPA, 2012a, b).

Les conditions hydrodynamiques qui régissent la circulation estuarienne sont la résultante de plusieurs processus physiques, chimiques et biologiques inhérents aux estuaires. Ces systèmes, très énergétiques, sont sujets à de fortes variations des niveaux d'eau et des courants, à des échelles spatiales et temporelles variables. Leur dynamique hautement complexe se caractérise par l'action combinée des marées et des débits fluviaux, la bathymétrie irrégulière du milieu, la présence d'un couvert de glace en hiver et de plantes aquatiques en été, de forts gradients de densité à la rencontre des eaux douces et salines, et des conditions météorologiques et climatiques changeantes. Il en résulte des patrons complexes de vitesses, spatialement distribués en fonction des caractéristiques du milieu et des conditions locales, et dont la variabilité temporelle se manifeste par des changements abrupts, périodiques ou séculiers (sans apparente périodicité), à des échelles pouvant varier de quelques heures à plusieurs années, voire décennies (Jay, 2010).

La modélisation numérique s'avère l'outil technologique idéal pour comprendre et analyser les liens entre la physique et le milieu naturel (Morin *et al.*, 2003b). Complémentée par des mesures de terrain, elle permet de faire le pont entre les différents processus, à diverses échelles spatiales et temporelles. Toutefois, la mesure et la modélisation des systèmes fluvio-estuariens est compliquée par trois facteurs : 1) leur taille, 2) la non-stationnarité des processus induits par l'interaction de la marée, des débits fluviaux et de la géométrie du milieu, et 3) la variabilité spatiale des phénomènes y ayant court. Pour augmenter nos connaissances et notre compréhension de ces systèmes et améliorer notre capacité prédictive, une combinaison d'observations et

de modèles est donc nécessaire, accompagnée de stratégies adaptées aux caractéristiques uniques de ces environnements.

### 1.1.1 Problématique

Le fleuve Saint-Laurent et son estuaire font partie de l'un des plus importants systèmes hydrographiques d'Amérique du Nord : le système Saint-Laurent – Grands Lacs. Avec un bassin de $1.6 \times 10^6$ km$^2$, ce dernier draine plus de 25 % des réserves mondiales d'eau douce. Il connecte les Grands Lacs avec l'océan Atlantique, formant la plus grande voie navigable intérieure au monde. Plus de 45 millions de personnes vivent à l'intérieur de son bassin, qui constitue le cœur industriel des États-Unis et un centre socio-économique majeur pour le Québec et le Canada. L'environnement naturel du Saint-Laurent renferme des ressources essentielles à une multitude d'espèces animales et végétales et représente une source d'approvisionnement en eau potable pour près de la moitié de la population du territoire (Hébert & Belley, 2005). Toutefois, l'aménagement et l'utilisation du chenal de navigation, la disparition de grandes superficies de milieux humides sous les remblais et l'empiètement, la contamination des sédiments près des aménagements portuaires et les industries du secteur sont autant de facteurs qui modifient l'hydrodynamique, détériorent la qualité des eaux, restreignent les activités récréatives et affectent les ressources halieutiques de la région.

L'estuaire fluvial du Saint-Laurent, composé d'eau douce, se trouve à la jonction entre le fleuve et l'estuaire supérieur du Saint-Laurent. Malgré son importance, il constitue l'une des régions les moins bien documentées du fleuve, tant en termes de données que de modèles. Ce manque de connaissances dans l'estuaire fluvial, là où la transition entre fleuve et estuaire s'effectue, résulte peut-être de la complexité des interactions non-linéaires et de la non-stationnarité des phénomènes en présence, qui nécessitent, si l'on veut les caractériser, des équipements de mesure de pointe et des outils numériques et informatiques très performants. Il devient donc crucial de poursuivre des recherches scientifiques qui visent à documenter ces processus, afin de comprendre la dynamique du système et de développer les outils qui vont permettre d'en anticiper l'évolution et d'évaluer l'impact à long terme de changements anthropiques et climatiques.

### *1.1.1.1 L'estuaire fluvial du Saint-Laurent*

L'estuaire fluvial du Saint-Laurent s'étend sur près de 180 km, de la sortie du lac Saint-Pierre à la pointe est de l'île d'Orléans (Figure 1.1.1), située à la limite de l'intrusion saline et du bouchon de turbidité, ou zone de transition estuarienne (D'Anglejan, 1990, Ingram & El-Sabh, 1990, Simons *et al.*, 2010). Cette région du fleuve est caractérisée par une topographie complexe, que l'on associe à des zones profondes (> 60 m), à une section de largeur variable (< 1 à 15 km), à l'imposant chenal de navigation et à la présence d'îles, de hauts-fonds, de marais et de nombreux ouvrages de génie. Elle présente également une forte hétérogénéité dans la composition du substrat, qui varie des argiles fines (< 2 µm) aux blocs rocheux (> 1 m), et dans la distribution des plantes aquatiques ou du couvert de glace, selon la saison. Ces caractéristiques physiques ont un impact significatif sur la circulation et sur la dynamique de transport sédimentaire.

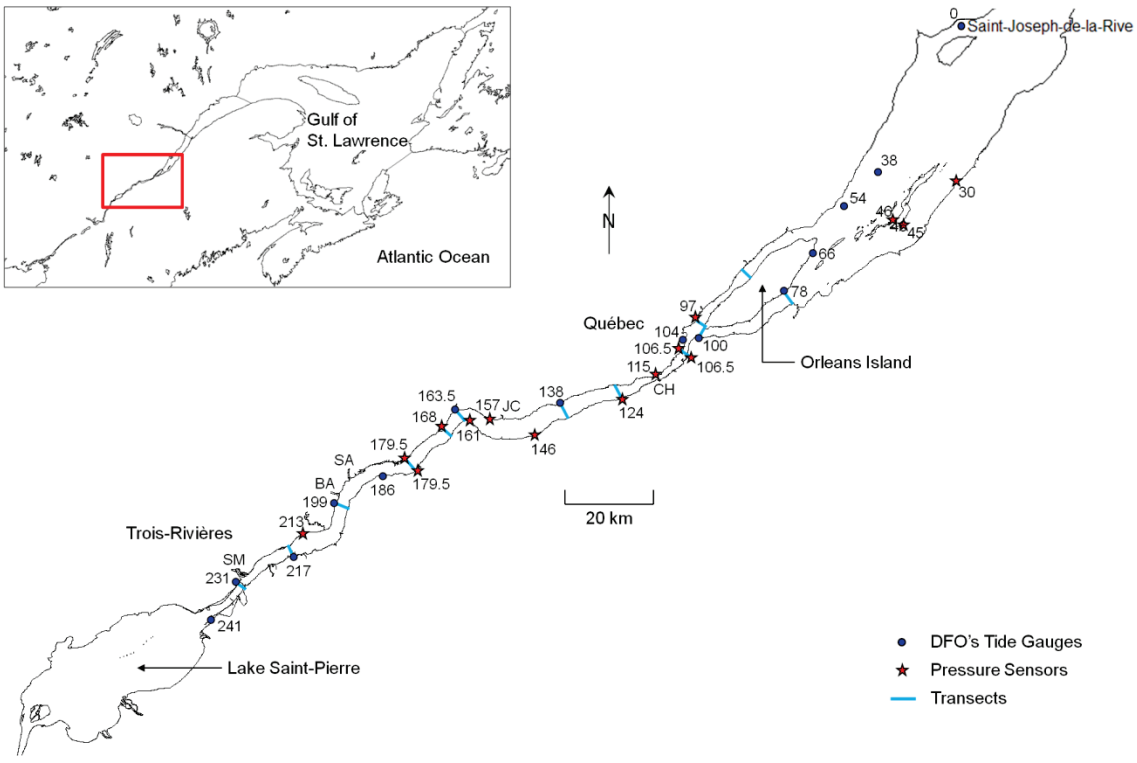


**Figure 1.1.1** **Carte de l'estuaire fluvial du Saint-Laurent (Québec, Canada), illustrant la position des marégraphes du MPO (cercles bleus foncés), des sondes de pression (étoiles rouges) et des sections de mesure (lignes bleues pâles). Les kilomètres de rivière (rkm) sont indiqués pour chaque station. Les principaux tributaires sont les rivières St-Maurice (SM), Batiscan (BA), Sainte-Anne (SA), Jacques-Cartier (JC) et Chaudière (CH).**

De l'aval vers l'amont, l'écoulement est soumis à l'influence d'une marée semi-diurne, avec des marnages culminant à 7 m à Saint-Joseph-de-la-Rive (défini comme kilomètre de rivière 0, ou rkm 0) lors des grandes marées de vives-eaux. Des augmentations du niveau de l'eau de plus de 1 m $h^{-1}$ sont observables en marée montante, menant à des changements rapides des conditions d'écoulement et des superficies inondées. De fortes inversions de courant sont ainsi générées, avec des débits de pointe jusqu'à cinq fois supérieurs à la moyenne journalière aux stations aval (ex.: Figure A.2.16, p. 281). Le signal de marée est progressivement déformé et atténué à mesure qu'il se propage vers l'amont dû aux effets de la friction (cf. section 2.3, Godin, 1999, Matte *et al.*, 2014c); la durée du jusant s'en trouve ainsi augmentée par rapport au flot, plus court et abrupt. La limite amont où cessent les inversions de courant (une seule étale) se déplace entre Grondines (rkm 179.5) et Bécancour (rkm 217) en fonction de la marée et du débit fluvial. À Trois-Rivières (rkm 231), la modulation semi-mensuelle des niveaux moyens induite par le cycle de marées de mortes-eaux et de vives-eaux excède en amplitude la marée semi-diurne (LeBlond, 1979), dont le marnage moyen est de 0.2 m. L'amplitude des composantes de marée de courtes périodes (c.-à-d. diurne, semi-diurne, etc.) est presque entièrement atténuée dans le lac Saint-Pierre (rkm 264), mais les fluctuations de longues périodes se font sentir jusqu'à Montréal (rkm 360). Ces propriétés de l'écoulement présentent une variabilité tant latérale que longitudinale, tel que confirmé par des mesures de terrain (cf. section 2.2, Matte *et al.*, 2014a).

Le débit fluvial dans l'estuaire fluvial du Saint-Laurent provient des débits sortants du lac Ontario, de la rivière des Outaouais et des différents tributaires le long de son cours. Bien que le débit moyen journalier à Québec soit de 12 200 $m^3s^{-1}$, les débits minimum et maximum observés pour la période de 1960–2010 ont été de 7000 et 32 700 $m^3s^{-1}$, respectivement, incluant la contribution des tributaires et des superficies drainées en amont de Québec (Bouchard & Morin, 2000). Les effets de telles variations (saisonnières et interannuelles) sur les niveaux moyens et le marnage de la marée sont sévères, particulièrement dans la portion amont de l'estuaire fluvial (cf. section 2.3, Matte *et al.*, 2014c).

Par ailleurs, certaines conditions météorologiques particulières, comme les tempêtes extratropicales se déplaçant entre le Saint-Laurent et le littoral Atlantique, provoquent occasionnellement une surélévation des niveaux d'eau pouvant atteindre quelques mètres; ces surcotes peuvent se produire à marée haute comme à marée basse (El-Sabh *et al.*, 1988, Drapeau, 2008). Une augmentation de la fréquence et de la force de ces événements a été observée dans la

dernière moitié du 20e siècle, suggérant des changements dans la dynamique de forçage des tempêtes (Xu *et al.*, 2006).

Ensemble, les caractéristiques du terrain, de la marée et des débits fluviaux, combinées à l'influence d'événements météorologiques extrêmes, font de l'estuaire fluvial du Saint-Laurent un laboratoire naturel unique pour l'étude de l'hydrodynamique fluvio-estuarienne.

#### *1.1.1.2 Données disponibles*

Un large réseau de stations marégraphiques, composé de stations permanentes et saisonnières, est maintenu par le Ministère des Pêches et Océans Canada (MPO) dans l'estuaire fluvial du Saint-Laurent (Figure 1.1.1) et comprend des données de niveaux d'eau remontant à la fin du 19e siècle ou au début du 20e siècle pour certaines stations (ex.: Lauzon, Batiscan, Trois-Rivières). Les données courantométriques, quant à elles, sont beaucoup moins abondantes. Parmi les campagnes de mesure de courants recensées, la majorité des mesures se limite généralement à quelques points dans l'espace, échantillonnés sur de courtes périodes (un mois au plus) à l'aide de courantomètres. Plusieurs de ces campagnes sont décrites par Dohler (1961), Godin (1971), Prandle (1971), Prandle & Crookshank (1972) et Long *et al.* (1980). Les seules mesures documentées dans l'estuaire fluvial réalisées à l'aide de méthodes acoustiques (ex.: ADCP), qui permettent une couverture spatiale très détaillée sur la verticale et sur l'horizontale, ont été recueillies en 1995 par Environnement Canada sur une section devant Québec durant 24 h (Bourgault & Koutitonsky, 1999). Ainsi, très peu de données récentes de vitesses sont disponibles et leur résolution spatiale et temporelle n'en fournit qu'une description limitée, pour une gamme de conditions tidales et fluviales restreinte. De plus, il n'existe à l'heure actuelle aucune mesure en continu du débit dans l'estuaire fluvial du Saint-Laurent. Un éventail détaillé des données disponibles est fourni en annexe, à la section A.2.2.2.

#### *1.1.1.3 Modèles existants*

Les premiers efforts de modélisation du Saint-Laurent, du Golfe jusqu'à Montréal, sont passés en revue par El-Sabh & Murty (1990). Plusieurs modèles analytiques ont notamment été développés (ex.: Vincent, 1965, Partenscky & Warmoes, 1970, Marche & Partenscky, 1974, Chassé *et al.*, 1993, Godin, 1999), fournissant une description générale de la propagation de la marée et de sa distorsion dans le fleuve. Le développement et l'application de modèles numériques unidimensionnels (1D) (ex.: Kamphuis, 1968, Prandle, 1970, Cheylus & Ouellet, 1971, Godin, 1971,

Prandle, 1971, Prandle & Crookshank, 1972, Prandle & Crookshank, 1974, Morse, 1990, Robert *et al.*, 1992, Bourgault & Koutitonsky, 1999) ont également permis de reproduire les principales caractéristiques tidales et fluviales rencontrées dans l'estuaire fluvial, bien que seulement qualitativement dans la portion amont du système, en raison du manque de précision des conditions limites en débit dans la plupart des modèles. Parmi les modèles numériques 1D développés, le modèle ONE-D (Dailey & Harleman, 1972, Morse, 1990) tourne actuellement en mode opérationnel dans le fleuve, alimenté par les prévisions sur 30 jours des débits sortants du lac Ontario et de la rivière des Outaouais, de même que par les prévisions de vents sur 48 h d'Environnement Canada (Service Météorologique du Canada) à la limite aval du modèle; l'effet des glaces est également pris en compte en hiver (Lefaivre *et al.*, 2009). Ce modèle opérationnel remplit son mandat de fournir une prévision des niveaux d'eau dans l'estuaire fluvial, mais trouve ses limites dans sa résolution spatiale et sa capacité à représenter les échanges latéraux, fondamentalement de nature bidimensionnelle (2D).

Un certain nombre de modèles numériques 2D ont été développés dans le Saint-Laurent (ex.: Prandle & Crookshank, 1972, Prandle & Crookshank, 1974, Lévesque, 1977, Lévesque *et al.*, 1979, Leclerc *et al.*, 1990). De même, quelques modèles tridimensionnels (3D) ont été présentés (ex.: Gagnon, 1994, Saucier & Chassé, 2000, Saucier *et al.*, 2003, Simons *et al.*, 2010), menant notamment à la production d'un atlas des courants de marée dans l'estuaire du Saint-Laurent (Saucier *et al.*, 1997, 1999). Plusieurs de ces modèles ne s'étendent pas en amont de l'île d'Orléans, alors que ceux qui incluent l'estuaire fluvial souffrent généralement d'un manque de données de validation et/ou d'une résolution spatiale insuffisante ($\geq 200$ m) pour capter les variations locales (latérales et longitudinales) associées au terrain (topographie, friction) et à l'hydrodynamique. Par ailleurs, le développement ponctuel de modèles par des firmes privées ou organisations gouvernementales pour des applications spécifiques (ex.: Doyon, 2011) est habituellement restreint à des zones d'intérêt qui n'englobent pas l'ensemble du système, ne fournissant ainsi qu'une description incomplète de l'hydrodynamique.

Il en ressort de ce bilan que l'estuaire fluvial du Saint-Laurent est largement non documenté, tant en ce qui a trait aux données disponibles qu'aux modèles existants.

### 1.1.2 Objectifs de recherche

La présente recherche a pour but de documenter l'hydrodynamique à l'eau libre de l'estuaire fluvial du Saint-Laurent au moyen de la modélisation numérique et de mesures de terrain, afin d'en améliorer la compréhension physique, d'identifier l'importance respective des facteurs qui en contrôlent la dynamique et d'en prédire l'évolution.

Ce but est poursuivi à travers les trois objectifs suivants :

1. Acquérir des données détaillées permettant de quantifier la variabilité spatiale et temporelle des niveaux d'eau et des vitesses dans l'estuaire fluvial du Saint-Laurent;
2. Développer une relation fonctionnelle spatiale entre le contenu fréquentiel de la marée et les conditions non-stationnaires de forçage fluvial et océanique, en vue d'améliorer la compréhension des processus fluvio-tidaux dans l'estuaire fluvial du Saint-Laurent;
3. Modéliser à haute résolution spatiale l'hydrodynamique 2D non-stationnaire de l'estuaire fluvial du Saint-Laurent, afin d'en fournir une description intégrée et synoptique.

Pour répondre à l'objectif 1, une campagne de terrain a été réalisée dans l'estuaire fluvial du Saint-Laurent, divisée en deux volets visant, d'une part, à densifier le réseau de marégraphes en place par l'installation de sondes de pression et, d'autre part, à mesurer les niveaux d'eau et les vitesses sur différentes sections contrastées de l'estuaire fluvial, sur les plans de l'hydrodynamique et de la géomorphologie. Une méthode combinant les technologies du RTK GPS (« Real-Time Kinematic Global Positioning System ») et de l'ADCP (« Acoustic Doppler Current Profiler ») a été développée pour la mesure simultanée des niveaux d'eau et des vitesses, à très haute fréquence d'acquisition ($\geq 1$ Hz) le long de trajets répétés par bateau. De plus, une stratégie d'analyse de données a été mise au point permettant la correction d'erreurs systématiques et la reconstruction de champs de niveaux d'eau et de vitesses continus et synoptiques sur un cycle semi-diurne de marée. Les données ainsi obtenues ont été utilisées pour valider les modèles développés aux objectifs 2 et 3.

Pour réaliser l'objectif 2, un modèle 1D non-stationnaire de propagation de la marée a été développé dans l'estuaire fluvial du Saint-Laurent, permettant d'analyser les variations spatiales et temporelles du niveau moyen et des propriétés tidales en fonction du débit fluvial et de la marée océanique. Une représentation harmonique non-stationnaire de la marée a été utilisée pour

exprimer la réponse de la marée aux forçages externes sous la forme d'une fonction continue, facilement réutilisable en mode prédictif. Ce modèle a été validé à partir des données aux stations marégraphiques obtenues à l'objectif 1, ainsi que par comparaison avec le modèle hydrodynamique ONE-D, opérationnel sur le fleuve. De plus, une extension du modèle pour l'estimation des débits tidaux, basée sur la résolution de l'équation de continuité, a été élaborée et validée aux sections de mesures de l'objectif 1.

Pour remplir l'objectif 3, un modèle hydrodynamique 2D non-stationnaire à haute résolution spatiale de l'estuaire fluvial du Saint-Laurent a été développé, basé sur une discrétisation par éléments finis des équations de Saint-Venant. Des données à haute densité, issues de sondages bathymétriques multifaisceaux et LIDAR pour la topographie des berges et des estrans, ont été incorporées au modèle numérique de terrain, de même que les principaux tributaires du Saint-Laurent. Une procédure a été élaborée pour l'étalonnage du modèle, faisant usage d'un réseau dense de marégraphes et de données transversales de niveaux d'eau et de vitesses, issues de la campagne de mesures décrite à l'objectif 1.

Les modèles numériques, tels que développés à l'objectif 3, offrent une vision spatialement intégrée et synoptique des niveaux d'eau et des vitesses à l'échelle du tronçon. Les modèles de régression, comme celui présenté à l'objectif 2, mettent quant à eux l'accent sur l'évolution du contenu fréquentiel de la marée, en fournissant une représentation intégrée dans le temps d'un signal, mesuré à un ou quelques points dans l'espace, sur des périodes pouvant couvrir jusqu'à plusieurs décennies (ex.: Jay *et al.*, 2011). Les modèles développés aux objectifs 2 et 3, combinés aux mesures de l'objectif 1, fournissent donc une description globale et détaillée de l'estuaire fluvial du Saint-Laurent, sous trois angles distincts mais complémentaires.

### 1.1.3 Contexte de la recherche

Le Groupe de Recherche et d'Étude en Écohydraulique Numérique de l'INRS et la section Hydrologie et Écohydraulique d'Environnement Canada (Service Météorologique du Canada) travaillent en partenariat depuis plus de 15 ans. Ils ont développé un modèle hydrodynamique 2D du fleuve Saint-Laurent couvrant la portion entre Cornwall et Trois-Rivières (plus de 260 km), fournissant ainsi un outil de description et de prévision environnementale pour l'ensemble du tronçon fluvial du Saint-Laurent (Morin *et al.*, 2000a, Morin *et al.*, 2000b, Champoux *et al.*,

2003, Morin *et al.*, 2003a, Morin *et al.*, 2003b, Morin *et al.*, 2005, Heniche *et al.*, 2006). Ce modèle s'appuie sur les outils logiciels développés à l'INRS, soit : Modeleur (Secretan & Leclerc, 1998, Roy *et al.*, 2000), Hydrosim (Heniche *et al.*, 2000a, Heniche *et al.*, 2000b), Dispersim (Heniche *et al.*, 2001) et H2D2 (Secretan, 2013). Il comprend un modèle numérique de terrain (MNT) 2D composé de la topographie du fond et de la plaine inondable et d'une caractérisation des substrats et des plantes aquatiques (Morin *et al.*, 2000b), le tout reporté sur un maillage aux éléments finis dont la résolution varie entre ~1 m et ~100 m selon la complexité du terrain et de l'hydrodynamique. Des simulations hydrodynamiques 2D et de transport-diffusion 2D pour des événements documentés ont permis d'étalonner et de valider le modèle. L'erreur sur les niveaux d'eau simulés est inférieure à 5 cm sur l'ensemble du domaine, tant à forts débits qu'à faibles débits. Une validation des vitesses a également été faite avec des mesures sur plus de 300 transects ADCP (*acoustic Doppler current profiler*) (Morin *et al.*, 2003b).

Le niveau de maturité des modèles varie en fonction du secteur considéré. Le lac Saint-François et le lac Saint-Louis ont fait l'objet de travaux de modélisation détaillés, incluant une validation serrée par des mesures de terrain (Morin, 2001, Morin *et al.*, 2003a). Le modèle de l'archipel de Montréal est quant à lui en cours de développement et vise à mettre à jour et à connecter les sections du lac Saint-Louis, du lac des Deux-Montagnes, de la rivière des Mille-Îles et de la rivière des Prairies. La section entre Montréal et Trois-Rivières, qui comprend le lac Saint-Pierre, est la plus mature du fleuve et tourne actuellement en mode opérationnel en moyenne journalière.

La démarche de modélisation de l'estuaire fluvial présentée à l'objectif 3 s'inscrit dans le projet d'opérationnalisation du modèle hydrodynamique du Saint-Laurent, des Grands Lacs jusqu'à Québec, et vise une utilisation en temps réel et en prévisionnel des modèles. Le modèle numérique développé dans le cadre de cette thèse couvre la section de Trois-Rivières à l'Île-aux-Coudres et sera joint au modèle opérationnel de la portion fluviale. L'étalonnage et la validation du modèle de l'estuaire fluvial suit donc les mêmes exigences de qualité que la partie amont. Un couplage du modèle avec le modèle océanique 3D de l'estuaire du Saint-Laurent (Saucier *et al.*, 2009) ou le modèle NEMO (Madec, 2008, Brickman & Drozdowski, 2012), unifiant les systèmes de modélisation océanique global et régional (Roy *et al.*, 2012, Smith *et al.*, 2013), est également envisagé.

Par ailleurs, un stage de recherche de six mois réalisé dans l'équipe du Prof. David A. Jay de la Portland State University (Oregon, États-Unis) a rendu possible le développement d'un nouvel outil d'analyse de la marée en rivière, NS_TIDE (Matte *et al.*, 2013), présenté à l'annexe A.1, sur lequel est basée la réalisation de l'objectif 2 de cette thèse. Ce stage a permis d'initier une collaboration de recherche. Le Prof. Jay détient une expertise en analyse et prédiction de la marée, mise à profit dans le cadre de recherches portant sur l'impact des changements anthropiques et climatiques sur la physique et les écosystèmes, notamment dans la rivière Columbia et l'océan Pacifique (ex.: Kukulka & Jay, 2003a, b, Jay, 2009, Jay *et al.*, 2011).

### 1.1.4 Structure de la thèse

La présente thèse a la forme d'une thèse par articles. La première partie comprend une synthèse qui fait le lien entre chacun des articles qui la composent. Cette synthèse présente les objectifs de la recherche, une description des méthodes employées et un résumé des résultats et conclusions obtenues au terme de leur réalisation. Elle permet ainsi de positionner la recherche dans la littérature et de faire le lien entre les différentes composantes de l'étude. La seconde partie de la thèse renferme l'ensemble des articles présentés, répondant aux trois objectifs de la thèse. Les deux premiers articles (sections 2.1 et 2.2) appuient le premier objectif de la thèse, tandis que les troisième et quatrième articles (sections 2.3 et 2.4) supportent les deuxième et troisième objectifs, respectivement. Des travaux connexes à la thèse sont également présentés en annexes. De plus, une seule liste des références a été incluse, rassemblant les travaux cités dans la synthèse, les articles et les annexes.

## 1.2 Éléments méthodologiques

La présente section décrit les méthodes employées, accompagnées d'une justification qui s'appuie sur la littérature. Elle se divise en trois sous-sections (1.2.1, 1.2.2 et 1.2.3), pour chacun des trois objectifs de la thèse, respectivement.

### 1.2.1 Campagne de terrain

Les gradients latéraux en niveaux d'eau et en vitesses jouent un rôle déterminant dans la circulation fluvio-estuarienne. La mesure de leur variabilité à l'intérieur d'un cycle semi-diurne de marée permet de décrire plusieurs processus liés à la formation de fronts de densité, la circulation et le mélange transversaux, et la répartition des forces en présence (ex.: Collignon & Stacey, 2012, Basdurak & Valle-Levinson, 2013). Quantifier ces variations requiert des observations à haute résolution spatiale et temporelle. Les stations de mesure permanentes, telles que les marégraphes ou les stations fixes de mesure des débits, fournissent des enregistrements à haute fréquence. Elles sont toutefois limitées en nombre et leur capacité à représenter les caractéristiques spatiales de l'écoulement s'en trouve réduite. Inversement, les mesures satellitaires ou aéroportées fournissent des images instantanées et synoptiques d'une région, mais trouvent leurs limites dans la faible résolution temporelle des données et dans l'interprétation des champs observés qui en découle. Les sondages par bateau permettent, quant à eux, la caractérisation de variables hydrodynamiques non-stationnaires. Ils garantissent une couverture spatiale et temporelle suffisante, pourvu que les stratégies d'échantillonnage et la résolution des mesures soient adaptées aux caractéristiques des patrons observés (ex.: Rixen *et al.*, 2001).

Cette section présente les aspects méthodologiques d'une campagne de terrain réalisée à l'été 2009 visant à quantifier les variations spatiales et temporelles des niveaux d'eau et des vitesses dans l'estuaire fluvial du Saint-Laurent. Elle inclut une description des stratégies employées pour la mesure et l'analyse des données (cf. sections 2.1.3, 2.2.3, 2.2.4 et 2.2.8).

#### *1.2.1.1 Mesures et instrumentation*

Les variations du niveau de l'eau sont mesurées à intervalles de 3 min à 13 stations marégraphiques, permanentes ou saisonnières, dans l'estuaire fluvial du Saint-Laurent, maintenues par le MPO. Pour augmenter la résolution spatiale du réseau existant et fournir des données de

validation aux sections de mesure, 15 sondes de pression hydrostatique HOBO U20-001-01 ont été installées de juin à octobre 2009, fournissant des enregistrements aux 15 minutes (Figure 1.1.1).

L'une des stratégies de sondage les plus répandues pour la mesure et l'analyse de variables hydrodynamiques non-stationnaires consiste à prendre des mesures répétitives le long d'un trajet prédéfini sur une période couvrant au minimum un cycle semi-diurne de marée (ex.: Geyer & Signell, 1990, Old & Vennell, 2001, Dinehart & Burau, 2005b). Des mesures par bateau ont été réalisées sur des périodes couvrant un cycle semi-diurne de marée (12h25) le long de 13 sections transversales de 1 à 4 km de large de l'estuaire fluvial du Saint-Laurent, représentatives de la variabilité longitudinale des propriétés hydrodynamiques et géomorphologiques (Figure 1.1.1). À chaque section, généralement alignée sur une station marégraphique, des allers-retours ont été répétés en continu suivant une même trajectoire, perpendiculaire à l'écoulement, à une vitesse de 1–2 m $s^{-1}$. Les mesures ont été effectuées du 15 juin au 25 août 2009, à différentes phases sur le cycle de marées de mortes-eaux et de vives-eaux. Les débits moyens journaliers durant cette période ont fluctué entre 11 100 et 14 600 $m^3s^{-1}$. Bien que l'instrumentation choisie permette des mesures rapides, ces dernières n'ont pu être considérées comme synoptiques à l'intérieur de chaque traversée en raison des fortes variations induites par la marée. Un résumé des sections sondées est présenté à la Table 2.2.4 (p. 117).

Les mesures de vitesse ont été réalisées à l'aide d'un ADCP de 600 kHz de marque RD Instruments Rio Grande, installé sur le côté du bateau. Une fréquence d'acquisition de 2.5 Hz et des profondeurs de cellules de 0.5 m ont été utilisées, en mode « bottom track ».

Un RTK GPS de marque Trimble R6 a été utilisé pour la mesure des niveaux le long des sections sondées. Deux récepteurs, la base (installée en berge) et le mobile (fixé sur le bateau), ont été opérés simultanément, récoltant des données satellitaires à un taux d'acquisition de 1 Hz. Un lien radio a été utilisé pour la transmission des observations de la base au mobile durant les mesures.

Pour une description des instruments et de leurs applications, se référer aux sections 2.1.2, 2.2.2 et 2.2.3.3.

*1.2.1.2 Analyses*

Un résumé des procédures d'analyse des données est fourni à la Figure 1.2.1; les procédures sont détaillées aux sections 2.1.3, 2.2.4 et 2.2.8.

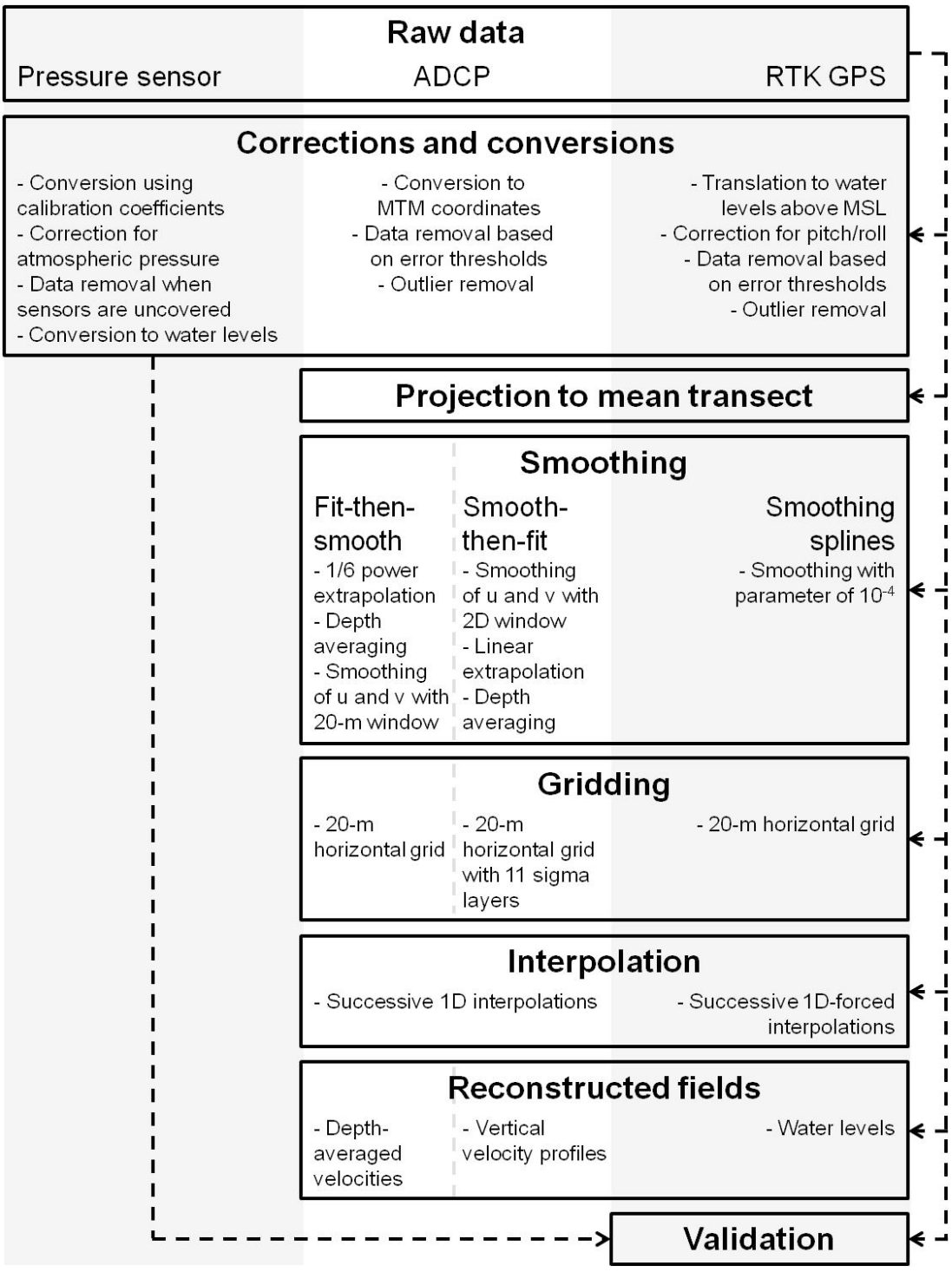


**Figure 1.2.1 Diagramme résumant la procédure d'analyse des données.**

#### 1.2.1.2.1 Corrections et conversions

La première étape des analyses consiste à corriger les données et les convertir dans une référence horizontale et verticale commune. Les pressions mesurées aux sondes ont été corrigées pour la pression atmosphérique et converties en niveaux d'eau, basé sur des niveaux de référence mesurés au RTK GPS [cf. Éq. (2.2.3)]. Les corrections appliquées aux données ADCP et RTK GPS, recueillies par bateau, comprennent la suppression des données erronées et aberrantes, sur la base de seuils de tolérance de l'erreur, définis à partir des distributions statistiques des données. Une attention particulière a été portée aux erreurs systématiques des données RTK GPS, attribuables aux changements dans le nombre de satellites et aux déplacements verticaux de basse fréquence induits par les angles de tangage et de roulis du bateau. En partie dû à la difficulté d'automatiser le processus, aucune correction n'a été réalisée dans le cas des variations corrélées avec le changement de satellites, lesquelles sont possiblement liées à des erreurs logiciel; ces biais se trouvent néanmoins lissées lors du traitement des données (cf. sections 1.2.1.2.2 et 1.2.1.2.3). Les mouvements de tangage et de roulis effectués par la plateforme de mesure, quant à eux, modifient les niveaux rapportés en faisant pivoter l'antenne GPS. Le tirant d'eau dynamique peut expliquer des variations verticales de quelques décimètres, associées à des changements dans la répartition du poids sur le bateau, du cap, de la vitesse, des vagues, du vent et du courant. Les oscillations aléatoires du niveau de l'eau, dues aux vagues par exemple, peuvent facilement être éliminées en lissant les données. Toutefois, les déplacements non-périodiques ou de basse fréquence contenus dans les mesures peuvent être attribuables aussi bien aux variations du niveau de l'eau qu'à l'effet du tirant d'eau dynamique. Alors qu'il est crucial de conserver les déplacements réels de la surface de l'eau, les variations résultant des mouvements du bateau doivent être identifiées et exclues des enregistrements. Pour ce faire, l'utilisation de modèles de squat ou d'unités de mesure inertielle est souvent préconisée (ex.: Work *et al.*, 1998, Hess, 2003, Hughes Clarke *et al.*, 2005); l'installation de multiples antennes GPS peut également être envisagée comme alternative (Beaulieu *et al.*, 2009), mais le coût élevé de ces équipements rend l'approche moins attrayante.

Le squat (enfoncement d'un navire se déplaçant dans l'eau) dépend de plusieurs facteurs, tels que la géométrie du chenal, la forme de la coque du bateau et sa vitesse (Barrass, 2004). Estimer les caractéristiques de squat d'un navire est donc une tâche non triviale (ex.: Beaulieu *et al.*, 2012). En revanche, l'utilisation de senseurs pour la mesure des paramètres d'attitude (orientation,

tangage et roulis) peut permettre le calcul des déplacements verticaux induits par les mouvements de rotation du bateau. Cette technique nécessite néanmoins une connaissance de la position de l'antenne GPS par rapport au centre de rotation de la plateforme de mesure (Alkan & Baykal, 2001). Elle présuppose également que la position du centre de rotation est connue et invariante dans le temps, deux conditions généralement difficiles à rencontrer dans plusieurs campagnes. En effet, cette position peut changer dans le temps dû à la consommation d'essence ou au mouvement du personnel à bord, ce qui rend sa détermination difficile. Une méthode a été développée pour corriger les erreurs systématiques dans les hauteurs GPS associées au tirant d'eau dynamique, en corrélant ces dernières aux déplacements verticaux induits par les angles d'inclinaison mesurés par l'ADCP. Le centre de rotation du bateau est déterminé à l'aide d'un modèle robuste d'estimation des paramètres par régression linéaire itérative [IRLS, ou « iteratively-reweighted least-squares » (Holland & Welsch, 1977, Huber, 1996)]. Les changements temporels dans la position du centre de rotation sont pris en compte en appliquant les régressions successivement sur des sous-segments des séries temporelles analysées. La méthode et son application dans l'estuaire fluvial du Saint-Laurent sont présentées à la section 2.1 (Matte *et al.*, 2014b); l'algorithme est présenté en détail à la section 2.1.3. Un résumé des corrections et conversions appliquées aux données est également présenté à la section 2.2.8.

##### 1.2.1.2.2 Lissage

Pour faciliter le traitement et l'analyse des données ADCP et RTK GPS mesurées par bateau, un transect moyen a été déterminé pour chaque section de mesure, à partir des coordonnées Est et Nord des données. Un système de coordonnées dans le référentiel du transect a été défini, selon lequel les vitesses longitudinales ($u$) et transversales ($v$) sont orientées perpendiculairement et parallèlement à la section, respectivement. Les données ont été lissées et ré-interpolées sur une grille régulière (d'une résolution horizontale de 20 m) le long du transect de référence, pour réduire les fluctuations aléatoires et faciliter les analyses subséquentes. Les données ont été interpolées sur la grille en conservant leur temps de mesure respectif, formant ainsi une grille régulière composée de données mesurées à des temps irréguliers (Figure 1.2.2). De plus, à chaque point de la grille horizontale, la colonne d'eau a été divisée en 10 couches sigma de profondeurs correspondant à un dixième de la profondeur totale.

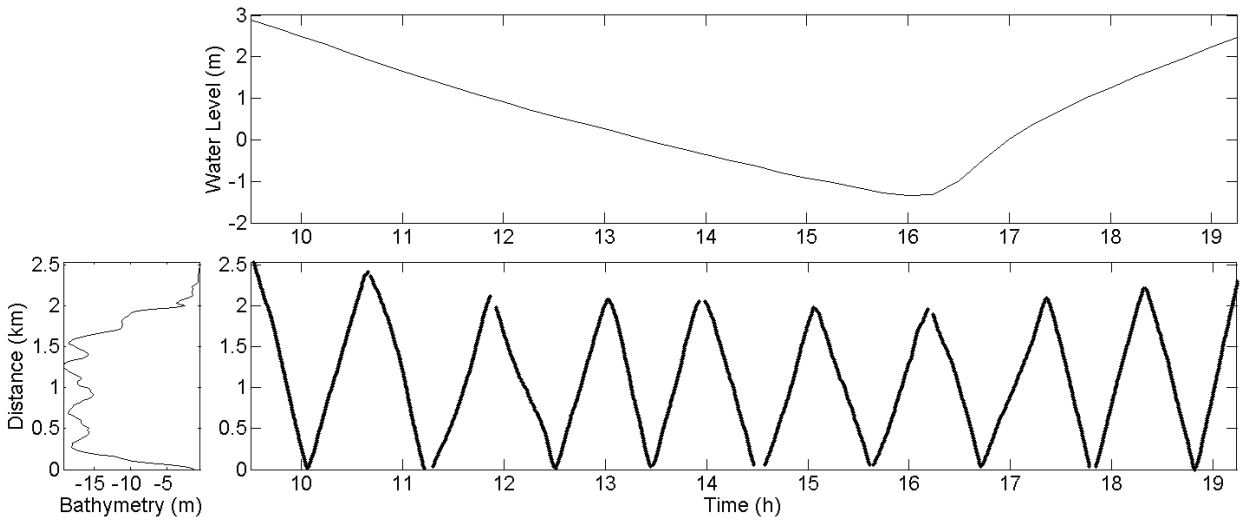


**Figure 1.2.2** **(bas) Diagramme spatiotemporel montrant la position, dans le temps et l'espace, des points de mesure tels que rapportés sur la grille, pour les traversées réalisées à la section de Saint-Nicolas. (haut) Signal de marée durant l'échantillonnage. (gauche) Bathymétrie de la section.**

Les vitesses mesurées à l'ADCP ont été extrapolées dans les couches non-mesurées du haut et du bas de la colonne d'eau suivant deux méthodes, respectivement appliquées avant et après lissage. Ces extrapolations ont pour but : 1) de calculer les vitesses moyennées sur la profondeur et 2) de fournir des données à chacune des couches sigma pour l'interpolation temporelle. La première approche testée, intitulée « fit-then-smooth » (f-t-s), consiste à faire passer une fonction de puissance à travers les données de chaque ensemble mesuré (Chen, 1991, Simpson & Oltmann, 1993) :

$$U = a' z^m , \tag{1.2.1}$$

où $U$ est le profil de vitesse, $a'$ est une constante déterminée par régression qui est fonction de la vitesse de cisaillement et de la rugosité du lit, $z$ est l'élévation mesurée à partir du lit (positif vers le haut), et $m = 1/6$. Les vitesses moyennées sur la verticale ainsi obtenues sont lissées, composante par composante, à l'aide d'une moyenne mobile horizontale de 20 m. La seconde méthode, nommée « smooth-then-fit » (s-t-f), commence par un lissage des composantes $u$ et $v$ de la vitesse à l'aide d'une moyenne mobile 2D d'une largeur de 20 m et d'une hauteur variable correspondant à un dixième de la profondeur d'eau instantanée, conforme avec la grille d'interpolation définie. Les composantes de vitesses sont ensuite extrapolées linéairement dans les couches non-mesurées, puis intégrées sur la verticale pour le calcul des vitesses moyennes.

Dans les deux cas, les composantes de vitesses $u$ et $v$ sont lissées séparément pour assurer une reconstruction précise des directions du vecteur de vitesse en chaque point de grille.

Les variations du niveau de l'eau sont par nature beaucoup plus lisses que les vitesses sur une section. Les élévations mesurées au RTK GPS ont donc été lissées dans le temps, une traversée à la fois, à l'aide de splines lissantes cubiques $s$, définies par la fonction de minimisation suivante (Reinsch, 1967, de Boor, 1978) :

$$p\sum_i w_i (y_i - s(t_i))^2 + (1-p)\int \left(\frac{d^2 s}{dt^2}\right)^2 dt\,, \qquad (1.2.2)$$

où $y_i$ est le niveau d'eau mesuré au temps $t_i$ durant une traversée; les poids $w_i$ sont fixés à 1 pour l'ensemble des points; le paramètre de lissage $p$ est fixé à $1\times10^{-4}$, permettant d'éliminer les oscillations aléatoires de la surface tout en conservant les variations apériodiques et de basses fréquences, telles que dues aux marées ou à des gradients locaux de bathymétrie. Le détail de la procédure de lissage des vitesses et des niveaux d'eau est présenté à la section 2.2.4.1.

#### 1.2.1.2.3 Interpolation

Un processus d'interpolation est nécessaire pour la reconstruction, à partir de données non-stationnaires, de champs continus dans le temps et l'espace (ex.: Sokolov & Rintoul, 1999, Vennell & Beatson, 2006). Les variables mesurées lors de chaque traversée n'ont pas été considérées comme synoptiques, c'est-à-dire comme ayant été acquises de façon simultanée, tel qu'illustré à la Figure 1.2.2. Poser une telle hypothèse peut introduire d'importants biais dans les analyses subséquentes lorsque les quantités mesurées varient rapidement, comme dans les estuaires macro-tidaux, résultant en une distorsion des champs interpolés (Matthews, 1997, Rixen & Beckers, 2002). Par conséquent, une procédure d'interpolation a été développée pour reconstruire des champs latéraux synoptiques à tout moment durant la période de mesure. Cette méthode conserve la position des données dans le temps et l'espace et évite ainsi de poser des hypothèses de départ erronées.

Les séries temporelles de vitesses ont été interpolées successivement à chaque point de grille à l'aide de splines lissantes 1D [cf. Éq. (1.2.2)]. L'interpolation des vitesses a été réalisée uniquement selon l'axe du temps pour éviter la propagation latérale indésirable de patrons locaux de vitesses. Les composantes $u$ et $v$ de la vitesse ont été interpolées séparément, avec des

paramètres de lissage $p$ de $5\times10^{-9}$ et $1\times10^{-10}$, respectivement. Les profils verticaux de vitesse ont été interpolés de la même manière, de façon indépendante pour chacune des couches sigma. L'interpolation des niveaux d'eau a, quant à elle, été réalisée à l'aide de trois méthodes, évaluées de manière comparative. La première méthode reprend la stratégie utilisée pour les vitesses et applique des splines lissantes 1D successivement à chaque point de grille. La seconde technique fait usage de splines lissantes 2D, ou « thin-plate splines » (TPS), pour permettre aux variations en niveau d'eau de se propager d'une rive à l'autre en dépit des trous dans les données (Candela *et al.*, 1992, Beatson *et al.*, 2004, Vennell & Beatson, 2006). La troisième méthode est un hybride des deux premières approches en ce sens où elle utilise une courbe de référence, définie à partir des interpolations 2D par TPS, comme fonction de base pour des optimisations successives réalisées à chaque point de grille. Les méthodes d'interpolation sont décrites en détails à la section 2.2.4.2.

### 1.2.2 Modèle 1D de propagation de la marée

Les marées en rivières sont le résultat de l'interaction non-linéaire de la marée océanique avec la bathymétrie, la friction et le débit fluvial. Elles peuvent être assimilées à un phénomène diffusif (LeBlond, 1978) selon lequel l'onde de marée, prenant origine de l'effet conjugué des forces gravitationnelles de la Lune et du Soleil sur les océans, subit une distorsion et une modification de son amplitude à mesure qu'elle se propage vers l'amont (Aubrey & Speer, 1985, Godin, 1985, Speer & Aubrey, 1985, Parker, 1991, Godin, 1999, Nayak & Shetye, 2003). Il en résulte une asymétrie dans la durée du jusant et du flot, et dans les temps d'arrivée et les hauteurs des marées hautes et basses (Godin, 1984, 1999, Nidzieko, 2010). Des oscillations semi-mensuelles des niveaux moyens suivant le cycle de marées de mortes-eaux et de vives-eaux augmentent également en force vers l'amont. Ces dernières surpassent éventuellement en amplitude la marée semi-diurne et se caractérisent par un renversement progressif des hauteurs des marées basses en période de marées de mortes-eaux par rapport aux marées de vives-eaux (LeBlond, 1979, 1991, Gallo & Vinzon, 2005).

Les marées en rivières se trouvent également modulées par divers facteurs externes, qu'ils soient océaniques, hydrologiques, météorologiques ou climatiques. Ces derniers perturbent le signal sur des périodes variant de quelques heures à plusieurs décennies. De plus, des modifications morphologiques, de source naturelle ou anthropique, sont susceptibles d'altérer les propriétés

tidales d'un système (Amin, 1983, 1985, Godin, 1985, DiLorenzo *et al.*, 1993, Horsburgh & Wilson, 2007, Jay, 2009, Jay *et al.*, 2011). La prédiction des marées en rivière n'est donc pas triviale, d'une part en raison de leur caractère non-linéaire et non-stationnaire et, d'autre part, puisqu'elle dépend de prédictions précises et à court terme du débit fluvial – et possiblement d'autres variables externes responsables de sa modulation – généralement difficiles à obtenir.

Cette section présente les aspects méthodologiques ayant mené au développement et à la validation d'un modèle 1D de propagation de la marée dans l'estuaire fluvial du Saint-Laurent, visant à prédire les variations spatiales et temporelles du niveau moyen et des propriétés tidales en fonction du débit fluvial et du marnage océanique (cf. sections 2.3.3 et A.1.3). Une application du modèle au calcul des débits tidaux est également présentée (cf. section A.2.3).

#### *1.2.2.1 Modèle de régression*

L'analyse harmonique classique est sans aucun doute l'approche la plus répandue pour l'analyse et la prédiction des marées. Ses fondements sont basés sur une compréhension moderne du potentiel de marée introduite par Doodson (1921), puis reformulée par Godin (1972). Elle représente le signal mesuré à une station donnée sous la forme d'une somme d'ondes sinusoïdales dont les fréquences sont dérivées du potentiel gravitationnel et d'interactions non-linéaires. Mathématiquement, les hauteurs de marées $h$, telles que représentées par le modèle harmonique classique, sont définies à chaque station comme :

$$h(t) = b_{0,0} + \sum_{k=1}^{n} [b_{1,k} \cos(\sigma_k t) + b_{2,k} \sin(\sigma_k t)], \tag{1.2.3}$$

où $t$ est le temps, $\sigma_k$ sont les fréquences connues *a priori*, $n$ est le nombre de composantes de marée, et $b_{0,0}$, $b_{1,k}$ et $b_{2,k}$ sont les coefficients déterminés par régression linéaire, à partir desquels sont extraites les amplitudes et les phases associées à chaque composante. Plusieurs améliorations récentes au modèle harmonique ont été proposées (ex.: Foreman *et al.*, 2009, Leffler & Jay, 2009, Codiga, 2011). Parmi elles, Leffler & Jay (2009) ont incorporé des statistiques robustes par le biais d'analyses IRLS (Holland & Welsch, 1977, Huber, 1996) pour réduire l'influence des valeurs aberrantes et augmenter le niveau de confiance dans les paramètres calculés. Avec cette inclusion, la solution à l'Éq. (1.2.3) est obtenue en minimisant la somme des résidus pondérés :

$$E = \sum_{j=1}^{m} w_j^2 (h_j - y_j)^2 , \tag{1.2.4}$$

où $y$ sont les observations, $m$ est la longueur du signal et $w$ est une fonction de poids.

L'analyse harmonique repose cependant sur les hypothèses de stationnarité du signal et d'indépendance des composantes de marée, qui vont à l'encontre du caractère non-stationnaire et non-linéaire de la marée en rivière (Jay & Flinchem, 1999). Par conséquent, aucune information sur l'évolution du contenu fréquentiel de la marée en fonction des conditions de forçage non-tidales ne peut être obtenue. Plusieurs méthodes ou adaptations du modèle harmonique traditionnel ont été proposées pour mieux représenter la non-stationnarité de certains processus tidaux [pour une revue, voir Jay & Kukulka (2003) et Parker (2007)]. Néanmoins, le succès de ces méthodes s'est trouvé en partie limité par une perte de résolution des composantes de marée à l'intérieur d'une bande de fréquence donnée (diurne, semi-diurne, etc.), ou par leur incapacité à analyser des signaux fortement non-stationnaires.

Plusieurs auteurs ont montré le potentiel de simples relations de régression pour prédire les modifications de la marée par le débit fluvial (ex.: Godin, 1985, Jay & Flinchem, 1997, Godin, 1999, Kukulka & Jay, 2003a, b, Buschman *et al.*, 2009, Jay *et al.*, 2011). Une généralisation de l'analyse harmonique traditionnelle aux marées non-stationnaires, NS_TIDE (cf. section A.1, Matte *et al.* 2013), basée sur les dernières améliorations du code T_TIDE (Pawlowicz *et al.*, 2002, Leffler & Jay, 2009), a été utilisée pour le développement du modèle de marée dans l'estuaire fluvial du Saint-Laurent. Conceptuellement, les constantes $b_{0,0}$, $b_{1,k}$ et $b_{2,k}$ de l'Éq. (1.2.3) sont remplacées par des fonctions du débit fluvial et du marnage océanique, basé sur une formulation dérivée de la théorie (Jay, 1991) et adaptée par Kukulka & Jay (2003a, b) et Jay *et al.* (2011), selon laquelle :

$$b_{l,k}(t) = a_{0,l,k} + a_{1,l,k} Q^{p_l}(t) + a_{2,l,k} \frac{R^{q_l}(t)}{Q^{r_l}(t)} , \tag{1.2.5}$$

où $Q$ est le débit fluvial ($m^3s^{-1}$); $R$ est le marnage diurne maximum (m); $p$, $q$, $r$ sont les exposants pour chaque station et bande de fréquence; $a_{0,l,k}$, $a_{1,l,k}$, $a_{2,l,k}$ sont les coefficients pour chaque station et fréquence; $k$ est l'indice des composantes de marée ($k$ = 1, $n$); et $l$ est l'indice des

coefficients ($l$ = 0, 2). L'application du modèle à l'estuaire fluvial considère des exposants égaux aux valeurs théoriques données par Kukulka & Jay (2003a, b). Aussi, à chaque station, un décalage temporel $\tau$ est appliqué aux variables de forçage $Q$ et $R$ pour tenir compte des temps de propagation moyens jusqu'à la station d'analyse. La forme finale du modèle, une fois les Éqs. (1.2.5) et (1.2.3) combinées, est donnée par :

$$h(t) = \underbrace{c_0 + c_1 Q^{2/3}(t-\tau_Q) + c_2 \frac{R^2(t-\tau_R)}{Q^{4/3}(t-\tau_Q)}}_{\text{stage model or } s(t)} + \underbrace{\sum_{k=1}^{n}\left[\left(d_{0,k}^{(c)} + d_{1,k}^{(c)} Q(t-\tau_Q) + d_{2,k}^{(c)} \frac{R^2(t-\tau_R)}{Q^{1/2}(t-\tau_Q)}\right)\cos(\sigma_k t) + \left(d_{0,k}^{(s)} + d_{1,k}^{(s)} Q(t-\tau_Q) + d_{2,k}^{(s)} \frac{R^2(t-\tau_R)}{Q^{1/2}(t-\tau_Q)}\right)\sin(\sigma_k t)\right]}_{\text{tidal - fluvial model or } f(t)} \tag{1.2.6}$$

où $s$ et $f$ désignent les modèles du niveau moyen et fluvio-tidal, respectivement; les exposants ($c$) et ($s$) réfèrent aux termes cosinus et sinus; $c_i$ ($i$ = 0, 2) sont les coefficients du modèle du niveau moyen et $d_{i,k}$ ($i$ = 0, 2) sont les coefficients du modèle fluvio-tidal, déterminés par régression [cf. Éq. (1.2.4)]. Les interactions fluvio-tidales se trouvent ainsi découplées, permettant aux propriétés du niveau moyen et de la marée (c.-à-d. les amplitudes et les phases des composantes harmoniques) d'être modélisées séparément en fonction du temps et du forçage externe par le débit fluvial et la marée océanique [cf. Éqs. (2.3.9) – (2.3.14)].

### *1.2.2.2 Spatialisation du modèle*

En utilisant le modèle de régression décrit à la section précédente, les propriétés du niveau moyen et de la marée ont été déterminées en un nombre fini de stations (13) le long du Saint-Laurent, réparties entre Saint-Joseph-de-la-Rive et Lanoraie (Figure 2.3.1, p. 129). Pour représenter ces propriétés de manière continue dans le système, les coefficients de l'Éq. (1.2.6) ont été interpolés spatialement à l'aide de fonctions cubiques d'Hermite (Fritsch & Carlson, 1980). Ainsi, une meilleure compréhension du phénomène de propagation de la marée est rendue possible, de même que des prédictions en tout point dans le système. Pour permettre une telle interpolation, les paramètres de l'analyse (c.-à-d. exposants, composantes harmoniques,

longueur des séries, etc.) ont été fixés au préalable et uniformisés d'une station à l'autre (cf. section 2.3.4.2).

#### *1.2.2.3 Validation*

Pour évaluer la performance du modèle, les prévisions du modèle non-stationnaire ont été comparées aux résultats d'analyses harmoniques classiques (Pawlowicz *et al.*, 2002) réalisées aux stations. De plus, pour juger des capacités prédictives du modèle, des prédictions du niveau d'eau ont été produites pour l'ensemble des 32 stations marégraphiques et des sondes de pression installées de mai à octobre 2009 (Figure 2.3.1, p. 129). Ces prédictions ont été comparées aux mesures ainsi qu'aux résultats du modèle hydrodynamique ONE-D, opérationnel dans le Saint-Laurent (Hicks, 1997, Lefaivre *et al.*, 2009).

#### *1.2.2.4 Méthode de cubature*

Une méthode d'estimation et de prédiction des débits tidaux, qui s'appuie sur le modèle de propagation de la marée développé, a été appliquée à l'estuaire fluvial du Saint-Laurent. Cette méthode, dite de cubature (Dronkers, 1964, Forrester, 1972), est basée sur la résolution de l'équation de continuité et requiert uniquement une connaissance des niveaux d'eau et de la géométrie de la rivière. Mathématiquement, l'équation de continuité sous sa forme intégrale peut s'écrire comme :

$$\int_{\Omega} \vec{\nabla} \cdot \vec{q} d\Omega = -\int_{\Omega} \frac{\partial h}{\partial t} d\Omega , \tag{1.2.7}$$

où $q$ est le débit spécifique ($m^2\ s^{-1}$), $h$ est le niveau d'eau (m), $t$ est le temps (s) et $\Omega$ est la surface d'intégration ($m^2$). La méthode ici proposée utilise une discrétisation 2D par éléments finis de l'estuaire fluvial, qui prend en compte l'inondation et l'exondation des estrans par le biais de données topographiques détaillées. Les niveaux d'eau $h$ sont quant à eux issus du modèle 1D de propagation de la marée, lesquels sont extrapolés sur le maillage 2D. Pour valider la méthode, les débits calculés ont été comparés aux débits mesurés aux sections de mesure lors de la campagne de terrain de 2009 (section 1.2.1). Le développement de la méthode et son application au Saint-Laurent sont présentés à la section A.2.3.

### 1.2.3 Modèle hydrodynamique 2D

Les modèles hydrodynamiques sont essentiels pour comprendre les interactions entre la marée, le débit fluvial et la géométrie du milieu. Un tel outil permet à la fois de recréer l'histoire hydrodynamique d'un système, d'en assurer le suivi en temps réel et de prédire les conséquences potentielles de pratiques de gestion, de modifications anthropiques, ou d'événements hydrologiques ou météorologiques extrêmes sur le système (ex.: Babu *et al.*, 2005, Morin & Champoux, 2006, Horsburgh & Wilson, 2007, Araújo *et al.*, 2008, Picado *et al.*, 2010). De plus, ces modèles peuvent être couplés ou utilisés comme entrée à des modèles morphodynamiques (Rinaldi *et al.*, 2008, Nabi *et al.*, 2012), hydrologiques (de Paiva *et al.*, 2013), océaniques (Saucier *et al.*, 2009), d'advection-diffusion (Simons *et al.*, 2006, Bárcena *et al.*, 2012), d'interactions vague-courant (Liu *et al.*, 2007) et d'habitats aquatiques (Morin *et al.*, 2003b). Une résolution spatiale très fine est souvent requise pour ce genre d'applications (ex.: Crowder & Diplas, 2000).

Cette section présente les aspects méthodologiques liés au développement d'un modèle hydrodynamique 2D non-stationnaire à haute résolution spatiale de l'estuaire fluvial du Saint-Laurent. Elle inclut une description des modèles numériques de terrain et hydrodynamique, ainsi que du processus d'étalonnage et d'assimilation de la condition limite aval (cf. section 2.4.3). Un supplément à la validation du modèle est présenté à la section A.3.

#### *1.2.3.1 Domaine de simulation*

La limite amont du domaine de simulation est enlignée sur la station marégraphique de Port Saint-François (rkm 241), située à la sortie du lac Saint-Pierre (Figure 1.1.1). La limite aval du modèle est, quant à elle, positionnée le long d'une ligne de cophase, quelques km en aval de la station de Saint-Joseph-de-la-Rive (rkm 0), située dans la zone de transition estuarienne de l'estuaire du Saint-Laurent (Simons *et al.*, 2010). Cette limite a été définie à proximité d'une station marégraphique permanente et suffisamment loin de la limite aval de l'estuaire fluvial pour permettre aux échanges entre les bras nord et sud de l'île d'Orléans de s'effectuer librement. Toutefois, puisque la station permanente de mesure des niveaux d'eau sur la rive nord de la limite n'a pas de vis-à-vis en rive sud, la distribution des niveaux le long de la limite est inconnue et a été déterminée par assimilation. Cette étape a consisté à utiliser les différences entre les niveaux mesurés et simulés aux stations avoisinantes pour orienter les modifications dans la distribution des niveaux d'eau de la condition limite.

Les principaux tributaires ont été inclus dans le modèle de façon à permettre à la marée de s'y propager. Ils comprennent les rivières Saint-Maurice, Batiscan, Sainte-Anne, Jacques-Cartier et Chaudière. Les limites ont été positionnées à l'intérieur des tributaires suffisamment en amont de l'influence de la marée pour permettre l'imposition de conditions de débits non influencées par la marée.

Le domaine de simulation global a été partitionné en deux sous-domaines qui se chevauchent, chacun partageant les mêmes points de grille et données que le modèle global. Cette séparation s'est avérée nécessaire pour permettre de dissocier le processus d'assimilation de celui d'étalonnage, en raison d'incertitudes liées à la répartition des niveaux d'eau le long de la limite aval du modèle. Ainsi, l'étalonnage du modèle s'est réalisé sur un domaine réduit s'étendant de Port Saint-François (rkm 241) à Québec (rkm 106.5), pour lequel les conditions de niveaux d'eau aux frontières sont connues. De son côté, l'assimilation des conditions limites aval, visant à déterminer la répartition optimale des niveaux d'eau le long de la limite, s'est faite sur un domaine réduit s'étendant de Neuville (rkm 138) à Saint-Joseph-de-la-Rive (rkm 0). L'impact de l'exclusion de la portion aval du processus d'étalonnage est faible, puisque l'erreur est dominée par la condition limite aval et la bathymétrie complexe du secteur, davantage que par la friction. Seule la friction autour de l'île d'Orléans a été ajustée dans ce segment. Une fois le modèle étalonné et assimilé séparément sur chacun des sous-domaines, les simulations ont été réalisées sur le modèle global.

#### *1.2.3.2 Modèle numérique de terrain*

Le développement du MNT s'est fait à l'aide du logiciel MODELEUR (Secretan & Leclerc, 1998, Secretan *et al.*, 2001). Le facteur explicatif premier de l'hydrodynamique est la topographie, qui comprend la bathymétrie du chenal, la plaine inondable et les structures de génie. Près de 42M de points de sondages multifaisceaux réalisés par le Service Hydrographique du Canada (SHC) ont été intégrés au MNT. Pour compléter les données dans les zones peu profondes, les données d'une campagne LIDAR réalisée dans l'estuaire fluvial du Saint-Laurent ont été obtenues, pour l'ensemble des zones intertidales et des hauts-fonds (cf. section 2.4.3.1). Au total, 420M de points LIDAR ont été intégrés au modèle. Par ailleurs, en raison d'un manque de données dans les tributaires, seule leur géométrie a pu être récupérée à partir des lignes de berge. Leur bathymétrie a été remplacée par un chenal régulier de pente constante, de largeur connue

(donnée par les rives) et de profondeur variable, déduite en supposant un débit moyen (connu) et une vitesse d'écoulement moyenne de 1 m $s^{-1}$. La topographie telle que représentée par le modèle est présentée à la Figure 1.2.3.

La composition du substrat a été définie sur des zones homogènes caractérisées par une topographie uniforme, sur la base de 6400 points de caractérisation de substrat du SHC. Cette classification a ensuite été convertie en coefficient de frottement de Manning, suivant la méthode de Morin *et al.* (2000a). La friction due aux macrophytes a été intégrée comme couche supplémentaire de frottement dans les régions où des plantes aquatiques sont observables durant l'été. Les coefficients de friction ont été ajustés lors de l'étalonnage à l'intérieur de la gamme de valeurs fournies par Morin *et al.* (2000b). Enfin, un frottement constant a été utilisé à l'intérieur des tributaires. La distribution des coefficients de Manning utilisés dans l'estuaire fluvial du Saint-Laurent est présentée à la Figure 1.2.4. Aucun vent ni glace n'ont été intégrés au modèle.

Par ailleurs, une condition de glissement libre (« free-slip ») a été imposée le long des structures verticales, bien que la plupart des limites latérales soient mobiles et contrôlées par le modèle de couvrant-découvrant (cf. section 2.4.3.2.3).

La topographie et le frottement ont été assemblés sur un maillage 2D aux éléments finis, composé de 1 347 515 nœuds et de 662 934 éléments (maillage global). Le maillage a été construit de manière à minimiser les erreurs dans les régions présentant de fortes variations morphologiques et ainsi représenter le terrain de façon précise. La résolution spatiale moyenne est de 50 m, avec des raffinements allant jusqu'à ~1 m autour des structures de génie (ex.: piliers de ponts, quais) et dans les régions de topographie complexe (ex.: forts gradients bathymétriques, chenaux étroits). Ces raffinements sont toutefois très localisés et visent à capter les effets de ces structures sur les processus à grande échelle (ex.: propagation de la marée, échanges latéraux), avec pour objectif de calibrer le modèle avec un niveau de détail comparable à celui fourni par les données hydrodynamiques disponibles (Matte *et al.*, 2014a). Le maillage global est présenté à la Figure 1.2.5.

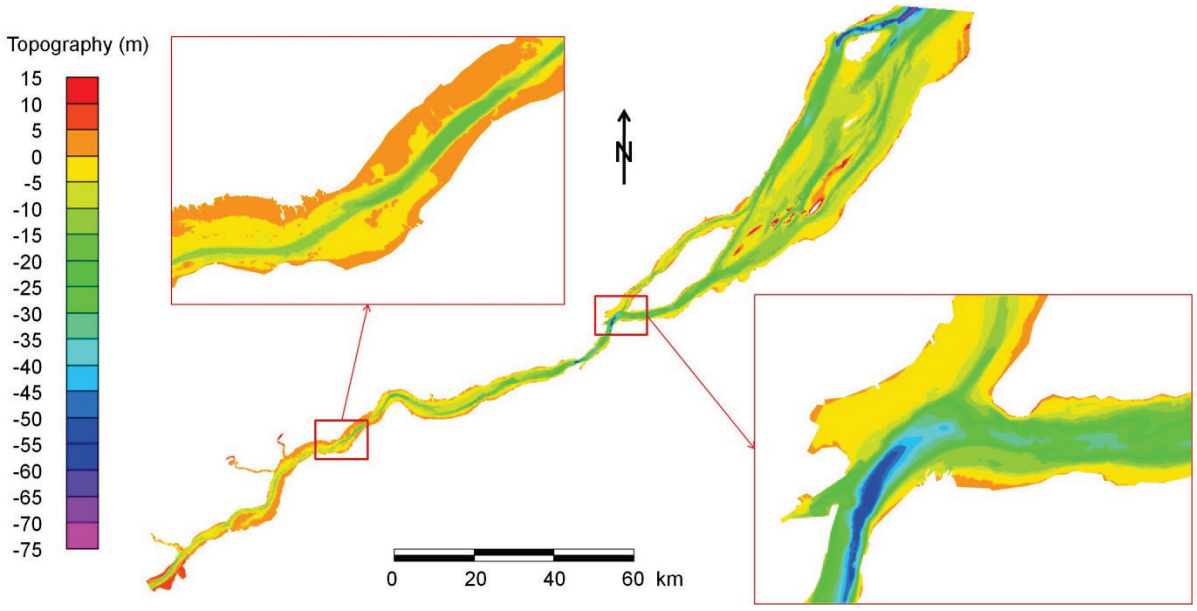


**Figure 1.2.3** **Topographie de l'estuaire fluvial du Saint-Laurent, projetée sur le maillage aux éléments finis, avec zooms sur Grondines et sur la jonction de l'île d'Orléans.**

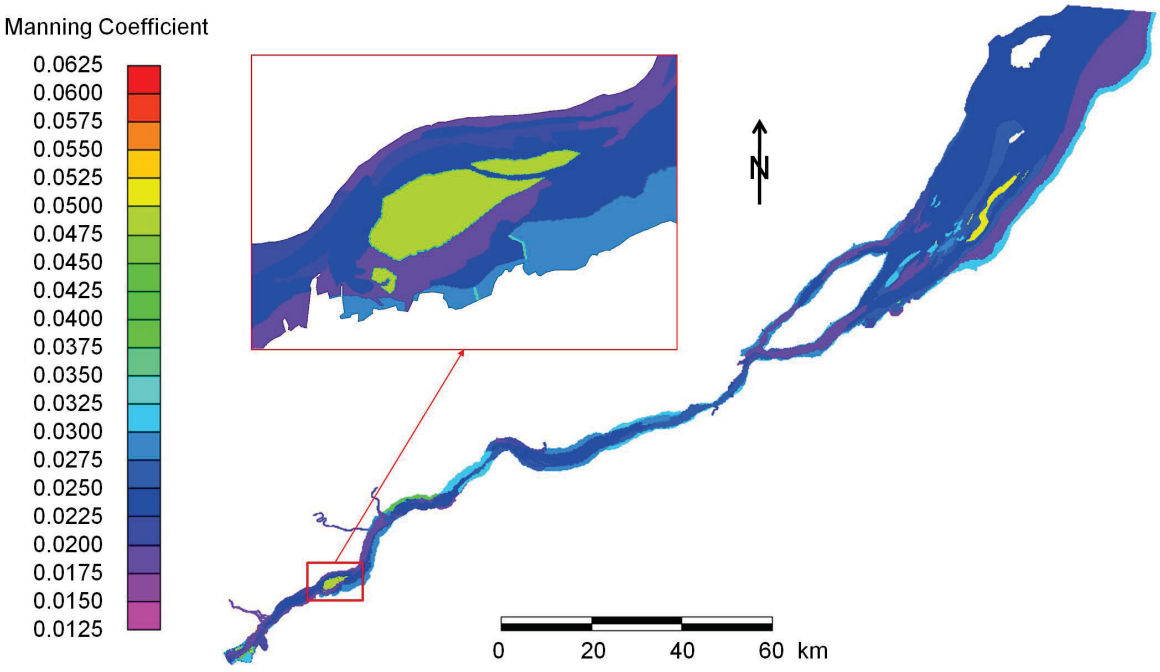


**Figure 1.2.4** **Coefficients de Manning dans l'estuaire fluvial du Saint-Laurent, basés sur une description du substrat et des macrophytes, avec zoom sur le haut-fond de Gentilly (Bécancour).**

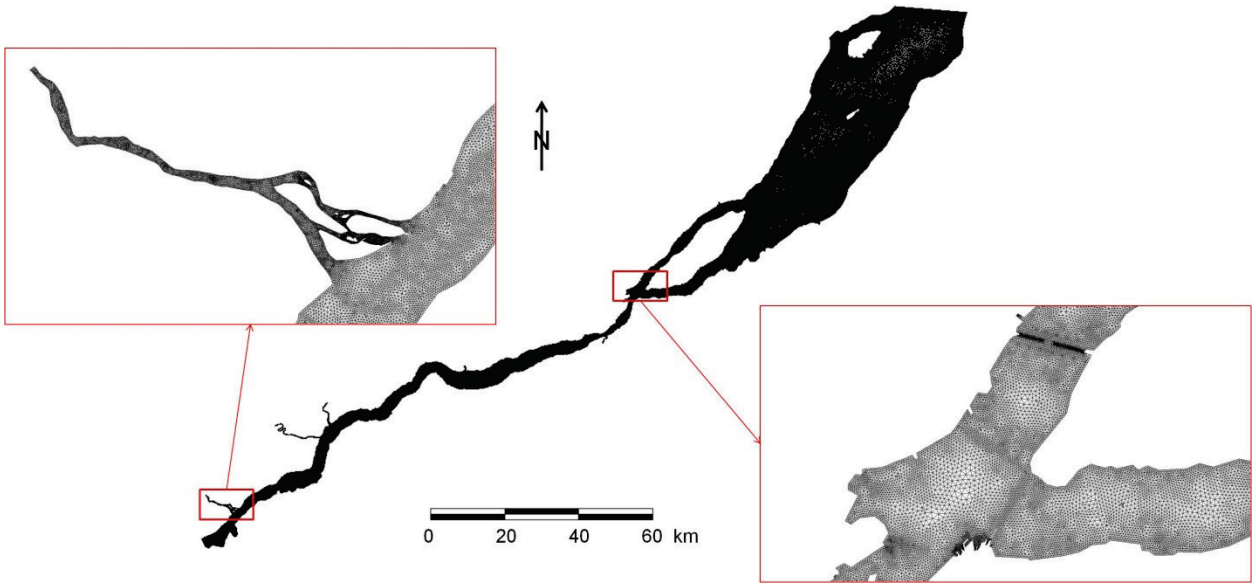


**Figure 1.2.5** **Maillage aux éléments finis dans l'estuaire fluvial du Saint-Laurent, avec zooms sur la rivière Saint-Maurice et sur la jonction de l'île d'Orléans.**

### *1.2.3.3 Modèle hydrodynamique*

Les simulations hydrodynamiques ont été réalisées à l'aide du logiciel H2D2 (Secretan, 2013), qui résout les équations de Saint-Venant 2D non-stationnaires, intégrées sur la verticale (cf. section 2.4.7). Il est basé sur une discrétisation des équations par éléments finis et comprend un modèle de couvrant-découvrant pour le traitement des zones intertidales. Les équations de Saint-Venant, telles qu'implantés dans H2D2, reposent sur les hypothèses d'incompressibilité, de pression hydrostatique et de stabilité du lit. La géométrie et la taille de l'estuaire fluvial du Saint-Laurent, combinées à l'effet des fortes marées dans un environnement d'eau douce, rendent l'approximation du 2D valide pour ce système. De plus, les mesures réalisées dans l'estuaire fluvial (cf. section 1.2.1, Matte *et al.*, 2014a) ont confirmé la non-stratification des vitesses sur la verticale pour l'ensemble des sections sondées.

Des conditions de niveaux d'eau, mesurés aux stations marégraphiques du MPO, ont été imposées aux limites amont et aval du modèle. Des conditions de débits moyens journaliers, reconstruits par la méthode de Bouchard & Morin (2000), adaptée de Morse (1990), ont été imposées aux limites amont des tributaires. Les équations de Saint-Venant 2D non-stationnaires sont intégrées dans le temps à l'aide d'un schéma implicite d'Euler, avec un pas de temps de simulation de 5 minutes combiné à un algorithme de coupure du pas de temps en cas de non-

convergence. Le système algébrique non-linéaire qui en résulte est résolu par la méthode itérative de Newton-Raphson (Dhatt *et al.*, 2005). Une période initiale équivalant à un cycle de marée est nécessaire pour dissiper les effets de la condition initiale et propager l'onde de marée d'un bout à l'autre du domaine.

#### *1.2.3.4 Étalonnage*

L'étalonnage du modèle a été réalisé sur deux périodes de simulation de 15 jours débutant le 14 juin 2009 00:00:00 HAE et le 19 août 2009 00:00:00 HAE, respectivement, correspondant aux périodes de mesures par bateau (cf. section 1.2.1.1). Le processus d'étalonnage a consisté à ajuster le modèle de façon à réduire les erreurs associées à la topographie, au substrat et à la friction. Durant l'étalonnage, les erreurs de topographie ont été détectées et corrigées en cherchant notamment la présence de patrons de vitesses incohérents ou de larges erreurs en niveaux d'eau. Le niveau moyen et le marnage de la marée ont ensuite été ajustés localement par des modifications dans la composition du substrat, de façon à reproduire les observations aux stations. Des ajustements du frottement de Manning ont ensuite été appliqués dans les zones peu profondes pour tenir compte de la présence de macrophytes.

Les niveaux moyens sont calculés à l'aide d'une moyenne mobile de 3 jours, similaire à l'éliminateur de marée de Godin (1972). Les marnages ont quant à eux été déterminés par la méthode de Kukulka & Jay (2003a), en calculant la différence entre les niveaux maximum et minimum sur une fenêtre mobile de 27 jours.

Pour évaluer la performance du modèle, deux critères ont été utilisés, soit l'erreur quadratique moyenne (RMSE) et la compétence (ou « skill ») (Willmott *et al.*, 1985) :

$$\mathrm{RMSE} = \sqrt{\frac{1}{n}\sum_{n}\left(X_{\mathrm{sim}} - X_{\mathrm{obs}}\right)^2} \tag{1.2.8}$$

et

$$\mathrm{Skill} = 1 - \frac{\sum_{n}\left(X_{\mathrm{sim}} - X_{\mathrm{obs}}\right)^2}{\sum_{n}\left(\left|X_{\mathrm{sim}} - \overline{X_{\mathrm{obs}}}\right| + \left|X_{\mathrm{obs}} - \overline{X_{\mathrm{obs}}}\right|\right)^2}, \tag{1.2.9}$$

où $X$ est la variable comparée et $\overline{X}$ est sa moyenne pour $n$ valeurs. Le RMSE est une mesure de l'erreur moyenne entre le modèle et les observations dans les unités de la quantité évaluée. La compétence, quant à elle, est une mesure sans unité de l'erreur moyenne relative entre le modèle et les observations. Une compétence de 1 indique une concordance parfaite du modèle et des observations, tandis qu'une compétence de 0 signifie que le modèle proposé est équivalent à la moyenne des observations.

#### *1.2.3.5 Assimilation*

Les niveaux d'eau imposés le long de la limite aval du modèle sont dérivés des observations à la station de Saint-Joseph-de-la-Rive (rkm 0), plutôt que des composantes harmoniques de la marée, de façon à permettre aux variations non-tidales (résiduelles) de se propager dans le système. Une assimilation des niveaux d'eau a été réalisée pour déterminer leur distribution le long de cette limite, qui reproduit le mieux les niveaux observés aux stations plus en amont. Durant l'assimilation, des déphasages temporels ont été appliqués de manière itérative aux niveaux imposés jusqu'à ce que les signaux simulés et observés aux stations soient en phase. Des gradients latéraux (positifs et négatifs) des niveaux moyens et des marnages ont également été testés pour évaluer la sensibilité du modèle aux conditions imposées. De façon générale, les variations simulées n'ont pas suffi à expliquer les différences entre les niveaux simulés et observés aux stations plus en amont, de sorte qu'aucun gradient n'a été appliqué aux mesures de Saint-Joseph-de-la-Rive, distribuées le long de la limite du modèle. L'assimilation de la condition limite s'est donc limitée, d'une part, à déterminer le déphasage optimal permettant de propager la marée de manière synchrone avec les observations aux stations et, d'autre part, à définir les corrections (constantes sur toute la limite) du niveau moyen et du marnage permettant de reproduire le signal mesuré à la station de Saint-Joseph-de-la-Rive.

## 1.3 Résultats

La présente section décrit les résultats obtenus pour chacun des trois objectifs de la thèse, regroupés en trois sous-sections (1.3.1, 1.3.2 et 1.3.3) pour chacun des trois objectifs de la thèse, respectivement.

### 1.3.1 Campagne de terrain

L'évaluation des données et des méthodes d'analyse, introduites à la section 1.2.1, est décrite dans cette section. Les résultats de ces analyses sont présentés en détails aux sections 2.2.5 et 2.2.9. Les mesures réalisées dans l'estuaire fluvial du Saint-Laurent sur l'ensemble des sections sont présentées en supplément à l'annexe A.3.

#### *1.3.1.1 Erreurs et précision*

L'erreur et la précision des mesures ont été déduites à partir des statistiques extraites des données. Dans le cas des sondes de pression installées en berge, la dérive des données a été estimée à -0.020 m en moyenne (Table 2.2.5, p. 118). Les erreurs moyennes en vitesses mesurées à l'ADCP ont, quant à elles, varié entre 0.09 et 0.16 m $s^{-1}$ sur l'ensemble des sections de mesure (Table 2.2.6, p. 119), tandis que les erreurs verticales moyennes des données RTK GPS ont oscillé entre 0.012 et 0.021 m (Table 2.2.7, p. 120), ce qui est conforme à l'erreur d'instrumentation attendue (Ghilani & Wolf, 2012).

Les erreurs systématiques en niveaux d'eau mesurés au RTK GPS sont attribuables à deux principales sources : 1) des changements dans le nombre et la géométrie des satellites et 2) les effets du tirant d'eau dynamique. Des variations verticales pouvant s'élever à 10 cm ont été observées à de rares occasions et corrélées à des changements dans le nombre de satellites (ex.: Figure 2.2.14, p. 122), fort probablement liées à des problèmes dans la version du logiciel du RTK GPS. La procédure d'interpolation développée étant presque insensible à ces variations, aucune correction n'a été appliquée. Par ailleurs, les erreurs systématiques associées aux mouvements de tangage et de roulis du bateau ont été corrigées et réduites en-deçà de l'erreur d'instrumentation [cf. Figure 2.1.3 (p. 73), Figure 2.2.15 (p. 122) et Table 2.2.8 (p. 124)].

Les erreurs aléatoires en niveaux d'eau et en vitesses, notamment attribuables aux conditions de vagues, de vent et de turbulence, ont été éliminées par lissage [cf. Figure 2.2.5 (p. 94) et Figure

2.2.6 (p. 94)]. Pour assurer une reconstruction adéquate de l'orientation des vecteurs de vitesse, le lissage et l'interpolation ont été réalisés séparément sur chaque composante *u* et *v*. Les modules de vitesses recalculés après lissage à partir des composantes diffèrent toutefois de ceux obtenus en lissant directement les modules mesurés. Des différences moyennes de moins de 4 cm $s^{-1}$ ont été calculées aux transects, avec des maximums pouvant s'élever à quelques dizaines de cm $s^{-1}$ par endroit (Table 2.2.1, p. 72).

Deux méthodes d'extrapolation des vitesses dans les couches non-mesurées de la colonne d'eau ont été testées et comparées. La Figure 1.3.1 (gauche) illustre un échantillon de vitesses mesurées à Neuville, accompagné de deux représentations des profils de vitesses obtenues des méthodes f-t-s et s-t-f. Dans la zone mesurée de la colonne d'eau, les deux profils sont équivalents en termes de représentativité des données, tandis que la fonction de puissance (méthode f-t-s) permet dans la zone non-mesurée du fond de ramener les vitesses à zéro. Cette caractéristique est conforme à l'allure générale des profils de vitesses observés sur la majeure partie du cycle de marée. Pour cette raison, la méthode f-t-s a été choisie pour le calcul des vitesses moyennées sur la profondeur. Toutefois, une forme de profil définie par une loi de puissance n'est généralement pas valable pour les composantes transversales (*v*) de la vitesse. Les composantes de vitesses aux profondeurs sigma, produites pour les besoins de l'interpolation temporelle, ont donc été obtenues via une extrapolation linéaire dans les zones non-mesurées, suivant la méthode s-t-f. Sur une section complète, les vitesses moyennées sur la profondeur issues des méthodes f-t-s et s-t-f diffèrent en moyenne de moins de 0.1 m $s^{-1}$ pour la plupart des transects [cf. Figure 1.3.1 et Table 2.2.1 (p. 72)]. De larges différences peuvent néanmoins apparaître entre les deux méthodes lorsque les profils de vitesses dévient des conditions standard, par exemple autour de fortes variations bathymétriques, en présence de courants secondaires ou durant l'étale de courant.

Les erreurs associées à la configuration des données dans le temps et l'espace ont été estimées à l'aide de signaux synthétiques, ré-interpolés sur les grilles spatio-temporelles définies pour chaque section (ex.: Figure 1.2.2). De façon générale, les splines lissantes 1D sont plus sensibles à la configuration des données que les autres méthodes testées. Pour les niveaux d'eau, la méthode d'interpolation 1D basée sur l'optimisation d'une courbe de référence s'est avérée la plus robuste [cf. Table 2.2.8 (p. 124) et Table 2.2.2 (p. 99)].

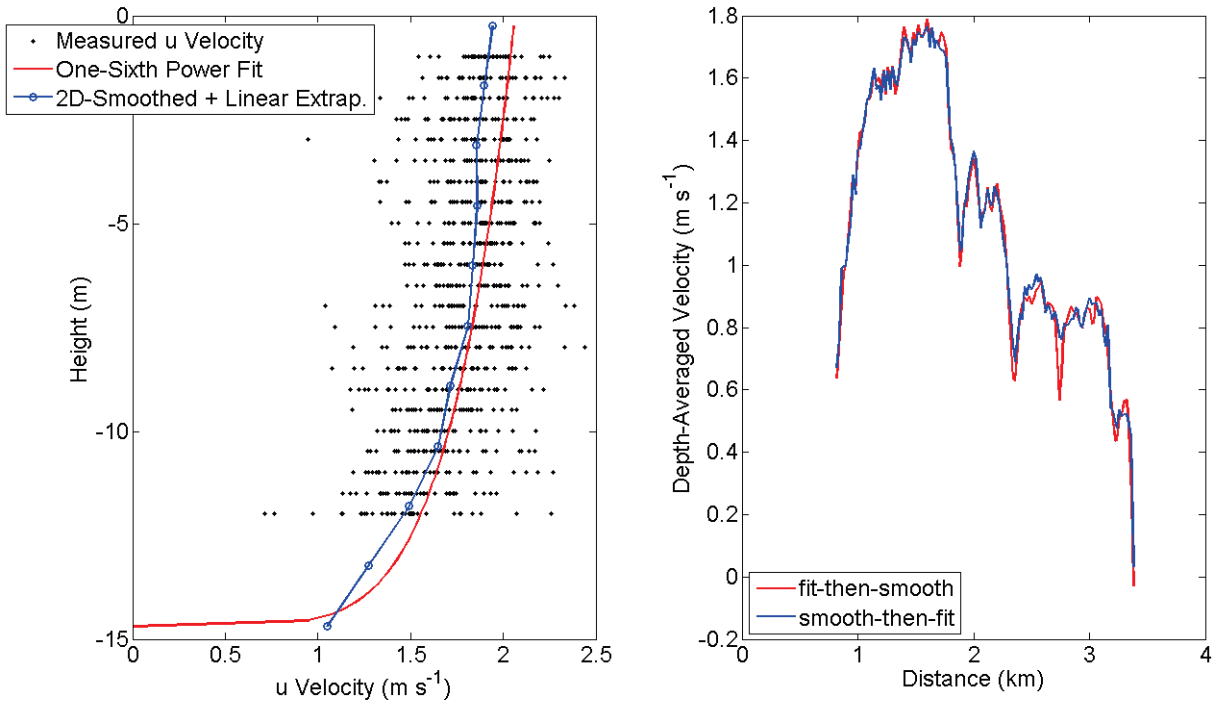


**Figure 1.3.1** **Comparaison des méthodes d'extrapolation des vitesses. (gauche) Profil de vitesses en *u* mesurées à Neuville; les points noirs sont les vitesses mesurées à chaque cellule sur une distance de 20 m; la ligne bleue illustre le lissage par la méthode 2D avec extrapolations linéaires; la ligne rouge est une fonction de puissance passée à travers les points de mesure. (droite) Vitesses moyennées sur la verticale et lissées à partir des méthodes f-t-s (rouge) et s-t-f (bleu).**

### *1.3.1.2 Reconstruction de champs hydrodynamiques continus*

La Figure 1.3.2 présente l'amplitude et la direction des vitesses moyennées sur la profondeur à Saint-Jean, reconstruites par interpolation des composantes *u* et *v*. D'importantes variations latérales et temporelles, liées à la forme du chenal et à l'effet de la marée, sont observées, notamment dans les temps d'inversion de courant. De plus, une forte cohérence latérale des vitesses est notée, en dépit du fait que les interpolations 1D aient été réalisées séparément sur chacun des points de grille. Cela suggère que les fonctions splines et les paramètres utilisés sont bien adaptés à la variabilité et à la distribution des données sous-jacentes. Les erreurs d'interpolation pour chaque section sont présentées à la Table 2.2.3 (p. 103).

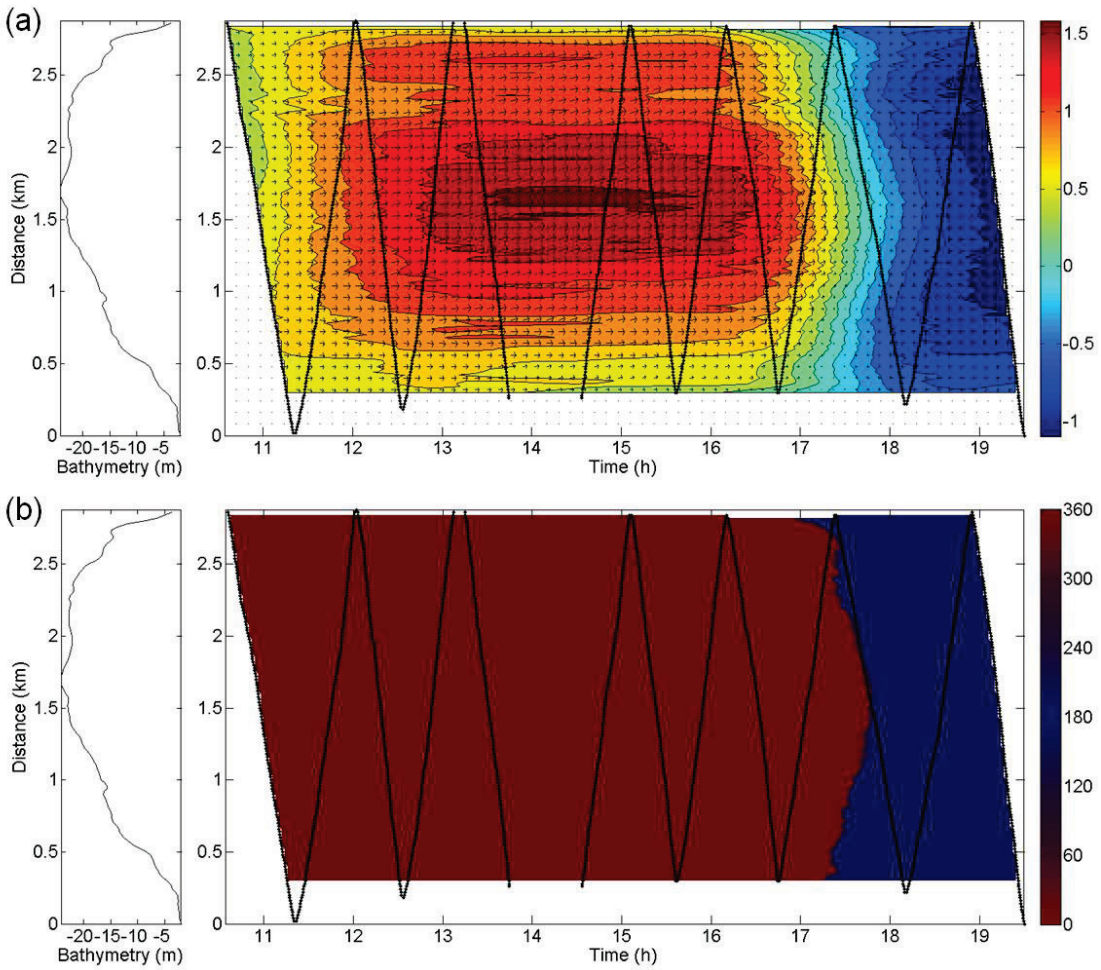


**Figure 1.3.2** **(a) Vitesses moyennées sur la verticale (en m $s^{-1}$) à Saint-Jean le 24 août 2009, reconstruites à partir des composantes interpolées *u* et *v*. (b) Orientation des vitesses (en degrés) illustrant les temps d'inversion de courant. Les points noirs correspondent à la position des données sur la grille. La bathymétrie est présentée sur les panneaux de gauche.**

Une comparaison des niveaux d'eau interpolés à partir des trois méthodes testées est présentée à la Figure 1.3.3. Les résultats démontrent la supériorité de la méthode hybride d'interpolation 1D par optimisations successives, en ce sens où elle conserve un lien spatial fort entre les données du transect, tout en permettant une certaine souplesse dans leur interpolation à travers des optimisations locales. Elle permet notamment, dans le cas présenté, de faire ressortir des gradients latéraux, fortement corrélés aux variations bathymétriques. La Table 2.2.3 (p. 103) et la Figure 1.3.4 présentent les erreurs d'interpolation pour chaque transect ainsi qu'une comparaison avec les données de niveaux d'eau mesurées aux stations marégraphiques. L'erreur maximale est généralement observée autour des marées hautes ou basses et est surtout fonction de la position des données autour de ces extrema.

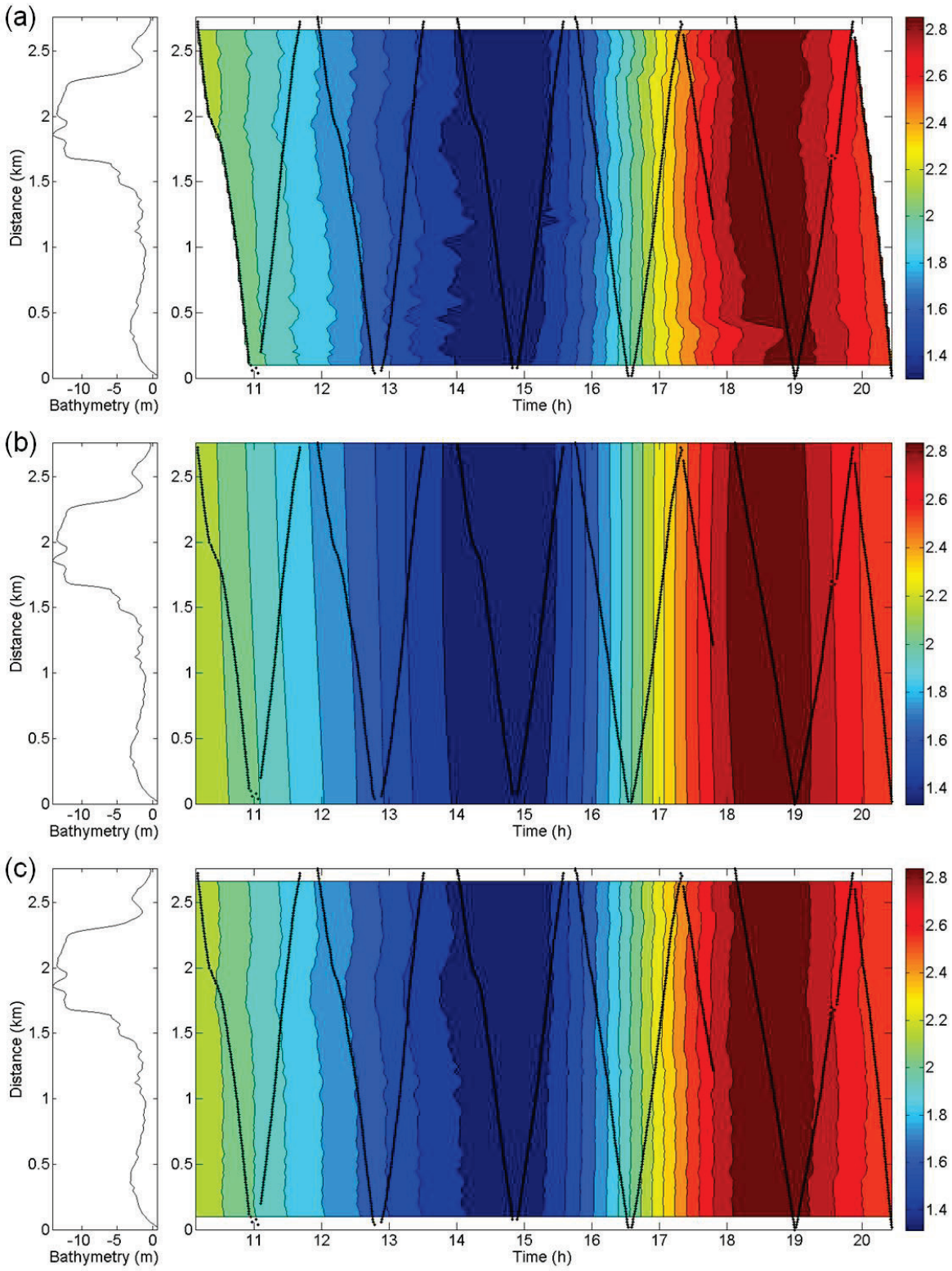


**Figure 1.3.3** **Niveaux d'eau interpolés (en m) à Grondines le 19 juin 2009 à partir (a) d'interpolations successives par splines lissantes 1D, (b) de TPS 2D, et (c) d'une courbe de référence 1D forcée aux points de grille. Les points noirs correspondent aux données sur la grille. La bathymétrie est présentée sur les panneaux de gauche.**

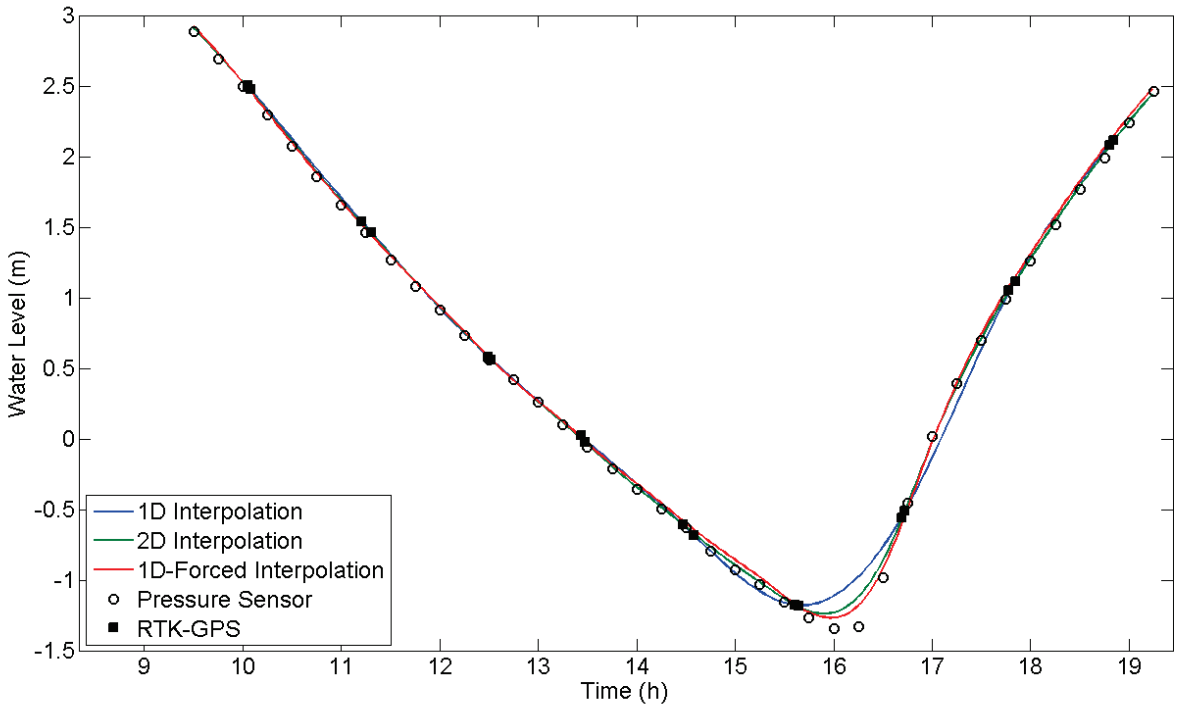


**Figure 1.3.4** **Validation des niveaux d'eau interpolés à Saint-Nicolas. Niveaux mesurés à la sonde de pression (cercles) et par le RTK GPS au point du transect le plus près (carrés). Les lignes bleue, verte et rouge représentent les interpolations 1D, 2D et 1D optimisée des données RTK GPS, respectivement.**

La procédure d'analyse ici présentée est basée sur la prémisse que les mesures prises à chaque traversée par bateau ne sont pas synoptiques. Une démonstration de la pertinence de cette hypothèse est faite à la Figure 1.3.5, pour deux champs de vitesses mesurés et interpolés. Dans cet exemple où les variations dues à la marée sont importantes (~1 m en 37 min) et la section de mesure est large (> 2 km), l'hypothèse de synopticité des mesures mène à une surestimation des vitesses et à un mauvais positionnement des vitesses maximales et des fronts d'inversion de courant. Ces derniers se propagent en réalité depuis les rives vers le chenal, alors que les mesures non-interpolées indiquent plutôt une inversion de courant s'initiant sur une rive uniquement. Les niveaux d'eau interpolés, quant à eux, sont relativement constants le long de la section, contrairement aux mesures qui présentent une augmentation de 1 m en cours de traversée. Pour reconstruire des champs hydrodynamiques physiquement plausibles, il est donc crucial de tester les hypothèses de départ afin de s'assurer de leur applicabilité locale. Ces considérations sont déterminantes dans le calcul des débits instantanés ou d'autres variables hydrodynamiques, notamment rendu possible par la mesure simultanée des niveaux d'eau et des vitesses.

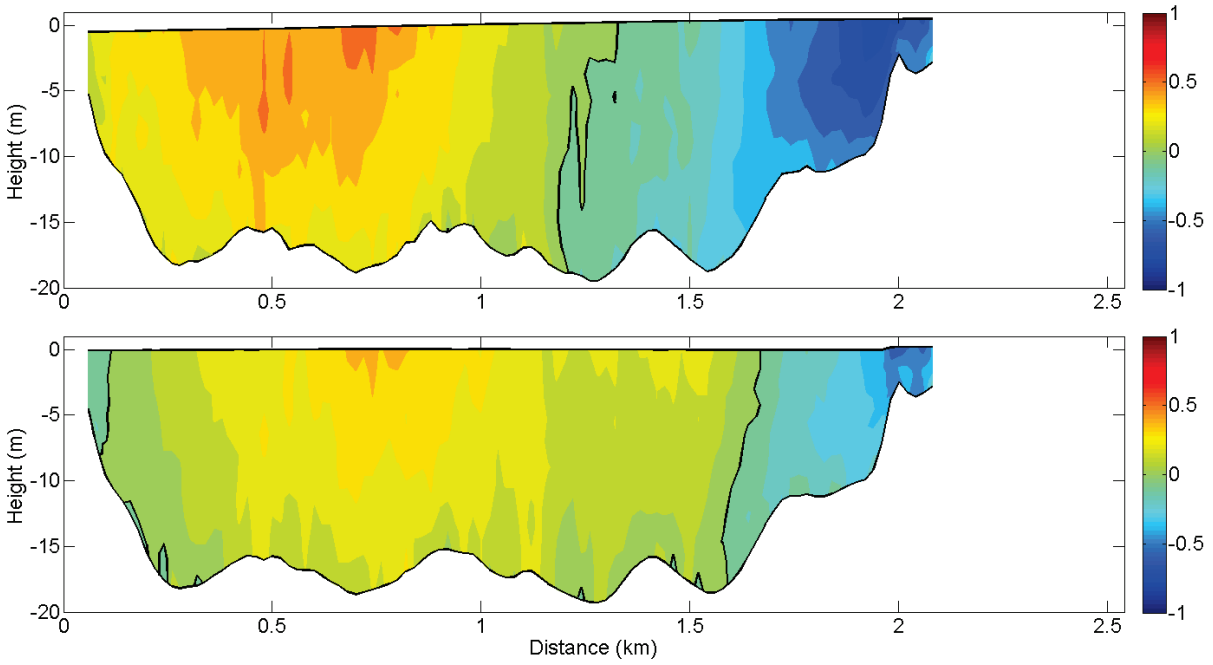


**Figure 1.3.5** **Erreur associée à l'hypothèse de synopticité pour une traversée le long de la section de Saint-Nicolas. (haut) Vitesses mesurées (en m $s^{-1}$) de 16h44 à 17h21. (bas) Vitesses interpolées à 17h02 (temps moyen). Les lignes noires indiquent la position de la surface de l'eau, du lit et des vitesses nulles.**

### 1.3.2 Modèle 1D de propagation de la marée

L'évaluation des capacités descriptives et prédictives du modèle 1D de propagation de la marée présenté à la section 1.2.2 est décrite dans cette section. Cette évaluation est présentée en détails à la section 2.3.4.3. Les résultats de l'application du modèle au calcul des débits tidaux sont présentés à la section A.2.4.

#### *1.3.2.1 Performance du modèle*

Une comparaison des analyses faites par le modèle NS_TIDE et l'analyse harmonique classique (HA) est présentée à la Figure 1.3.6 pour les stations de la Table 2.3.1 (p. 137) et une période d'analyse de 1999-2009. Le nombre de composantes incluses dans l'analyse harmonique classique est plus élevé qu'avec NS_TIDE, qui comprend la moitié moins de composantes. Néanmoins, le nombre de coefficients du modèle non-stationnaire est supérieur à celui de l'analyse harmonique en raison du nombre de termes qui le composent [cf. Éq. (1.2.6)]. Aux stations aval, de Saint-Joseph-de-la-Rive (rkm 0) à Portneuf (rkm 163.5), les deux méthodes sont

comparables. Passé Portneuf, la performance de l'analyse harmonique se dégrade considérablement, avec des variances du résidu qui augmentent de façon drastique et des erreurs quadratiques moyennes et maximales qui surpassent celles de l'analyse non-stationnaire. Ce changement de comportement coïncide avec la présence de rapides devant Deschambault (rkm 168) combinée à une augmentation rapide de la pente du fond, marquant la transition entre les régimes tidal et fluvio-tidal, où l'influence du débit sur les niveaux moyens et les amplitudes de marée s'intensifie. Les variations résultant de ces interactions ne sont pas représentées adéquatement par le modèle harmonique standard.

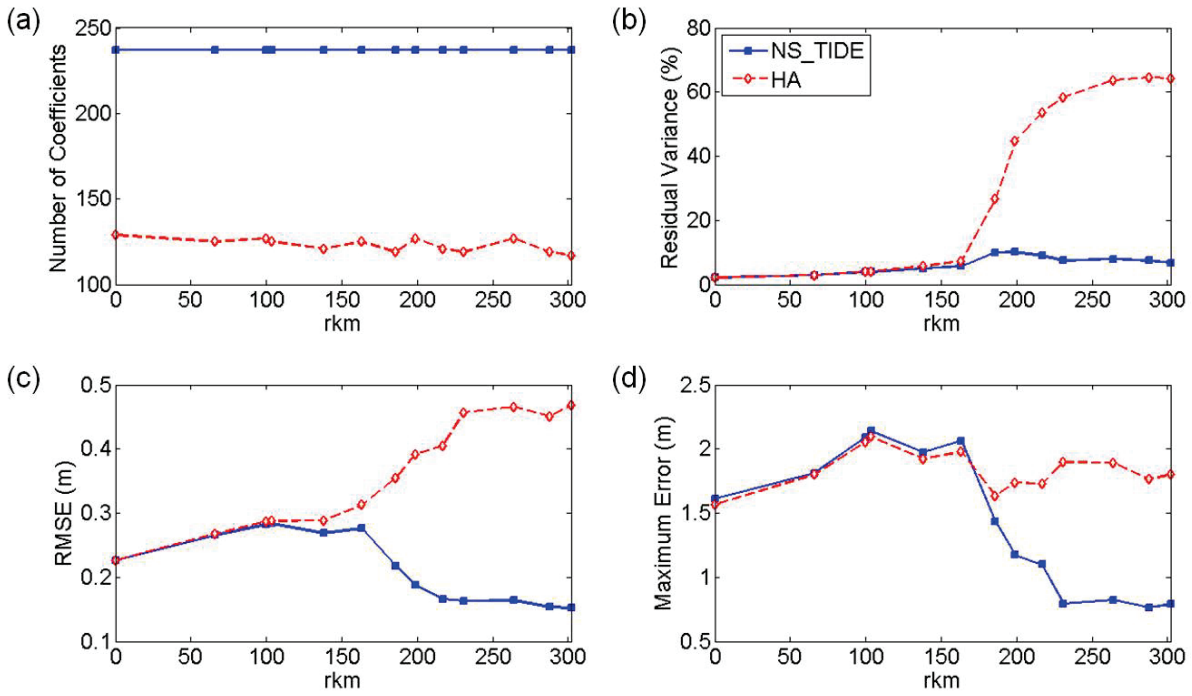


**Figure 1.3.6** **Statistiques sur les niveaux d'eau reproduits par NS_TIDE et par l'analyse harmonique classique (HA) aux stations d'analyse pour la période 1999-2009.**

Pour valider le modèle, des prédictions du niveau d'eau ont été produites et comparées aux observations sur une période allant du 21 mai au 21 octobre 2009, pour l'ensemble des 32 stations [cf. Table 2.3.1 (p. 137) et Table 2.3.2 (p. 137)]. Les performances du modèle ONE-D ont également été évaluées pour la même période (Figure 1.3.7). De façon générale, les variances et les erreurs moyennes quadratiques et maximales sont inférieures avec ONE-D qu'avec NS_TIDE, à l'exception de quelques stations à l'amont. Ce résultat est conforme aux attentes du modèle ONE-D, qui comprend beaucoup plus de degrés de liberté que NS_TIDE. Composé de 1241 sections, décrites en termes de leur géométrie et de leur friction, ONE-D résout les

équations de Saint-Venant 1D en non-stationnaire sur la période définie. En comparaison, le modèle NS_TIDE est basé sur une solution analytique des équations de Saint-Venant (Jay, 1991) et est composé de 237 paramètres (ou 237 fonctions polynomiales d'Hermite pour le modèle spatial), invariants dans le temps. Bien que plus simple, ce modèle arrive à des erreurs quadratiques moyennes inférieures à 0.3 m sur l'ensemble des stations. Considérant les marnages de la marée dans l'estuaire fluvial du Saint-Laurent, pouvant excéder 5 m à l'aval, ces erreurs sont relativement faibles. De plus, le modèle NS_TIDE se démarque par sa simplicité, son efficacité et sa capacité à représenter les variations du niveau moyen et de la marée de manière très compacte, sans avoir recours à une description détaillée du terrain, par opposition aux modèles hydrodynamiques. La Figure 2.3.8 (p. 148) présente une analyse plus poussée des erreurs quadratiques moyennes obtenues séparément sur les niveaux moyens, les marnages, et les temps et hauteurs des marées hautes et basses; ces résultats sont discutés à la section 2.3.4.3.3.

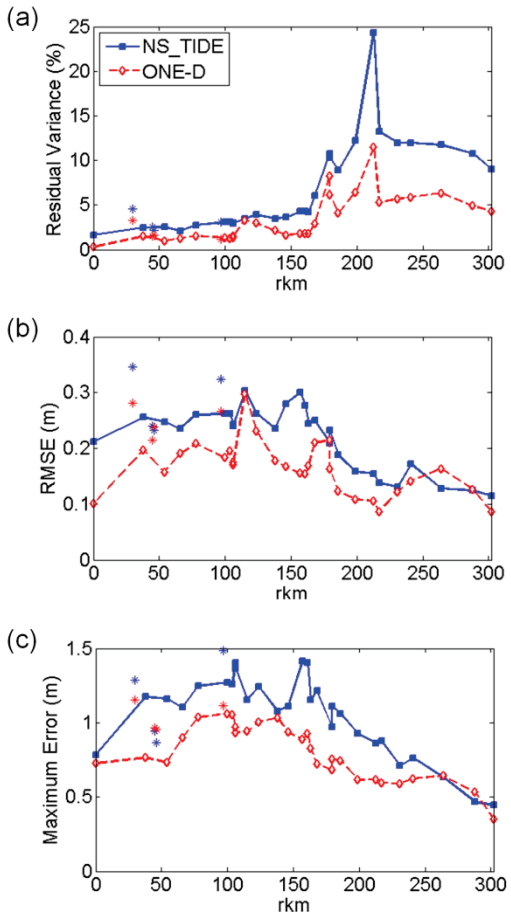


**Figure 1.3.7** **Statistiques sur les niveaux d'eau prédits par NS_TIDE et ONE-D sur l'ensemble des stations pour la période du 21 mai au 21 octobre 2009. Les stations identifiées par un astérisque ne sont pas couvertes par la branche principale du modèle ONE-D.**

### *1.3.2.2 Processus fluvio-tidaux*

Une démonstration du potentiel du modèle à améliorer les connaissances des processus fluvio-tidaux l'estuaire fluvial du Saint-Laurent est faite aux Figure 1.3.8 à Figure 1.3.11. L'objectif n'étant pas de fournir une analyse exhaustive des processus dynamiques en place, les résultats ont été restreints au modèle du niveau moyen et à cinq composantes majeures du modèle fluvio-tidal, pour les bandes diurne, semi-diurne et quart-diurne (cf. section 2.3.4.3.4).

Les profils longitudinaux du niveau moyen sont présentés à la Figure 1.3.8 pour les quantiles 0.1, 0.5 et 0.9 du débit fluvial et du marnage océanique. Les pentes du niveau moyen font clairement ressortir trois zones contrastées dans l'estuaire fluvial, tel que suggéré par Godin (1999), séparées par des brisures de pentes autour de Portneuf (rkm 163.5) et Cap-à-la-Roche (rkm 186). La région délimitée par ces deux stations forme une zone de transition entre les régimes tidal et fluvio-tidal, caractérisée par une forte augmentation de la pente du lit aux rapides Richelieu près de Deschambault (rkm 168). Cette observation supporte l'idée que des changements morphologiques abrupts soient responsables de la séparation d'un système en une partie dominée par la marée et une partie contrôlée par les variations du débit fluvial (Sassi *et al.*, 2012). Un saut dans les niveaux moyens apparait également au rkm 235, qui correspond à l'emplacement du pont Laviolette, lequel agit comme une restriction majeure à l'écoulement. Une quatrième zone peut donc être définie à partir de ce point, situé près de l'entrée du lac Saint-Pierre, jusqu'à Lanoraie, où la marée semi-diurne s'éteint complètement en marées de mortes-eaux. Dans la zone amont, la sensibilité des niveaux moyens aux variations du débit augmente considérablement, alors qu'ils sont peu affectés par le débit aux stations les plus en aval. De plus, à plus fort marnage, les niveaux moyens sont plus élevés, et vice versa, ce qui est en accord avec les variations semi-mensuelles de la marée décrites par LeBlond (1979). Aussi, ces variations dues au marnage sont plus importantes à faible débit.

La Figure 1.3.9 présente les profils longitudinaux des amplitudes et phases des composantes diurnes dominantes, $O_1$ et $K_1$. Comme les niveaux moyens (Figure 1.3.8), leurs variations longitudinales peuvent être groupées selon les quatre mêmes zones. Une diminution lente des amplitudes se fait sentir dans la portion en aval de Portneuf (rkm 163.5), suivie d'une diminution rapide en amont. Ce n'est toutefois qu'à partir de Cap-à-la-Roche (rkm 186) que les amplitudes s'atténuent avec une augmentation du débit. Passé le pont Laviolette (rkm 235), la diminution

des amplitudes est ralentie. Jusqu'à Portneuf, $K_1$ est la composante diurne dominante et son amplitude est supérieure à $O_1$. Toutefois, les amplitudes de $K_1$ et $O_1$ se rejoignent autour de Portneuf et $K_1$ se trouve atténuée légèrement plus rapidement que $O_1$, possiblement en raison de sa fréquence plus élevée (Godin, 1999). De même, des changements de pente dans les phases de $O_1$ et $K_1$ à partir de Portneuf signifient une propagation plus lente de l'onde de marée vers l'amont. Les temps de propagation présentent également des comportements inverses entre l'amont et l'aval en fonction du marnage. Des observations similaires peuvent être faites à partir des composantes semi-diurnes dominantes, $M_2$ et $S_2$ (Figure 1.3.10). L'une des caractéristiques que font ressortir les analyses, à première vue contre-intuitive, concerne l'effet du marnage sur les amplitudes de $M_2$ et $S_2$. Ces composantes, lorsque combinées, sont responsables des modulations semi-mensuelles (14.77 jours) de la marée. À fort marnage (c.-à-d. en marées de vives-eaux), $M_2$ et $S_2$ sont en phase et leur amplitude s'additionne l'une avec l'autre. Toutefois, tel qu'illustré à la Figure 1.3.10, l'augmentation du marnage a pour effet de réduire l'amplitude de $S_2$, alors que l'effet sur $M_2$ est faible, à l'exception des premiers ~80 rkm. Cela signifie qu'en marées de vives-eaux la somme de leur amplitude est plus petite qu'elle le serait en l'absence de friction. Par ailleurs, en comparant les profils de décroissance de l'amplitude des composantes diurnes et semi-diurnes des Figure 1.3.9 et Figure 1.3.10, on note une atténuation plus rapide des amplitudes des composantes semi-diurnes par rapport aux composantes diurnes.

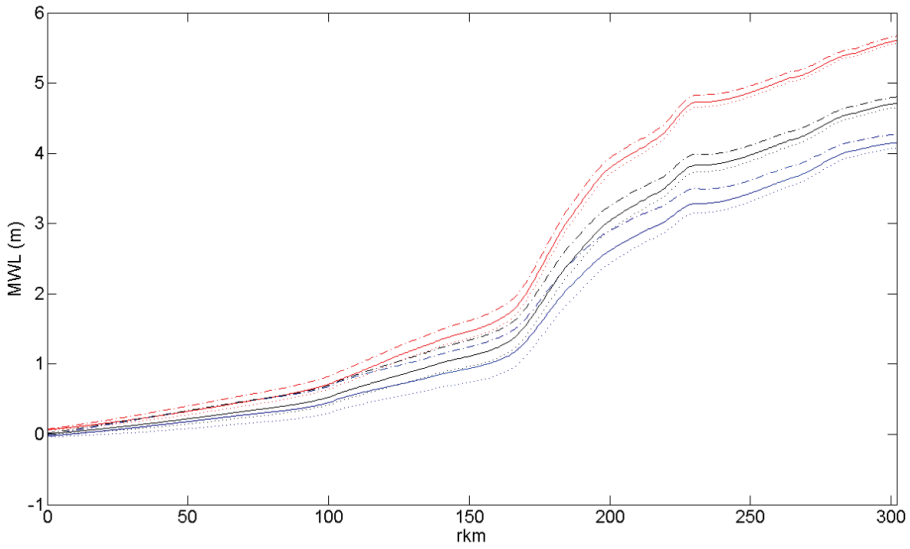


**Figure 1.3.8** **Profils longitudinaux des niveaux moyens (MWL) pour des quantiles de débit fluvial et de marnage océanique. Les lignes bleue, noire et rouge correspondent aux quantiles 0.1, 0.5 et 0.9 du débit; les lignes pointillée, pleine et tiret-pointillée correspondent aux quantiles 0.1, 0.5 et 0.9 du marnage, respectivement.**

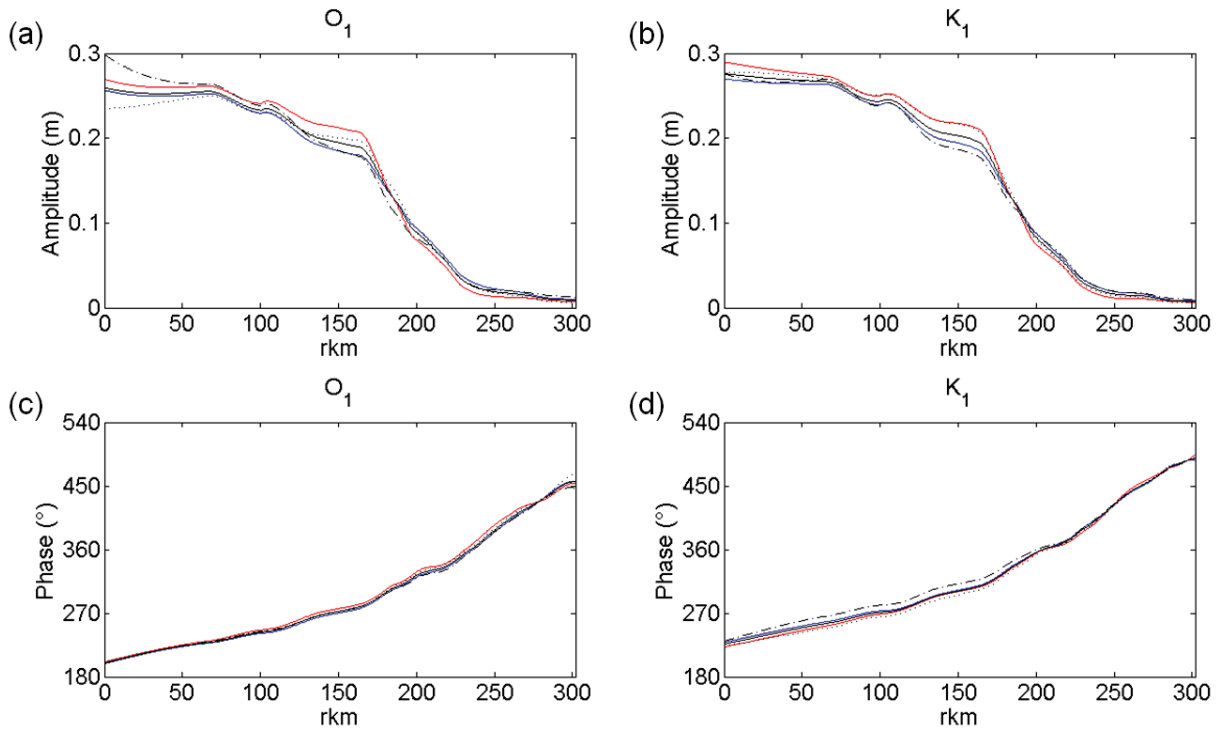


**Figure 1.3.9** **Similaire à la Figure 1.3.8 pour les amplitudes et les phases des composantes $O_1$ et $K_1$.**

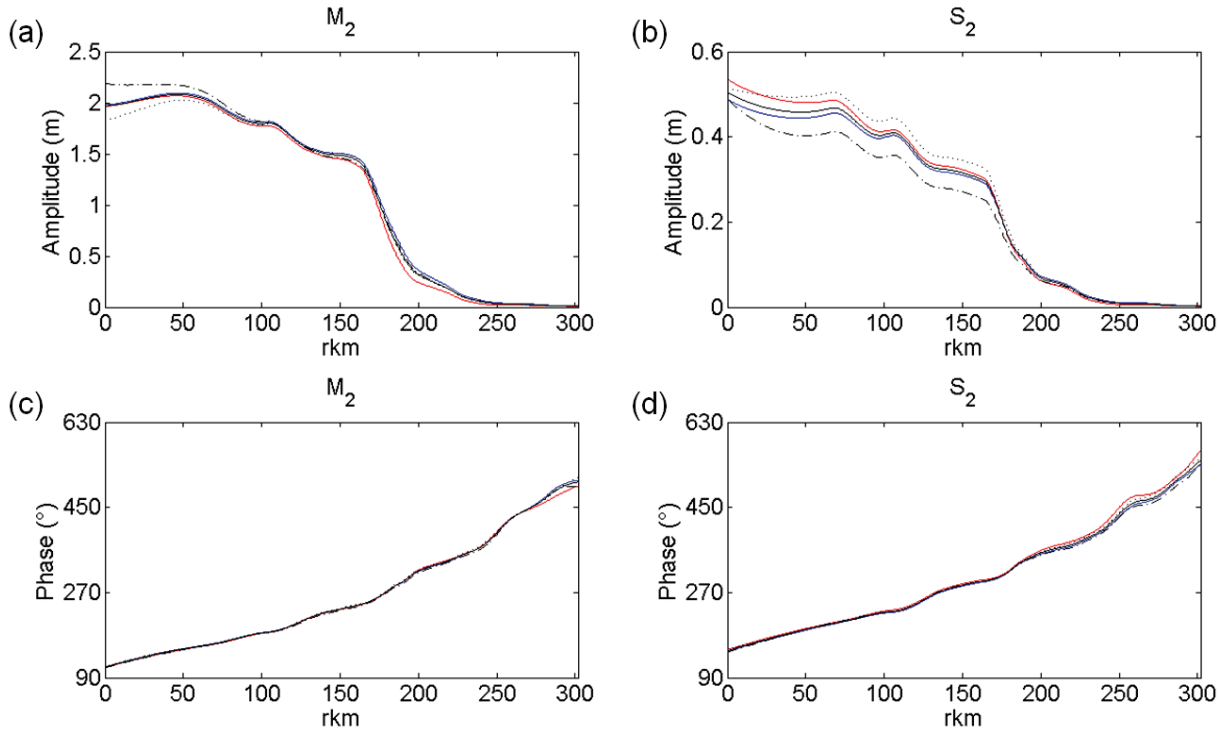


**Figure 1.3.10** **Similaire à la Figure 1.3.8 pour les amplitudes et les phases des composantes $M_2$ et $S_2$.**

La Figure 1.3.11 présente le ratio des amplitudes $M_4/M_2$ et les différences de phases $2M_2–M_4$ en fonction de la distance. En dépit des oscillations observées, une augmentation du ratio des amplitudes $M_4/M_2$ est observée jusqu'à Port Saint-François (rkm 241), indiquant un transfert d'énergie de $M_2$ vers $M_4$ à travers la friction, amplifié en amont dû à l'influence grandissante du débit. Le ratio des amplitudes subit une rapide diminution dans le lac Saint-Pierre alors que la majeure partie du signal de marée est atténuée, $M_4$ étant amortie plus rapidement que $M_2$ en raison de sa fréquence plus élevée. Des observations similaires peuvent être faites en relation avec les variations du débit fluvial (cf. section 2.3.4.3.4). Passé Cap-à-la-Roche (rkm 186), $M_4$ se trouve davantage atténuée par le débit que créée via les interactions non-linéaires à partir de $M_2$. Les variations associées au marnage, quant à elles, peuvent une fois de plus sembler contre-intuitive. En effet, le ratio des amplitudes $M_4/M_2$ se trouve réduit à mesure qu'augmente le marnage, contrairement à ce qui serait attendu. L'une des explications les plus probables est que l'approche utilisée dans ce dernier cas diffère drastiquement des méthodes traditionnelles [par exemple, les méthodes d'analyse par ondelettes (Jay & Flinchem, 1997, 1999, Jay & Kukulka, 2003) ou le concept de vecteur réduit (George & Simon, 1984)] qui ne permettent pas la séparation des fréquences voisines à l'intérieur d'une bande de fréquences donnée, ou espèce (diurne, semi-diurne, etc.). L'amplitude des composantes calculée par ces méthodes correspond donc à l'énergie totale contenue dans leur bande respective. La comparaison directe des résultats de NS_TIDE avec les méthodes traditionnelles doit donc tenir compte de cette caractéristique. Ainsi, prises individuellement, les composantes d'une même espèce sont susceptibles de répondre différemment à des variations de débit et de marnage. Par exemple, le transfert d'énergie de $M_2$ vers les fréquences supérieures implique non seulement $M_4$, mais aussi $MN_4$, $MS_4$, etc. Les résultats sont donc dépendants du nombre de composantes incluses dans l'analyse. Enfin, les différences de phases $2M_2–M_4$ dans la Figure 1.3.11, inférieures à 180°, indiquent une asymétrie de la marée caractérisée par une durée du flot écourtée et une montée plus abrupte des niveaux d'eau par comparaison avec le jusant (Friedrichs & Aubrey, 1988). À mesure que ces différences de phases approchent les 180°, cette asymétrie se voit accentuée.

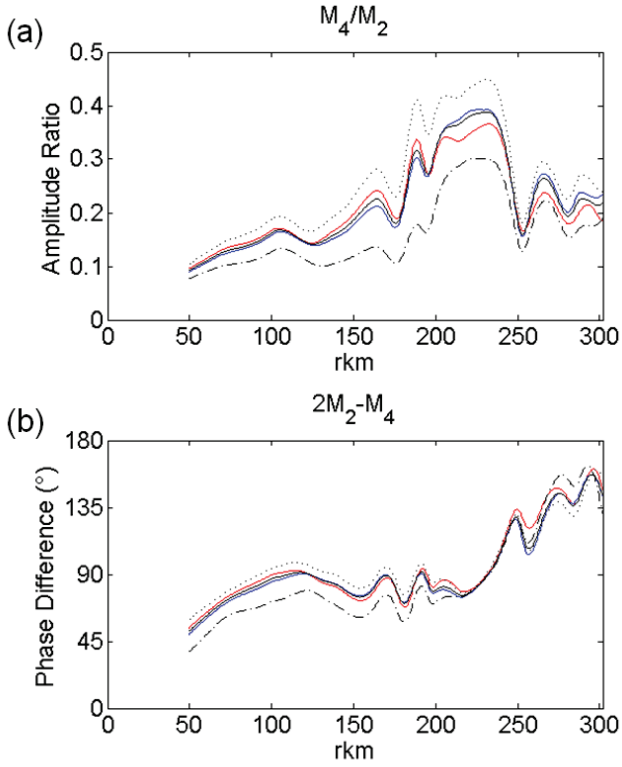


**Figure 1.3.11** **Similaire à la Figure 1.3.8 pour les ratios d'amplitudes $M_4/M_2$ et les différences de phases $2M_2–M_4$.**

### *1.3.2.3 Reconstruction des débits tidaux*

La Figure 1.3.12 présente pour la période du 18 au 19 juin 2009 les débits tidaux calculés par la méthode de cubature pour l'ensemble des transects. Les débits tidaux représentent uniquement la composante des débits associée à la marée, à laquelle s'ajoute le débit moyen pour former le débit total. De façon générale, les prédictions de débits suivent bien les variations des débits mesurés lors de la campagne de 2009. Notamment, les temps d'occurrence des étales de courants et des débits minimums et maximums sont très bien reproduits pour les stations en aval de Deschambault (Figure A.2.11 à Figure A.2.15, pp. 277–279). L'amplitude des variations de débits sur un cycle de marée est toutefois légèrement sous-estimée par la méthode. En amont de Deschambault (Figure A.2.7 à Figure A.2.10, pp. 275–276), les cycles de débits se trouvent légèrement déphasés par rapport aux débits mesurés. Les niveaux extraits du modèle de propagation de la marée, utilisés lors du calcul, sont entachés d'une plus grande erreur aux

stations en amont du système, lorsque mis en relation avec le marnage (cf. section 2.3.4.3); les différences entre les niveaux prédits et mesurés en témoignent. Les marées sont en effet très non-linéaires et difficiles à prédire dans cette portion du fleuve, particulièrement les temps d'arrivée des marées basses et l'asymétrie de la marée, tous deux dictés en majeure partie par les composantes quart-diurnes. Ces dernières souffrent d'une erreur d'interpolation plus importante en raison de leur courte longueur d'onde (cf. section 2.3.5), qui se répercute sur les débits calculés. À ces erreurs s'ajoutent le transfert des niveaux du modèle 1D vers un maillage 2D, les erreurs de topographie des berges servant à définir le domaine d'intégration, de même que les variations latérales des niveaux d'eau dans les régions où des gradients latéraux sont attendus (ex.: estrans, zones de forte courbure du chenal). La méthode permet néanmoins de reconstruire, à relativement faible coût et avec une bonne précision, les débits tidaux en n'importe quelle section du domaine, pour n'importe quelle période passée ou future, ce qui représente un avantage considérable. La disponibilité d'une description 2D de la topographie, bien que plus complexe, est un atout pour la prise en compte des estrans dans le calcul, mais peut facilement être remplacée par une représentation 1D, ou par sections (ex.: Forrester, 1972), de la géométrie du système.

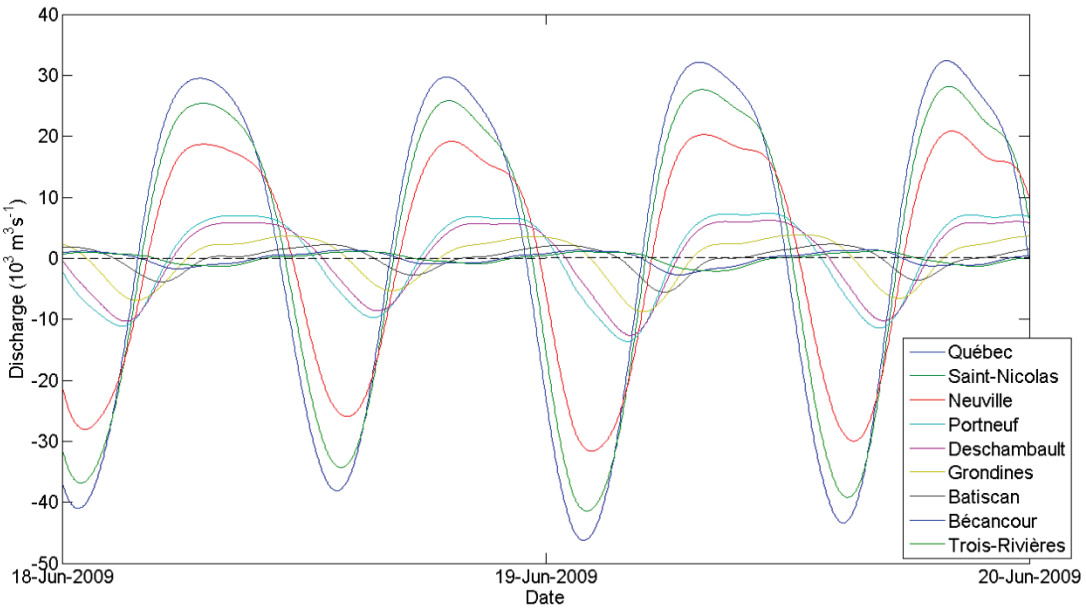


**Figure 1.3.12 Débits tidaux calculés par la méthode de cubature pour l'ensemble des stations, pour la période du 18 au 19 juin 2009.**

### 1.3.3 Modèle hydrodynamique 2D

Dans cette section, les résultats d'étalonnage du modèle hydrodynamique décrit à la section 1.2.3 sont présentés. L'habileté du modèle à reproduire les caractéristiques de la marée et des écoulements, telles qu'observées dans les données, est également évaluée. Cette évaluation est présentée de manière détaillée à la section 2.4.4 de cette thèse. Les résultats du modèle sur l'ensemble des sections de mesure sont présentés en supplément à l'annexe A.3.

#### *1.3.3.1 Performance du modèle*

Les résultats d'étalonnage et d'assimilation du modèle hydrodynamique 2D de l'estuaire fluvial du Saint-Laurent sont présentés, séparément pour les segments amont et aval du modèle, aux Table 2.4.1 (p. 178) et Table 2.4.2 (p. 178), respectivement. La Table 1.3.1 présente, quant à elle, les résultats pour l'ensemble des stations du modèle global (cf. Figure 1.1.1). Les erreurs faites dans la portion aval du modèle (Table 2.4.2, p. 178) se propagent vers l'amont, augmentant par le fait même les écarts entre les niveaux observés et simulés de plusieurs cm aux stations amont, par comparaison avec les résultats de la Table 2.4.1 (p. 178). Globalement, les erreurs en niveaux d'eau s'expliquent par des marnages trop faibles dans les premiers 78 rkm et sont dominées par des niveaux moyens trop bas à Beauport (rkm 97), avec des écarts moyens de l'ordre de 20 cm. Une augmentation du frottement autour de l'île d'Orléans est donc susceptible d'améliorer les prédictions du modèle sur l'ensemble du domaine (les tests d'assimilation de la condition limite aval n'ayant pas été concluants). Malgré ces différences, la compétence (« skill ») du modèle est supérieure à 0.992 pour l'ensemble des stations. Ces valeurs élevées s'expliquent par les forts marnages caractérisant la région, qui excèdent régulièrement les 5 m. Ainsi, pour les stations en aval de Batiscan (rkm 199), les erreurs quadratiques moyennes sont inférieures à 5% du marnage local. Aux stations en amont, ce ratio augmente dû à l'atténuation rapide du signal de marée, alors que les erreurs quadratiques moyennes demeurent inférieures à 6 cm.

Par ailleurs, une augmentation des écarts entre les niveaux d'eau mesurés et simulés est observable entre les périodes de simulation de juin et août, particulièrement à Bécancour (cf. Figure 2.4.6, p. 181). Les niveaux moyens se trouvent en effet sous-estimés en août par rapport à juin. Ces différences s'expliquent par une hausse graduelle des frottements dans le haut-fond de Gentilly, quelques km en aval de Bécancour, qui suit la croissance des macrophytes durant l'été. Cette augmentation n'est pas prise en compte par le modèle, puisque la même répartition des

frottements (cf. Figure 1.2.4) a été utilisée pour les deux périodes. Une friction qui varie dans le temps en fonction de la densité et de la phase de croissance des plantes aquatiques présentes pourrait être utilisée pour tenir compte de ces variations (Morin *et al.*, 2000b).

**Table 1.3.1** **Validation du modèle global: RMSE et compétence (« skill ») pour les niveaux simulés (original), les niveaux moyens (MWL) et le marnage sur l'ensemble des stations pour chaque période de simulation de 15 jours.**

| rkm | Stations | 14–29 Juin, 2009 | | | | 19 Août–3 Sept, 2009 | | | |
|---|---|---|---|---|---|---|---|---|---|
| | | RMSE (m) | | | Skill | RMSE (m) | | | Skill |
| | | Original | MWL | Marnage | | Original | MWL | Marnage | |
| 0 | Saint-Joseph-de-la-Rive | 0.095 | 0.013 | 0.064 | 0.999 | 0.091 | 0.021 | 0.066 | 0.999 |
| 30 | Islet-sur-Mer | 0.130 | 0.031 | 0.303 | 0.998 | 0.143 | 0.051 | 0.319 | 0.998 |
| 38 | Rocher Neptune | 0.103 | 0.067 | 0.198 | 0.999 | – | – | – | – |
| 45 | Ile-aux-Grues Sud | 0.110 | 0.057 | 0.212 | 0.999 | 0.145 | 0.107 | 0.193 | 0.998 |
| 46 | Ile-aux-Grues Nord | 0.154 | 0.115 | 0.293 | 0.998 | 0.135 | 0.098 | 0.271 | 0.998 |
| 54 | Banc du Cap Brûlé | 0.100 | 0.047 | 0.195 | 0.999 | 0.113 | 0.049 | 0.192 | 0.999 |
| 66 | Saint-François | 0.124 | 0.078 | 0.243 | 0.999 | 0.121 | 0.061 | 0.249 | 0.998 |
| 78 | Saint-Jean | 0.166 | 0.147 | 0.194 | 0.997 | 0.108 | 0.058 | 0.202 | 0.999 |
| 97 | Beauport | 0.221 | 0.198 | 0.064 | 0.995 | 0.160 | 0.120 | 0.058 | 0.997 |
| 100 | Lauzon | 0.185 | 0.155 | 0.074 | 0.996 | 0.133 | 0.076 | 0.084 | 0.998 |
| 104 | Saint-Charles River | 0.182 | 0.147 | 0.102 | 0.996 | 0.136 | 0.075 | 0.099 | 0.998 |
| 106.5 | Lévis | 0.175 | 0.137 | 0.102 | 0.997 | 0.133 | 0.069 | 0.086 | 0.998 |
| 106.5 | Québec | 0.177 | 0.141 | 0.086 | 0.997 | 0.132 | 0.072 | 0.088 | 0.998 |
| 115 | Québec Bridge | 0.177 | 0.140 | 0.040 | 0.996 | 0.131 | 0.069 | 0.079 | 0.998 |
| 124 | Saint-Nicolas | 0.138 | 0.112 | 0.087 | 0.998 | 0.104 | 0.062 | 0.078 | 0.999 |
| 138 | Neuville | 0.135 | 0.107 | 0.135 | 0.997 | 0.107 | 0.057 | 0.116 | 0.998 |
| 146 | Sainte-Croix-Est | 0.123 | 0.096 | 0.062 | 0.997 | 0.111 | 0.061 | 0.103 | 0.998 |
| 157 | Cap-Santé | 0.125 | 0.102 | 0.109 | 0.997 | 0.107 | 0.066 | 0.095 | 0.998 |
| 161 | Pointe-Platon | 0.118 | 0.094 | 0.083 | 0.997 | 0.109 | 0.066 | 0.085 | 0.998 |
| 163.5 | Portneuf | 0.089 | 0.062 | 0.056 | 0.999 | 0.121 | 0.086 | 0.076 | 0.997 |
| 168 | Deschambault | 0.106 | 0.069 | 0.139 | 0.997 | 0.126 | 0.074 | 0.222 | 0.996 |
| 179.5 | Leclercville | – | – | 0.029 | – | – | – | 0.042 | – |
| 179.5 | Grondines | 0.070 | 0.054 | 0.029 | 0.997 | 0.111 | 0.087 | 0.044 | 0.993 |
| 186 | Cap-à-la-Roche | 0.070 | 0.055 | 0.036 | 0.996 | 0.080 | 0.050 | 0.061 | 0.996 |
| 199 | Batiscan | 0.040 | 0.027 | 0.037 | 0.996 | 0.060 | 0.044 | 0.063 | 0.994 |
| 213 | Champlain | 0.046 | 0.035 | 0.074 | 0.992 | 0.058 | 0.037 | 0.056 | 0.992 |
| 217 | Bécancour | 0.027 | 0.010 | 0.042 | 0.997 | 0.056 | 0.048 | 0.036 | 0.992 |
| 231 | Trois-Rivières | 0.025 | 0.022 | 0.019 | 0.992 | 0.015 | 0.005 | 0.008 | 0.999 |
| 241 | Port Saint-François | 0.008 | 0.007 | 0.007 | 0.999 | 0.007 | 0.006 | 0.005 | 1.000 |

Pour évaluer la capacité du modèle à représenter le contenu fréquentiel de la marée, une analyse harmonique (Pawlowicz *et al.*, 2002) des signaux mesurés et simulés a été réalisée pour chaque station du modèle global, séparément pour les deux périodes de simulation. Les erreurs quadratiques moyennes et la compétence (« skill ») du modèle ont été calculées pour les 9

composantes les plus significatives, parmi 17 résolues. Les résultats sont présentés à la Table 1.3.2. Il en ressort que les niveaux moyens sont bien représentés par la composante de basse fréquence MSf. Les RMSE les plus élevées sont obtenues avec la composante dominante $M_2$; toutefois, l'amplitude de cette dernière excède les 2 m aux stations aval, d'où les valeurs de compétence parmi les plus élevées (0.998) des composantes analysées. Les phases sont également bien reproduites par le modèle, indiquant un bon synchronisme des marées hautes et basses. De plus, l'asymétrie de la marée, qui s'estime par l'importance relative des composantes $M_2$ et $M_4$, est représentée de manière adéquate par le modèle, leurs critères de compétence respectifs figurant parmi les plus élevés ($\geq 0.996$). Les erreurs de phase se dégradent pour les composantes de hautes fréquences $M_6$ et $M_8$. Toutefois, ces erreurs sont minimales aux stations les plus en amont, là où ces composantes sont les plus significatives, se trouvant amplifiées par les interactions non-linéaires de $M_2$ dues à la friction et au débit fluvial.

**Table 1.3.2 Statistiques des amplitudes et phases des principales composantes de la marée calculées sur l'ensemble des stations du modèle global, pour chaque période de simulation de 15 jours.**

| Composante | 14–29 Juin, 2009 | | | 19 Août–3 Sept, 2009 | | |
|---|---|---|---|---|---|---|
| | Amplitude | | Phase | Amplitude | | Phase |
| | RMSE (m) | Skill | RMSE (°) | RMSE (m) | Skill | RMSE (°) |
| MSf | 0.020 | 0.981 | 5.5 | 0.034 | 0.966 | 4.1 |
| $O_1$ | 0.009 | 0.997 | 2.9 | 0.011 | 0.992 | 2.6 |
| $K_1$ | 0.019 | 0.988 | 2.7 | 0.008 | 0.997 | 4.4 |
| $M_2$ | 0.066 | 0.998 | 1.5 | 0.059 | 0.998 | 1.9 |
| $S_2$ | 0.010 | 0.997 | 7.4 | 0.035 | 0.993 | 4.3 |
| $M_3$ | 0.010 | 0.975 | 2.4 | 0.005 | 0.980 | 9.2 |
| $M_4$ | 0.015 | 0.996 | 7.2 | 0.019 | 0.996 | 6.7 |
| $M_6$ | 0.009 | 0.986 | 17.8 | 0.016 | 0.982 | 15.5 |
| $M_8$ | 0.006 | 0.991 | 15.8 | 0.011 | 0.961 | 23.4 |

### *1.3.3.2 Reproduction des caractéristiques de l'écoulement*

Une comparaison des niveaux d'eau observés et simulés le long de la section de Grondines est présentée à la Figure 1.3.13, pour un cycle semi-diurne de marée. La concordance des niveaux simulés avec les champs interpolés à partir des mesures est bonne. De façon générale, les marées basses et hautes sont synchronisées et les patrons latéraux sont bien reproduits. Plus particulièrement, un gradient latéral des niveaux se forme en marée descendante, responsable du vidage des estrans vers le chenal. La Figure 2.4.8 (p. 184) quantifie ces variations sur la section pour

différentes variables extraites des champs de niveaux d'eau. Les hauteurs de marées basse et haute se trouvent légèrement surestimées par le modèle ($\sim<$ 10 cm) et le marnage est sous-estimé, indicateurs d'une friction légèrement trop importante aux environs de Grondines. Seule une partie de ces différences peut être attribuable aux erreurs de mesure et d'interpolation, ces dernières ne s'élevant qu'à quelques cm [cf. Table 2.2.3 (p. 103) et Table 2.2.7 (p. 120)].

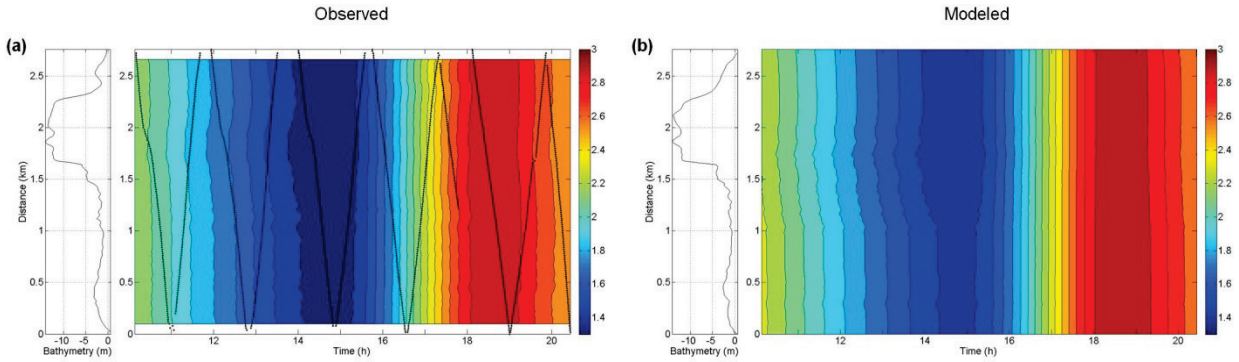


**Figure 1.3.13** **(a) Niveaux d'eau observés et (b) simulés (en m) à Grondines le 19 juin 2009, en fonction du temps et de la distance le long de la section.**

Les variations latérales des composantes *u* et *v* de la vitesse, moyennées sur la verticale, sont présentées à la Figure 1.3.14, pour un cycle semi-diurne de marée à Grondines. Les vitesses longitudinales (*u*) sont maximales au centre du chenal, alors que les vitesses transversales (*v*) présentent deux zones de forte vitesse distinctes, dont les valeurs sont légèrement supérieures dans le modèle par rapport aux mesures. Les vitesses *v* plus élevées dans la région la plus au sud (entre les km 1 et 1.5) résultent de la vidange des estrans. Dans la seconde zone (entre les km 1.5 et 2), on associe cette augmentation à l'effet de la courbure du chenal sur la direction du courant. Une inversion de courant est également observée, uniquement sur la rive nord. Ces caractéristiques de l'écoulement sont bien reproduites par le modèle, ce qui suggère que les variations latérales de la topographie et de la friction telles que modélisées représentent la réalité du terrain de manière adéquate. Une évaluation des différences entre le modèle et les mesures est faite à la Figure 2.4.10 (p. 186) à partir de variables directement extraites des champs de vitesses. Une partie des différences observées s'explique par les erreurs en vitesses issues des données, qui avoisinent les 0.1 m $s^{-1}$ en moyenne à Grondines (cf. Table 2.2.6, p. 119).

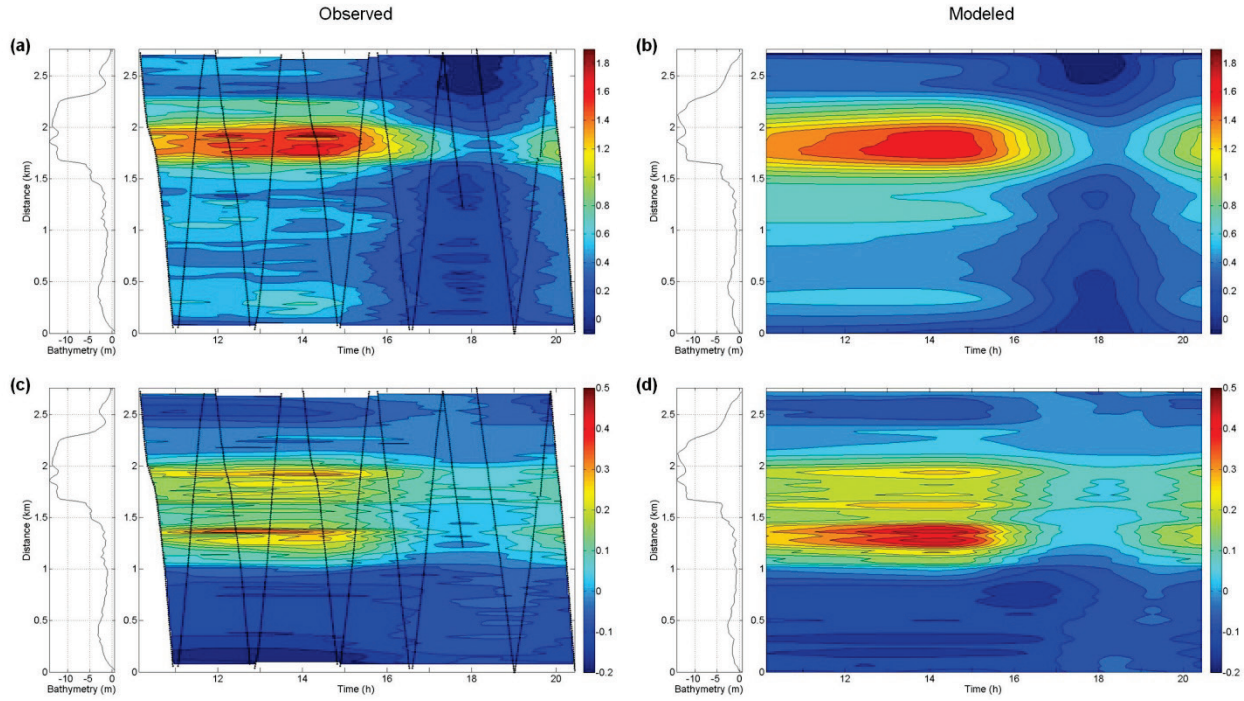


**Figure 1.3.14** **(a) Vitesses *u* observées et (b) simulées (en m $s^{-1}$) à Grondines le 19 juin 2009, en fonction du temps et de la distance le long de la section. (c) Vitesses *v* observées et (d) simulées.**

L'une des manifestations de la variabilité semi-mensuelle associée au cycle de marées de mortes-eaux et de vives-eaux s'observe dans la position de la limite amont d'inversion de courant, qui se déplace entre Grondines et Bécancour en fonction du marnage de la marée et du débit fluvial. La Figure 1.3.15 en fait l'illustration, où l'orientation des vitesses est présentée le long des sections de Grondines (rkm 179.5) et de Batiscan (rkm 199) sur un cycle semi-diurne de marée, à deux différents stades sur le cycle de marées de mortes-eaux et de vives-eaux. En marée de mortes-eaux, les courants s'inversent à peine à Grondines; l'inversion se produit sur une distance d'environ 200 m à partir de la rive nord. En marée de vives-eaux, une inversion de courant complète se produit à Batiscan (~20 km en amont de Grondines), sur toute la section, avec une durée écourtée au centre du chenal. Le modèle parvient donc à bien décrire la variabilité latérale et longitudinale des inversions de courant sur le cycle semi-mensuel de la marée, en comparaison avec les mesures.

La division du débit à la jonction de chenaux multiples soumis à la marée est en partie influencée par la topographie et la friction des branches individuelles (Buschman *et al.*, 2010). Au niveau de l'île d'Orléans, la division du débit sur un cycle semi-diurne de marée a été mesurée pour chacun des bras nord et sud, puis comparée au modèle (Figure 2.4.12, p. 189). Ce dernier distribue de

façon adéquate les débits de chaque côté de l'île. En marée de vives-eaux, les débits dépassent les 60 000 $m^3s^{-1}$ au jusant dans le bras sud, alors qu'ils atteignent les 10 000 $m^3s^{-1}$ dans le bras nord. Ces différences sont attribuables à la géométrie des chenaux, les plus grandes profondeurs et les plus larges sections se trouvant dans le bras sud de l'île d'Orléans.

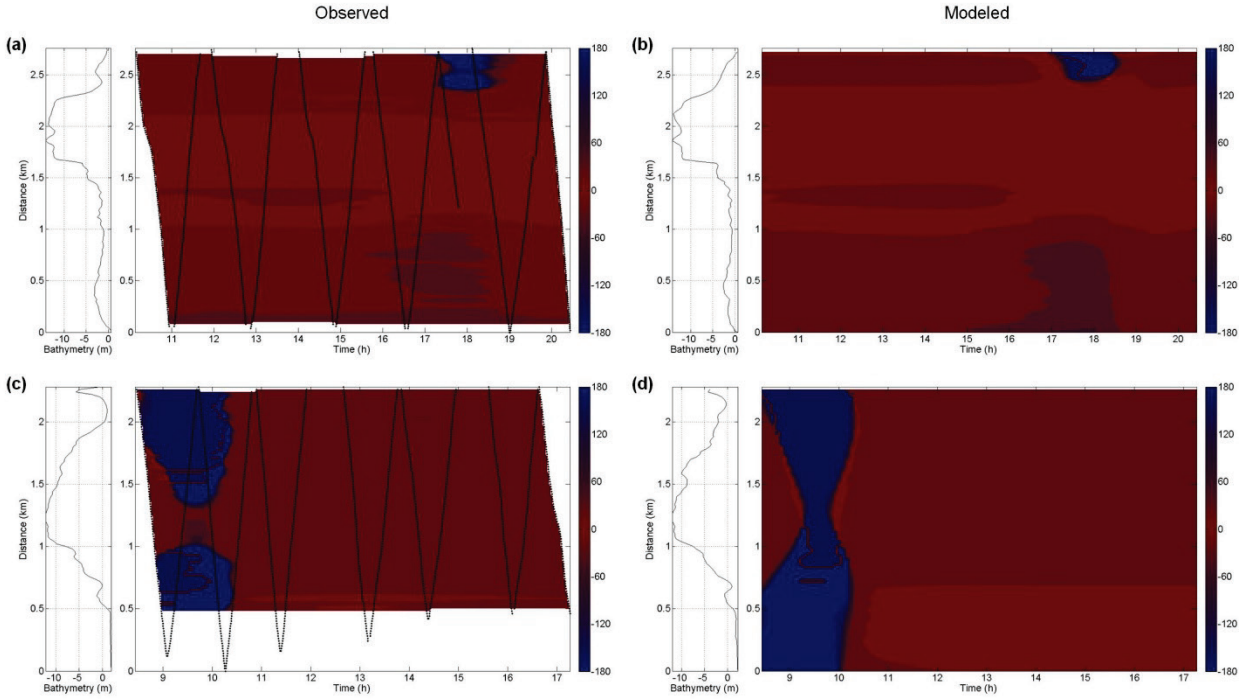


**Figure 1.3.15** **Variabilité semi-mensuelle dans la position de la limite amont d'inversion de courant. (a) Orientation des vitesses mesurées et (b) simulées (en m $s^{-1}$) à Grondines (rkm 179.5) le 19 juin 2009 (marée de morte-eau), en fonction du temps et de la distance le long de la section. (c) Orientation des vitesses mesurées et (b) simulées à Batiscan (rkm 199) le 23 juin 2009 (marée de vive-eau). Un vecteur d'angle 0° est orienté vers l'aval et perpendiculaire à la section.**

La Figure 1.3.16 présente les vitesses simulées à la jonction de l'île d'Orléans à différents stades de la marée. Les résultats présentés correspondent à une marée de vive-eau, mesurée à Lauzon le 24 juin 2009, en conditions de débit moyen (11 100 $m^3$ $s^{-1}$). À marée haute, les courants sont inversés dans les deux bras de l'île d'Orléans, avec des vitesses atteignant 1.5 m $s^{-1}$ dans les zones les plus profondes. Une heure après la marée haute, les courants sont considérablement affaiblis et des recirculations apparaissent dans les zones peu profondes où les courants sont redirigés vers l'aval. Deux heures après la marée haute, les courants sont orientés vers l'aval et gagnent en importance à mesure que la marée baisse; les zones intertidales se trouvent progressivement exondées. Les courants atteignent leur maximum environ une heure avant la marée

basse, avec des vitesses de 2.3 $m\,s^{-1}$. À marée basse, les courants diminuent; ils changent rapidement dans les heures qui suivent, la marée montante étant plus abrupte que la marée descendante. Une heure après la marée basse, l'étale de courant atteint Lauzon, mais les courants du jusant demeurent forts dans le bras nord de l'île d'Orléans. Deux heures après la marée basse, les courants sont complètement renversés dans le bras sud, alors qu'ils le sont partiellement dans le bras nord, une partie de l'eau provenant du bras sud étant déversée dans le bras nord. L'étale de courant arrive finalement dans le bras nord une heure avant la prochaine marée haute, les courants se renversant complètement de nouveau, pour une durée supplémentaire d'environ trois heures.

Une évaluation de la contribution respective de chacun des termes de l'équilibre des forces est présentée à la Figure 2.4.14 (p. 192). Cet équilibre oscille entre deux états dynamiques, similaires à ceux décrits par Hench and Luettich (2003), selon que la phase de la marée se situe près des vitesses maximales de jusant ou de flot, ou aux environs des étales de courant. L'écoulement est dominé par les gradients de pression lors du plein jusant et du plein flot, lesquels s'équilibrent avec les termes d'accélération convective et de friction – et dans une moindre mesure la force de Coriolis. La friction au fond excède en importance l'effet du gradient de pression presque exclusivement en zones peu profondes, tandis que le terme de Coriolis domine sur l'accélération convective pour des vitesses typiquement inférieure à 1 $m\,s^{-1}$. La turbulence, quant à elle, est un ordre de grandeur inférieure aux autres termes. Lors des étales, seuls les gradients de pression demeurent significatifs; ils s'équilibrent avec le terme d'accélération locale.

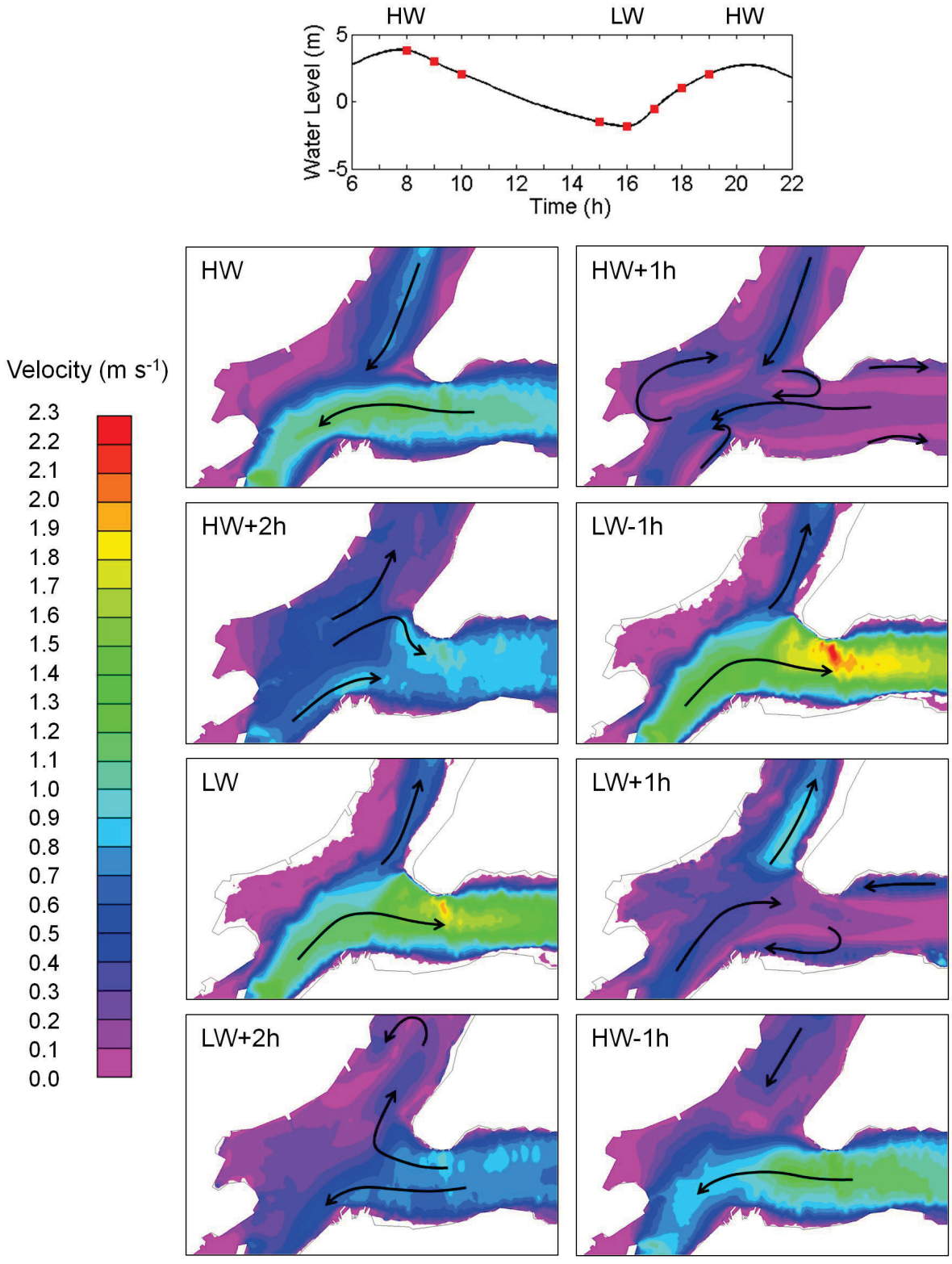


**Figure 1.3.16** **Vitesses simulées (en m $s^{-1}$) à la jonction de l'île d'Orléans à différents stades de la marée; les flèches indiquent la direction des courants. (haut) Signal de marée mesuré à Lauzon le 24 juin 2009 (marée de vive-eau), ainsi que les marées hautes (HW) et la marée basse (LW) correspondantes.**

## 1.4 Conclusion

Les travaux réalisés dans le cadre de cette thèse ont permis de décrire l'hydrodynamique complexe et peu documentée de l'estuaire fluvial du Saint-Laurent, tant par le biais de données de terrain que par l'entremise d'outils de modélisation, fournissant ainsi des moyens pour analyser et prédire l'évolution du système en réponse aux facteurs externes qui le contrôlent. Une grande emphase a été mise sur le développement de nouvelles méthodes d'analyse et de prédiction, afin de poser les bases de l'étude des systèmes fluvio-estuariens en général. Les caractéristiques physiques particulières de l'estuaire fluvial du Saint-Laurent, notamment sa taille et la variabilité spatiale et temporelle des processus, ont joué un rôle de premier plan dans l'élaboration des campagnes de terrain et le développement des outils, en orientant le choix des stratégies de mesure et d'analyse.

Les campagnes de mesures visant à décrire l'hydrodynamique non-stationnaire de systèmes très énergétiques comme le Saint-Laurent nécessitent une phase de planification rigoureuse, qui tient compte des critères et contraintes du terrain, des instruments et des utilisateurs. L'arrivée d'instruments à haute précision, tels que l'ADCP et le RTK GPS, a permis de faciliter la réalisation d'un tel travail. La combinaison de ces deux technologies dans l'estuaire fluvial du Saint-Laurent a permis l'acquisition simultanée de données de niveaux d'eau et de vitesses, essentielles à la caractérisation du milieu et au calcul précis des variables hydrodynamiques non-stationnaires comme le débit. Une stratégie d'échantillonnage par bateau et une procédure d'analyse des données ont été mises au point pour permettre la reconstruction de champs latéraux à la fois synoptiques et continus, en s'affranchissant d'hypothèses simplificatrices liées à la stationnarité ou à l'homogénéité des variables mesurées. Une quantification de l'erreur et une validation par l'entremise de mesures indépendantes ont permis d'établir un niveau de confiance élevé dans les données et leurs sous-produits. Ces dernières constituent le jeu de données le plus complet et détaillé à ce jour dans l'estuaire fluvial du Saint-Laurent, fournissant des connaissances nouvelles sur les propriétés de l'écoulement dans des régions contrastées du fleuve, à l'échelle intratidale – notamment les échanges entre les estrans et le chenal, qui affectent la propagation de la marée aussi bien que la dynamique d'inversion des courants. Ces données sont indispensables à la validation des modèles.

La prédiction des marées en rivières est compliquée par les interactions non-linéaires de la marée océanique avec la friction, le débit fluvial et la géométrie du milieu. De plus, l'influence externe de facteurs comme le débit perturbe le signal en modulant son amplitude et sa phase. Le potentiel de l'analyse harmonique non-stationnaire par NS_TIDE pour analyser et prédire les marées dans l'estuaire fluvial du Saint-Laurent a été démontré et validé à l'aide d'un réseau densifié de stations marégraphiques, et par comparaison avec l'analyse harmonique classique et le modèle hydrodynamique ONE-D, opérationnel sur le fleuve. L'interpolation spatiale des coefficients du modèle ont permis de reconstruire les propriétés du niveau moyen et de la marée de manière continue dans le système, en tenant compte de la contribution respective du débit fluvial et de la marée océanique. Ainsi, le modèle développé est capable de fournir une prédiction des niveaux d'eau en n'importe quel point du système. De plus, contrairement aux méthodes d'analyse traditionnelles, ce dernier présente l'avantage de pouvoir différencier plus d'une composante à l'intérieur de chaque bande de fréquences tidale, permettant une analyse plus approfondie des processus fluvio-tidaux. Notamment, les résultats suggèrent la séparation de l'estuaire fluvial en quatre zones contrastées et font ressortir les effets de la friction sur l'asymétrie du signal et sur l'amplitude et la phase des composantes dominantes de la marée. Bénéficiant de la compacité et de l'efficacité de l'analyse harmonique classique, cette approche basée sur des analyses par régression ne nécessite aucune description de terrain ni étalonnage, minimisant ainsi la sensibilité aux erreurs de topographie et de friction. Le modèle développé dans l'estuaire fluvial du Saint-Laurent vient ainsi complémenter les efforts de modélisation du système en permettant d'analyser les variations temporelles et spatiales dans le contenu fréquentiel de la marée.

L'évaluation, l'étalonnage et la validation des modèles hydrodynamiques non-stationnaires représentent un grand défi. Plusieurs auteurs ont décrit ce processus avec détails (ex.: Willmott, 1982, Willmott *et al.*, 1985, Hsu *et al.*, 1999, Umgiesser *et al.*, 2004, Warner *et al.*, 2005, Espino *et al.*, 2007, Jung *et al.*, 2012). L'évaluation de la performance d'un modèle est souvent limitée à une comparaison à des stations fixes de mesure (ex.: marégraphes). De plus, les sondages réalisés le long de sections transversales d'une rivière pour la mesure des vitesses, lorsque disponibles, accordent habituellement peu d'attention aux gradients latéraux en niveaux d'eau. Ces variations des niveaux et des vitesses sont toutefois fortement corrélées, surtout à proximité de fortes pentes de bathymétrie, renforçant la nécessité de considérer ces deux variables de façon conjointe dans le processus d'étalonnage et de validation d'un modèle.

La force des modèles hydrodynamiques réside dans leur capacité à déterminer la contribution respective des termes de l'équation de conservation du mouvement à la dynamique des écoulements, essentiels à une compréhension approfondie d'un système. Un modèle hydrodynamique 2D à haute résolution spatiale (~50 m en moyenne) de l'estuaire fluvial du Saint-Laurent a été développé en réponse au manque de connaissances dans cette région complexe du Saint-Laurent. Le modèle a été construit, étalonné et validé à partir du jeu de données le plus récent et détaillé dans ce secteur du fleuve, permettant d'atteindre des standards de qualité élevés – avec, notamment, des erreurs quadratiques moyennes inférieures à 5% du marnage local aux stations en aval de Batiscan (rkm 199) et inférieures à 6 cm aux stations en amont, ainsi que des critères de compétence (ou « skill ») supérieurs à 0.99 pour l'ensemble des stations. Ces résultats sont une preuve indirecte de la cohérence des données et de la validité du MNT. Une reproduction adéquate des propriétés de la marée et de la variabilité latérale et intratidale des niveaux d'eau et des vitesses a également été rendue possible sur un ensemble de sections de mesure réparties sur tout le système. De plus, la variabilité longitudinale des inversions de courant sur un cycle semi-mensuel de marées, aussi bien que la répartition des débits de part et d'autre de l'île d'Orléans ont pu être évaluées, démontrant par le fait même la validité et la capacité descriptive du modèle. L'ensemble de ces caractéristiques, se manifestant à des échelles spatiales et temporelles variées, a pu être observé grâce à une combinaison de mesures et de modèles utilisés conjointement pour arriver à une compréhension plus globale de l'estuaire fluvial du Saint-Laurent.

Plusieurs avancées ont été réalisées dans le cadre de cette thèse, susceptibles de trouver application dans de nombreux contextes. Par exemple, les ADCP et les RTK GPS sont des instruments versatiles avec le potentiel de fournir des observations précises dans plusieurs environnements caractérisés par des écoulements complexes (ex.: Seim *et al.*, 2006, Sime *et al.*, 2007, Rennie & Church, 2010). La combinaison de ces deux technologies permet la mesure simultanée des niveaux d'eau et des vitesses, cruciale dans le calcul des débits en rivières. Ce type de mesures devient particulièrement utile en absence de stations de mesure des niveaux d'eau à proximité des sites d'étude, ou lorsque les variations latérales, liées aux caractéristiques géographiques locales ou à des phénomènes transitoires, ne peuvent être représentées par des stations situées en berge. De plus, les techniques d'interpolation mises au point pour la reconstruction de champs synoptiques continus peuvent facilement être généralisées à une variété de contextes non-stationnaires. En effet, l'optimisation d'une fonction de référence arbitraire définie

à partir des données rend cette méthode facilement transposable. En présence de variables complexes comme la vitesse, l'usage de splines lissantes représente une alternative intéressante pour l'interpolation de champs non-stationnaires. Alors que l'emphase a été mise sur l'analyse des vitesses horizontales ($u$ et $v$), certaines avenues restent encore à explorer, notamment l'analyse des courants secondaires à partir des vitesses verticales mesurées. De plus, l'installation d'une station permanente de mesure des vitesses dans l'estuaire fluvial permettrait un suivi en continu des débits du fleuve et l'acquisition de données de validation en temps réel pour les modèles opérationnels, en complément aux mesures de niveaux d'eau.

Par ailleurs, l'application de NS_TIDE dans les rivières à marées représente un avantage considérable par rapport à la modélisation numérique en termes d'efficacité de calcul, en particulier dans des contextes où les données de terrain sont limitées ou lorsque le développement d'un modèle numérique est une option difficilement envisageable. Une fois les paramètres du modèle NS_TIDE spatialisés, cet outil de diagnostic permet d'inférer la variabilité temporelle et spatiale des processus fluvio-tidaux dans un estuaire. De plus, l'utilisation d'un tel modèle pour le calcul des débits tidaux, via une méthode de cubature, a été démontrée et validée sur plusieurs sections de l'estuaire fluvial du Saint-Laurent, une technique facilement généralisable à d'autres systèmes. Il devient ainsi possible de reconstruire des séries historiques de débit et de prédire les débits tidaux attendus pour différents scénarios de débit fluvial et de marée. Pour améliorer l'interpolation des composantes de marée de haute fréquence, l'utilisation de modèles numériques peut être envisagée, afin de profiter d'une résolution spatiale plus grande. Combiné à la modélisation hydrodynamique, cet outil a le potentiel d'améliorer notre compréhension des systèmes fortement non-linéaires comme les rivières à marées, poussant ainsi les limites des outils de prévision conventionnels.

Dans les rivières à marée et les estuaires, l'accent est le plus souvent mis sur l'habileté des modèles à reproduire adéquatement les amplitudes et phases des principales composantes astronomiques et en eaux peu profondes de la marée (ex.: Hsu *et al.*, 1999, Espino *et al.*, 2007, Picado *et al.*, 2010). Pour des périodes de simulation courtes (ex.: 15 jours), seul un nombre limité de composantes de marée peut être résolu par l'analyse harmonique traditionnelle. De plus, de par la nature non-stationnaire des marées en rivière, les résultats de telles analyses n'expliquent qu'une fraction de la variance totale du signal. Pour de courtes séries temporelles, même les méthodes d'analyse harmonique non-stationnaire (ex.: Matte *et al.*, 2013) ou de

décomposition par ondelettes de la marée (ex.: Jay & Kukulka, 2003, Buschman *et al.*, 2009, Sassi *et al.*, 2011) présentent des capacités descriptives limitées. La performance du modèle de l'estuaire fluvial du Saint-Laurent a donc été évaluée, non seulement en termes du contenu fréquentiel de la marée, mais également sur la base des variations temporelles des niveaux moyens et du marnage, extraites des signaux observés et simulés aux stations marégraphiques. De plus, certaines variables explicatives – comme les temps d'arrivée et hauteurs des marées hautes et basses, le marnage, les temps d'inversion de courant, les vitesses maximales, et l'orientation des vitesses – extraites aux sections de mesure sur un cycle semi-diurne de marée ont été utilisées pour fins de validation. Comme l'analyse cycle-par-cycle décrite par Parker (2007), ces variables forment une base de comparaison à un site donné et d'un site à l'autre, entre les différents cycles du mois (des marées de mortes-eaux aux marées de vives-eaux) et les différentes conditions non-tidales observables (ex.: débits fluviaux, vents). Une telle approche, plus versatile qu'une évaluation uniquement basée sur une comparaison des harmoniques, peut potentiellement trouver application dans plusieurs contextes non-stationnaires, autres que tidaux.

L'estuaire fluvial du Saint-Laurent constitue l'un des plus grands systèmes fluvio-estuariens en Amérique du Nord, de par sa taille et les volumes d'eau qu'il transporte. La modélisation de ce système permet de mettre au jour d'importants processus présents au sein des estuaires à travers le monde. Le modèle hydrodynamique développé ouvre la voie à une série d'applications visant à évaluer les impacts de modifications anthropiques ou naturelles sur le système, notamment via un couplage de modèles. Une description quantitative approfondie des processus physiques dans l'estuaire fluvial du Saint-Laurent doit être poursuivie, en exploitant les données et modèles actuels et en planifiant de futures campagnes de mesure. De plus, un exercice de validation reste à faire pour différents scénarios de débits et de vents, et pour divers stades de croissance des macrophytes ou conditions de glace. Ce travail permettra de couvrir le spectre des conditions possibles et ainsi de mettre en place des stratégies pour répondre aux changements à venir. Cette recherche constitue la première étape dans le développement d'un modèle global détaillé et opérationnel de l'écosystème du Saint-Laurent, qui inclura une série de variables pour l'évaluation de la qualité de l'eau et des habitats aquatiques (ex.: Morin *et al.*, 2003b). Le modèle de l'estuaire fluvial viendra ainsi se greffer aux modèles opérationnels et en développement sur les tronçons amont et aval du fleuve.

# CHAPITRE 2 : ARTICLES

## 2.1 A robust estimation method for correcting dynamic draft error in PPK GPS elevation using ADCP tilt data

Cet article présente une méthode robuste de régression linéaire itérative pour la correction des erreurs systématiques dans les hauteurs GPS, associées au tirant d'eau dynamique. Elle corrèle ces dernières aux déplacements verticaux induits par les angles d'inclinaison du bateau mesurés à l'ADCP. Cette contribution constitue l'un des volets de l'objectif 1 de cette thèse visant l'acquisition de données de niveaux d'eau détaillées et précises dans l'estuaire fluvial du Saint-Laurent. L'article a été publié dans la revue *Journal of Atmospheric and Oceanic Technology*.

L'idée de combiner les mesures RTK GPS et ADCP pour la mesure simultanée des niveaux d'eau et des vitesses a été proposée par Jean Morin (troisième auteur). L'acquisition et l'analyse des données ont été réalisées par l'auteur de cette thèse (premier auteur). Des erreurs systématiques dans les hauteurs GPS observées lors des analyses ont poussé ce dernier à élaborer une méthode pour leur correction. Yves Secretan (second auteur) a participé à la réflexion sur le modèle. Le développement de la méthode, la production des résultats et l'écriture de l'article ont été réalisés par l'auteur principal; les coauteurs ont contribué au manuscrit en en révisant le contenu.

La référence complète de l'article est donnée ci-dessous :

Matte P, Secretan Y & Morin J (2014) A robust estimation method for correcting dynamic draft error in PPK GPS elevation using ADCP tilt data. *J. Atmos. Oceanic Technol.* 31(3):729-738.

### 2.1.1 Abstract

Measuring temporal and spatial variations in water level with high resolution and accuracy can provide fundamental insights into the hydrodynamics of marine and riverine systems. Real-time kinematic global positioning systems (RTK GPS), and by extension post-processed kinematic (PPK) positioning, have provided the opportunity to achieve this goal, by allowing fast and straightforward measurements with sub-decimeter accuracy. However, boat-mounted GPS are subject to movements of the water surface (e.g., waves, long-period heaves) as well as to the

effects of dynamic draft. The latter contaminates the records and needs to be separated and removed from the data. A method is proposed to post-correct the elevation data using tilt information measured by an attitude sensor, in this case, an acoustic Doppler current profiler (ADCP) equipped with internal pitch and roll sensors. The technique uses iteratively-reweighted least-squares (IRLS) regressions to determine the position of the center of rotation (COR) of the boat that leads to optimal corrections. The COR is also allowed to change in time by performing the IRLS analyses on data subsamples, thus accounting for changes in weight distribution, e.g., due to personnel movements. An example of application is presented using data collected in the St. Lawrence fluvial estuary. The corrections exhibit significant reductions associated with the boat motion, while keeping subtle variations in water levels likely related to local hydrodynamics.

### 2.1.2 Introduction

In recent years, real-time kinematic global positioning systems (RTK GPS), and by extension post-processed kinematic (PPK) positioning, have played an increasingly important role in the study of marine and riverine environments. Aboard survey vessels or mounted on buoys, kinematic GPS record any motion of the water surface and measurement platform across the whole frequency spectrum. Relying on differential carrier-phase measurements, they are capable of sub-decimeter accuracy in both horizontal and vertical positioning (Awange, 2012, Ghilani & Wolf, 2012). Such vertical accuracy is required in order to measure variations in water level associated with waves, long-period heave, tides and non-periodic motions such as those due to morphological features, currents and dynamic draft effects (Bisnath *et al.*, 2004b). When acquired with precision, temporal and spatial variations in water level can provide new insights into dynamical processes (e.g., Sime *et al.*, 2007) and can be very helpful in the calibration of numerical models (e.g., Church *et al.*, 2008, Capra *et al.*, 2010) or satellite altimetric measurements (e.g., Watson *et al.*, 2003).

More specifically, RTK and PPK GPS have proven very beneficial in hydrographic surveys for the determination of chart and tidal datum (e.g., Riley *et al.*, 2003, Bisnath *et al.*, 2004a, Moegling *et al.*, 2009) and for monitoring changes in seabed morphology when combined to multibeam echosounders (e.g., Church *et al.*, 2009). In bathymetric soundings, they represent an advantage over traditional tidal and heave compensation methods typically restricted only to

long- and short-period motions, respectively (Work *et al.*, 1998, Blake, 2007). Kinematic GPS have also been used for the measurement of tides as a complement to shore-based gauges or in offshore regions where stations are remote or nonexistent (e.g., Hess, 2003, Zhao *et al.*, 2004, Hughes Clarke *et al.*, 2005). Notably, centimeter-level differences were obtained by Rocken *et al.* (1990) and Bisnath *et al.* (2003) between GPS and tide gauge water levels. Furthermore, reliable estimates of the vertical motion of sea surface have been achieved with buoy-mounted GPS for mean sea level and ocean wave measurements (e.g., Rocken *et al.*, 1990, Kelecy *et al.*, 1994). Similarly, estimates of wave heights made by Bender *et al.* (2010a, 2010b) in the context of hurricane Katrina were shown to be as accurate as obtained from a strapped-down, one-axis accelerometer, if properly corrected for tilting.

In rivers and estuaries, local variations in water level profiles are important to characterize. For example, Bauer *et al.* (2007) were able to identify pools with potential sand deposition in the Sandy River, by comparing water surface profiles taken at different years with a RTK GPS. Similarly, Sime *et al.* (2007) surveyed the main thalweg and branch channels of the Lower Fraser River using RTK GPS and observed strong streamwise fluctuations in water surface slope reflecting the pronounced riffle-pool variations, as well as the backwater and acceleration effects induced by diagonal bar complexes. Likewise, Rennie & Church (2010) identified local variations in water surface slope over a succession of riffles and pools in the Fraser River, using RTK GPS.

During vessel surveys, pitch and roll motions modify the reported water levels as they both rotate and translate the GPS antenna. The measured vertical positions can fluctuate by a few decimeters as the boat shifts position, due to changes in boat loading, weight distribution, heading, speed, wave, wind and current action. These effects are referred to as dynamic draft, which is the sum of static draft, settlement and squat. Static draft is the draft of the vessel at rest, when fully loaded (with equipment, fuel and personnel). Settlement is the vertical lowering of the moving vessel, relative to what its level would be if it were motionless; it is measured at the vessel's COR. Squat refers to the sinking of the vessel's stern into the water as speed increases; it acts as a lever arm from the COR to the mounted instrument, thus changing its angle and draft (CHS, 2008, NOAA, 2010).

Random oscillations, e.g. due to waves, can easily be removed from the records by smoothing. However, non-periodic and low-frequency vertical displacements can either be attributed to variations of the water surface elevation or to dynamic draft effects and need to be accounted for. While it is crucial to keep the actual displacements of the water surface, shifts arising from the boat movements have to be identified and removed from the records.

In many of the above-mentioned studies (Kelecy *et al.*, 1994, Work *et al.*, 1998, Bisnath *et al.*, 2003, Hess, 2003, Riley *et al.*, 2003, Zhao *et al.*, 2004, Hughes Clarke *et al.*, 2005, Church *et al.*, 2009, Moegling *et al.*, 2009, Bender *et al.*, 2010a, Bender *et al.*, 2010b), the effects of pitch and roll and/or dynamic draft on the measured water levels have been examined, by use of either squat models or sensors for attitude determination. Because squat depends on several factors, such as channel depth and cross-section, shape of the ship hull and ship speed (Barrass, 2004), estimating the vessel squat characteristics as a function of speed through the water is not a trivial task (e.g., Beaulieu *et al.*, 2012). On the other hand, using attitude sensors implicitly means that the position of GPS antennas relative to the center of rotation (COR) of the measurement platform is known and constant over time, two conditions not easily met in many surveys. In fact, the position of the COR, if not *a priori* known, must first be determined to calculate the vertical displacements of the antennas induced by pitch and roll motions. For this purpose, Alkan & Baykal (2001), for example, lifted their survey boat from the sea to the shore and mapped it in three dimensions with all the equipment in place. However, this technique is unpractical and most often impossible to achieve. Furthermore, the weight distribution, and thereby the position of the COR, may change in time due to fuel consumption and personnel movements on board, which limits the applicability of the method. As an alternative to attitude sensors, Beaulieu *et al.* (2009) applied the on-the-fly (OTF) GPS technology, which is a class of RTK surveys, using the Canadian Coast Guard's GPS network to measure ship squat in the St. Lawrence Waterway. The ship and escort boat were each equipped with two OTF GPS antennas on the longitudinal axis (bow and stern) and two others on the starboard and port sides to ensure simultaneous measurements of all vessel movements (rolling, sinkage, trim, etc.). Although the vertical accuracy can be high (±5 cm in 95 % of cases, as confirmed by validation pretests), the required number of antennas (four per boat) makes this technique less attractive.

A method is presented here for post-correcting systematic errors in GPS elevations associated with dynamic draft effects, using tilt information measured by an attitude sensor, in this case, an

acoustic Doppler current profiler (ADCP) equipped with internal pitch and roll sensors. It is assumed that the low-frequency motions of the water surface do not induce changes in the pitch and roll angles of the boat and that these rotations are exclusively related to dynamic draft effects. Hence, high-frequency oscillations are first removed from the records by smoothing, and the resulting low-passed PPK GPS and ADCP time series are re-sampled to a common time vector and lagged to eliminate any synchronization issues. The implemented procedure applies iteratively-reweighted least-squares (IRLS) regressions to determine the position of the COR of the boat that leads to optimal tilt corrections. The COR is also allowed to change in time, by performing the IRLS analyses on smaller segments of the time series, thus accounting for changes in weight distribution over time. The method is tested using data collected in the St. Lawrence fluvial estuary along repeated transects, aimed at documenting the lateral and intratidal variations in water levels and currents, at cross-sections characterized by complex geometries (e.g., river bends, tidal flats) and in regions of contrasting tidal ranges and/or degrees of ebb-flood asymmetry.

The paper is divided as follows. Section 2.1.3 details the implemented method, section 2.1.4 applies the procedure to the St. Lawrence River data, section 2.1.5 discusses the results and section 2.1.6 follows with concluding remarks.

### 2.1.3 Methods

To calculate the vertical corrections, a coordinate system is defined with the origin located at the COR of the boat (Figure 2.1.1). The $x$ axis is relative to the centerline of the boat and is positive to the bow. The $y$ axis is perpendicular to the $x$ and is positive to port. The $z$ axis points to the nadir direction, and is positive upward. Pitch is described as the forward and backward rotation of the boat about the transverse $y$ axis and is positive when the bow of the boat goes up. Roll is described as the side-to-side rotation about the longitudinal $x$ axis and is positive when the port of the boat goes up.

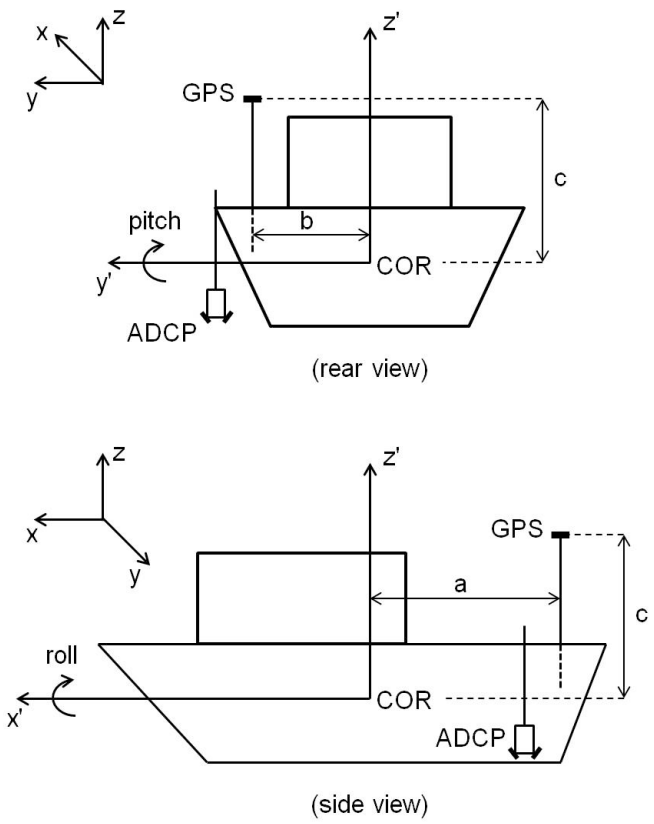


**Figure 2.1.1** **Configuration of the GPS and ADCP on the boat and its associated coordinate system, with the origin located at the COR.**

The corrections applied to the data are aimed at reducing systematic errors in the recorded GPS elevations by minimizing the variations in water levels that correlate the most with the long-period movements induced by pitch and roll. The input time series of observations (i.e. water surface elevations, and pitch and roll angles) are thus filtered versions of the original time series. The GPS elevations are detrended to remove the effects of tides, by subtracting a cubic smoothing spline function from the original time series. The cubic smoothing spline $s$ is constructed for the specified smoothing parameter $p$ and weigths $w_i$ so that it minimizes (Reinsch, 1967, de Boor, 1978)

$$p\sum_i w_i (y_i - s(t_i))^2 + (1-p)\int\left(\frac{d^2 s}{dt^2}\right)^2 dt\,, \qquad (2.1.1)$$

where $y_i$ is the observed water levels measured at times $t_i$. Here, $p = 0$ would produce a straight line fit to the data, while $p = 1$ corresponds to the cubic spline (exact) interpolant. The *csaps*

Matlab function (MathWorks, 2012) is used with a very low smoothing parameter ($p = 10^{-7}$), well suited to the slowly varying character of tides. The weights $w_i$ are set to 1 for all data points. Similarly, mean values in the pitch and roll data are subtracted to correct for sensor misalignment, using the *detrend* Matlab function (MathWorks, 2012). The input time series are then smoothed to remove random oscillations due to waves, using cubic smoothing spline functions [cf. Eq. (2.1.1)] with a smoothing parameter of $p = 0.05$, thus keeping enough variations in the records to allow corrections for systematic errors. As a result of filtering, the computed corrections only become effective when the low-passed pitch and roll signals are departing from zero.

The ADCP time series are also re-interpolated to a common time vector (that of the GPS), and lagged in such a way that the correlation between observed water levels and vertical corrections for pitch and roll is maximal, thus eliminating any synchronization issues. Moreover, to account for temporal variations in the position of the COR, e.g., due to changes in the weight distribution of the boat, the time series are divided into subsets, or transects, each of which being analysed separately.

Mathematically, the observed water levels can be represented by a linear model of the form:

$$\mathbf{h} = \mathbf{A}\mathbf{x} + \boldsymbol{\varepsilon}, \tag{2.1.2}$$

where $\mathbf{h}$ is a $n \times 1$ vector of the filtered GPS elevations, $\mathbf{A}$ is a $n \times m$ tilt correction matrix (here $m = 3$), $\mathbf{x}$ is a $m \times 1$ vector of unknown COR parameters, and $\boldsymbol{\varepsilon}$ is a $n \times 1$ vector of observational error. Corrections for the motion of a measurement platform can be performed by use of rotation matrices (e.g., Edson *et al.*, 1998, Miller *et al.*, 2008). To transform the GPS elevations from ship coordinates to earth coordinates, a first rotation about the $x$ axis (roll), followed by a rotation about the intermediate $y$ axis (pitch), are calculated (cf. Teledyne RD Instruments, 2010). A translation along the $z$ axis is then applied to transform GPS rotated heights into true GPS orthometric heights. The resulting tilt corrections $\Delta\mathbf{z}$ applied to the data are defined as:

$$\Delta\mathbf{z}(\mathbf{t}) \equiv \mathbf{A}\mathbf{x} = \begin{bmatrix} \sin\mathbf{P}(t_1) & \sin\mathbf{R}(t_1)\cos\mathbf{P}(t_1) & 1-\cos\mathbf{R}(t_1)\cos\mathbf{P}(t_1) \\ \vdots & \vdots & \vdots \\ \sin\mathbf{P}(t_n) & \sin\mathbf{R}(t_n)\cos\mathbf{P}(t_n) & 1-\cos\mathbf{R}(t_n)\cos\mathbf{P}(t_n) \end{bmatrix} \times \begin{bmatrix} a \\ b \\ c \end{bmatrix}, \tag{2.1.3}$$

where **P** and **R** are the low-passed pitch and roll time series of length $n$, **t** is a $n \times 1$ time vector, and $a$, $b$ and $c$ are the $x$-$y$-$z$ coordinates of the GPS antenna relative to the COR, respectively (Figure 2.1.1). Hence, the further the antenna is from the COR, the larger the displacements $\Delta\mathbf{z}$ are, for given angles of rotation. The first two columns of **A** correspond to vertical translations of the antenna due to the pitch and roll movements, while the third column is the vertical shift associated with its rotation. The latter correction is either strictly positive or strictly negative, depending on the sign of $c$, and is up to two orders of magnitude smaller than the translations, for small $P$ and $R$ angles.

Robust parameter estimation models can be used to solve Eq. (2.1.2) in a way to reduce the influence of variations in water levels other than those associated with dynamic draft effects. A number of techniques with various levels of efficiency and effectiveness have been proposed, some of which were described by Huber (1996), Awange & Aduol (1999), and Gonclaves *et al.* (2012). Among them, IRLS regression analysis (Holland & Welsch, 1977, Huber, 1996) has successfully been applied to geophysical problems (see, e.g., Bube & Langan, 1997, Leffler & Jay, 2009). The IRLS algorithm reduces the influence of high-leverage data points that increase residual variance, by down-weighting the outliers. The level of confidence in the computed parameters is therefore increased compared to ordinary least-squares (OLS) analyses.

The IRLS solution to Eq. (2.1.2) is given by

$$\mathbf{x} = \left(\mathbf{A}^{\mathrm{T}}\mathbf{W}\mathbf{A}\right)^{-1}\mathbf{A}^{\mathrm{T}}\mathbf{W}\mathbf{h}\,, \tag{2.1.4}$$

where **W** is a $n \times n$ diagonal weight matrix. The initial solution is obtained from OLS regression by setting the weight matrix to the identity matrix, i.e. $\mathbf{W} = \mathbf{I}$. Iterations are then performed on **x** and **W** until there is convergence of the residual. At each iteration $j$, the following steps are repeated:

1. The residual **R** is computed from previous fit [i.e. Eq. (2.1.4)]:

$$\mathbf{R}^{j} = \mathbf{W}^{j-1}\left(\mathbf{h} - \mathbf{A}\mathbf{x}\right)^{j-1}; \tag{2.1.5}$$

2. The residuals are adjusted using leverage $l_i$, as advised by DuMouchel & O'Brien (1989), which is a measure of the influence of each point $i$ on the least-squares fit:

$$R_i' = \frac{R_i}{\sqrt{1-l_i}}, \tag{2.1.6}$$

where $R_i$ are the $i$th-elements of vector $\mathbf{R}$, $R_i'$ is the adjusted residuals and $l_i = \text{diag}\left(\mathbf{A}\left(\mathbf{A}^{\mathrm{T}}\mathbf{A}\right)^{-1}\mathbf{A}^{\mathrm{T}}\right)$ (Weisberg, 2005);

3. A standard deviation estimate $s$ is computed using the median absolute deviation (MAD) of adjusted residuals from zero:

$$s = \frac{\text{MAD}(R_i')}{0.6745}; \tag{2.1.7}$$

where the constant 0.6745 makes the estimate unbiased for the normal distribution;

4. New weights are calculated using the specified weight function $f$ and tuning parameter $\tau$:

$$w_i = f\left(r_i\right), \tag{2.1.8}$$

where $r_i = \frac{R_i'}{s\tau}$;

5. A new solution is obtained by application of Eq. (2.1.4), with $w_i = \text{diag}\left(\mathbf{W}\right)$.

IRLS regression analyses are performed using the *robustfit* Matlab function (MathWorks, 2012). A bisquare weighting function is used, defined as:

$$w_i = \begin{cases} (1-r_i^2)^2, & |r_i| < 1 \\ 0, & |r_i| \geq 1 \end{cases}, \tag{2.1.9}$$

with a (default) tuning constant $\tau$ of 4.685. The latter can be adjusted to penalize the outliers more or less heavily, depending on the level of filtering needed. In the present application, the default Matlab value is used, yielding coefficient estimates that are approximately 95% as statistically efficient as the OLS estimates, assuming that the response has a normal distribution with no outliers (MathWorks, 2012). In general, for small pitch and roll angles, departure from the default function and parameter suggested by Matlab has little effect on the corrections (i.e. of

the order of a few millimeters). A list of available weight functions can be found in Matlab documentation (MathWorks, 2012), also summarized in Leffler & Jay (2009).

To assess the significance of the corrections $\Delta z$, the *p*-values are computed for the relative standard errors of coefficient estimates *a*, *b* and *c*. They represent the probability of obtaining a test statistic at least as extreme as the observed error. For *p*-values less than 0.001, the null hypothesis is rejected – i.e. the correlation between the calculated corrections and the observations is highly unlikely to be the result of random chance alone. Otherwise, for *p*-values superior to 0.001, the correlation is not significant and coefficients are rejected (i.e. set to zero), in which case the solution is recalculated using only the columns of **A** corresponding to non-zero coefficients **x**. Threshold values on the coefficients can also be used to ensure that realistic distances between the antenna and the COR are obtained.

### 2.1.4 Data analysis

Data were collected at 13 cross-sections of 1–4-km width of the St. Lawrence fluvial estuary, Quebec, Canada, during the summer of 2009. Each cross-section was surveyed repeatedly over a period of approximately 12 h, corresponding to the semi-diurnal tidal period. Boat speed was maintained at 1–2 m $s^{-1}$ on average to ensure data of good quality. Two Trimble R6 RTK GPS receivers – the base, located on the shore, and the rover, mounted at the rear of the boat (Figure 2.1.1) – were used for positioning and water level measurements along the transects (Trimble, 2003). They were operated simultaneously, collecting data at a frequency of 1 Hz. Tilt information was obtained from the internal pitch and roll sensors of a 600-kHz RD Instruments Rio Grande ADCP, mounted on the side of the boat (Figure 2.1.1). The frequency of acquisition was set to 2.5 Hz.

For the purpose of testing, the elevation data measured during one crossing at Portneuf were used, which present systematic shifts typically encountered during the campaign due to dynamic draft effects. As shown in Figure 2.1.2a, measured water levels are indeed highly correlated with the variations in pitch and roll angles. Before using the data, the input time series were detrended and/or demeaned to remove variations associated with tides or sensor misalignment, then smoothed to remove random oscillations due to waves. Note that GPS elevations are detrended solely for the sake of regression analysis; once the correction $\Delta z$ is made, the trend is reapplied

to the elevation time series. The resulting filtered time series are shown in Figure 2.1.2b. It can be seen that even the sharpest variations appearing in the original records (Figure 2.1.2a) are preserved in the filtered time series.

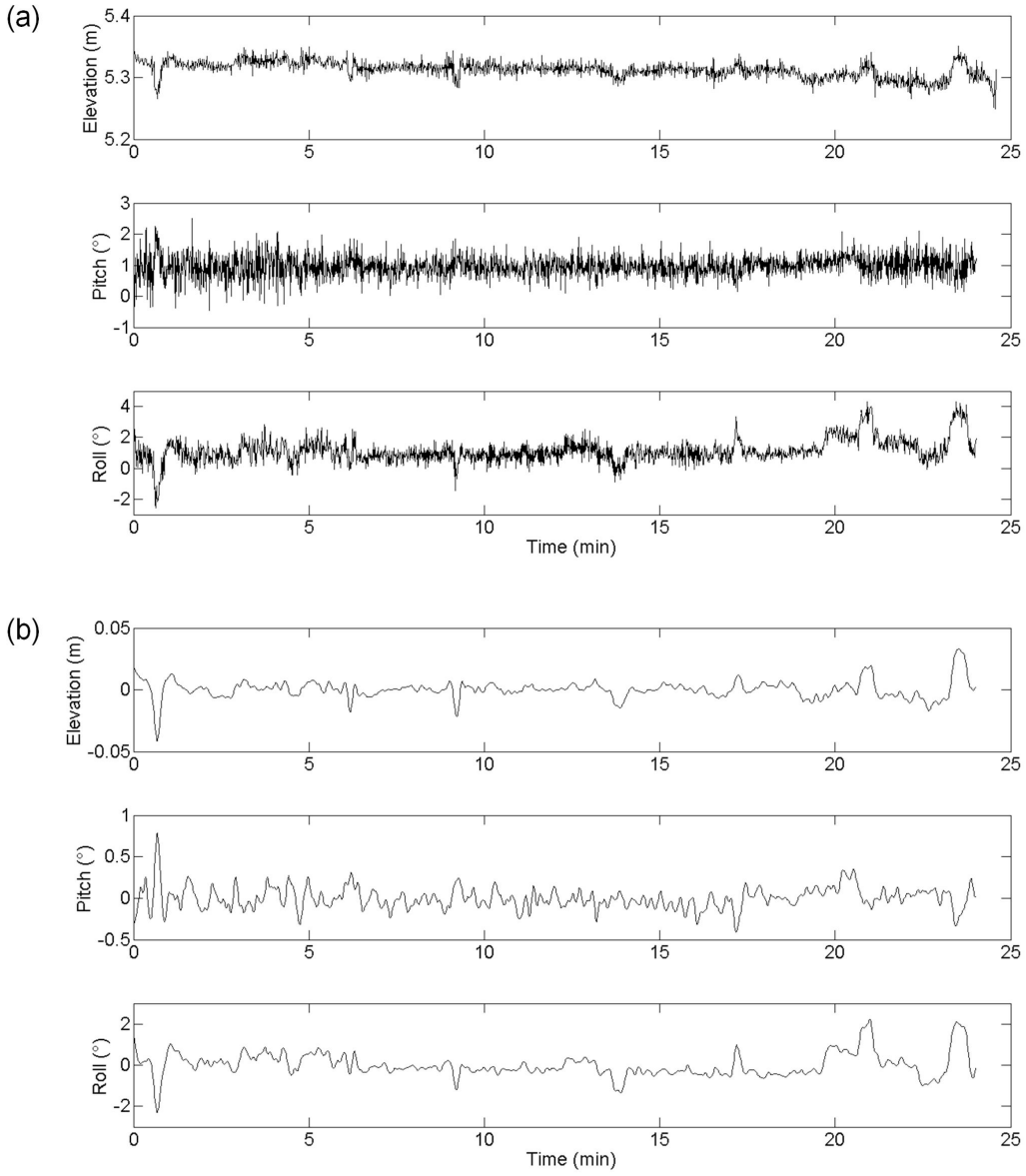


**Figure 2.1.2** **(a) Elevation data for a transect at Portneuf measured with a kinematic GPS, compared to pitch and roll data from an ADCP. (b) Filtered time series of elevations, and pitch and roll angles.**

The first entry of Table 2.1.1 shows the regression coefficients [*a*, *b*, *c*] obtained for the chosen transect, representing the position of the antenna that leads to the optimal corrections. Because the pitch and roll angles are relatively small (cf. Figure 2.1.2b), vertical corrections from the

third column of **A** in Eq. (2.1.3) were very small too. Consequently, the value of $c$ was not significant according to its $p$-value, which was much higher than 0.001; it was thus set to zero. The zero time lag indicates that the elevation and pitch and roll time series were synchronous. Furthermore, the correlation coefficient (0.790) highlights the strong relation that exists between the computed correction and the elevation time series.

**Table 2.1.1** **Regression coefficients for a transect at Portneuf, along with their associated statistics. First entry shows results for the entire crossing (24.6-min interval), while the other entries correspond to 5-min subsets of the transect.**

| Time interval (min) | [$a$, $b$, $c$] (m) | Standard deviation (m) | Time lag (s) | Correlation coefficient |
|---|---|---|---|---|
| | *Entire transect* | | | |
| 24.6 | [-0.854, 0.468, 0.000] | 0.0047 | 0 | 0.790 |
| | *5-min subsets* | | | |
| 5 | [0.000, 0.673, 0.000] | 0.0041 | 0 | 0.880 |
| 5 | [-0.865, 0.630,0.000] | 0.0028 | 0 | 0.809 |
| 5 | [0.394, 0.409, 0.000] | 0.0025 | 0 | 0.695 |
| 5 | [-0.629, 0.000, 0.000] | 0.0050 | 0 | 0.277 |
| 4.6 | [0.782, 0.782, 0.000] | 0.0039 | 0 | 0.948 |

The impact of dividing the time series into smaller subsets and performing successive IRLS analyses was assessed. In Table 2.1.1, results are presented from consecutive 5-min intervals of the same transect as in the first entry. The optimized coefficients slightly differ from each other, highlighting the respective influence of pitch and roll on each subsample. The corresponding standard deviations are thus smaller than for the total transect (24.6-min interval), with the exception of the fourth 5-min subset, because coefficients are adjusted to the local conditions prevailing during each time interval. Correlation coefficients are also higher in subsets where water level variations induced by dynamic draft movements are the strongest. Overall, the displacement of the COR is within ±1 m in all directions, reflecting the combined action of external factors (such as currents, winds, weight distribution, etc.) on the position of the COR. Despite these dissimilarities, maximum absolute differences in water levels between the analyses performed using the whole transect (first entry) and using 5-min intervals were less than 1 cm (given maximum absolute corrections of ~3 cm; cf. Figure 2.1.3).

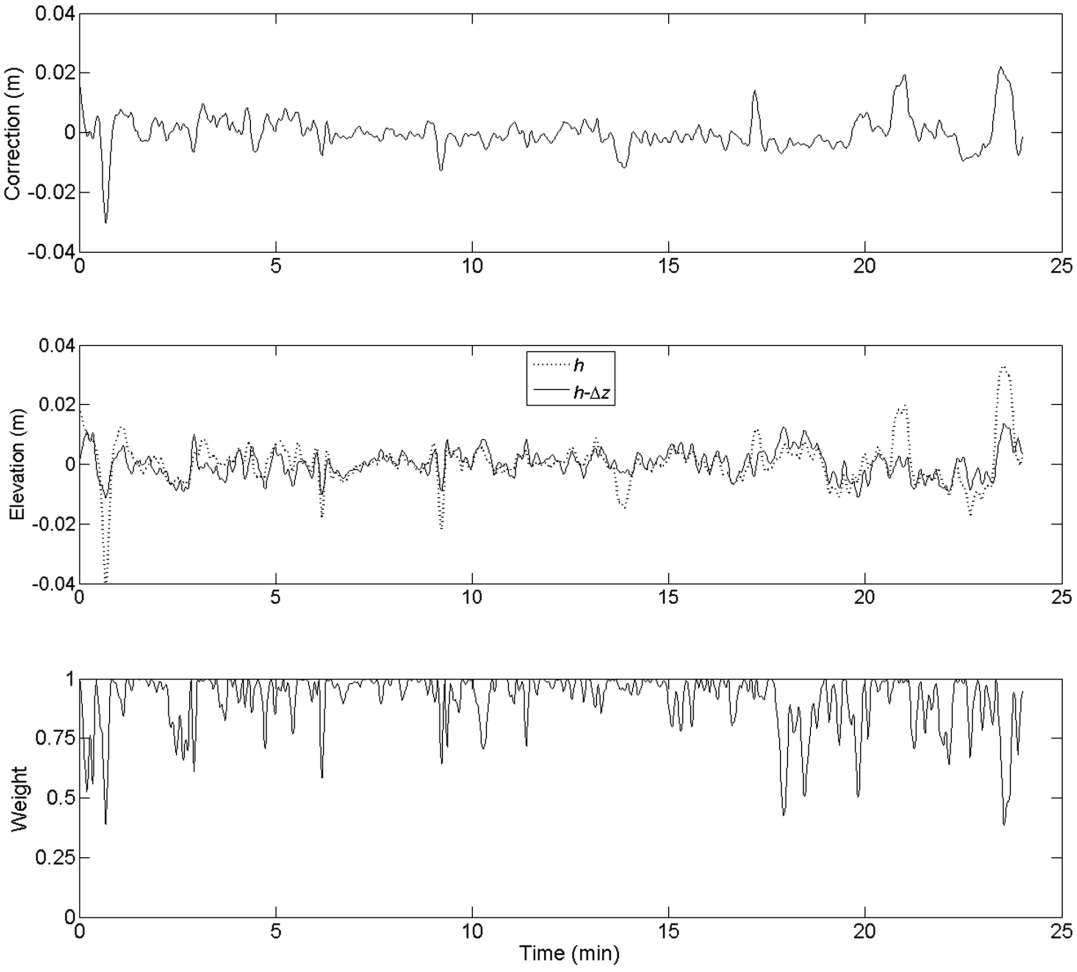


**Figure 2.1.3** **(top) Computed correction for a transect at Portneuf; (middle) original (filtered) and corrected elevations; (bottom) bisquare weights from the IRLS analysis.**

The corrections obtained by IRLS analyses for the transect at Portneuf are shown in Figure 2.1.3. The computed correction is shown in top panel, while the signals before and after correction are presented in middle panel. Variations associated with pitch and roll motions are significantly reduced, although not completely eliminated in some instances. The fluctuations however remain within an interval of ±1 cm once corrected, which is comparable to the data vertical accuracy at Portneuf, as generally expected for kinematic GPS surveys (Ghilani & Wolf, 2012). The weight time series appearing in bottom panel of Figure 2.1.3 follows the variations in the residual and shows how the IRLS regression analysis reduces the influence of non-zero residuals on calculated coefficients. Lower weights are attributed to portions of the signal where variations

caused by pitch and roll motions still remain, as well as where variations with no apparent correlation with the boat motion appear, possibly related to local hydrodynamics.

### 2.1.5 Discussion

GPS elevations are subject to errors other than related to dynamic draft effects. These include data latency associated with the motion of the rover during data transmission from the base receiver, reception and processing at the rover. In the present application, positioning errors caused by this time difference tend to be small since boat speed was maintained around 1–2 m $s^{-1}$ on average. Other factors that limit the positioning accuracy of kinematic surveys are errors associated with spikes in positional dilution of precision (PDOP), tropospheric and ionospheric refraction, weak satellite geometry, ephemeris error, multipathing, obstructions to satellite signals due to topography or infrastructure, base station coordinate errors, firmware algorithms and weather (Blake, 2007, Ghilani & Wolf, 2012). These factors should be taken into account when possible in the planning of a field campaign. During the St. Lawrence campaign, the number and configuration of available satellites was not considered, due to time and resources constraints; only the weather was, mainly for security reasons. However, the number of available satellites was always high (> 10 in the example shown, with PDOP < 2) due to a very open survey environment, thus limiting the associated errors. Moreover, errors associated with tropospheric delay were limited by short-baseline surveys (< 4 km). Some of the remaining errors were directly filtered out in the receivers (e.g., multipath effects), the rest being partly cancelled by data smoothing. In the robust model, only the variations in measured heights that are significantly correlated with pitch and roll (through the *p*-value criterion) were corrected. Also, the weights attributed to uncorrelated variations were reduced, leaving them almost unchanged. This allows a separation between dynamic draft and GPS-related errors. The latter perturb the robust model only if they are synchronized with the boat movements, which is improbable.

Due to the strategy of repeated transects used in the St. Lawrence fluvial estuary, data from each river crossing was analysed and corrected separately. Although smaller regression intervals than the transect length might be desired (e.g., Table 2.1.1), care must be taken at the junctions of neighbouring subsets because of discontinuities appearing between successive corrections. More tests are needed to determine the optimal time interval to apply to each subset at a given location.

Although the GPS antenna is fixed on the boat, the position of the COR is generally unknown and can move due to changes in weight distribution, e.g., caused by personnel movements on board. The use of IRLS weighting functions allows obtaining robust coefficients, corresponding to the optimal distances between the antenna and the COR in terms of residual variance reduction. More work is however necessary to assess the performance of other weighting functions and to define practical limits for the tuning parameters, which may vary from place to place and as a function of the conditions that prevail. In the example shown, pitch and roll angles were relatively small, so that the impact of the choice of the weighting function and tuning constant on the corrected water levels was minor (of the order of a few millimeters). This may not be the case under more extreme dynamic draft conditions.

The regression approach put forward here is intended to be used in a context where the position of the COR is unknown and/or changes in time. Its position can only be determined when time variations in tilt angles occur and when these variations are significantly correlated with changes in the measured GPS elevations. Therefore, the presented method does not apply in contexts where the boat is tilted by a constant angle during the whole survey, unless the ADCP is perfectly aligned in the vertical. In this case, the average pitch and roll can be used to shift the GPS data, using the known or iteratively-determined COR.

### 2.1.6 Conclusion

ADCPs are used in a wide variety of applications, from discharge monitoring to the investigation of sediment transport, turbulence or habitat quality (e.g., Lu & Lueck, 1999b, Yorke & Oberg, 2002, Shields & Rigby, 2005, Rennie & Church, 2010). In the present application, the tilt information provided by an ADCP was used in place of traditional attitude sensors, thus broadening its range of applicability. In contrast, the use of kinematic GPS technology in the study of riverine and marine systems is relatively new. As experience is gained in the field, measurement techniques and data analysis procedures are refined. As argued by Work *et al.* (1998), extreme care and detail must be maintained during data collection and processing to yield useful data.

A simple method was presented to post-correct elevation data obtained from a boat-mounted GPS. Using data collected in the St. Lawrence fluvial estuary, contamination of the measured

elevations was shown, arising from dynamic draft effects undergone by the boat as it followed its survey path. The observed systematic errors were correlated with pitch and roll data obtained from an ADCP, which were used to correct the PPK GPS data, thereby reducing the error to within instrumentation accuracy. This improved accuracy demonstrates the potential of using boat-mounted PPK GPS in a variety of environments and conditions, as long as there is no signal obstruction and sufficient information is available to compensate for boat movements. Even when the measured tilt angles are relatively small, there is no reason not to perform the corrections if tilt information is available. Under more extreme dynamic draft conditions, as the tilt angles increase, the need for such a correction becomes increasingly important.

The combination of kinematic GPS and ADCP technologies allows simultaneous acquisition of both water level and velocity data, which is crucial for the calculation of accurate discharges in rivers. This becomes especially useful when there is no water level gauge close to the study site, or when cross-sectional variations cannot be adequately captured by shore-based gauges. Likewise, local variations in water levels either due to local geographic features or to transient processes can only be precisely measured using instruments capable of high resolution and accuracy, such as PPK GPS.

### 2.1.7 Acknowledgements

This work was supported by scholarships from the Natural Sciences and Engineering Research Council of Canada and the Fonds de recherche du Québec – Nature et technologies. The field campaign was funded by Environment Canada (Meteorological Service of Canada). Special thanks go to Guy Morin, Jean-François Cantin, Patrice Fortin, Olivier Champoux, and Catherine Leblanc for their contribution to the field work, as well as to two anonymous reviewers for their constructive comments on the manuscript.

## 2.2 Quantifying lateral and intratidal variability in water level and velocity in a tide-dominated river using combined RTK GPS and ADCP measurements

Cet article présente une méthode combinant les technologies du RTK GPS et de l'ADCP pour la mesure simultanée des niveaux d'eau et des vitesses le long de trajets répétés par bateau. À partir de données recueillies sur différentes sections contrastées de l'estuaire fluvial du Saint-Laurent et grâce à un réseau densifié de stations marégraphiques, une stratégie d'analyse est présentée pour la reconstruction de champs de niveaux d'eau et de vitesses continus et synoptiques sur un cycle semi-diurne de marée. L'article contribue à la réalisation de l'objectif 1 de cette thèse en fournissant les données nécessaires à la caractérisation de la variabilité latérale et intratidale des niveaux d'eau et des vitesses, et à la validation des modèles développés aux objectifs 2 et 3. L'article a été publié dans la revue *Limnology and Oceanography: Methods*.

La campagne de terrain a été planifiée et réalisée par l'auteur de cette thèse (premier auteur), en étroite collaboration avec les coauteurs. Yves Secretan (second auteur) a participé activement à l'élaboration de la stratégie de mesure; Jean Morin (troisième auteur), qui détient une large expérience de terrain, a participé aux réflexions entourant la planification de la campagne et a fourni les moyens financiers et techniques pour la réalisation des travaux, par l'entremise d'Environnement Canada. La collecte et l'analyse des données, la production des résultats et l'écriture de l'article ont été réalisées par l'auteur principal. Les coauteurs ont contribué aux discussions entourant la collecte et le traitement des données, ainsi qu'à la révision du manuscrit.

La référence complète de l'article est donnée ci-dessous :

Matte P, Secretan Y & Morin J (2014) Quantifying lateral and intratidal variability in water level and velocity in a tide-dominated river using combined RTK GPS and ADCP measurements. *Limnology and Oceanography: Methods* 12: 279-300.

### 2.2.1 Abstract

Cross-sectional gradients in water levels and velocities play a determining role in the circulation dynamics of tidal rivers and estuaries. Documenting and analysing their variability throughout a tidal cycle require observations with high spatial and temporal resolution. A survey strategy and a data analysis procedure have been designed to obtain continuous and synoptic water level and

velocity fields over a tidal cycle, along 13 cross-sections of the St. Lawrence fluvial estuary dominated by large tidal ranges. The method combines both RTK GPS and ADCP technologies for the simultaneous measurement of water levels and velocities along repeated boat transects, allowing fast data acquisition over wide river sections and under rapidly changing conditions. The reconstruction of continuous and synoptic fields is made by interpolation. Simplifying assumptions about data stationarity and/or homogeneity are avoided by adapting the interpolation procedures to the shape and distribution of the underlying data in a space-time reference frame, thus minimizing distortion in the reconstructed quantities. The capabilities and limitations of the method are assessed through error computations and comparisons with alternate data analysis methods and complementary data sets from tide gauges. With these latest observations, new insights into the tidal hydrodynamics of the St. Lawrence fluvial estuary are gained in regions of contrasting tidal and fluvial properties, specifically related to the effects of channel curvature and bathymetry on tidal propagation and cross-channel flow properties at the intratidal scale.

### 2.2.2 Introduction

Direct measurement of water levels and velocities can provide fundamental insight into the hydrodynamics of tidal rivers and estuaries. They represent a reliable source of data for the verification and calibration of numerical models. Such knowledge is also crucial for navigation, environmental assessments, and coastal protection and development. To reach a high level of description, measured data must cover a wide range of spatial and temporal variability. Long-term monitoring stations provide high-frequency records, but they are usually limited in number, thereby limiting their ability to represent spatial features of the flow. Conversely, satellite-based measurements provide synoptic snapshots of a region, but they are limited in their temporal resolution and interpretation of the velocity field. Boat surveys remain the best compromise between fixed measurements and remote sensing observations for the characterization of nonstationary hydrodynamic fields. They can ensure both spatial and temporal coverage, provided that the sampling strategy and resolution is adapted to the size and rate of evolution of the structures measured (e.g., Rixen *et al.*, 2001).

In the field, meeting these requirements is often a challenge, as both the instrumentation and survey strategy must meet the criteria and constraints set by the users (e.g., sampling require-

ments, finite measurement time and resources) and by the environment (e.g., presence of tides, size of the river). This has been facilitated in part by the development of new technologies over the last decades, including acoustic Doppler current profilers (ADCP) for water velocity measurements and real-time kinematic global positioning systems (RTK GPS) for three-dimensional positioning, thus enabling a higher resolution and accuracy in the data.

Boat-mounted ADCPs allow rapid measurement of vertical profiles of the three components of water velocity along a transect line. Frequency differences (i.e. Doppler shifts) between emitted and received sound pulses at the transducers are measured, which arise from the reflection of the transmitted pulses on small, suspended particles moving with the water. They are used to obtain the speed of water at a variety of depth cells, or bins, within the water column (Muste *et al.*, 2004b, Kostaschuk *et al.*, 2005, Gunawan *et al.*, 2010, Rennie & Church, 2010). Due to their ease of use and versatility, ADCPs have been increasingly used over the last two decades in systems ranging from small rivers to shelf seas (Howarth & Proctor, 1992, Gunawan *et al.*, 2010), thus being favoured over conventional current measurement techniques. Their applications have expanded beyond the simple measurement of velocity fields, to river bathymetry and discharge monitoring (Simpson, 2001, Yorke & Oberg, 2002), the investigation of sediment transport (Kostaschuk *et al.*, 2005, Rennie & Church, 2010), secondary flow (Dinehart & Burau, 2005a, Szupiany *et al.*, 2007), shear stress (Lu & Lueck, 1999a, Sime *et al.*, 2007), turbulence (Lu & Lueck, 1999b, Nystrom *et al.*, 2007, Stone & Hotchkiss, 2007), habitat quality (Shields & Rigby, 2005), gravity currents (García *et al.*, 2007), and the validation of numerical models (Morin, 2001).

Water levels are typically monitored using near-shore pressure sensors or inferred from ADCP depth data at different locations over a surveyed region (Li *et al.*, 2000). While the first method is limited to a pointwise (0D) description, the second is dependent on prior knowledge of bathymetry and can be largely inaccurate when spatial deviations between repeated tracks occur over large bottom slopes. Vertical and horizontal positions can be adequately determined with sub-decimeter accuracy by differentially correcting GPS signals recorded at two separate GPS receivers (Ghilani & Wolf, 2012). Non-periodic and low frequency vertical motions, such as due to tides, squat, long-period heave, and other dynamic draft effects, can only be effectively measured by post-processing kinematic (PPK) or RTK GPS (Bisnath *et al.*, 2004b, Beaulieu *et al.*, 2009). Providing real-time measurements in the field, RTK GPS have been used to resolve

water velocities measured with an ADCP into earth coordinates when bottom tracking is not possible (Rennie & Rainville, 2006), to measure water levels from buoys (Rocken *et al.*, 1990, Kelecy *et al.*, 1994, Bisnath *et al.*, 2003), water surface profiles from river shores (Kessler & Lorenz, 2010) or from a moving boat (Hess, 2003, Zhao *et al.*, 2004, Bauer *et al.*, 2007, Sime *et al.*, 2007), wave heights (Bender *et al.*, 2010b), in support to hydrographic surveys (Bisnath *et al.*, 2004a, Moegling *et al.*, 2009), and to verify and calibrate hydrodynamic models (Church *et al.*, 2008, Capra *et al.*, 2010).

In addition to the advent of new technologies, many attempts have been made for effectively sampling nonstationary hydrodynamic fields using strategies where data are collected repeatedly along the same survey path (e.g., Geyer & Signell, 1990, Old & Vennell, 2001, Dinehart & Burau, 2005b). The irregular mixed space-time data series obtained from such surveys have led to improvements in flow interpolation procedures for spatially nonstationary fields (e.g., Sokolov & Rintoul, 1999, Vennell & Beatson, 2006). These procedures are generally restricted to data sets for which synopticity is assumed within the duration of individual surveys. However, this assumption may introduce strong biases in subsequent analyses when the measured quantities undergo significant temporal changes during the survey (Matthews, 1997, Rixen & Beckers, 2002). This usually results in a distortion of the reconstructed fields. To prevent this, both the survey strategies and data analysis procedures must be adapted to the scale and nature of the dynamical processes involved, rather than making *a posteriori* assumptions about the data to conform to existing procedures.

In this paper, a survey strategy and its associated data analysis are presented, to quantify intratidal variations in the lateral distribution of water levels and velocities in a tide-dominated river. The collected data are expected to express this variability in time – throughout a tidal cycle – and in space – as a function of upriver distance and at contrasting river sections in terms of tidal-fluvial dynamics and geomorphology. Previous studies have shown the importance of such information. For example, Collignon & Stacey (2012) described the intratidal dynamics of shear fronts and lateral flows across a shoal-channel interface in south San Francisco Bay, using a combination of moored and boat-mounted instruments. Basdurak & Valle-Levinson (2013), for their part, performed continuous velocity measurements and station density profiles to determine the intratidal and spatial changes in lateral advection of momentum and its contribution to along-channel flow at the James River entrance in Chesapeake Bay. However, water level variations

associated with these flow features are usually not examined, but rather implicitly considered as invariant along the surveyed transects and extracted from nearby tide gauges. Yet, in presence of curved channels, shoals, tidal flats, or other bathymetric features, lateral variations in flow and tidal properties can induce significant changes in both water levels and velocities.

The method presented here combines both RTK GPS and ADCP technologies for the simultaneous measurement of water levels and currents at a very high sampling frequency (≥1 Hz) along repeated boat paths. The sampling strategy is designed in such a way that each survey line is travelled repeatedly to ensure temporal coverage of the studied phenomena. The data set thus obtained contains information on both the lateral and temporal variability of water levels and currents, with a high spatial resolution along the boat track and unevenly spaced data in time between successive tracks, depending on how the survey lines are covered. An interpolation procedure that uses the actual position of the data in a space-time reference system is put forward, thus allowing the reconstruction of synoptic fields at any given time within the surveyed period without prior assumptions on synopticity. A combination of tide gauges and pressure sensors distributed throughout the studied system is also used to provide continuous and simultaneous water level measurements during the surveys for data validation. The methodology is applied to a series of surveys realized under nonstationary, tide-driven conditions in the St. Lawrence fluvial estuary, Quebec, Canada, but it is quite general with respect to its applicability to many hydrographic systems, including rivers, estuaries and bays, as well as to a variety of nonstationary contexts, such as in the presence of tides or discharge waves.

### 2.2.3 Materials and Data Acquisition

#### *2.2.3.1 Study Area*

The St. Lawrence fluvial estuary is part of the St. Lawrence River – Great Lakes waterway. It spans 180 river kilometers (rkm), from the eastern end of Lake Saint-Pierre to the eastern tip of Orleans Island (Saint-François), located at the upper limit of saline intrusion (Figure 2.2.1). Its width varies from < 1 to 15 km, with maximum water depths in the navigational channel exceeding 60 m. The bathymetry features extensive intertidal areas, river bends, shoals and islands. The flow is characterised by vertically well-mixed freshwater, with an average discharge of 12,200 $m^3s^{-1}$ at Quebec City, which can more than double during the freshet season. Ocean

tides are amplified as they enter the St. Lawrence until they reach their highest level (~ 7 m in range) in the upper estuary at Saint-Joseph-de-la-Rive – hereafter referred to as rkm 0. About 66 rkm upstream, tidal ranges still exceed 6 m during the largest spring tides at Saint-François, i.e. the downstream limit of the fluvial estuary. Increases in water levels of more than 1 m $h^{-1}$ can be observed during the rising tide, leading to rapid changes in flow conditions as well as in the wetted areas. This generates strong current reversals and peak tidal discharges up to five times larger than the daily average. The tide is increasingly distorted and damped as it propagates upstream (Godin, 1999). Most of the short period tide (i.e. diurnal, semidiurnal, etc.) is damped in Lake Saint-Pierre (rkm 264), but long period oscillations are still noticeable as far as Montreal (rkm 360). The combination of strong tides, large river flows, wide river sections and variable bathymetry makes measurements in this particular environment challenging.

*2.2.3.2 Survey Strategy*

Boat surveys were conducted over semi-diurnal tidal periods (12h25) along 13 cross-sections of 1 to 4 km in width of the St. Lawrence fluvial estuary, representative of the longitudinal variability in geomorphological and tidal-fluvial properties (Figure 2.2.1). The cross-sections were aligned, when possible, with shore-based water level stations and distributed between Trois-Rivières and the Orleans Island, in regions of contrasting tidal ranges and/or degrees of ebb-flood asymmetry, as well as sections of complex geometries that are likely to present lateral gradients in flow properties (e.g., river bends, tidal flats). At each transect, the boat repeatedly moved back and forth across the channel following the same transect line, perpendicular to the mean flow direction. Boat speed was maintained at 1–2 m $s^{-1}$ on average to ensure data of good quality. In some instances, shorter surveys were made, due to field constraints (i.e. weather, length of daytime, travel time, etc.) or at upstream locations of low tidal variability [cf. Table 2.2.4 in section 2.2.9 (appendix B)].

The measurements were carried out between June 15 and August 25, 2009, so that most transects were surveyed at different phases on the neap-spring tidal cycle. Daily averaged net discharges at Quebec City varied between 11,100 and 14,600 $m^3s^{-1}$ during that period. Although the chosen instrumentation allows rapid measurements, synopticity was still difficult, if not impossible, to attain within individual crossings because of the combination of wide river sections and rapidly changing conditions associated with large tidal ranges and/or steep flood tides. The number of

crossings along with statistics on travel times, traveled distances and boat velocity for each transect are shown in Table 2.2.4 in section 2.2.9 (appendix B). Differences between the minimum and maximum travel times and distances indicate how extensive the tidal flats are at each transect, as they usually cannot be surveyed at or around low tide.

Measurements from boat surveys were used in combination with data from fixed stations distributed throughout the fluvial estuary (Figure 2.2.1), thus filling the gaps in time between consecutive crossings of a given survey and between surveys performed at different locations.

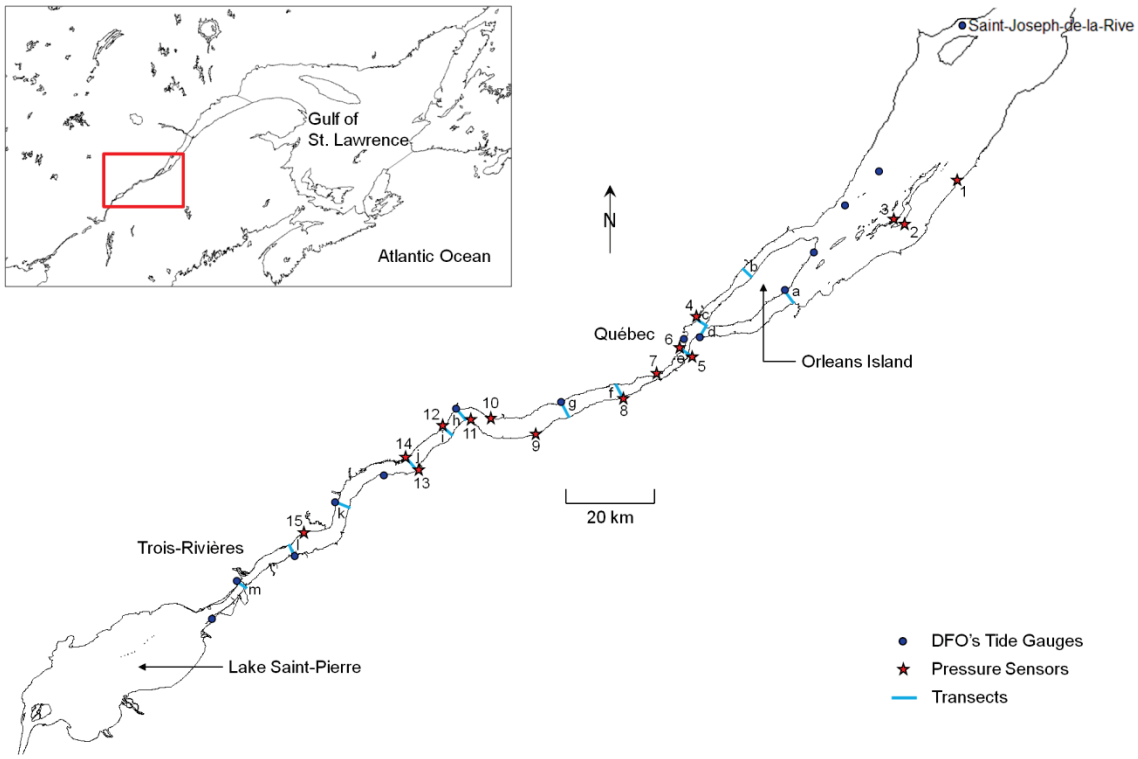


**Figure 2.2.1** **Map of the St. Lawrence fluvial estuary (Quebec, Canada) showing locations of the DFO's tide gauges (dark blue circles), pressure sensors (red stars), and transects (light blue lines).**

### *2.2.3.3 Instrumentation*

#### 2.2.3.3.1 Survey Boat

The boat used during the field campaign is owned by Environment Canada. It is 7-m long, 2.6-m wide and 1-m high. The hull and hardware are made of aluminum and stainless steel, respective-

ly, to avoid magnetic effects that could bias the ADCP internal compass. The boat has a static draft of approximately 0.5 m under normal loading, i.e. fuel tanks full, three people on board and 300 kg of equipment; it can thus be manoeuvred in rather shallow waters.

#### 2.2.3.3.2 Pressure Sensors

Water level variations were continuously monitored during the campaign, at a 3-min interval, at 13 tide gauges in the St. Lawrence fluvial estuary (Figure 2.2.1), maintained by Canada's Department of Fisheries and Oceans (DFO). To increase spatial resolution of the existing network and provide data for validation at the transects, 15 HOBO U20-001-01 hydrostatic pressure sensors were installed from June to October 2009 at one or both ends of the cross-sections as well as at critical points along the estuary where tide gauges are non-existent (Figure 2.2.1). Each sensor was mounted on a metal rod that was sunken into the river bed at low tide. Sampling interval was set to 15 min, thus allowing for a maximum of ~7.5 months of measurements, given a memory of 64K bytes (or, equivalently, ~21,700 pressure and temperature samples). The operation range of the sensors is approximately 0–9 m and the water level accuracy is typically 0.005 m, with a maximum error of 0.01 m (Onset Computer Corporation, 2012).

#### 2.2.3.3.3 ADCP

Velocity measurements were made using a 600-kHz RD Instruments Rio Grande ADCP, with firmware version 10.16, mounted on the side of the boat. The transducers were set between 0.25 and 0.35 m below the water surface depending on wave conditions. The frequency of acquisition was set to 2.5 Hz and the vertical bin size to 0.5 m with a 0.25-m blanking distance. The ADCP worked in bottom track mode 5 and water mode 12 (cf. Teledyne RD Instruments, 2009). The internal ADCP compass measures the ADCP orientation relative to the earth's magnetic field. A correction for local magnetic variation was calculated at each location, following the compass correction procedure described in WinRiver II User's Guide (Teledyne RD Instruments, 2009). Corrections varying around $-17.0 \pm 0.5°$ were applied; the heading information was thus used to output velocities in earth coordinates. Velocity measurements were compensated for rocking and tilting of the ADCP by means of internal pitch and roll sensors. Navigation data were acquired using a NovAtel PRO-PACK G2-D89-RT20W DGPS placed on top of the ADCP and connected to the same computer; the DGPS is capable of sub-meter horizontal accuracy.

#### 2.2.3.3.4 RTK GPS

An independent Trimble R6 RTK GPS receiver was used for positioning and water level measurements along the transects. Two receivers, the base and the rover, were operated simultaneously, collecting data from common satellites at the same epoch rate (1 s), using both GPS and GLONASS satellite systems. The base receiver was positioned on the shore in sight of the rover. The latter was mounted at the rear of the boat, about 1 m from the ADCP. A radio link was used to transmit the base receiver coordinates and its observations to the rover during data acquisition. Carrier phase corrections (19-cm wavelength) enable the position of points to be determined in real-time as the rover moves (Ghilani & Wolf, 2012).

This setup was tested for the first time during this campaign, while years of experience had been cumulated with the ADCP/Novatel DGPS system by our team. Thus, to allow independent testing of the setup, the Trimble GPS was not connected to the ADCP. They should however be integrated in the future, to prevent synchronization issues between velocity and water level data.

### 2.2.4 Data Analysis Procedures

The data analysis procedures are summarized in Figure 2.2.2 and detailed in the following paragraphs. Methods for the correction and conversion of the data are presented in section 2.2.8 (appendix A).

#### *2.2.4.1 Smoothing and Gridding*

A mean transect, whose length corresponds to the longest crossing made, was defined for each survey by fitting a first-degree polynomial function to the East and North data coordinates from all crossings (Figure 2.2.3). The data points were projected onto the mean transect and new coordinates were calculated, corresponding to the closest points on the line to the data. A coordinate system in the mean transect referential was thus defined, in which velocity directions increase in the counter-clockwise direction, with the 0° vector oriented downstream and perpendicular to the mean transect. Velocity components were rotated accordingly so that the u- and v-components represent the along- and cross-channel velocities, respectively oriented perpendicular and parallel to the mean transect. Data points distanced from the mean transect by more than 150 m were removed from the records.

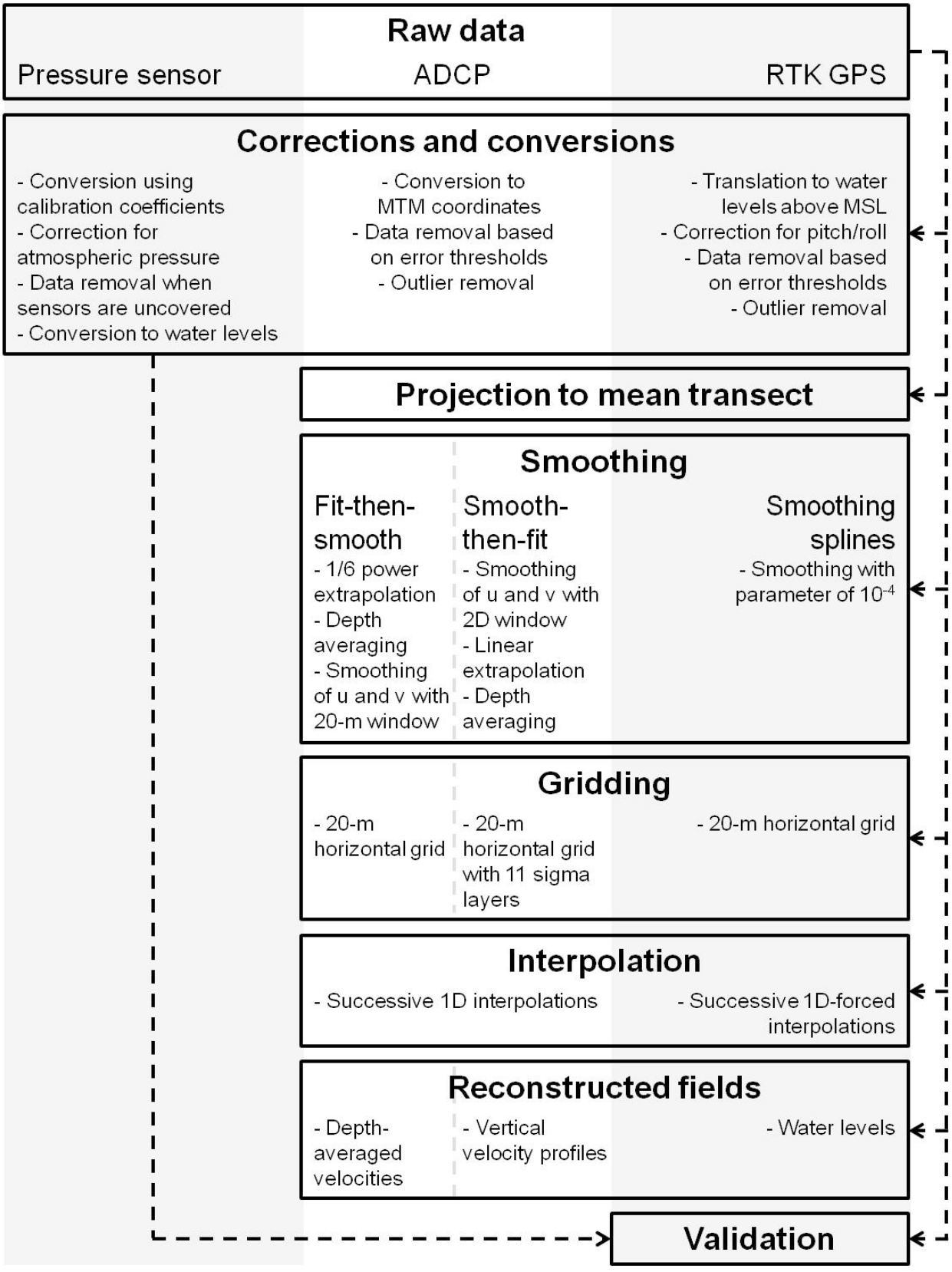


**Figure 2.2.2** **Flow diagram summarizing the data analysis procedure.**

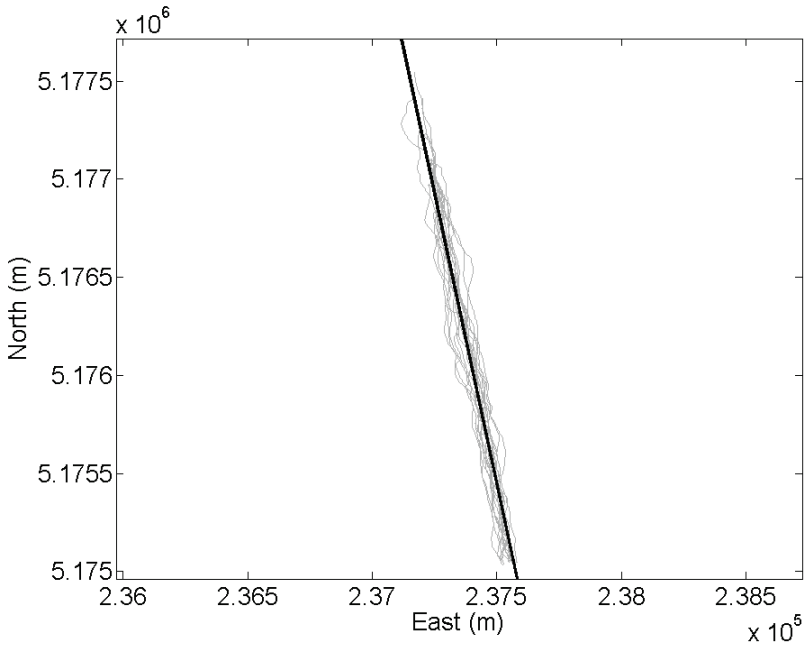


**Figure 2.2.3** **Mean transect line (black) fitted through all the crossings made at Saint-Nicolas (grey). Coordinates are in MTM zone 7 (NAD83).**

All data were smoothed and gridded, one crossing at a time, to reduce random variations in the data and facilitate subsequent analyses. ADCP data points from each crossing were first sorted according to the along-transect direction to correct for boat turns or deviations from the transect line, e.g., to give priority to ships. Two curve-fitting approaches, either performed before or after smoothing, were tested for the extrapolation of velocities in the unmeasured layers at the top and bottom of the water column, which are associated with the transducer depth and blank after transmit (top layer) and side-lobe interference (bottom layer).

The first procedure is referred to as "fit-then-smooth" (f-t-s), following a slightly different terminology and approach than Sime *et al.* (2007). Depth-averaged velocity magnitudes are calculated from the raw ADCP data by summing, for each ensemble, the discharges in both the measured and unmeasured layers, then dividing by the ensemble area. In the measured layer, the discharge is computed by summing the bin velocities using the default nearest neighbor routine. Discharge in the unmeasured layers is extrapolated by fitting a one-sixth power curve through the measured data. Following Chen (1991), the power-law equivalent of Manning's formula for open channels has the form (Simpson & Oltmann, 1993):

$$U = a' z^m , \tag{2.2.1}$$

where $U$ is the velocity profile, $a'$ is a constant determined by regression that is function of shear velocity and bed roughness, $z$ is the elevation measured from the bed (positive upward), and $m = 1/6$. Depth-averaged flow directions are obtained from the measured velocity components only, summed independently, by calculating the arctangent of the ratio of the summed components, i.e. $\arctan\left( \sum_{i=1}^{n} u_i \Big/ \sum_{i=1}^{n} v_i \right)$, where $n$ is the number of measured bins. Depth-averaged u- and v-velocities are then computed using the depth-averaged magnitudes and directions. Once depth-averaged components are obtained, they are smoothed separately with a horizontal 20-m moving average, using the *smooth* Matlab function (MathWorks, 2012). The window size was chosen small enough to keep subtle variations in velocity around the steepest gradients in bathymetry, but large enough to filter out the effects of small-scale turbulence. Smoothed, depth-averaged velocity magnitudes are obtained by computing the (signed) modulus of the smoothed components (denoted $u_{sm}$ and $v_{sm}$), i.e. $\text{sign}(u_{sm}) \times \sqrt{u_{sm}^2 + v_{sm}^2}$ .

The second procedure, called "smooth-then-fit" (s-t-f), begins with smoothing the binned u- and v-velocities using a two-dimensional (2D) moving window of 20 m in width and of a height corresponding to one tenth of the instantaneous water depth, yielding a constant number of sigma layers in the vertical. Water depths are assumed constant during the time interval encompassed by each window. The window heights however vary in space and in time as a function of channel bathymetry and tidal height. Smoothed velocity components are linearly extrapolated in the unmeasured layers, then summed vertically and divided by the number of sigma layers to obtain smoothed, depth-averaged u- and v-velocities. Smoothed, depth-averaged velocity magnitudes are calculated from the smoothed components, as described in the f-t-s procedure. Depth-averaged flow directions are retrieved from the smoothed components by computing the $\arctan\left(u_{sm}/v_{sm}\right)$. As opposed to the f-t-s procedure, this method not only yields smoothed, depth-averaged velocities, but is capable of providing smoothed velocity components at various (sigma) depths in the water column, which are used for time interpolations in a subsequent step (cf. Figure 2.2.2).

Several other methods exist to extrapolate velocities in the unmeasured layers (see, e.g., Muste *et al.*, 2004b). Although only two contrasting methods were tested in the present analysis to demonstrate the usefulness of the approach, virtually any method could be used in place of the ones used here. It is however suggested that tests be performed to ensure that the chosen extrapolation methods are representative of the measured data. Also, direct measurements in the unmeasured layers would be an excellent way to validate the methods, although this was not done here.

Water level variations are expected to be much smoother spatially than cross-channel velocities. RTK GPS elevations were therefore smoothed in time, one crossing at a time, using smoothing splines, which are continuous up to the second derivative. The *csaps* Matlab function was used (MathWorks, 2012). The cubic smoothing spline $s$ is constructed for the specified smoothing parameter $p$ and weigths $w_i$ so that it minimizes (Reinsch, 1967, de Boor, 1978)

$$p\sum_i w_i (y_i - s(t_i))^2 + (1-p)\int \left(\frac{d^2 s}{dt^2}\right)^2 dt\,, \tag{2.2.2}$$

where $y_i$ is the water level data measured at times $t_i$ during one crossing. The weights $w_i$ were set to 1 for all data points. The smoothing parameter $p$ was set to $1\times10^{-4}$; here, $p = 0$ produces a least-squares straight line fit to the data, while $p = 1$ corresponds to the cubic spline (exact) interpolant. The value of $p$ was chosen after some numerical experimentation to eliminate random oscillations of the water surface while still capturing aperiodic and low-frequency variations such as due to tides or local gradients in bathymetry. Alternatively, an error tolerance based on measurement accuracy could be used instead of a constant smoothing parameter, or $L^1/L^2$ minimizations could be performed to down-weight erroneous data (e.g., Bube & Langan, 1997), although these tests were not carried out. Once smoothed, the data points were sorted according to the along-transect direction before gridding.

A horizontal grid with a 20-m resolution was defined along the mean transect. Smoothed, depth-averaged velocity and water level data were interpolated at the grid points along with their respective times of measurement, thus forming a spatially regular grid composed of measurements taken at irregular times. Not only the measurement times are irregular within individual crossings, but an unevenly distributed time series is obtained at each grid point composed of data

from successive crossings. Figure 2.2.4 shows an example of how the data points are positioned in a space-time referential. In the time axis direction, data points are the most evenly distributed around mid-transect, while they are the most unevenly separated near the shores. The length of each crossing also varies as a function of the tide; as tide decreases, tidal flats gradually empty and become too shallow to be surveyed, thus creating gaps in the time series.

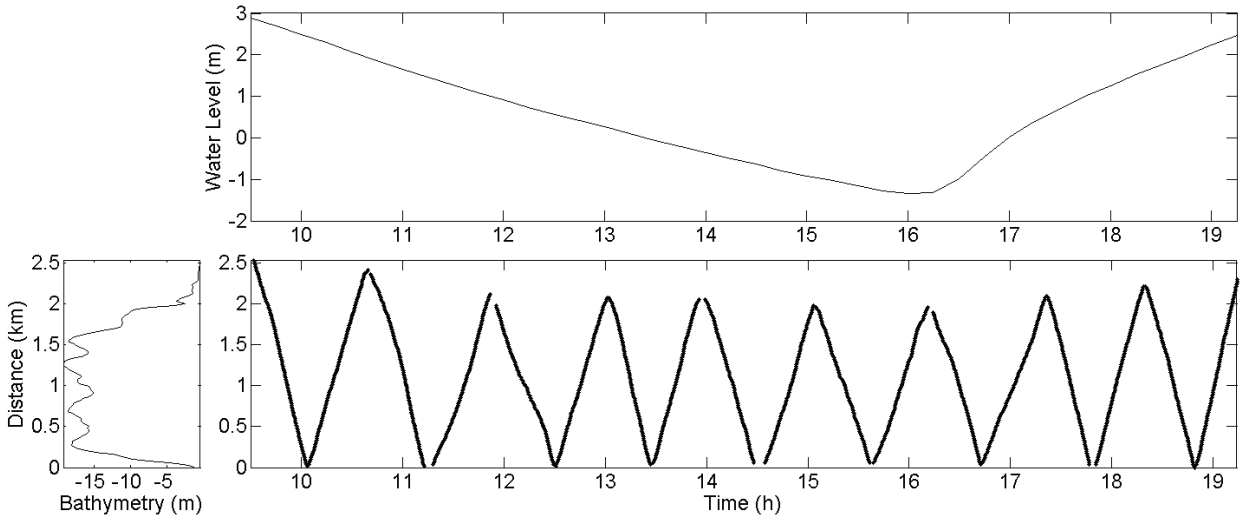


**Figure 2.2.4** **Space-time diagram (bottom-right) showing the position, both in time and in space, of the gridded data points along the boat tracks at Saint-Nicolas. (top) Tidal signal during the survey. (bottom-left) Cross-channel bathymetry from north to south shores. Local time reference is Eastern Daylight Time.**

A sigma-coordinate system was used to represent vertical velocity profiles continuously in space and in time, regardless of the variations in cross-channel bathymetry and water surface elevation. At each point on the 20-m horizontal grid and at each time of measurement, the water column was divided into tenths of the total depth and normalized to the water depth, yielding relative depths distributed between 0 and 1, respectively corresponding to the water surface and river bed. Smoothed u- and v-velocity profiles stemming from the s-t-f procedure were interpolated at the sigma coordinates, thus forming a spatiotemporal grid similar to that of Figure 2.2.4 at each sigma depth.

### *2.2.4.2 Interpolation*

Synopticity was not assumed within individual crossings (as shown in Figure 2.2.4). An interpolation procedure was thus applied to the gridded velocity and water level data in order to reconstruct synoptic lateral fields at any time within the surveyed period. Various interpolation

methods were tested by Matte *et al.* (2010) in order to demonstrate their respective potential in reconstructing continuous fields from measured data points, given their configuration and variability. Tested interpolation methods were grouped into two categories: one-dimensional (1D) interpolations in the time axis direction successively performed at each point on the spatial grid, and 2D space-time interpolations. They included piecewise linear, polynomial, cubic spline, smoothing spline, piecewise cubic Hermite polynomial, Fourier, and thin-plate spline interpolations (Matte *et al.*, 2010). The authors showed that, among the methods tested, successive 1D interpolations using smoothing splines and 2D interpolations using thin-plate splines (TPS) were best-suited for reconstructing continuous velocity and water level fields, respectively. These preferences were mainly attributed to the inability of 2D TPS to represent spatially non-uniform velocity fields, characterized by much sharper lateral gradients than water levels. These methods are the basis for the techniques presented herein. Other interpolation methods can be found in Sokolov & Rintoul (1999) and Emery & Thomson (2001), although not tested here.

In the following, the independent data are assumed to be 2D (i.e. 1D in space and 1D in time) and the dependent data a scalar (e.g., water level, u- and v-component velocity) obtained from a series of measurements $i = 1..N$ taken at locations $x_i$ and instant $t_i$. This is a surface interpolation problem in which measured data values $y_i$ are defined at a set of points $(x_i, t_i)$. An interpolation function $f(x,t)$ is sought, which comprises the data, i.e. $f(x_i, t_i) \cong y_i$, and provides a continuous field that may be evaluated at any set of points $(x,t)$, on which the information from the data is smoothly propagated.

Velocity time series from each grid point were successively interpolated using 1D smoothing splines [cf. Eq. (2.2.2)]. The interpolations were made only in the time axis direction to prevent local variations in the data to be propagated laterally. As a result, a near-zero velocity at the bank is not propagated to the deeper sections of the channel, as it would if 2D interpolation methods were improperly used. The spatial gaps between the interpolated curves were filled by linear interpolations. The radius of influence of any data point is thus equal to twice the spatial grid resolution, i.e. 40 m, except at the transect ends where it is 20 m. Time interpolations were only made between consecutive crossings, since they usually do a poor job when large gaps occur in the time series around low tide due to unmeasured intertidal areas. Depth-averaged u- and v-component velocities were interpolated separately using a smoothing parameter $p$ of $5\times10^{-9}$ and

$1\times10^{-10}$, respectively. These values were chosen in such a way to control the trade-off between smoothness and closeness of fit. Vertical velocity profiles were interpolated in a similar fashion, one sigma layer at a time, the time series from each sigma depth being treated independently.

Interpolation of water level data was first made using 2D TPS, which enables features appearing in the record at one specific point in space and in time (e.g., the tide extrema) to be smoothly propagated from one end of the transect to the other, regardless of the gaps in the data (Matte *et al.*, 2010). TPS are one class of radial basis functions (Beatson *et al.*, 2004). The biharmonic TPS have continuity up to the first derivatives, thus making them smooth enough for interpolating across wide gaps in the data (Vennell & Beatson, 2006). In 2D, the TPS minimize a function similar to Eq. (2.2.2), where the terms are 2D in time and in space, and the derivatives replaced by a set of partial derivatives with respect to $t$ and $x$. Description and application of TPS in oceanographic studies can be found in Candela *et al.* (1992) and Vennell & Beatson (2006), among others. Here, the *tpaps* Matlab function was used to generate a 2D interpolation surface from the gridded water level data. The default smoothing parameter $p$ was used (MathWorks, 2012).

The performance of 2D TPS interpolators was assessed by comparing the reconstructed water level fields to successive 1D smoothing spline interpolations, with $p$ set to $5\times10^{-9}$. A third method, described in the following, was also tested, referred to as 1D-forced interpolation, which is a combination of the other two. Starting from the assumption that water levels smoothly vary from one shore to another, a reference tidal curve is defined from the 2D TPS interpolation, serving as a basis function for successive optimizations performed at the grid points. To determine the reference curve, individual interpolated time series are retrieved at the grid points from the 2D TPS interpolation; they are shifted to make their minimum and/or maximum coincide, and the median curve is found and used as the reference. This curve is iteratively optimised to best fit the data in time, one grid point at a time, by applying a vertical shift (in m), an amplitude factor, and a stretching factor in time. These three parameters serve as input to a non-linear constrained minimization performed using the *fmincon* Matlab function (MathWorks, 2012), with bounds respectively defined as [-0.2, 0.2], [0.95, 1.05] and [0.95, 1.05]. The optimization uses an interior-point algorithm (Byrd *et al.*, 2000, Waltz *et al.*, 2006) where a sequence of approximate minimization problems is solved using a direct (Newton) step, or a conjugate gradient step if a direct step cannot be taken – e.g. when the approximate problem is

not locally convex near the current iteration. Because the form of the curve is given *a priori*, gaps in the time series due to shorter surveys over tidal flats are also filled. The spatial gaps between the final interpolated curves are filled by linear interpolations.

### 2.2.5 Assessment

Assessment of the methods introduced in the previous section is made in the following paragraphs. Raw data statistics and accuracy are presented in section 2.2.9 (appendix B).

#### *2.2.5.1 Smoothing of Random Errors*

Random errors in both water levels and velocities were removed by smoothing, after being corrected for outliers and systematic errors, leaving only the low-frequency variations associated with local tidal hydrodynamics. An example of raw and smoothed water levels and depth-averaged velocity components is presented in Figure 2.2.5 for a crossing made at Saint-Nicolas. Velocity extrapolations in the unmeasured layers were made following the f-t-s method. As shown in the figure, smoothing splines are well-suited to water level data, because the low-frequency variations are expected to be smooth both spatially and temporally. Cross-channel velocities, however, generally exhibit large variations in space that are correlated with the shape of the channel; in that case, the use of smoothing splines may lead to oscillations. These can typically be removed by reducing $p$ [cf. Eq. (2.2.2)], but at the cost of a loss of representativeness of the actual gradients present in the data. The moving average was therefore preferred to smoothing splines for velocity data as its performance is not sensitive to those variations.

The magnitude of random oscillations in each time series varies as a function of both time and space depending on the wave, wind, and turbulence conditions. Smoothing thus consists of both time and space averaging. For example, with an average boat speed of 1 m $s^{-1}$ and a 20-m smoothing window, eddy fluctuations with time scales smaller than 20 s are removed from the velocity records. The same applies to oscillations in water levels due to waves, where the smoothing window is replaced by a smoothing parameter.

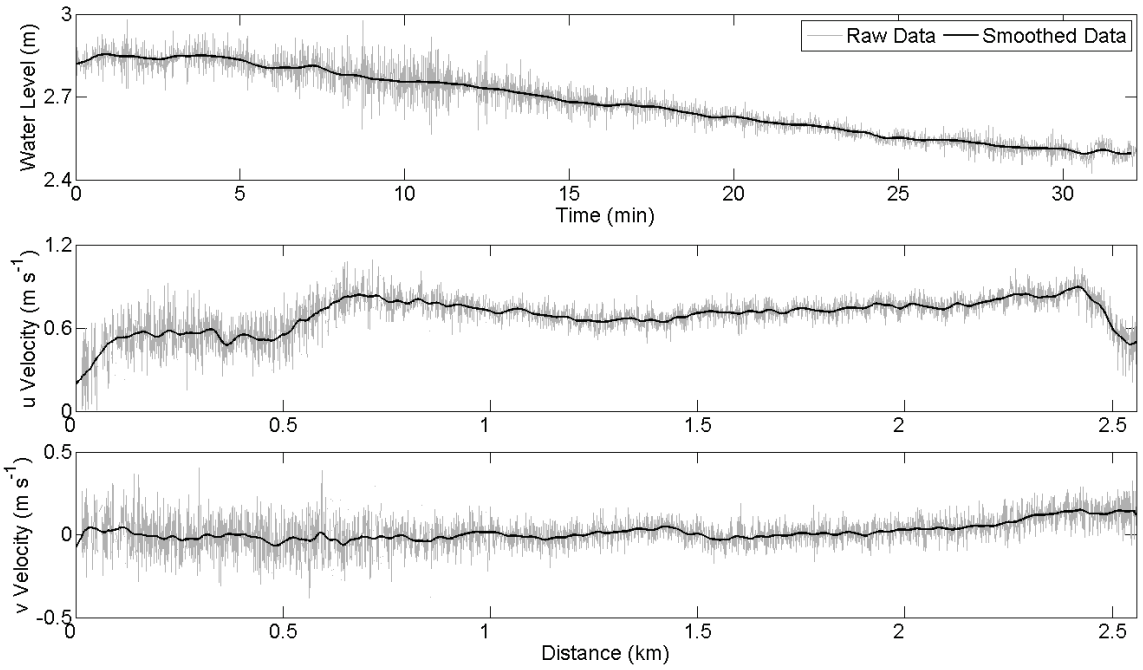


**Figure 2.2.5** **Data smoothing of a crossing at Saint-Nicolas. (top) Raw and smoothed water levels, depth-averaged u- (middle) and v-component velocities (bottom), as a function of time (water levels) and space (velocities).**

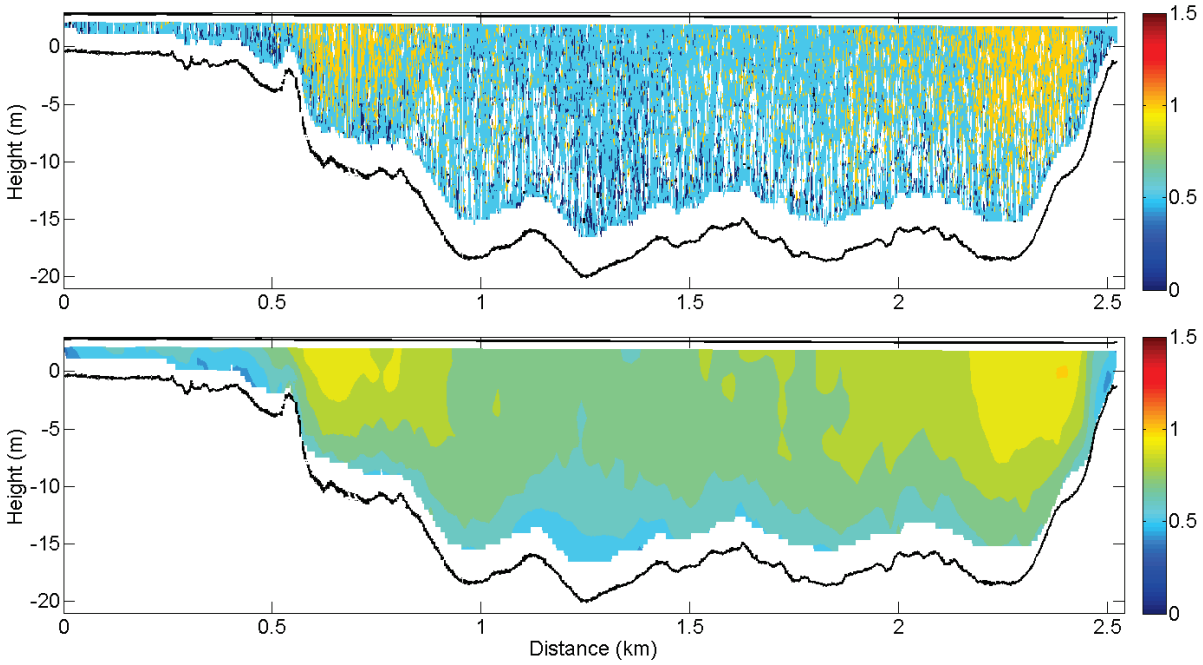


**Figure 2.2.6** **Bin velocity smoothing of a crossing at Saint-Nicolas. (top) Raw and (bottom) smoothed, u-component velocity (in m s$^{-1}$). Black lines indicate the position of the water surface and river bed.**

Raw and smoothed u-component velocities are compared in Figure 2.2.6 for all vertical bins of the same crossing at Saint-Nicolas. The smoothed velocities were obtained from the 2D smoothing window implemented in the s-t-f method (extrapolations in the unmeasured layers are not shown). The resulting smoothed field bring out the local variability present in the data, while reducing the random fluctuations that characterize the raw data.

**Table 2.2.1** **Mean and maximum absolute differences between smoothed, depth-averaged velocity magnitudes: (first column) obtained directly by smoothing the amplitudes and calculated from the smoothed u- and v-components; (second column) calculated from the f-t-s and s-t-f methods.**

| Transect Location | Depth-Avg. Vel. Err. ($m\ s^{-1}$) | | Difference f-t-s/s-t-f ($m\ s^{-1}$) | |
|---|---|---|---|---|
| | Mean | Max | Mean | Max |
| Saint-Jean | 0.007 | 0.036 | 0.027 | 0.203 |
| Château-Richer | 0.009 | 0.110 | 0.182 | 0.870 |
| Beauport | 0.039 | 0.562 | 0.032 | 0.367 |
| Lauzon | 0.007 | 0.088 | 0.107 | 0.930 |
| Québec | 0.010 | 0.446 | 0.046 | 0.273 |
| Saint-Nicolas | 0.007 | 0.036 | 0.046 | 0.479 |
| Neuville | 0.010 | 0.240 | 0.025 | 0.172 |
| Portneuf | 0.012 | 0.126 | 0.113 | 0.676 |
| Deschambault | 0.020 | 0.347 | 0.033 | 0.230 |
| Grondines | 0.009 | 0.059 | 0.058 | 0.444 |
| Batiscan | 0.035 | 0.335 | 0.049 | 0.368 |
| Bécancour | 0.003 | 0.039 | 0.033 | 0.271 |
| Trois-Rivières | 0.004 | 0.020 | 0.028 | 0.096 |

As shown in Figure 2.2.5 and Figure 2.2.6, velocity components were smoothed separately. In both f-t-s and s-t-f techniques, velocity directions are computed from the u and v components, which is preferable to averaging individual directions, because erroneous values can otherwise be obtained due to angle ambiguity. For example, neighbouring vectors whose angles oscillate between 0 and 360° (i.e. in the mean flow direction) will average to 180°, which is incorrect. Such ambiguities are avoided by working with components. Smoothed velocity magnitudes and directions are therefore calculated from the smoothed u- and v-components, rather than smoothed directly. The resulting smoothed magnitudes, however, slightly differ from the magnitudes that would be obtained by smoothing the amplitudes directly, rather than from the components, as shown in Table 2.2.1 (first column). Mean differences are $\leq 4$ cm $s^{-1}$ at all locations, but differences as high as a few tens of cm $s^{-1}$ can be observed at some points.

#### *2.2.5.2 Comparison of Velocity Extrapolation Methods*

Velocity extrapolations were made in the unmeasured layers at the top and bottom of the water column, in order 1) to calculate depth-averaged velocities and 2) to provide data at each sigma-depth for time interpolation. Two curve-fitting procedures, leading respectively to two representations of cross-channel velocities, are compared in Figure 2.2.7. The first one (f-t-s) uses a one-sixth power fit through the measured data to provide values in the unmeasured layers and the second one (s-t-f) makes a linear extrapolation of the smoothed data. Left panel of Figure 2.2.7 shows a sample of u-component velocities measured at Neuville, vertically distributed in 0.5-m deep bins, over a 20-m distance. The blue curve shows the data smoothed with a 2D moving average, as done in the s-t-f method, and is compared to a one-sixth power fit (red curve). Both curves are equivalent in terms of representativeness of the underlying data. However, the moving average tends to be closer to the actual variations in the measured data as it is not restricted by any predetermined function. On the other hand, the one-sixth power fit may be more accurate in the unmeasured layers, especially near the bed where velocities tend to zero, provided that this assumption holds true. The power fit in Figure 2.2.7 is presented for illustrative purposes only, as this fit is applied to the total velocity in the f-t-s method, not to the components [cf. Eq. (2.2.1)], as well as to individual ensembles rather than to a set of ensembles falling within a given window. The u-velocity profile is nonetheless representative of the total velocity since it is oriented in the mean flow direction, perpendicular to the mean transect line. In comparison, the shape of the v-component profile (not shown) would not necessarily follow that of a one-sixth power law. Therefore, for the purposes of time interpolation, the smoothed velocity components needed at the sigma-depths are obtained using the 2D moving average with linear extrapolations in the unmeasured layers, as implemented in the s-t-f procedure.

Right panel of Figure 2.2.7 shows smoothed, depth-averaged velocities for a crossing made at Neuville, obtained from the f-t-s and s-t-f methods (red and blue curves, respectively). Overall, both curves follow the same patterns in velocities. Differences observed between the two curves are mostly influenced by the extrapolation made in the unmeasured layers and by the fact that the fit either precedes or follows smoothing in the two procedures. Table 2.2.1 (second column) presents the mean and maximum absolute differences between the two methods for each transect. These are below 0.1 $m\ s^{-1}$ on average at most locations, but can reach very high maximum values. Large differences are partly explained by non-standard velocity profiles, associated with

local changes in bathymetry, secondary currents, turbulence, or a transitory state of the river (e.g., near slack water). In such cases, fitting a predetermined function such as a one-sixth power law may be misleading (Muste *et al.*, 2004b). On the other hand, large errors in velocity either near the top or bottom of the measured layer necessarily lead to errors in the extrapolated velocities when linear extrapolation is applied. Thus, when comparing both approaches for extrapolation, large differences arise when either one of the methods (or both) falls outside of its respective range of applicability.

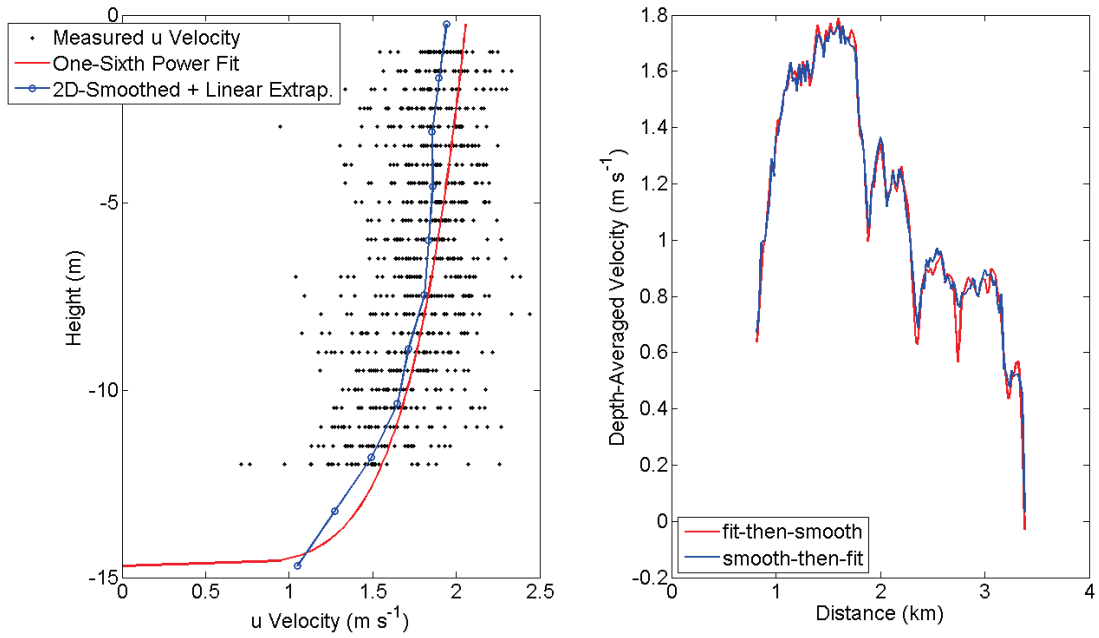


**Figure 2.2.7** **Comparison of velocity extrapolation methods. (left) u-component velocity profile measured at Neuville; black dots are the velocities measured in each 0.5-m deep bin over a 20-m distance; blue line shows the 2D-smoothed data centered at the sigma coordinates (blue circles) with linear extrapolations made in the top and bottom layers; red line is a one-sixth power fit through the measured velocities. (right) Smoothed, depth-averaged velocities for a crossing at Neuville obtained from the f-t-s (red) and s-t-f (blue) methods.**

Here, we opted for the f-t-s method to produce depth-averaged velocities, because experimentation showed that a vertical velocity profile that mimics a one-sixth power curve in the unmeasured layers is more appropriate than linear extrapolation during most of the tidal cycle. As hypothesized by Smith (1971), the dynamic effects related to rapid changes in flow conditions seem, on average, to have little effect on the velocity distribution relations, except near slack water (Simpson & Oltmann, 1993); more experimentation may however be needed to define suitable velocity profile functions if non-standard conditions prevail (e.g., due to changes in

bathymetry, secondary currents, strong shears and turbulence). Although the f-t-s method was used to produce depth-averaged velocities, velocity components were linearly extrapolated using the s-t-f method (cf. Figure 2.2.2), only for the sake of interpolation in the sigma layers, since fitting a one-sixth power curve separately to each velocity component was improper.

#### *2.2.5.3 Interpolation Error Due to Data Configuration*

The developed interpolation procedure is intended to fill gaps in time between successive crossings of a river cross-section, without prior assumption on synopticity. To assess the impact of data configuration and spacing on the interpolated fields at all 13 cross-sections, interpolations were performed on synthetic time series, re-interpolated to the same spatiotemporal grid constructed from the original data at the transects (e.g., Figure 2.2.4). At each location, the synthetic signal for water levels was constructed using the reference curve used in the 1D-forced interpolation method. For velocities, the synthetic signal was built using the calculated discharge time series, normalized between -1 and 1, which is representative of the average velocity. Errors in water levels were expressed in terms of differences in the height and time of occurrence of low or high water (LW or HW) between the synthetic and interpolated signals, while errors in velocities were translated into differences in the minimum or maximum velocity and time of slack water.

**Table 2.2.2** **Maximum interpolation errors in water levels and velocities due to data configuration in space and in time, calculated from synthetic signals for each interpolation method tested. Errors in water levels are expressed in terms of differences in the height and time of occurrence of LW or HW between the synthetic and interpolated signals; errors in velocities are translated into differences in the minimum or maximum velocity and time of slack water.**

| Transect Location | Water level | | | | | | Velocity | |
|---|---|---|---|---|---|---|---|---|
| | 1D | | 2D | | 1D-Forced | | 1D | |
| | LW/HW (m) | LW/HW (min) | LW/HW (m) | LW/HW (min) | LW/HW (m) | LW/HW (min) | Min/Max ($m\ s^{-1}$) | Slack (min) |
| Saint-Jean | 0.035 | 15.0 | 0.053 | 7.8 | 0.015 | 6.3 | 0.001 | 5.6 |
| Château-Richer | 0.026 | 11.7 | 0.057 | 5.7 | 0.029 | 3.6 | 0.013 | 2.5 |
| Beauport | 0.076 | 8.5 | 0.094 | 6.0 | 0.046 | 4.0 | 0.099 | 2.3 |
| Lauzon | 0.039 | 6.8 | 0.064 | 6.0 | 0.033 | 2.7 | 0.006 | 1.3 |
| Québec | 0.008 | 2.8 | 0.021 | 2.7 | 0.009 | 0.9 | 0.004 | 0.7 |
| Saint-Nicolas | 0.073 | 15.6 | 0.087 | 6.6 | 0.035 | 2.8 | 0.010 | 2.8 |
| Neuville | 0.140 | 12.3 | 0.151 | 9.8 | 0.039 | 6.4 | 0.016 | 3.5 |
| Portneuf | 0.021 | 2.9 | 0.030 | 1.8 | 0.022 | 2.3 | 0.032 | 2.9 |
| Deschambault | 0.006 | 1.4 | 0.090 | 6.8 | 0.040 | 2.3 | 0.008 | 0.2 |
| Grondines | 0.019 | 14.4 | 0.017 | 4.5 | 0.003 | 1.8 | 0.096 | – |
| Batiscan | 0.027 | 7.6 | 0.017 | 2.3 | 0.004 | 0.4 | 0.069 | 7.5 |
| Bécancour | 0.001 | 2.7 | 0.001 | 2.8 | 0.001 | 0.1 | 0.004 | – |
| Trois-Rivières | – | – | – | – | – | – | – | – |

Results are shown in Table 2.2.2 for every interpolation method tested. In general, errors in height and timing of LW and HW are the lowest with the 1D-forced method. Deschambault is the only location where errors are significantly lower with 1D smoothing spline interpolations. At Deschambault, the channel occupies only one fourth of the section, the rest being composed of tidal flats that are not covered by the surveys during several hours around low tide [cf. Table 2.2.4 in section 2.2.9 (appendix B)]. While the 2D and 1D-forced methods allow to fill gaps associated with shorter surveys (as opposed to the 1D method), the ability of the interpolators to reproduce low tide decreases in return, with errors that increase as a function of the extent (in space and in time) of the uncovered areas. This explains the larger errors at Deschambault. Moreover, error in 1D-forced interpolations is dominated by errors in the reference curve, derived from 2D TPS, whereas the optimization alone is responsible for errors several orders of magnitude lower (not shown). In an attempt to reduce errors, a reference curve could alternatively be defined using data at the pressure sensors, though compromising their use for independent validation. In its current form, the 1D-forced method leads to errors in the heights of LW or HW not exceeding 5 cm and errors in their timing less than 7 min at all locations.

As for velocities, interpolations are only made using 1D smoothing splines and therefore are more sensitive to data spacing. The error amounts to a few cm $s^{-1}$ for maximum or minimum velocities, as shown in Table 2.2.2, which still is one order of magnitude lower than measurement errors globally [cf. Table 2.2.6 in section 2.2.9 (appendix B)]. The time of slack waters are also well captured, with errors well below 8 min at all locations. The error however increases for velocity magnitudes as they are obtained from two interpolations, separately performed on the u- and v-components.

In Figure 2.2.8 is an example of the performance of all three methods in interpolating a synthetic water level signal with the same data configuration as in Batiscan. The time and height of HW extracted from the interpolated fields are compared to what is expected from the reference synthetic signal at all points across the section. It can be seen that errors from the 1D and 2D interpolations are the lowest around mid-transect and increase approaching the boundaries, where data points are the most irregularly spaced. Also, the interpolated HW tend to be lower and to occur later than expected, unless the data points are positioned exactly at the tide maxima. Conversely, the interpolated LW would tend to be higher and to occur earlier. This produces artificial gradients in interpolated quantities in the cross-channel direction. In contrast, the error

made with the 1D-forced method is systematic and barely changes along the transect, showing more robustness to changes in data distribution and spacing.

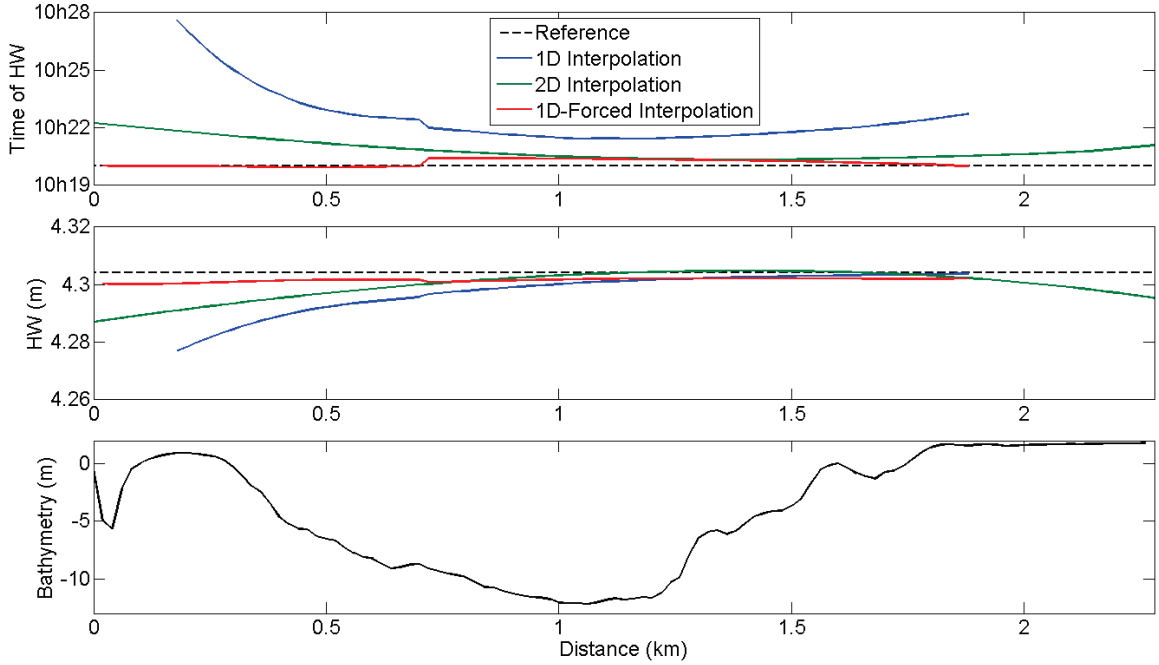


**Figure 2.2.8** **Interpolation error due to data configuration. Time and height of HW calculated from 1D (blue), 2D (green) and 1D-forced (red) interpolations of a synthetic (reference) signal with the same data configuration as in Batiscan. Local time reference is Eastern Daylight Time.**

### *2.2.5.4 Reconstruction of Continuous Velocity Fields*

Figure 2.2.9 shows the reconstructed depth-averaged velocity magnitudes and directions resulting from the interpolated u- and v-components at Saint-Jean. The velocity field in Figure 2.2.9a presents significant lateral and temporal variations that are related to the shape of the channel and to the effect of the tide. Despite the fact that 1D-time interpolations were performed separately at each grid point, there is a strong lateral coherence between the interpolated data from adjacent grid points. This suggests that the spline functions used, along with their respective smoothing parameters, are well adapted to the variability and distribution of the underlying data. This is confirmed by the tests performed using synthetic signals (cf. Table 2.2.2).

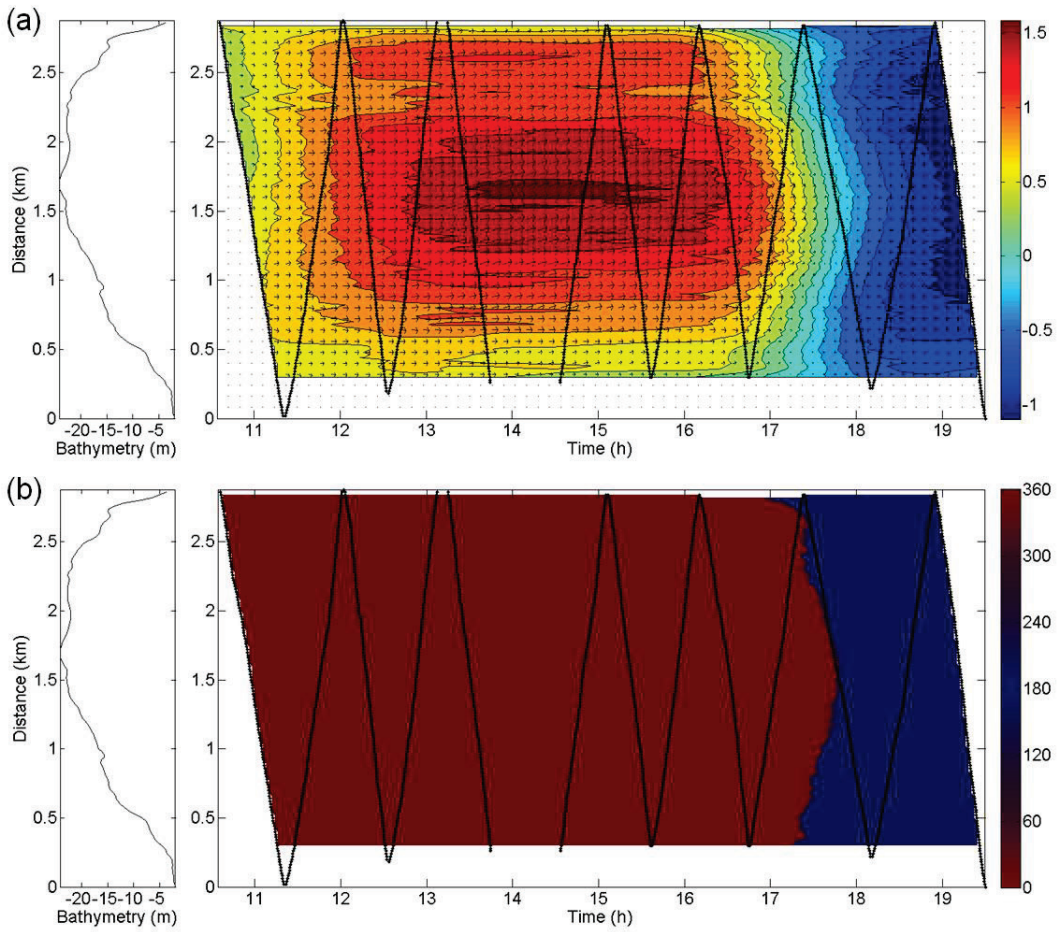


**Figure 2.2.9** **(a) Reconstructed depth-averaged velocity magnitudes (in m $s^{-1}$) at Saint-Jean from interpolated u- and v-components, along with their respective vectors. (b) Velocity directions (in degrees) showing the time of current reversal. Black dots correspond to the gridded data along the boat tracks. Cross-channel bathymetry from north to south shores is shown on the left panels. Local time reference is Eastern Daylight Time.**

Velocity vectors in Figure 2.2.9a are mainly oriented in the along-channel direction and only show small cross-channel variations in their orientation, with v-component velocities not exceeding 0.13 m $s^{-1}$. Velocity directions in Figure 2.2.9b were calculated from the interpolated u- and v-velocity fields. The transition from 0° to 180° highlights the time of current reversal, which presents lateral variations of almost one hour between the shore and the center of the channel, much higher than the interpolation error in the time of slack water calculated at Saint-Jean (5.6 min) from synthetic fields (Table 2.2.2). Such features can only be adequately captured when interpolations are performed on the velocity components, because they do not necessarily change at the same rate or synchronously, especially around slack water. In fact, results from

angle interpolations (not presented) were strongly correlated in space and very sensitive to the position and spacing of the data.

**Table 2.2.3** **Interpolation errors in water levels and depth-averaged velocities when compared to water level data at the tide gauges (first column), and to the gridded RTK GPS and ADCP data (last two columns). The first comparison serves as validation for water levels, whereas the last two are a measure of closeness of fit. Among the three interpolation methods tested for water levels, only results from the 1D-forced method are shown.**

| Transect Location | Tide Gauge (m) | | RTK GPS (m) | | ADCP ($m\ s^{-1}$) | |
|---|---|---|---|---|---|---|
| | Mean | Max | Mean | Max | Mean | Max |
| Saint-Jean | 0.066 | 0.187 | 0.032 | 0.106 | 0.014 | 0.074 |
| Château-Richer | – | – | 0.025 | 0.083 | 0.029 | 0.219 |
| Beauport | 0.128 | 0.334 | 0.038 | 0.129 | 0.036 | 0.322 |
| Lauzon | 0.104 | 0.443 | 0.033 | 0.142 | 0.024 | 0.168 |
| Québec | 0.077 | 0.111 | 0.015 | 0.058 | 0.034 | 0.368 |
| Saint-Nicolas | 0.046 | 0.147 | 0.023 | 0.083 | 0.018 | 0.124 |
| Neuville | 0.033 | 0.091 | 0.017 | 0.096 | 0.012 | 0.052 |
| Portneuf | 0.150 | 0.204 | 0.011 | 0.050 | 0.020 | 0.171 |
| Deschambault | 0.072 | 0.133 | 0.022 | 0.087 | 0.062 | 0.490 |
| Grondines | 0.029 | 0.093 | 0.014 | 0.065 | 0.006 | 0.044 |
| Batiscan | 0.023 | 0.079 | 0.022 | 0.077 | 0.010 | 0.082 |
| Bécancour | 0.036 | 0.047 | 0.005 | 0.020 | 0.016 | 0.181 |
| Trois-Rivières | 0.077 | 0.089 | 0.002 | 0.011 | 0.010 | 0.063 |

Mean and maximum (absolute) differences between the interpolated depth-averaged velocities and the gridded ADCP data are shown in Table 2.2.3 (last column), as a measure of closeness of fit. Errors are inferior to 4 cm $s^{-1}$ on average at all locations with the exception of Deschambault (6.2 cm $s^{-1}$). Higher absolute errors can partly be explained by larger range and magnitude in measured velocities [cf. Table 2.2.6 in section 2.2.9 (appendix B)]. At Deschambault, for example, velocities exceed 4 m $s^{-1}$ around low tide, which is significantly higher than anywhere else. The number of crossings and distribution and spacing of the data may also affect the performance of the interpolation, as shown above.

### *2.2.5.5 Comparison of Interpolation Methods for Water Levels*

A comparison of interpolated water levels obtained from the 1D, 2D, and 1D-forced methods is made in Figure 2.2.10 using data from a highly channelized cross-section at Grondines, for which significant lateral variations in water levels are observed. Results from successive 1D smoothing splines (Figure 2.2.10a) show high sensitivity to errors in the data especially around

high and low tides, either associated with changes in satellite number [cf. Figure 2.2.14 in section 2.2.9 (appendix B)], residual dynamic draft effects or data spacing, as revealed by an artificial bump in the interpolation near the south shore between the 8th and 10th crossings. Because water levels are expected to vary smoothly in space, results from 2D TPS (Figure 2.2.10b) are better suited for the interpolation of water levels than the 1D method. It maintains a much stronger link between data from adjacent grid points, by enabling the information to be smoothly propagated from one end of the section to the other. However, the degree of smoothness obtained from the default smoothing parameter $p$ is so high that subtle lateral variations are lost in the process. Yet, increasing $p$ most often led to a failure in the convergence of the algorithm; the default $p$ therefore was the only obvious choice of smoothing parameter. For its part, the interpolated field obtained from the 1D-forced method (Figure 2.2.10c) lies midway between the results of the two other methods. The use of a reference curve as a basis for the interpolation preserves the strong link between data from adjacent grid points, while allowing freedom in the interpolation through local optimization. The lateral variations thus obtained are smooth, but they exhibit gradients that are closely related to the shape of the channel, most likely of physical origin. Errors due to data spacing are also significantly reduced (cf. Table 2.2.2) and measurement errors seem to have little effect on the result.

Differences between the interpolated water levels from the 1D-forced method and the gridded RTK GPS data are presented in Table 2.2.3 (middle column). Mean errors are inferior to 4 cm at all locations, indicating a good fit of the data. Errors in water levels made with the 1D and 2D interpolation methods (not presented) were often lower, partly because they have much more degrees of freedom than the 3-parameter optimization implemented in the 1D-forced method. The latter, however, is more robust to measurement error and less sensitive to data configuration than the other two methods, as shown in Figure 2.2.10 and Table 2.2.2. In seeking an interpolation function, the aim is to minimize the error down to a certain level, beyond which the ability of the interpolator to represent the physics degrades even if error is decreased. This critical level is strongly linked to measurement and instrumentation accuracies. Closeness of fit and representativeness of the physics are, in that sense, orthogonal.

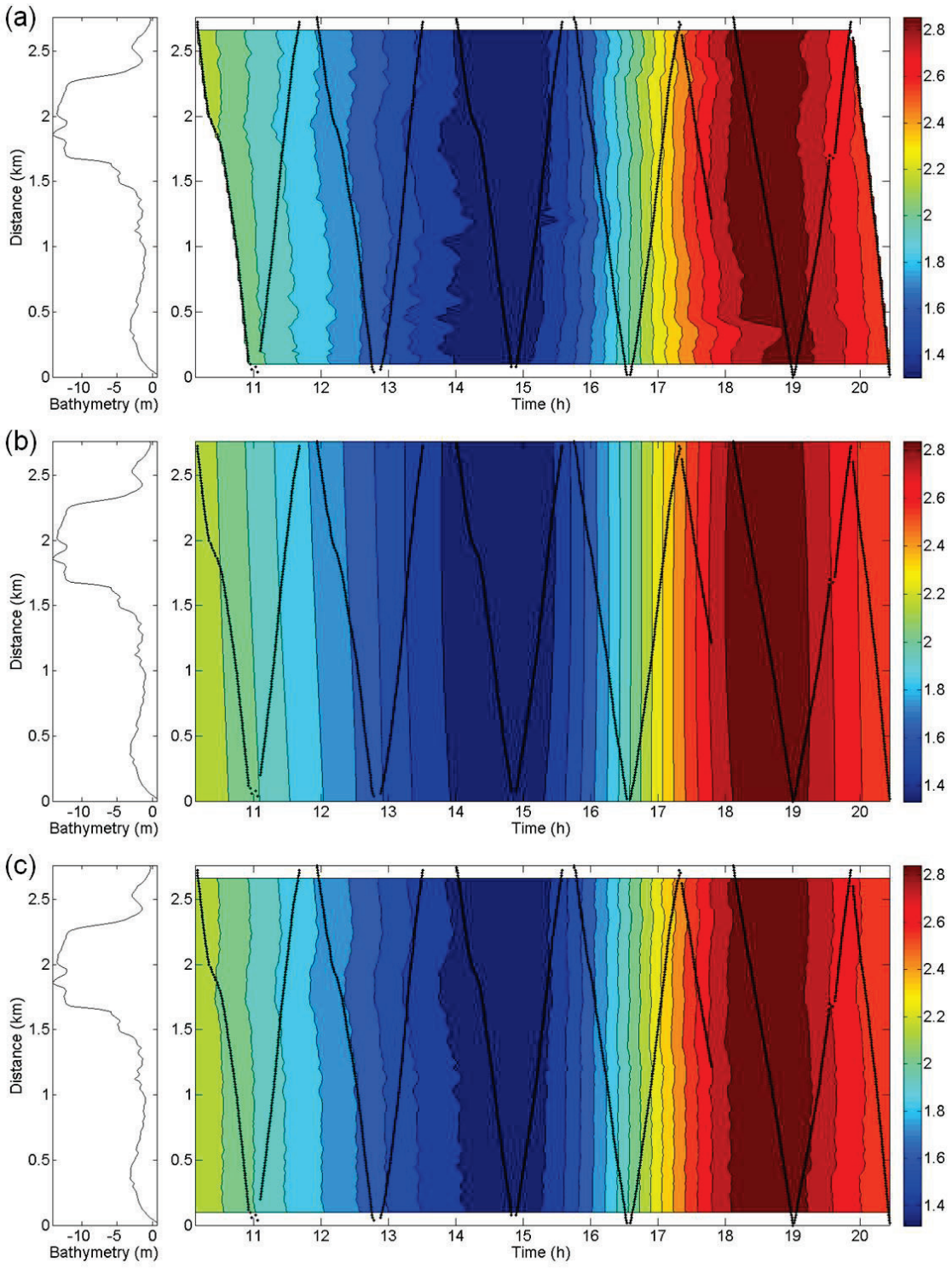


**Figure 2.2.10** **Comparison of water level interpolations (in m) at Grondines using (a) successive 1D smoothing splines, (b) 2D TPS, and (c) a 1D-forced reference curve. Black dots correspond to the gridded data along the boat tracks. Local time reference is Eastern Daylight Time.**

To further validate the interpolated water levels, they were compared to water level data measured at nearby tide gauges (first column of Table 2.2.3). At each location, errors are calculated based on the interpolated water levels at the grid point closest to the tide gauge. Mean differences are as high as 15 cm, with maximum errors reaching 44.3 cm. This is partly attributed to the tide extrema that are well captured at the tide gauges, but not so well at some transects depending on the position of the gridded data in time and in space. The maximum errors generally occur around LW or HW, generating artificial lateral slopes in the interpolated fields; part of this error has been quantified in Table 2.2.2. Other possible error sources include errors in the reference curve derived from 2D TPS, errors in the reduction of measured elevations to MSL, residual dynamic draft effects, measurement errors in the tide gauge data, including drift of the pressure sensors [cf. Table 2.2.5 in section 2.2.9 (appendix B)], and differences associated with the distance separating the tide gauge from the closest point on the grid. The mean differences presented in Table 2.2.3 are thus an estimation of the remaining systematic errors in RTK GPS elevations.

A similar comparison is made in Figure 2.2.11 for water levels measured at Saint-Nicolas at the south end of the transect. Measured data, both at the tide gauge and from the RTK GPS, are compared to the three interpolated curves tested. The 1D-forced interpolation yields very similar results to those of the 2D TPS interpolation, while the 1D smoothing spline is the poorest interpolator, especially around low tide. Clearly, the RTK GPS measurements did not capture the low tide at this end of the transect, mainly because of the cross-section width (~2 km at low tide). This reinforces the need for robust interpolation techniques for water levels capable of adequately reconstructing their variability at a higher temporal resolution. In this regard, the 1D-forced interpolation helps improve the representation of water levels, by keeping the average form of the signal as a starting basis for optimization.

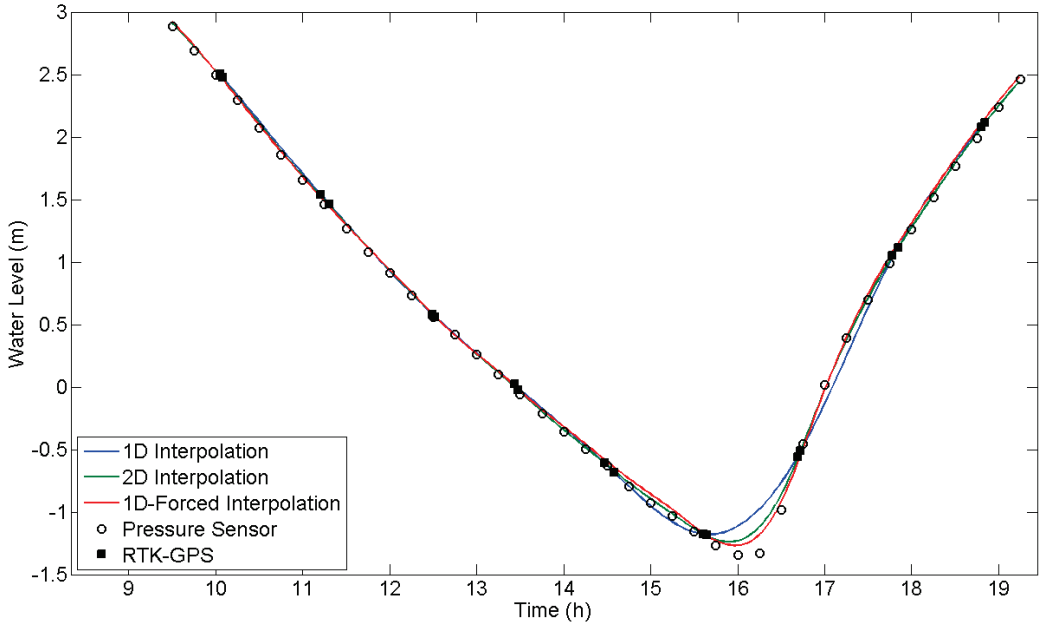


**Figure 2.2.11** **Validation of water level interpolations at Saint-Nicolas. Measured water levels by the pressure sensor (circles) and by the RTK GPS at the closest (southernmost) transect grid point (squares). Blue, green and red lines show 1D, 2D and 1D-forced interpolations of the RTK GPS data, respectively. Local time reference is Eastern Daylight Time.**

### *2.2.5.6 Error Made When Assuming Synopticity*

The data analysis procedure presented herein is based on the premise that measurements taken during each crossing are not synoptic. In this section we assess the relevance of not making this assumption, through an example, shown in Figure 2.2.12. Cross-sectional velocity magnitudes measured during a crossing at Saint-Nicolas are compared to velocities interpolated at the time when the boat was halfway through the transect. The measured data shown in top panel of Figure 2.2.12 were collected during a period of 37 min. The water surface increased by 1 m during that period and currents reversed slightly passed mid-transect, after 1.2 km. In rivers where tidal range is much lower, this velocity distribution would normally be treated as if each ensemble had been collected at an identical time, corresponding to the mean time of the crossing (e.g., Dinehart & Burau, 2005b). In the present case, however, the tidal variation is too large and the river cross-section too wide for the same reasoning to be applied. In fact, making such an assumption would lead to false interpretations on the dynamics of the system. When looking at the bottom panel of

Figure 2.2.12, we can see the actual (interpolated) velocity distribution occurring at mid-time. Several features differ from the top panel: the velocity magnitudes are lower on average and both the region of maximum velocity and the zero-velocity fronts of current reversal are shifted horizontally, with current reversals propagating from both shores rather than only one. Hence, the difference between the two velocity distributions presented in Figure 2.2.12 is an indication of the error made if synopticity was assumed.

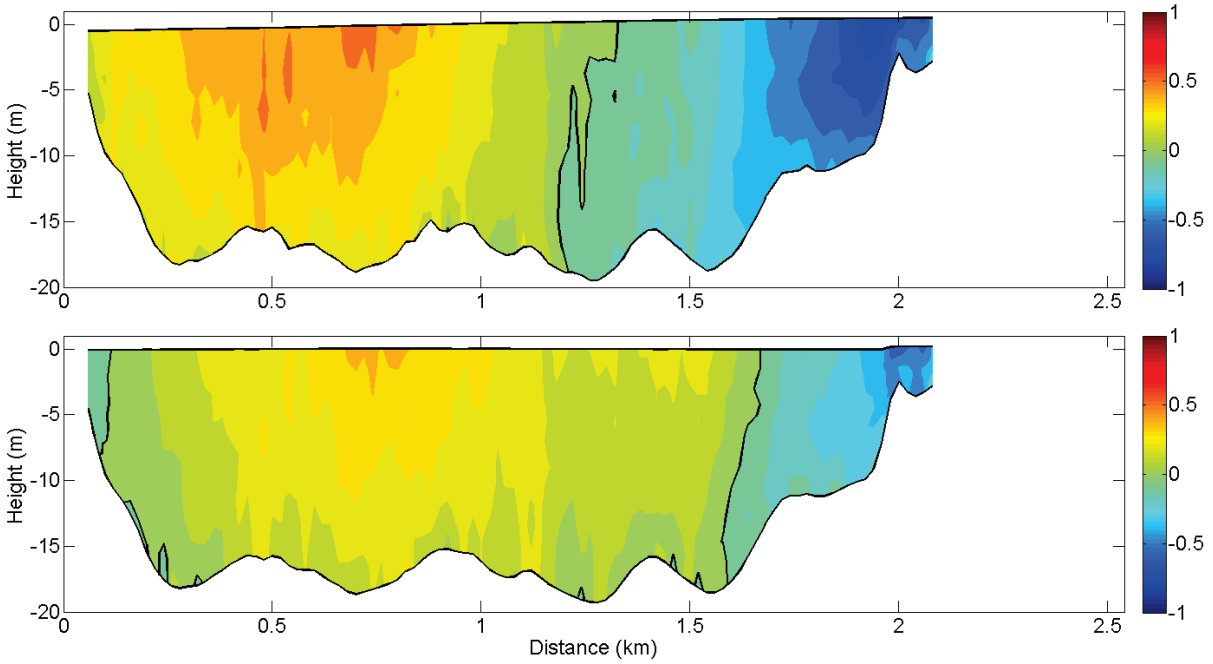


**Figure 2.2.12** **Error associated with assuming synopticity during a crossing at Saint-Nicolas. (top) Measured velocity magnitude (in m $s^{-1}$) from 16h44 to 17h21. (bottom) Time-interpolated velocity magnitude at mid-time (17h02). Black lines indicate the position of the water surface, river bed and zero velocities.**

### 2.2.6 Discussion

A survey strategy and a data analysis procedure were designed to obtain the time evolution of the lateral distribution of water levels and currents in the St. Lawrence fluvial estuary over the semi-diurnal tidal cycle. Measurements simultaneously performed with an ADCP and a RTK GPS were made with sufficient detail to reveal local features in water levels and velocities that had never previously been observed. This includes, for instance, the exchanges between the intertidal

shoals and the channel, which affects both the propagation of the tide and the dynamics of current reversals (see, e.g., Figure 2.2.9, Figure 2.2.10 and Figure 2.2.12; Le Hir *et al.*, 2000, Nidzieko & Ralston, 2012). Such features cannot be captured using fixed apparatus such as near-shore pressure sensors or fixed ADCPs (either side-looking or bottom-moored), because they are generally installed below lower low water.

Moving boat measurements are well-adapted to time-varying flow conditions as they can cover large regions in short periods of time [see, e.g., Table 2.2.4 in section 2.2.9 (appendix B)]. Despite their simplicity and rapidity, a certain amount of averaging is necessary in order to reduce errors present in the recorded data (e.g., Gunawan *et al.*, 2010). Measuring at fixed locations over long time intervals or averaging data from repeated transects are usually recommended to accurately characterize the mean velocity distributions with ADCPs (Muste *et al.*, 2004a, Muste *et al.*, 2004b, Szupiany *et al.*, 2007). However, fixed measurements are impractical when data along a river cross-section are needed; likewise, averaging repeated transects is inadequate under nonstationary conditions as it conflicts with the requirement to monitor the time variations induced by the nonstationary processes (e.g., tides, discharge waves). The smoothing procedure presented here was applied individually at each crossing, using slightly different approaches for water levels and velocities. Smoothing splines are well adapted to the slowly varying nature of water levels. They are however less suitable to velocities since they usually present sharp gradients leading to oscillations of the spline functions; in this case, moving averages proved to be a more robust choice than reducing the smoothing parameter of the spline functions. These methods along with their respective parameters were thus chosen in such a way to obtain smoothed time series that best represents the variations in the signal, but smooth enough that no artifacts associated with the smoothing methods are left behind.

Velocity components were smoothed and interpolated separately to ensure accurate reconstruction of the velocity directions. The reconstructed magnitudes resulting from this separation, however, slightly differ from those that would be obtained if magnitudes were directly used instead of components (cf. Table 2.2.1, first column). In constricted channels, the tidal ellipses formed by the velocity vectors resemble a straight line, meaning that both velocity components vanish at the same time. However, in wider systems or in presence of changes in bathymetry or variations in channel curvature, the tidal current is rotary, i.e. 2D (Parker, 2007). Treating the velocity components separately thus allows them to vanish at different times, as in a rotary

current, while working with velocity magnitudes forces a slack water to occur even in regions where a residual transverse current would normally remain, e.g., between a tidal flat and the deeper channel. Although we limited our analysis to horizontal velocity components (i.e. u and v), vertical w-velocities could be used to investigate the presence of secondary currents, especially in the vicinity of river bends. In doing so, special attention must be paid to errors associated with misalignment of the ADCP (Marsden & Gratton, 1997).

The reconstruction of continuous fields was made by interpolation, taking into account the temporal changes occurring during each crossing by use of a spatiotemporal grid (see, e.g., Figure 2.2.4). That way, distortions in the reconstructed quantities associated with the assumption of synopticity were avoided (e.g., Figure 2.2.12), thus allowing accurate computations of the instantaneous discharge and other relevant variables. Velocities were interpolated in time using 1D smoothing spline interpolations, performed sequentially at each grid point. As for water levels, among the three methods tested for interpolation, the 1D-forced method proved to have the needed characteristics, both in terms of smoothness and robustness, that best conformed to the underlying physics. Results for water levels and velocities showed a high spatial coherence between consecutive interpolations at the grid points and highlighted both the lateral and intratidal variations in the data in a continuous manner (cf. Figure 2.2.9 and Figure 2.2.10). These features can only be revealed after interpolation of the data.

These interpolation techniques can easily be generalized and applied to a variety of nonstationary signals where instantaneous cross-sectional profiles are needed, as long as the smoothness assumption is respected and a reference curve or function can be defined. In this regard, the use of an arbitrary basis function, defined from the data, is more versatile than fitting harmonic constituents, especially for signal lengths shorter or equal to the semi-diurnal tidal period. For particularly complex variables such as velocities characterized by high spatiotemporal variability, or signals for which basis functions describing the measured phenomena are not readily available, smoothing spline functions are a good alternative for interpolation.

Explanatory variables that arise directly from the reconstructed fields can be obtained, providing insights into the hydrodynamics of a system. As shown in Figure 2.2.8, lateral variations in the timing and height of LW and HW, as well as in the tidal range, can be extracted from the interpolated water levels. Similarly, the timing of current reversal, the maximum current

velocities, or the inclination and direction of rotation of the velocity vector as a function of depth and cross-sectional distance can be deduced from the reconstructed velocity fields. Like the cycle-by-cycle analysis described by Parker (2007), these variables can form the basis for comparisons at a given site between different tidal cycles throughout the month (e.g., from neap to spring tides) and different non-tidal conditions (e.g., winds, river discharge), as well as between regions of contrasting tidal and fluvial properties, channel geometries, and geographic features.

### 2.2.7 Comments and Recommendations

Surveys aimed at describing the tidal hydrodynamics of very energetic systems are not easy to conduct and necessitate cautious planning. Before going in the field, numerical models can be used to develop and test synthetic surveys, and assess synopticity problems associated with sampling configurations (Blain, 1997, Rixen *et al.*, 2001).

The method described in this paper highlighted the elements of a field campaign that need to be carefully examined with reference to the surveyed environment; they include the size of the system, the degree of non-stationarity in the measured processes, and main geographic features that can possibly influence the choice of survey locations and configuration. The data analysis procedure presented here was devised by making the least possible simplifying hypotheses about the data, adapting it to its shape and distribution. The implemented methods were little sensitive to the position of the sampling points and measurement errors, and allowed the reconstruction of continuous, synoptic fields. They were adapted to the underlying physics, basing the analyses on different strategies for velocities – typically characterized by sharp lateral variations – than for water levels – usually much smoother spatially. At each step of the analysis, errors were quantified or estimated through comparisons with alternate data analysis methods and complementary data sets. As a result, new knowledge was acquired in the St. Lawrence fluvial estuary in regions of contrasting tidal and fluvial properties, specifically related to the effects of channel curvature and bathymetry on tidal propagation and cross-channel flow properties at the intratidal scale.

ADCP and RTK GPS are versatile instruments that can provide accurate observations in many situations characterized by complex flow features (e.g., Seim *et al.*, 2006, Sime *et al.*, 2007,

Rennie & Church, 2010). Application of the method in other environments or contexts should therefore be rather straightforward.

### 2.2.8 Appendix A: Corrections and Conversions

#### *2.2.8.1 Pressure Sensor Data*

Pressure sensors were individually calibrated to control the accuracy of measured pressure data. During calibration, data were collected at 12 known pressures over the range of 100–200 kPa (at every 8–9 kPa, approximately), using a closed reservoir connected to compressed air wherein the sensors were placed. Calibration coefficients were generated for each sensor and used to convert the measured pressures to actual pressures. This step is crucial as it will affect subsequent conversions of pressures to water levels, for which a constant slope of $1/g$ is assumed (see text below).

Pressure data were corrected for atmospheric pressure measured at nearby meteorological stations or at the DFO's tide gauges of the St. Lawrence River, located generally at a distance of less than 20 km from the sensors. Between June and October 2009, river flow at the fluvial estuary entrance decreased by more than 4,500 $m^3s^{-1}$, thus gradually dropping the low waters at upstream stations below the level at which the sensors were installed. Corrected pressure values below 0.1 kPa were thus removed from the record, assuming an error in the atmospheric pressure of ±0.1 kPa, as the sensors were likely out of the water under these conditions.

The vertical position of the sensors was difficult to measure with accuracy, due to low underwater visibility, waves, and rapidly increasing water levels during the installation. Instead, pressure data were converted to water level elevations based on reference water level measurements taken with a RTK GPS at the beginning and end of the deployment, at different stages of the tidal cycle. These elevations were associated with the pressure values measured by the sensors using the relation:

$$P = \rho g H = \rho g (h_{MSL} - b), \tag{2.2.3}$$

where $P$ is the measured pressure in Pa (corrected for atmospheric pressure), $\rho$ is the water density in kg $m^{-3}$ (which is a function of temperature), $g$ is the gravitational acceleration (= 9.81

m $s^{-2}$), $H$ is the depth of the water column above the sensor in m, and $h_{MSL}$ is the water level above mean sea level (MSL) in m. Here, $h_{MSL}$ is related to $H$ through an offset coefficient $b$, which corresponds to the height of the sensor above MSL. Figure 2.2.13 shows, for one of the sensors located at Deschambault, measured water levels above MSL ($h_{MSL}$) plotted against adjusted pressures (i.e. $P/\rho$, compensated for temperature variations). The first-degree polynomial that best fits the reference level data, given a slope equal to $1/g$, is calculated (black line) and used to convert all adjusted pressures to water levels. The latter are used for validation of measured and interpolated data at the transect ends and provide a means to define and compare tidal properties at each survey site.

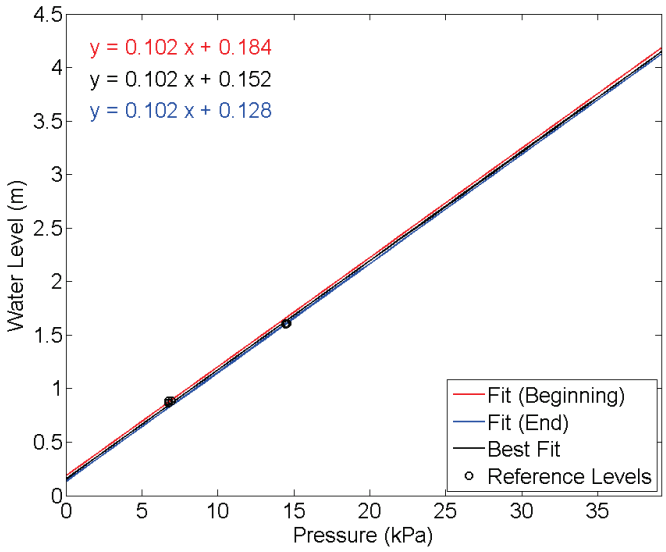


**Figure 2.2.13** **Reference levels (black circles) measured with a RTK GPS at the beginning and end of the deployment at Deschambault. The first-degree polynomial that best fits the data (black line), given a slope of 1/9.81, is used to obtain water levels above MSL from pressures measured by the sensor over the range shown in the abscise (corrected for atmospheric pressure and temperature). Drift of the sensor is estimated from the data, separately fitted for the beginning (red) and end (blue) of the deployment, and amounts to -0.056 in this case.**

### *2.2.8.2 ADCP Data*

Velocity data were collected and extracted from the ADCP files using WinRiver II, version 2.06 (Teledyne RD Instruments, 2009). The extracted data are, for each ensemble: the time of measurement, longitude, latitude, horizontal and vertical velocity components, error velocity,

depth-averaged velocity, heading, pitch and roll angles, boat and water speed, river depth, number of satellites, and horizontal dilution of precision (HDOP).

Navigational longitude and latitude positions were converted to Modified Transverse Mercator (MTM) coordinates (zone 7 or 8) in the NAD83 datum. The ADCP flags the data as bad whenever a wrong depth is reported, the echo intensity, correlation or percent-good are not met, or velocity thresholds are exceeded. The latter are set to 1 $m\,s^{-1}$ for both upward and error velocities. Data for which the HDOP was greater than 6 were eliminated from the records. Velocity outliers were also identified, based on depth-averaged values, and their corresponding ensembles were removed. An iterative procedure was followed for outlier removal. Large along-transect variations in velocities sometimes hid locally extreme values; therefore, velocity data from each crossing was first separated into sub-transects, each encompassing data from successive 2-min intervals (i.e. 300 data points). Any linear trend in depth-averaged velocity was locally removed within the 2-min window. A minimum and maximum threshold for rejection that contains 99.99% of the values was then defined for each sub-transect, using the mean and standard deviation of the detrended data, by computing the inverse of the normal cumulative distribution function, using the *norminv* Matlab function (MathWorks, 2012). Data values outside the range defined by the thresholds were removed from the records. Recursive checks for outliers were made until no outliers were found or the maximum number of iterations was reached; the latter was set to 5.

#### *2.2.8.3 RTK GPS Data*

Measured RTK GPS data were extracted using the ASCII File Generator from Trimble Office. They include the time of measurement, North and East MTM coordinates, elevations, horizontal and vertical precisions, positional (3D) dilution of precision (PDOP), and number of satellites. All elevations were reduced to MSL based on nearby, permanently established benchmarks, maintained by the Quebec's Ministry of Natural Resources. Vertical positions at geodetic points were taken with the rover at the beginning and end of each day of measurements, and then averaged to obtain the translation to apply to the data. The precision of these conversions is primarily determined by the precision class of the geodetic points and quality of the GPS signal.

The vertical distance between the rover and the water surface, once attached to the boat, was manually measured before each survey and used to convert the data into water surface eleva-

tions. This height is accurate as long as the boat remains static, but once in motion it varies in time as a function of the wave conditions, changes in weight distribution and dynamic draft. Oscillations of the water level due to waves are regarded as random errors and can easily be eliminated by smoothing. Systematic errors generally occur when the boat moves, as the difference between the forward and aft drafts (or the trim) changes as a function of boat speed, heading, current action and movement of people on board. These shifts were correlated with the low-frequency pitch and roll movements measured by the ADCP. Corrections were made following a procedure described in Matte *et al.* (2014b), where low-frequency variations in water level are regressed with the vertical displacements induced by the pitch and roll angles of the boat. Further vertical movements appearing in the measurements can be attributed to actual movements of the water surface due to tides, long-period heaves or local bathymetry, and were left unchanged. Remaining systematic errors were evaluated by comparison with tide gauge data at the transect ends.

Data for which the PDOP exceeded 6 or the vertical error was greater than 0.05 m were removed from the records. A similar procedure for outlier removal as used for ADCP data was applied (described above). A 5-min window was used to detrend the data, due to the lower sampling rate, and the maximum number of iterations was set to 10.

### 2.2.9 Appendix B: Raw Data Statistics and Accuracy

#### *2.2.9.1 Pressure Sensor Data*

To verify the accuracy of the measurements, calibration coefficients for each pressure sensor were determined in a controlled environment and used to convert the measured pressures to actual pressures. They are shown in Table 2.2.5. For most sensors the coefficients do not deviate significantly from one, with the exception of the sensor installed at Québec Bridge, followed by the one at Islet-sur-Mer. In the most extreme case (0.9831), this represents an error of 0.017 m per meter of water.

To determine the amount of drift of the pressure sensor data during the period of measurement, the reference levels taken with a RTK GPS at the beginning and end of the deployment were fitted separately [red and blue lines in Figure 2.2.13 in section 2.2.8 (appendix A)]. The vertical shift between the two curves gives an indication of the drift, assuming accurate reference levels.

The measured drifts are presented in Table 2.2.5 for each sensor. Their values average to -0.020 m with a maximum absolute value of 0.076 m. The elevations taken with the RTK GPS are likely contaminated by errors in the GPS signal and by the presence of waves or ripples on the water surface during the measurements. The calculated drift values therefore represent the total error from both sensor drift and reference level measurements. Because it is virtually impossible to separate the two sources of error, data were used as is.

Also shown in Table 2.2.5 is the total number of pressure data points before and after data deletion for periods where the pressure sensors were out of the water. The number of deleted points is only significant at upstream stations, which are the most affected by fluctuations in discharge.

*2.2.9.2 ADCP Data*

Table 2.2.6 shows statistics on the ADCP raw data, calculated from all crossings at each location. Differences between the mean and maximum water depths are influenced by both the extent of tidal flats and amplitude of the local tide. Negative depth-averaged velocities are the maximum measured values in the upstream direction, i.e. during current reversal. Their magnitude is generally lower than downstream currents, with the exception of Québec. Bin velocity magnitudes were calculated using all measured bins. Their maximum values are therefore higher than depth-averaged velocities. Mean absolute values are slightly lower than 1 m $s^{-1}$ on average. Current velocities in the St. Lawrence fluvial estuary increase in strength from Deschambault to Richelieu rapids (located a few km upstream), explaining the significantly higher mean values measured at Deschambault. Error velocities are between 0.09 and 0.16 m $s^{-1}$ on average. For each transect location in Table 2.2.6, the total number of ADCP data points is shown before and after outlier removal and data deletion for exceeding the error threshold values specified. Since transects were surveyed at different periods on the neap-spring tidal cycle and under different flow and wind conditions, the values presented in Table 2.2.6 are specific to the conditions prevailing during each survey.

**Table 2.2.4** **Surveys made in the St. Lawrence fluvial estuary in 2009. Transect locations are listed from downstream to upstream and numbered as they appear in Figure 2.2.1. River kilometer (rkm) 0 is located at Saint-Joseph-de-la-Rive in the upper estuary.**

| | rkm | Transect Location | Date | Time (hh:mm) | | Crossings | Travel Time (mm:ss) | | Traveled Distance (m) | | Boat Vel. ($m\ s^{-1}$) |
|---|---|---|---|---|---|---|---|---|---|---|---|
| | | | | Start | End | | Min | Max | Min | Max | Mean |
| a | 78 | Saint-Jean | 24 Aug 09 | 10:35 | 19:30 | 13 | 30:06 | 46:59 | 2536 | 2868 | 1.26 |
| b | 79 | Château-Richer | 25 Aug 09 | 09:28 | 19:17 | 19 | 18:33 | 50:05 | 1218 | 2249 | 0.98 |
| c | 97 | Beauport | 24 Jun 09 | 09:21 | 20:55 | 12 | 18:32 | 34:04 | 1203 | 2210 | 1.15 |
| d | 100 | Lauzon | 24 Jun 09 | 08:58 | 21:18 | 12 | 22:45 | 37:07 | 1990 | 2152 | 1.22 |
| e | 106.5 | Québec | 15 Jun 09 | 10:50 | 22:25 | 32 | 11:00 | 25:01 | 1336 | 1459 | 1.17 |
| f | 124 | Saint-Nicolas | 21 Aug 09 | 09:31 | 19:15 | 18 | 24:45 | 37:54 | 1924 | 2547 | 1.18 |
| g | 138 | Neuville | 25 Jun 09 | 10:13 | 20:35 | 12 | 24:02 | 53:27 | 2547 | 3361 | 1.25 |
| h | 163.5 | Portneuf | 26 Jun 09 | 09:47 | 17:15 | 12 | 20:35 | 36:16 | 1265 | 2045 | 1.15 |
| i | 168 | Deschambault | 20 Aug 09 | 09:14 | 20:22 | 32 | 07:49 | 41:07 | 560 | 1909 | 1.02 |
| j | 179.5 | Grondines | 19 Jun 09 | 10:10 | 20:26 | 12 | 34:18 | 52:58 | 2653 | 2764 | 1.04 |
| k | 199 | Batiscan | 23 Jun 09 | 08:27 | 17:16 | 13 | 29:22 | 38:03 | 1782 | 2267 | 1.06 |
| l | 217 | Bécancour | 18 Jun 09 | 14:23 | 19:52 | 16 | 16:01 | 21:12 | 1158 | 1180 | 1.09 |
| m | 231 | Trois-Rivières | 18 Jun 09 | 10:45 | 12:17 | 4 | 19:54 | 23:04 | 1279 | 1402 | 1.07 |

**Table 2.2.5** **Drift of the pressure sensor data calculated using reference level measurements at the beginning and end of the deployment. Negative drifts indicate a decrease in the measured water levels over time. The total number of data points is shown before (initial) and after (final) removal for periods where sensors are out of the water. Sensor locations are listed from downstream to upstream and numbered as they appear in Figure 2.2.1. River kilometer (rkm) 0 is located at Saint-Joseph-de-la-Rive in the upper estuary.**

| | rkm | Sensor Location | Start Date | End Date | Calibration Coefficient | Drift (m) | Initial | Final |
|---|---|---|---|---|---|---|---|---|
| 1 | 30 | Islet-sur-Mer | 28 May 09 | 16 Oct 09 | 0.9964 | -0.031 | 13522 | 13522 |
| 2 | 45 | Île-aux-Grues South | 30 May 09 | 09 Sep 09 | 1.0010 | -0.019 | 9780 | 9780 |
| 3 | 46 | Île-aux-Grues North | 30 May 09 | 09 Sep 09 | 1.0014 | – | 9785 | 9785 |
| 4 | 97 | Beauport | 27 May 09 | 15 Oct 09 | 1.0012 | 0.075 | 13410 | 13410 |
| 5 | 106.5 | Lévis | 28 May 09 | 15 Oct 09 | 1.0015 | – | 13415 | 13415 |
| 6 | 106.5 | Québec | 03 Jun 09 | 15 Oct 09 | 1.0002 | -0.021 | 12769 | 12769 |
| 7 | 115 | Québec Bridge | 25 May 09 | 15 Oct 09 | 0.9831 | -0.076 | 13617 | 13617 |
| 8 | 124 | Saint-Nicolas | 02 Jun 09 | 15 Oct 09 | 1.0001 | -0.007 | 12966 | 12963 |
| 9 | 146 | Sainte-Croix Est | 01 Jun 09 | 15 Oct 09 | 1.0014 | -0.030 | 13066 | 13052 |
| 10 | 157 | Cap-Santé | 03 Jun 09 | 15 Oct 09 | 0.9994 | -0.025 | 12765 | 12765 |
| 11 | 161 | Pointe-Platon | 02 Jun 09 | 15 Oct 09 | 0.9992 | -0.011 | 12967 | 12964 |
| 12 | 168 | Deschambault | 03 Jun 09 | 15 Oct 09 | 1.0000 | -0.056 | 12755 | 11243 |
| 13 | 179.5 | Leclercville | 01 Jun 09 | 15 Oct 09 | 1.0020 | – | 13057 | 11966 |
| 14 | 179.5 | Grondines | 29 May 09 | 15 Oct 09 | 1.0010 | -0.010 | 13261 | 12431 |
| 15 | 213 | Champlain | 29 May 09 | 15 Oct 09 | 1.0023 | -0.023 | 13250 | 11786 |

**Table 2.2.6 Statistics of ADCP raw data. The total number of data points is shown before (initial) and after (final) data removal for exceeding the error threshold values.**

| Transect Location | Water Depth (m) | | Depth-Avg. Vel. ($m\ s^{-1}$) | | Bin Vel. Magnitude ($m\ s^{-1}$) | | Error Vel. ($m\ s^{-1}$) | Satellites | HDOP | Initial | Final |
|---|---|---|---|---|---|---|---|---|---|---|---|
| | Mean | Max | Min | Max | Mean | Max | Mean | Mean | Mean | | |
| Saint-Jean | 16.5 | 26.0 | -1.40 | 1.94 | 0.98 | 5.04 | 0.14 | 6.7 | 1.3 | 48124 | 46513 |
| Château-Richer | 7.2 | 15.0 | -0.95 | 2.13 | 0.71 | 2.38 | 0.13 | 6.8 | 1.3 | 73050 | 69593 |
| Beauport | 7.7 | 21.1 | -1.87 | 2.33 | 0.51 | 2.72 | 0.11 | 7.6 | 1.2 | 24526 | 23719 |
| Lauzon | 18.4 | 33.0 | -1.68 | 2.22 | 1.01 | 4.18 | 0.13 | 7.6 | 1.3 | 27380 | 25435 |
| Québec | 24.4 | 39.3 | -1.99 | 1.95 | 0.93 | 5.14 | 0.13 | 7.4 | 1.3 | 43159 | 40723 |
| Saint-Nicolas | 14.6 | 22.7 | -1.52 | 2.02 | 1.16 | 5.88 | 0.14 | 6.8 | 1.3 | 61384 | 60281 |
| Neuville | 10.7 | 21.6 | -1.20 | 2.11 | 0.96 | 3.55 | 0.13 | 7.5 | 1.3 | 53321 | 52205 |
| Portneuf | 14.1 | 31.6 | -0.91 | 2.31 | 0.71 | 3.91 | 0.13 | 7.0 | 1.4 | 29103 | 27960 |
| Deschambault | 9.5 | 22.2 | -1.41 | 4.17 | 1.30 | 5.13 | 0.16 | 6.0 | 1.8 | 53730 | 49915 |
| Grondines | 7.4 | 17.8 | -0.40 | 2.28 | 0.85 | 2.59 | 0.11 | 7.2 | 1.3 | 47673 | 43595 |
| Batiscan | 8.9 | 16.7 | -1.12 | 1.45 | 0.62 | 1.88 | 0.09 | 7.6 | 1.3 | 40363 | 37465 |
| Bécancour | 12.4 | 15.7 | 0.01 | 1.34 | 0.89 | 2.09 | 0.10 | 7.7 | 1.2 | 28318 | 27741 |
| Trois-Rivières | 11.7 | 21.6 | -0.25 | 1.17 | 0.82 | 1.88 | 0.10 | 7.8 | 1.3 | 8036 | 7589 |

**Table 2.2.7** **Statistics of RTK GPS raw data. The total number of data points is shown before (initial) and after (final) data removal for exceeding the error threshold values. Elevation differences are calculated from single crossings.**

| Transect Location | Elevation (m) | | Elevation Difference (m) | | Horiz. Error (m) | Vert. Error (m) | Satellites | PDOP | Initial | Final |
|---|---|---|---|---|---|---|---|---|---|---|
| | Min | Max | Mean | Max | Mean | Mean | Mean | Mean | | |
| Saint-Jean | -2.24 | 2.02 | 0.66 | 1.38 | 0.011 | 0.018 | 11.6 | 1.7 | 27748 | 27462 |
| Château-Richer | -2.08 | 3.09 | 0.39 | 0.99 | 0.009 | 0.014 | 13.1 | 1.5 | 33594 | 33149 |
| Beauport | -1.91 | 2.99 | 0.50 | 1.00 | 0.011 | 0.017 | 13.3 | 1.5 | 18722 | 17968 |
| Lauzon | -1.89 | 3.26 | 0.59 | 1.02 | 0.010 | 0.015 | 13.7 | 1.4 | 20311 | 18950 |
| Québec | -1.34 | 2.69 | 0.31 | 0.58 | 0.009 | 0.015 | 12.9 | 1.6 | 37336 | 33973 |
| Saint-Nicolas | -1.45 | 2.98 | 0.54 | 1.08 | 0.011 | 0.017 | 11.6 | 1.7 | 33050 | 32613 |
| Neuville | -0.71 | 3.86 | 0.53 | 0.82 | 0.008 | 0.012 | 13.6 | 1.5 | 27927 | 26732 |
| Portneuf | 1.02 | 4.24 | 0.33 | 0.61 | 0.008 | 0.013 | 12.8 | 1.5 | 18169 | 17539 |
| Deschambault | -0.38 | 3.62 | 0.33 | 0.71 | 0.008 | 0.013 | 12.3 | 1.6 | 29035 | 27712 |
| Grondines | 1.15 | 3.23 | 0.51 | 0.77 | 0.011 | 0.016 | 12.3 | 1.6 | 30857 | 29656 |
| Batiscan | 2.92 | 4.47 | 0.30 | 0.42 | 0.013 | 0.021 | 10.1 | 2.3 | 23729 | 20736 |
| Bécancour | 3.30 | 3.60 | 0.08 | 0.11 | 0.008 | 0.013 | 14.2 | 1.5 | 17519 | 16787 |
| Trois-Rivières | 3.97 | 4.21 | 0.16 | 0.24 | 0.013 | 0.019 | 12.6 | 1.5 | 5119 | 4446 |

#### *2.2.9.3 RTK GPS Data*

Table 2.2.7 shows statistics on the RTK GPS raw data. Minimum and maximum measured elevations are an indication of the tidal variations during the period of measurements, although contaminated by the boat movement due to waves. Only a small amount of this variation can be attributed to lateral pressure gradients. At locations where measurements were taken during a time period inferior to the semi-diurnal tidal cycle (cf. Table 2.2.4), the measured range is lower than the actual tidal range. The mean and maximum differences in measured water levels during each crossing are also presented in Table 2.2.7. During the first hour after low tide, the increase in water level is generally the fastest. Variations exceeding 1 m were measured within single crossings at more than one location; on average, these variations exceeded 30 cm at all but the most upstream locations. Given these variations in water level, synoptic measurements were not obtained during single crossings. Also of interest in our application is the vertical error associated with RTK GPS measurements, averaging between 0.012 and 0.021 m during the campaign, which conforms to the expected error (Ghilani & Wolf, 2012). For each survey presented in Table 2.2.7, the total number of RTK GPS data points is shown before and after outlier removal and data deletion for exceeding the error threshold values specified. Again, transect data must be compared with caution, because the conditions (tides, river discharge, etc.) prevailing during each survey differed from each other.

Systematic errors in water surface elevations measured by the RTK GPS can be attributed to two main sources: changes in satellite number and low-frequency pitch and roll movements. They were detected both visually and by correlating the data with variations in PDOP and pitch and roll angles, respectively. Shifts in vertical positions of up to 10 cm were observed in rare occasions due to changes in satellite number (Figure 2.2.14). Since the number of satellites was greater than 10 on average (cf. Table 2.2.7), these shifts were most likely related to problems in the firmware version used at the time of the campaign, which has been updated since (J.-P. Simard, personal communication). The time interpolation procedure developed for water level data is nearly insensitive to such variations, so that no corrections were made.

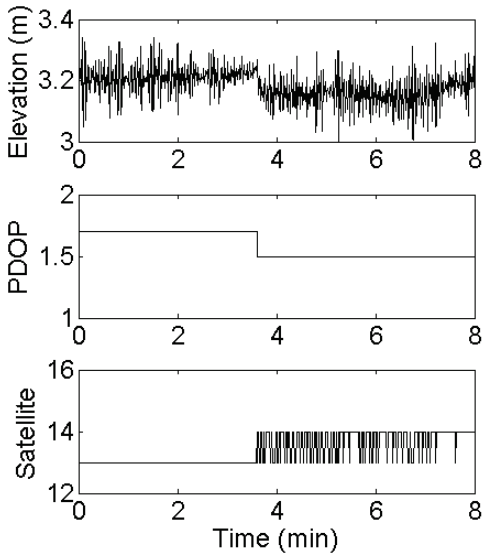


**Figure 2.2.14** **Shifts in water elevations observed at Grondines due to changes in the number of satellites. A change in the PDOP also appears.**

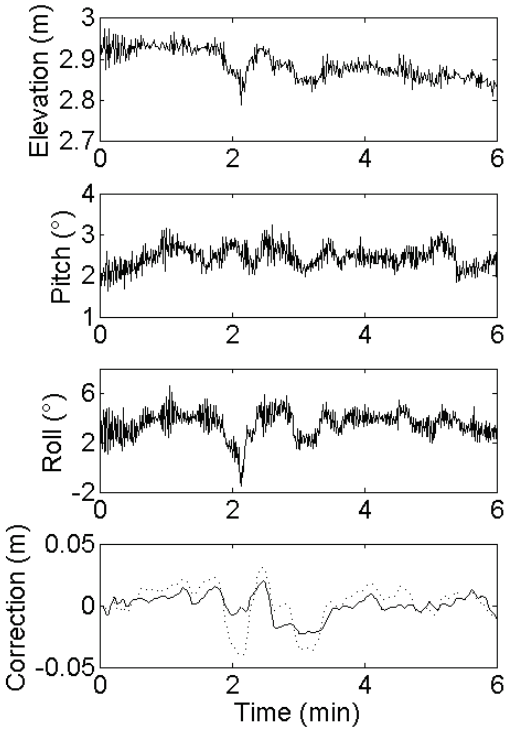


**Figure 2.2.15** **Shifts in water elevations at Deschambault caused by the pitch and roll movements of the boat, along with the smoothed, detrended elevations before (dotted line) and after (solid line) correction.**

Boat movements due to dynamic draft, on the other hand, can significantly bias the measured water levels and therefore need to be accounted for. The internal pitch and roll sensor of the ADCP was used to quantify and remove the low-frequency boat displacements from the measured records. Figure 2.2.15 shows the correction made to a record measured at Deschambault, where the correlation between the pitch and roll variations and the resulting systematic errors in water level is clear. The maximum correction applied to each transect is shown in Table 2.2.8 (first column); it exceeds 4 cm in the case of Deschambault. For most transects, the biases are of the same order of magnitude as the mean vertical error in RTK GPS elevations (cf. Table 2.2.7). Although relatively small, the corrections were made because information readily available from the ADCP was at disposal. As a result, systematic errors were reduced to within instrumentation accuracy (see also Matte *et al.*, 2014b). The remaining systematic errors are constant and most likely attributed to the reduction of the measured elevations to MSL. They are estimated by comparison with tide gauge data (cf. Table 2.2.3 and Figure 2.2.11).

#### *2.2.9.4 Projection Error*

Projection errors are defined as the perpendicular distance between a measurement point and the mean transect, the latter being fitted through all the data from a given survey (cf. Figure 2.2.3). Table 2.2.8 (second column) presents the mean and maximum errors for each transect. Average distances are $\leq 96$ m at all locations, and maximum values are $\leq 208$ m; the points whose distance was greater than 150 m were excluded from the records. This distance corresponds to less than 10 % of the river width at most locations. The impact of having measurement points slightly off the mean transect is little in the St. Lawrence fluvial estuary as the longitudinal bottom slopes are typically low.

**Table 2.2.8** **(first column) Maximum corrections for pitch and roll movements, applied to the RTK GPS elevations. (second column) Projection error, defined as the perpendicular distance between a measurement point and the mean transect.**

| Transect Location | Pitch/Roll (m) | Projection Error (m) | |
|---|---|---|---|
| | Max | Mean | Max |
| Saint-Jean | 0.017 | 29.0 | 96.0 |
| Château-Richer | 0.021 | 27.9 | 98.3 |
| Beauport | 0.013 | 27.3 | 144.5 |
| Lauzon | 0.018 | 52.7 | 196.0 |
| Québec | 0.030 | 70.0 | 208.0 |
| Saint-Nicolas | 0.025 | 26.7 | 90.0 |
| Neuville | 0.012 | 29.6 | 108.0 |
| Portneuf | 0.031 | 18.8 | 90.5 |
| Deschambault | 0.042 | 47.5 | 189.6 |
| Grondines | 0.036 | 19.7 | 109.7 |
| Batiscan | 0.029 | 16.8 | 70.0 |
| Bécancour | 0.026 | 11.7 | 58.9 |
| Trois-Rivières | 0.005 | 15.1 | 55.2 |

## 2.2.10 Acknowledgements

Work by Pascal Matte was supported by scholarships from the Natural Sciences and Engineering Research Council of Canada and Fonds de recherche du Québec – Nature et technologies. We thank Environment Canada (Meteorological Service of Canada) for providing the equipment and boat, and supporting the logistic and financial aspects of the field work. Special thanks go to Guy Morin, Jean-François Cantin, Patrice Fortin, Olivier Champoux, and Catherine Leblanc for their contribution to the field campaign, and to two reviewers for their comments on the manuscript.

## 2.3 Temporal and spatial variability of tidal-fluvial dynamics in the St. Lawrence fluvial estuary: An application of nonstationary tidal harmonic analysis

Cet article présente un modèle 1D basé sur une représentation harmonique non-stationnaire de la marée, permettant d'exprimer la réponse de la marée aux forçages du débit fluvial et de la marée océanique sous la forme d'une fonction continue. Une validation du modèle à partir des données issues de l'objectif 1 et du modèle opérationnel ONE-D est réalisée. L'article répond à l'objectif 2 de cette thèse en fournissant une analyse des variations spatiales et temporelles du contenu fréquentiel de la marée et des processus fluvio-tidaux dans l'estuaire fluvial du Saint-Laurent. Il a été publié dans la revue *Journal of Geophysical Research: Oceans*.

L'application dans le Saint-Laurent de l'outil NS_TIDE (présenté à l'annexe A.1) et le développement d'un modèle spatial de propagation de la marée ont été réalisés par l'auteur de cette thèse (premier auteur). Yves Secretan (second auteur) et Jean Morin (troisième auteur) ont participé à l'analyse des résultats et à la révision du manuscrit, écrit par l'auteur principal.

La référence complète de l'article est donnée ci-dessous :

Matte P, Secretan Y & Morin J (2014) Temporal and spatial variability of tidal-fluvial dynamics in the St. Lawrence fluvial estuary: An application of nonstationary tidal harmonic analysis. *J. Geophys. Res* 119: 5724-5744.

### 2.3.1 Abstract

Predicting tides in upstream reaches of rivers is a challenge, because tides are highly nonlinear and nonstationary, and accurate short-time predictions of river flow are hard to obtain. In the St. Lawrence fluvial estuary, tide forecasts are produced using a one-dimensional model (ONE-D), forced downstream with harmonic constituents and upstream with daily discharges using 30-day flow forecasts from Lake Ontario and the Ottawa River. Although this operational forecast system serves its purpose of predicting water levels, information about nonstationary tidal-fluvial processes that can be gained from it is limited, particularly the temporal changes in mean water level and tidal properties (i.e. constituent amplitudes and phases), which are function of river flow and ocean tidal range. In this paper, a harmonic model adapted to nonstationary tides, NS_TIDE, was applied to the St. Lawrence fluvial estuary, where the time-varying external

forcing is directly built into the tidal basis functions. Model coefficients from 13 analysis stations were spatially interpolated to allow tide predictions at arbitrary locations as well as to provide insights into the spatiotemporal evolution of tides. Model hindcasts showed substantial improvements compared to classical harmonic analyses at upstream stations. The model was further validated by comparison with ONE-D predictions at a total of 32 stations. The slightly lower accuracy obtained with NS_TIDE is compensated by model simplicity, efficiency and capacity to represent stage and tidal variations in a very compact way, and thus represents a new means for understanding tidal rivers.

### 2.3.2 Introduction

Tides in rivers are the result of nonlinear interactions of the oceanic tide with channel geometry, bottom friction, and river flow. They are best represented by a diffusive phenomenon in which the tidal wave, originating from tidal forces in the ocean, is increasingly distorted and damped as it propagates upriver (LeBlond, 1978). This results in asymmetries in the duration of ebb and flood, as well as in the timing and height of high and low water (Godin, 1984, 1999, Nidzieko, 2010). Fortnightly oscillations of mean water levels (MWL) following the neap-spring cycle also increase in strength upstream and eventually surpass the semidiurnal tidal amplitude, with mean low water progressively being lowered during neap tides rather than spring tides (LeBlond, 1979, 1991, Gallo & Vinzon, 2005).

Classical harmonic analysis (HA) is possibly the most widely used approach to analyse and predict tides. It performs very well in semi-enclosed basins, coastal shelves and seas, but usually fails in representing river tides, as the assumptions of stationarity and independence of the tidal components are not fulfilled due to nontidal modulating processes (Jay & Flinchem, 1999). As a consequence, no information on the evolution of the tidal content in time as a function of the nontidal forcing (e.g., annual river flow cycle) can be extracted. Some authors (e.g., Godin, 1985, Jay & Flinchem, 1997, Godin, 1999) showed the potential of simple regression relations to predict the modification of the tide by variations in river flow, but most investigators have turned to numerical modeling in order to get around the problem of nonstationary signals (i.e. tidal signals influenced by nonstationary external forcing). One- and two-dimensional models are notably used in estuaries to represent longitudinal variations in tidal properties and to produce cotidal charts, respectively. In these models, imposed discharges are generally kept constant at

the upstream boundaries, with tidal components forced at the downstream entrance, and simulations are performed for a sufficiently long period (typically one year) to extract tidal properties at the grid nodes using traditional HA methods (see, e.g., El-Sabh & Murty, 1990, Parker, 1991). Although these models provide a basis for understanding the nonlinear interactions of tides with friction and river flow, continuous functions of the response of tidal properties (i.e. amplitudes and phases of tidal constituents) to river flow and ocean tidal forcing are generally not incorporated in the analyses, thus limiting the predictive capabilities of the models.

Several methods or improvements to traditional harmonic methods have been developed to better represent transient tidal processes [for an overview, see, e.g., Jay & Kukulka (2003) and Parker (2007)]. Among the latest, an adaptation of classical HA to nonstationary tides, NS_TIDE, has been proposed and successfully applied in the Columbia River to a tidal signal strongly altered by river flow (Matte *et al.*, 2013). In NS_TIDE, the nonstationary forcing is built directly into the HA basis functions using a functional representation derived from river-tide propagation theory (Jay, 1991) and adapted from Kukulka & Jay (2003a, b) and Jay *et al.* (2011). Tidal-fluvial interactions are decoupled, allowing stage and tidal properties to be modeled separately as a function of time, in terms of time-varying external forcing by river flow and ocean tides. Moreover, the independence of the tidal components is ensured through redefined constituent selection and error estimation procedures.

In the St. Lawrence River, tide tables are produced using HA for all ports in the gulf and estuary up to Saint-Joseph-de-la-Rive (Figure 2.3.1). Upstream of Saint-Joseph-de-la-Rive, the influence of river discharge is included in the prediction using a one-dimensional model (ONE-D) of the St. Lawrence River (Dailey & Harleman, 1972, Morse, 1990). The ONE-D model solves the one-dimensional St. Venant equations. It is forced downstream with harmonic constituents at Saint-Joseph-de-la-Rive and upstream with daily discharges at the outlets of Lake Saint-Louis and Lake Des-Deux-Montagnes for a typical year, i.e. an average spring freshet followed by low flows in summer and rising flows in fall. The model is run for the entire year and hourly water levels, along with the times and heights of high and low tides, are extracted to produce tide tables at the stations.

The model is also run in operational mode, fed by the freshwater outflows from Lake Ontario and the Ottawa River. These outflows are forecast 30 days ahead and carefully regulated to

prevent flooding in the spring and to avoid low water conditions throughout the year, for navigation safety purposes. For the first 48 hours, the wind forecast of Environment Canada (Meteorological Service of Canada) for the St. Lawrence Estuary is used to calculate wind-induced storm surge at the downstream boundary. The effect of ice cover on the flow is also included in winter time, by restricting the flow on some sections (Lefaivre *et al.*, 2009).

This operational forecast system meets the need for a water level prediction throughout the entire St. Lawrence system and has proven to be quite valuable to the Canadian Coast Guard, the Canadian Port Authorities, ship owners, and in diverse applications from coastal flooding forecasts and ice cover management to hydrodynamic and climate change impact studies (Lefaivre *et al.*, 2009). However, a discrepancy remains between the harmonic-based predictions made in the estuary and gulf and the hydrodynamic-based predictions made upstream, which is strongly linked to the nature of the tides in both regions. Traditional harmonic methods assume that tides at a coastal station can be represented by a sum of sine waves with constant amplitudes and phases, whose frequencies are derived from tidal potential and nonlinear shallow-water interactions. Hydrodynamic models, for their part, solve the shallow water equations for the conservation of mass and momentum. They offer a spatially integrated representation of water levels and velocities in a system at the scale of the grid element size, whereas regression models such as HA or others offer temporally integrated views of a tidal signal measured at one or a few points in space, but usually over much larger periods of time (e.g., Jay *et al.*, 2011), typically expressed in terms of its frequency content. Consequently, the dynamical understanding that can be gained in the upstream and downstream portions of the St. Lawrence is inherently different due to drastically different methods used to represent the tides.

In this paper, a harmonic-based, nonstationary tidal propagation model of the St. Lawrence fluvial estuary is developed through application of NS_TIDE to 13 tide gauges distributed between Saint-Joseph-de-la-Rive and Lanoraie (Figure 2.3.1). In order to represent tidal properties in a continuous manner throughout the system, model coefficients are spatially interpolated between the stations, thus yielding a spatial model of the evolution of stage and tidal properties as a function of upriver location and forcing conditions. To validate the model, water level predictions are produced at 19 intermediate (mostly temporary) stations and compared to observations as well as to forecasts made by the operational ONE-D model. The objectives of this work are 1) to develop a spatial harmonic model capable of predicting variations in stage and

tidal properties as a function of nonstationary forcing variables, and 2) to improve current knowledge on tidal-fluvial processes in the St. Lawrence fluvial estuary. The goal is not to supplant the operational ONE-D forecast model, which serves its purpose of predicting water levels in the St. Lawrence River, but to complement it by exploring temporal changes in the frequency content of the tides, thereby bringing new insights into tidal-fluvial interactions. Such a treatment also guarantees continuity between predictions made in the upper and lower St. Lawrence by use of harmonic methods throughout.

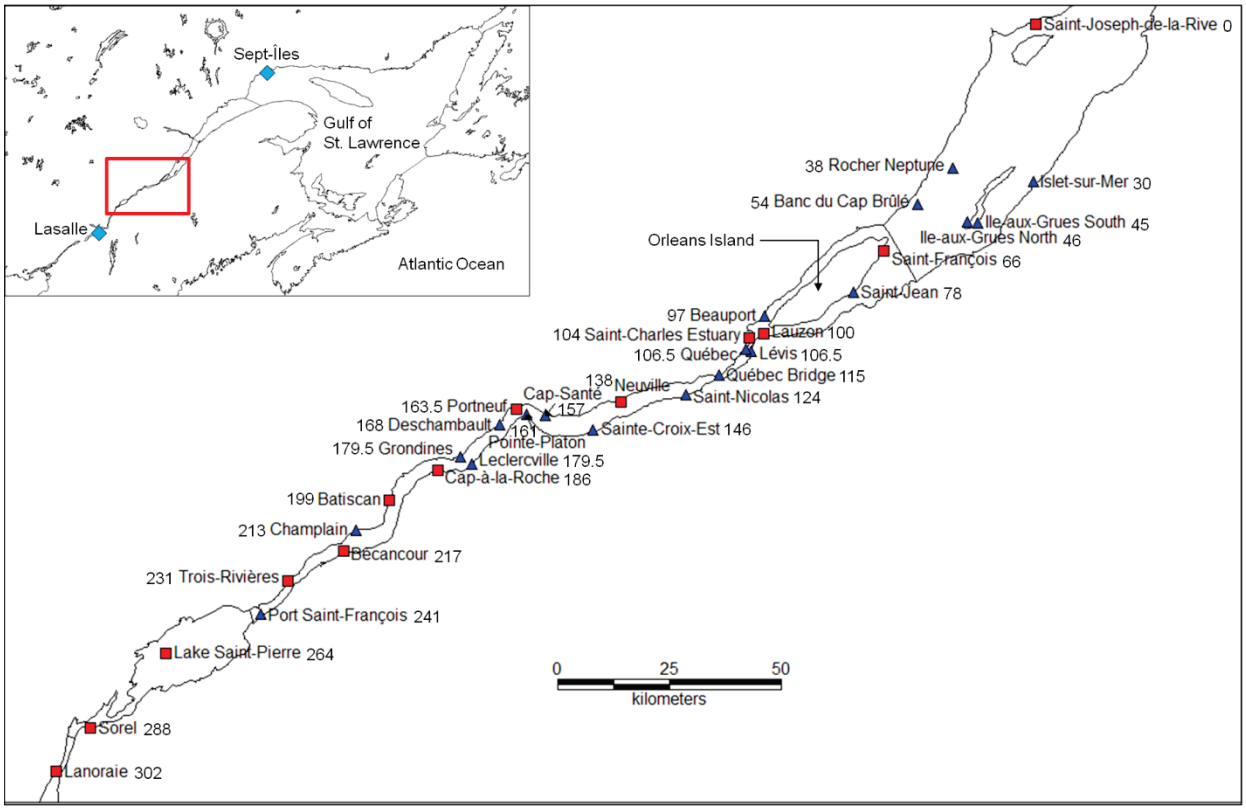


**Figure 2.3.1** **Map showing tide gauges in the St. Lawrence fluvial estuary: (red squares) analysis stations; (blue triangles) validation stations; (light blue diamonds) reference stations for ocean tidal range (Sept-Îles) and river discharge (Lasalle). River kilometers are shown beside each station name.**

### 2.3.3 Methods

#### *2.3.3.1 Regression Models*

Classical HA was given a structure based on a modern understanding of the tidal potential by Doodson (1921). Following a reformulation of Doodson's work by Godin (1972), tidal heights $h$ are typically modeled as:

$$h(t) = b_{0,0} + \sum_{k=1}^{n} [b_{1,k} \cos(\sigma_k t) + b_{2,k} \sin(\sigma_k t)], \tag{2.3.1}$$

where $t$ is time, $\sigma_k$ are *a priori* known frequencies, $n$ is the number of constituents, and $b_{0,0}$, $b_{1,k}$ and $b_{2,k}$ are unknown coefficients determined by regression analysis to best fit the observations.

Improvements to traditional harmonic methods have been made in the recent years (e.g., Foreman *et al.*, 2009, Leffler & Jay, 2009, Codiga, 2011). Among those, Leffler & Jay (2009) incorporated robust statistical fitting through iteratively reweighted least-squares (IRLS) analyses (Holland & Welsch, 1977, Huber, 1996) to increase the level of confidence in computed parameters. With these inclusions, the solution to Eq. (2.3.1) is obtained by minimizing $E$, the sum of weighted residuals:

$$E = \sum_{j=1}^{m} w_j^2 (h_j - y_j)^2, \tag{2.3.2}$$

where $y$ is the observations, $m$ is the record length and $w$ is a weighting function. Setting all $w_j$ ($j = 1..m$) values to 1 reduces the equation to the ordinary least-squares (OLS) solution, while introducing a weighting function allows one to penalize outliers with lower values of $w_j$, thus downweighting observations that increase residual variance.

A generalization of traditional HA has also been proposed by Matte *et al.* (2013) for the study of nonstationary tides, more specifically, river tides, implemented through modifications of the T_TIDE toolbox in Matlab (Pawlowicz *et al.*, 2002). To include contributions caused by external forcing (river flow and ocean tides) and nonlinear interactions, a functional representation, derived from a theory of river-tide propagation (Jay, 1991) by Kukulka & Jay (2003a, b) and Jay *et al.* (2011), was embedded directly in the HA basis functions implemented in NS_TIDE (Matte *et al.*, 2013). This formulation is based on the Tschebyschev decomposition of the bed stress

$\tau_B = \rho C_D |U| U$ of the one-dimensional St. Venant equations (Dronkers, 1964), which is the dominant source of nonlinearities in shallow rivers; here, $\rho$ is the water density, $C_D$ is the drag coefficient, and $U$ is the velocity. It is obtained for the critical convergence regime defined by Jay (1991), in which case tides can be considered as diffusive (LeBlond, 1978). In this regime, tidal and fluvial flows are assumed to be of similar magnitude and channel convergence moderate. Conceptually, the constants $b_{0,0}$, $b_{1,k}$ and $b_{2,k}$ in Eq. (2.3.1) are replaced by functions of river flow and greater diurnal tidal range (i.e. the difference between higher high water and lower low water within a day) at a convenient station removed from fluvial influence:

$$b_{l,k}(t) = a_{0,l,k} + a_{1,l,k} Q^{p_l}(t) + a_{2,l,k} \frac{R^{q_l}(t)}{Q^{r_l}(t)}, \tag{2.3.3}$$

where $Q$ is the river flow ($m^3s^{-1}$); $R$ is the greater diurnal tidal range (m); $p$, $q$, $r$ are the exponents for each station and frequency band; $a_{0,l,k}$, $a_{1,l,k}$, $a_{2,l,k}$ are the model coefficients for each station and frequency; $k$ is the index for tidal constituents ($k$ = 1, $n$); $l$ is the index for coefficients ($l$ = 0, 2).

The coefficient $a_{0,l,k}$ in Eq. (2.3.3) is primarily determined by the convergence or divergence of the channel cross-section. The second term represents the nonlinear response of tidal parameters to river flow, approximated in theory by a two-term function (Jay, 1991), but reduced in Eq. (2.3.3) to one discharge term with its associated coefficient and exponent. Also, the variable $Q$ appearing in Eq. (2.3.3) is itself a simplification of $U = Q/A(Q)$, where $A(Q)$ is the cross-channel area. Variations in channel geometry and peripheral intertidal areas are thus absorbed into the model parameters. The last term in Eq. (2.3.3) represents the effects of frictional interaction due to neap-spring variability, responsible for the tidal monthly changes in MWL and tidal properties. In practice, deviations from theory, due to time-varying channel geometries and variations in the ratio of river flow to tidal currents as a function of upriver distance, can be accounted for by tuning the exponents by station (e.g., Jay *et al.*, 2011).

In the following application, exponents are set to the theoretical values of Kukulka & Jay (2003a, b), rather than iteratively optimized, to allow comparisons between stations and development of a spatial model (see next section). Also, at each station, a time lag is applied to the forcing variables $Q$ and $R$, representing the average time of propagation of the waves to the station. The

$Q$ and $R$ time series are lagged by calculating the maximum correlation between $Q$ or $R$ and the observations $y$ (either low-passed or range-filtered). More complex lag functions could be used to better capture the varying propagation times as a function of river stage and improve synchronism between the input time series, although they are not applied here. The final form of the model, with the exponents replaced by their theoretical values, is obtained by distributing Eq. (2.3.3) into Eq. (2.3.1):

$$h(t) = \underbrace{c_0 + c_1 Q^{2/3}(t-\tau_Q) + c_2 \frac{R^2(t-\tau_R)}{Q^{4/3}(t-\tau_Q)}}_{\text{stage model or } s(t)} + \underbrace{\sum_{k=1}^{n}\left[\left(d_{0,k}^{(c)} + d_{1,k}^{(c)} Q(t-\tau_Q) + d_{2,k}^{(c)} \frac{R^2(t-\tau_R)}{Q^{1/2}(t-\tau_Q)}\right)\cos(\sigma_k t) + \left(d_{0,k}^{(s)} + d_{1,k}^{(s)} Q(t-\tau_Q) + d_{2,k}^{(s)} \frac{R^2(t-\tau_R)}{Q^{1/2}(t-\tau_Q)}\right)\sin(\sigma_k t)\right]}_{\text{tidal - fluvial model or } f(t)}, \tag{2.3.4}$$

where $s$ and $f$ denote the stage and tidal-fluvial models, respectively; the superscripts ($c$) and ($s$) refer to the cosine and sine terms, respectively; $c_i$ ($i$ = 0, 2) are the model parameters for the stage model; $d_{i,k}$ ($i$ = 0, 2) are the model parameters for the tidal-fluvial model; $\tau_Q$ and $\tau_R$ are the time lags applied to the $Q$ and $R$ time series, respectively. The regression coefficients ($c_0$, $c_1$, $c_2$, $d_{0,k}$, $d_{1,k}$, and $d_{2,k}$) in Eq. (2.3.4) are determined by application of Eq. (2.3.2).

Each tidal component of the tidal-fluvial model can be represented in the form of a time series:

$$Z_k(t) = z_k(t)\mathrm{e}^{\mathrm{i}\sigma_k t} + z_{-k}(t)\mathrm{e}^{-\mathrm{i}\sigma_k t} = \left|z_k(t)\right|\mathrm{e}^{-\mathrm{i}\phi_k(t)}\mathrm{e}^{\mathrm{i}\sigma_k t} + \left|z_{-k}(t)\right|\mathrm{e}^{\mathrm{i}\phi_k(t)}\mathrm{e}^{-\mathrm{i}\sigma_k t}, \tag{2.3.5}$$

with time-dependent amplitudes and phases respectively given by:

$$\left|Z_k(t)\right| = \left|z_k(t)\right| + \left|z_{-k}(t)\right| \tag{2.3.6}$$

and

$$\phi_k(t) = \arctan\left[\mathrm{Im}\left(z_{-k}(t)\right)/\mathrm{Re}\left(z_{-k}(t)\right)\right]. \tag{2.3.7}$$

In terms of the coefficients in Eq. (2.3.4), $z_{-k}(t)$ can be rewritten as:

$$z_{-k}(t) = z_k^*(t) = \frac{1}{2}\left(A_k \cos\alpha_k + B_k \cos\beta_k + C_k \cos\gamma_k\right) + \mathrm{i}\frac{1}{2}\left(A_k \sin\alpha_k + B_k \sin\beta_k + C_k \sin\gamma_k\right) \quad (2.3.8)$$

where the amplitudes $A_k$, $B_k$, and $C_k$, and phases $\alpha_k$, $\beta_k$, and $\gamma_k$ are defined as:

$$A_k = \sqrt{\left(d_{0,k}^{(c)}\right)^2 + \left(d_{0,k}^{(s)}\right)^2}\,, \quad (2.3.9)$$

$$B_k = Q(t-\tau_Q)\sqrt{\left(d_{1,k}^{(c)}\right)^2 + \left(d_{1,k}^{(s)}\right)^2}\,, \quad (2.3.10)$$

$$C_k = \frac{R^2(t-\tau_R)}{Q^{1/2}(t-\tau_Q)}\sqrt{\left(d_{2,k}^{(c)}\right)^2 + \left(d_{2,k}^{(s)}\right)^2}\,, \quad (2.3.11)$$

$$\alpha_k = \arctan\left(d_{0,k}^{(s)} / d_{0,k}^{(c)}\right), \quad (2.3.12)$$

$$\beta_k = \arctan\left(d_{1,k}^{(s)} / d_{1,k}^{(c)}\right), \quad (2.3.13)$$

$$\gamma_k = \arctan\left(d_{2,k}^{(s)} / d_{2,k}^{(c)}\right). \quad (2.3.14)$$

Hence, time series of MWL and tidal amplitudes and phases for each resolved frequency can be generated for any given forcing time series $Q$ and $R$.

*2.3.3.2 Spatial Model*

Using the regression models described in the previous section, stage and tidal properties were determined at a finite number of stations located along the St. Lawrence. A spatial model is required to represent these properties in a continuous manner so that spatial interpretation of the physics becomes possible as well as predictions at arbitrary locations. The criteria used in the selection of interpolating functions were the smoothness properties and degree of approximation. Here, interpolation of the coefficients in Eq. (2.3.4) is made between the stations using piecewise cubic Hermite interpolants (Fritsch & Carlson, 1980). Cubic Hermite functions are exact interpolants. They are continuous up to the first derivatives only and do not generate extrema or oscillations. Furthermore, slopes between stations are determined in a way that the shape of the data (e.g., local extrema, convexity) is preserved and monotonicity is respected.

Spatial interpolation of tidal harmonic fields is more robust and accurate when performed in complex amplitude form, in this case using model coefficients, rather than interpolating amplitudes and phases directly. Large errors can otherwise be introduced; for example, the average of 350° and 10° is 0°, not 180° if inappropriately interpolated (Martin *et al.*, 2009, Park *et al.*, 2012). Hence, model coefficients in Eq. (2.3.4) were spatially interpolated, so that they become a function of the distance *x*, i.e. $c_i \Rightarrow c_i(x)$ and $d_{i,k} \Rightarrow d_{i,k}(x)$. For the interpolation to be relevant, the analysis parameters (i.e. model exponents, tidal constituents, record length and analysis period, etc.) must be the same at all stations. They are detailed in the next section.

### 2.3.4 Application to the St. Lawrence Fluvial Estuary

#### *2.3.4.1 Setting*

The St. Lawrence River connects the Atlantic Ocean with the Great Lakes (Figure 2.3.1). It is the third largest river in North America, with a catchment area of ~$1.6 \times 10^6$ km$^2$ and an average freshwater discharge of 12 200 m$^3$s$^{-1}$ at Québec. Minimum and maximum daily net discharges in the St. Lawrence respectively amounted to 7000 and 32 700 m$^3$s$^{-1}$ at Québec over the 1960–2010 period, taking into account the contribution of all tributaries (Bouchard & Morin, 2000). The effects of such variations on MWL and tidal range are severe, particularly in the upper portion of the St. Lawrence fluvial estuary above Deschambault (Godin, 1999).

Ocean tides are amplified as they enter the St. Lawrence until they reach their maximum amplitude in the upper estuary at Saint-Joseph-de-la-Rive [hereafter defined as river kilometer (rkm) 0] with a 7-m range during the largest spring tides. They are then damped on their way upstream due to frictional effects. Tides are mixed diurnal, semi-diurnal, with ratios of major semidiurnal to diurnal amplitudes, i.e. $(|M_2|+|S_2|)/(|K_1|+|O_1|)$, around 5:1 at Saint-Joseph-de-la-Rive and decreasing upstream, the diurnal components being damped less rapidly than the semidiurnals.

The St. Lawrence fluvial estuary spans 180 rkm from the eastern tip of Orleans Island, located at the upper limit of saline intrusion, to the eastern end of Lake Saint-Pierre (Figure 2.3.1). While tides can be considered as stationary in the estuary and gulf, they are highly nonlinear and nonstationary in the fluvial estuary. Godin (1999) suggested separation of the fluvial estuary into three zones: 1) Québec – Portneuf (rkm 100 to 163.5), 2) Portneuf – Cap-à-la-Roche (rkm 163.5

to 186), and 3) Cap-à-la-Roche – Trois-Rivières (rkm 186 to 231). Observed water levels at these stations are presented in Figure 2.3.2 for a one-year period characterized by both very low and very high flows (see Figure 2.3.3). In the first zone (Québec – Portneuf), tidal ranges vary between approximately 3 and 6 m depending on the station and phase of the neap-spring cycle. Increases in water levels of more than 1 $m\,h^{-1}$ occur during the rising tide, leading to rapid changes in flow conditions as well as in the surfaces of wetted areas. This generates strong current reversals with daily peak tidal discharges being up to five times greater than the daily average in both upstream and downstream directions. The second zone (Portneuf – Cap-à-la-Roche) marks the transition between the tidal and tidal-fluvial regime. It is characterized by a sharp increase in bed slope at the Richelieu Rapid near Deschambault (rkm 168). The tidal signal is strongly distorted and progressively damped as a result of friction and river discharge. Ebb tides are lengthened and flood tides are steepened and shortened, part of the energy from the primary tidal constituents being nonlinearly transferred to their super-harmonics. The limit where the flow becomes unidirectional (i.e. only one slack water) moves between Grondines (rkm 179.5) and Becancour (rkm 217) as a function of tidal range and river flow, near the limit between zones 2 and 3. In the third zone (Cap-à-la-Roche – Trois-Rivières), water level variations are dominated by the river flow cycle. At Trois-Rivieres (rkm 231), the fortnightly modulation of MWL induced by the neap-spring cycle exceeds in amplitude the semidiurnal tide (LeBlond, 1979), whose range is 0.2 m for a mean tide. Leaving the tidal river per se, most of the short period tide (i.e. diurnal, semidiurnal, etc.) is damped in Lake Saint-Pierre (rkm 264), but long period oscillations are still noticeable as far as Montreal (rkm 360).

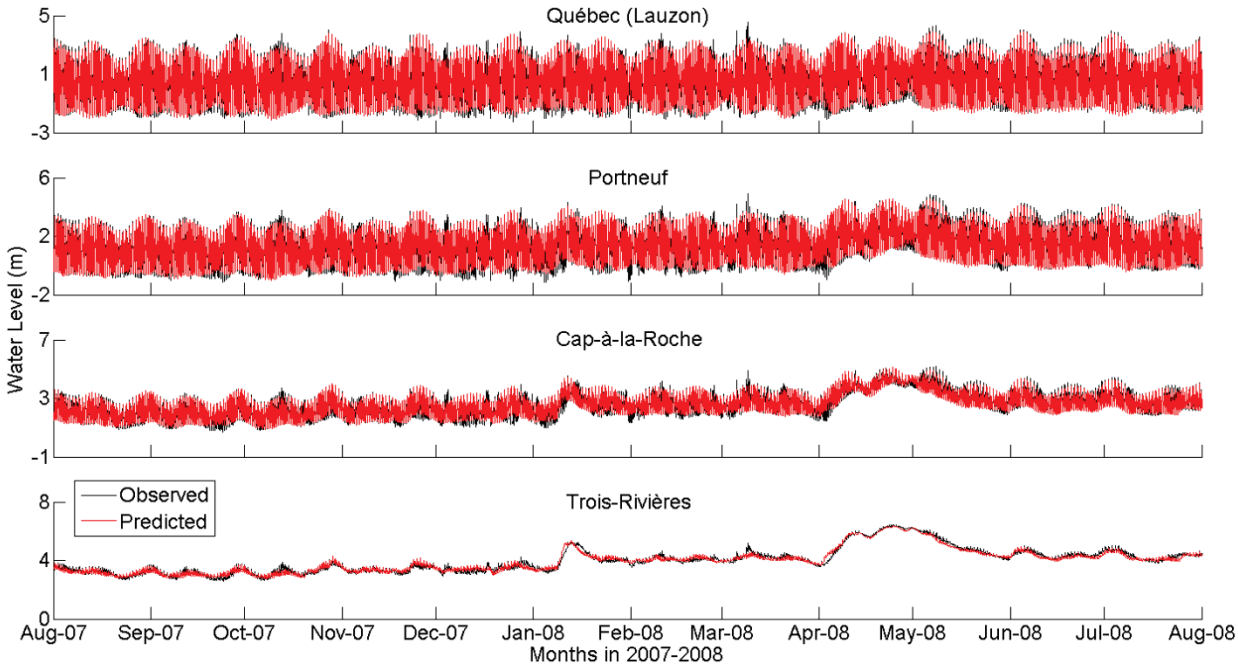


**Figure 2.3.2** **(black) Observed water levels at Québec (Lauzon), Portneuf, Cap-à-la-Roche and Trois-Rivières from August 2007 to August 2008. (red) Water level hindcast from NS_TIDE.**

### *2.3.4.2 Analysis Parameters*

NS_TIDE was applied to hourly water level data at 13 tide gauges, maintained by Canada's Department of Fisheries and Oceans (DFO), distributed between Saint-Joseph-de-la-Rive and Lanoraie (Figure 2.3.1); they are listed in Table 2.3.1. Time series composed of more than 90 000 good data points were selected for the analysis, for a reference period extending from 1999 to 2009 inclusively, the remaining 19 stations being used for validation (Table 2.3.2). Validation stations are a mix of temporary DFO's tide gauges and pressure sensors installed from May to October 2009 (Figure 2.3.1; Matte *et al.*, 2014a). The 11-yr analysis period was chosen for its wide range in river flow. Also, no major construction or dredging work was done after 1998 (Côté & Morin, 2007), so that stage and tidal properties are expected to be rather stable during that time period. Moreover, the proportion of fine materials is about 20 % in the St. Lawrence, between Sorel and Orleans Island, with an average sedimentation rate of 4 mm $yr^{-1}$ (Couillard, 1987). Most of the silting-up is dredged for maintenance of the navigational channel or flushed in fall and spring (Gagnon, 1995, Robitaille, 1998a, b), and thus has a limited effect on tidal propagation.

**Table 2.3.1** **Parameters of the NS_TIDE analyses at the tide gauges for the 1999-2009 period, including the number of good data points, and their corresponding discharge time series and time lags.**

| rkm | Station | Good data | $Q$ time series | $\tau_Q$ (h) | $\tau_R$ (h) |
|---|---|---|---|---|---|
| 0 | Saint-Joseph-de-la-Rive | 93149 | Québec | -14 | 5 |
| 66 | Saint-François | 95418 | Québec | -14 | 5 |
| 100 | Lauzon | 95048 | Québec | -14 | 5 |
| 104 | Saint-Charles River | 94608 | Québec | -14 | 5 |
| 138 | Neuville | 95449 | Neuville | -6 | 6 |
| 163.5 | Portneuf | 94833 | Neuville | -6 | 6 |
| 186 | Cap-à-la-Roche | 95301 | Batiscan | 16 | 7 |
| 199 | Batiscan | 93062 | Batiscan | 16 | 7 |
| 217 | Bécancour | 95649 | Bécancour | 26 | 9 |
| 231 | Trois-Rivières | 95583 | Bécancour | 26 | 9 |
| 264 | Lake Saint-Pierre | 90395 | Bécancour | 26 | 9 |
| 288 | Sorel | 95718 | Trois-Rivières | 28 | 10 |
| 302 | Lanoraie | 96119 | Trois-Rivières | 28 | 10 |

**Table 2.3.2** **Validation stations from DFO and pressure sensors, along with their corresponding discharge time series, record lengths and number of good data points for the 1999-2009 period. Pressure sensor data are sampled at a 15-min interval, while DFO's data are hourly. Stations in italics are not covered by the main branch of the ONE-D model.**

| rkm | Station | Source | Record length (yr) | Good data | $Q$ time series |
|---|---|---|---|---|---|
| *30* | *Islet-sur-Mer* | *Pressure sensor* | *0.4* | *13522* | *Québec* |
| 38 | Rocher Neptune | DFO | 4.4 | 19433 | Québec |
| *45* | *Ile-aux-Grues South* | *Pressure sensor* | *0.3* | *9780* | *Québec* |
| *46* | *Ile-aux-Grues North* | *Pressure sensor* | *0.3* | *9785* | *Québec* |
| 54 | Banc du Cap Brûlé | DFO | 3.1 | 12436 | Québec |
| 78 | Saint-Jean | DFO | 3.5 | 16988 | Québec |
| *97* | *Beauport* | *Pressure sensor* | *0.4* | *13410* | *Québec* |
| 106.5 | Lévis | Pressure sensor | 0.4 | 13415 | Québec |
| 106.5 | Québec | Pressure sensor | 0.4 | 12769 | Québec |
| 115 | Québec Bridge | Pressure sensor | 0.4 | 13617 | Québec |
| 124 | Saint-Nicolas | Pressure sensor | 0.4 | 12963 | Québec |
| 146 | Sainte-Croix-Est | Pressure sensor | 0.4 | 13052 | Neuville |
| 157 | Cap-Santé | Pressure sensor | 0.4 | 12765 | Neuville |
| 161 | Pointe-Platon | Pressure sensor | 0.4 | 12964 | Neuville |
| 168 | Deschambault | Pressure sensor | 0.4 | 11243 | Batiscan |
| 179.5 | Leclercville | Pressure sensor | 0.4 | 11966 | Batiscan |
| 179.5 | Grondines | Pressure sensor | 0.4 | 12431 | Batiscan |
| 213 | Champlain | Pressure sensor | 0.4 | 11452 | Bécancour |
| 241 | Port Saint-François | DFO | 10.3 | 63857 | Bécancour |

Five daily discharge time series $Q$ were used as forcing conditions, each of which is an estimate based upon continuous water level measurements at the station of Lasalle (Figure 2.3.1) and has been modified to account for flows from tributaries. The data were produced based on a stage-discharge relation at Lasalle. Fortnightly variations of MWL due to low-frequency tides were considered as part of the noise. The flows from tributaries were reconstructed by adding the discharge measured at an upstream station to the estimated lateral inflow, consisting of surface water runoff and groundwater inflow. Virtually no data is available for groundwater inflow, so that only surface water runoff was considered, based on gauged areas. For ungauged areas, the inflow was estimated from the runoff coefficient of an adjoining gauged area. Relations for each tributary to the St. Lawrence were developed by Morse (1990) and adapted by Bouchard & Morin (2000). Since the drainage area in the St. Lawrence increases moving downstream, the contribution of tributaries was progressively added to the total discharge time series used at the stations. The reconstructed discharge time series used in the analyses are presented in Figure 2.3.3 and listed in Table 2.3.1 for each station. Discharge time series used at the validation stations are shown in Table 2.3.2. Differences in discharge between Trois-Rivières and Québec for the 1999-2009 period reached a maximum of 8700 $m^3s^{-1}$ in April 2008 during the freshet (Figure 2.3.3). Minimum and maximum discharges at Québec for that period were observed in September 2007 (7600 $m^3s^{-1}$) and April 2008 (26 400 $m^3s^{-1}$), respectively, which are fairly extreme when compared to the most extreme flows that occurred in March 1965 (7000 $m^3s^{-1}$) and April 1976 (32 700 $m^3s^{-1}$) for the 1960–2009 period. Empirical cumulative distribution functions are shown in Figure 2.3.3 for each discharge time series and were used to define quantiles of river flow (see next section).

Sept-Îles was chosen as the reference station for ocean tidal forcing (Figure 2.3.1), similarly to Godin's (1999) regression model, because it is removed from fluvial influence and sufficient data are available. Greater diurnal tidal ranges $R$ were extracted from hourly data at Sept-Îles. Water levels were high-pass filtered, then re-interpolated using (exact) cubic spline functions to a 6-min interval in order to capture the tidal extrema (data are smooth and regularly sampled so that no oscillations are generated during interpolation). Tidal ranges were calculated as the difference between higher high water and lower low water using a 27-h moving window with 1-h steps, then smoothed to eliminate discontinuities, similarly to Kukulka & Jay (2003a)'s tidal range filter. The time series of tidal range for the analysis period is presented in Figure 2.3.4,

along with its corresponding empirical cumulative distribution function, used to define quantiles of tidal range.

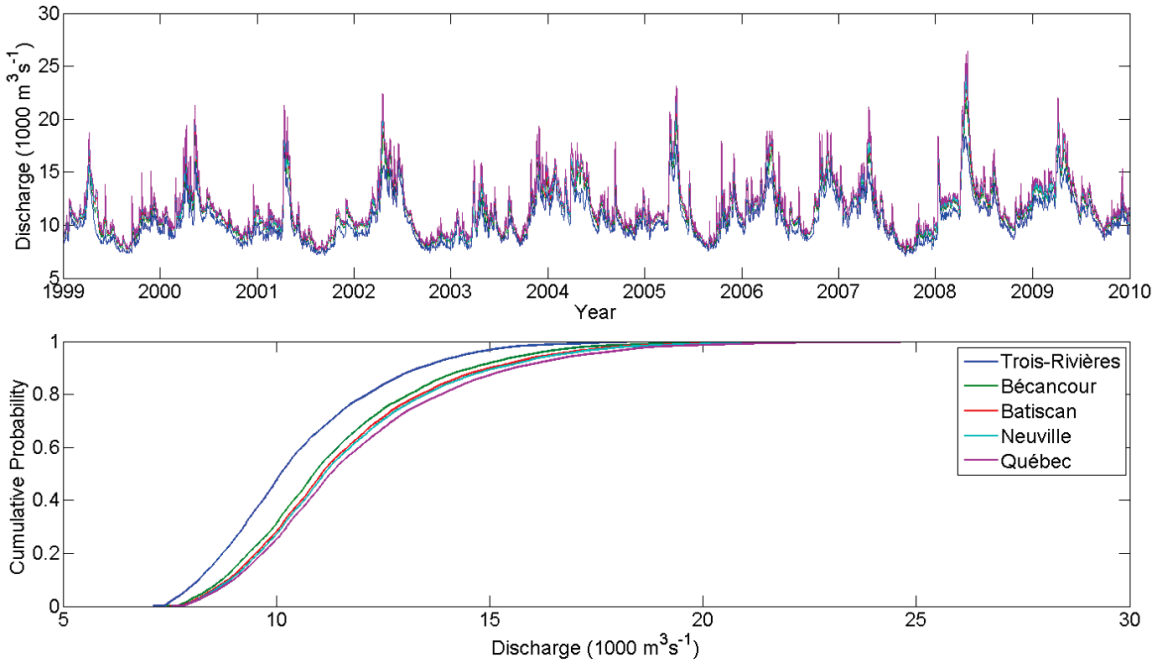


**Figure 2.3.3** **Forcing discharges in the St. Lawrence River for the 1999-2009 period: (top) discharge time series at Trois-Rivières, Bécancour, Batiscan, Neuville and Québec; (bottom) empirical cumulative distribution function.**

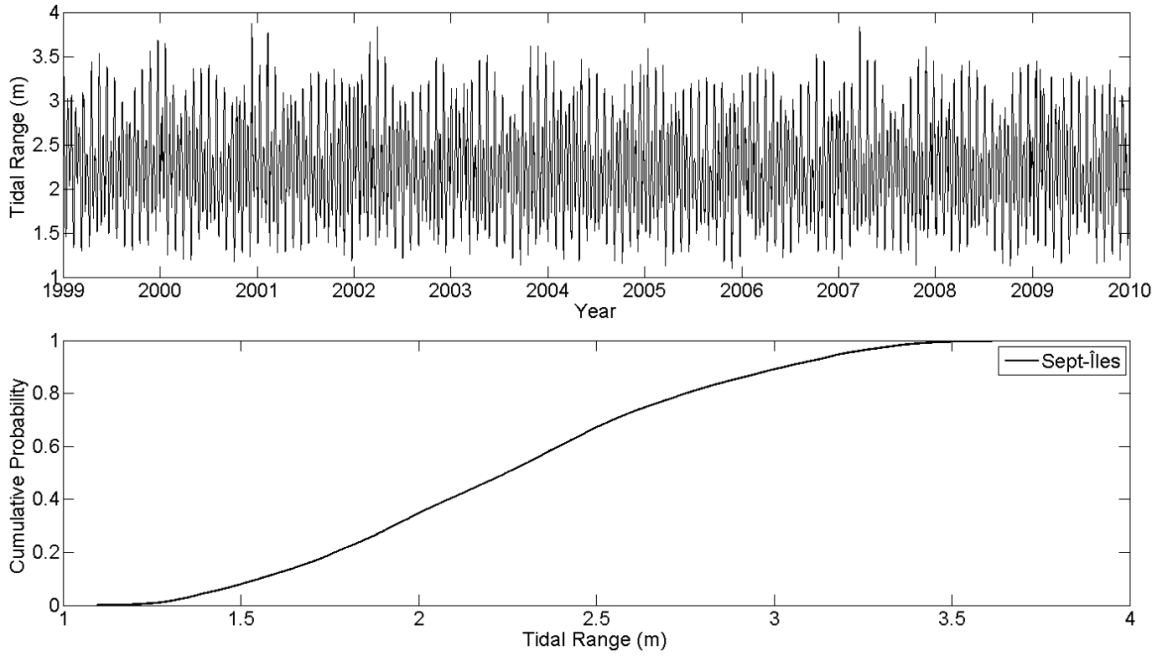


**Figure 2.3.4** **Forcing tidal range in the St. Lawrence River for the 1999-2009 period: (top) tidal range time series at Sept-Îles; (bottom) empirical cumulative distribution function.**

Time lags $\tau_Q$ and $\tau_R$ for both $Q$ and $R$ time series are presented in Table 2.3.1. They were set to identical values for stations sharing the same discharge time series, corresponding to the average lags for the stations concerned. For predictions made at arbitrary locations, e.g., at the validation stations, the same lags as the ones used at neighbouring stations were applied to the time series. It is noteworthy that for the Trois-Rivières station, the discharge time series for Bécancour was used instead of that of Trois-Rivières, in order to include the backwater effects from the Saint-Maurice River, located 1 km downstream of the station. This effect propagates up to the station of Lake Saint-Pierre.

In the development of a spatial model, identical analysis parameters must be applied to each station to ensure that spatial variations in the coefficients are not the result of changes in model properties, but that they are attributable to tidal-fluvial processes. Preliminary tests on the model exponents in Eq. (2.3.3) showed that model performance was little sensitive to their value, as deviations from theoretical exponents were compensated by changes in the regression coefficients. Similar conclusions were drawn from the sensitivity analysis performed by Matte *et al.* (2013). Therefore, model exponents were set to the theoretical values used by Kukulka & Jay (2003a, b), as they appear in Eq. (2.3.4). The same tidal constituents were imposed at all stations to allow interpolation of model coefficients throughout the system. As a consequence, errors for some constituents may grow upstream, while some other constituents become less significant downstream. The IRLS analyses [cf. Eq. (2.3.2)] were performed using a Cauchy weighting function with a default tuning constant of 2.385 (Leffler & Jay, 2009, MathWorks, 2012).

The allowed frequency separation in NS_TIDE is dictated by a redefined Rayleigh criterion, which takes into account the overlap between frequencies associated with their tidal cusps (Munk *et al.*, 1965). The width of these cusps reflects the intensity of modulation of the tidal components. Therefore, the inclusion of too many constituents with overlapping cusps can lead to erroneous estimates of tidal properties (e.g., Godin, 1999). One typical symptom of an over-determined solution (i.e. too many constituents) is that closely spaced components take very large (unreal) amplitudes, their phases are almost 180° out of phase, so they cancel partially, and phase errors are very large (typically exceeding 100°). Conversely, not resolving enough constituents may result in oscillation of the tidal amplitudes as a compensation for modulations that would normally occur between pairs of constituents not included in the analyses. In the most extreme case, only including one component per tidal band would yield similar results as

continuous wavelet transform (CWT) (Flinchem & Jay, 2000). Here, tidal constituents were selected, partly based on rather permissive constituent selection criteria [$\eta = 0.5$ and mean signal-to-noise ratio (SNR) $\geq 2$; see Matte *et al.* (2013) for a definition of the parameters]. Constituent amplitudes and phases were then carefully inspected to detect artefacts arising from the method. To ensure that included constituents have a physical meaning, comparisons of time-averaged tidal properties (especially the phases) with those given by standard HA were made, assuming that HA accurately represents the average frequency content of the time series. Constituents presenting non-physical characteristics were excluded from the analyses, while some others were progressively added to reduce oscillations in the tidal amplitudes of principal components. In the end, the tidal-fluvial model was forced using the same 39 components at all stations, listed in Table 2.3.3. At Saint-Joseph-de-la-Rive (rkm 0), these 39 constituents explain 98% of the variance in water levels, with classical HA. Low-frequency variations in water levels, for their part, are represented by the stage model [cf. Eq. (2.3.4)], rather than the usual low-frequency harmonic constituents.

**Table 2.3.3 Tidal constituents included in the analyses, for each tidal band from diurnal to eight-diurnal (D1 to D8).**

| Tidal bands | Constituents |
|---|---|
| $D_1$ | $\sigma_1$, $Q_1$, $O_1$, $P_1$, $K_1$, $J_1$ |
| $D_2$ | $2N_2$, $N_2$, $\nu_2$, $M_2$, $\lambda_2$, $L_2$, $S_2$, $K_2$, $MSN_2$ |
| $D_3$ | $MO_3$, $SO_3$, $MK_3$ |
| $D_4$ | $MN_4$, $M_4$, $SN_4$, $MS_4$, $MK_4$, $S_4$, $SK_4$ |
| $D_5$ | $2MK_5$, $2SK_5$ |
| $D_6$ | $2MN_6$, $M_6$, $2MS_6$, $2MK_6$, $2SM_6$, $MSK_6$ |
| $D_7$ | $3MK_7$ |
| $D_8$ | $M_8$ |

The time reference for the analyses was Eastern Standard Time. Greenwich phases were computed, with no nodal corrections. The latter are performed in NS_TIDE in the same manner as T_TIDE (Pawlowicz *et al.*, 2002) and should be applied in overlapping 366-day periods. However, for the coefficients of the nonstationary analysis to be robust, a record length that covers the widest dynamic range of flow conditions is sought. The chosen 11-year period met this criterion. NS_TIDE does not currently embed the nodal corrections in the least-squares matrix, which would remove the need for assumptions that underlie usual post-fit corrections and that may restrict the length of the analysis period (Foreman *et al.*, 2009). Nevertheless, modula-

tions of the main tidal constituents by their satellites are small in rivers relative to the effects of stage variations. Nodal modulations are also modified by fluvial modulations. In fact, deviations from the equilibrium constants may occur due to friction and shallow-water effects, which may lead to systematic errors in the estimation of tidal constituents (Amin, 1983, 1985, 1993, Shaw & Tsimplis, 2010). In practice, it is virtually impossible to separate the modulation effects on the main tidal constituents by river flow and tidal range from those stemming from changes in lunar declination (see, e.g., Matte *et al.*, 2013, for further discussion). For these reasons, nodal corrections were not included in the analyses.

To assess model performance, water level hindcasts were compared to results from classical HA at the stations. Standard HA (Pawlowicz *et al.*, 2002, Leffler & Jay, 2009) were performed using a threshold SNR of 2 for constituent rejection. The number of replicates for the error estimation was set to 300 and a correlated noise model was used. The same weighting function and tuning constant as for the nonstationary analyses were used. To further validate model predicting capabilities, water level forecasts were produced at all stations for a period free of ice extending from May 21 to October 21, 2009, during which pressure sensors were in place. Results were compared to simulations from the ONE-D model of the St. Lawrence without considering the effects of wind. The numerical scheme and formulation of the model are detailed in Hicks (1997), along with a thorough analysis of its performance.

#### *2.3.4.3 Results*

##### 2.3.4.3.1 Model Performance

Figure 2.3.2 shows water level hindcasts from NS_TIDE compared to observations at four selected stations for the 2007-2008 period, characterized by very low and very high flows (cf. Figure 2.3.3). Predicted signals follow the variations in tidal amplitude and in MWL with good accuracy at both upstream and downstream stations.

Statistics obtained from classical HA and NS_TIDE at the analysis stations of Table 2.3.1 for the 1999-2009 period are presented in Figure 2.3.5. They include the number of model coefficients solved for [different from $n$, the number of tidal constituents; see Eq. (2.3.4)], the residual variance, root-mean-square errors (RMSE), and maximum absolute errors. The only criteria for constituent selection and rejection in HA are based on the record length and error level in coefficients, respectively. As shown in Figure 2.3.5a, the total number of model coefficients is

higher with NS_TIDE, with nearly half the constituents of HA, due to the higher number of terms composing the nonstationary model. The ability of classical HA to explain the signal variance is comparable to NS_TIDE at downstream stations, from Saint-Joseph-de-la-Rive (rkm 0) to Portneuf (rkm 163.5), landward of which the residual variance drastically increases for HA (Figure 2.3.5b). This coincides with the presence of rapids near Deschambault (rkm 168) combined with a rapid increase of the bottom slope, marking the transition from tidal to tidal-fluvial regimes where the influence of discharge becomes prominent.

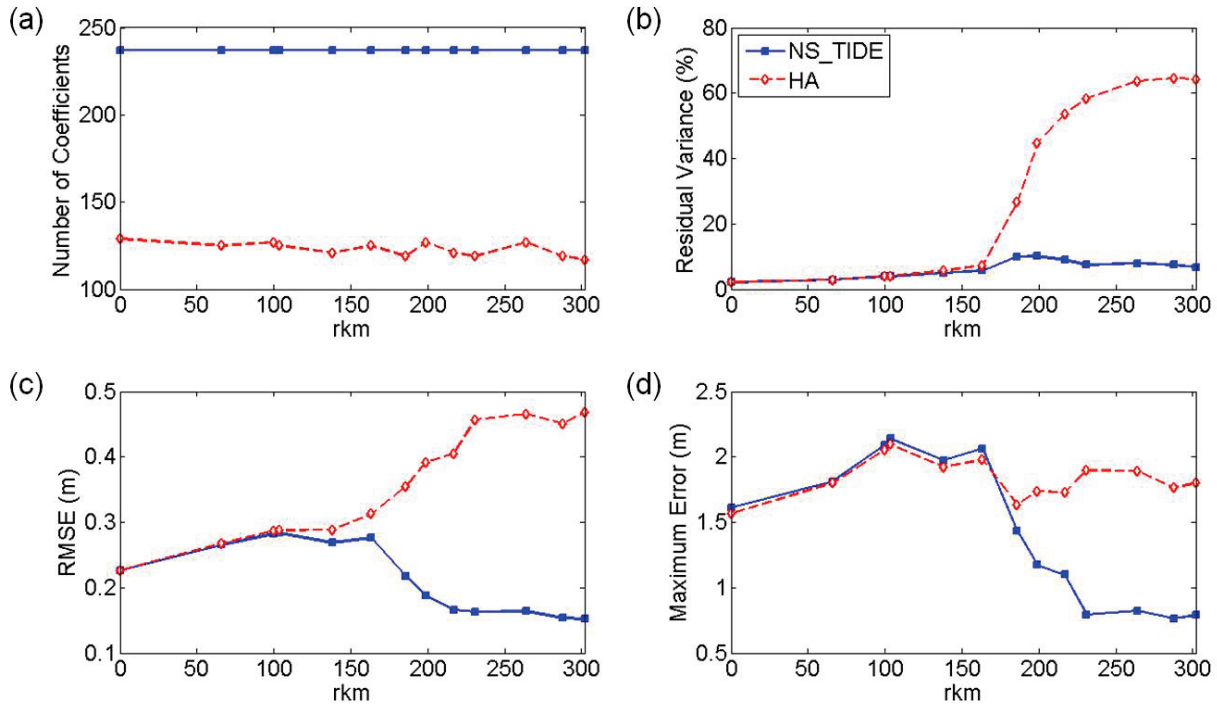


**Figure 2.3.5** **Statistics on water level hindcasts from NS_TIDE and classical HA at the analysis stations of Table 1 for the 1999-2009 period: (a) number of model coefficients solved for; (b) residual variance; (c) root-mean-square errors (RMSE); (d) maximum absolute errors. RMSE and maximum errors are absolute values, thus decreasing with tidal range.**

In Figure 2.3.5c, RMSE from both methods are plotted at the stations. The curves coincide in the first 100 rkm, but the RMSE associated with NS_TIDE sharply decrease upstream, while those of HA increase. On average, the NS_TIDE analyses are far more representative of the tidal-fluvial dynamics than HA in upstream reaches of tidal rivers. At downstream stations, where the tidal signals are much more stationary (see Figure 2.3.2), NS_TIDE is comparable to HA, thus demonstrating the validity of the model under these conditions too.

Maximum absolute errors shown in Figure 2.3.5d are again comparable between the two methods up to Portneuf (rkm 163.5), where they split. They then show a significant decrease with NS_TIDE, attributable to a better representation of the physics by the nonstationary model. Note that both RMSE and maximum errors are absolute values; their sharp decrease passed Portneuf thus also follows the decrease in tidal range.

#### 2.3.4.3.2 Spatial Interpolations

The model coefficients in Eq. (2.3.4) were spatially interpolated using Hermite polynomials so that tidal properties may be retrieved at any points in space. Figure 2.3.6a-b show an example of interpolated coefficients for the stage model and the $M_2$ component of the tidal-fluvial model, respectively. For clarity, second and third coefficients were multiplied by the average discharge and tidal range for the 1999-2009 period, as shown in the legend. In the stage model (Figure 2.3.6a), the coefficient $c_0$ is primarily determined by river geometry. In the first ~160 rkm, its contribution to the MWL is partly balanced by the discharge term $c_1$. From Portneuf (rkm 163.5) and upstream, the $c_0$ term increases following the rapid rising of the bed slope. This may be due to a long-term water level setup caused by river-tide interaction that steepens the water surface profile (e.g., Sassi & Hoitink, 2013). The discharge coefficient $c_1$ increases from downstream to upstream; its effect is more pronounced past Portneuf, where changes in the tidal-fluvial regime occur. The range term $c_2$ is responsible for fortnightly variations in MWL. The value of $c_2$ increases gradually up to Cap-à-la-Roche (rkm 186), where the amplitude of the fortnightly wave reaches a maximum; it then decreases upstream. This tendency is consistent with the variations in Mf, MSf and Mm amplitudes (not shown) calculated from classical HA at the stations.

In Figure 2.3.6b, the coefficients of the $M_2$ component of the tidal-fluvial model are presented, where the blue curves represent the cosine part of Eq. (2.3.4) and the red curves represent the sine part. Both sine and cosine parts of the constant term $d_0$ (solid lines), representing the astronomical tide, are strongly damped moving upstream. The discharge terms $d_1$ (dashed lines) are in general opposite in sign with $d_0$, each pair of curves of a given part (cosine or sine) intercepting around zero, so that they cancel each other once they are summed. In other words, the sign difference between $d_1$ and $d_0$ means that an increase in discharge is reflected as a decrease in tidal amplitude. The range terms $d_2$ are not consistently opposed in sign with $d_0$, so

that their effect on $M_2$ amplitudes varies along the river. The amplitudes and phases can be retrieved for each term from Eqs. (2.3.9) through (2.3.14) for further analysis (see next sections).

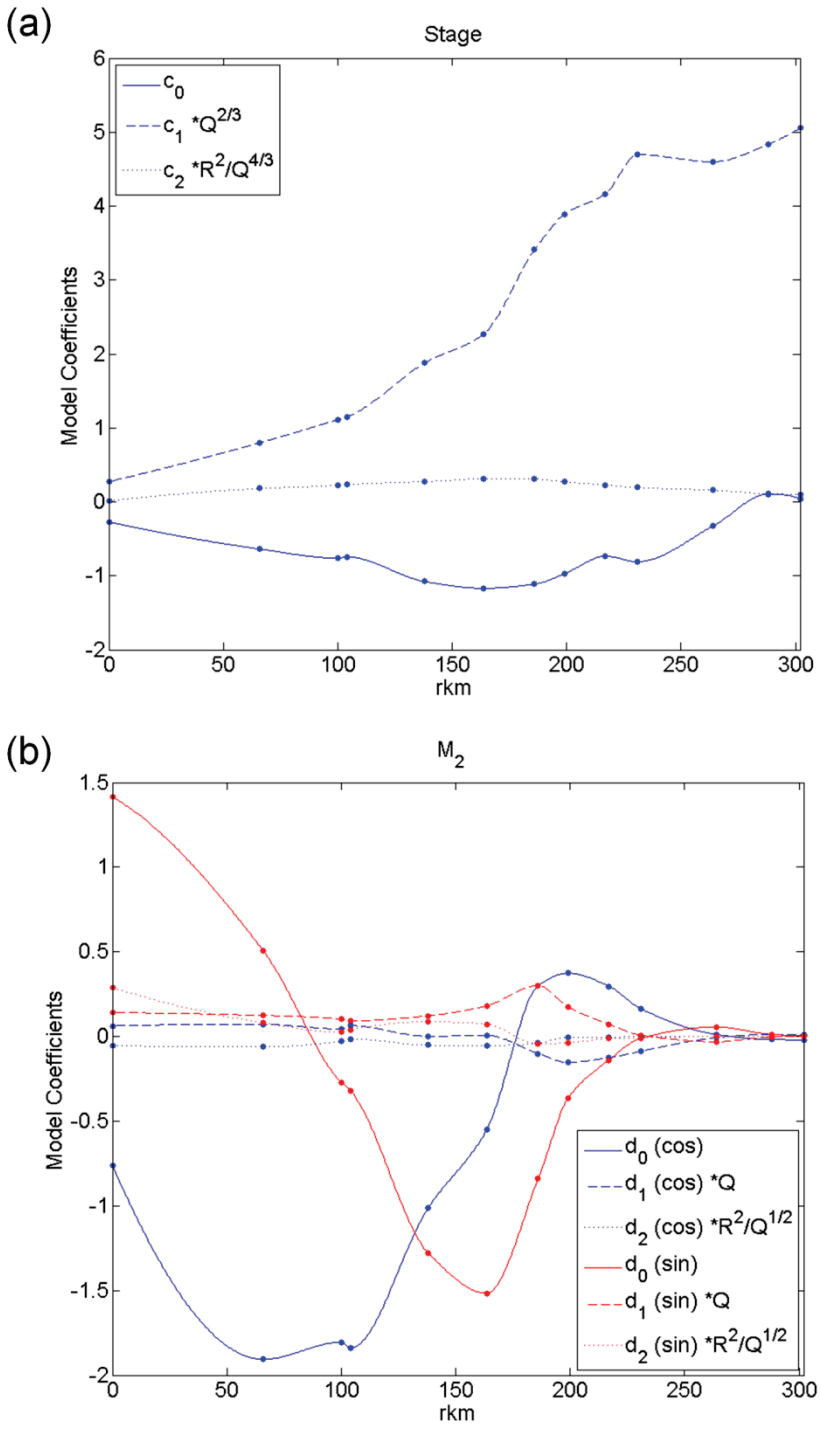


**Figure 2.3.6** **Spatially-interpolated coefficients of the (a) stage model and (b) $M_2$ component from the tidal-fluvial model. Second and third coefficients in (a) and (b) were multiplied by their average discharge and tidal range for the 1999-2009 period.**

#### 2.3.4.3.3 Validation

To validate the model, water level predictions were generated at all 32 stations from Table 2.3.1 and Table 2.3.2 and compared with observations, for the period extending from May 21 to October 21, 2009. The same exercise was done for the ONE-D model for comparison purposes. Results are presented in Figure 2.3.7. Stations identified with asterisks are not covered by the main branch of the ONE-D model and should be interpreted with caution; they are either located on the south shore of the upper estuary (downstream of Orleans Island) or in the north arm of Orleans Island. In general, residual variances, RMSE and maximum errors are lower with the ONE-D model than with NS_TIDE, with the exception of a few upstream stations. This is not a surprising result since ONE-D has many more degrees of freedom than NS_TIDE. The ONE-D model of the St. Lawrence is composed of 1241 sections, each described in terms of geometry and friction. It solves the one-dimensional St. Venant equations at every time step of the validation period. In comparison, the NS_TIDE model is based on an analytical solution of the St. Venant equations for the critical convergence regime (Jay, 1991). It is composed of 237 parameters per station or, equivalently, 237 Hermite polynomial functions for the spatial model which are invariant in time (i.e. no need for time integration). Although much simpler, the NS_TIDE model is capable of good accuracy, with RMSE lower than 0.3 m at all stations. This is quite low considering that tidal ranges often exceed 5 m in the downstream portion of the river. Furthermore, error at the validation stations is not systematically higher than at the analysis stations, which is an indication that the station network is dense enough to allow accurate interpolation. It also shows that the interpolation functions are well adapted to the variations in modeled parameters, and thereby to the physics of the river. Interpolation errors are discussed in section 2.3.5. Higher residual variances were obtained at the station of Champlain (rkm 213) due to a higher noise level in the observed data (Figure 2.3.7a).

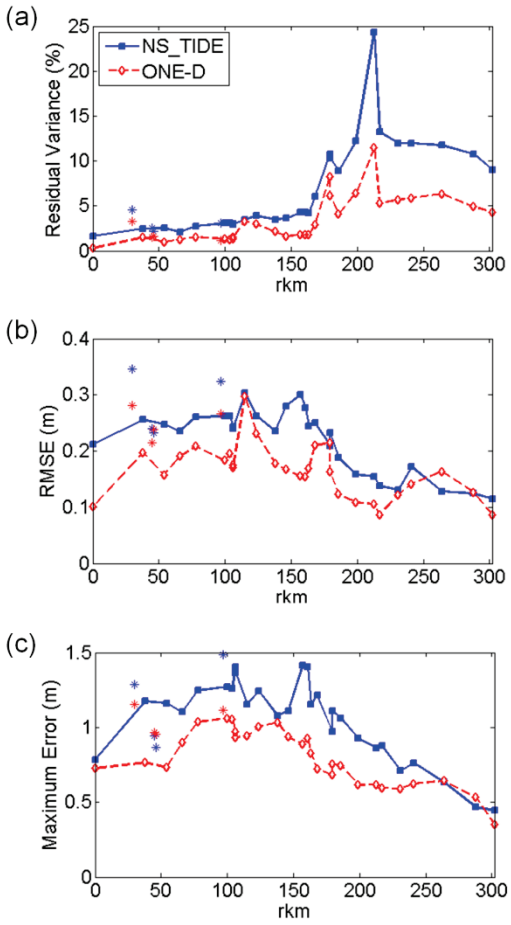


**Figure 2.3.7** **Statistics on water level predictions from NS_TIDE and ONE-D at the stations for the period from May 21 to October 21, 2009. Stations identified with asterisks are not covered by the main branch of the ONE-D model.**

To better characterize the model predicting capabilities, RMSE values were computed separately on MWL, tidal range, and height and time of high water (HW) and low water (LW). Results are shown in Figure 2.3.8. MWL are better reproduced by the ONE-D model at most stations except a few where the two models are comparable. With NS_TIDE, the highest errors in MWL occur between Neuville (rkm 138) and Portneuf (rkm 163.5), possibly due to lateral gradients in water levels associated with channel curvature. Errors in tidal range decrease with upriver distance as tidal amplitudes are damped. They reach a maximum between Québec Bridge (rkm 115) and Saint-Nicolas (rkm 124), which can be explained by very large water depths between Lauzon (rkm 100) and Saint-Nicolas, varying approximately from 30 to 60 m. The tidal wave propagates faster with increased water depth and is less rapidly damped by bottom friction. Because the interpolation is made between Saint-Charles River estuary (rkm 104) and Neuville (rkm 138)

assuming smooth variations in tidal properties, the resulting tidal ranges at intermediate stations are less accurate. This is confirmed by errors in LW heights, which are significantly higher at Québec Bridge and Saint-Nicolas, as LW are the most sensitive to depth variations. It is however a little surprising to observe the same behaviour with ONE-D considering that water depths are taken into account in the model; this might be related to a lack of stations for calibration between Lauzon and Neuville. Furthermore, errors in the heights and times of HW are rather stable downstream of Trois-Rivières (rkm 231), while errors in the times of occurrence of LW gradually increase from downstream to upstream. They reach values of about 2 h at Trois-Rivières. LW are more sensitive to friction and river flow than HW (e.g., Godin, 1999), thus explaining the higher and increasing errors in the timing of LW. Timing errors of HW and LW upstream of Trois-Rivières were excluded, because tide completely vanishes during high discharge events. Here, the comparison of the times of occurrence of HW and LW is an indirect evaluation of tidal asymmetry.

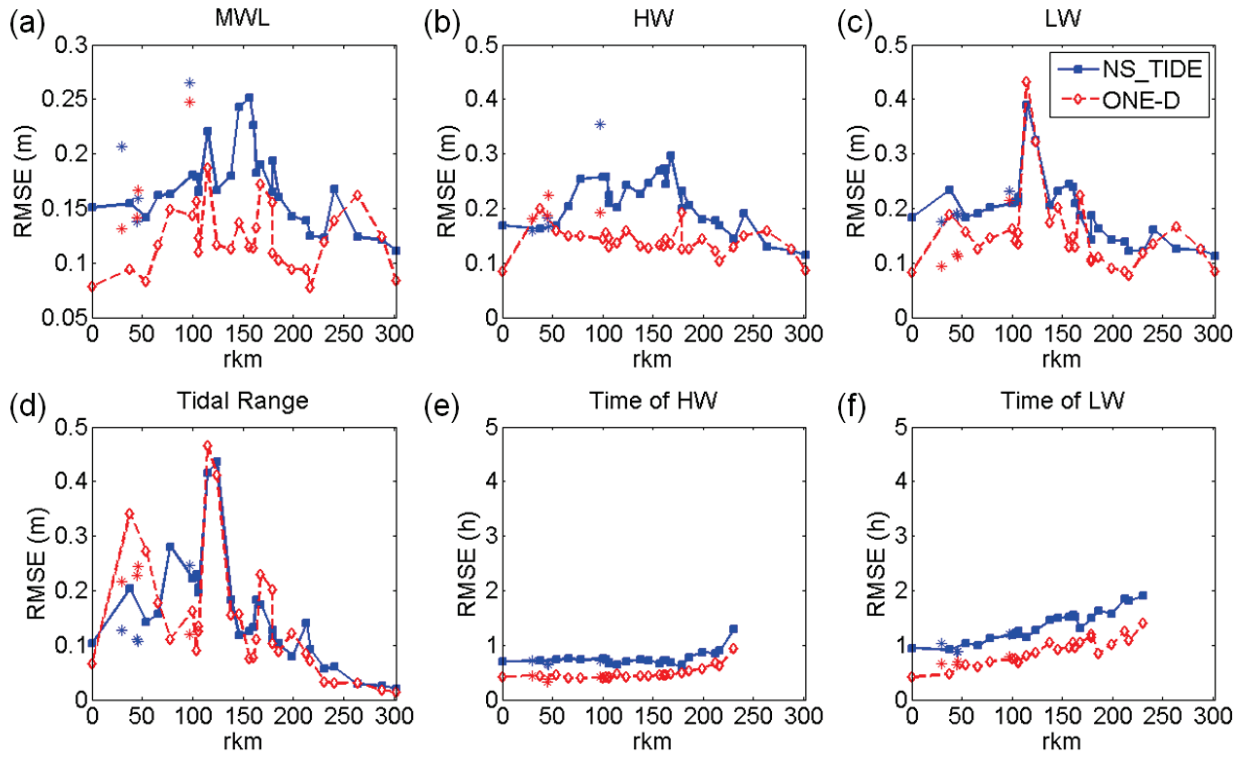


**Figure 2.3.8** **Root-mean-square error (RMSE) on predicted mean water level (MWL), tidal range, and height and time of high water (HW) and low water (LW) from NS_TIDE and ONE-D at the stations for the period from May 21 to October 21, 2009. Stations identified with asterisks are not covered by the main branch of the ONE-D model.**

#### 2.3.4.3.4 Tidal-Fluvial Processes

To demonstrate the ability of the model to improve current knowledge on tidal-fluvial processes, results in the St. Lawrence fluvial estuary are presented in Figure 2.3.9 through Figure 2.3.12. Because the objective is not to present a thorough analysis of the dynamical processes in play, results are restricted to the stage model and to five major constituents from the diurnal, semidiurnal and quarter-diurnal bands of the tidal-fluvial model.

The harmonic representation of low frequencies in traditional HA, composed of semi-monthly (Mf, MSf), monthly (Mm, MSm), semi-annual (Ssa), and annual (Sa) constituents, is unable to adequately represent low-frequency river motions dominated by nonlinear interactions of tides with river flow (Parker, 2007). In contrast, these interactions are well accounted for in NS_TIDE because river flow and ocean tidal range are included directly in the basis functions. Longitudinal profiles of MWL are shown in Figure 2.3.9 for the 0.1, 0.5 and 0.9 quantiles of discharge and tidal range. The water surface slopes clearly exhibit three contrasting zones in the fluvial estuary, as suggested by Godin (1999), with marked changes in the slopes around Portneuf (rkm 163.5) and Cap-à-la-Roche (rkm 186). The region delimited by these two stations forms a transition zone from the tidal to the tidal-fluvial regime, characterized by a rapid increase in bottom slope at the Richelieu Rapid near Deschambault (rkm 168). This supports the idea that breaks in morphology are responsible for splitting the system into river- and tide-dominated parts, similarly to the results obtained by Sassi *et al.* (2012) – in their case, however, they associated this separation with the point where the exponential width decrease stops. A jump in MWL also occurs around rkm 235, corresponding to the location of Laviolette Bridge, which acts as a major restriction to the flow. A fourth region can therefore be defined from this point, located near the entrance of Lake Saint-Pierre, up to Lanoraie where the semi-diurnal tide completely extinguishes during neap tides. The sensitivity of MWL to variations in discharge considerably increases in the upstream region of the fluvial estuary, while it is little affected at the most downstream stations. Increases in tidal range are also reflected by increases in MWL, and vice versa, which is in accordance with the fortnightly rise and fall of MWL during spring and neap tides, respectively (LeBlond, 1979). Further modulations of the MWL induced by frictional interactions between tidal constituents are accounted for by the stage model through the range term. Moreover, the response of the system to variations in tidal range is greater at lower

discharges. At downstream stations, MWL under conditions of low discharge and high tidal range are similar to MWL observed during high discharge and mean tidal range.

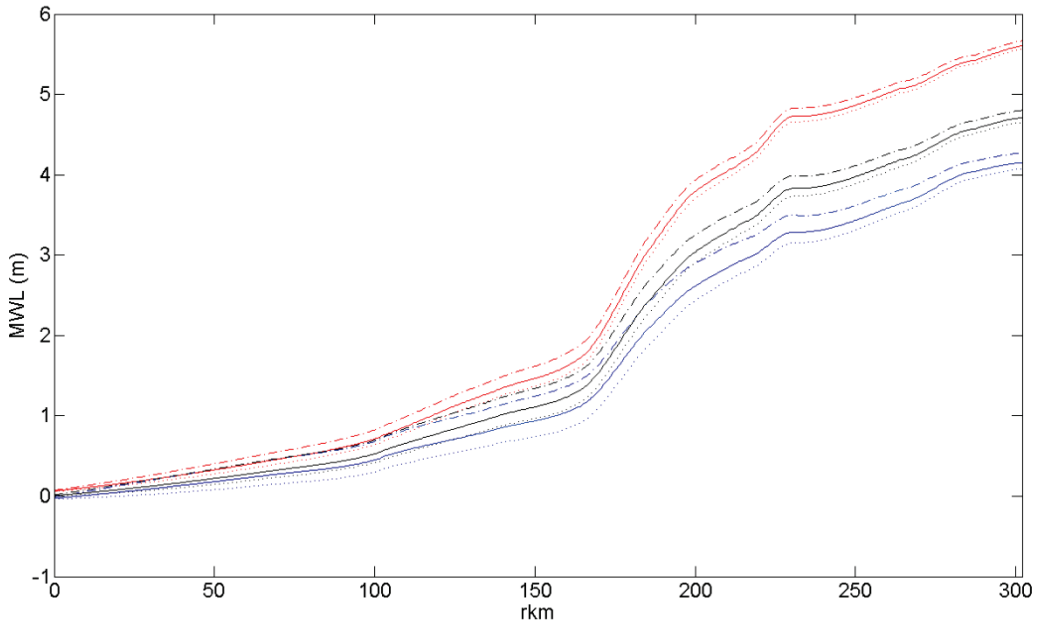


**Figure 2.3.9** **Longitudinal profiles of mean water levels (MWL) for quantiles of discharge and tidal range. Blue, black and red lines correspond to 0.1, 0.5 and 0.9 quantiles of discharge, respectively; dotted, solid and dash-dotted lines correspond to 0.1, 0.5 and 0.9 quantiles of tidal range, respectively.**

In Figure 2.3.10a-b, longitudinal profiles of amplitudes and phases are shown for the two dominant diurnal constituents, $O_1$ and $K_1$. In general, they suggest a similar separation of the fluvial estuary into four distinct regions. Tidal amplitudes are characterized by a slow decrease downstream to Portneuf (rkm 163.5), followed by a sharp diminution upstream. At downstream stations, tidal amplitudes increase with discharge, because of larger water depth. Although amplitudes are being damped considerably from Portneuf, it is only around Cap-à-la-Roche (rkm 186) that tidal amplitudes start to decrease with increases in discharge. From that point, amplitudes are more severely damped by the discharge. Past the Laviolette Bridge (rkm 235), the decrease in tidal amplitudes slows as it approaches zero.

$K_1$ is the dominant diurnal constituent and has higher amplitudes than $O_1$ downstream of Portneuf. However, the amplitudes of $O_1$ and $K_1$ reach similar values around Portneuf, $K_1$ being damped slightly more rapidly than $O_1$, possibly due to the higher frequency of $K_1$ (Godin,

1999). According to the development of the tidal potential (Doodson, 1921), $O_1$ should consistently be smaller than $K_1$. One possible explanation for $O_1$ and $K_1$ being of similar amplitude is to attribute this discrepancy to the effect of $M_2$ on $K_1$ and $O_1$ in presence of strong bottom friction (Godin & Martinez, 1994).

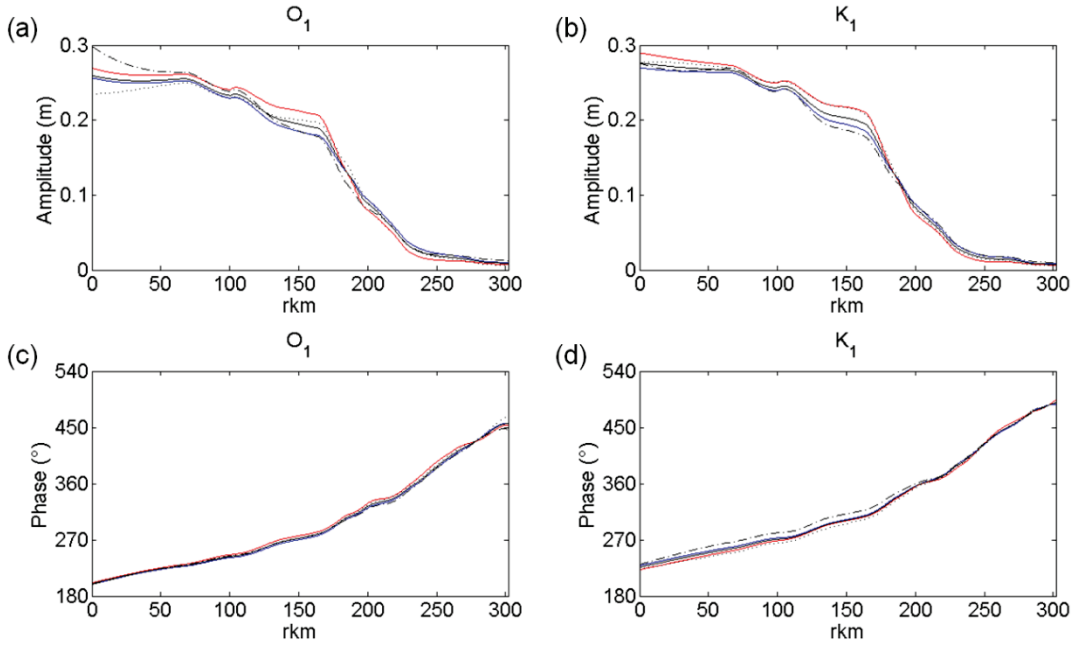


**Figure 2.3.10 Same as Figure 2.3.9 for $O_1$ and $K_1$ amplitudes and phases.**

$O_1$ and $K_1$ are responsible for the diurnal inequality associated with lunar declination. Their combined effect leads to a modulation with a period of 27.32 days, reaching a minimum every 13.66 days when the moon is over the equator. However, in presence of friction, their summed amplitude is also modulated by tidal range. In fact, taken individually, the amplitude of $K_1$ is damped during spring tides (higher tidal range) and amplified during neap tides (lower tidal range) due to nonlinear interactions, as observed in Figure 2.3.10. As for $O_1$, higher amplitudes are obtained at spring tides downstream of Portneuf (rkm 163.5), while they are lower upstream. This effect reverses upstream of Laviolette Bridge (rkm 235) in the case of $O_1$ and upstream of Cap-à-la-Roche (rkm 186) for $K_1$.

As for the phases of $O_1$ and $K_1$ in Figure 2.3.10c-d, they show a constant increase with distance up to Portneuf (rkm 163.5) where a change in slope occurs, meaning that tide propagation is delayed due to the increasing influence of river flow (here, a steeper slope means a slower

propagation of the tidal wave). However, for $O_1$, phase lags are slightly larger at high discharges compared to low discharges, while the opposite is observed for $K_1$. Although this may be an artefact of the method, the consequence is a modification of their combined effect on a semi-monthly basis. Finally, with larger tidal ranges the phases of both components are increased downstream while they are reduced upstream; this is another effect of the reversal of mean low waters during spring and neap tides.

In Figure 2.3.11, longitudinal profiles of amplitudes and phases are shown for the two dominant semidiurnal constituents, $M_2$ and $S_2$. Similar observations as in Figure 2.3.10 can be made with respect to the general aspect of the curves. Both $M_2$ and $S_2$ show little variations in amplitude with discharge throughout the system, relative to their amplitude. Overall, slightly lower amplitudes are obtained at higher discharges with $M_2$, where damping is more influenced by discharge upstream of Portneuf (rkm 163.5). With $S_2$, higher amplitudes are observed down-stream of Portneuf at higher discharges, while damping occurs upstream. The effects of tidal range on the amplitudes of $M_2$ are little, except in the first ~80 rkm, while the amplitudes of $S_2$ are much more sensitive. In presence of larger tidal ranges, the amplitudes of $S_2$ decrease, which might seem counterintuitive. In fact, $M_2$ and $S_2$ interact together to produce neap-spring variations with a modulation period of 14.77 days. When tidal ranges are large (at spring tides), $M_2$ and $S_2$ are in phase, their amplitude being added to each other. However, as shown in Figure 2.3.11a-b, the individual amplitude of $S_2$ is smaller during spring tide compared to neap tides, meaning that the summed amplitude of $M_2$ and $S_2$ is smaller than it would be in absence of friction. In other words, $M_2$ and $S_2$ are responsible for the generation of the neap-spring cycle, but they may be, in turn, affected by these fortnightly variations through friction, by a feedback mechanism.

As for the phases of $M_2$ and $S_2$, shown in Figure 2.3.11c-d, variations are more subtle. Increases in discharge lead to slightly higher phases of $S_2$, while increases in tidal range lead to lower phases. Variations for $M_2$ are almost imperceptible, but they show similar trends.

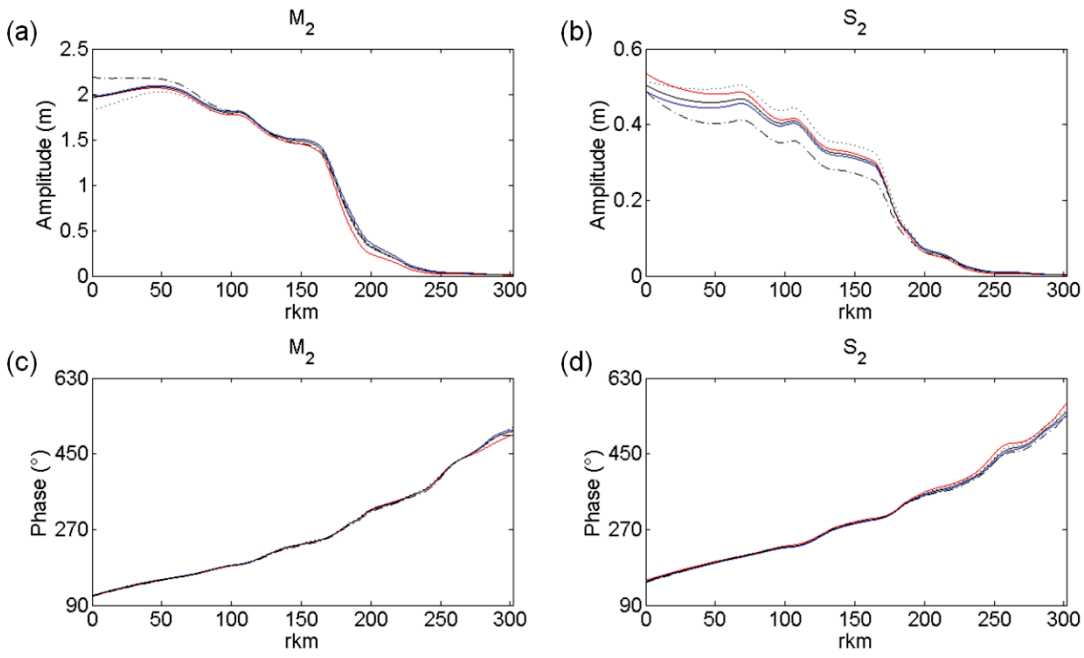


**Figure 2.3.11 Same as Figure 2.3.9 for $M_2$ and $S_2$ amplitudes and phases.**

In upstream reaches of rivers, discharge has the effect of damping constituents of higher frequency more effectively (Godin, 1991, Godin & Martinez, 1994). As a result, semidiurnal constituents are being damped faster than diurnal tides (e.g., Godin, 1999). The decay profiles of the diurnal and semidiurnal components in Figure 2.3.10 and Figure 2.3.11 between Saint-Joseph-de-la-Rive (rkm 0) and Lanoraie (rkm 302) are highly similar, but damping ratios seem to confirm this trend. In fact, for an average discharge, approximately 3% of the original diurnal amplitude remains at Lanoraie, while only 0.7% of the semidiurnal amplitude measured at Saint-Joseph-de-la-Rive is still observable at Lanoraie. While damping and phase speed may be frequency dependent, frictional nonlinearities also act as a generating mechanism for overtides and compound tides, hence contributing to the modification of the principal components.

In Figure 2.3.12 are shown the $M_4/M_2$ amplitude ratios and $2M_2–M_4$ phase differences as a function of upriver distance. The first 50 rkm were removed due to interpolation errors between the first two stations for frequencies higher or equal to that of $M_4$ (see discussion in section 2.3.5). Other oscillations are most likely artefacts of the interpolation functions. In general, an increase in $M_4/M_2$ amplitudes is observed up to Port Saint-François (rkm 241), indicating a transfer of energy from $M_2$ to $M_4$ through friction that is amplified upstream due to the increas-

ing influence of discharge. The amplitude ratio then undergoes a rapid decrease in Lake Saint-Pierre as most of the tidal signal is damped, $M_4$ being attenuated more rapidly than $M_2$ due to its higher frequency. Similar observations can be made between scenarios of low and high discharge. Downstream of Cap-à-la-Roche (rkm 186), the $M_4/M_2$ ratio increases with increasing discharges, while the reverse holds upstream. Past Cap-à-la-Roche, $M_4$ is damped more rapidly by discharge than it is created from $M_2$, while downstream the energy transfer from $M_2$ to $M_4$ at higher discharge overcomes its damping effects.

As for tidal ranges, their effect on $M_4/M_2$ amplitude ratio is consistent throughout the domain: a larger tidal range is expressed through smaller $M_4/M_2$ ratios, and vice versa. This is counterintuitive, as increases in the $M_4/M_2$ ratio are generally expected at spring tide rather than neap tide. One possible explanation is that the relative decrease in amplitude of $M_4$, even more pronounced than that of $M_2$ during spring tide, may be related to the lowering of low waters at neap tides rather than spring tides, with correspondingly stronger bottom friction.

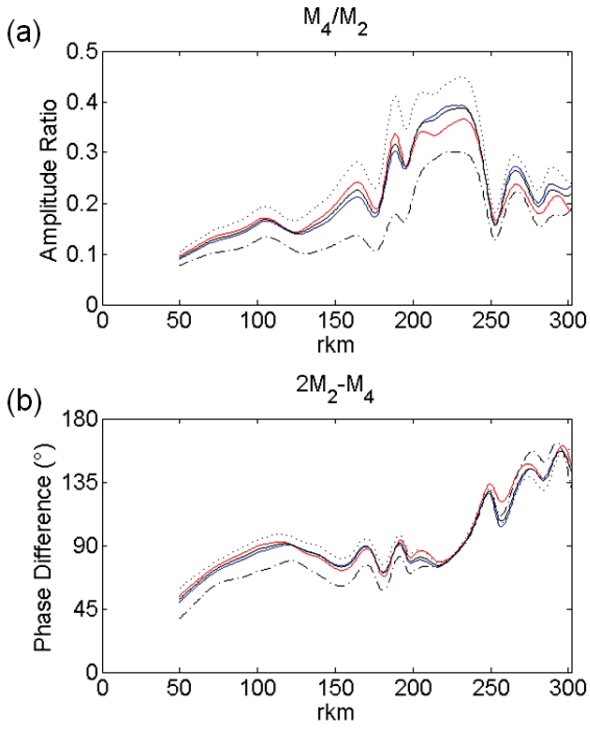


**Figure 2.3.12 Same as Figure 2.3.9 for $M_4/M_2$ amplitude ratios and $2M_2–M_4$ phase differences.**

The key to explain this unusual observation may lie in the tidal analysis approach used and in how river tides are conceptualized. For example, CWT tidal analysis methods (Jay & Flinchem, 1997, 1999, Jay & Kukulka, 2003, Buschman *et al.*, 2009) are able to express time variations in the tidal content of a signal, although with no distinction between frequencies of a given tidal band. Ratios of $D_4/D_2$ amplitudes (where $D_2$ and $D_4$ refer to the semidiurnal and quarter-diurnal species, respectively) thus represent the relative energy contained in the quarter-diurnal and semidiurnal bands, all frequencies combined. Similarly, the concept of "reduced vector" introduced by George & Simon (1984), and notably applied by Godin (1999), yields daily-averaged band estimates of the major tidal components, again with no possible separation between neighbouring frequencies. The amplitudes associated with $M_2$ and $M_4$ thus correspond to the total energy of their respective tidal band, much like CWT. Because NS_TIDE allows for the inclusion of multiple frequencies within each tidal band, direct comparisons with conventional methods is not straightforward. In fact, to actually reproduce the variations in $M_4/M_2$ ratios as traditionally expected from conventional methods, the total contribution from quarter-diurnal and semidiurnal bands needs to be taken into account. For example, plots of the dominant semidiurnal and quarter-diurnal constituents (not shown) confirm that their summed amplitudes in each tidal band are synchronized with tidal range, and so are the amplitude ratios. This is because both fortnightly and monthly modulations are induced by the interactions between pairs of frequencies. Taken individually, however, these constituents may respond differently to changes in discharge and ocean tidal range. Moreover, the energy transfer through friction from $M_2$ to higher frequencies not only involves $M_4$, but also $MN_4$, $MS_4$, and so on. As such, results are dependent on the number of included constituents within each tidal band.

Finally, in Figure 2.3.12b, the $2M_2–M_4$ phase differences show a gradual increase as a function of upriver distance. The relative phase differences are below 180°, which indicates a flood tidal asymmetry (Friedrichs & Aubrey, 1988). As these differences approach 180°, tidal asymmetry increases, with a signal characterized by short and abrupt flood tides and slowly decreasing ebb tides. The phase differences tend to increase with discharge, except for stations located between Neuville (rkm 138) and Cap-à-la-Roche (rkm 186); this is not clear whether it is the result of interpolations or river-tide interactions. Moreover, in the first ~250 rkm, flood tidal asymmetry is enhanced during neap tides compared to spring tides, which is coherent with the variations in $M_4/M_2$ ratios. The other quarter-diurnal tides possibly play a role in reinforcing tidal asymmetry.

### 2.3.5 Discussion and Conclusion

The potential of NS_TIDE to predict tides in upstream reaches of tidal rivers has been demonstrated. Signal analyses from 13 contrasting stations in terms of tidal-fluvial dynamics showed significantly better statistics than classical HA at upstream stations, while model performance at downstream stations was comparable to classical HA. Despite all assumptions made on the physics, the predicting capability of NS_TIDE was surprisingly high. In fact, many parameters such as the model exponents were set to constant values, while in reality they may be influenced by the river geometry, including the cross-sectional area, the wetted perimeter, the convergence rate, or other factors. Furthermore, the model implemented in NS_TIDE was developed for systems where tidal and fluvial flows are of similar magnitude. Knowing that tidal discharges can be more than five times greater than the residual flow at downstream locations, the agreement between the predicted and the observed water levels is remarkable. Even with these simplifications, tidal-fluvial processes that are explained by the method are physically plausible. When time-averaged, the amplitudes and phases resemble those obtained from HA, which confirms that the energy is well distributed between the constituents. Furthermore, predicting water levels from hindcast results for a time period other than the analysis period (e.g., Matte *et al.*, 2013), or equivalently, at intermediate stations if coefficients are spatially interpolated (like here), is a good way to test the validity of a model. Non-physical variations (e.g., unreal amplitudes and phases), which sometimes improve the harmonic fits, are likely to degrade the predictions when transposed to other time periods or stations. Here, the addition of constituents in the analysis was carried out until the point was reached where prediction accuracy decreased or artefacts started to appear (e.g., incoherent phases compared to classical HA). While resolving for too few components could lead to oscillations in the tidal amplitudes, the modulations observed in the results for the dominant frequencies were not eliminated by adding more constituents. The remaining variations may be attributable to increased errors under specific discharge and tidal range conditions, or they may be of physical origin. Further investigation may be needed to identify the sources of variation.

The model was validated with observations at a total of 32 stations and by comparison with the operational ONE-D model of the St. Lawrence River. Better statistics were obtained with the ONE-D model, but at the price of a more complex and time-consuming modeling process

(including the time devoted to develop and calibrate the model). In contrast, NS_TIDE provided still very good accuracy from a simpler but more informative model in terms of tidal-fluvial dynamics. In fact, numerical models and tidal analysis tools have very different strengths and weaknesses. Much can be learned from the existing operational model, especially if all terms in the momentum balance can be stored. However, no information on the time-varying frequency content of water levels or velocities can be obtained if not combined with other tidal analysis methods. By contrast, NS_TIDE uses a functional representation of tides (i.e. constituent amplitudes and phases) expressed in terms of external nonstationary forcing, which can be used for prediction in a straightforward manner. With an approach based on regression analysis, no field description is needed (topography, substrate friction, etc.), thus minimizing sensitivity to local topographic or frictional uncertainty. Instead, model parameters are optimized by stations to account for changes in these variables, as experienced by the water levels. NS_TIDE also preserves the compactness and efficiency of HA and ensures continuity between analyses performed in the St. Lawrence fluvial estuary, marine estuary and gulf. Furthermore, its capacity to distinguish frequencies within tidal species represents a considerable improvement compared to conventional tidal analysis methods that offers new possibilities for dynamical inquiry.

In NS_TIDE, the inclusion of river discharge in the basis function drastically improves the predictions at upstream stations, which had been demonstrated before, notably by Godin (1985, 1999) and Jay & Flinchem (1997). Similar adaptations of the models developed by Kukulka & Jay (2003a, b) were made to hindcast lower low water (LLW) and higher high water (HHW) as a function of river flow and external tidal forcing in the Columbia River (Jay *et al.*, 2011). Likewise, an inverse model based on analysis of tidal statistics was derived from Kukulka & Jay's (2003a, b) approach to produce monthly-averaged tidal discharge estimates in the San Francisco Bay (Moftakhari *et al.*, 2013); in their analysis, however, the tidal range term was neglected, because of the 31.7-day averaging period used.

Buschman *et al.* (2009) presented a method to analyze subtidal water levels in tidal rivers. Unlike Kukulka & Jay's (2003a, b) models, they used Godin's approximation of the friction term (Godin, 1999), rather than the Tschebyschev polynomial approach (Dronkers, 1964), to derive a new expression for subtidal friction, and successfully applied their model in the Berau River (Indonesia). They attribute subtidal motion to three sources, namely the river flow, river-tide interactions and tides alone. The river-tide interaction was mainly responsible for fortnightly

variations in water levels at the station under study. By comparison, the stage model implemented in NS_TIDE, derived from Kukulka & Jay's (2003b) model, decompose variations in MWL into contributions from river forcing, tides, atmospheric pressure (not included here), and topographic offset. As shown in the present application, NS_TIDE is able to reproduce the nonlinearly-generated fortnightly variations in MWL, as well as seasonal variations associated with river discharge. The frequency content of the stage model contains energy at annual and semiannual periods due to seasonal cycles in discharge ($c_1$ term), and at monthly and semimonthly periods due to the influence of the tidal range ($c_2$ term). These low frequencies are generated by tidal-fluvial interactions and nonlinear compound tides, which are inadequately represented in tidal rivers by the usual harmonic apparatus (Parker, 2007, Matte *et al.*, 2013). The improved statistics in the upstream reach of the St. Lawrence fluvial estuary (cf. Figure 2.3.5) is directly related to the ability of the stage model to accurately represent subharmonics.

Part of the error in the spatial model is related to the position of the analysis stations, the distance that separates them and the interpolation functions used. It was shown that Hermite polynomials are good interpolators in the present case, given the spatial variations in the coefficients in the St. Lawrence. However, as the frequency of the constituents increases, the wavelength decreases, leading to more oscillations in the coefficients due to a higher number of cycles. When the distance separating the stations approaches half the wavelength of the constituent, interpolation errors may increase drastically. In that case, components of higher frequencies should be neglected or more stations should be added to the available network. In the present application, the average distance between the stations is 25 km (cf. Table 2.3.1), which is less than half the wavelength of $M_8$ (roughly ~70 km). Between Saint-Joseph-de-la-Rive (rkm 0) and Saint-François (rkm 66), however, the interpolation of $M_4$ (wavelength ~140 km) and higher frequencies is questionable due to the distance separating the two stations, as mentioned above (cf. Figure 2.3.12). Using numerical models to improve the interpolation, by taking advantage of a higher spatial resolution, may be an interesting avenue to explore.

NS_TIDE does not currently differentiate between the rising and falling limbs of a hydrograph, mainly because coefficients determined by regression are constant in time. This feature allows general applicability of the model, although it cannot account for hysteresis phenomena. For example, as shown by Sassi & Hoitink (2013), tides are damped faster during the rising limb of a discharge wave than inversely. The fact that nonstationary (rather than constant) river discharges

are built directly in the basis function matrix of NS_TIDE offers the possibility of analysing such mechanisms; they should be addressed in the future. Moreover, recent studies show that flow division in tidal branching systems is controlled by river flow, tides and the interactions between the two (Buschman *et al.*, 2010, Sassi *et al.*, 2011). Notably, the discharge asymmetry features fortnightly oscillations attributable to neap-spring variations in tidal range. The use of NS_TIDE to further examine these interactions would be interesting, especially at the junction of Orleans Island in the St. Lawrence fluvial estuary.

The spatial, nonstationary harmonic model presented in this paper represents a new way to look at river tides. Applied to the St. Lawrence fluvial estuary, it successfully reproduced stage and tidal properties in an unprecedented way, by expressing their variations in terms of nonstationary forcing variables, i.e. river discharge and ocean tidal range, for a broad range of conditions. Several characteristics of the St. Lawrence and, by extension, of tidal rivers in general were brought to light by the model. They can be summarized as follows:

- The decrease in predictive skill of classical HA compared to NS_TIDE coincides with a break in river morphology, in the present case associated with the presence of rapids combined with a rapid increase of the bottom slope, which marks the transition from the tidal to tidal-fluvial regimes.
- A mean water level setup is observed, starting in the transition zone between the tidal and tidal-fluvial regimes (Portneuf; rkm 163.5).
- The sensitivity of mean water levels to variations in discharge considerably increases upstream. The response of the system to variations in tidal range is greater at lower discharges.
- A fortnightly rise and fall of the mean water levels is observed during spring and neap tides, respectively. The amplitude of the fortnightly wave reaches a maximum as it enters into the tidal-fluvial regime (Cap-à-la-Roche; rkm 186).
- Tides are rapidly damped in the transition zone between the tidal and tidal-fluvial regimes, and tide propagation is delayed.

- The response of tidal constituents to external forcing by discharge and ocean tides is both spatially and frequency dependent; it differs between constituents in different tidal species, but also between frequencies of a single tidal species.
- Frictional nonlinearities act as a generating mechanism for overtides, until they reach a point upstream where they are damped more rapidly by friction than they are generated through nonlinear interactions.

Together with numerical modeling, nonstationary HA has the potential to improve current knowledge on tidal-fluvial processes in highly nonlinear environments such as tidal rivers, pushing the limits of conventional tidal prediction tools. Furthermore, it can be used to assess the temporal and spatial variability of tidal-fluvial dynamics in systems where the development of a numerical model is not possible.

### 2.3.6 Acknowledgements

This work was supported by scholarships from the Natural Sciences and Engineering Research Council of Canada and Fonds de recherche du Québec – Nature et technologies. The authors wish to thank Denis Lefaivre and Alain D'Astous for providing simulation results from the ONE-D model, David A. Jay for discussions regarding the analysis of tides in rivers, and two anonymous reviewers for their constructive comments on the manuscript.

## 2.4 Development of a high-resolution, two-dimensional hydrodynamic model of the St. Lawrence fluvial estuary

Cet article présente le développement d'un modèle hydrodynamique 2D non-stationnaire à haute résolution spatiale de l'estuaire fluvial du Saint-Laurent. Une procédure d'étalonnage et de validation du modèle est décrite, basée sur des données de terrain détaillées en partie issues de l'objectif 1. L'article remplit l'objectif 3 de cette thèse en fournissant une description intégrée et synoptique du système via la modélisation numérique. L'article a été soumis à la revue *Water Resources Research*.

Le développement, l'étalonnage et la validation du modèle hydrodynamique ont été réalisés par l'auteur de cette thèse (premier auteur), en étroite collaboration avec Yves Secretan (second auteur) et Jean Morin (troisième auteur), qui détiennent une expérience complémentaire en modélisation sur de grands systèmes fluviaux, incluant le Saint-Laurent. Ces derniers ont participé de près à chacune des étapes de développement du modèle, à la réflexion entourant l'étalonnage en non-stationnaire et à l'analyse des résultats. Les coauteurs ont également contribué à ce travail en fournissant les ressources informatiques et humaines nécessaires au développement et à l'intégration de certaines composantes du modèle. L'écriture de l'article a été réalisée en totalité par le principal auteur, avec une contribution des coauteurs à la révision du manuscrit.

La référence complète de l'article est donnée ci-dessous :

Matte P, Secretan Y & Morin J (2014) Development of a high-resolution, two-dimensional hydrodynamic model of the St. Lawrence fluvial estuary. *Water Resour. Res.*: submitted.

### 2.4.1 Abstract

A two-dimensional (2D) non-stationary, high-resolution hydrodynamic model of the St. Lawrence fluvial estuary (SLFE) has been developed with the objective of providing detailed spatiotemporal description of the hydrodynamics in response to tidal and fluvial forcings. It is based on high density topographic data stemming from LIDAR surveys and multibeam bathymetric soundings. A finite-element mesh with an average spatial resolution of 50 m was designed, far denser than previous/existing models. The model includes a drying-wetting

component allowing water in intertidal areas to be cyclically stored and evacuated. Calibration and validation was performed using detailed field data composed of water level data from 29 tide gauges and cross-sectional water level and velocity data collected along 13 transects, repeatedly surveyed during semidiurnal tidal cycles. Results show very good agreement between modeled and observed water levels, with predicting skills higher than 0.99 at all stations and root-mean-square errors (RMSE) corresponding to less than 5% of the local tidal ranges in the first 186 river km; at upstream stations, where tidal ranges are significantly reduced, RMSE are lower than 6 cm. Harmonic properties as well as tidal and flow features observed in the field data are all reproduced satisfactorily. The model adequately represents lateral exchanges between the intertidal flats and the channel, neap-spring variability in the location of the upstream limit of current reversal, flow division at the junction of Orleans Island, and momentum balance as a function of space and tidal phase. This work provides for the first time a detailed and validated 2D description of the tidal hydrodynamics of this complex region where knowledge is very limited.

### 2.4.2 Introduction

The St. Lawrence River is the third largest river in North America, with a drainage basin of ~$1.6 \times 10^6$ $km^2$ and an average freshwater discharge of 12 200 $m^3s^{-1}$ at Québec. It connects the Great Lakes with the Atlantic Ocean and is the primary drainage of the Great Lakes basin, one of the most industrialized regions of the world. This river is one of diverse economical activity for both Canada and the United States, involving commercial navigation, numerous industries, recreational activities and tourism. It accounts simultaneously for the drinking water source and effluent receptor of major cities, and encompasses great aquatic habitat diversity.

The St. Lawrence fluvial estuary (SLFE) spans 180 river kilometers (rkm) from the eastern end of Lake Saint-Pierre to the eastern tip of Orleans Island, located at the upper limit of saline intrusion (Figure 2.4.1). The circulation of the SLFE is characterized by vertically well-mixed freshwater (Simons *et al.*, 2010) and driven by strong tidal and river flows. Ocean tides are amplified as they enter the St. Lawrence until they reach their highest level (~7 m in range) in the upper estuary at Saint-Joseph-de-la-Rive – hereafter referred to as rkm 0. About 66 rkm upstream, tidal ranges still exceed 6 m during the largest spring tides at Saint-François, i.e. the downstream limit of the SLFE. Increases in water levels of more than 1 m $h^{-1}$ can be observed at

these locations during the rising tide, leading to rapid changes in flow conditions as well as in the wetted areas. This generates strong current reversals with peak tidal discharges up to five times larger than the daily average in both upstream and downstream directions. The tidal signal is increasingly distorted and damped as it propagates upstream due to frictional effects (Godin, 1999, Matte *et al.*, 2014c); the ebb tides are lengthened and the flood tides are steepened and shortened. The limit where the flow becomes unidirectional (i.e. only one slack water) moves between Grondines (rkm 179.5) and Bécancour (rkm 217) as a function of tidal range and river flow. At Trois-Rivières (rkm 231), the fortnightly modulation of mean water levels induced by the neap-spring cycle exceeds in amplitude the semidiurnal tide (LeBlond, 1979), whose range is 0.2 m for a mean tide. Most of the short period tide (i.e. diurnal, semidiurnal, etc.) is damped in Lake Saint-Pierre (rkm 264), but long period oscillations are still noticeable as far as Montreal (rkm 360). These flow properties exhibit both lateral and longitudinal variations that were confirmed by field measurements (Matte *et al.*, 2014a).

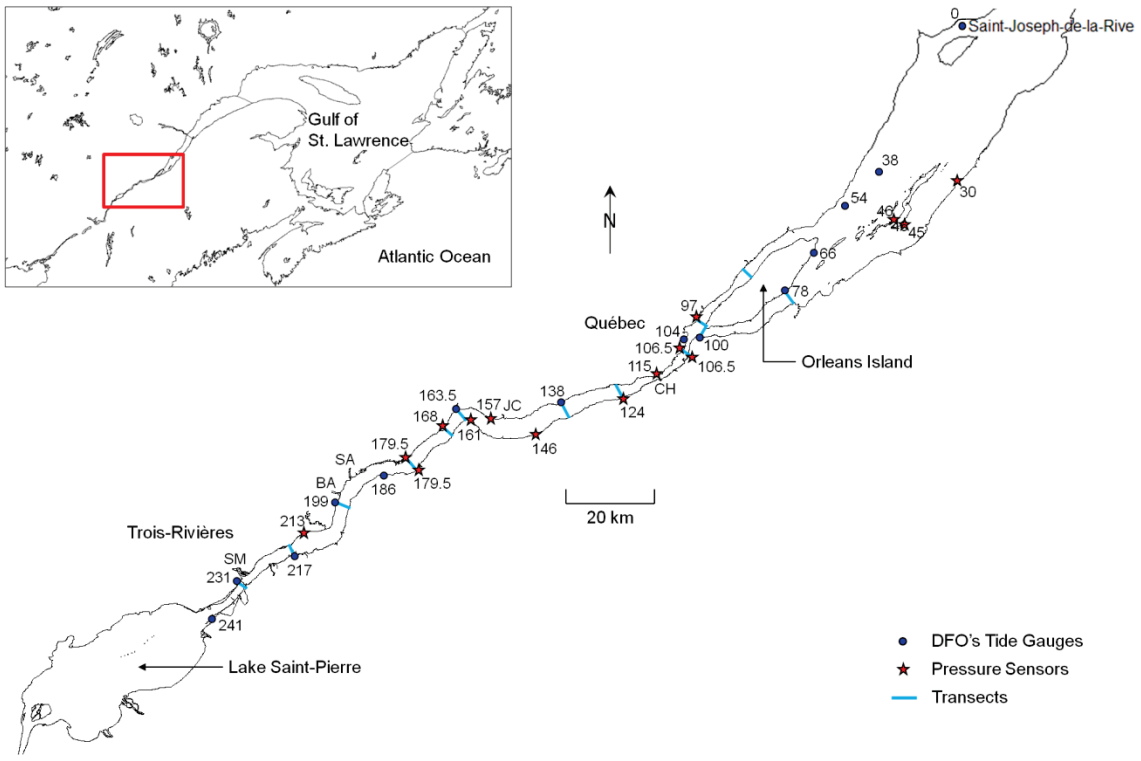


**Figure 2.4.1** **Map of the SLFE (Quebec, Canada) showing locations of the DFO's tide gauges (dark blue circles), pressure sensors (red stars), and measurement transects (light blue lines). River kilometers (rkm) are indicated for each station. Major tributaries are the St-Maurice (SM), Batiscan (BA), Sainte-Anne (SA), Jacques-Cartier (JC) and Chaudière (CH) rivers.**

River forcing in the SLFE comes from the freshwater outflows of Lake Ontario, Ottawa River and other tributaries along its course. Although the average discharge is 12 200 $m^3s^{-1}$ at Québec, observed minimum and maximum daily net discharges in the St. Lawrence amounted to 7000 and 32 700 $m^3s^{-1}$ over the 1960–2010 period, taking into account the contribution of all tributaries and drainage areas upstream of Québec (Bouchard & Morin, 2000). The effects of such variations on mean water level and tidal range are severe, particularly in the upper portion of the SLFE (Matte *et al.*, 2014c).

Combined to the strong tidal and fluvial forcing are the effects of variable bathymetry, characterized by deep channels (> 60 m), a section width that varies from less than 1 to 15 km, extensive intertidal areas, river bends, shoals and islands, as well as high spatial heterogeneity in substrate composition, distribution of macrophytes, ice and wind. Together, these characteristics provide a unique environment for the study of tidal hydrodynamics.

High-resolution hydrodynamic models are essential to understand the complex interaction between tides, river flow and geometry. Such tools enable reliable and sustainable ecosystem monitoring, and are a prerequisite for predicting the likely consequences of management practices, anthropogenic changes, and meteorological events on the system (e.g., Babu *et al.*, 2005, Morin & Champoux, 2006, Horsburgh & Wilson, 2007, Araújo *et al.*, 2008, Picado *et al.*, 2010). Furthermore, hydrodynamic models can be coupled or used as input to morphodynamic models (Rinaldi *et al.*, 2008, Nabi *et al.*, 2012), hydrologic models (de Paiva *et al.*, 2013), advection-diffusion models (Simons *et al.*, 2006, Bárcena *et al.*, 2012), wave-current interaction models (Liu *et al.*, 2007), and aquatic habitat models (Morin *et al.*, 2003b), among others.

Previous numerical studies conducted in the SLFE only provided limited knowledge on the circulation complexities of the river. El-Sabh & Murty (1990) give an overview of early modeling efforts made in the St. Lawrence, from the Gulf entrance up to Montreal in some instances. Numerous analytical or tidal models have notably been developed (e.g., Vincent, 1965, Partenscky & Warmoes, 1970, Marche & Partenscky, 1974, Chassé *et al.*, 1993, Godin, 1999, Matte *et al.*, 2014c), providing valuable insights into the propagation of tides and associated upstream distortions. Development and application of one-dimensional (1D) numerical models of the St. Lawrence have also been conducted (e.g., Kamphuis, 1968, Prandle, 1970, Cheylus & Ouellet, 1971, Godin, 1971, Prandle, 1971, Prandle & Crookshank, 1972,

Prandle & Crookshank, 1974, Morse, 1990, Robert *et al.*, 1992, Bourgault & Koutitonsky, 1999). These models were able to reproduce the main tidal and fluvial characteristics encountered in the system, although only qualitatively in the upstream portion of the SLFE, for most of them, partly due to imprecise discharge conditions at the boundaries. Among the models, the ONE-D model (Dailey & Harleman, 1972, Morse, 1990) is currently run in operational mode, fed by the 30-day outflow forecast from Lake Ontario and Ottawa River and by the 48-hour wind forecast of Environment Canada (Meteorological Service of Canada) at the downstream boundary; the effect of ice is also included in winter time (Lefaivre *et al.*, 2009). This operational model meets the need for a water level prediction in the SLFE, but it cannot account for lateral exchanges (e.g., Matte *et al.*, 2014a), which are fundamentally two-dimensional (2D).

A number of 2D (depth- or laterally-averaged) numerical models have been developed in the St. Lawrence (e.g., Prandle & Crookshank, 1972, Prandle & Crookshank, 1974, Ouellet & Cerceau, 1975, Lévesque, 1977, Lévesque *et al.*, 1979, De Borne de Grandpre *et al.*, 1981, Tee & Lim, 1987, Leclerc *et al.*, 1990). Three-dimensional (3D) models have also been presented (e.g., Gagnon, 1994, Saucier & Chassé, 2000, Saucier *et al.*, 2003, Simons *et al.*, 2010), notably leading to the production of an atlas of tidal currents in the St. Lawrence Estuary (Saucier *et al.*, 1997, 1999). Most of these models do not include the SLFE upstream of Orleans Island. When they do, they usually suffer from a lack of data for validation and their spatial resolution is generally too coarse ($\geq$ 200 m) to account for local variations (both lateral and longitudinal) in topography, friction and hydrodynamic properties. In parallel, model development for specific applications have been conducted by private or government agencies (e.g., Doyon, 2011), but they are usually restricted to smaller areas of interest and thereby do not provide a complete description of the system hydrodynamics. The SLFE thus remains largely not documented.

In this paper, a 2D non-stationary, high-resolution hydrodynamic model of the SLFE has been developed with the objective of providing detailed spatial and temporal description of the hydrodynamics in response to tidal and fluvial forcings. It is based on high density topographic data stemming from LIDAR surveys and multibeam bathymetric soundings. The finite-element model includes a drying-wetting component allowing water in intertidal areas to be cyclically stored and evacuated. The model was calibrated and validated using an extensive data set composed of water level data from 29 tide gauges and cross-sectional water level and velocity data collected along 13 transects, repeatedly surveyed during complete semidiurnal tidal cycles.

This research provides for the first time a detailed and validated 2D description of the tidal hydrodynamics of this complex region where knowledge is very limited. It is the first step in the development of a comprehensive model of the SLFE ecosystem.

### 2.4.3 Methodology

#### *2.4.3.1 Field Campaigns*

A field campaign, the most extensive to date, was conducted in the SLFE during the summer of 2009 for the measurement of water levels and velocities (Matte *et al.*, 2014a). The objective was twofold: 1) document the hydrodynamics and improve current knowledge of the system; and 2) obtain recent and detailed data for the calibration and validation of the hydrodynamic model.

A set of 15 pressure sensors was installed from June to October 2009 for water level measurements, adding to the 14 tide gauges operated by Canada's Department of Fisheries and Oceans (DFO) already available (Figure 2.4.1). Boat surveys were also conducted over semi-diurnal tidal periods along 13 cross-sections of 1 to 4 km in width of the SLFE, representative of the longitudinal variability in geomorphological and tidal-fluvial properties. At each transect, the boat repeatedly moved back and forth across the channel following the same transect line, perpendicular to the mean flow direction. Water levels and velocities were measured during each crossing, using mounted RTK GPS and ADCP, respectively. The measurements were carried out between June 15, 2009, and August 25, 2009, so that most transects were surveyed at different phases on the neap-spring tidal cycle. Daily averaged net discharges at Québec varied between 11 100 and 14 600 $m^3s^{-1}$ during that period. Details of the data acquisition and analyses are provided in Matte *et al.* (2014a, b).

A LIDAR campaign was also conducted during the summer of 2012 to collect topographic data in shallow areas. Topography of all intertidal zones of a 200-km reach of the St. Lawrence, extending from Trois-Rivières (rkm 231) to Islet-sur-Mer (rkm 30), was measured around low tide. The survey was carried out from June 16, 2012, to July 7, 2012. This time period was chosen after the spring freshet and at a time where aquatic plants are not at their peak in terms of density and coverage. A total of 8 days of measurements were necessary to cover the entire domain. The LIDAR system used during the campaign (Optech ALTM Gemini No. 07sen209)

allowed a scanning frequency of 37 Hz, with an angle of 20°. Flight height was 1350 m above ground, yielding a scanning width of 877 m. Line spacing was 614 m, allowing a 30 % overlap.

The low tide propagates upstream at a speed of about 15–30 km $h^{-1}$, depending on channel depth, while the speed of the plane is about 10 times faster (i.e. 256 km $h^{-1}$). The propagation times and heights of low water also vary over the neap-spring cycle and as a function of discharge (LeBlond, 1979, Godin, 1984). Reliable information on the times of arrival of low water was thus essential to the planning of the LIDAR campaign in order for the measurement to be synchronized with the low tide. Tidal predictions from the ONE-D model of the St. Lawrence (Lefaivre *et al.*, 2009) were used to determine the times of arrival of low water at different stations in the SLFE, under the discharge and tidal conditions prevailing during the period of survey. The flight lines and time of survey were determined according to these predictions. Therefore, the extent of dry areas covered is highly dependent on the prediction accuracy of the model and the concordance between the planned and executed flight lines.

Due to the very energetic tidal environment, measurements taken slightly before or after low tide represent a significant loss in the dry superficies surveyed. A tolerance of 20 cm around the low tide was considered in the delimitation of zones of measurement. At stations of moderate to strong tidal range (i.e. between Grondines and Saint-François), this tolerance is respected for time intervals from 20 min before low tide to 10 min after low tide (the rising tide is more abrupt than the falling tide). This gave the operator some latitude in the determination of flight lines and times. The flight lines were delineated in such a way to cover the entire area from the chart datum elevation in the river to the bank limit inland, based on the approximate limit of a 1000-yr recurrence flood. The limits were further extended by 500 m inside the major tributaries. During measurements, the flight lines were executed in a predetermined order, from the channel to the bank, to ensure that the most critical areas (intertidal zone, shoals, etc.) are surveyed as close as possible to the low tide.

*2.4.3.2 Model Description*

2.4.3.2.1 Simulation Domain

The simulation domain of the SLFE model extends beyond the actual downstream limit of the system, situated at the eastern tip of Orleans Island. In the model, the downstream boundary is located in the estuarine transition zone of the St. Lawrence Estuary (Simons *et al.*, 2010). It is

positioned along a 15-km wide cotidal line of constant phase, a few km downstream of the nearest tide gauge, located on the north shore at Saint-Joseph-de-la-Rive (rkm 0). This station is the closest permanent tide gauge to the Orleans Island. It was chosen as the downstream boundary, far enough from the SLFE downstream limit, to allow the exchanges between the North and South arms of Orleans Island to occur freely. However, because a permanent station exists only on the North side of the boundary, water level distribution across the section is unknown and was determined by assimilation. In the present case, assimilation consisted in using differences between observed and modeled water levels at nearby stations to orient changes in the water level distribution of the downstream boundary.

The upstream boundary, for its part, is positioned in alignment with the Port Saint-François station (rkm 241), at the exit of Lake Saint-Pierre, i.e. the upstream limit of the SLFE. Due to the small section width, imposed water levels were the same on both sides of the boundary.

Major tributaries were included in the model to allow water to be cyclically stored and evacuated as a function of the tide. They are the Saint-Maurice, Batiscan, Sainte-Anne, Jacques-Cartier and Chaudière rivers (Figure 2.4.1). The boundaries were positioned at upstream locations removed from tidal influence for the imposition of discharges uninfluenced by the tide.

The global simulation domain was partitioned into two smaller overlapping domains, each sharing the same grid configuration and data as the global model. This separation was necessary to dissociate the assimilation process from the calibration process. Hence, calibration in the upstream portion of the model was performed on a reduced domain extending from Port Saint-François (rkm 241) to Québec (rkm 106.5) where water level conditions are defined at the boundaries from tide gauge data. The downstream portion was calibrated on a reduced domain extending from Neuville (rkm 138) to Saint-Joseph-de-la-Rive (rkm 0), where assimilation of the downstream boundary conditions was carried out to determine the optimal water level distribution along the boundary. In the downstream reach past Orleans Island, the most significant error sources are related to the downstream boundary conditions and the particularly complex bathymetry, characterized by a large amount of islands. The strong tides typical of this area are therefore much more likely to be impacted by these components than influenced by variations in bottom friction, so that the effect of excluding this segment from the calibration process is believed to be little. Friction in the downstream model was thus only adjusted in the North and

South arms of Orleans Island. Once the two models were calibrated and assimilated, simulations were performed using the global domain.

#### 2.4.3.2.2 Numerical Terrain Model

Development of the numerical terrain model (NTM) was made using the MODELEUR software, a geographic information system (GIS) adapted to fluvial hydrodynamics (Secretan & Leclerc, 1998, Secretan *et al.*, 2001). The NTM is horizontally positioned in a UTM projection in the NAD83 referential. The vertical datum is mean sea level (MSL), or, equivalently, CGVD28. The different components composing the NTM are described in the following.

The main explanatory factor of the hydrodynamics is the topography, which includes channel bathymetry, floodplains, and engineering structures. Around 42M data points were obtained from multibeam bathymetric soundings performed by the Canadian Hydrographic Service (CHS). Data were reduced from chart datum to MSL using a kriging grid based on known conversions at the tide gauges. Data density is a function of the year of acquisition and location, and shallow regions are generally not covered.

To complete the topography in shallow areas, data from the LIDAR campaign were used. The water lines were identified from the data and used to separate points on the water from those on the ground. Data was validated with supplementary LIDAR and bathymetric data sets in overlapping regions. A total of 420M LIDAR data points were integrated to the NTM.

As for the tributaries, the geometry of the river shores was extracted using geospatial data from Natural Resources Canada's GeoBase website (http://www.geobase.ca/). Their bathymetry was emulated, due to a lack of data, by a regularly shaped trapezoidal channel of constant slope and variable depth and width. Channel depth was determined by calculating the depth needed to discharge the average river flow at an approximate mean velocity of 1 m $s^{-1}$, given the local width of the river.

Engineering structures, such as bridge pillars, peers, marinas and ports, were also included in the NTM. A free-slip condition was used along vertical walls, but most lateral boundaries are mobile and controlled by the drying-wetting component (detailed later). The topography, as described by the SLFE model, is presented in Figure 2.4.2.

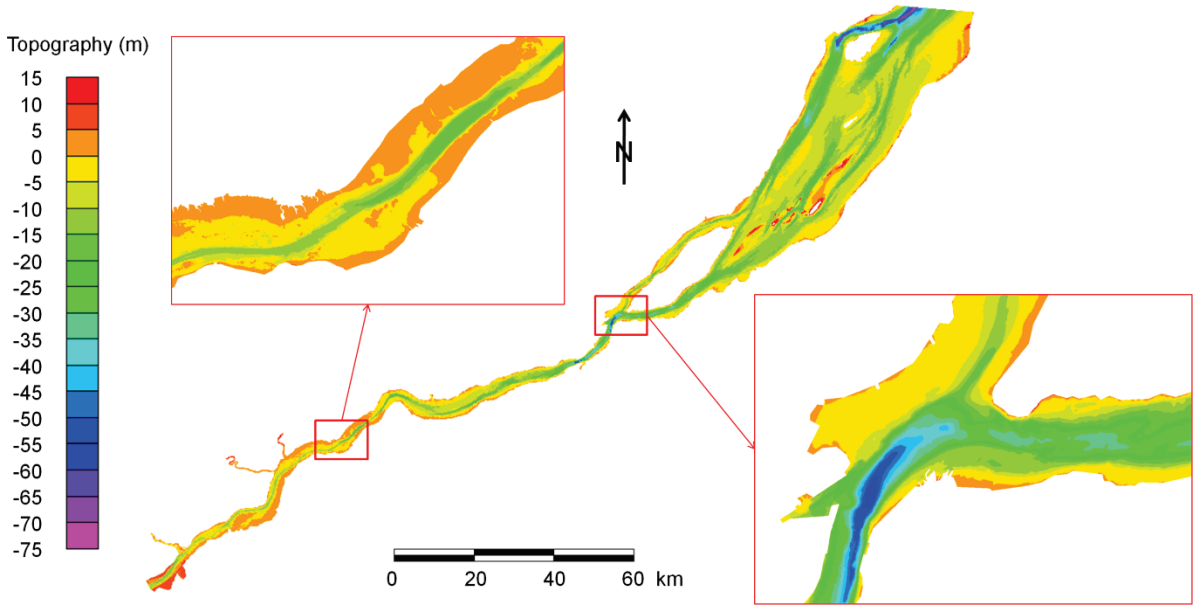


**Figure 2.4.2** **Topography of the SLFE as projected on the finite-element mesh, with zoom-ins at Grondines and at the junction of Orleans Island.**

Information on bottom substrate and macrophytes was added to the NTM for friction description. Substratum composition was defined for homogeneous regions based on 6400 substratum observation points obtained from the CHS. They were converted into Manning coefficients following Morin *et al.* (2000a). Friction due to macrophytes was included as an additional layer in regions where aquatic plants are observed during summer. Friction coefficients were adjusted during calibration, within the range of values provided by Morin *et al.* (2000b). Finally, a constant friction coefficient was used inside the tributaries. The distribution map of Manning coefficients used in the SLFE during the calibration period is shown in Figure 2.4.3. Surface friction by wind or ice was set to zero.

Both topography and friction data were assembled onto a computing grid, in this case a 2D finite-element mesh composed of triangular $P_1$–$P_1$isoP$_2$ elements of continuity $C^0$. The latter are based on linear approximations for water levels, calculated at the element summits, and on piecewise linear approximations for specific discharges, computed on sub-elements, i.e. at both summit and middle nodes (Heniche *et al.*, 2000a). The mesh for the global model forms a triangular irregular network composed of 1 347 515 nodes and 662 934 elements. The calibration and assimilation domains include 585 798 and 849 480 nodes, and 286 300 and 419 318 elements, respectively. The mesh was built following the river morphology in such a way to

reduce errors in regions of strong variability and to represent the terrain adequately. Hence, average grid resolution is 50 m, with refinements down to ~1 m around engineering structures (e.g., bridge pillars, piers) and over regions of complex topography (e.g., steep bathymetry, narrow channels). The resolution is sufficiently high to describe the complex geometry of the river and of the man-made structures therein, evidenced by the very detailed bathymetric data. Refinements in the mesh are, however, very localized (e.g., in the near surroundings of bridge pillars) and do not propagate very far from the refined regions. In fact, the grid was built in such a way to capture the effects of engineering constructions to the flow on large-scale phenomena (e.g., tidal propagation, cross-sectional velocities), as well as of water exchanges between shallow intertidal areas and the main channel, with the aim of calibrating the model with a similar level of detail as provided by the available hydrodynamic data (Matte *et al.*, 2014a). An even finer spatial resolution would be necessary, with an accordingly increasing computational cost, in order to capture small-scale structures of the flow that result from turbulence and that develop beyond the geometric elements present in the field (e.g., von Karman vortexes); this is not the objective here. The finite-element mesh is shown in Figure 2.4.4.

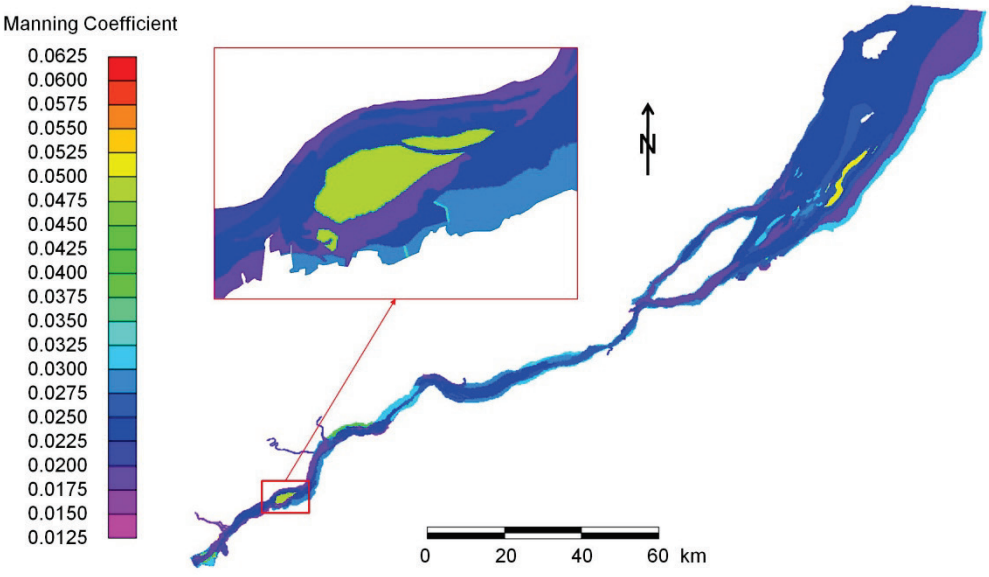


**Figure 2.4.3** **Manning coefficients in the SLFE, based on substrate composition and macrophytes distribution, with a zoom-in on Gentilly shoal (Bécancour).**

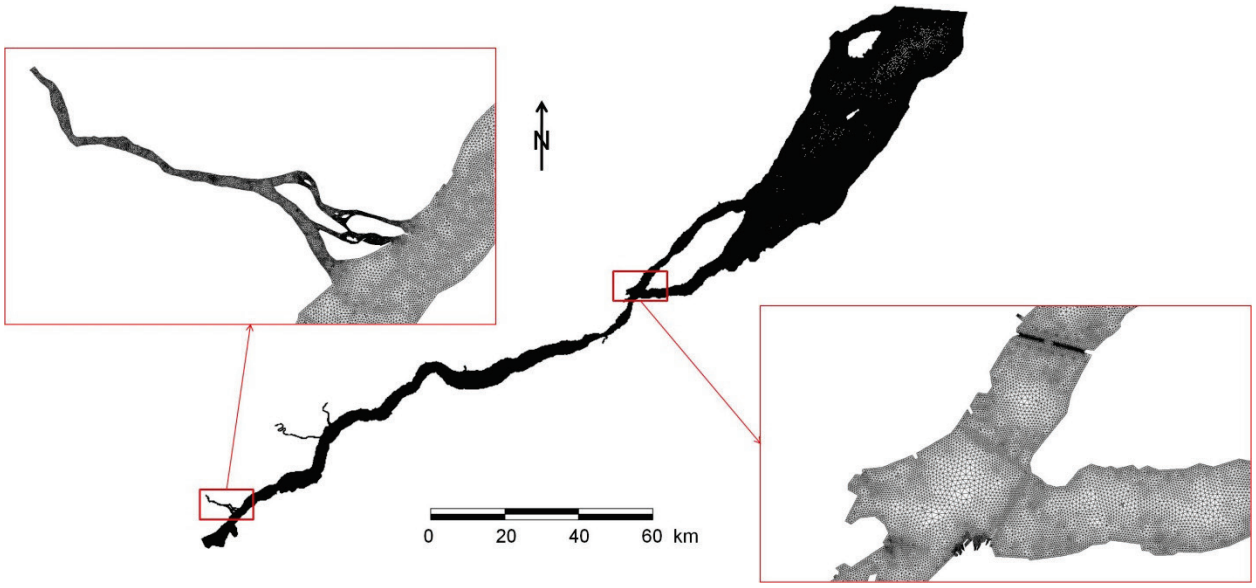


**Figure 2.4.4** **Finite-element mesh of the SLFE, with zoom-ins in the Saint-Maurice River and at the junction of Orleans Island.**

#### 2.4.3.2.3 Hydrodynamic Model

Hydrodynamic simulations were performed using the H2D2 software (Secretan, 2013), which allows robust and distributed computing for large systems and non-stationary problems. It solves the 2D vertically-integrated shallow water equations over a finite-element discretized domain, with special treatment of drying-wetting areas. The shallow water model, as implemented in H2D2, is based on the assumptions of incompressibility, hydrostatic pressure, and stable riverbed [for a derivation of the shallow water equations, see, e.g., Dronkers (1964) and Bois (2000)]. The weak variational formulation and finite-element model are detailed in Heniche *et al.* (2000a). A brief summary of the model equations is provided in section 2.4.7 (appendix). Description and application of the model to the SLFE is presented in the following.

An Eulerian approach is used for the prediction of drying-wetting areas (Heniche *et al.*, 2000a), in which the water level can plunge under the bed level and generate both positive (i.e. wet) and negative (i.e. dry) water depths. The effective depth in the dry area is however limited to a minimum depth $H_{min}$ (Figure 2.4.5), allowing only a thin layer of water to subsist that mimics a groundwater flow. The goal being to freeze the flow in the dry area, for mass to be conserved, the Manning coefficient $n$ is drastically increased, while in the wet area it is set in accordance

with local flow properties. Increased viscosity is also imposed in the dry area to reduce to a minimum the contribution of velocities to momentum conservation. Moreover, a Darcy viscosity (via the hydraulic conductivity $\delta$) is added to further smooth the free surface in dry areas (see section 2.4.7). In general, to ensure a smoother transition, changes in the parameters between the wet and dry areas are made over a certain distance, delimited by the position of $H_{\text{min}}$ and $H_{\text{threshold}}$ (Figure 2.4.5). Within this transitory depth zone, all the parameters (e.g., Manning's $n$) vary linearly from their wet value to their dry value. Furthermore, this transition follows a hysteresis loop, identified by the dashed lines in Figure 2.4.5, so that the passage of a node from the wet to the dry state is made differently than inversely. This feature reduces the rigidity of the system in allowing faster convergences.

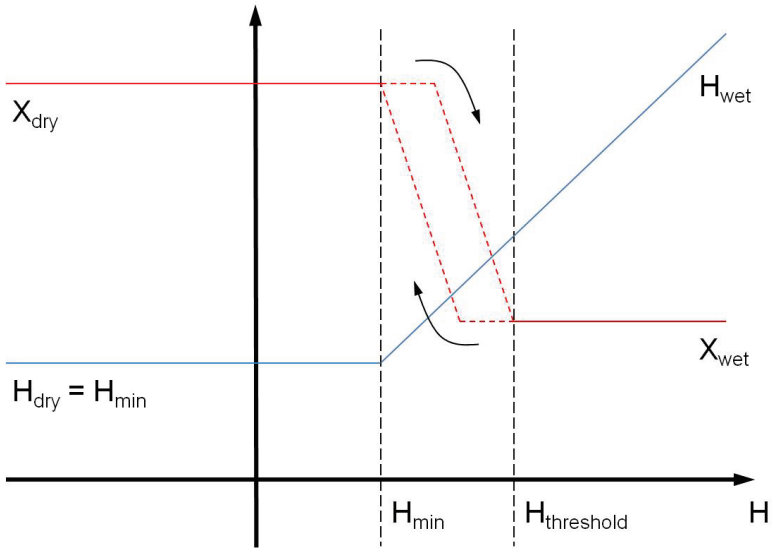


**Figure 2.4.5** **Schematization of the drying-wetting model, where $H$ is the water depth (blue) and $X$ is an arbitrary parameter (e.g., Manning's $n$) (red). Positive and negative depths are identified as wet and dry, respectively. The arrows show the hysteresis loop made in the transitory depth zone delimited by $H_{\text{min}}$ and $H_{\text{threshold}}$.**

Measured water levels are imposed at both upstream and downstream open boundaries. They are obtained from permanent tide gauges operated by Canada's DFO. In the global model, conditions for the upstream boundary are taken from the station of Port Saint-François (rkm 241). Imposed water levels along the downstream boundary are assimilated from measurements at the tide gauge of Saint-Joseph-de-la-Rive (rkm 0). In the upstream model (calibration segment), the same upstream boundary as in the global model is used, while data from a pressure sensor installed at Québec (rkm 106.5) are imposed downstream. In the downstream model (assimila-

tion segment), conditions at the upstream boundary are taken from the tide station of Neuville (rkm 138), while water levels at the downstream boundary are assimilated following a procedure described in a later section.

Daily-averaged discharges are imposed at the tributaries. They are reconstructed by adding the discharge measured at an upstream station to the estimated lateral inflow, consisting in theory of surface water runoff and groundwater inflow. Because virtually no data is available for groundwater inflow, only surface water runoff is considered, approximated based on gauged areas. For ungauged areas, the inflow is estimated from the runoff coefficient of an adjoining gauged area. Relations for each tributary to the St. Lawrence were developed by Morse (1990) and adapted by Bouchard & Morin (2000).

The time-varying 2D discretized shallow water equations are integrated in time using an implicit Euler time scheme. The resulting non-linear algebraic system is solved by Newton-Raphson iterations (Dhatt *et al.*, 2005). A spin-up of approximately one tidal cycle is needed to dissipate the effects of initial conditions and to propagate the tidal wave from one end of the domain to the other.

Implicit temporal schemes do not constrain the time step size. Simulations are thus run at a 5-min nominal time step, with a time-step halving algorithm in case of non-convergence. This time step size is fine enough to accurately represent the tidal dynamics of the SLFE, but acts also as a temporal filter for small-scale processes by smoothing any motion whose frequency is higher than that prescribed by the time step. With a 50-m average spatial resolution $\Delta x$ and a 5-min time step $\Delta t$, the Courant number ($C = u\,\Delta t/\Delta x$) is equal to 6, assuming a velocity $u$ of 1 m $s^{-1}$; however, its value increases to 300 where the spatial resolution reaches 1 m. Numerical experiments using explicit, semi-implicit and implicit time integration scheme, with time steps varying between 1 and 300 s, were made (not presented) to assess the impact of the chosen spatial and temporal resolutions.

Numerical experiments were also conducted to adjust turbulent and numerical viscosities through the mixing length and Peclet number, respectively (see section 2.4.7), within their limit of stability and/or applicability. Values between 0.01 and 1 for the mixing length coefficient and between 1 and 5 for the Peclet number were tested. Overall, velocity fields were little sensitive to these changes when compared to the reference simulation (5-min time step, mixing length

coefficient of 1, Peclet number equal to 1). This is coherent with the fact that refinements in the mesh are very localized and do not allow small-scale turbulent motions to develop and propagate. Only larger-scale structures are observed, which remain unaffected by a reduction of the time step.

Using a relatively large time step is also consistent with the hydrostatic assumption of the 2D shallow water model. In fact, by low-pass filtering small-scale, and hence nonhydrostatic, flow features, it maintains the solution hydrostatic. As demonstrated by Wang *et al.* (2009), the effect of nonhydrostatic pressure on tidal variations of water levels and depth-averaged velocities is negligible. Furthermore, nonhydrostatic pressure does not accumulate over time and has a minimal effect on large-scale quantities, its effect being rather localized in space.

*2.4.3.3 Calibration*

Calibration was conducted for two simulation periods of 15 days starting on 14 June 2009 00:00:00 EDT and 19 August 2009 00:00:00 EDT, respectively, corresponding to the periods of transect surveys. Calibration consisted in model adjustments to reduce errors associated with topography, substrate and friction. Topographic errors were detected and corrected by looking for the presence of incoherent velocity patterns or large errors in water levels. In a second step, substrate composition was locally controlled to ensure that mean surface slopes and tidal ranges are adequately reproduced by the model. Further adjustments in Manning friction coefficients were made, especially in shallow regions where macrophytes are present, until errors in water levels were minimized. Increases in bottom friction act on the tides by reducing its amplitude and increasing the mean water levels upstream of the modification. Because the model is controlled in water levels at both upstream and downstream boundaries, tidal amplitudes are also slightly increased downstream of the modification when friction is increased. Experimentation showed that a performance criterion based on these two variables (mean water level and tidal range) is much simpler than a calibration based on tidal amplitudes and phases of harmonic constituents, especially for short simulation periods.

Mean water levels were calculated using a 3-day moving average, similar to Godin (1972)'s tidal eliminator. Greater diurnal tidal ranges were extracted from the high-passed data by calculating the difference between higher high water and lower low water using a 27-h moving window, similar to Kukulka & Jay (2003a)'s tidal range filter.

To assess the performance of the model, two criteria were used, namely the root-mean-square error (RMSE) and skill (Willmott *et al.*, 1985), based on quantitative comparisons between simulated and observed values; they are respectively given by:

$$\mathrm{RMSE} = \sqrt{\frac{1}{n}\sum_{n}\left(X_{\mathrm{sim}} - X_{\mathrm{obs}}\right)^2} \tag{2.4.1}$$

and

$$\mathrm{Skill} = 1 - \frac{\sum_{n}\left(X_{\mathrm{sim}} - X_{\mathrm{obs}}\right)^2}{\sum_{n}\left(\left|X_{\mathrm{sim}} - \overline{X_{\mathrm{obs}}}\right| + \left|X_{\mathrm{obs}} - \overline{X_{\mathrm{obs}}}\right|\right)^2}, \tag{2.4.2}$$

where $X$ is the variable being compared and $\overline{X}$ is the time average of $n$ values. RMSE is a measure of the average error between model and observations in the units of the quantities assessed. Skill is a unitless measure of the relative average error between model and observations, where a skill of 1 means perfect agreement and a skill of 0 means that the model is equivalent to the mean of the observations.

*2.4.3.4 Assimilation*

Imposed water levels along the downstream boundary are derived from observations at Saint-Joseph-de-la-Rive (rkm 0), rather than tidal harmonic constituents, to allow non-tidal (residual) variations to be propagated in the system. Water levels along the boundary were assimilated in order to determine the distribution that best reproduces observations at upstream tide gauges, located on both sides of the river. During assimilation, time shifts were iteratively applied on the imposed water levels until simulated and observed signals were in phase at the stations. Lateral gradients (both positive and negative) in mean water level and tidal range were also tested along the boundary to assess model sensitivity to the imposed conditions. The simulated variations were generally not sufficient to explain the differences between observed and simulated water levels at the stations, so that it was chosen to impose the same (time-shifted) water level time series on every node of the downstream boundary, with no lateral gradient. Assimilation of the boundary condition was thus limited to 1) determining the optimal time shift needed for the tide to propagate in phase with observations at the stations, and 2) defining the corrections, constant

along the boundary, in mean water level (i.e. vertical shift) and tidal range (i.e. amplitude factor) that best reproduce the tidal signal at Saint-Joseph-de-la-Rive.

### 2.4.4 Results

In this section, calibration results are presented and the ability of the model to reproduce tidal and flow features observed in the field data is evaluated.

#### *2.4.4.1 Statistics on Water Levels*

Results from the calibrated model are presented separately on the upstream and downstream segments (Table 2.4.1 and Table 2.4.2, respectively), as well as on the global model (Table 2.4.3), for the two simulation periods of June 14–29, 2009 and Aug 19–Sep 3, 2009. Because friction acts on both mean water levels and tidal ranges, statistics on these two quantities were also calculated. They were used during calibration to orient the local modifications towards an increase or a decrease in friction. In the upstream model (Table 2.4.1), RMSE between observed and simulated water levels are lower than 10 cm at all 16 stations (141-km long reach). Modeled water levels are almost in perfect agreement with observations at the stations, with predicting skills varying between 0.993 and 1.000. The highest RMSE (0.094 m) is obtained at Grondines and is mostly dominated by errors in MWL. These are likely related to topographic errors in the intertidal flats between Deschambault (rkm 168) and Grondines (rkm 179.5), combined to an overestimated friction.

Results for the downstream model are presented in Table 2.4.2. Errors in water levels are larger than in the upstream segment, with maximum RMSE of nearly 20 cm occurring at Beauport. In an attempt to reduce these errors by assimilation, lateral variations in mean water levels and tidal ranges were imposed along the downstream boundary, with little success; variations in modeled water levels were not sufficient to explain the observed differences at the stations. The error is likely attributed to an underestimated friction in the intertidal zones of Orleans Island, particularly in the North arm, due to the presence of aquatic plants during summer. This error has a repercussion on upstream water levels and efforts should be put in the future to reduce it below 10 cm, in order to meet the same quality standards as the upstream operational model of the St. Lawrence. Nonetheless, predicting skills are very high (> 0.997) at all stations, indicating a good performance of the model.

**Table 2.4.1** **Calibration results for the upstream model: RMSE and skill for modeled water levels (original), mean water levels (MWL) and tidal range at the stations for each 15-day simulation period.**

| rkm | Stations | June 14–29, 2009 | | | | Aug 19–Sep 3, 2009 | | | |
|---|---|---|---|---|---|---|---|---|---|
| | | RMSE (m) | | | Skill | RMSE (m) | | | Skill |
| | | Original | MWL | Range | | Original | MWL | Range | |
| 115 | Québec Bridge | 0.053 | 0.028 | 0.057 | 1.000 | 0.051 | 0.022 | 0.085 | 1.000 |
| 124 | Saint-Nicolas | 0.027 | 0.005 | 0.020 | 1.000 | 0.030 | 0.005 | 0.015 | 1.000 |
| 138 | Neuville | 0.043 | 0.015 | 0.083 | 1.000 | 0.042 | 0.013 | 0.061 | 1.000 |
| 146 | Sainte-Croix-Est | 0.046 | 0.013 | 0.052 | 1.000 | 0.057 | 0.018 | 0.082 | 0.999 |
| 157 | Cap-Santé | 0.046 | 0.019 | 0.077 | 1.000 | 0.047 | 0.021 | 0.051 | 1.000 |
| 161 | Pointe-Platon | 0.042 | 0.014 | 0.048 | 1.000 | 0.043 | 0.020 | 0.022 | 1.000 |
| 163.5 | Portneuf | 0.061 | 0.050 | 0.033 | 0.999 | 0.076 | 0.066 | 0.027 | 0.999 |
| 168 | Deschambault | 0.062 | 0.025 | 0.124 | 0.999 | 0.067 | 0.030 | 0.193 | 0.999 |
| 179.5 | Leclercville | – | – | 0.021 | – | – | – | 0.020 | – |
| 179.5 | Grondines | 0.094 | 0.090 | 0.021 | 0.995 | 0.087 | 0.082 | 0.017 | 0.996 |
| 186 | Cap-à-la-Roche | 0.028 | 0.006 | 0.032 | 0.999 | 0.037 | 0.022 | 0.027 | 0.999 |
| 199 | Batiscan | 0.045 | 0.039 | 0.053 | 0.996 | 0.041 | 0.033 | 0.051 | 0.997 |
| 213 | Champlain | 0.054 | 0.047 | 0.068 | 0.990 | 0.045 | 0.032 | 0.063 | 0.995 |
| 217 | Bécancour | 0.016 | 0.006 | 0.014 | 0.999 | 0.050 | 0.047 | 0.022 | 0.993 |
| 231 | Trois-Rivières | 0.028 | 0.026 | 0.007 | 0.989 | 0.014 | 0.006 | 0.008 | 0.999 |
| 241 | Port Saint-François | 0.008 | 0.007 | 0.007 | 0.999 | 0.007 | 0.006 | 0.006 | 1.000 |

**Table 2.4.2** **Calibration and assimilation results for the downstream model: RMSE and skill for modeled water levels (original), mean water levels (MWL) and tidal range at the stations for each 15-day simulation period.**

| rkm | Stations | June 14–29, 2009 | | | | Aug 19–Sep 3, 2009 | | | |
|---|---|---|---|---|---|---|---|---|---|
| | | RMSE (m) | | | Skill | RMSE (m) | | | Skill |
| | | Original | MWL | Range | | Original | MWL | Range | |
| 0 | Saint-Joseph-de-la-Rive | 0.095 | 0.014 | 0.066 | 0.999 | 0.091 | 0.020 | 0.069 | 0.999 |
| 30 | Islet-sur-Mer | 0.130 | 0.026 | 0.292 | 0.998 | 0.143 | 0.047 | 0.304 | 0.998 |
| 38 | Rocher Neptune | 0.106 | 0.069 | 0.198 | 0.999 | – | – | – | – |
| 45 | Ile-aux-Grues South | 0.114 | 0.059 | 0.213 | 0.999 | 0.143 | 0.102 | 0.196 | 0.998 |
| 46 | Ile-aux-Grues North | 0.160 | 0.119 | 0.297 | 0.997 | 0.133 | 0.092 | 0.274 | 0.998 |
| 54 | Banc du Cap Brûlé | 0.102 | 0.043 | 0.192 | 0.999 | 0.113 | 0.042 | 0.189 | 0.999 |
| 66 | Saint-François | 0.120 | 0.066 | 0.257 | 0.999 | 0.120 | 0.052 | 0.257 | 0.998 |
| 78 | Saint-Jean | 0.155 | 0.131 | 0.233 | 0.998 | 0.106 | 0.048 | 0.224 | 0.999 |
| 97 | Beauport | 0.197 | 0.173 | 0.047 | 0.996 | 0.157 | 0.122 | 0.068 | 0.997 |
| 100 | Lauzon | 0.163 | 0.128 | 0.039 | 0.997 | 0.124 | 0.071 | 0.047 | 0.998 |
| 104 | Saint-Charles River | 0.157 | 0.120 | 0.029 | 0.997 | 0.126 | 0.070 | 0.039 | 0.998 |
| 106.5 | Lévis | 0.148 | 0.106 | 0.040 | 0.997 | 0.119 | 0.061 | 0.043 | 0.998 |
| 106.5 | Québec | 0.151 | 0.111 | 0.037 | 0.997 | 0.119 | 0.065 | 0.036 | 0.998 |
| 115 | Québec Bridge | 0.151 | 0.103 | 0.127 | 0.997 | 0.117 | 0.061 | 0.168 | 0.998 |
| 124 | Saint-Nicolas | 0.082 | 0.056 | 0.086 | 0.999 | 0.067 | 0.041 | 0.098 | 0.999 |
| 138 | Neuville | 0.005 | 0.002 | 0.006 | 1.000 | 0.006 | 0.003 | 0.005 | 1.000 |

Table 2.4.3 presents statistics on water levels obtained with the global model. The errors made in the downstream segment propagate upstream, increasing the gaps between observed and modeled water levels by several cm at upstream stations, by comparison with results from Table 2.4.1. Errors in water levels are mostly explained by too low tidal ranges in the first 78 rkm. They are dominated by errors in mean water levels (MWL) at Beauport (rkm 97) and relatively balanced between errors in MWL and tidal ranges upstream, depending on the station and simulation period considered. Increases in friction around the Orleans Island are likely to improve model predictions, both at stations close to the modifications and stations further away. Despite these discrepancies, predicting skills are still higher than 0.992 at all stations. These very high skills are explained by the large tidal ranges characterizing the region, which often exceed 5 m. In fact, for stations downstream of Batiscan (rkm 199), the RMSE correspond to less than 5% of the local tidal ranges. At upstream stations, the ratio of the error to tidal range increases, due to rapidly decreasing tidal ranges, but RMSE are lower than 6 cm. This confirms that longitudinal variations in friction are well captured by the model.

Figure 2.4.6 shows a comparison between modeled and observed water levels from the global model at 7 selected permanent tide gauges, for each simulation period. Overall, observed water levels are well reproduced by the model, during both neap and spring tides. Fortnightly variations in MWL are also well captured at upstream stations (e.g., Trois-Rivières and Bécancour). However, differences between observed and modeled water levels at Bécancour are larger in August than June, with MWL being lower than expected in August (cf. Table 2.4.3). This points towards a gradual underestimation of friction in the Gentilly shoal, located 2 km downstream of Bécancour, following the growth of macrophytes during summer. The same friction field (Figure 2.4.3) was used during both simulation periods, but time-varying friction based on density and growth phase factors could be implemented in order to take this effect into account (Morin *et al.*, 2000b).

**Table 2.4.3 Validation on the global model: RMSE and skill for modeled water levels, mean water levels and tidal range at all stations for each 15-day simulation period.**

| rkm | Stations | June 14–29, 2009 | | | | Aug 19–Sep 3, 2009 | | | |
|---|---|---|---|---|---|---|---|---|---|
| | | RMSE (m) | | | Skill | RMSE (m) | | | Skill |
| | | Original | MWL | Range | | Original | MWL | Range | |
| 0 | Saint-Joseph-de-la-Rive | 0.095 | 0.013 | 0.064 | 0.999 | 0.091 | 0.021 | 0.066 | 0.999 |
| 30 | Islet-sur-Mer | 0.130 | 0.031 | 0.303 | 0.998 | 0.143 | 0.051 | 0.319 | 0.998 |
| 38 | Rocher Neptune | 0.103 | 0.067 | 0.198 | 0.999 | – | – | – | – |
| 45 | Ile-aux-Grues South | 0.110 | 0.057 | 0.212 | 0.999 | 0.145 | 0.107 | 0.193 | 0.998 |
| 46 | Ile-aux-Grues North | 0.154 | 0.115 | 0.293 | 0.998 | 0.135 | 0.098 | 0.271 | 0.998 |
| 54 | Banc du Cap Brûlé | 0.100 | 0.047 | 0.195 | 0.999 | 0.113 | 0.049 | 0.192 | 0.999 |
| 66 | Saint-François | 0.124 | 0.078 | 0.243 | 0.999 | 0.121 | 0.061 | 0.249 | 0.998 |
| 78 | Saint-Jean | 0.166 | 0.147 | 0.194 | 0.997 | 0.108 | 0.058 | 0.202 | 0.999 |
| 97 | Beauport | 0.221 | 0.198 | 0.064 | 0.995 | 0.160 | 0.120 | 0.058 | 0.997 |
| 100 | Lauzon | 0.185 | 0.155 | 0.074 | 0.996 | 0.133 | 0.076 | 0.084 | 0.998 |
| 104 | Saint-Charles River | 0.182 | 0.147 | 0.102 | 0.996 | 0.136 | 0.075 | 0.099 | 0.998 |
| 106.5 | Lévis | 0.175 | 0.137 | 0.102 | 0.997 | 0.133 | 0.069 | 0.086 | 0.998 |
| 106.5 | Québec | 0.177 | 0.141 | 0.086 | 0.997 | 0.132 | 0.072 | 0.088 | 0.998 |
| 115 | Québec Bridge | 0.177 | 0.140 | 0.040 | 0.996 | 0.131 | 0.069 | 0.079 | 0.998 |
| 124 | Saint-Nicolas | 0.138 | 0.112 | 0.087 | 0.998 | 0.104 | 0.062 | 0.078 | 0.999 |
| 138 | Neuville | 0.135 | 0.107 | 0.135 | 0.997 | 0.107 | 0.057 | 0.116 | 0.998 |
| 146 | Sainte-Croix-Est | 0.123 | 0.096 | 0.062 | 0.997 | 0.111 | 0.061 | 0.103 | 0.998 |
| 157 | Cap-Santé | 0.125 | 0.102 | 0.109 | 0.997 | 0.107 | 0.066 | 0.095 | 0.998 |
| 161 | Pointe-Platon | 0.118 | 0.094 | 0.083 | 0.997 | 0.109 | 0.066 | 0.085 | 0.998 |
| 163.5 | Portneuf | 0.089 | 0.062 | 0.056 | 0.999 | 0.121 | 0.086 | 0.076 | 0.997 |
| 168 | Deschambault | 0.106 | 0.069 | 0.139 | 0.997 | 0.126 | 0.074 | 0.222 | 0.996 |
| 179.5 | Leclercville | – | – | 0.029 | – | – | – | 0.042 | – |
| 179.5 | Grondines | 0.070 | 0.054 | 0.029 | 0.997 | 0.111 | 0.087 | 0.044 | 0.993 |
| 186 | Cap-à-la-Roche | 0.070 | 0.055 | 0.036 | 0.996 | 0.080 | 0.050 | 0.061 | 0.996 |
| 199 | Batiscan | 0.040 | 0.027 | 0.037 | 0.996 | 0.060 | 0.044 | 0.063 | 0.994 |
| 213 | Champlain | 0.046 | 0.035 | 0.074 | 0.992 | 0.058 | 0.037 | 0.056 | 0.992 |
| 217 | Bécancour | 0.027 | 0.010 | 0.042 | 0.997 | 0.056 | 0.048 | 0.036 | 0.992 |
| 231 | Trois-Rivières | 0.025 | 0.022 | 0.019 | 0.992 | 0.015 | 0.005 | 0.008 | 0.999 |
| 241 | Port Saint-François | 0.008 | 0.007 | 0.007 | 0.999 | 0.007 | 0.006 | 0.005 | 1.000 |

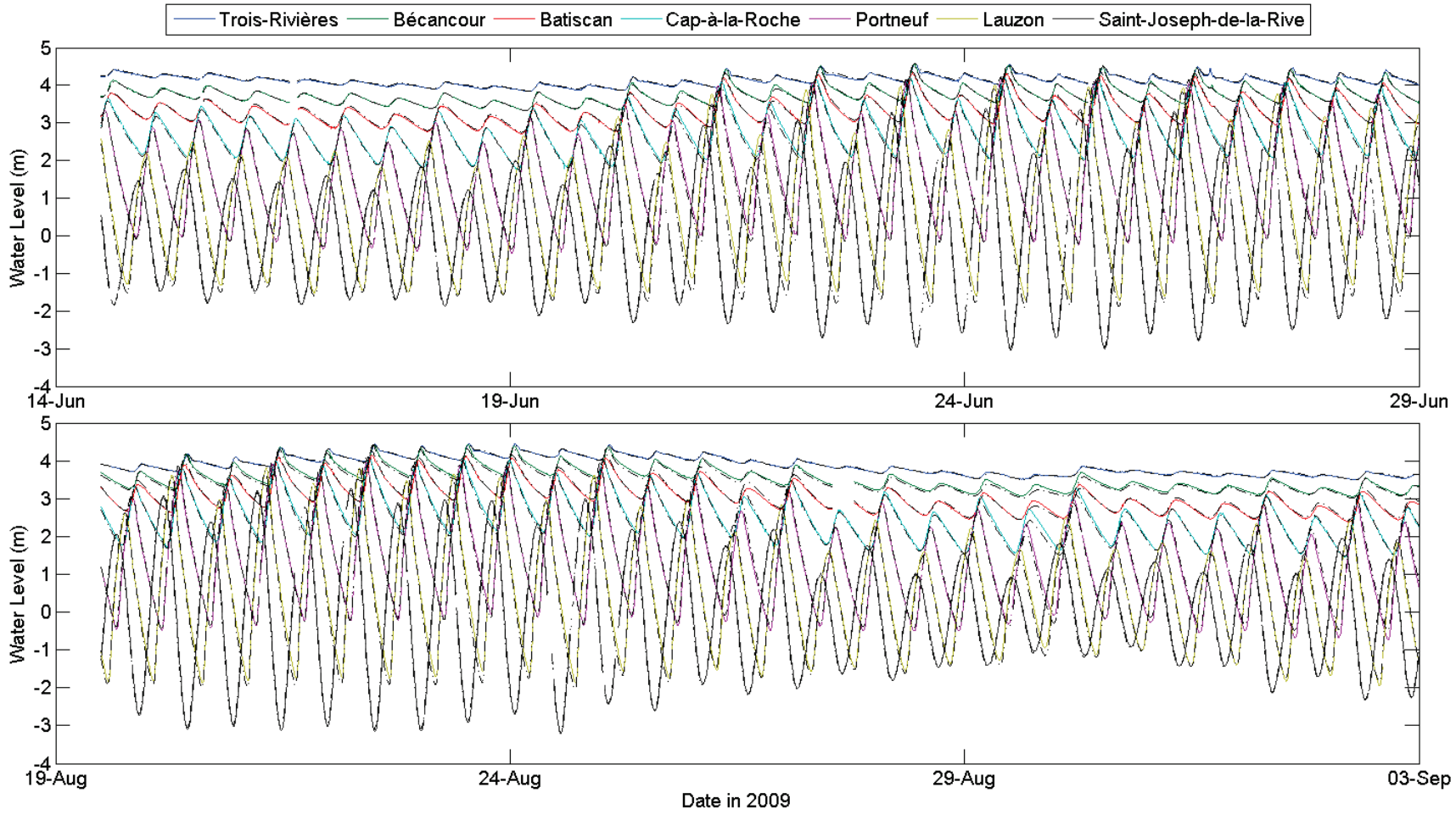


**Figure 2.4.6** **(solid lines) Observed and (dash-dotted lines) modeled water levels from the global model at 7 permanent tide gauges for the two simulation periods of June 14–29, 2009, and Aug 19–Sep 3, 2009.**

*2.4.4.2 Harmonic Properties*

To further evaluate the model, statistics from observed and modeled amplitudes and phases of major tidal constituents were computed for each 15-day simulation period (Table 2.4.4), by performing classical harmonic analyses at all stations of the global model (Pawlowicz *et al.*, 2002). Results for the 9 dominant constituents, among the 17 resolved ones, are presented in Table 2.4.4. For each tidal constituent, RMSE and skill are calculated by summing results at all 29 stations. Classical harmonic analysis implies that tides are stationary. In reality, daily discharges at Québec varied by 2000 $m^3s^{-1}$ and 1200 $m^3s^{-1}$ during the two simulation periods, respectively. Therefore, only the average frequency content of the tides can be retrieved from the analyses. For longer signals, however, nonstationary harmonic analyses could be performed to extract the time-varying amplitudes and phases of the tides (e.g., Matte *et al.*, 2013, Matte *et al.*, 2014c).

**Table 2.4.4 Statistics from observed and modeled amplitudes and phases of principal tidal constituents at all stations of the global model for each 15-day simulation period.**

| Constituent | June 14–29, 2009 | | | Aug 19–Sep 3, 2009 | | |
|---|---|---|---|---|---|---|
| | Amplitude | | Phase | Amplitude | | Phase |
| | RMSE (m) | Skill | RMSE (°) | RMSE (m) | Skill | RMSE (°) |
| MSf | 0.020 | 0.981 | 5.5 | 0.034 | 0.966 | 4.1 |
| $O_1$ | 0.009 | 0.997 | 2.9 | 0.011 | 0.992 | 2.6 |
| $K_1$ | 0.019 | 0.988 | 2.7 | 0.008 | 0.997 | 4.4 |
| $M_2$ | 0.066 | 0.998 | 1.5 | 0.059 | 0.998 | 1.9 |
| $S_2$ | 0.010 | 0.997 | 7.4 | 0.035 | 0.993 | 4.3 |
| $M_3$ | 0.010 | 0.975 | 2.4 | 0.005 | 0.980 | 9.2 |
| $M_4$ | 0.015 | 0.996 | 7.2 | 0.019 | 0.996 | 6.7 |
| $M_6$ | 0.009 | 0.986 | 17.8 | 0.016 | 0.982 | 15.5 |
| $M_8$ | 0.006 | 0.991 | 15.8 | 0.011 | 0.961 | 23.4 |

Results in Table 2.4.4 highlight the capacity of the model to represent the tidal frequency content of the observed signals with very high accuracy, with skills greater than 0.961 for all tidal constituents. MWL are well accounted for by the low-frequency MSf component. The larger RMSE was obtained for the $M_2$ (dominant) constituent, whose amplitude exceeds 2 m at the most downstream stations. The relative error for $M_2$ is therefore the lowest, presenting the highest skills among analyzed constituents. Phases are also well reproduced by the model, indicating a good synchronism with observations of the high and low tides. Furthermore, tidal

asymmetry, which can be assessed through the relative importance of $M_2$ and $M_4$ components, is expected to be well accounted for by the model. In fact, the skills associated with these two components are among the highest ($\geq 0.996$). Phase errors degrade with constituents of higher frequency, namely $M_6$ and $M_8$. However, the lowest errors for these components are observed at upstream locations, where they are the most significant, as they are generated by energy transfer from $M_2$ through nonlinear frictional interactions.

*2.4.4.3 Lateral and Intratidal Variability*

The model was further validated by comparison with water level and velocity measurements at the surveyed transects. The irregular mixed space-time data series were interpolated in space and in time to allow reconstruction of continuous and synoptic fields (cf. Matte *et al.*, 2014a). Comparisons between observed and modeled cross-channel water levels and velocities are made in Figure 2.4.7–Figure 2.4.10 for a river cross-section located at Grondines (rkm 179.5).

Observed and modeled water levels are shown in Figure 2.4.7. The agreement between the two is good, both in terms of synchronicity of the signals and reproducibility of the lateral patterns. Of particular interest is the lateral gradient forming during the falling tide between 1.0 and 1.7 km from the South shore, responsible for the emptying of the tidal flats into the channel. Variables extracted from the water level fields are shown in Figure 2.4.8, allowing a quantitative assessment of model performance at the transect. Time and height of high and low water (HW and LW, respectively), as well as tidal range, are plotted as a function of cross-sectional distance. LW is occurring slightly (~1–5 min) earlier in the model than observed, with a later arrival on the southern tidal flat (first km). Modeled LW is also ~10 cm higher than expected. Timing of HW in the model is relatively similar to observations, but exhibits less lateral variability. Modeled heights of HW are also higher than observed, with differences smaller than LW (<10 cm); they remain almost unchanged across the section. The tidal ranges are lower in the model compared to observations, but they follow a similar trend. Slightly decreasing friction near Grondines would therefore reduce the local predicted tidal heights and increase tidal range. The observed differences can also be partly explained by differences between the bathymetry measured along the section and obtained from the CHS soundings; they are referred to as observed and modeled bathymetries in bottom panel of Figure 2.4.8, the latter being the one actually incorporated in the NTM.

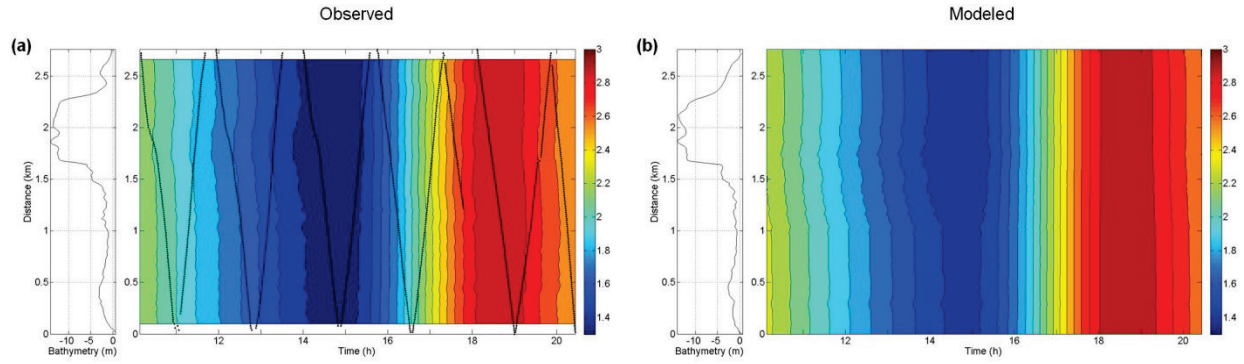


**Figure 2.4.7** **(a) Observed and (b) modeled water levels (in m) at Grondines on June 19, 2009, as a function of cross-sectional distance and time. Bathymetry is shown on the left panels. Black dots represent the gridded data points along the boat track. Time reference is EDT.**

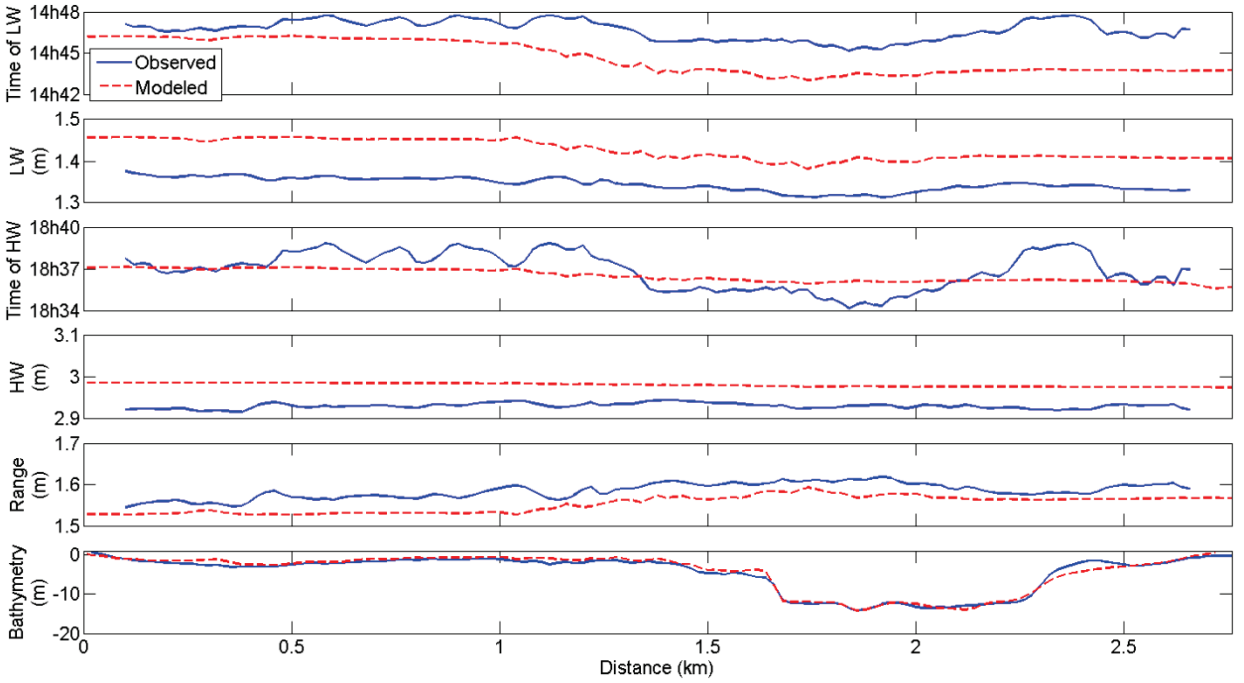


**Figure 2.4.8** **Comparison between observed and modeled variables extracted from the water level fields at Grondines on June 19, 2009: times and heights of high water (HW) and low water (LW), tidal range, and bathymetry across the section.**

Depth-averaged *u* and *v* velocity components are shown in Figure 2.4.9, corresponding to the along- and cross-channel velocities, respectively. The highest *u* velocities are concentrated in the channel, while *v* velocities present two distinct regions characterized by large positive values (oriented to the North). The southernmost region is the result of the tidal flats emptying into the channel and is in concordance with the observed lateral gradients in water levels

(cf. Figure 2.4.7). The second region is in the channel and likely corresponds to the effects of local channel curvature on the velocity directions. Current reversal only occurred on the North shore during the surveyed period, which is also corroborated by the model. These general flow features are adequately reproduced by the model, which strongly suggests that the lateral variations in topography and friction are well captured by the model. Figure 2.4.10 is a comparison based on variables directly extracted from the velocity fields in Figure 2.4.9. Maximum absolute velocities show very similar patterns in the model than in the observations, although modeled $u$ and $v$ velocities are slightly higher in the tidal flat, between 1.0 and 1.7 km. The observed times of slack water in both the ebb-to-flood and flood-to-ebb transitions are relatively well synchronized with the model. Current reversals however occur on a shorter distance from the North shore in the model. The inclination of the tidal ellipse formed by the velocity vector over a tidal cycle is a measure of the relative strength of lateral and longitudinal velocity components. Differences between observed and modeled inclinations are generally small. Highest inclinations are found in the southern tidal flat, where lateral exchanges are maximal.

These results stress the need for accurate bathymetric and hydrodynamic data in order to adequately model the flooding-drying processes that occur over shallow intertidal flats. These processes play a key role not only in the simulation of water transport over shallow areas, but also of tidal currents in the main river channel. In fact, the convergence of lateral flow towards the channel tend to add mass and to increase the magnitude of the along-estuary flow in the channel (Valle-Levinson *et al.*, 2000). Ignoring them could lead to significant underestimation of the amplitude of the latter (Zheng *et al.*, 2003). Furthermore, as observed by Valle-Levinson *et al.* (2000), lateral convergences are produced by phase lags of the tidal flow between the channel and the shoals, with magnitudes that are proportional to the along-estuary bathymetry gradients and to the tidal range. In the present application, the availability of LIDAR data, detailed cross-sectional hydrodynamic data (i.e. water levels and velocities) combined with a high-resolution mesh allowed a precise description and validation of the lateral exchanges occurring between the intertidal flats and the channel. Although comparisons are herein limited to one cross-section, detailed results for all transects can be found in section A.3.

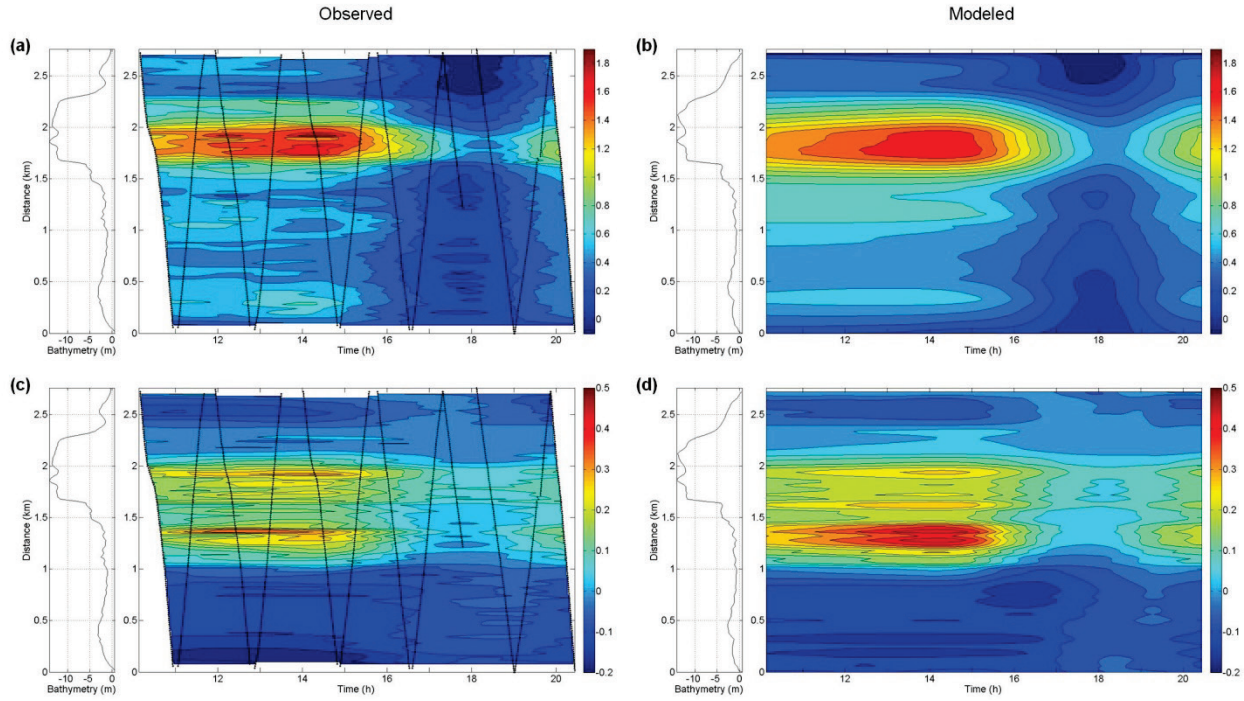


**Figure 2.4.9** **(a) Observed and (b) modeled u-component velocities (in m $s^{-1}$) at Grondines on June 19, 2009, as a function of cross-sectional distance and time. (c) Observed and (d) modeled v-component velocities. Bathymetry is shown on the left panels. Black dots represent the gridded data points along the boat track. Time reference is EDT.**

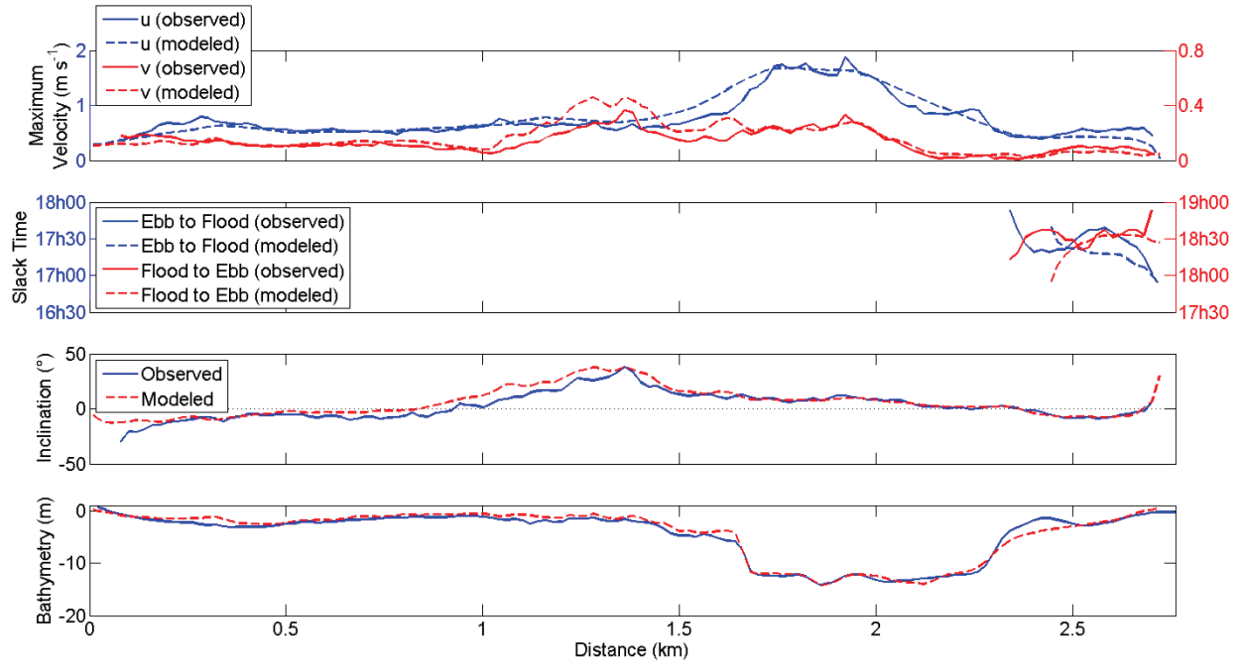


**Figure 2.4.10** **Comparison between observed and modeled variables extracted from the velocity fields at Grondines on June 19, 2009: maximum absolute u- and v-velocities, times of slack water, inclination of the tidal ellipse, and bathymetry across the section.**

*2.4.4.4 Neap-Spring Variability*

An appreciation of the neap-spring variability in the system can be gained by looking at the tide gauge water levels (Figure 2.4.6) for the two simulation periods. Tidal damping and signal distortion from downstream to upstream are marked. Over the neap-spring cycle, modulations of the tidal range as well as of MWL occur, the amplitude of the latter exceeding that of the semidiurnal tide at Trois-Rivières (rkm 231). Another striking manifestation of the neap-spring cycle can be observed in the location of the upstream limit of current reversal, which moves between Grondines (rkm 179.5) and Bécancour (rkm 217) depending on tidal range and river flow. This is illustrated in Figure 2.4.11 where velocity directions are shown over a tidal cycle at Grondines and Batiscan (rkm 199), at two different phases on the neap-spring cycle, around neap and spring tides, respectively. During neap tides, currents barely reverse at Grondines, only on a small portion of the cross-section. During spring tides, the current reversal as shown by the model occurs on the entire section of Batiscan (~20 rkm upstream). Measured velocity directions at Batiscan show a remaining section in the middle of the channel still resisting current reversals, although this may be an artifact of interpolation between the transects (Matte *et al.*, 2014a). The lateral and longitudinal variability in the location of current reversals are thus well reproduced by the model over the neap-spring cycle.

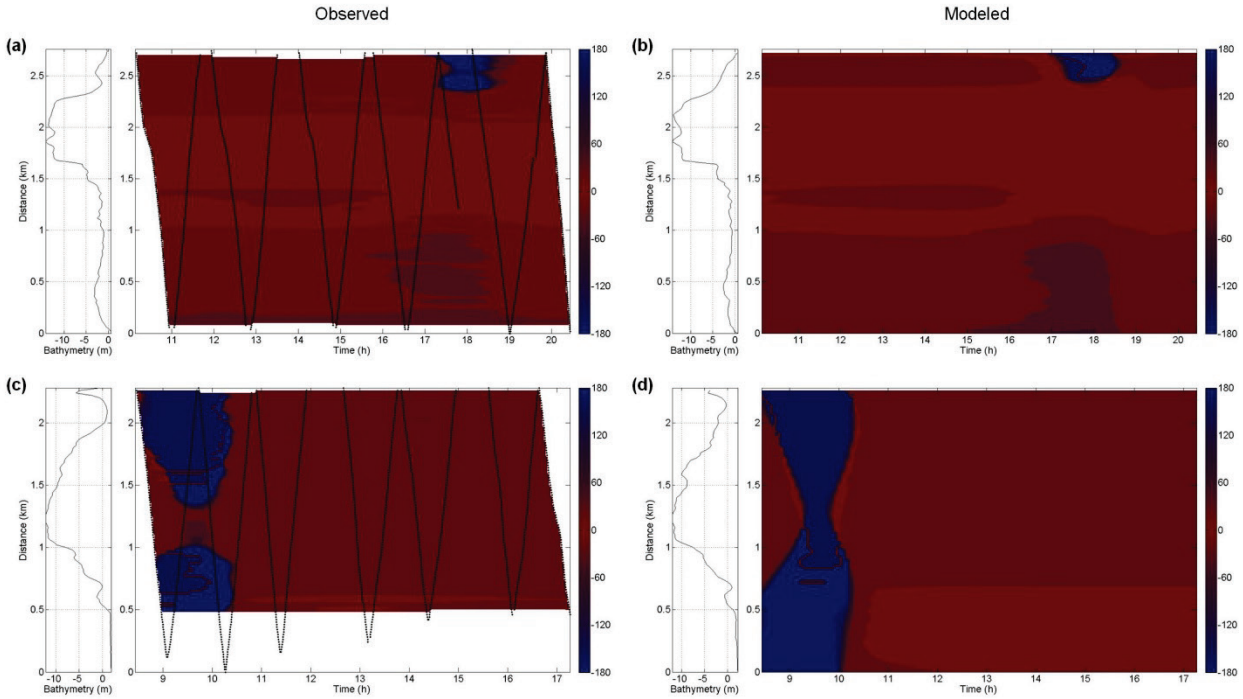


**Figure 2.4.11** **Neap-spring variability in the upstream limit of current reversals. (a) Observed and (b) modeled velocity directions (in degrees) at Grondines (rkm 179.5) on June 19, 2009 (around neap tides), as a function of cross-sectional distance and time. (c) Observed and (d) modeled velocity directions at Batiscan (rkm 199) on June 23, 2009 (around spring tides). The 0° vector is oriented downstream and perpendicular to the mean transect. Bathymetry is shown on the left panels. Black dots represent the gridded data points along the boat track. Time reference is EDT.**

### *2.4.4.5 Flow Division at a Tidal Junction*

Computed discharges in the North and South arms of Orleans Island are presented in Figure 2.4.12 to illustrate flow distribution at this tidal junction. Measurements in the two arms were taken one day apart from each other, so that the tidal and discharge conditions during each survey are comparable. Observed and modeled discharges over the tidal cycle are very similar at both locations, meaning that flow is well distributed in the channels. This also indicates that the topography and friction are well balanced between the sections, which are known to be critical components affecting flow division at shallow tidal junctions (Buschman *et al.*, 2010). Daily-averaged discharges in the SLFE are of 12 200 $m^3s^{-1}$ at Québec. In Figure 2.4.12, peak discharges exceed 60 000 $m^3s^{-1}$ during ebb tide and reach almost the same (negative) value during flood tide, in the South arm of Orleans Island. In the North arm, another 10 000 $m^3s^{-1}$ is discharged during ebb tide at its peak. These differences in discharge, measured during spring tide, follow

the geometry of the channels, the higher depths and wider sections being encountered in the South arm.

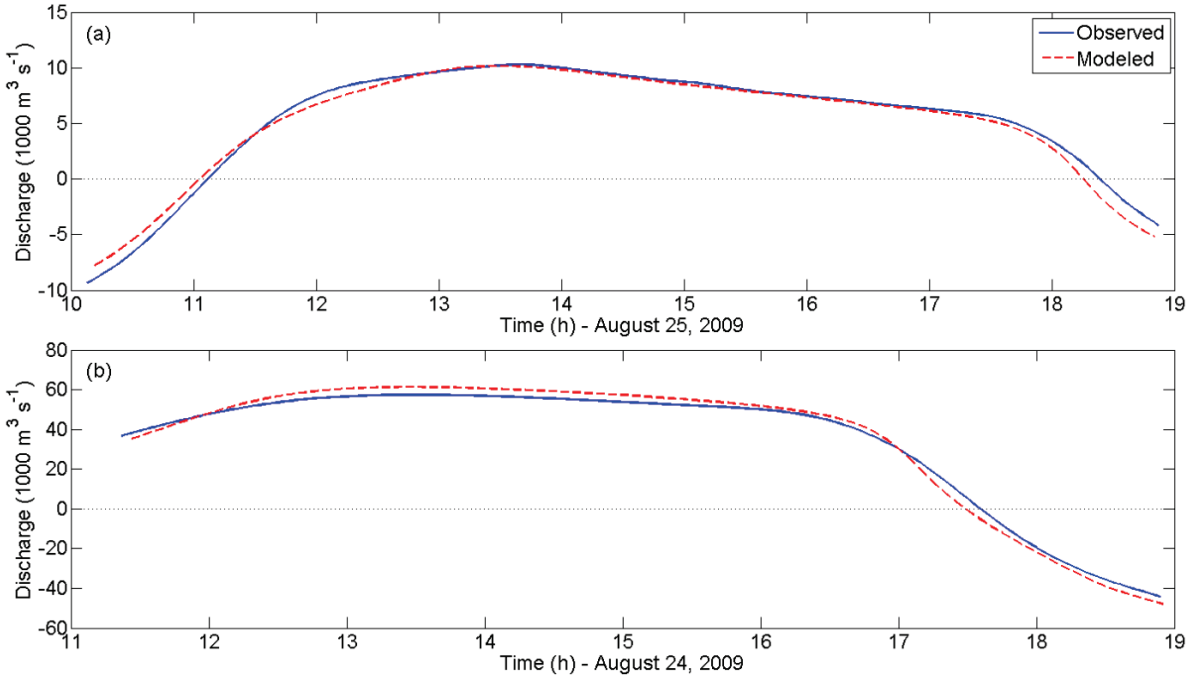


**Figure 2.4.12 Observed and modeled flow division in the (a) North and (b) South arms of Orleans Island.**

Figure 2.4.13 presents simulation results at the junction of Orleans Island at different stages of the tidal cycle. Results are presented for a spring tide, measured at Lauzon (rkm 100) on June 24, 2009, under approximately average discharge conditions (11 100 $m^3s^{-1}$). Arrows indicate the mean direction of currents and recirculations. At high tide, currents are reversed in both arms of Orleans Island, with velocities reaching about 1.5 m $s^{-1}$ in the deepest regions. One hour after HW, currents are weakened and recirculation appears in shallow regions where water is redirected downstream. Two hours after HW, currents are oriented downstream and increase in importance with the falling tide; tidal flats are also progressively dried. Currents are at their maximum approximately one hour before low tide, with velocities reaching 2.3 m $s^{-1}$. At low tide, currents start decreasing; they rapidly change in the following hours, due to the more abrupt rising tide. One hour after LW, slack water has reached Lauzon, but ebb currents are still strong in the North arm of Orleans Island. Two hours after LW, currents are completely reversed in the South arm; they are partly diverted into the North arm and partly directed upstream. Slack water finally arrives in the North arm one hour before the next HW, and currents are completely reversed thereafter, for the next three hours approximately.

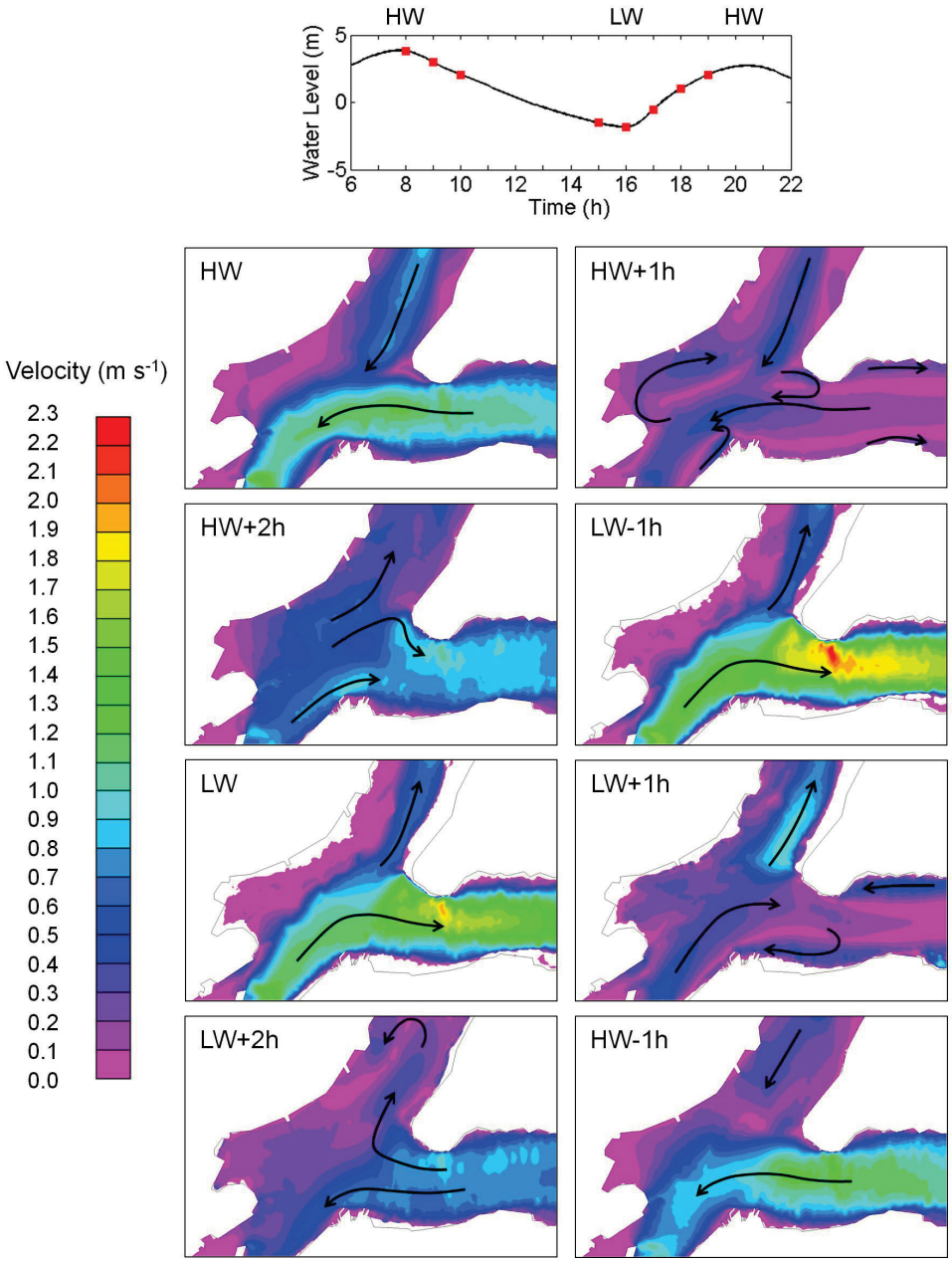


**Figure 2.4.13** **Modeled velocities (in m $s^{-1}$) at the junction of Orleans Island at different stages of the tidal cycle. (top panel) Tidal signal at Lauzon on June 24, 2009 (spring tide), with corresponding high waters (HW) and low water (LW). Arrows indicate the direction of currents and recirculations.**

The flow patterns described above are in concordance with continuous water level and velocity measurements taken at the junction of Orleans Island during the same tidal cycle as the one presented in Figure 2.4.13 (cf. section A.3). In general, timing of current reversals is strongly dependent on the geometry of the two channels, which affect both tidal propagation and flow distribution. Use of accurate bathymetric data is therefore essential.

*2.4.4.6 Momentum Balance*

Instantaneous momentum balances were computed for the spring tide of June 24, 2009, 08:00:00 EDT; their modulus are reported in Figure 2.4.14, calculated from the *x* and *y* components of the balance. This snapshot encompasses the various features that can be observed during a tidal cycle, by opposition to momentum balances averaged over a complete semidiurnal tidal cycle, much less contrasted spatially. Upstream, the flow is unidirectional down to approximately Batiscan (rkm 199). A slack water before flood occurs at Deschambault (rkm 168), as shown by near-zero velocities and a minimum in water levels (Figure 2.4.14a-b). This is then followed by a flood tide where currents are reversed and water level gradients are positive. A slack before ebb is observed at the eastern end of Orleans island, followed by increasing ebb currents in the seaward direction that are accompanied by a sharp decrease in water levels.

Figure 2.4.14c-g shows the contribution of advective acceleration, pressure gradient, bottom friction, Coriolis acceleration and turbulent viscosity to the momentum balance, respectively. Clearly, the balance is dominated by the pressure gradients, which are the major driving force of the flow. As a first approximation, LeBlond (1978) had showed that the dynamic balance in shallow tidal reaches of the St. Lawrence and Fraser rivers reduces to an equilibrium between friction and surface slope over most of the tidal cycle, except near slack. Here, at both full ebb and flood, it is shown that both advective accelerations and bottom friction – and, to a lesser extent, Coriolis accelerations – balance the pressure gradients. In the two upstream regions of high velocities, the advective accelerations are comparable to the pressure gradients because of the relatively low water level slopes. By opposition, in the downstream ebb, the flow is primarily driven by gravity due to the much steeper gradients of water levels. Ratios calculated between the terms (not presented) show that bottom friction dominates over the effects of pressure gradient almost exclusively in shallow areas (e.g., intertidal flats, shoals). The Coriolis acceleration, for its part, typically exceeds the advective acceleration in regions where velocities are lower than 1 m $s^{-1}$. As for turbulence, it is one order of magnitude smaller than the other terms. The highest values are located in the deepest portions of the river, in front of Québec and Île-aux-Coudres, as well as around engineering structures and islands. They are also higher in the channel than in the intertidal regions. Near slack, only the pressure gradients remain significant, which are balanced by local acceleration (not shown).

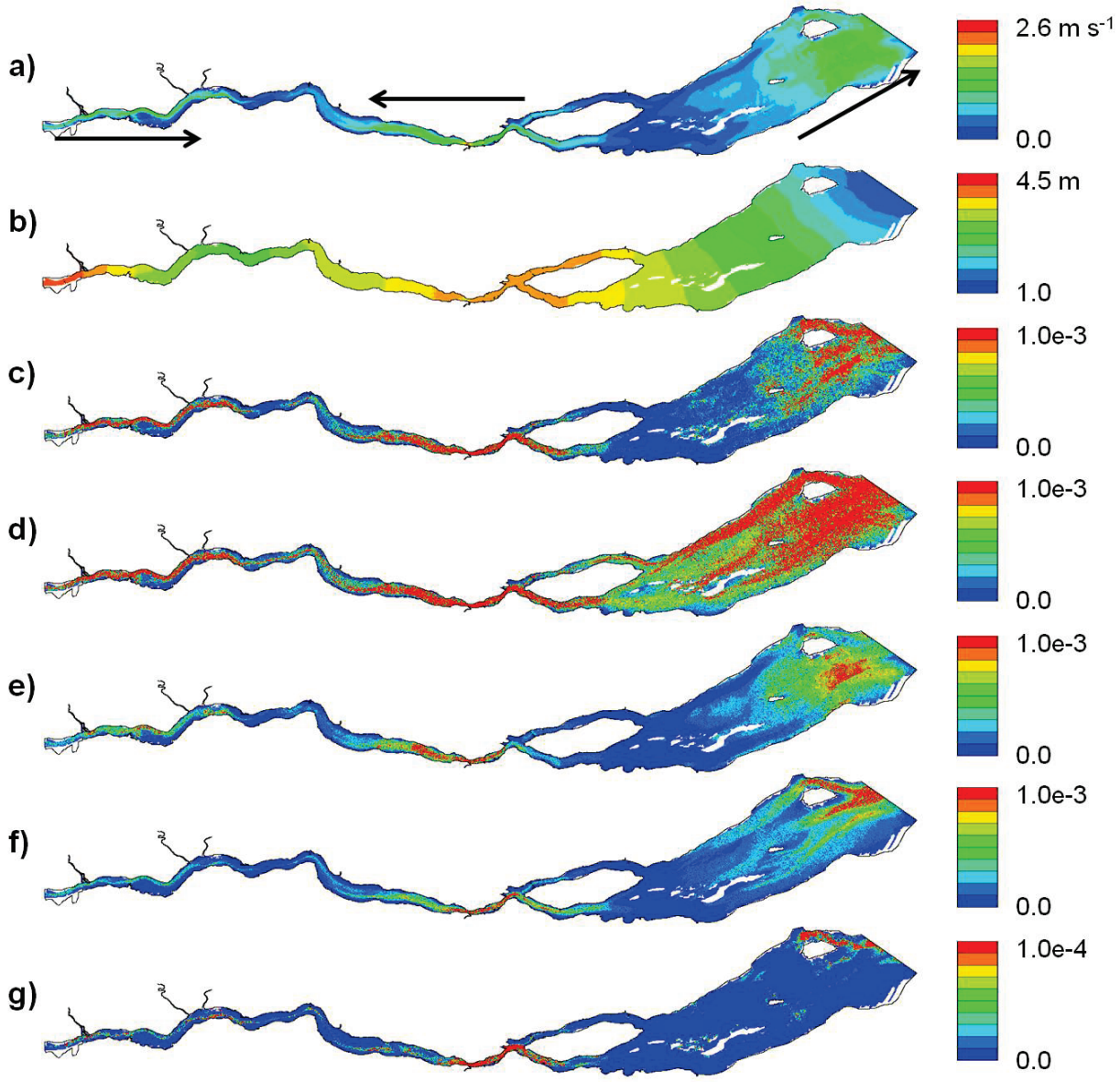


**Figure 2.4.14** **Terms of the momentum balance (modulus in $m^2s^{-2}$) on June 24, 2009, 08:00:00 EDT (spring tide): (a) velocities with arrows indicating the direction of currents, (b) water levels, (c) advective acceleration, (d) pressure gradient, (e) bottom friction, (f) Coriolis acceleration, (g) turbulent viscosity, whose scale is one order of magnitude smaller than the other terms.**

Hench & Luettich (2003) analyzed the transient momentum balances at shallow barotropic tidal inlets and found that they oscillate between two dynamical states, depending on whether the phase of the tide is near maximum ebb or flood, or near slack. Here, similar analyses were carried out with a complete coverage of the tidal cycle in space rather than in time. Similar conclusions can be drawn from the analyzed fields with respect to the differing dynamical states observed at high velocity versus near slack. Hench & Luettich (2003) further divided their

momentum balance calculations into along-stream and cross-stream components. While such a separation may facilitate physical interpretation in the case of strongly curving flow fields, here we limited our analysis to the modulus of the momentum balance terms due to the dominance of the streamwise velocities. However, a more thorough analysis of momentum balances that includes cross-stream components could be very informative, especially with regards to lateral exchanges of momentum between the tidal flats and the channel (e.g., Cáceres *et al.*, 2003, Basdurak & Valle-Levinson, 2013), although this is outside the scope of this work.

### 2.4.5 Discussion

Several authors have thoroughly described the process of model evaluation, calibration and validation (e.g., Willmott, 1982, Willmott *et al.*, 1985, Hsu *et al.*, 1999, Umgiesser *et al.*, 2004, Warner *et al.*, 2005, Espino *et al.*, 2007, Jung *et al.*, 2012). Here, a procedure for the calibration and validation of non-stationary hydrodynamic models has been presented, which makes use of very detailed cross-sectional water level and velocity data. Because such comprehensive data sets are rarely available in tidal rivers, model evaluation is most often limited to fixed stations. Here, various lateral features that were revealed in the data were adequately reproduced by the model. Furthermore, transect surveys are usually devised for the measurement of velocity distributions only and little attention is generally paid to lateral gradients in water levels. Results presented herein showed that lateral variations in velocity are strongly linked to lateral water level gradients, especially over strong bathymetry, reinforcing the need for both variables to be considered conjointly in the calibration and validation process.

When modeling tidal rivers and estuaries, the main focus is most often oriented towards the ability of the models to adequately reproduce tidal amplitudes and phases of major astronomical and shallow water constituents (e.g., Hsu *et al.*, 1999, Espino *et al.*, 2007, Picado *et al.*, 2010). Here, the simulation periods were limited to 15 days due to the high computational cost associated with grid resolution and size of the domain. As a result, only a limited number of tidal constituents could be resolved by traditional harmonic analysis. Furthermore, tides in upstream reaches of rivers are highly non-stationary, so that results from harmonic analysis can only explain a fraction of the total signal variance. With short records, even non-stationary harmonic analysis methods (e.g., Matte *et al.*, 2013) or wavelet decomposition of tidal species (e.g., Jay & Kukulka, 2003, Buschman *et al.*, 2009, Sassi *et al.*, 2011) present limited descriptive capabilities.

Here, model performance was further assessed based on time variations in surface elevation, mean water level and tidal range, extracted from the modeled and observed signals at the tide stations. Moreover, meaningful variables (i.e. time and height of high and low water, tidal range, time of slack water, maximum velocity, inclination of the tidal ellipse) extracted from both transect data and model results over the semidiurnal tidal period were also used for validation. Basing model evaluation on these variables is consistent with the type of boundary conditions used, where observed water levels rather than tidal harmonics were imposed. Like the cycle-by-cycle analysis described by Parker (2007), such variables can form the basis for comparisons at a given site between different tidal cycles throughout the month (e.g., from neap to spring tides) and different non-tidal conditions (e.g., winds, river discharge), as well as between regions of contrasting tidal and fluvial properties and channel geometries. Such an approach is believed to be more versatile than harmonic-based validation alone, as it can be applied to a variety of non-stationary contexts other than tidal.

The geometry and size of the SLFE (notably the small depth relative to horizontal width), combined to the effects of strong tides in a freshwater environment, make the assumptions leading to a 2D approximation valid. Furthermore, recent velocity measurements made in the SLFE (Matte *et al.*, 2014a) have shown that virtually no vertical structures were present in the data. In fact, current reversals generally occur in a very short period of time and are nearly simultaneous within the water column. Secondary circulation, on the other hand, was observed only at Portneuf, a region of high channel curvature. Improvements to the 2D shallow water model could be made to account for the vertical variability in velocity, for example by adding a dispersive term in the equations (Secretan & Dubos, 2005), although this was not done here. In the estuarine transition zone, however, the presence of density currents and stratification was observed by Simons *et al.* (2010), which present variability at both semidiurnal and fortnightly time scales. The 2D vertically-averaged model developed here cannot account for these effects, but their impact on water levels is assumed to be low.

High-resolution modeling allows decreasing the overall discretization error. However, accurate predictions are strongly dependent on the precision of tidal and river forcing at the boundaries, bathymetry and bottom roughness. In fact, in regions of complex bathymetry, increase in the grid resolution cannot come without an increase in the bathymetric resolution, and greater care must be taken in parameterizing bottom friction. Moreover, nonhydrostatic effects may become

important for small-scale flow structures, but has a small effect on the large-scale dynamics (Wang *et al.*, 2009). Because our main focus here was to model tidal- to intratidal-scale processes reported in recently acquired field data, the model was not configured to reproduce phenomena at scales that are influenced by the nonhydrostatic pressure. Local refinements of the mesh were rather intended for a better inclusion of topographic elements influencing the mean flow, including shallow intertidal areas.

Model results in the downstream segment presented larger errors than in the upstream portion of the SLFE. Part of these errors is associated with the distribution of water levels along the downstream boundary. The assimilation performed here only allowed defining the appropriate time shift and vertical and amplitude corrections in water levels to apply at the boundary; therefore, the actual lateral distribution could not be optimized entirely. Coupling with a 3D ocean model of the St. Lawrence Estuary (Saucier & Chassé, 2000, Saucier *et al.*, 2009, Smith *et al.*, 2013) may allow us to improve water level forcing at the downstream boundary. Numerical experimentation showed it to be non-trivial, stressing the need for it to be complemented with field data. Increasing friction around the Orleans Island may also reduce the gaps between modeled and observed water levels at nearby stations by increasing the MWL and reducing tidal ranges, thereby correcting for the discrepancies upstream. Moreover, although detailed LIDAR topographic data was acquired in shallow areas, bathymetry in the Montmagny archipelago, downstream of Orleans Island, is very complex and the only available data in some areas were measured several decades ago. Also, data reduction from chart datum to mean sea level is not trivial in this region due to the high spatial variability in tidal properties. This therefore introduces further errors in the model, which are likely to be more pronounced during low spring tides (Falcão *et al.*, 2013). One possible way to improve model performance would be to treat the various sources of error in bathymetry as a calibration parameter (Cea & French, 2012).

### 2.4.6 Conclusion

A 2D hydrodynamic model of the SLFE was developed, using a finite-element grid with an average spatial resolution of 50 m, far denser than previous/existing models. Various challenges were addressed, associated with model calibration and validation, the description of topography in shallow areas using LIDAR data, the inclusion of main tributaries with limited terrain data, the assimilation of boundary conditions, and the integration of a large amount of high-resolution

terrain data from numerous sources. The model was calibrated and validated using water level and velocity data collected in the summer of 2009, constituting the most detailed data set to date in this section of the St. Lawrence. Results showed good agreement between modeled and observed water levels, with predicting skills higher than 0.99 at all stations and root-mean-square errors (RMSE) corresponding to less than 5% of the local tidal ranges in the first 186 rkm; at upstream stations, where tidal ranges are significantly reduced, RMSE are lower than 6 cm. These results confirm that the boundary conditions and parameterizations used in the model are well adjusted. Furthermore, harmonic properties as well as tidal and flow features observed in part in the field data were all reproduced satisfactorily, including the lateral exchanges between the intertidal flats and the channel, the neap-spring variability in the upstream limit of current reversal, flow division at the junction of Orleans Island, and momentum balance as a function of space and tidal phase. This research provides for the first time a detailed 2D description of the tidal hydrodynamics of this complex region where knowledge is very limited, thoroughly validated from recent field data under a variety of tidal-fluvial conditions. This is the first step towards a comprehensive model of the SLFE that will be run in operational mode and include variables for the assessment of habitat and water quality (e.g., Morin *et al.*, 2003b).

Future work should focus on the validation of the model under varying discharge, wind, macrophytes distribution, and ice conditions. As much as computational time permit, the mesh should be extended to include floodplain topography for the simulation of extreme events.

### 2.4.7 Appendix: Shallow Water Equations

The shallow water equations can be written as follows; for mass conservation:

$$\frac{\partial h}{\partial t}+\frac{\partial q_x}{\partial x}+\frac{\partial q_y}{\partial y}+(\gamma+\delta)\left(\frac{\partial^2 h}{\partial x^2}+\frac{\partial^2 h}{\partial y^2}\right)=0 \qquad (2.4.3)$$

and momentum conservation:

$$\frac{\partial q_x}{\partial t}+\frac{\partial}{\partial x}\left(\frac{q_x q_x}{H}\right)+\frac{\partial}{\partial y}\left(\frac{q_x q_y}{H}\right)+c^2\frac{\partial h}{\partial x}-\frac{1}{\rho}\left[\frac{\partial}{\partial x}(H\tau_{xx})+\frac{\partial}{\partial y}(H\tau_{xy})+\tau_x^s-\tau_x^b\right]-f_c q_y=0 \qquad (2.4.4)$$

$$\frac{\partial q_y}{\partial t}+\frac{\partial}{\partial x}\left(\frac{q_y q_x}{H}\right)+\frac{\partial}{\partial y}\left(\frac{q_y q_y}{H}\right)+c^2\frac{\partial h}{\partial y}-\frac{1}{\rho}\left[\frac{\partial}{\partial x}\left(H\tau_{yx}\right)+\frac{\partial}{\partial y}\left(H\tau_{yy}\right)+\tau_y^s-\tau_y^b\right]+f_c q_x=0 \quad (2.4.5)$$

where:

**x**($x$,$y$) East and North Cartesian coordinates (m);

**q**($q_x$,$q_y$) specific discharge ($m^2s^{-1}$), defined as:

$$\mathbf{q}=\mathbf{u}H \quad (2.4.6)$$

where **u**($u_x$,$u_y$) is the water velocity ($m\ s^{-1}$);

$h$ water level (m);

$t$ time (s);

$H$ water depth (m), defined as:

$$H=h-z_b \quad (2.4.7)$$

where $z_b$ is the bed level with respect to the mean sea level;

$g$ gravitational acceleration (= 9.81 $m\ s^{-2}$)

$c$ celerity of waves ($m\ s^{-1}$), defined as:

$$c=\sqrt{gH} \quad (2.4.8)$$

$\rho$ density of water (= $10^3$ $kg\ m^{-3}$);

$\gamma$ Lapidus coefficient, defined as (Lapidus, 1967, Heniche *et al.*, 2000a):

$$\gamma=\gamma_0\Delta^2\sqrt{\left(\frac{\partial h}{\partial x}\right)^2+\left(\frac{\partial h}{\partial y}\right)^2} \quad (2.4.9)$$

where $\gamma_0$ is a constant value in the range of $10^{-5}$ and $\Delta$ is the local element size; this added viscosity damps the solution only in regions of high water level gradient, thus preventing oscillations of the free surface;

$\delta$ hydraulic conductivity; it is set to zero in wet areas and in the range of 10 in dry areas;

$\tau_{ij}$ Reynolds stress (kg $s^{-2}m^{-1}$), each stress component being defined as:

$$\frac{1}{\rho}\begin{bmatrix}\tau_{xx} & \tau_{xy}\\ \tau_{yx} & \tau_{yy}\end{bmatrix} = \left(\nu_l + \nu_t + \nu_n\right)\begin{bmatrix} 2\frac{\partial u_x}{\partial x} & \left(\frac{\partial u_x}{\partial y} + \frac{\partial u_y}{\partial x}\right)\\ \left(\frac{\partial u_x}{\partial y} + \frac{\partial u_y}{\partial x}\right) & 2\frac{\partial u_y}{\partial y}\end{bmatrix} \tag{2.4.10}$$

where $\nu_l$ is the laminar viscosity; $\nu_t$ is the turbulent viscosity, and $\nu_n$ is the numerical viscosity; $\nu_t$ is expressed either as a constant viscosity or as a function of the flow gradient, derived from the mixing length theory as (Rodi, 1984):

$$\nu_t = l_m^2\sqrt{2\left(\frac{\partial u_x}{\partial x}\right)^2 + 2\left(\frac{\partial u_y}{\partial y}\right)^2 + \left(\frac{\partial u_x}{\partial y} + \frac{\partial u_y}{\partial x}\right)^2} \tag{2.4.11}$$

where $l_m$ is the mixing length and is defined as (Soulaïmani, 1983, Ouellet *et al.*, 1986):

$$l_m = \lambda H \tag{2.4.12}$$

with a calibration coefficient $\lambda$[1]; $\nu_n$ is controlled by the Peclet number $Pe$ (Zienkiewicz *et al.*, 2014):

$$\nu_n = \left|\frac{q}{H}\right|\frac{\Delta}{Pe} \tag{2.4.13}$$

[1] This representation of the mixing length differs from Smagorinsky's (1963) subgrid model in that the length scale at which turbulent processes can be represented is limited by a fraction of the local depth instead of the element size $\Delta$. In the present application, the mean depth is overall smaller than the average element size, although spatial variations of the depth do not necessarily follow the variations in mesh resolution.

$\tau_i^s$ surface friction (N m$^{-2}$), defined as:

$$\tau_i^s = \rho_a C_w |w| w_i \tag{2.4.14}$$

where $\rho_a$ is the air density, $C_w$ is the wind drag coefficient, and $\mathbf{w}(w_x,w_y)$ is the wind velocity;

$\tau_i^b$ bottom friction (N m$^{-2}$), defined as:

$$\tau_i^b = \left( \alpha + \frac{\rho g n^2 |q|}{H^{7/3}} \right) q_i \tag{2.4.15}$$

where $\alpha$ is a damping coefficient acting as a linear friction parameter (set to zero in the present application), $n$ is the Manning coefficient which defines quadratic resistance to flow by substrate, macrophytes, macrorugosity, etc., each being quadratically added as follows (Boudreau *et al.*, 1994):

$$n^2 = \sum_m n_m^2 \tag{2.4.16}$$

$f_c$ Coriolis factor (s$^{-1}$), defined as:

$$f_c = 2\omega \sin\phi \tag{2.4.17}$$

where $\omega$ is the Earth's rotational rate and $\phi$ is the site latitude.

The weak form is derived from the Galerkin weighted residuals method (Heniche *et al.*, 2000a, Dhatt *et al.*, 2005). The higher order terms and the continuity are integrated by parts, leading to the apparition of a natural condition of impermeability on solid boundaries where no explicit condition is specified (i.e. $q_n = 0$, where $q_n$ is the specific discharge normal to the boundary).

### 2.4.8 Acknowledgements

Work by Pascal Matte was supported by scholarships from the Natural Sciences and Engineering Research Council of Canada and Fonds de recherche du Québec – Nature et technologies. The authors wish to thank Environment Canada (Meteorological Service of Canada) for their

financial support, the Ministère du Développement Durable, de l'Environnement, de la Faune et des Parcs (MDDEFP) for financing the LIDAR campaign, and the Canadian Hydrographic Service (CHS) and Ministère des Transports du Québec (MTQ) for providing bathymetric and topographic data. Special thanks go to Jimmy Poulin, Charles Gignac, Olivier Champoux and Patrice Fortin for their contribution to this work as well as Daniel Bourgault for his valued comments on a previous version of the manuscript. Tide gauge data are available for download on DFO's Canadian Tides and Water Levels Data Archive (http://www.meds-sdmm.dfo-mpo.gc.ca/isdm-gdsi/twl-mne/index-eng.htm). Other field data are in the process of being made available, but can be requested directly to Pascal Matte (corresponding author). The H2D2 software and source code are freely available for download, upon request to Yves Secretan, at http://www.gre-ehn.ete.inrs.ca/H2D2/contenu_download.

# RÉFÉRENCES


Alkan RM & Baykal O (2001) Survey boat attitude determination with GPS/IMU systems. *J. Navigation* 54(1):135-144.

Amin M (1983) On perturbations of harmonic constants in the Thames Estuary. *Geophys. J. Roy. Astron. Soc.* 73(3):587-603.

Amin M (1985) Temporal variations of tides on the west coast of Great Britain. *Geophys. J. Roy. Astron. Soc.* 82(2):279-299.

Amin M (1993) The mutual influence of tidal constituents in the presence of bottom stress. *Estuar. Coast. Shelf Sci.* 37(6):625-633.

Araújo IB, Dias JM & Pugh DT (2008) Model simulations of tidal changes in a coastal lagoon, the Ria de Aveiro (Portugal). *Contin. Shelf Res.* 28(8):1010-1025.

Aubrey DG & Speer PE (1985) A study of non-linear tidal propagation in shallow inlet/estuarine systems Part I: Observations. *Estuar. Coast. Shelf Sci.* 21(2):185-205.

Awange JL (2012) *Environmental Monitoring Using GNSS.* Springer-Verlag. 386 p.

Awange JL & Aduol FWO (1999) An evaluation of some robust estimation techniques in the estimation of geodetic parameters. *Surv. Rev.* 35(273):146-162.

Babu MT, Vethamony P & Desa E (2005) Modelling tide-driven currents and residual eddies in the Gulf of Kachchh and their seasonal variability: A marine environmental planning perspective. *Ecol. Model.* 184(2-4):299-312.

Bárcena JF, García A, Gómez AG, Álvarez C, Juanes JA & Revilla JA (2012) Spatial and temporal flushing time approach in estuaries influenced by river and tide. An application in Suances Estuary (Northern Spain). *Estuar. Coast. Shelf Sci.* 112(0):40-51.

Barrass CB (2004) *Ship Design and Performance for Masters and Mates.* Elsevier, Burlington, MA. 265 p.

Basdurak NB & Valle-Levinson A (2013) Tidal variability of lateral advection in a coastal plain estuary. *Contin. Shelf Res.* 61–62(0):85-97.

Bauer TR, Bountry J & Hilldale RC (2007) 2007 Profile survey of the Sandy River for Marmot Dam removal. (U.S. Department of the Interior, Bureau of Reclamation, Technical Service Center, Denver, CO). 25 p.

Beatson RK, Cherrie JB, McLennan TJ, Mitchell TJ, Carr JC, Fright WR & McCallum BC (2004) Surface reconstruction via smoothest restricted range approximation. *Geometric Modeling and Computing*, Lucian ML & Neamtu M (Édit.) Nashboro Press, Nashboro, Brentwood, Tennessee. p 41-52.

Beaulieu C, Gharbi S, Ouarda T, Charron C & Aissia M (2012) Improved model of deep-draft ship squat in shallow waterways using stepwise regression trees. *J. Waterw. Port Coast. Ocean Eng.* 138(2):115-121.

Beaulieu C, Gharbi S, Ouarda TBMJ & Seidou O (2009) Statistical approach to model the deep draft ships' squat in the St. Lawrence Waterway. *J. Waterw. Port Coast. Ocean Eng.* 135(3):80-90.

Bender LC, Guinasso NL, Walpert JN & Howden SD (2010a) A comparison of methods for determining significant wave heights—Applied to a 3-m discus buoy during Hurricane Katrina. *J. Atmos. Oceanic Technol.* 27(6):1012-1028.

Bender LC, Howden SD, Dodd D & Guinasso NL (2010b) Wave heights during Hurricane Katrina: An evaluation of PPP and PPK measurements of the vertical displacement of the GPS antenna. *J. Atmos. Oceanic Technol.* 27(10):1760-1768.

Bisnath S, Wells D, Howden S, Dodd D & Wiesenburg D (2004a) Development of an operational RTK GPS-equipped buoy for tidal datum determination. *Int. Hydrogr. Rev.* 5(1):54-64.

Bisnath S, Wells D, Howden S & Stone G (2003) The use of a GPS-equipped buoy for water level determination. *OCEANS 2003.* (San Diego, CA, 22-26 Sept. 2003) The Marine Technology Society, p 1241-1246.

Bisnath S, Wells D, Santos M & Cove K (2004b) Initial results from a long baseline, kinematic, differential GPS carrier phase experiment in a marine environment. *Position Location and Navigation Symposium (PLANS) 2004.* (Monterey, CA, 26-29 April 2004) IEEE, p 625-631.

Blain CA (1997) Development of a data sampling strategy for semienclosed seas using a shallow-water model. *J. Atmos. Oceanic Technol.* 14(5):1157-1173.

Blake SJ (2007) *Heave compensation using time-differenced carrier observations from low cost GPS receivers*. Ph.D. thesis (University of Nottingham, Nottingham). 209 p.

Bois P-A (2000) *Introduction à la mécanique théorique des fluides.* Ellipses, Paris. 418 p.

Bottom DL, Simenstad CA, Burke J, Baptista AM, Jay DA, Jones KK, Casillas E & Schiewe MH (2005) Salmon at river's end: The role of the estuary in the decline and recovery of Columbia River salmon. NMFS-NWFSC-68 (U.S. Dept. of Commerce, NOAA Tech. Memo.). 246 p.

Bouchard A & Morin J (2000) Reconstitution des débits du fleuve Saint-Laurent entre 1932 et 1998. Rapport Technique RT-101 (Environnement Canada, Sainte-Foy). 71 p.

Boudreau P, Leclerc M & Fortin GR (1994) Modélisation hydrodynamique du lac Saint-Pierre, fleuve Saint-Laurent : l'influence de la végétation aquatique. *Can. J. Civ. Eng.* 21:471-489.

Bourgault D & Koutitonsky VG (1999) Real-time monitoring of the freshwater discharge at the head of the St. Lawrence Estuary. *Atmos. Ocean* 37(2):203-220.

Brickman D & Drozdowski A (2012) Development and validation of a regional shelf model for maritime Canada based on the NEMO-OPA circulation model. Canadian Technical Report of Hydrography and Ocean Sciences 278. 66 p.

Bube KP & Langan RT (1997) Hybrid $l^1/l^2$ minimization with applications to tomography. *Geophysics* 62(4):1183-1195.

Buschman FA, Hoitink AJF, van der Vegt M & Hoekstra P (2009) Subtidal water level variation controlled by river flow and tides. *Water Resour. Res.* 45(10):W10420.

Buschman FA, Hoitink AJF, van der Vegt M & Hoekstra P (2010) Subtidal flow division at a shallow tidal junction. *Water Resour. Res.* 46(12):W12515.

Byrd RH, Gilbert JC & Nocedal J (2000) A trust region method based on interior point techniques for nonlinear programming. *Math. Program.* 89(1):149-185.

Cáceres M, Valle-Levinson A & Atkinson L (2003) Observations of cross-channel structure of flow in an energetic tidal channel. *J. Geophys. Res.* 108(C4):3114.

Candela J, Beardsley RC & Limeburner R (1992) Separation of tidal and subtidal currents in ship-mounted acoustic Doppler current profiler observations. *J. Geophys. Res.* 97(C1):769-788.

Capra H, Pella H, Morin J, LePichon C, Perraud C, Datry T, Secretan Y, Jouve P & Matte P (2010) Conséquences de l'artificialisation de l'hydrologie du Rhône sur la structuration des communautés d'invertébrés et de poissons - Rapport final. Rapport Cemagref - Agence de l'Eau RM&C. 104 p.

Cea L & French JR (2012) Bathymetric error estimation for the calibration and validation of estuarine hydrodynamic models. *Estuar. Coast. Shelf Sci.* 100(0):124-132.

Champoux O, Morin J, Doyon B, Bouchard A, Dallaire É, Morin A, Roy N & Côté J-P (2003) Floodplain mapping of Lake des Deux-Montagnes, modelling of wind-generated waves for Lake St. Louis and Lake des Deux-Montagnes, integration of landside datasets. Rapport technique RT-126 (Environnement Canada, Sainte-Foy). 58 p.

Chassé J, El-Sabh MI & Murty TS (1993) A numerical model for water level oscillations in the St. Lawrence estuary, Canada Part I: Tides. *Mar. Geod.* 16(2):109-124.

Chen C-l (1991) Unified theory on power laws for flow resistance. *J. Hydraul. Eng.* 117(3):371-389.

Chen Y-C & Chiu C-L (2002) An efficient method of discharge measurement in tidal streams. *J. Hydrology* 265(1-4):212-224.

Cheylus JF & Ouellet Y (1971) Étude du modèle mathématique de la propagation des marées dans le fleuve Saint-Laurent. Application du modèle mathématique et étude de la Région de l'Île d'Orléans. Rapport CRE-71/05 (Université Laval, Québec). 37 p.

CHS (2008) *Hydrographic survey management guidelines.* Canadian Hydrographic Service, Fisheries and Oceans Canada. 63 p.

Church I, Brucker S, Hughes Clarke JE, Haigh S, Bartlett J & Janzen T (2009) Developing strategies to facilitate long term seabed monitoring in the Canadian Arctic using post processed GPS and tidal models. *U.S. Hydro 2009 Conference.* (Norfolk, VA) Hydrographic Society of America.

Church I, Clarke JEH, Haigh S, Santos M, Lamplugh M, Griffin J & Parrott R (2008) Using Globally-corrected GPS solutions to assess the viability of hydrodynamic modeling in the Bay of Fundy. *Canadian Hydrographic Conference and National Surveyors Conference.* (Victoria, BC, Canada) IIC Technologies.

Codiga DL (2011) Unified tidal analysis and prediction using the UTide Matlab functions. Technical Report 2011-01 (Graduate School of Oceanography, University of Rhode Island, Narragansett). 59 p.

Collignon AG & Stacey MT (2012) Intratidal dynamics of fronts and lateral circulation at the shoal–channel interface in a partially stratified estuary. *J. Phys. Oceanogr.* 42(5):869-883.

Côté J-P & Morin J (2007) Principales interventions humaines survenues dans le fleuve Saint-Laurent entre Montréal et Québec au 20e siècle: 1907-2005. Rapport technique SMC Québec - Section Hydrologie, RT-141 (Environnement Canada, Sainte-Foy). 65 p.

Couillard D (1987) Qualité des sédiments en suspension et de fond du système Saint-Laurent (Canada). *Hydrol. Sci. J.* 32(4):445-467.

Crowder DW & Diplas P (2000) Using two-dimensional hydrodynamic models at scales of ecological importance. *J. Hydrology* 230(3-4):172-191.

D'Anglejan B (1990) Recent sediments and sediment transport processes in the St. Lawrence Estuary. *Oceanography of a large-scale estuarine system: The St. Lawrence*, El-Sabh MI & Silverberg N (Édit.) Springler-Verlag, New York. p 109-129.

Dailey JE & Harleman DRF (1972) Numerical model for the prediction of transient water quality in estuary networks. Report No. 158, RT72-72 (Hydrodynamics Laboratory, Massachusetts Institute of Technology, Cambridge, Massachusetts). 226 p.

Daniell PJ (1946) Discussion of "On the theoretical specification and sampling properties of autocorrelated time-series". *Suppl. J. Roy. Stat. Soc.* 8(1):88-90.

Darwin GH (1891) Bakerian lecture: On tidal prediction. *Philos. Trans. Roy. Soc. London* A182:159-229.

de Boor C (1978) *A practical guide to splines.* Springer-Verlag, New York. 372 p.

De Borne de Grandpre C, El-Sabh MI & Salomon JC (1981) A two-dimensional numerical model of the vertical circulation of tides in the St. Lawrence estuary. *Estuar. Coast. Shelf Sci.* 12(4):375-387.

de Paiva RCD, Buarque DC, Collischonn W, Bonnet M-P, Frappart F, Calmant S & Bulhões Mendes CA (2013) Large-scale hydrologic and hydrodynamic modeling of the Amazon River basin. *Water Resour. Res.* 49(3):1226-1243.

Dhatt G, Touzot G & Lefrançois E (2005) *Méthode des éléments finis - Une présentation.* Hermes - Lavoisier. 601 p.

Dierckx P, Smets E, Piessens R & Temmerman M (1981) A new method of cubature using spline functions. *Ocean Dyn.* 34(2):61-79.

DiLorenzo JL, Huang P, Thatcher ML & Najarian TO (1993) Dredging impacts on Delaware Estuary tides. *3rd International Conference on Estuarine and Coastal Modeling.* (Oak Brook, IL, September 8-10, 1993), Spaulding ML (Édit.) ASCE, p 86-104.

Dinehart RL & Burau JR (2005a) Averaged indicators of secondary flow in repeated acoustic Doppler current profiler crossings of bends. *Water Resour. Res.* 41(9):1-18.

Dinehart RL & Burau JR (2005b) Repeated surveys by acoustic Doppler current profiler for flow and sediment dynamics in a tidal river. *J. Hydrology* 314(1-4):1-21.

Dohler GC (1961) Current survey, St-Lawrence River, Montréal-Québec, 1960. (Can. Hydro. Serv. Dept. of Mines and Technical Surveys, Ottawa). 58 p.

Doodson AT (1921) The harmonic development of the tide-generating potential. *Proc. Roy. Soc. London* A100(704):305-329.

Doyon B (2011) Recherche de nouvelles aires de dépôt de matériaux dragués dans le secteur de Saint-Pierre-les-Becquets. Rapport technique (Secteur Génie hydraulique de la Garde côtière canadienne - Région du Québec, Québec). 69 p.

Drapeau G (2008) Surélévations de la marée dans la région de Québec. *76e Congrès de l'Acfas.* (Québec, 5-9 mai 2008).

Dronkers JJ (1964) *Tidal Computations in Rivers and Coastal Waters.* North-Holland Publishing Company, Amsterdam. 518 p.

DuMouchel WH & O'Brien FL (1989) Integrating a robust option into a multiple regression computing environment. *Computer Science and Statistics: Proceedings of the 21st Symposium*

*on the Interface*. (Alexandria, VA), Malone L & Berk K (Édit.) American Statistical Association, p 297-301.

Edson JB, Hinton AA, Prada KE, Hare JE & Fairall CW (1998) Direct covariance flux estimates from mobile platforms at sea. *J. Atmos. Oceanic Technol.* 15(2):547-562.

El-Sabh MI & Murty TS (1990) Mathematical modelling of tides in the St. Lawrence Estuary. *Oceanography of a large-scale estuarine system: The St. Lawrence*, El-Sabh MI & Silverberg N (Édit.) Springler-Verlag, New York. p 10-50.

El-Sabh MI, Murty TS & Briand J-M (1988) Negative storm surges on Canada's East coast. *Natural and Man-Made Hazards*, El-Sabh MI & Murty TS (Édit.) Springer Netherlands. p 305-316.

Emery WJ & Thomson RE (2001) *Data Analysis Methods in Physical Oceanography*. Elsevier, Amsterdam, Netherlands. 654 p.

Espino M, Maidana MA, Sánchez-Arcilla A & German A (2007) Hydrodynamics in the Huelva Estuary: Tidal model calibration using field data. *J. Waterw. Port Coast. Ocean Eng.* 133(5):313-323.

Falcão AP, Mazzolari A, Gonçalves AB, Araújo MAVC & Trigo-Teixeira A (2013) Influence of elevation modelling on hydrodynamic simulations of a tidally-dominated estuary. *J. Hydrology* 497(0):152-164.

Flinchem EP & Jay DA (2000) An introduction to wavelet transform tidal analysis methods. *Estuar. Coast. Shelf Sci.* 51(2):177-200.

Foreman MGG (1977) Manual for tidal heights analysis and prediction. Pacific Marine Science Report 77-10 (Institute of Ocean Sciences, Patricia Bay, Sidney, BC). 58 p.

Foreman MGG, Cherniawsky JY & Ballantyne VA (2009) Versatile harmonic tidal analysis: Improvements and applications. *J. Atmos. Oceanic Technol.* 26(4):806-817.

Foreman MGG & Henry RF (1989) The harmonic analysis of tidal model time series. *Adv. Water Resour.* 12(3):109-120.

Forrester WD (1972) Tidal transports and streams in the St. Lawrence River and Estuary. *Int. Hydrogr. Rev.* 49:95-108.

Friedrichs CT & Aubrey DG (1988) Non-linear tidal distortion in shallow well-mixed estuaries: A synthesis. *Estuar. Coast. Shelf Sci.* 27(5):521-545.

Fritsch F & Carlson R (1980) Monotone piecewise cubic interpolation. *SIAM J. Numer. Anal.* 17(2):238-246.

Gagnon M (1994) *Modélisation tridimentionnelle des courants de marée et de densité dans l'estuaire du Saint-Laurent par la méthode des éléments finis*. Ph.D. thesis (Université Laval, Québec, Canada). 454 p.

Gagnon M (1995) Bilan régional - Québec-Lévis. Zone d'intervention prioritaire 14. (Centre Saint-Laurent, Environnement Canada, Plan Saint-Laurent). 65 p.

Gallo MN & Vinzon SB (2005) Generation of overtides and compound tides in Amazon estuary. *Ocean Dyn.* 55(5-6):441-448.

García C, Oberg K & García M (2007) ADCP measurements of gravity currents in the Chicago River, Illinois. *J. Hydraul. Eng.* 133(12):1356-1366.

George KJ & Simon B (1984) The species concordance method of tide predictions in estuaries. *Int. Hydrogr. Rev.* 61(1):121-145.

Geyer WR & Signell RP (1990) Measurements of tidal flow around a headland with a shipboard acoustic Doppler current profiler. *J. Geophys. Res.* 95(C3):3189-3197.

Ghilani CD & Wolf PR (2012) *Elementary Surveying: An Introduction to Geomatics.* Prentice-Hall, 13th edition. 983 p.

Godin G (1971) Hydrodynamical studies in the St. Lawrence river. MS Report No. 18 (Marine Sciences Branch, Department of Energy, Mines and Resources). 116 p.

Godin G (1972) *The Analysis of Tides.* University of Toronto Press, Toronto. 264 p.

Godin G (1984) The tide in rivers. *Int. Hydrogr. Rev.* 61:159-170.

Godin G (1985) Modification of river tides by the discharge. *J. Waterw. Port Coast. Ocean Eng.* 111(2):257-274.

Godin G (1991) Compact approximations to the bottom friction term, for the study of tides propagating in channels. *Contin. Shelf Res.* 11(7):579-589.

Godin G (1999) The propagation of tides up rivers with special considerations on the Upper Saint Lawrence River. *Estuar. Coast. Shelf Sci.* 48(3):307-324.

Godin G & Martinez A (1994) Numerical experiments to investigate the effects of quadratic friction on the propagation of tides in a channel. *Contin. Shelf Res.* 14(7-8):723-748.

Goncalves RM, Awange JL, Krueger CP, Heck B & Coelho LdS (2012) A comparison between three short-term shoreline prediction models. *Ocean Coastal Manage.* 69(0):102-110.

Gunawan B, Sterling M & Knight DW (2010) Using an acoustic Doppler current profiler in a small river. *Water Environ. J.* 24(2):147-158.

Hébert S & Belley J (2005) Le Saint-Laurent - La qualité des eaux du fleuve 1990-2003. Envirodoq n° ENV/2005/0095, collection n° QE/156 (Ministère de l'Environnement, Direction du suivi de l'état de l'environnement, Québec). 25 p.

Hench JL & Luettich RA (2003) Transient Tidal Circulation and Momentum Balances at a Shallow Inlet. *J. Phys. Oceanogr.* 33(4):913-932.

Heniche M, Secretan Y, Boudreau P & Leclerc M (2000a) A two-dimensional finite element drying-wetting shallow water model for rivers and estuaries. *Adv. Water Resour.* 23(4):359-372.

Heniche M, Secretan Y & Leclerc M (2000b) HYDROSIM 1.0a06: Guide d'utilisation. Rapport R482-G2 (INRS-Eau, Québec). 100 p.

Heniche M, Secretan Y & Leclerc M (2001) DISPERSIM 1.0a02: Guide d'utilisation. Rapport R558-G2 (INRS-Eau, Québec). 115 p.

Heniche M, Secretan Y, Morin J, Cantin J-F & Leclerc M (2006) Two-dimensional depth averaged fluvial thermal regime prediction. Rapport R-859 (INRS-ETE). 33 p.

Hess K (2003) Water level simulation in bays by spatial interpolation of tidal constituents, residual water levels, and datums. *Contin. Shelf Res.* 23(5):395-414.

Hicks F (1997) Accuracy and conservation characteristics of the numerical algorithm in Environment Canada's ONE-D model. *Can. J. Civ. Eng.* 24(4):560-569.

Holland PW & Welsch RE (1977) Robust regression using iteratively reweighted least-squares. *Commun. Stat.-Theor. M.* 6(9):813-827.

Horsburgh KJ & Wilson C (2007) Tide-surge interaction and its role in the distribution of surge residuals in the North Sea. *J. Geophys. Res.* 112(C8):C08003.

Howarth MJ & Proctor R (1992) Ship ADCP measurements and tidal models of the North Sea. *Contin. Shelf Res.* 12(5-6):601-623.

Hsu M-H, Kuo AY, Kuo J-T & Liu W-C (1999) Procedure to calibrate and verify numerical models of estuarine hydrodynamics. *J. Hydraul. Eng.* 125(2):166-182.

Huber PJ (1996) *Robust Statistical Procedures.* CBMS-NSF Regional Conference Series in Applied Mathematics, Society of Industrial and Applied Mathematics, Bayreuth, Germany, 2nd edition. 67 p.

Hughes Clarke JE, Dare P, Beaudoin J & Bartlett J (2005) A stable vertical reference for bathymetric surveying and tidal analysis in the high Arctic. *U.S. Hydrographic Conference.* (San Diego, CA) Hydrographic Society of America.

Ingram RG & El-Sabh MI (1990) Fronts and mesoscale features in the St. Lawrence Estuary. *Oceanography of a large-scale estuarine system: The St. Lawrence*, El-Sabh MI & Silverberg N (Édit.) Springler-Verlag, New York. p 71-93.

Jay DA (1991) Green's law revisited: Tidal long wave propagation in channels with strong topography. *J. Geophys. Res.* 96(20):585-598.

Jay DA (2009) Evolution of tidal amplitudes in the eastern Pacific Ocean. *Geophys. Res. Lett.* 36(4):L04603.

Jay DA (2010) Estuarine variability. *Contemporary Issues in Estuarine Physics*, Valle-Levinson A (Édit.) Cambridge University Press, New York. p 62-99.

Jay DA & Flinchem EP (1995) Wavelet transform analyses of non-stationary tidal currents. *IEEE Fifth Working Conference on Current Measurement.* (St. Petersburg, FL, 7-9 Feb., 1995), Anderson SP, Appell GF & Williams AJ (Édit.), p 100-105.

Jay DA & Flinchem EP (1997) Interaction of fluctuating river flow with a barotropic tide: A demonstration of wavelet tidal analysis methods. *J. Geophys. Res.* 102(C3):5705-5720.

Jay DA & Flinchem EP (1999) A comparison of methods for analysis of tidal records containing multi-scale non-tidal background energy. *Contin. Shelf Res.* 19(13):1695-1732.

Jay DA & Kukulka T (2003) Revising the paradigm of tidal analysis – the uses of non-stationary data. *Ocean Dyn.* 53(3):110-125.

Jay DA, Leffler K & Degens S (2011) Long-term evolution of Columbia River tides. *J. Waterw. Port Coast. Ocean Eng.* 137(4):182-191.

Jung HC, Jasinski M, Kim J-W, Shum CK, Bates P, Neal J, Lee H & Alsdorf D (2012) Calibration of two-dimensional floodplain modeling in the central Atchafalaya Basin Floodway System using SAR interferometry. *Water Resour. Res.* 48(7):W07511.

Kamphuis JW (1968) Mathematical model study of the propagation of tides in the St. Lawrence River and Estuary. Report MH 105 (Nat. Res. Coun. Rep., DME, Ottawa). 62 p.

Kelecy TM, Born GH, Parke ME & Rocken C (1994) Precise mean sea level measurements using the Global Positioning System. *J. Geophys. Res.* 99(C4):7951-7959.

Kessler E & Lorenz DL (2010) Low-flow characteristics of the Mississippi River upstream from the Twin Cities Metropolitan Area, Minnesota, 1932-2007. Scientific Investigations Report 2010-5163 (U.S. Geological Survey). 14 p.

Kostaschuk R, Best J, Villard P, Peakall J & Franklin M (2005) Measuring flow velocity and sediment transport with an acoustic Doppler current profiler. *Geomorphology* 68(1-2):25-37.

Kukulka T & Jay DA (2003a) Impacts of Columbia River discharge on salmonid habitat: 1. A nonstationary fluvial tide model. *J. Geophys. Res.* 108(C9):3293.

Kukulka T & Jay DA (2003b) Impacts of Columbia River discharge on salmonid habitat: 2. Changes in shallow-water habitat. *J. Geophys. Res.* 108(C9):3294.

Lapidus A (1967) A detached shock calculation by second-order finite differences. *Journal of Computational Physics* 2(2):154-177.

Le Hir P, Roberts W, Cazaillet O, Christie M, Bassoullet P & Bacher C (2000) Characterization of intertidal flat hydrodynamics. *Contin. Shelf Res.* 20(12-13):1433-1459.

LeBlond PH (1978) On tidal propagation in shallow rivers. *J. Geophys. Res.* 83(C9):4717-4721.

LeBlond PH (1979) Forced fortnightly tides in shallow rivers. *Atmos. Ocean* 17(3):253-264.

LeBlond PH (1991) Tides and their interactions with other oceanographic phenomena in shallow water (Review). *Tidal Hydrodynamics*, Parker BB (Édit.) Wiley, New York. p 357-378.

Leclerc M, Bellemare J-F & Trussard S (1990) Simulation hydrodynamique de l'estuaire supérieur du fleuve Saint-Laurent (Canada) avec un modèle aux éléments finis couvrant-découvrant. *Can. J. Civ. Eng.* 17:739-751.

Lefaivre D, Hamdi S & Morse B (2009) Statistical analysis of the 30-day water level forecasts in the St. Lawrence River. *Mar. Geod.* 32(1):30-41.

Leffler KE & Jay DA (2009) Enhancing tidal harmonic analysis: Robust (hybrid $L^1/L^2$) solutions. *Contin. Shelf Res.* 29(1):78-88.

Lévesque L (1977) Étude du modèle mathématique de la propagation de la marée dans l'Estuaire du Saint-Laurent. Cahier d'Information, N°2 (Section d'Océanographie, Université du Québec à Rimouski). 160 p.

Lévesque L, Murty TS & El-Sabh MI (1979) Numerical modeling of tidal propagation in the St. Lawrence Estuary. *Int. Hydrogr. Rev.* 56(2):117-132.

Li C, Valle-Levinson A, Atkinson LP & Royer TC (2000) Inference of tidal elevation in shallow water using a vessel-towed acoustic Doppler current profiler. *J. Geophys. Res.* 105(C11):26225-26236.

Liu Y-Z, Shi JZ & Perrie W (2007) A theoretical formulation for modeling 3D wave and current interactions in estuaries. *Adv. Water Resour.* 30(8):1737-1745.

Long B, Bouchard D & Dumas J-P (1980) Étude des variations de la charge solide du fleuve Saint-Laurent entre Trois-Rivières et Gentilly. Compte rendu des campagnes de terrain (1978-1979). (Université du Québec à Rimouski, INRS-Océanologie, Rimouski).

Lu Y & Lueck RG (1999a) Using a broadband ADCP in a tidal channel. Part I: Mean flow and shear. *J. Atmos. Oceanic Technol.* 16(11):1556-1567.

Lu Y & Lueck RG (1999b) Using a broadband ADCP in a tidal channel. Part II: Turbulence. *J. Atmos. Oceanic Technol.* 16(11):1568-1579.

Madec G (2008) NEMO reference manual, ocean dynamics component : NEMO-OPA. Preliminary version. No 27 ISSN No 1288-1619 (Note du Pole de modélisation, Institut Pierre-Simon Laplace (IPSL), France).

Marche C & Partenscky HW (1974) Étude de la déformation progressive de l'onde de marée dans l'Estuaire du Saint-Laurent. Rapport de la section hydraulique (École Polytechnique, Université de Montréal). 126 p.

Marsden RF & Gratton Y (1997) A method for correcting vertical velocities measured from a vessel-mounted acoustic Doppler current profiler. *J. Atmos. Oceanic Technol.* 14(6):1533-1538.

Martin PJ, Smith SR, Posey PG, Dawson GM & Riedlinger SH (2009) Use of the Oregon State University tidal inversion software (OTIS) to generate improved tidal prediction in the East-Asian Seas. NRL/MR/7320-09-9176 (Naval Research Laboratory, Stennis Space Center, MS). 29 p.

MathWorks (2012) *R2010a MathWorks documentation.* http://www.mathworks.com/help/releases/R2010a/helpdesk.html (Consulté le 22 avril 2014).

Matte P, Jay DA & Zaron ED (2013) Adaptation of classical tidal harmonic analysis to nonstationary tides, with application to river tides. *J. Atmos. Oceanic Technol.* 30(3):569-589.

Matte P, Secretan Y & Morin J (2010) Deriving continuous hydrodynamic data from non-synoptic measurements in the St. Lawrence fluvial estuary. *6th International Symposium on Environmental Hydraulics.* (Athens, Greece, 23-25 June, 2010), Christodoulou GC & Stamou AI (Édit.), p 851-856.

Matte P, Secretan Y & Morin J (2014a) Quantifying lateral and intratidal variability in water level and velocity in a tide-dominated river using combined RTK GPS and ADCP measurements. *Limnol. Oceanogr.: Methods* 12:279-300.

Matte P, Secretan Y & Morin J (2014b) A robust estimation method for correcting dynamic draft error in PPK GPS elevation using ADCP tilt data. *J. Atmos. Oceanic Technol.* 31(3):729-738.

Matte P, Secretan Y & Morin J (2014c) Temporal and spatial variability of tidal-fluvial dynamics in the St. Lawrence fluvial estuary: An application of nonstationary tidal harmonic analysis. *J. Geophys. Res.* 119:5724–5744.

Matthews PA (1997) The impact of nonsynoptic sampling on mesoscale oceanographic surveys with towed instruments. *J. Atmos. Oceanic Technol.* 14(1):162-174.

Miller SD, Hristov TS, Edson JB & Friehe CA (2008) Platform motion effects on measurements of turbulence and air–sea exchange over the open ocean. *J. Atmos. Oceanic Technol.* 25(9):1683-1694.

Moegling CH, Dasler JL, Creech JC & Canter P (2009) GPS derived water levels for large scale hydrographic surveys: Implementation of a separation model of the Columbia River datum, a case study. *U.S. Hydro 2009 Conference.* (Norfolk, VA) Hydrographic Society of America.

Moftakhari HR, Jay DA, Talke SA, Kukulka T & Bromirski PD (2013) A novel approach to flow estimation in tidal rivers. *Water Resour. Res.* 49(8):4817-4832.

Morin J (2001) *Modélisation des facteurs abiotiques de l'écosystème fluvial du lac Saint-François, fleuve Saint-Laurent*. Ph.D. thesis (INRS-Eau, Québec). 71 p.

Morin J, Boudreau P, Secretan Y & Leclerc M (2000a) Pristine Lake Saint-François, St. Lawrence River: Hydrodynamic simulation and cumulative impact. *J. Great Lakes Res.* 26(4):384-401.

Morin J & Champoux O (2006) Integrated modelling of the physical processes and habitats of the St. Lawrence River. *Water Availability Issues for the St. Lawrence River: An Environmental Synthesis*, Talbot A (Édit.) Environment Canada, Montreal. p 24-39.

Morin J, Champoux O, Bouchard A & Rioux D (2003a) High resolution 2D hydrodynamic modelling of Lake Saint-Louis: Definition of scenarios, simulation and validation/calibration. Technical Report MSC Québec – Hydrology RT-125 (Environnement Canada, Sainte-Foy). 90 p.

Morin J, Champoux O, Martin S & Turgeon K (2005) Modélisation intégrée de la réponse de l'écosystème dans le fleuve Saint-Laurent : Rapport final des activités entreprises dans le cadre du Plan d'étude sur la régularisation du lac Ontario et du fleuve Saint-Laurent. Rapport scientifique SMC Québec – Section Hydrologie RS-108 (Environnement Canada, Sainte-Foy). 130 p.

Morin J, Leclerc M, Secretan Y & Boudreau P (2000b) Integrated two-dimensional macrophytes-hydrodynamic modeling. *J. Hydraul. Res.* 38:163-172.

Morin J, Mingelbier M, Bechara JA, Champoux O, Secretan Y, Jean M & Frenette J-J (2003b) Emergence of new explanatory variables for 2D habitat modelling in large rivers: The St. Lawrence Experience. *Can. Water Resour. J.* 28(2):249-272.

Morse B (1990) St-Lawrence River water-levels study: Application of the ONE-D hydrodynamic model. (Transport Canada, Waterways Development Division, Canadian Coast Guard).

Munk WH, Zetler B & Groves GW (1965) Tidal cusps. *Geophys. J. Roy. Astron. Soc.* 10(2):211-219.

Muste M, Yu K, Pratt T & Abraham D (2004a) Practical aspects of ADCP data use for quantification of mean river flow characteristics; Part II: fixed-vessel measurements. *Flow Meas. Instrum.* 15(1):17-28.

Muste M, Yu K & Spasojevic M (2004b) Practical aspects of ADCP data use for quantification of mean river flow characteristics; Part I: moving-vessel measurements. *Flow Meas. Instrum.* 15(1):1-16.

Nabi M, de Vriend HJ, Mosselman E, Sloff CJ & Shimizu Y (2012) Detailed simulation of morphodynamics: 1. Hydrodynamic model. *Water Resour. Res.* 48(12):W12523.

Nayak RK & Shetye SR (2003) Tides in the Gulf of Khambhat, west coast of India. *Estuar. Coast. Shelf Sci.* 57:249-254.

Nidzieko NJ (2010) Tidal asymmetry in estuaries with mixed semidiurnal/diurnal tides. *J. Geophys. Res.* 115(C8):C08006.

Nidzieko NJ & Ralston DK (2012) Tidal asymmetry and velocity skew over tidal flats and shallow channels within a macrotidal river delta. *J. Geophys. Res.* 117(C3):C03001.

NOAA (2010) Field procedures manual. (National Oceanic and Atmospheric Administration, Office of Coast Survey). 326 p.

Nystrom E, Rehmann C & Oberg K (2007) Evaluation of mean velocity and turbulence measurements with ADCPs. *J. Hydraul. Eng.* 133(12):1310-1318.

Old CP & Vennell R (2001) Acoustic Doppler current profiler measurements of the velocity field of an ebb tidal jet. *J. Geophys. Res.* 106(C4):7037-7049.

Onset Computer Corporation (2012) HOBO U20 water level logger manual. 7 p.

Ouellet Y & Cerceau J (1975) Simulation of the salinity distribution in the St. Lawrence Estuary by a two-dimensional mathematical model. *Symposium on Modeling Techniques for Waterways, Harbors and Coastal Engineering, ASCE.* (San Francisco, CA, September 3-5, 1975), p 1249-1269.

Ouellet Y, Dupuis P & Soulaïmani A (1986) Modélisation d'un écoulement tourbillonnaire en régime permanent. *Can. J. Civ. Eng.* 13:310-317.

Park S-Y, Byun D-S & Hart D (2012) A solution for the correct interpolation of data across regions with abrupt changes in tidal phase-lag. *Ocean Sci. J.* 47(3):215-219.

Parker BB (1991) The relative importance of the various nonlinear mechanisms in a wide range of tidal interactions (Review). *Tidal Hydrodynamics*, Parker BB (Édit.) Wiley, New York. p 237-268.

Parker BB (2007) Tidal analysis and prediction. NOS CO-OPS 3 (U.S. Department of Commerce, Silver Spring, Maryland). 378 p.

Partenscky HW & Warmoes JC (1970) Étude des marées dans l'Estuaire du Saint-Laurent à l'aide d'un modèle mathématique linéarisé. (Rapport soumis au Conseil National de Recherche du Canada). 677 p.

Pawlowicz R, Beardsley B & Lentz S (2002) Classical tidal harmonic analysis including error estimates in MATLAB using T_TIDE. *Comput. Geosci.* 28(8):929-937.

Picado A, Dias JM & Fortunato AB (2010) Tidal changes in estuarine systems induced by local geomorphologic modifications. *Contin. Shelf Res.* 30(17):1854-1864.

Prandle D (1970) Combined one and two-dimensional mathematical model of the St. Lawrence River. LTR-HY-13 (National Research Council Canada, Canadian Hydraulics Centre).

Prandle D (1971) St. Lawrence River tidal model study – Quebec Harbour study – Results of numerical model tests. LTR-HY-18 (National Research Council Canada, Canadian Hydraulics Centre).

Prandle D (2009) *Estuaries: Dynamics, Mixing, Sedimentation and Morphology.* Cambridge University Press, New York. 248 p.

Prandle D & Crookshank NL (1972) Numerical studies of the St. Lawrence River. Technical Report (Division of Mechanical Engineering, Ottawa). 104 p.

Prandle D & Crookshank NL (1974) Numerical model of the St. Lawrence River Estuary. *J. Hydr. Eng. Div.-ASCE* 100(4):517-529.

Pugh DT & Vassie JM (1976) Tide and surge propagation off-shore in the Dowsing region of the North Sea. *Deutsche Hydrografische Zeitschrift* 29(5):163-213.

Reinsch C (1967) Smoothing by spline functions. *Numer. Math.* 10:177-183.

Rennie CD & Church M (2010) Mapping spatial distributions and uncertainty of water and sediment flux in a large gravel bed river reach using an acoustic Doppler current profiler. *J. Geophys. Res.* 115(F3):F03035.

Rennie CD & Rainville F (2006) Case study of precision of GPS differential correction strategies: Influence on aDcp velocity and discharge estimates. *J. Hydraul. Eng.* 132(3):225-234.

Riley JL, Milbert DG & Mader GL (2003) Hydrographic surveying on a tidal datum with kinematic GPS: NOS case study in Delaware Bay. *U.S. Hydro 2003 Conference.* (Biloxi, MS) Hydrographic Society of America.

Rinaldi M, Mengoni B, Luppi L, Darby SE & Mosselman E (2008) Numerical simulation of hydrodynamics and bank erosion in a river bend. *Water Resour. Res.* 44(9):W09428.

Rixen M, Allen JT & Beckers JM (2001) Non-synoptic versus pseudo-synoptic data sets: an assimilation experiment. *J. Mar. Syst.* 29(1-4):313-333.

Rixen M & Beckers J-M (2002) A synopticity test of a sampling pattern in the Alboran Sea. *J. Mar. Syst.* 35(1-2):111-130.

Robert S, Piotte D, Rassam J-C, Boivin R, Larivière R & Hausser R (1992) Study of the hydraulic regime of the St. Lawrence River between Montreal and the city of Québec. *Can. J. Civ. Eng.* 19:78-85.

Robitaille J (1998a) Bilan régional - Pointe-du-Lac-Deschambault. Zone d'intervention prioritaire 12. (Environnement Canada - région de Québec, Conservation de l'environnement, Centre Saint-Laurent). 90 p.

Robitaille J (1998b) Bilan régional - Portneuf-Saint-Nicolas. Zone d'intervention prioritaire 13. (Environnement Canada - région de Québec, Conservation de l'environnement, Centre Saint-Laurent). 78 p.

Rocken C, Kelecy TM, Born GH, Young LE, Purcell GH & Wolf SK (1990) Measuring precise sea level from a buoy using the global positioning system. *Geophys. Res. Lett.* 17(12):2145-2148.

Rodi W (1984) Turbulence models and their application in hydraulics. State of the art paper. *IAHR-AIRH*.

Roy F, Smith G, Senneville S, Dupont F, Chanut J & Erfani A (2012) Evaluation of NEMO oceanic simulations for high-resolution coupled weather forecasts in the Gulf of St. Lawrence. *CMOS.* (Montréal, Canada).

Roy Y, Secretan Y, Granger Y & Leclerc M (2000) MODELEUR 1.0a07: Guide d'utilisation. Rapport R482-G3F (INRS-Eau, Québec). 286 p.

Sassi M, Hoitink A, de Brye B, Vermeulen B & Deleersnijder E (2011) Tidal impact on the division of river discharge over distributary channels in the Mahakam Delta. *Ocean Dyn.* 61(12):2211-2228.

Sassi MG & Hoitink AJF (2013) River flow controls on tides and tide-mean water level profiles in a tidal freshwater river. *J. Geophys. Res.* 118(9):4139-4151.

Sassi MG, Hoitink AJF, de Brye B & Deleersnijder E (2012) Downstream hydraulic geometry of a tidally influenced river delta. *Journal of Geophysical Research: Earth Surface* 117(F4):F04022.

Saucier FJ & Chassé J (2000) Tidal circulation and buoyancy effects in the St. Lawrence Estuary. *Atmos. Ocean* 38(4):1-52.

Saucier FJ, Chassé J, Couture M, Dorais R, D'Astous A, Lefaivre D & Gosselin A (1997) *Atlas of tidal currents: St. Lawrence Estuary, from Cap de Bon-Désir to Trois-Rivières.* Canadian Hydrographic Service, Fisheries and Oceans Canada, Ottawa. 108 p.

Saucier FJ, Chassé J, Couture M, Dorais R, D'Astous A, Lefaivre D & Gosselin A (1999) The making of a surface current atlas of the St. Lawrence Estuary, Canada. *Fourth international*

*conference on computer modelling of seas and coastal regions.*Brebbia CA & Anagnostopoulos P (Édit.) Wessex Institute of Technology Press, p 87-97.

Saucier FJ, Roy F, Gilbert D, Pellerin P & Ritchie H (2003) Modeling the formation and circulation processes of water masses and sea ice in the Gulf of St. Lawrence, Canada. *J. Geophys. Res.* 103(C8):3269-3289.

Saucier FJ, Roy F, Senneville S, Smith G, Lefaivre D, Zakardjian B & Dumais J-F (2009) Modélisation de la circulation dans l'estuaire et le golfe du Saint-Laurent en réponse aux variations du débit d'eau douce et des vents. *Rev. Sci. Eau* 22(2):159-176.

Secretan Y (2013) *H2D2 Software.* http://www.gre-ehn.ete.inrs.ca/H2D2 (Consulté le 22 avril 2014).

Secretan Y & Dubos V (2005) Modélisation de la variabilité verticale des vitesses dans un modèle hydrodynamique 2D horizontal. *Rev. Europ. Élem. Finis* 14(1):115-138.

Secretan Y & Leclerc M (1998) MODELEUR: a 2D hydrodynamic G.I.S. and simulation software. *3rd International Conference on Hydroinformatics '98, IAHR.* (Copenhagen, Denmark, August 24-26,), p 1-8.

Secretan Y, Leclerc M, Duchesne S & Heniche M (2001) Une méthodologie de modélisation numérique de terrain pour la simulation hydrodynamique bidimensionnelle. *Rev. Sci. Eau* 14(2):189-214.

Seim H, Blanton J & Elston S (2006) Tidal circulation and energy dissipation in a shallow, sinuous estuary. *Ocean Dyn.* 56(3-4):360-375.

Shaw AGP & Tsimplis MN (2010) The 18.6 yr nodal modulation in the tides of Southern European coasts. *Contin. Shelf Res.* 30(2):138-151.

Shields F & Rigby J (2005) River habitat quality from river velocities measured using acoustic Doppler current profiler. *Environ. Manage.* 36(4):565-575.

Sime LC, Ferguson RI & Church M (2007) Estimating shear stress from moving boat acoustic Doppler velocity measurements in a large gravel bed river. *Water Resour. Res.* 43:W03418.

Simons RD, Monismith SG, Johnson LE, Winkler G & Saucier FJ (2006) Zooplankton retention in the estuarine transition zone of the St. Lawrence Estuary. *Limnol. Oceanogr.* 51(6):2621-2631.

Simons RD, Monismith SG, Saucier FJ, Johnson LE & Winkler G (2010) Modelling stratification and baroclinic flow in the estuarine transition zone of the St. Lawrence estuary. *Atmos. Ocean* 48(2):132-146.

Simpson MR (2001) Discharge measurements using a broad-band acoustic Doppler current profiler. Open-File Report 01-1 (U.S. Geological Survey, Sacramento, California). 134 p.

Simpson MR & Oltmann RN (1993) Discharge-measurement system using an acoustic Doppler current profiler with applications to large rivers and estuaries. Water-Supply Paper 2395 (U.S. Geological Survey, Denver, Colorado). 37 p.

Smagorinsky J (1963) General circulation experiments with the primitive equations. *Monthly Weather Review* 91(3):99-164.

Smith GC, Roy F & Brasnett B (2013) Evaluation of an operational ice–ocean analysis and forecasting system for the Gulf of St Lawrence. *Q. J. Roy. Meteor. Soc.* 139(671):419-433.

Smith W (1971) Techniques and equipment required for precise stream gaging in tide-affected fresh-water reaches of the Sacramento River, California. Water-Supply Paper 1869-G (U.S. Geological Survey). 46 p.

Sokolov S & Rintoul SR (1999) Some remarks on interpolation of nonstationary oceanographic fields. *J. Atmos. Oceanic Technol.* 16(10):1434-1449.

Soulaïmani A (1983) *Nouveaux aspects de l'application de la méthode des éléments finis en hydrodynamique*. Master (Université Laval, Québec, QC). 192 p.

Speer PE & Aubrey DG (1985) A study of non-linear tidal propagation in shallow inlet/estuarine systems Part II: Theory. *Estuar. Coast. Shelf Sci.* 21(2):207-224.

Stone M & Hotchkiss R (2007) Turbulence descriptions in two cobble-bed river reaches. *J. Hydraul. Eng.* 133(12):1367-1378.

Szupiany RN, Amsler ML, Best JL & Parsons DR (2007) Comparison of fixed- and moving-vessel flow measurements with an aDp in a large river. *J. Hydraul. Eng.* 133(12):1299-1309.

Tee K-T & Lim T-H (1987) The freshwater pulse - a numerical model with application to the St. Lawrence Estuary. *J. Mar. Res.* 45(4):871-909.

Teledyne RD Instruments (2009) WinRiver II User's Guide. 178 p.

Teledyne RD Instruments (2010) ADCP coordinate transformation: Formulas and calculations. 36 p.

Trimble (2003) *Real-Time Kinematic Surveying: Training Guide.* Trimble Navigation Limited. 368 p.

U.S. EPA (2012a) Vulnerability assessments in support of the Climate Ready Estuaries Program: A novel approach using expert judgement, Volume I: Results for the San Francisco Estuary Partnership (final report). EPA/600/R-11/058Fa (U.S. Environmental Protection Agency, Washington, DC). 157 p.

U.S. EPA (2012b) Vulnerability assessments in support of the Climate Ready Estuaries Program: A novel approach using expert judgement, Volume II: Results for the Massachusetts Bays Program (final report). EPA/600/R-11/058Fb (U.S. Environmental Protection Agency, Washington, DC). 157 p.

Umgiesser G, Canu DM, Cucco A & Solidoro C (2004) A finite element model for the Venice Lagoon. Development, set up, calibration and validation. *J. Mar. Syst.* 51(1-4):123-145.

Valle-Levinson A, Li C, Wong K-C & Lwiza KMM (2000) Convergence of lateral flow along a coastal plain estuary. *J. Geophys. Res.* 105(C7):17045-17061.

Vennell R & Beatson R (2006) Moving vessel acoustic Doppler current profiler measurement of tidal stream function using radial basis functions. *J. Geophys. Res.* 111:C09002.

Vincent R (1965) *An investigation of the tidal characteristics of the St. Lawrence Estuary by a mathematical model*. M.Sc. thesis (Université Laval, Québec). 119 p.

Waltz RA, Morales JL, Nocedal J & Orban D (2006) An interior algorithm for nonlinear optimization that combines line search and trust region steps. *Math. Program.* 107(3):391-408.

Wang B, Fringer OB, Giddings SN & Fong DA (2009) High-resolution simulations of a macrotidal estuary using SUNTANS. *Ocean Modelling* 28(1–3):167-192.

Warner JC, Geyer WR & Lerczak JA (2005) Numerical modeling of an estuary: A comprehensive skill assessment. *J. Geophys. Res.* 110(C5):C05001.

Watson C, Coleman R, White N, Church J & Govind R (2003) Absolute calibration of TOPEX/Poseidon and Jason-1 using GPS buoys in Bass Strait, Australia. *Mar. Geod.* 26(3-4):285-304.

Weisberg S (2005) *Applied Linear Regression.* Wiley, New York, 3rd edition. 336 p.

Willmott CJ (1982) Some comments on the evaluation of model performance. *B. Am. Meteorol. Soc.* 63:1309-1313.

Willmott CJ, Ackleson SG, Davis RE, Feddema JJ, Klink KM, Legates DR, O'Donnell J & Rowe CM (1985) Statistics for the evaluation and comparison of models. *J. Geophys. Res.* 90(C5):8995-9005.

Work PA, Hansen M & Rogers WE (1998) Bathymetric surveying with GPS and heave, pitch, and roll compensation. *J. Surv. Eng.* 124(2):73.

Xu Z, Saucier FJ & Lefaivre D (2006) Water level variations in the Estuary and Gulf of St. Lawrence. *Understanding Sea-Level Rise and Variability Workshop.* (Paris, France, June 6-9, 2006).

Yorke TH & Oberg KA (2002) Measuring river velocity and discharge with acoustic Doppler profilers. *Flow Meas. Instrum.* 13(5-6):191-195.

Zhao J, Hughes Clarke JE, Brucker S & Duffy G (2004) On the fly GPS tide measurement along the Saint John River. *Int. Hydrogr. Rev.* 5(3):48-58.

Zheng L, Chen C & Liu H (2003) A Modeling Study of the Satilla River Estuary, Georgia. I: Flooding-Drying Process and Water Exchange over the Salt Marsh-Estuary-Shelf Complex. *Estuaries* 26(3):651-669.

Zienkiewicz OC, Taylor RL & Nithiarasu P (2014) *The finite element method for fluid dynamics.* Butterworth-Heinemann, Elsevier, Waltham, MA, USA, 7th.

# ANNEXES

## A.1 Adaptation of classical tidal harmonic analysis to nonstationary tides, with application to river tides

Cet article présente un nouvel outil d'analyse de la marée en rivière, NS_TIDE, développé dans le cadre d'un stage de recherche (Travail dirigé I; 4 crédits) réalisé dans l'équipe du Prof. David A. Jay de la Portland State University (Oregon, États-Unis). Cet outil permet une analyse harmonique non-stationnaire de la marée en rivières en exprimant les niveaux moyens et les propriétés de la marée en une station en fonction des conditions de forçage externe du débit fluvial et de la marée océanique. L'outil NS_TIDE est à la base du modèle 1D développé dans l'objectif 2 de cette thèse. L'article est publié dans la revue *Journal of Atmospheric and Oceanic Technology*.

L'idée d'inclure les variables de forçage du débit et de la marée océanique directement dans les fonctions de base du modèle harmonique classique a été proposée par David A. Jay (second auteur). Ce dernier a participé à l'élaboration du modèle mathématique inclus dans NS_TIDE. Le développement du programme, basé sur un outil existant (T_TIDE), et l'application à la rivière Columbia ont été réalisés par l'auteur de cette thèse (premier auteur). Edward D. Zaron (troisième auteur) a contribué avec l'auteur principal à l'élaboration du modèle d'erreur et à la redéfinition des critères de sélection des composantes de marée. L'écriture de l'article a été réalisée en totalité par l'auteur principal; les coauteurs en ont révisé le contenu.

La référence complète de l'article est donnée ci-dessous :

Matte P, Jay DA & Zaron ED (2013) Adaptation of classical tidal harmonic analysis to nonstationary tides, with application to river tides. *J. Atmos. Oceanic Technol.* 30(3):569-589.

### A.1.1 Abstract

One of the most challenging areas in tidal analysis is the study of nonstationary signals with a tidal component, as they confront both current analysis methods and dynamical understanding. A new analysis tool has been developed, NS_TIDE, adapted to the study of nonstationary signals, in this case, river tides. It builds the nonstationary forcing directly into the tidal basis functions.

It is implemented by modification of T_TIDE; however, certain concepts, particularly the meaning of a constituent and the Rayleigh criterion, are redefined to account for the smearing effects on the tidal spectral lines by nontidal energy. An error estimation procedure is included that constructs a covariance matrix of the regression coefficients, based on either an uncorrelated or a correlated noise model. The output of NS_TIDE consists of time series of subtidal water levels [mean water level (MWL)] and tidal properties (amplitudes and phases), expressed in terms of external forcing functions. The method was tested using records from a station on the Columbia River, 172 km from the ocean entrance, where the tides are strongly altered by river flow. NS_TIDE hindcast explains 96.4% of the signal variance with a root-mean-square error of 0.165 m obtained from 288 parameters, far better than traditional harmonic analysis (38.5%, 0.604 m, and 127 parameters). While keeping the benefits of harmonic analysis, its advantages compared to existing tidal analysis methods include its capacity to distinguish frequencies within tidal bands without losing resolution in the time domain or data at the endpoints of the time series.

### A.1.2 Introduction

Surface tides in the deep ocean are predictable at most locations because they are nearly periodic. There are many situations, however, in which the observed tides (a combination of barotropic and baroclinic waves) are modulated by nontidal processes, some of which occur in the tidal frequency band. Perturbations of the tidal signal may arise from variations in external forcing – either oceanic, meteorological, hydrologic, or climatic. They may be abrupt and aperiodic (with energy at periods of a few hours to a few days), quasi periodic (e.g., a diurnal sea breeze or annual river flow cycle), long term (periods of years to decades), or secular (without an apparent period within the length of the available tidal record). Also, morphological modifications leading to changes in bed friction, surface slope, and/or vegetation may all alter tidal properties (Amin, 1983, 1985, Godin, 1985, DiLorenzo *et al.*, 1993, Horsburgh & Wilson, 2007, Jay, 2009, Jay *et al.*, 2011). Such circumstances present a severe challenge for conventional tidal prediction methods, but also an opportunity for dynamical inquiry, provided that adequate analytical tools are available. Our purpose here is to generalize traditional harmonic analysis (HA) to allow for the study of nonstationary tides. We accomplish this by building the forcing that causes the nonstationary tidal response into the basis functions employed in the analysis. To demonstrate

the utility of the method, we apply it to the problem of river tides, because they are ‘‘conceptually the simplest nonstationary tidal process, and the only one for which both ample data and a detailed theoretical analysis are available’’ (Jay & Flinchem, 1997, p. 5705).

Tides in rivers do not respond simply to astronomical forcing, but are the result of nonlinear interactions of the oceanic tide with channel geometry, bottom friction, and river flow. As a consequence, the tide is increasingly distorted and damped as it propagates upriver (Aubrey & Speer, 1985, Godin, 1985, Speer & Aubrey, 1985, Parker, 1991, Godin, 1999). This leads to asymmetries in the river tide that are manifested by unequal duration of ebb and flood, resulting in irregularities in the timing and height of high and low water (Godin, 1984, 1999, Nidzieko, 2010). Tidal monthly oscillations of mean water level (MWL) induced by the neap-spring cycle also increase in strength upstream. The amplitude of this fortnightly tide eventually surpasses that of the dominant diurnal and semidiurnal tides, leading to the reversal of the relative levels of mean low water at spring and neap tides (LeBlond, 1979, 1991, Gallo & Vinzon, 2005).

Tidal motion in shallow rivers is best represented by a first-order differential equation with only one (incident) wave, which diffuses in from time-varying forcing conditions at the river mouth (LeBlond, 1978). The dynamic balance is between surface slope and friction, whose effects on subtidal and tidal water level variations can be captured in analytical solutions of the one-dimensional St. Venant equations. The solutions are based on a decomposition of the nonlinear friction term (e.g., Dronkers, 1964, Godin, 1999) into contributions caused by external parameters and nonlinear interactions. Simple regression models, exploiting the results of tidal analysis [whether HA, continuous wavelet transform (CWT), or some other form], can be used to identify and predict the relative importance of these contributions to local tidal dynamics.

Jay & Flinchem (1997) and Godin (1999) were among the first ones to show the predicting potential of such models. Jay & Flinchem (1997) obtained analytical predictions of the response of the low-frequency, diurnal, semidiurnal, and quarterdiurnal tidal elevations to variations in river flow and successfully compared them to CWT analyses of tidal height records in the Columbia River. Godin (1999) demonstrated that variations in MWL and tidal properties at upriver stations in the St. Lawrence River can be predicted from forcing conditions (i.e., tidal constituents amplitudes, tidal range, and/or river discharge). He further showed the correlation

between river discharge and the amplitude and phase variations of the semidiurnal tide, the local tidal range, and the times of arrival of high and low water.

Kukulka & Jay (2003a, b) derived from a theory of river-tide propagation in convergent channels with strong friction (Jay, 1991) a functional representation that uncouples the nonlinear interactions of fluvial tides and river stage (i.e., MWL). They used a CWT analysis of Columbia River tides to provide time series of stage, tidal amplitudes and phases, and tidal range, which they regressed against coastal tidal range and river flow. Their models agreed remarkably well with observations even at seaward stations, achieving better agreement with observation than hindcasts available from conventional HA. Elaborating on this work, Jay *et al.* (2011) adapted the method to model tidal extrema – that is, lower low water (LLW) and higher high water (HHW) – as a function of river flow and external tidal forcing.

Buschman *et al.* (2009) presented a method to analyze subtidal water levels in tidal rivers. Unlike Kukulka & Jay's (2003a, b) models, they used Godin's approximation of the friction term (Godin, 1999), rather than the Tschebyschev polynomial approach (Dronkers, 1964), to derive a new expression for subtidal friction, and successfully applied their model on the Berau River (Indonesia). Together, these studies have shown the potential of including the contributions of external tidal and fluvial forcing to improve tide predictions in the upper regions of rivers.

We introduce here a generalization of classical tidal HA to nonstationary tidal records. An analytical model, adapted from Kukulka & Jay (2003a, b) and Jay *et al.* (2011), is directly embedded into the HA basis functions to allow the treatment of tidal-fluvial interactions. Although we focus on the problem of river tides, the method is applicable in any situation in which tides are modulated by a quantifiable nontidal process. We seek an analysis tool that is able to

- embed an analytical model of nontidal perturbations into the HA basis functions;
- provide time series of subtidal and tidal properties (MWL, amplitudes, and phases), expressed in terms of external forcing;
- distinguish frequencies within tidal species;
- improve the predictive power of HA in highly nonlinear environment (e.g., upstream reaches of tidal rivers);

- evaluate errors in constituent properties.

HA is possibly the most widely used approach in tidal analysis. It determines the phase and amplitude coefficients of *a priori* known frequencies via a least squares fitting procedure. Each tidal constituent is represented by a sine wave whose frequency is derived from the tidal potential and nonlinear interactions. HA relies, however, on the assumptions that the analyzed signal is stationary and that constituents are independent. For a nonstationary signal, it provides approximate values of tidal constituent properties, but with no information regarding their evolution in time and the underlying dynamics involved (Jay & Flinchem, 1997, 1999). Several methods have been applied to time series to extract information on transient tidal processes. They are generally devised to transform the content of a signal in the time domain into frequency information that expresses the amplitude and phase behaviour of the input as a function of both frequency and time [for an overview of existing methods, see e.g. Jay & Kukulka (2003) and Parker (2007)]. While these methods allow a representation of the modulations induced by nonstationary processes, their success has been limited either by a loss of resolution of constituents within a tidal band [e.g. short-term HA (STHA), complex demodulation, CWT, empirical mode decomposition] or by their inability to treat signals with strong nonlinearities or sharp variations in non-tidal forcing (e.g. STHA, response method, species concordance method).

Our implementation of HA for nonstationary records, NS_TIDE, is carried out through modifications of the T_TIDE package in MATLAB (Pawlowicz *et al.*, 2002, Leffler & Jay, 2009). In common with traditional HA, our method assumes that the analysis frequencies are *a priori* known, even if some of them are non-tidal. However, changes are made to make the method suitable for the analysis of nonstationary signals. We first rethink the concept of harmonic constants because constituent amplitudes and phases for any station are modulated by time-dependent non-tidal forcing. Second, for the assumption of prior knowledge of tidal frequencies to be maintained, new criteria are defined to select and determine the significance of selected constituents.

This paper is structured as follows. The models implemented in NS_TIDE are presented in section A.1.3, together with a redefinition of the Rayleigh criterion and of the error estimation. In section A.1.4, the method is applied to tidal records for the Lower Columbia River and compared

to results from traditional HA. Section A.1.5 discusses and summarizes the results. The appendix in section A.1.6 explains details regarding the analysis method.

### A.1.3 Model Description

#### *A.1.3.1 Harmonic Models*

HA methods originated in the late 19th Century (e.g., Darwin, 1891) and were given a structure based on a modern understanding of the tidal potential by Doodson (1921). Several contemporary tidal analysis codes stem from Godin's (1972) reformulation of Doodson's work, in particular the FORTRAN code of Foreman (1977) and the MATLAB code of T_TIDE (Pawlowicz *et al.*, 2002). HA codes model tidal heights $h(t_j)$ as a function of time $t_j$, with known tidal constituent frequencies $\sigma_k$ and unknown amplitudes $b_0$, $b_{1,k}$ and $b_{2,k}$; thus:

$$h(t_j) = b_0 + \sum_{k=1}^{n} [b_{1,k} \cos(\sigma_k t_j) + b_{2,k} \sin(\sigma_k t_j)]. \qquad \text{(A.1.1)}$$

Improvements to traditional harmonic methods have been made in the recent years in the inverse technique used and the estimation of confidence limits. Leffler & Jay (2009) incorporated robust estimators (Huber, 1996) via iteratively reweighted least-squares (IRLS) into T_TIDE to reduce the influence of non-tidal variation on the overall fit by down-weighting outliers. Foreman *et al.* (2009) enhanced HA by embedding nodal and astronomical argument corrections and multiple inference calculations directly in the least-square matrix, thereby removing the need for post-fit adjustments. The most direct consequence of this is that corrections and inferences influence all constituents included in the analysis rather than the specific constituents actually corrected. These improvements are included in Foreman's FORTRAN code, as well as in the UTide MATLAB functions (Codiga, 2011). NS_TIDE is implemented as a modification to T_TIDE. It is similar to Foreman *et al.* (2009) in that the models describing stage and tidal-fluvial variations are directly embedded into the basis functions of the matrix system to be solved. It differs from previous software in its conception of tides as fundamentally nonstationary, in its implementation of the Rayleigh criterion, and in its error analysis.

*A.1.3.2 Stage and Tidal-Fluvial Models*

The conceptual approach we advance here is quite general with respect to the physical processes that perturb the tidal "constants". To provide a concrete example, we apply the method to river tides, using the framework provided by Kukulka & Jay (2003a, b) and Jay *et al.* (2011), summarized below. Kukulka & Jay (2003a, b) expressed the bed stress $\tau_B = \rho C_D |U| U$ using the Tschebyschev polynomial representation of $|U|U$ provided by Dronkers (1964), where $U$ is velocity, $\rho$ is water density, and $C_D$ is the drag coefficient. The bed stress $\tau_B$ controls the complex wave number $q = k + \mathrm{i}r$ and, therefore, governs tidal propagation; here, $k$ is the wave number and $r$ is the damping modulus. For the critical convergence regime (Jay, 1991) where tidal and fluvial flows are of similar magnitude and convergence is moderate, $k = -r$ and $q = (\mathrm{i} - 1)r$. Under these conditions, Kukulka & Jay (2003a) derived models for constituent amplitude (or tidal range) ratios between a station of interest and a reference station in terms of the damping modulus $r$:

$$\frac{\zeta(x)}{\zeta_0} = \mathrm{e}^{-\mathrm{i}q(x - x_0)}, \tag{A.1.2}$$

$$\ln\left[\frac{|\zeta(x)|}{|\zeta_0|}\right] = +r(x - x_0), \tag{A.1.3}$$

where $\zeta(x)$ is a tidal property (amplitude or range) at position $x$, and $\zeta_0$ is the same property at the reference station at position $x_0$. The phase difference $\Delta\phi$ is modeled by analogy to $\zeta$: $\Delta\phi = -k(x - x_0) + a_0'$, where $a_0'$ is an offset coefficient. Kukulka & Jay (2003a) used the Dronkers (1964) representation of $|U|U$ to parameterize Eq. (A.1.3) in terms of external variables $Q$ and $R$, respectively representing river flow and greater diurnal tidal range at the reference station, yielding:

$$\ln\left[\frac{|\zeta(x)|}{|\zeta_0|}\right] = a_0 + a_1 Q^p + a_2 \frac{R^2}{Q^{0.5}}, \tag{A.1.4}$$

where $(x - x_0)$ is assumed fixed and absorbed into the parameters, and $p = 1$.

The coefficient $a_0$ in Eq. (A.1.4) is primarily determined by the convergence or divergence of the channel cross-section, while $a_1$ represents nonlinear interactions with river flow. Kukulka & Jay (2003a) assumed that river flow $Q$ should appear linearly in Eq. (A.1.4). This simplifies the actual nonlinear response of tidal parameters to river flow in Jay (1991) without loss of accuracy (Kukulka & Jay, 2003a). Moreover, the appearance of $Q$ in Eq. (A.1.4) is itself a simplification – in theory, $U = Q/A(Q)$ should be used, where $A(Q)$ is cross-sectional area. The variation of $A$ with $Q$ can cause deviations of the exponent $p$ from unity depending on channel geometry at the site and seaward of the tide gauge, through which the tidal wave propagates. While $p$ may be kept constant by adding additional regression terms that represent the variation in $A$ with $Q$, this has an unfavourable effect on model confidence limits. A pragmatic solution is to optimize the exponents by station, as in Jay *et al.* (2011).

The last term in Eq. (A.1.4) represents the effects of nonlinear tidal-fluvial interactions due to neap-spring variability, whose importance decreases as river flow increases. It is responsible for the tidal monthly changes in MWL and tidal properties, attributable to frictional interactions. In theory, this interaction is quadratic in $R$, but only for stations where river flow and tidal currents are comparable in strength. Again, optimal exponents can be obtained to account for deviations from theory (e.g., Jay *et al.*, 2011).

Eq. (A.1.4) is dimensionally inhomogeneous, in that the values of $a_1$ and $a_2$ depend on the units of measurement, and their units depend on the exponents of $Q$ and $R$. These constants ought to involve the geometry of the river, including, for example, the cross-sectional area, the convergence rate, the wetted perimeter, and possibly other factors. In other words, placing this formula into dimensionally homogenous form would involve explicitly writing the dependence of $a_i$ ($i = 1, 2$) and the exponents on the appropriate non-dimensional parameters. These parameters will vary from place-to-place, and their values will often be unknown or uncertain. Rather than explicitly modeling these relationships, we have taken the pragmatic approach of adjusting the exponents and the coefficients to fit the data. And, interestingly enough, the sensitivity of the results to the exponents is little (see section A.1.4).

Expressions such as Eq. (A.1.4) can be used to describe tidal amplitude, phase, or range variations in time. Kukulka & Jay (2003b) derived a similar expression to model mean river

stage (MWL), with an additional term to account for variations in atmospheric pressure. Jay *et al.* (2011) further extended these functional representations to model LLW and HHW, which are quantities that combine river stage and tidal properties.

*A.1.3.3 Practical Regression Models*

The present analysis uses a functional representation derived from the latest version of the model by Jay *et al.* (2011), in which the exponents associated with the various terms in Eq. (A.1.4) are iteratively optimized to account for deviations from theory, due to the effects of time-varying channel geometries and variations in the ratio of river flow to tidal currents as a function of upriver distance. In practice, the variations in tidal parameters are small enough that the logarithm of the left-hand side of Eq. (A.1.4) can be replaced by a linear term, using the first term in the Taylor series expansion of the natural logarithm, $\ln(1+\delta) \sim \delta$, where $\delta$ is the departure of the ratio in Eq. (A.1.4) from unity (cf. Jay *et al.*, 2011).

Conceptually, we replace the constants $b_0$, $b_{1,k}$ and $b_{2,k}$ in Eq. (A.1.1) by functions of river flow $Q$ and greater diurnal tidal range $R$ at a convenient station removed from fluvial influence:

$$h(t_j) = b_{0,0}[Q(t_j), R(t_j)] + \sum_{k=1}^{n} \left\{ b_{1,k}[Q(t_j), R(t_j)] \cos(\sigma_k t_j) + b_{2,k}[Q(t_j), R(t_j)] \sin(\sigma_k t_j) \right\}, \quad \text{(A.1.5)}$$

$$b_{l,k}(t_j) = a_{0,l,k} + a_{1,l,k} Q^p(t_j) + a_{2,l,k} \frac{R^q(t_j)}{Q^r(t_j)}, \quad \text{(A.1.6)}$$

where $h$ is tidal heights (m); $t$ is time (s); $Q$ is river flow (thousands of $m^3s^{-1}$); $R$ is the greater diurnal tidal range (m); $p$, $q$, $r$ are the exponents for each station and frequency band; $a_0$, $a_1$, $a_2$ are the model parameters for each station and frequency; $b_0$, $b_{1,k}$, $b_{2,k}$ are the harmonic model amplitudes for each station and frequency; $j$ is the index for time ($j$ = 1, $m$); $k$ is the index for tidal constituents ($k$ = 1, $n$); $l$ is the index for coefficients ($l$ = 0, 2); $m$ is the number of observations in the time series; $n$ is the number of tidal constituents.

The $Q$ and $R$ time series are lagged to account for the distance separating the stations where they were measured and the station at which the analysis is performed. Time lags are determined by calculating the maximum correlation between $Q$ or $R$ and the filtered (i.e. low-passed or range-filtered) time series of measured tidal heights. A constant time lag representing the average time

of propagation of the waves is applied to each forcing variable $Q$ and $R$. More complex lag functions could be used to better capture the varying propagation times as a function of river stage, but they are not currently implemented in NS_TIDE.

To separately include the influence of multiple rivers and tidal inlets, the second and third terms of Eq. (A.1.6) are generalized as follows (indices $l$ and $k$ are dropped for clarity):

$$a_1 Q^p(t_j) \Rightarrow \sum_{u=1}^{n_Q} a_{1u} Q_u^{p_u}(t_j), \tag{A.1.7}$$

$$a_2 \frac{R^q(t_j)}{Q^r(t_j)} \Rightarrow \sum_{v=1}^{n_R} a_{2v} \frac{R_v^{q_v}(t_j)}{\left(\sum_{u=1}^{n_Q} Q_u(t_j)\right)^{r_v}}, \tag{A.1.8}$$

where $u$ and $v$ are indices for the added terms, and $n_Q$ and $n_R$ are the number of rivers and tidal inlets, respectively. Through Eqs. (A.1.7) and (A.1.8), each river and tidal inlet included in the analysis has its own term with its associated exponents, thus allowing a separation of their respective influence on tidal heights.

The terms in Eqs. (A.1.5) and (A.1.6) can be rewritten for use in a regression into two components, a stage model $s(t_j)$ and a tidal-fluvial model $f(t_j)$; by setting $n_Q = n_R = 1$ in Eqs. (A.1.7) and (A.1.8), we have:

$$h(t_j) = \underbrace{c_0 + c_1 Q^{p_s}(t_j) + c_2 \frac{R^{q_s}(t_j)}{Q^{r_s}(t_j)}}_{\text{stage model or } s(t_j)} + \underbrace{\sum_{k=1}^{n} \left[ \left( d_{0,k}^{(c)} + d_{1,k}^{(c)} Q^{p_f}(t_j) + d_{2,k}^{(c)} \frac{R^{q_f}(t_j)}{Q^{r_f}(t_j)} \right) \cos(\sigma_k t_j) + \left( d_{0,k}^{(s)} + d_{1,k}^{(s)} Q^{p_f}(t_j) + d_{2,k}^{(s)} \frac{R^{q_f}(t_j)}{Q^{r_f}(t_j)} \right) \sin(\sigma_k t_j) \right]}_{\text{tidal - fluvial model or } f(t_j)} \tag{A.1.9}$$

where the subscripts $s$ and $f$ denote, respectively, the stage and tidal-fluvial models; the superscripts ($c$) and ($s$) refer to the cosine and sine terms, respectively; $c_i$ ($i$ = 0, 2) are the model parameters for the stage model; $d_{i,k}$ ($i$ = 0, 2) are the model parameters for the tidal-fluvial model; and $p_s$, $q_s$, $r_s$, $p_f$, $q_f$, and $r_f$ are the exponents, determined using an iterative procedure. Iterative regression analyses are run for a representative time series that covers the widest dynamic range

in river flow possible, from very low to very high flows, to find the optimal exponents at the analysed station. Each model is optimized separately, using the original time series of tidal heights for the stage model and a high-passed version of the time series for the tidal-fluvial model. At each iteration of the optimization process, the Rayleigh criterion (defined in next section) is recalculated based on the exponents of the current iteration and the number of included constituents is adjusted accordingly. An ordinary least-squares (OLS) regression is then performed, leading to a new set of coefficients and statistics. The optimization procedure is based on a nonlinear constrained minimization of the residual standard deviation. It uses an interior-point algorithm (Byrd *et al.*, 2000, Waltz *et al.*, 2006) where a sequence of approximate minimization problems is solved using a direct (Newton) step, or a conjugate gradient step if a direct step cannot be taken – for example, when the approximate problem is not locally convex near the current iteration. The procedure is implemented in the MATLAB's *fmincon* function (Mathworks 2010). Exponents are allowed to vary over the range of $0.2 \le p \le 2$, $1 \le q \le 2.5$, and $0.2 \le r \le 1.5$, for both the stage and tidal-fluvial models, and initial guesses are set to the theoretical values used by Kukulka & Jay (2003a, b), summarized in Table A.1.1.

**Table A.1.1** **Selected constituents, optimized exponents, and Rayleigh criteria for the stage and tidal-fluvial models ($D_1$ to $D_8$), compared to theoretical exponent values (KJ) from Kukulka & Jay (2003a, b), for an 8-year-long record (June 2003 – June 2011) at Vancouver, WA. Results were obtained with two separate discharge terms ($n_Q = 2$), $\eta = 0.15$, and mean SNR ≥ 2 based on a correlated noise model.**

| LOR | Models | Constituents | Exponents | | | | Rayleigh Criteria ($h^{-1}$) |
|---|---|---|---|---|---|---|---|
| | | | Discharge Terms | | Range Term | | |
| | | | $Q_{\mathrm{Bon}}^{p_1}$ | $Q_{\mathrm{Wil}}^{p_2}$ | $R_{\mathrm{Ast}}^{q}$ | $Q_{\mathrm{tot}}^{r}$ | |
| 8 yr | Stage, KJ | – | 0.67 | 0.67 | 2.00 | 1.33 | – |
| | $D_1$ to $D_8$, KJ | Same as below | 1.00 | 1.00 | 2.00 | 0.50 | 1.089E-03 |
| 8 yr | Stage | – | 1.39 | 1.07 | 1.04 | 0.37 | – |
| | $D_1$ | $\sigma_1$, $Q_1$, $O_1$, $NO_1$, $K_1$, $J_1$, $SO_1$, $\upsilon_1$ | 1.46 | 0.71 | 2.48 | 0.26 | 9.304E-04 |
| | $D_2$ | $\varepsilon_2$, $\mu_2$, $N_2$, $M_2$, $L_2$, $S_2$, $MSN_2$ | 1.20 | 0.86 | 1.30 | 1.03 | 1.006E-03 |
| | $D_3$ | $MO_3$, $MK_3$, $SK_3$ | 0.53 | 0.48 | 2.38 | 0.53 | 8.402E-04 |
| | $D_4$ | $MN_4$, $M_4$, $SN_4$, $MS_4$, $SK_4$ | 0.79 | 0.68 | 2.44 | 0.25 | 9.149E-04 |
| | $D_5$ | $2MK_5$, $2SK_5$ | 0.96 | 0.96 | 2.14 | 0.20 | 1.065E-03 |
| | $D_6$ | $2MN_6$, $M_6$, $2MS_6$, $MSK_6$ | 1.00 | 1.00 | 2.00 | 0.50 | 1.089E-03 |
| | $D_7$ | $3MK_7$ | 1.00 | 1.00 | 2.00 | 0.50 | 1.089E-03 |
| | $D_8$ | $M_8$ | 1.00 | 1.00 | 2.00 | 0.50 | 1.089E-03 |

Since a different response can be expected from the diurnal, semidiurnal, etc. frequencies, band-specific exponents are calculated by dividing the tidal-fluvial model into sub-models, one per frequency band of interest:

$$f(t_j) = f_{D_1}(t_j) + f_{D_2}(t_j) + \ldots + f_{D_{n_f}}(t_j), \tag{A.1.10}$$

where the $D_i$ models ($i$ = 1, 2, ..., $n_f$) are composed of all frequencies within the diurnal, semidiurnal, etc. frequency bands. This division relies on the assumption that each of the constituents within a given tidal band is influenced by discharge and ocean tidal range in a similar way and can be represented by the same set of exponents. In NS_TIDE, $n_f$ is allowed to be as high as 12, which corresponds to half the sampling frequency (usually 1 h) or Nyquist frequency.

The final coefficients ($c_0$, $c_1$, $c_2$, $d_{0,k}$, $d_{1,k}$, and $d_{2,k}$) in Eq. (A.1.9) are determined, once the exponents are optimized, by IRLS regression analyses (Huber, 1996, Leffler & Jay, 2009) to best fit the observations, denoted $y(t_j)$. This takes the form of an overdetermined system composed of all models and sub-models (see the appendix in section A.1.6), whose solution to the IRLS fit is obtained by minimizing the sum of weighted residuals:

$$E = \sum_{j=1}^{m} w_j^2 [h(t_j) - y(t_j)]^2 , \tag{A.1.11}$$

where $w$ is a weighting function. NS_TIDE uses the matrix inversion mechanism built into MATLAB's *robustfit* function (MathWorks, 2012). The IRLS naturally de-weighs events that increase residual variance, so that the final coefficients may differ slightly from the coefficients from the last OLS iteration. The level of confidence in the computed parameters is however increased, leading to better hindcast under most conditions. Details of the solution are given in the appendix (section A.1.6).

When tidal amplitude vanishes, any increase in discharge should leave the tide unchanged (i.e. vanished). The equations, in their current form, may produce artificial, negative amplitudes beyond that point. In fact, the discharge term $d_{1,k}Q^{p_f}$ is usually opposed in phase with the constant term $d_0$ and thus represents a correction to $d_0$. It increases indefinitely as the discharge

$Q$ increases, regardless of the value of $d_0$. Consequently, when the correction exceeds the value actually corrected, an artificial tide is created that is out of phase with the rest of the signal, thus tainting the hindcast. To reduce this effect, a correction factor based on the total discharge can be applied to the tidal-fluvial model $f(t_j)$ of Eq. (A.1.9):

$$f(t_j) = f(t_j) \times \min\left[1, \left(Q_{\text{th}} \Big/ \sum_{u=1}^{n_Q} Q_u(t_j)\right)^{\kappa}\right], \tag{A.1.12}$$

where the threshold discharge value, $Q_{\text{th}}$, and exponent $\kappa$ can either be determined automatically (i.e., included as a parameter to be optimized) or specified by the user for each frequency band. Roughly, this correction switches gradually the tidal-fluvial model off when the threshold discharge is exceeded, such that most of the variations in water levels are accounted by the stage model alone. It prevents the tidal amplitudes from becoming negative – or the phases to be artificially shifted by ~180° – as the discharge increases beyond the point where the tide vanishes. This only occurs in extreme cases where the river flow is so strong that the tide is completely extinguished. In less extreme cases (when tides do not disappear), such a correction is not needed. If activated, the correction is applied after the Rayleigh criterion is determined and before the IRLS fit as opposed to a post-fit correction.

#### *A.1.3.4 Constituent Selection and Rayleigh Criterion*

Most HA codes use a twofold strategy to select constituents for analysis. The Rayleigh criterion (Godin, 1972) is used *a priori* to select constituents to include in the analysis, and the significance of constituents based on error estimates (detailed in next section) is used *a posteriori* to exclude those that are not significant. The Rayleigh criterion determines a minimal allowable frequency separation between neighbouring constituents. Frequencies are selected in accordance with the Rayleigh criterion in a predetermined order following a decision tree based on tidal potential amplitudes (e.g., Foreman, 1977). In traditional HA, the Rayleigh criterion states that, given a record composed of $m$ samples evenly spaced by a time step $\Delta t$, only constituents whose frequencies are more than $(m\Delta t)^{-1}$ apart from each other can be resolved. By this definition, the length of record (LOR = $m\Delta t$) is the only parameter that determines which constituents are selected, but the Rayleigh criterion may be either too exclusive for low frequencies or too inclusive for higher frequencies (Jay & Flinchem, 1999). Such a treatment is valid for stationary

signals where only pure spectral lines are considered. In contrast, non-stationarity adds a continuous spectral background that broadens and transforms the tidal spectral lines into cusp-like shaped peaks that reflect the intensity of modulation of the tides (Munk *et al.*, 1965). As a result, even though the LOR suggests that close frequencies can be resolved, their overlapping cusps lead to erroneous estimates of tidal properties (e.g., Godin, 1999). Preliminary tests performed on the implemented model with a LOR-based Rayleigh criterion highlighted this tendency, with the energy of the estimated spectrum greatly exceeding the energy of the original signal due to ill-conditioning of the IRLS system.

In order to obtain a meaningful spectrum, the Rayleigh criterion is redefined in NS_TIDE in such a way that "contaminated" frequencies are eliminated, thereby providing an independent set of constituent basis functions. Furthermore, the constituent selection is performed following a decision tree that is based on the actual order of importance of the constituents rather than on tidal potential amplitude, thus naturally incorporating nonlinear constituents in shallow water. For example, the constituent $M_3$, which is the dominant terdiurnal constituent according to tidal potential amplitudes (Foreman, 1977), comes after $MO_3$ and $MK_3$ in shallow water in terms of importance. A new decision tree is implemented in NS_TIDE through the computation of a standard HA prior to each nonstationary analysis, to decide on the order of inclusion of the constituents. Thus, the average tidal amplitudes of the analysed signal in a standard HA are the basis from which constituents are selected.

A new Rayleigh criterion $\Delta\sigma$ is defined, starting from the fact that the width of the cusps formed around the tidal spectral lines is related to the low-frequency spectrum of the nonlinear forcing. For two adjacent tidal frequencies $\sigma_1$ and $\sigma_2$, the minimal allowable frequency separation $\Delta\sigma$ is given by:

$$\left|\sigma_1 - \sigma_2\right| > \Delta\sigma \;\text{ with }\; \frac{\int_0^{\Delta\sigma} \hat{h}(\sigma)\mathrm{d}\sigma}{\int_0^{\infty} \hat{h}(\sigma)\mathrm{d}\sigma} = 1-\eta\,, \tag{A.1.13}$$

where $\hat{h}(\sigma)$ is the normalized power spectrum of either $Q^p$ or $1/Q^r$, and $\eta$ is a user-defined criterion representing a fraction of its total spectral power. The numerator in Eq. (A.1.13) represents a region of high power in the low frequency band, whose width $\Delta\sigma$ increases as a

function of the background modulations. The power spectrum $\hat{h}(\sigma)$ of $Q^p$ and $1/Q^r$ typically has maximum amplitude around annual and semi-annual periods and then decays with increasing frequency at a rate that is function of both the exponents $p$ and $r$ and forcing $Q$. $\hat{h}(\sigma)$ is calculated separately for each term in Eqs. (A.1.7) and (A.1.8), by letting $R$ be equal to 1 since energy at periods of ~15 and ~28 days would otherwise appear in the spectrum $\hat{h}(\sigma)$ due to neap-spring variations in $R$, with the adverse effect of lengthening $\Delta\sigma$. The final value for $\Delta\sigma$ is calculated as the maximum of the LOR-based Rayleigh criterion, $\Delta\sigma_{LOR} = (m\Delta t)^{-1}$, and all $\Delta\sigma_i$ ($i = 1,\ n_Q + n_R$) obtained from Eq. (A.1.13) for each term in Eqs. (A.1.7) and (A.1.8): $\Delta\sigma = \max(\Delta\sigma_{LOR}, \Delta\sigma_i)$.

Since more than one tidal-fluvial sub-model (one per tidal band) can be defined through Eq. (A.1.10), their associated exponents will lead to band-specific Rayleigh criteria (e.g. Table A.1.1), even if the parameter $\eta$ remains unchanged. This is made possible because $\hat{h}(\sigma)$ in Eq. (A.1.13) is not calculated from the subtidal continuum of the input tidal heights, but from the low-frequency power of $Q^p$ and $1/Q^r$, which varies from one sub-model to another due to differences in $p$ and $r$ amongst the bands. Thus, the more variability in the forcing $Q$ and the higher the exponents $p$ and $r$, the more restrictive the Rayleigh criterion must be. The width of the cusp formed around each dominant frequency is therefore proportional to the width of the low-frequency power associated with its corresponding sub-model basis function. Other attempts to establish fixed ratios relating the intensities of major constituent cusps to that of the near zero frequency (e.g., Munk *et al.*, 1965) were not very successful and are hard to generalize from one station to another.

There is a trade-off between the number of constituents included in the analysis and the independence of the terms composing the basis functions. With fewer constituents (smaller $\eta$) the overlap between frequencies is less, but the calculated amplitudes will include unknown contributions from nearby unresolved frequencies; and vice versa. For stationary tides, this problem is avoided by inferring unresolvable constituents from resolved constituents using known (constant) amplitude ratios and phase differences. Such a course is not applicable to nonlinear and nonstationary tides by definition. When nonstationary processes occur on short time scales relative to the period needed to separate frequencies, trying to distinguish the satellite

peaks by inference (e.g., $P_1$ from $K_1$) is meaningless. Moreover, nonlinear mechanisms transfer energy from the major constituents to adjacent frequencies, making the admittance discontinuous. For example, near $M_2$, $H_1$ and $H_2$ have an apparent admittance orders of magnitude greater than that of $M_2$, because almost all the energy at $H_1$ and $H_2$ comes from nonlinear transfer (e.g., Pugh & Vassie, 1976). The number of tidal components thus needs to be restricted, through the parameter $\eta$, in order to keep the spectral elements as independent as possible. In NS_TIDE, the user-defined $\eta$ parameter allows the user to tighten the tolerance related to constituent selection. If $\eta$ is set too high, the error calculation (detailed next) will help identify constituents that covary with others, so that they can be excluded *a posteriori*. Thus, the modified Rayleigh criterion and the error analysis work together to arrive at an analysis with an optimal number of constituents. With strongly nonstationary tidal signals, however, more experimentation with these criteria may be needed than is the case with nearly stationary signals.

For stationary tidal signals, nodal modulations of the main tidal constituents by their satellites are an important consideration. But nodal modulations are, as a rule, small in rivers relative to the effects of stage variations. They are dominated – and any attempt to resolve them is contaminated – by fluvial modulations. In practice, it is virtually impossible to separate the modulation effects on the main tidal constituents by river flow and tidal range from those stemming from changes in lunar declination, even for time series longer than 18.6 years; this follows directly from the redefinition of the Rayleigh criterion. In standard HA, all satellites are usually ignored and amplitudes and phases are determined for all major constituents that can be resolved given the length of the record. Post-fit corrections are then applied to account for the presence of the satellites, which modulate the calculated amplitudes and phases. They are defined in terms of a nodal amplitude amplification factor and a nodal angle, which are assumed to vary in the same way as the gravitational potential. This assumption, if invalidated, may lead to systematic errors in the estimation of tidal constituents, as shown by Shaw & Tsimplis (2010). Thus, an underestimation of the equilibrium nodal variation can be associated with nonlinear frictional damping (e.g., Amin, 1983, 1985), whereas an overestimation of the equilibrium nodal variation may be due to strong shallow-water interactions (e.g., Amin, 1993). Similarly, significant deviations from the equilibrium constants may occur in rivers due to friction and shallow-water effects. Moreover, these relationships are likely to change over time as the river conditions change. Therefore, tidal potential theory is not used in NS_TIDE to dictate relationships between tidal

constituents in rivers. Although nodal corrections were not included in our analyses, the time series of tidal range $R$ includes nodal modulations of the dominant diurnal and semi-diurnal constituents at the ocean entrance, which are nonlinearly propagated up to the analysis station.

*A.1.3.5 Error Estimation*

The least-squares solution of a HA produces statistical estimates of the constituent properties, whose error variances need to be evaluated in order to determine their significance. Two error models that differ from the models in T_TIDE (see Pawlowicz *et al.*, 2002) were implemented in NS_TIDE, namely an uncorrelated noise model and a correlated noise model. Each model constructs a covariance matrix of the regression coefficients and generates an ensemble of replicates – assuming a multivariate normal distribution – to compute uncertainty estimates for the stage and tidal-fluvial model parameters in Eq. (A.1.9). Each replicate is then converted into constituent parameters using Eqs. (A.1.25) – (A.1.30) and (A.1.32) – (A.1.33) and confidence bounds are estimated for both the regression coefficients and the constituent amplitudes and phases as a function of time. An IRLS solution is used, following Leffler & Jay (2009), to provide robust statistics on the regression coefficients.

In the following development, we define the covariance matrices needed in each of the error models. The error models assume a signal model of the form $\mathbf{h} = \mathbf{A}\mathbf{x} + \boldsymbol{\varepsilon}$, where $\mathbf{h}$ is a vector of the observed values, $\mathbf{A}$ a matrix of the basis functions evaluated at measurement times, $\mathbf{x}$ the model parameter vector, and $\boldsymbol{\varepsilon}$ the measurement noise vector including non-harmonic signals (i.e. correlated in time). The least-squares, maximum likelihood, best linear unbiased estimate of $\mathbf{x}$ is given by:

$$\mathbf{x} = \left(\mathbf{A}^{\mathrm{T}}\mathbf{C}_{\boldsymbol{\varepsilon}}^{-1}\mathbf{A}\right)^{-1}\mathbf{A}^{\mathrm{T}}\mathbf{C}_{\boldsymbol{\varepsilon}}^{-1}\mathbf{h}, \tag{A.1.14}$$

where $\mathbf{C}_{\boldsymbol{\varepsilon}}$ is the covariance of $\boldsymbol{\varepsilon}$. For the uncorrelated noise model, $\mathbf{C}_{\boldsymbol{\varepsilon}} = \sigma^2\mathbf{I}$, where $\mathbf{I}$ is the identity matrix and $\sigma^2$ is estimated from the residual as follows:

$$\sigma^2 = \frac{1}{N-M}\left(\mathbf{A}\mathbf{x}-\mathbf{h}\right)^{\mathrm{T}}\left(\mathbf{A}\mathbf{x}-\mathbf{h}\right), \tag{A.1.15}$$

where $N$ is the number of data samples and $M$ the number of harmonic coefficients. This yields the covariance matrix of $x$ for uncorrelated noise:

$$\mathbf{C}_{xu} = \left(\mathbf{A}^{\mathrm{T}}\mathbf{C}_{\boldsymbol{\varepsilon}}^{-1}\mathbf{A}\right)^{-1} = \left(\mathbf{A}^{\mathrm{T}}\mathbf{A}\right)^{-1}\sigma^2 . \tag{A.1.16}$$

For the correlated noise model, we consider the Fourier representation of $\boldsymbol{\varepsilon} = \mathbf{F}\hat{\boldsymbol{\varepsilon}}$ (strictly valid only if sample interval is constant), where $\mathbf{F}$ is the Fourier matrix of sines and cosines evaluated at the observation times and $\hat{\boldsymbol{\varepsilon}}$ is a vector of Fourier components. Thus, via the Fourier transform, $\hat{\boldsymbol{\varepsilon}}$ and $\boldsymbol{\varepsilon}$ are related by $\hat{\boldsymbol{\varepsilon}} = \mathbf{F}^{-1}\boldsymbol{\varepsilon}$. The covariance of $\boldsymbol{\varepsilon}$ is given by $\mathbf{C}_{\boldsymbol{\varepsilon}} = \mathbf{F}\mathbf{C}_{\hat{\boldsymbol{\varepsilon}}}\mathbf{F}^{\mathrm{T}}$, where $\mathbf{C}_{\hat{\boldsymbol{\varepsilon}}}$ is assumed diagonal (i.e. each Fourier component of $\boldsymbol{\varepsilon}$ is uncorrelated) and is estimated from the power spectrum of residuals. A Daniell average (Daniell, 1946) over the Rayleigh bandwidth is used to achieve a stable estimate. The covariance matrix of $\mathbf{x}$ for correlated noise is thus given by:

$$\mathbf{C}_{xc} = \left[\left(\mathbf{F}^{-1}\mathbf{A}\right)^{\mathrm{T}}\mathbf{C}_{\hat{\boldsymbol{\varepsilon}}}^{-1}\mathbf{F}^{-1}\mathbf{A}\right]^{-1} . \tag{A.1.17}$$

For evenly-spaced data the error estimate is essentially the same as the correlated noise model in T_TIDE, except for the different bandwidth used to estimate the non-tidal noise. The singular value decomposition of $C_{xc}$ could be computed to analyse the stability and conditioning of the non-harmonic analysis, similar to the approach of Foreman *et al.* (2009), although we have not pursued this.

Including the weighting matrix $\mathbf{W}$ of the IRLS yields the following covariance matrices for the uncorrelated and correlated noise models, respectively:

$$\mathbf{C}_{xu} = \left(\mathbf{A}^{\mathrm{T}}\mathbf{W}\mathbf{A}\right)^{-1}\sigma^2 \tag{A.1.18}$$

$$\mathbf{C}_{xc} = \left[\left(\mathbf{F}^{-1}\mathbf{W}^{1/2}\mathbf{A}\right)^{\mathrm{T}}\mathbf{C}_{\hat{\boldsymbol{\varepsilon}}}^{-1}\mathbf{F}^{-1}\mathbf{W}^{1/2}\mathbf{A}\right]^{-1} . \tag{A.1.19}$$

Since the amplitude and phase errors are functions of time in NS_TIDE, the significance of the constituents is assessed based on a time-averaged signal-to-noise ratio (SNR), which is the square of the ratio of tidal amplitude to amplitude error. Constituents whose mean SNR is below

the SNR lower limit are excluded from the analysis. The solution is recalculated using the significant constituents only.

### A.1.4 Application to River Tides

#### *A.1.4.1 Setting: The Lower Columbia River*

The Columbia River enters the Northeast Pacific Ocean 30 km seaward of the Tongue Pt tide gauge at Astoria, OR, USA (Figure A.1.1). It is the third largest river in the United States, with an annual average discharge of ~7,300 $m^3s^{-1}$ and a watershed of ~660,500 $km^2$ (Bottom *et al.*, 2005). The Lower Columbia River (LCR) spans 235 river kilometres (rkm) from the mouth to Bonneville Dam, located at the natural head of the tide. The maximum salinity intrusion length is 5-50 km, depending on the river flow and tides. Tidal amplitudes may vary by an order of magnitude due to the annual river flow cycle, and the propagation time from the entrance to rkm 170 almost doubles during high flow periods. Thus, the LCR is a good natural laboratory for the analysis of nonstationary tides. The Willamette River is the largest tributary to the LCR and enters the river mainstem at Portland, 160 rkm from the ocean. Its average discharge of 950 $m^3s^{-1}$ accounts for >40% of the average flow entering the mainstem below Bonneville Dam.

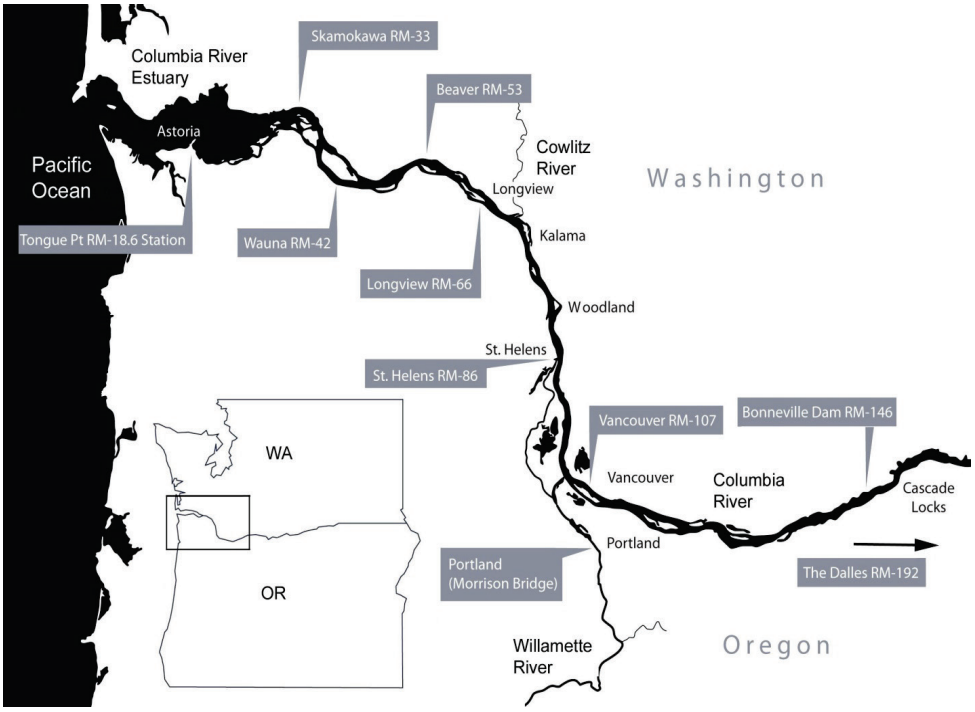


**Figure A.1.1 Map showing tide stations in the Lower Columbia River, with official river-mile designations; map courtesy of the Port of Portland.**

### *A.1.4.2 Harmonic Analysis Properties*

NS_TIDE was applied to hourly water level data for an 8-year period (June 2003 – June 2011) from Vancouver, WA (rkm 172), the second most landward of 10 tide gauges in the LCR (Figure A.1.1). These data were used here because they illustrate very well the difficult characteristics of river tides. The tides at Vancouver (Figure A.1.2) exhibit semidiurnal and diurnal tidal variations and have a range that varies from a few centimetres during high flow periods to ~1 m during fall spring tides. MWL varies by 3–8 m seasonally with river flow and by ~0.5 m over stronger neap-spring cycles in fall. The average frequency content of the tidal signal at Vancouver, obtained from a standard HA for the 8-year time series, contains 63 significant constituents. The admittance varies radically across the diurnal and semidiurnal bands due to nonlinear effects and daily cycles in hydropower demand at Bonneville Dam. Figure A.1.2 shows forcing data used to test NS_TIDE, which include hourly flow in the Columbia River at Bonneville Dam, daily flow in the Willamette River at Portland, and greater diurnal tidal range at Astoria-Tongue Pt (rkm 29).

Hourly discharge data at the Bonneville Dam were low-passed using a 3-day smoothing window, similar to Godin's (1972) tidal eliminator, in order to remove daily fluctuations caused by hydroelectric operations ("power-peaking"). Although our method does not require data pre-filtering of forcing data, this was done to eliminate undesirable oscillations in the modeled signal associated with irregular discharge waves at Bonneville Dam. However, the diurnal constituents at Vancouver are still affected by these fluctuations in river flow, propagating from the dam seaward. Fluctuations with periods of 3.5 and 7 days related to power-peaking remain in the filtered Bonneville time series and will be propagated to the analysis station. No filtering was applied to the daily discharge data of the Willamette River.

Greater diurnal tidal range was extracted from hourly data at Astoria-Tongue Pt. We chose Astoria-Tongue Pt at rkm 29 as reference station for the ocean tidal forcing, because tides at this location are only weakly influenced by river flow and it is the most seaward station for which sufficient data are available. To determine extrema, the hourly water level was high-passed, and then spline interpolated to 6 min intervals. Maximum and minimum heights were retrieved using a 27-hr moving window with 1-hr steps. Tidal ranges were calculated from the difference

between the maximum and minimum values, and smoothed using a 27-hr moving average to eliminate discontinuities due to steps in the tidal ranges.

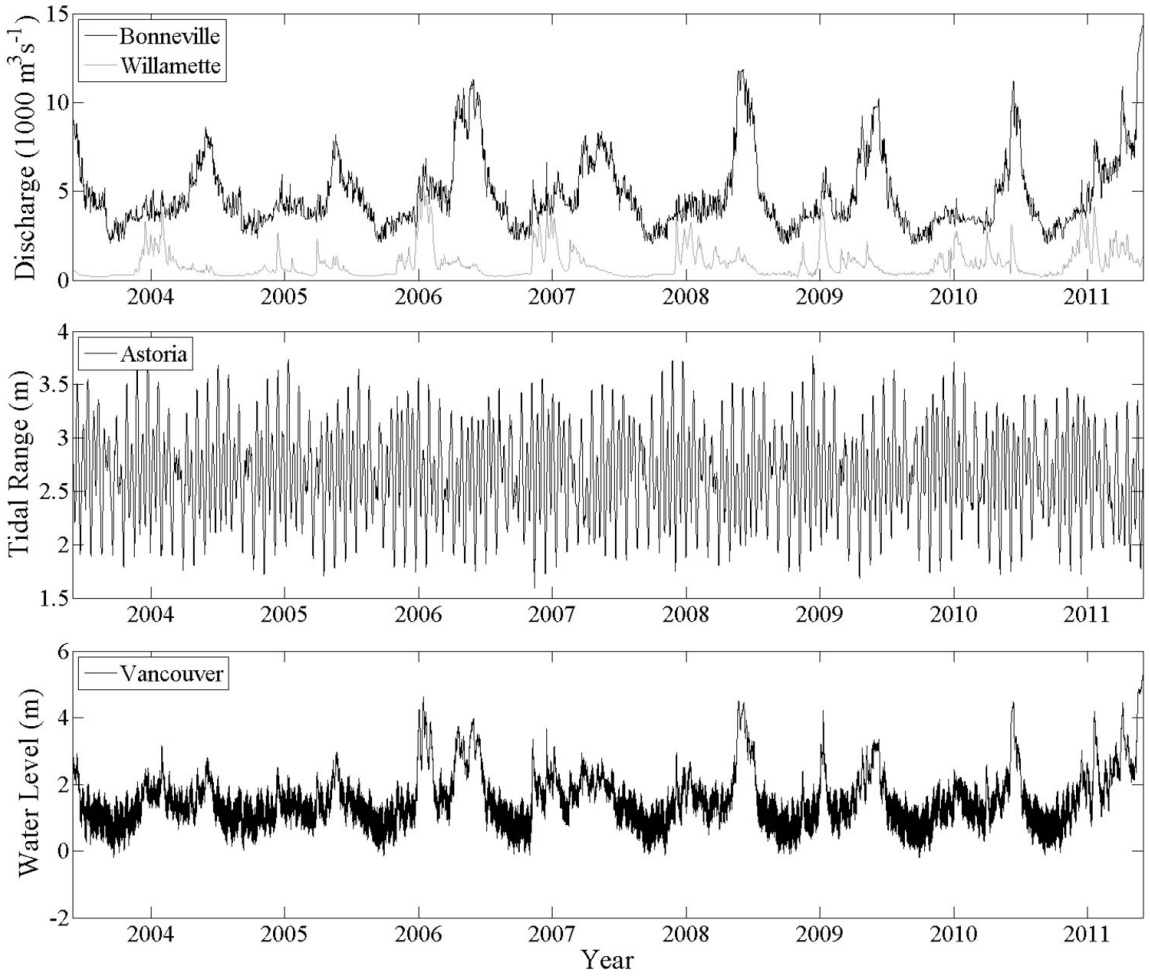


**Figure A.1.2** **Forcing variables and tidal response in the Lower Columbia River from June 2003 to June 2011: (top) discharge forcing at the Bonneville Dam and in the Willamette River, (middle) ocean tidal range forcing at Astoria, and (bottom) tidal response at Vancouver.**

The stage and tidal-fluvial models applied to the LCR have the form shown in Eq. (A.1.9), modified per Eq. (A.1.7) to include separately the river flows at Bonneville Dam and from the Willamette River (i.e. $n_Q = 2$, $n_R = 1$). While including the two discharges separately adds regression parameters and therefore increases error bounds, this adverse effect is compensated by a more accurate representation of the distinct effects of both rivers on tidal heights, especially marked during high flows (see Figure A.1.2). In fact, high flows are usually not synchronized in the Columbia and Willamette rivers, and they affect the tide at Vancouver with different lags. Also, the Willamette river flow affects tidal dissipation in the LCR and may reverse in the

mainstem beyond Vancouver, thus impacting Vancouver water levels (Jay *et al.*, 2011). Sensitivity of the results to this separation was tested for the cases 1) without the Willamette River, 2) with the Willamette and Bonneville Dam flows summed and added as a single discharge term (i.e. $n_Q = 1$), and 3) with the Willamette River included as a separate term (i.e. $n_Q = 2$). Sensitivity of MWL, constituent amplitudes and phases, and tidal range to the exponent values and the LOR was also assessed. The discharge threshold $Q_{th}$ and exponent $\kappa$ in Eq. (A.1.12) were set to 11,000 $m^3s^{-1}$ and 10, respectively, with the effect of switching the tidal-fluvial model off for discharges exceeding this limit. Since there were very few high-discharge/low-tide events during the 8-year time series analysed at Vancouver, these parameters were optimized using shorter analysis windows centered around these events. The final $Q_{th}$ and $\kappa$ values were chosen based on the optimization results and visual inspection of the tidal record; they are applied to all the analyses.

The tidal-fluvial model $f(t_j)$ was divided according to Eq. (A.1.10) into eight $D_i$ sub-models ($i = 1, 8$), each having a different set of exponents. The parameter $\eta$ for the Rayleigh criterion was set to 0.15, allowing for the resolution of a reasonable number of constituents while keeping the error bounds relatively low, given the non-stationarity of the analysed signal. Values of 0.05 and 0.5 were also tested to assess the sensitivity of the model to the parameter $\eta$. The significance of the constituents was determined using a correlated noise model with a mean SNR $\geq 2$; a mean SNR $\geq 10$ was also tested for comparison purposes, as well as an uncorrelated noise model. The number of realizations for the error estimation was set to 300. A Cauchy IRLS function with a tuning constant of 2.385 was used.

### *A.1.4.3 Results*

#### A.1.4.3.1 Model Parameters

Table A.1.1 summarizes the derived model exponents and compares them to the theoretical values of Kukulka & Jay (2003a, b). Departure of the exponents from theoretical values are observed for the stage and $D_1$ to $D_5$ models, while the $D_6$ to $D_8$ models present the same values as in Eq. (A.1.4), meaning that the optimization algorithm does not find the error to be decreasing in any direction. Deviations are partly explained by the linear form of the present model, as opposed to the logarithmic form of Kukulka & Jay's models. Differences from theory also arise from the highly nonlinear character of the tides at Vancouver and the fact that channel geometry

(e.g. flow-variable width) affects tides in a frequency-dependent manner, leading to band-specific exponents. The differences in the exponents of the two discharge terms are quite significant for the stage, $D_1$ and $D_2$ models. Their inclusion as two separate terms is therefore essential in order to adequately capture their respective effects on MWL and tidal properties.

Also shown in Table A.1.1 are the selected constituents for each tidal-fluvial sub-model ($D_1$ to $D_8$), along with their respective Rayleigh criterion. A total of 31 constituents are included in the analysis, compared to 63 with a LOR-based Rayleigh criterion of $1.422 \times 10^{-5}$. This reduction is due to the redefined Rayleigh criterion. For example, $P_1$ – the third largest diurnal constituent in terms of tidal potential amplitudes – cannot be separated from $K_1$ with an 8-year analysis, because of the non-stationarity of the signal. In fact, in highly nonstationary environments, the LOR does not dictate the frequency separation between neighbouring constituents anymore, as shown by Eq. (A.1.13). Another feature related to the redefinition of the Rayleigh criterion is its associated decision tree, based on the local importance of constituents as opposed to the order of inclusion presented by Foreman (1977). This explains for example why $M_3$ does not appear in the $D_3$ model.

#### A.1.4.3.2 Model Performance and Sensitivity

Shown in Figure A.1.3 is a comparison of results obtained from standard HA and NS_TIDE at Vancouver, for the analysis period extending from June 2003 to June 2011. Two constituents with periods of 3.5 and 7 days were added in the standard HA to account for low-frequency fluctuations associated with power-peaking at Bonneville Dam. For classical HA, the hindcast explains 38.5 % of the original signal variance and has a root-mean-square error (RMSE) of 0.604 m and a maximum absolute error of 3.26 m for tidal heights, as evidenced by the HA residual (Figure A.1.3a). These results clearly show the inability of HA to resolve the non-tidal fluctuations associated with changing river flow. Results for NS_TIDE sharply contrast with those for HA: the hindcast explains 96.4 % of the original signal variance and has a RMSE of 0.165 m and a maximum absolute error of 0.99 m. Furthermore, the NS_TIDE hindcast shown in Figure A.1.3a not only follows the low-frequency stage fluctuations of the MWL, but exhibits reductions in tidal amplitudes during very high flow periods, unlike HA. This performance was achieved with half the constituents used in traditional HA, because of more restrictive Rayleigh criteria, but with a larger number of parameters. The latter is 127 for the HA, which corresponds

to $2n + 1$, with $n$ equal to the number of constituents, plus the mean sea level. For NS_TIDE, the number of parameters is 288, which is $2n_Q + 3n_R + 1$ for the stage model, and $2n\,(n_Q + n_R + 1) + n_f\,(n_Q + 2n_R)$ for the tidal-fluvial model. While it is vital to recognize the limits on the amount of information in a signal (related to the LOR, number of data and noise level), the larger number of parameters considerably increases the explained variance and significantly reduces the residual error, compared to standard HA. Because the additional parameters are related to the actual dynamics of river tides, their use also increases the ability of NS_TIDE to predict tides outside of the analysis period.

In Figure A.1.3b, the IRLS fits obtained from both HA and NS_TIDE are compared to the observed spectrum. The NS_TIDE fit encompasses more of the observed signal energy than classical HA, especially at low frequencies (bottom left panel) where the harmonics from HA present the largest deviations from the observed spectrum. Because traditional HA assumes low-frequency oscillations to be perfectly sinusoidal and consistent from year to year, the sub-tidal forecasts computed with HA programs is generally found to be unsatisfactory. In fact, the usual harmonic apparatus, which provides semi-monthly (Mf, MSf), monthly (Mm, MSm), semi-annual (Ssa), and annual (Sa) constituents, is unable to adequately represent low-frequency river motions that are dominated by tidal-fluvial interactions and nonlinearly-generated low-frequency compound tides (Parker, 2007). In contrast, the low-frequency spectrum from NS_TIDE shows energy at annual and semi-annual periods due to seasonal cycles in discharge, at monthly and semi-monthly periods due to the influence of the tidal range term, and at periods of 3.5 and 7 days due to power-peaking fluctuations appearing in the Bonneville discharge term. In the semidiurnal band (bottom right panel), the NS_TIDE fit almost perfectly coincides with the observed spectrum and reproduces the cusp-like shapes formed around the dominant frequencies with great accuracy. Many constituents appearing in the HA fit (e.g., $H_1$ and $H_2$, which differ from $M_2$ by ±1 cpy) are far larger than expected from astronomical forcing, because they represent the modulation of major constituents (e.g. $M_2$) by the flow. In the fluvial context, astronomical $H_1$ and $H_2$ – as well as other frequencies of the HA fit separated by only a few cycles per year from major constituents – are insignificant, and these constituents are not resolved in NS_TIDE, because river flow is included directly in the basis functions. Similar observations can be made for the other tidal bands (not shown).

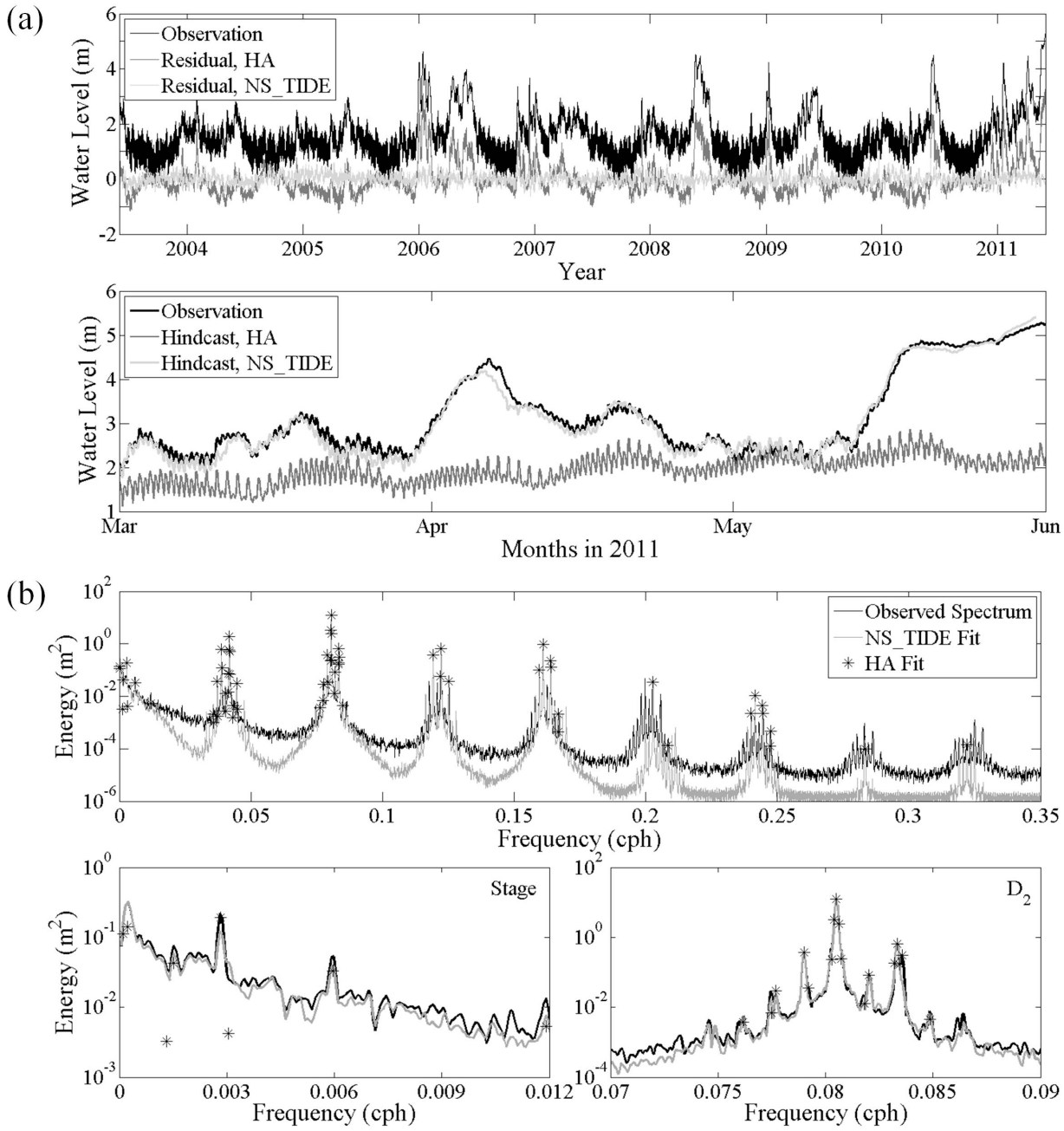


**Figure A.1.3** **Results for standard HA and NS_TIDE at Vancouver, WA, from June 2003 to June 2011. (a) (top) Residuals and (bottom) hindcasts are shown for both methods, for the complete time series and a three-month period in 2011, respectively. (b) (top) Power spectra of the observed signal and IRLS fits for both methods. (bottom) Zoom-ins of the power spectra for the low-frequency (stage) and semi-diurnal ($D_2$) bands.**

**Table A.1.2 Results for standard HA and NS_TIDE.**

| Method | Test | Specifications | LOR (yr) | Data Points | Parameters | Variance (%) | RMSE (m) | Max. Error (m) |
|---|---|---|---|---|---|---|---|---|
| HA | Reference | Hindcast for 2003-2011[a] | 8 | 70 247 | 127 | 38.5 | 0.604 | 3.26 |
| NS_TIDE | | Hindcast for 2003-2011[b] | 8 | 70 197 | 288 | 96.4 | 0.165 | 0.99 |
| NS_TIDE | Sensitivity to exponents and LOR | Hindcast with KJ's exponents[c] | 8 | 70 197 | 288 | 91.6 | 0.197 | 1.06 |
| | | Hindcast for a high flow year | 1 | 8812 | 260 | 97.7 | 0.153 | 0.76 |
| | | Hindcast for a low flow year | 1 | 8842 | 184 | 92.6 | 0.152 | 0.54 |
| NS_TIDE | Sensitivity to constituent selection and rejection | Hindcast with $\eta = 0.05$ | 8 | 70 197 | 184 | 96.2 | 0.169 | 0.94 |
| | | Hindcast with $\eta = 0.5$ | 8 | 70 197 | 352 | 96.6 | 0.163 | 0.97 |
| | | Hindcast with mean SNR $\geq 10$ | 8 | 70 197 | 228 | 96.4 | 0.166 | 0.99 |
| | | Hindcast with uncorrelated noise model | 8 | 70 197 | 204 | 96.4 | 0.165 | 0.98 |
| NS_TIDE | Sensitivity to separation of discharge terms | Hindcast without Willamette | 8 | 70 222 | 216 | 73.8 | 0.429 | 2.84 |
| | | Hindcast with Columbia and Willamette summed ($n_Q = 1$) | 8 | 70 197 | 216 | 91.6 | 0.211 | 1.16 |
| NS_TIDE | Predicting capabilities | Prediction for 2007-2011 from 2003-2007 analysis | 4 | 35 230 | 296 | 94.7 | 0.168 | 0.84 |
| | | Prediction for 2003-2007 from 2007-2011 analysis | 4 | 35 141 | 240 | 96.9 | 0.171 | 1.01 |
| | | Prediction from a high flow year analysis | 8 | 70 197 | 260 | 99.5 | 0.180 | 1.01 |
| | | Prediction from a low flow year analysis | 8 | 70 197 | 184 | 78.4 | 0.211 | 1.25 |
| | | Prediction using average flow by year-day | 8 | 69 925 | 288 | 46.5 | 0.561 | 2.79 |

[a] *Two constituents with periods of 3.5 and 7d were added to account for power-peaking at Bonneville Dam.*
[b] *With optimized exponents shown in Table A.1.1, two separate discharge terms ($n_Q = 2$), $\eta = 0.15$, and mean SNR $\geq 2$ based on a correlated noise model.*
[c] *Theoretical exponent values from Kukulka & Jay (2003a, b), as shown in Table A.1.1.*

The preceding results are summarized in Table A.1.2 and compared to a series of tests aimed at assessing the sensitivity of the model. First presented is the performance obtained when Kukulka & Jay's (2003a, b) exponents are used for the stage and tidal-fluvial models, in place of the optimized exponents shown in Table A.1.1. Results compare well with the reference analysis, with an explained variance $\geq 90$ %. The RMSE is increased by about 3 cm, mainly due to differences in MWL during very high flow conditions. Differences in tidal amplitudes and phases are minor and their variations as a function of the forcing conditions are well reproduced. The low sensitivity of model results to the exponents is partly due to the fact that variations in exponents are compensated by changes in model coefficients in a way that the resulting time series remain almost unaffected.

Two one-year analyses were also performed for a year with very strong river flow variations – June 2010 to June 2011 – and a year characterized by much lower flows – June 2004 to June 2005 (Figure A.1.2). Results show similar performances to the reference hindcast despite the smaller number of data points used, because the parameters are tuned to the conditions prevailing during each period of analysis. However, predictions based on the low flow year analysis are likely to be inaccurate if used under conditions that fall outside the range within which the model parameters were determined. This is shown in Table A.1.2 through predictions made for the June 2003 to June 2011 period using the parameters from the high and low flow year hindcasts. The analysis period must therefore cover most conditions encountered in the system in order for the tidal properties to be predicted with precision. In some cases, this can only be achieved using longer analysis windows or periods of greater range of flow conditions.

Model sensitivity to constituent selection and rejection was assessed through variations of the $\eta$ parameter of the Rayleigh criterion and the tolerance on the mean SNR for the error model. By varying $\eta$ from 0.05 to 0.5, the number of included constituents increases and, by extension, the number of parameters. Reducing the number of constituents only slightly degrades model performance. Similarly, the inclusion of more constituents does not significantly improve the results. On one extreme, if only one constituent per tidal band is included, the analysis is similar to CWT where all the energy contained in a tidal band is carried by a single frequency, with no distinction made between constituents. The resulting fit would explain most of the variance but with insufficient energy at minor tidal frequencies. On the other extreme, if the LOR is the only criterion controlling constituent selection, the included constituents are more dependent, and

phase shifts appear between constituents of a given tidal band that represent energy cancellation at nearby frequencies. The resulting linkage between constituents becomes more apparent as the nonlinear interactions between tidal components increase. Although the resulting fit is good, the properties of some minor constituents are not physical but rather an artefact of the analysis method, with correspondingly negative effects on the ability of the results to predict tides outside the analysis period. A moderate $\eta$ value, combined with a sufficiently high SNR tolerance, together lead to a selection that conforms to the local dynamics. Increasing the mean SNR lower limit to 10 actually led to the rejection of 7 constituents without affecting model performance. The use of an uncorrelated noise model, instead of the correlated noise model, also led to the rejection of a higher number of constituents, mainly those composing the $D_6$ to $D_8$ tidal bands.

As stressed above, the inclusion of the Willamette River as a separate discharge term is a crucial element in modeling the tides at Vancouver. This is reflected in Table A.1.2, first in a hindcast made without the Willamette River, and second in a hindcast where the same exponents are attributed to both discharge terms by combining them into a single term. Model performance is greatly affected by the exclusion of the Willamette River contribution. The effect of summing both discharges is lesser, but significant, and compares to the results obtained with the Kukulka & Jay's (2003a, b) exponents.

Also presented in Table A.1.2 are the prediction performances obtained with NS_TIDE by dividing the 8-year period into two equal halves and using the analysis of each half to predict tides for the other. For both predictions, the explained variances are around 95 % or higher, and the RMSE and maximum absolute errors are very close to the 8-year reference hindcast. This is due to the fact that both analysis windows encompass essentially the entire range of present flow conditions. An analysis performed using less dynamic years would likely provide poorer predictions. This is illustrated in Table A.1.2 through two 8-year predictions made using parameters from a high and low flow year hindcast, respectively, the latter presenting poorer performances during periods of high flows due to an inadequate choice of the reference analysis window. The last entry of Table A.1.2 shows results of a prediction made using the coefficients of the reference hindcast and a discharge time series based on an average river flow by year-day, which, for some systems, would be the only available forecast for discharge. Results are better than for HA, but errors remain large due to the large interannual variability of the river flow cycle.

A.1.4.3.3 Stage Model

Low-frequency fluctuations at Vancouver are represented by the stage model $s(t_j)$. Figure A.1.4 presents reconstructed time series for each term of the stage model. Results show that the MWL is mostly influenced by the discharge from Bonneville Dam, which follows sharp seasonal cycles with maximum flows usually occurring between March and June. Differences in MWL between high and low flow periods can be as high as 5 m during high flow years (e.g., 2011). The Willamette River flow, in turn, is much lower on average than the Columbia River flow, but often exhibits high peaks during the winter. Changes in MWL illustrated in Figure A.1.4 due to high flows in the Willamette River exceed 2.5 m during the analysis period. Inclusion of the influence of the Willamette River flow as a separate term is therefore justified, given its marked effect on MWL and its asynchronicity with the Columbia River flow. The range term of the stage model represents the influence of the neap-spring cycle on MWL. Semi-monthly oscillations appear in the reconstructed signal shown in Figure A.1.4, typical of what is usually observed at upstream stations in tidal rivers. These oscillations increase in importance as the flow decreases. As for the constant term $c_0$ in $s(t_j)$ (not shown), it gives the vertical shift that best fits the data, which is -0.61 m in this case. This represents the difference between the average MWL and the gauge datum, which is set at an estimate of historic extreme low water.

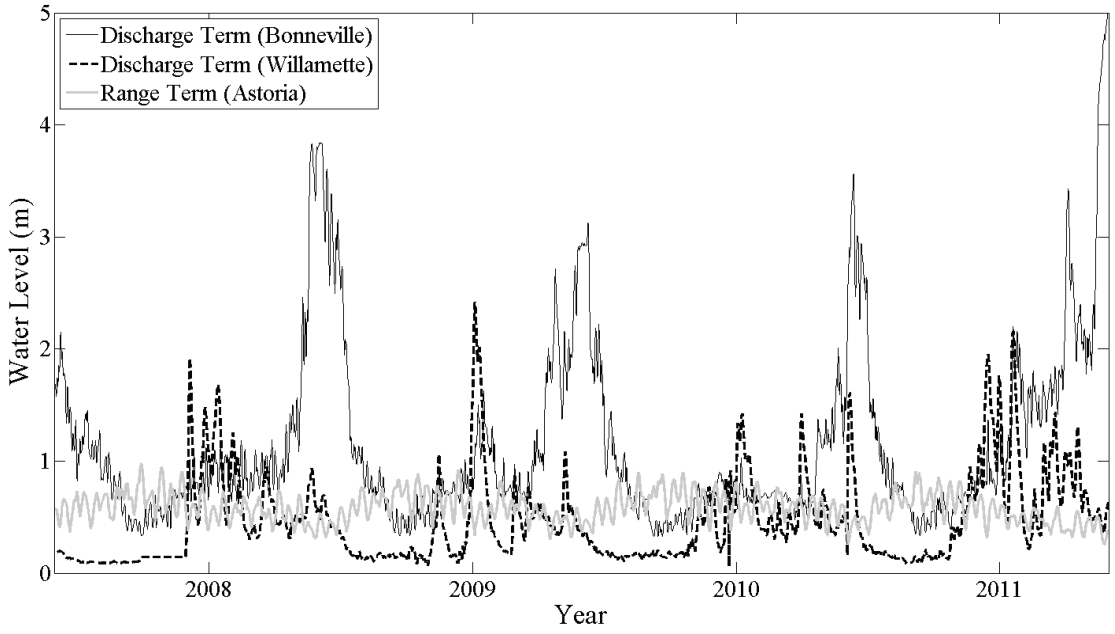


**Figure A.1.4** **Individual contributions of each term of the stage model to the MWL at Vancouver, WA, from June 2007 to June 2011, representing the discharge at Bonneville Dam, the discharge in the Willamette River, and the tidal range at Astoria, respectively.**

#### A.1.4.3.4 Tidal-Fluvial Model

Figure A.1.5 shows the contribution of each term of the tidal-fluvial model $f(t_j)$ to the total tidal variance, respectively representing the astronomical forcing (constant term), the discharge at Bonneville Dam, the discharge in the Willamette River, and the tidal range at Astoria. The sum of all terms yields the high-passed time series of predicted tidal heights. To better understand how tidal heights are dynamically connected to each of these terms, we can look at the amplitudes and phases of the constituents that compose the signal. Figure A.1.6 shows the amplitude variations of each separate term as a function of time for the $M_2$ tide alone. Their respective phases are 89.1°, 257.0°, 256.6°, and 4.1°. Properties of the constant term are an indicator of the amplitude and phase that the $M_2$ constituent would reach in the absence of river flow. The phases of both discharge terms differ by about 168° from that of the constant term, meaning that, to the lowest order, flow reduces tidal amplitudes. In other words, the time-dependent amplitudes of the discharge terms are essentially subtracted from the constant term. Since the phase difference is not exactly 180°, the phase of the resulting $M_2$ tide will gradually tend towards that of the discharge terms as their amplitude increases. This is consistent with tidal dynamics, as we expect the propagation times to increase as river flow increases. The tidal range term, in turn, makes the constituent properties (both amplitudes and phases) oscillate in accordance with the neap-spring cycle.

The resulting amplitudes and phases as a function of time, all terms combined, are shown in Figure A.1.7, for the $K_1$ and $M_2$ tides. Traditional HA gives, for $K_1$ and $M_2$, average amplitudes of 0.13 and 0.22 m and average phases of 9.3 and 60.4°, respectively. Results from NS_TIDE show fluctuations around these mean values following the variations in forcing. Amplitudes are significantly reduced and phases shifted as the river flow increases, and both constituent properties show fluctuations that follow the neap-spring cycle, as they react to its associated fortnightly variations in friction.

Amplitude and phase errors, shown as dotted lines in Figure A.1.7, increase during highly nonstationary events, as the signal becomes more nonlinear. Large errors during very high flows ($Q > Q_{th}$) are however reduced by use of Eq. (A.1.12). In NS_TIDE, error bounds also increase as more constituents are included in the analysis, since they become more dependent on each

other. Applying a more restrictive Rayleigh criterion therefore improves the confidence limits and decreases the dependence among constituents, but determines fewer of them.

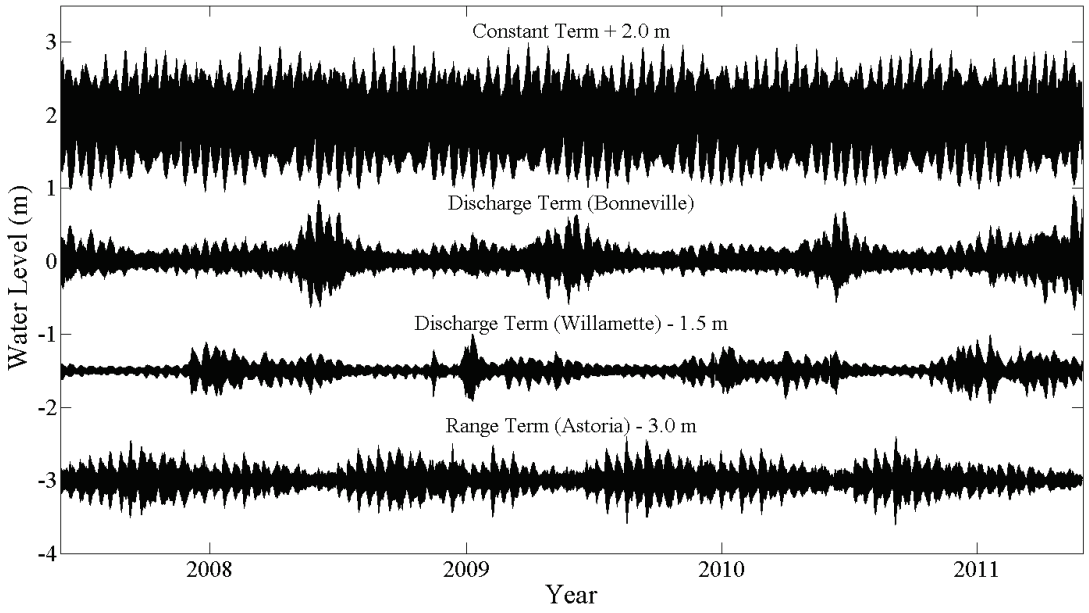


**Figure A.1.5** **Individual contributions of each term of the tidal-fluvial model to the tidal heights at Vancouver, WA, from June 2007 to June 2011, representing the astronomical forcing (constant term), the discharge at Bonneville Dam, the discharge in the Willamette River, and the tidal range at Astoria, respectively. Time series are shifted vertically for clarity.**

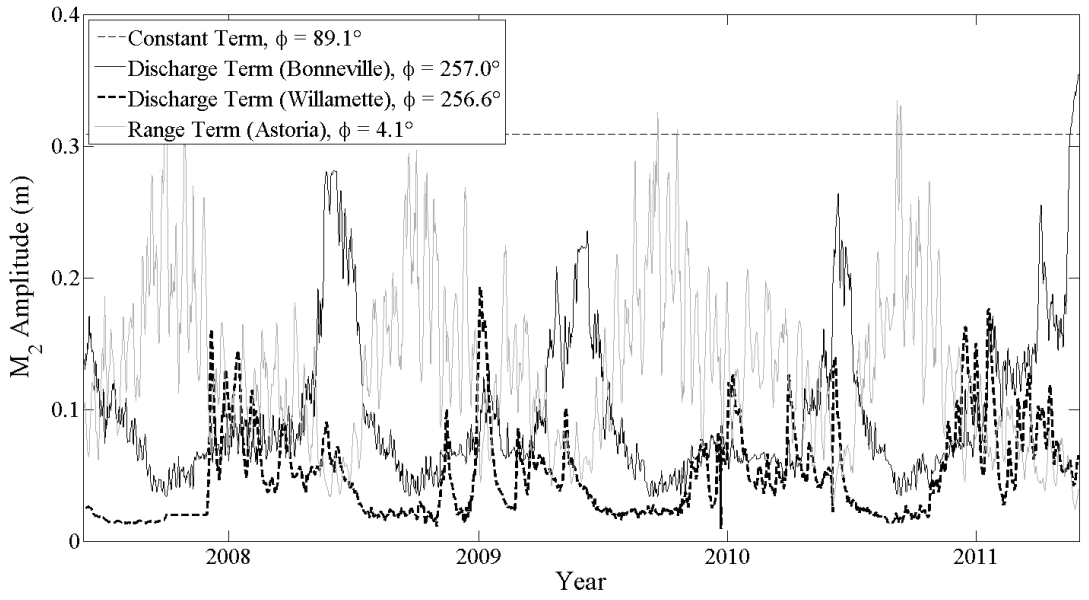


**Figure A.1.6** **Individual contributions of each term of the tidal fluvial-model to the $M_2$ amplitudes at Vancouver, WA, from June 2007 to June 2011, representing the astronomical forcing (constant term), the discharge at Bonneville Dam, the discharge in the Willamette River, and the tidal range at Astoria, respectively. Phases are shown in the legend.**

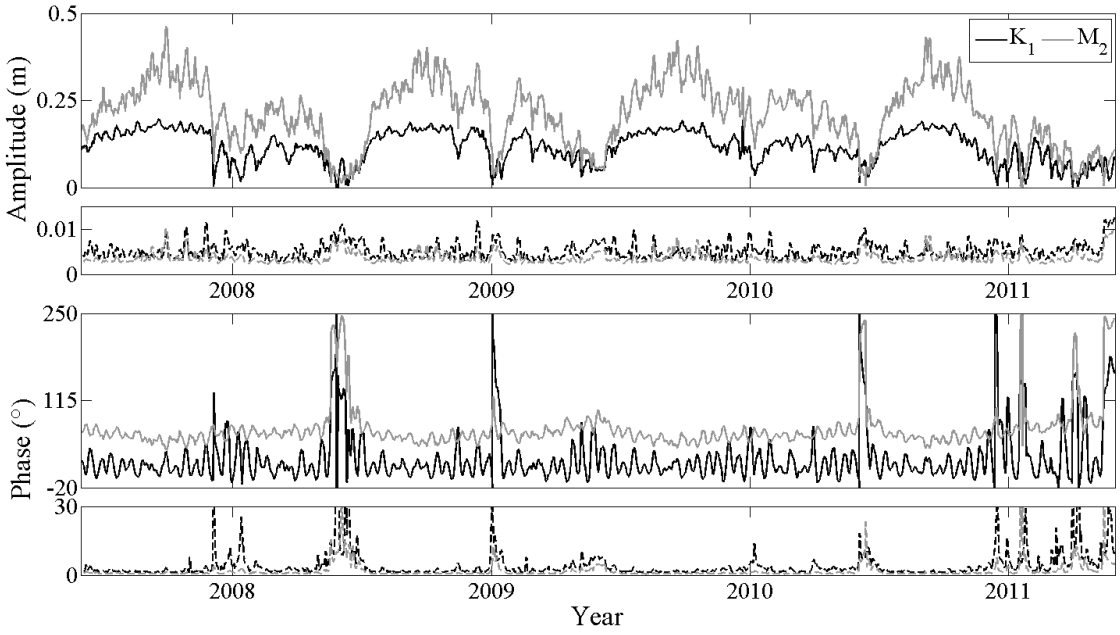


**Figure A.1.7** **$K_1$ and $M_2$ amplitudes and phases (solid lines) at Vancouver, WA, from June 2007 to June 2011, along with their error bounds (dotted lines), based on a correlated noise model.**

## A.1.5 Discussion and Conclusions

### *A.1.5.1 Improvements over Conventional Tidal Analysis Methods*

Conventional tidal analysis methods are usually unable to represent the nonstationary nature of river tides, because they are either limited in their time or frequency representation of the phenomenon. Traditional HA gives average amplitudes and phases for a wide range of constituents, but with no information in the time domain. Time series obtained from STHA, using a relatively short moving window compared to the analysis period, typically exhibit increased tidal damping during periods of high discharge accompanied by phase shifts due to increased propagation times of the tidal wave. The effects of tidal range are however smoothed out with window lengths that exceed the duration of the neap-spring cycle. In addition, each individual analysis can only be used to predict tides under the exact same flow and tide conditions, which makes STHA useless for prediction. Interpretation of results from STHA is also laborious, because there is no easy way to separate the influence of discharge from different rivers or tidal range on the resulting tide. CWT, in turn, proved to be very successful in the study of nonstationary time series as it provides a good localization of events in time and is invertible (Jay &

Flinchem, 1995). It nonetheless lacks frequency resolution within tidal bands and is sensitive to side-lobe effects near the ends of the time series.

In contrast, NS_TIDE gives, with a single analysis, time series of amplitudes and phases for each resolved constituent with the same time resolution as the original signal. It is able to solve for more than one frequency per tidal band – although fewer than with standard HA – under highly nonstationary tidal conditions without losing information in the time domain. Moreover, this is done in such a way that the respective contribution of flow and tidal forcing can be quantified and used for hindcast or prediction purposes, if flow predictions are available. Thus, NS_TIDE is able to facilitate dynamical inquiries regarding the evolution of tides as a function of the changing forcing conditions.

#### *A.1.5.2 Merits of the Approach Compared to Dynamic Circulation Models*

The presented method provides a pointwise (0D) description of the tides and MWL that can potentially be extended to a 1D description by spatial interpolation of the model parameters. In comparison, dynamic circulation models (1D, 2D or 3D) provide a detailed description of the tidal hydrodynamics at the scale of the grid element size. They offer a spatially integrating view of a system, whereas our method offers a temporally integrated view of a signal, measured at one point in space but over a much larger period of time, ranging from a few years to a century or more (e.g., Jay *et al.*, 2011). This information is usually not obtained from high-resolution numerical models. The main advantage of an approach based on regression analysis is that no terrain description is needed (topography, substrate friction, etc.), thus minimizing sensitivity to local topographic uncertainty, which is especially a problem for historical analyses. Also, the parameter calibration is completely automated and replaced by rather simple functions whose exponents are optimized to account for local topographic and frictional effects, and whose coefficients are determined from IRLS analyses. Another advantage of NS_TIDE is that it can separate the influences of discharge and oceanic tides on the resulting tidal signal, whereas this is not as straightforward with numerical models. This approach can therefore be used with confidence in rivers where no dynamical model exists, or as a complement to these models. Hence, it provides an alternate way to look at river tides. Finally, use of NS_TIDE on model output would be an excellent way to test a numerical model of a strongly nonstationary system (cf. Foreman & Henry, 1989).

*A.1.5.3 Summary*

We have developed a new HA-based method for the analysis of nonstationary tides and successfully applied it to the modeling and hindcast of river tides in the LCR. We generalized traditional HA by embedding the nonstationary fluvial and tidal forcing into the HA basis functions. The model is based on an analytical solution for incident tidal waves in frictional, convergent channels (Kukulka & Jay, 2003a, b) adapted to linear regression analysis. The treatment of non-tidal forcing is iteratively optimized, one tidal band at a time, to provide band-specific models that best describe the local interactions of river tides. The model output is in the form of time series of subtidal and tidal properties, expressed in terms of external forcing, for each resolved tidal frequency. They are given, along with their error time series calculated from either uncorrelated or correlated noise models. The method differs from other tidal analysis tools for nonstationary tides in that it can distinguish frequencies within a given tidal band, without any loss of resolution in the time domain. This was made possible through the redefinition of the Rayleigh criterion and the decision tree for constituent selection, which account for the smearing of the constituent spectral lines and the importance of shallow water constituents. Applied to a tide gauge 172 km from the ocean with very nonstationary tides, the model gave surprisingly accurate results for river tides, with a hindcast explaining 96.4 % of the original signal variance and a RMSE of 0.165 m for an 8-year analysis period with highly variable river flow. Although NS_TIDE maintains the compactness of HA, it has the potential to be an effective tool for the prediction of tides in tidal rivers, provided that reasonably accurate flow predictions are available. It can be extended to other problems involving nonstationary tides, provided that suitable time series are available to quantify the relevant factors altering the tide. Our MATLAB implementation of NS_TIDE is available upon request.

### A.1.6 Appendix: Solution Details

The time series of tidal heights in Eq. (A.1.9) can be rewritten in matrix form as:

$$h(t) = s(t) + f(t) = \left[\mathbf{A}_s \quad \mathbf{A}_f\right] \times \left[\mathbf{x}_s \quad \mathbf{x}_f\right]^{\mathrm{T}} \tag{A.1.20}$$

with basis functions $\mathbf{A}_s$ and $\mathbf{A}_f$ such as:

$$\mathbf{A}_s = \begin{bmatrix} 1 & Q^{p_s}(t_1) & \dfrac{R^{q_s}(t_1)}{Q^{r_s}(t_1)} \\ \vdots & \vdots & \vdots \\ 1 & Q^{p_s}(t_m) & \dfrac{R^{q_s}(t_m)}{Q^{r_s}(t_m)} \end{bmatrix} \tag{A.1.21}$$

$$\mathbf{A}_f = \begin{bmatrix} \cos(\sigma_1 t_1) & \cdots & \cos(\sigma_n t_1) & \sin(\sigma_1 t_1) & \cdots & \sin(\sigma_n t_1) \\ \vdots & \cdots & \vdots & \vdots & \cdots & \vdots \\ \cos(\sigma_1 t_m) & \cdots & \cos(\sigma_n t_m) & \sin(\sigma_1 t_m) & \cdots & \sin(\sigma_n t_m) \end{bmatrix}$$

$$\begin{matrix} Q^{p_f}(t_1)\cos(\sigma_1 t_1) & \cdots & Q^{p_f}(t_1)\cos(\sigma_n t_1) & Q^{p_f}(t_1)\sin(\sigma_1 t_1) & \cdots & Q^{p_f}(t_1)\sin(\sigma_n t_1) \\ \vdots & \cdots & \vdots & \vdots & \cdots & \vdots \\ Q^{p_f}(t_m)\cos(\sigma_1 t_m) & \cdots & Q^{p_f}(t_m)\cos(\sigma_n t_m) & Q^{p_f}(t_m)\sin(\sigma_1 t_m) & \cdots & Q^{p_f}(t_m)\sin(\sigma_n t_m) \end{matrix} \tag{A.1.22}$$

$$\begin{bmatrix} \dfrac{R^{q_f}(t_1)}{Q^{r_f}(t_1)}\cos(\sigma_1 t_1) & \cdots & \dfrac{R^{q_f}(t_1)}{Q^{r_f}(t_1)}\cos(\sigma_n t_1) & \dfrac{R^{q_f}(t_1)}{Q^{r_f}(t_1)}\sin(\sigma_1 t_1) & \cdots & \dfrac{R^{q_f}(t_1)}{Q^{r_f}(t_1)}\sin(\sigma_n t_1) \\ \vdots & \cdots & \vdots & \vdots & \cdots & \vdots \\ \dfrac{R^{q_f}(t_m)}{Q^{r_f}(t_m)}\cos(\sigma_1 t_m) & \cdots & \dfrac{R^{q_f}(t_m)}{Q^{r_f}(t_m)}\cos(\sigma_n t_m) & \dfrac{R^{q_f}(t_m)}{Q^{r_f}(t_m)}\sin(\sigma_1 t_m) & \cdots & \dfrac{R^{q_f}(t_m)}{Q^{r_f}(t_m)}\sin(\sigma_n t_m) \end{bmatrix}$$

and unknown parameters $\mathbf{x}_s$ and $\mathbf{x}_f$:

$$\mathbf{x}_s = \begin{bmatrix} c_0 & c_1 & c_2 \end{bmatrix} \tag{A.1.23}$$

$$\mathbf{x}_f = \begin{bmatrix} d_{0,1}^{(c)} & \cdots & d_{0,n}^{(c)} & d_{0,1}^{(s)} & \cdots & d_{0,n}^{(s)} & d_{1,1}^{(c)} & \cdots & d_{1,n}^{(c)} & d_{1,1}^{(s)} & \cdots & d_{1,n}^{(s)} & d_{2,1}^{(c)} & \cdots & d_{2,n}^{(c)} & d_{2,1}^{(s)} & \cdots & d_{2,n}^{(s)} \end{bmatrix} \tag{A.1.24}$$

From the coefficients $\mathbf{x}_s$, the respective contribution of the freshwater discharge and the neap-spring cycle to the total stage variation can be deduced and low-frequency variation in water levels reconstructed. As for the coefficients $\mathbf{x}_f$, it is useful to express each constituent ($k = 1, n$) in terms of their time-dependent amplitude and phase; hence the expected results take the form of a time series. We define, for each term of the tidal-fluvial model, the amplitudes $A_k$, $B_k$ and $C_k$, and phases $\alpha_k$, $\beta_k$ and $\gamma_k$ for a given constituent $k$ as:

$$A_k = \sqrt{\left(d_{0,k}^{(c)}\right)^2 + \left(d_{0,k}^{(s)}\right)^2} \tag{A.1.25}$$

$$B_k = Q^{p_f}(t)\sqrt{\left(d_{1,k}^{(c)}\right)^2 + \left(d_{1,k}^{(s)}\right)^2} \tag{A.1.26}$$

$$C_k = \frac{R^{q_f}(t)}{Q^{r_f}(t)}\sqrt{\left(d_{2,k}^{(c)}\right)^2 + \left(d_{2,k}^{(s)}\right)^2} \tag{A.1.27}$$

$$\alpha_k = \arctan\left(d_{0,k}^{(s)} / d_{0,k}^{(c)}\right) \tag{A.1.28}$$

$$\beta_k = \arctan\left(d_{1,k}^{(s)} / d_{1,k}^{(c)}\right) \tag{A.1.29}$$

$$\gamma_k = \arctan\left(d_{2,k}^{(s)} / d_{2,k}^{(c)}\right) \tag{A.1.30}$$

$B_k$ and $C_k$ are a function of time, while the other parameters are constant. Eqs. (A.1.25) – (A.1.27) express the contribution of astronomical, river flow and neap-spring forcing to the total variance in tidal heights, respectively, while Eqs. (A.1.28) – (A.1.30) are their corresponding (constant) phases. In order to obtain the total amplitude and phase variation of a given constituent, we combine Eqs. (A.1.25) – (A.1.30) such that time series of amplitudes and phases are obtained. For the constituent $k$, the time series of tidal heights has the form:

$$Z_k(t) = z_k(t)\mathrm{e}^{\mathrm{i}\sigma_k t} + z_{-k}(t)\mathrm{e}^{-\mathrm{i}\sigma_k t} = \left|z_k(t)\right|\mathrm{e}^{-\mathrm{i}\phi_k(t)}\mathrm{e}^{\mathrm{i}\sigma_k t} + \left|z_{-k}(t)\right|\mathrm{e}^{\mathrm{i}\phi_k(t)}\mathrm{e}^{-\mathrm{i}\sigma_k t} \tag{A.1.31}$$

where the time-dependent amplitudes and phases are given, respectively, by:

$$\left|Z_k(t)\right| = \left|z_k(t)\right| + \left|z_{-k}(t)\right| \tag{A.1.32}$$

$$\phi_k(t) = \arctan\left[\mathrm{Im}\left(z_{-k}(t)\right)/\mathrm{Re}\left(z_{-k}(t)\right)\right] \tag{A.1.33}$$

with, in terms of the amplitudes $A_k$, $B_k$, and $C_k$, and phases $\alpha_k$, $\beta_k$, and $\gamma_k$:

$$z_{-k}(t) = z_k^*(t) = \frac{1}{2}\left(A_k\cos\alpha_k + B_k\cos\beta_k + C_k\cos\gamma_k\right) + \mathrm{i}\frac{1}{2}\left(A_k\sin\alpha_k + B_k\sin\beta_k + C_k\sin\gamma_k\right) \tag{A.1.34}$$

### A.1.7 Acknowledgements

Work by Pascal Matte was supported by scholarships from the Natural Sciences and Engineering Research Council of Canada and from the Ministère de l'Éducation du Québec. Support for David A. Jay and Edward D. Zaron came from the National Science Foundation grant, "Secular trends in Pacific Tides", and from the Miller Foundation Grant to Portland State University. Tide and flow data were provided by the National Oceanic and Atmospheric Administration, and the U.S. Geological Survey. The authors thank Rich Pawlowicz, Bob Beardsley and Steve Lentz for distributing the T_TIDE package, which is the basis for the adaptations proposed in this paper, Yves Secretan who provided useful input regarding code and model verification, and four anonymous reviewers for their constructive comments on the manuscript.

## A.2 Estimation des débits tidaux dans l'estuaire fluvial du Saint-Laurent

Ce rapport présente une estimation des débits tidaux dans l'estuaire fluvial du Saint-Laurent basée sur une méthode de cubature, développée dans le cadre d'un stage de recherche (Travail dirigé II; 4 crédits) réalisé à Environnement Canada, Section Hydrologie et Écohydraulique. La méthode développée est une extension du modèle 1D de propagation de la marée présenté à l'objectif 2 et fait usage du MNT issu du modèle hydrodynamique 2D du Saint-Laurent présenté à l'objectif 3. Elle repose sur une intégration de l'équation de continuité et permet de reconstruire les débits en n'importe quel point du système. Les résultats sont validés aux sections de mesure.

### A.2.1 Introduction

La compréhension de plusieurs des processus dynamiques présents au sein des rivières à marée, comme le transport des sédiments en suspension, repose en grande partie sur une connaissance des débits tidaux (Chen & Chiu, 2002). Elle permet non seulement de mieux comprendre les processus physiques et hydrologiques qui caractérisent le milieu, mais également d'orienter le développement de plans d'intervention en cas de déversement toxique ou d'inondation. Aussi, l'information des débits est généralement utilisée comme condition limite dans les modèles numériques. La mesure directe des débits dans les grandes rivières à marée et les estuaires est toutefois compliquée par deux facteurs : la nature non-stationnaire de l'écoulement et la taille du système (typiquement avec des largeurs de sections de plusieurs km), qui rendent l'obtention de données simultanées (ou synoptiques) difficile. Il en résulte que les enregistrements historiques de débits sont généralement très courts comparés aux données historiques de niveaux d'eau disponibles.

Dans l'estuaire fluvial du Saint-Laurent, aucune station ni information sur les débits n'est disponible en temps réel pour le suivi des fluctuations du débit en fonction de la marée. Les seules estimations sont celles faites par Bourgault & Koutitonsky (1999), qui dérivent les débits mensuels d'eau douce à Québec à partir d'une relation de régression basée sur les niveaux mesurés à la station de Neuville. Forrester (1972), de son côté, fournit une approximation des courants et débits moyens dans le fleuve et l'estuaire déduits indirectement à partir de l'équation de continuité et d'observations de niveaux d'eau aux stations marégraphiques. Cette dernière

estimation, validée par les analyses faites par Godin (1971), trouve ses limites dans la représentation très simplifiée du système. Le modèle de Bourgault & Koutitonsky (1999) se limite, quant à lui, à des prédictions mensuelles à Québec qui ne tiennent pas compte de l'influence des estrans sur les volumes emmagasinés ni des variations associées à la marée. Par ailleurs, le modèle ONE-D (Dailey & Harleman, 1972, Morse, 1990) qui tourne en mode opérationnel dans le fleuve (Lefaivre *et al.*, 2009), ne publie pas d'information sur les débits en temps réel, en partie en raison d'un manque de données pour leur validation.

La méthode ici présentée vise à reconstruire, en différents endroits le long de l'estuaire fluvial du Saint-Laurent, des séries temporelles subhoraires de débits tidaux en utilisant les observations historiques de niveaux d'eau aux stations, la topographie de la rivière et les débits moyens journaliers en provenance de l'amont et des tributaires. Cette méthode, dite de cubature, est basée sur la résolution de l'équation de continuité. Elle se veut une extension du travail de Forrester (1972) et prend en compte la nature bidimensionnelle de la topographie en considérant l'inondation et l'exondation des estrans en fonction du cycle de marée. La méthode proposée utilise les niveaux mesurés aux stations marégraphiques, génère une interpolation 1D longitudinale (c.-à-d. entre les stations) basée sur une décomposition du signal de marée par composantes (Matte *et al.*, 2014c), et projette les niveaux sur un maillage 2D aux éléments finis pour déterminer la surface inondée, influencée par la topographie des estrans. L'équation de continuité est alors résolue à différents temps et pour différentes sections le long du système. Les résultats sont validés à partir des débits mesurés lors d'une campagne de terrain réalisée en 2009 (Matte *et al.*, 2014a).

### A.2.2 Contexte

#### *A.2.2.1 L'estuaire fluvial du Saint-Laurent*

Le fleuve Saint-Laurent relie l'Océan Atlantique et les Grands Lacs (Figure A.2.1). Il est la troisième plus grande rivière en Amérique du Nord, avec un bassin versant de ~$1.6 \times 10^6$ km$^2$ et un débit d'eau douce moyen de 12 200 m$^3$s$^{-1}$ à Québec. Les débits nets journaliers historiques du Saint-Laurent atteignent des valeurs minimum et maximum de 7000 et 32 700 m$^3$s$^{-1}$ à Québec, respectivement, pour la période de 1960 à 2010, prenant en compte la contribution des tributaires et des superficies drainées (Bouchard & Morin, 2000). Les effets de telles variations sur les

niveaux moyens et le marnage de la marée sont sévères, particulièrement dans la partie amont de l'estuaire fluvial, passé Deschambault (Godin, 1999).

Les marées océaniques sont amplifiées en entrant dans le Saint-Laurent, atteignant leur plus haut niveau dans l'estuaire supérieur à Saint-Joseph-de-la-Rive (ici défini comme kilomètre de rivière de référence, c.-à-d. rkm 0), avec 7 m de marnage lors des grandes marées de vives-eaux. Elles se trouvent progressivement atténuées en amont dû aux effets de la friction. Les marées sont de type mixte semi-diurne, avec un ratio des composantes majeures semi-diurnes et diurnes, c.-à-d. $(|M_2|+|S_2|)/(|K_1|+|O_1|)$, de 5:1 à Saint-Joseph-de-la-Rive et diminuant en amont, les composantes semi-diurnes étant atténuées plus rapidement que les composantes diurnes.

L'estuaire fluvial du Saint-Laurent s'étend sur 180 km, de la pointe est de l'île d'Orléans, située à la limite de l'intrusion saline, jusqu'à la sortie du lac Saint-Pierre (Figure A.2.1). Sa largeur fait quelques km, variant d'environ 600 m sous les ponts de Québec à 15 km en aval de l'île d'Orléans. La profondeur moyenne du chenal de navigation varie de 13 m à plus de 60 m.

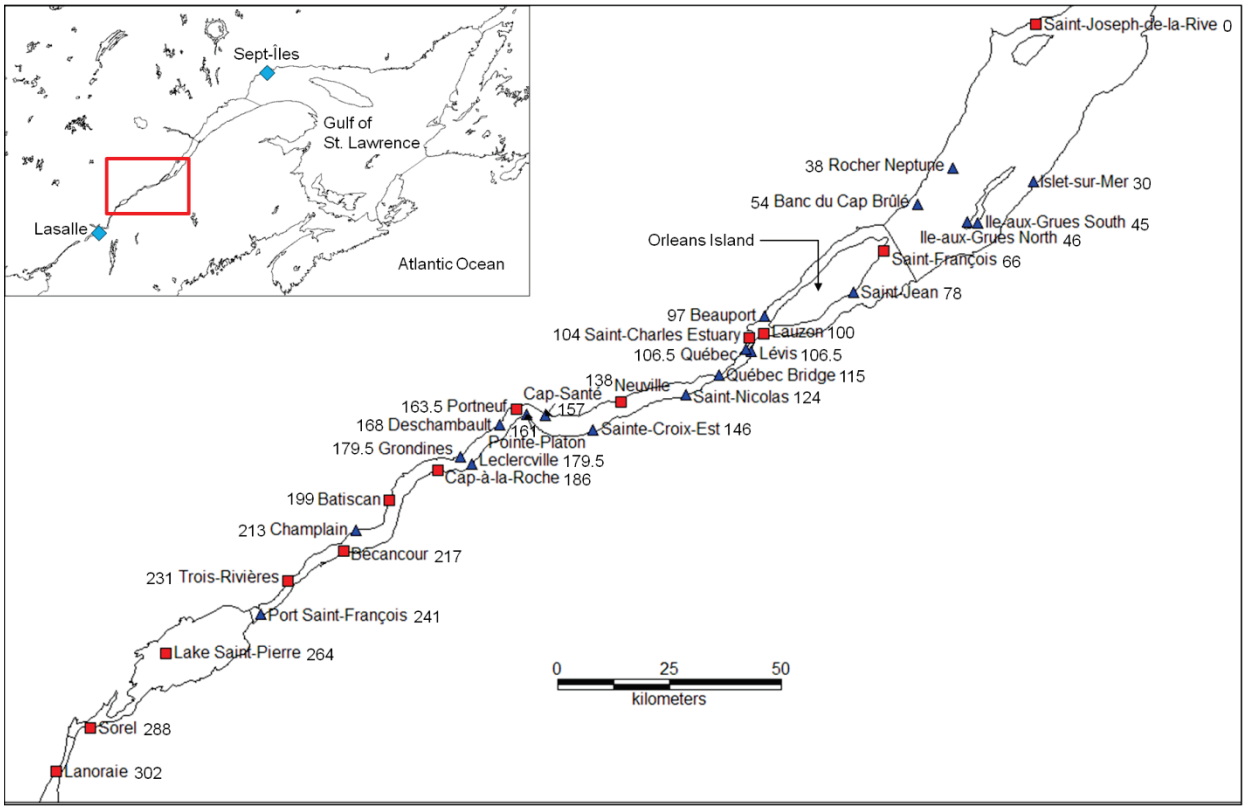


**Figure A.2.1** **Carte de l'estuaire fluvial du Saint-Laurent; (carrés rouges) stations marégraphiques permanentes; (triangles bleus) stations temporaires; (losanges bleus pâle) stations de référence pour la marée océanique (Sept-Îles) et le débit fluvial (Lasalle). Les kilomètres de rivière sont inscrits à côté de chaque station.**

Alors que les marées peuvent être considérées comme stationnaires dans l'estuaire et le golfe, elles sont fortement non-linéaires et non-stationnaires dans l'estuaire fluvial. Godin (1999) suggère la séparation de l'estuaire fluvial en trois zones : 1) Québec – Portneuf (rkm 100 à 163.5), 2) Portneuf – Cap-à-la-Roche (rkm 163.5 à 186), et 3) Cap-à-la-Roche – Trois-Rivières (rkm 186 à 231). Cette subdivision est corroborée par les travaux de Matte *et al.* (2014c). Les niveaux d'eau observés à ces stations sont présentés à la Figure A.2.2 pour une période d'un an, caractérisée par de très faibles et de très forts débits. Dans la première zone (Québec – Portneuf), les marnages varient de 3 à 6 m en fonction de la station et de la phase sur le cycle de marées de mortes-eaux et de vives-eaux. Les niveaux d'eau s'élèvent de plus d'un mètre par heure en marée montante, entraînant des changements rapides dans les conditions d'écoulement et les superficies inondées. De fortes inversions de courant sont générées avec des débits de pointe atteignant cinq fois le débit moyen journalier, autant vers l'aval que vers l'amont. La deuxième zone (Portneuf – Cap-à-la-Roche) marque la transition entre les régimes tidal et fluvio-tidal. Elle se caractérise par une forte augmentation de la pente du lit aux rapides Richelieu près de Deschambault (rkm 168). Le signal de marée est fortement distorsionné et progressivement atténué en raison de la friction, du débit fluvial et de la géométrie du milieu. La durée du jusant est augmentée, le flot est plus abrupt et court, puisqu'une partie de l'énergie des principales composantes de marée est transférée non-linéairement aux harmoniques supérieures. La limite où l'écoulement devient unidirectionnel (c.-à-d. seulement une étale de courant) se déplace entre Grondines (rkm 179.5) et Bécancour (rkm 217) en fonction du marnage de la marée et du débit, dans la transition entre les zones 2 et 3. Dans la zone 3 (Cap-à-la-Roche – Trois-Rivières), les variations du niveau d'eau sont dominées par le cycle saisonnier du débit fluvial. À Trois-Rivières (rkm 231), les modulations semi-mensuelles du niveau moyen induites par le cycle de mortes-eaux/vives-eaux excèdent en amplitude la marée semi-diurne (LeBlond, 1979), dont le marnage est de 0.2 m pour une marée moyenne. La majeure partie des composantes de marée de courte période (c.-à-d. diurne, semi-diurne, etc.) se trouve atténuée dans le lac Saint-Pierre (rkm 264), mais les oscillations de longue période sont toujours perceptibles à Montréal (rkm 360).

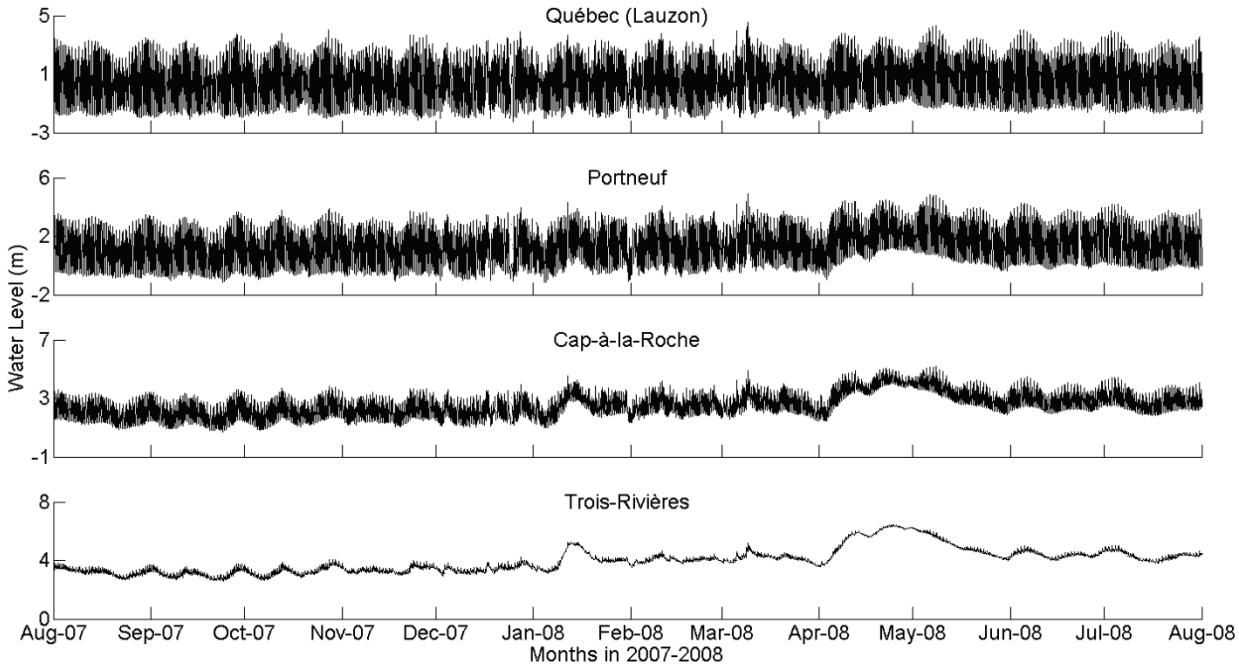


**Figure A.2.2 Niveaux d'eau observés à Québec (Lauzon), Portneuf, Cap-à-la-Roche et Trois-Rivières pour la période d'août 2007 à août 2008.**

### *A.2.2.2 Données disponibles*

Un large réseau de stations marégraphiques est maintenu par Pêches et Océans Canada dans l'estuaire fluvial et comprend des données de niveaux d'eau remontant à la fin du 19$^{e}$ siècle ou le début du 20$^{e}$ siècle pour certaines stations (Lauzon, Batiscan, Trois-Rivières). Actuellement, dix stations permanentes sont en place entre Port Saint-François et l'île d'Orléans. Quelques stations temporaires sont parfois installées durant les mois d'été, par exemple à Saint-Jean d'Orléans et à l'est de l'île d'Orléans (banc du Cap-Brûlé, rocher Neptune). D'autres stations ont été installées à différents endroits dans l'estuaire fluvial, mais ont été démantelées; elles fournissent généralement des données durant quelques années. Dans l'ensemble, ces stations fournissent des données de niveaux d'eau à un pas de temps horaire jusqu'en 1993, puis à un pas de 15 minutes de 1993 à 2000; depuis 2000, les données sont fournies à toutes les 3 minutes.

En 1960, des données de courant ont été recueillies manuellement par Dohler (1961) à différents endroits entre Montréal et Neuville et à différentes profondeurs d'eau, à l'aide d'un couranto-

mètre; la durée des observations excède rarement 48 h. Une partie de ces données est présentée dans les rapports de Dohler (1961) et de Godin (1971).

En 1968, la division du chenal de navigation du Saint-Laurent (St. Lawrence Ship Channel Division) a installé deux paires de courantomètres à quelques km en amont du pont de Québec (Pointe à Basile). Chaque paire était constituée de deux courantomètres très rapprochés, dont les données discontinues sont considérées comme appartenant à un seul et même enregistrement. La première paire a été installée au centre du chenal et la seconde près de la rive sud du fleuve. Des mesures aux 30 minutes ont été recueillies du 2 octobre au 5 novembre 1968. On peut trouver une analyse harmonique de ces données dans Godin (1971). Des mesures similaires ont aussi été recueillies à la hauteur de l'Île-aux-Coudres durant la même campagne. En août de la même année, des données de vitesses ont été recueillies à Saint-François sur une période de huit jours (Prandle & Crookshank, 1972). En juin 1971, des mesures de vitesses ont aussi été récoltées devant Québec et dans les bras nord et sud de l'île d'Orléans (Prandle, 1971).

Forrester (1972), de son côté, donne des valeurs moyennes de courants de marée obtenues à partir de l'équation de continuité pour 22 sections du fleuve et de l'estuaire du Saint-Laurent. Il fournit également les amplitudes et phases moyennes de sept composantes harmoniques et leur débit et courant tidaux moyens respectifs pour chaque section. Les valeurs prédites concordent avec les valeurs mesurées avec des écarts de l'ordre de 10 % (Godin, 1971).

En septembre 1978 et en avril et juin 1979, des mesures de vitesses ont été réalisées par Long *et al.* (1980), à l'aide de courantomètres, le long de quatre sections situées respectivement en amont de la rivière Bécancour, en amont du quai de Bécancour, sur trois lignes comprises entre le quai de Bécancour et la batture de Gentilly, et entre la batture de Gentilly et la centrale nucléaire.

Les seules données de courant récentes ayant fait l'objet d'une publication sont celles d'une campagne de mesures à l'ADCP où la distribution verticale des vitesses a été mesurée sur une section du fleuve située à Québec, pendant une durée de 24 h, par la section Hydrologie et Écohydraulique d'Environnement Canada. Les données ont permis de calculer les fluctuations du débit sur deux cycles de marée complets et ont été utilisées pour valider le modèle numérique de Bourgault & Koutitonsky (1999). Plus récemment, à l'été 2009, une large campagne de terrain a été réalisée dans l'estuaire fluvial du Saint-Laurent où des mesures de niveaux d'eau et de vitesses ont été recueillies le long de 13 transects, chacun couvrant approximativement un cycle

de marée (Matte *et al.*, 2014a). Les données de débit issues de cette campagne sont utilisées pour la validation de la présente méthode.

Pour reconstruire les séries temporelles de débits tidaux le long de l'estuaire fluvial, l'utilisation de modèles numériques, statistiques, ou autre est nécessaire. Dans la section qui suit, une reconstruction des séries historiques de débits par la méthode de cubature est présentée comme alternative à la modélisation numérique, avec comme avantages la possibilité de reconstruire de longues périodes de données historiques (de l'ordre de plusieurs décennies), de s'affranchir de toute phase d'étalonnage et de prédire les débits tidaux attendus pour des conditions de débit fluvial et de marées données.

### A.2.3 Méthodes

#### *A.2.3.1 Méthode de cubature*

La méthode de cubature (Dronkers, 1964, Forrester, 1972) consiste à calculer le débit d'une rivière en se basant uniquement sur la connaissance des niveaux d'eau et de la géométrie de la rivière, à travers l'équation de continuité (ou conservation de la masse). Diverses adaptations de la méthode de cubature ont été proposées, comme celle de Dierckx *et al.* (1981), qui utilise des splines pour obtenir une représentation en continu des niveaux et des débits en rivière en fonction de la marée. Alternativement, une description simplifiée de la géométrie par zones ou à l'aide de largeurs de section prédéfinies, à la manière d'un modèle hydrodynamique 1D, peut être utilisée. La méthode ici proposée utilise une discrétisation 2D par éléments finis de l'estuaire fluvial pour résoudre l'équation de continuité à différents temps et à différentes stations le long du système. Bien que plus complexe qu'une discrétisation 1D, ce type de représentation a été choisi en raison de la disponibilité de maillages 2D et de données spatiales détaillées dans le fleuve Saint-Laurent, ce qui représente un atout pour la prise en compte des estrans dans le calcul.

Mathématiquement, l'équation de continuité sous sa forme intégrale peut s'écrire comme :

$$\int_{\Omega} \vec{\nabla} \cdot \vec{q} d\Omega = -\int_{\Omega} \frac{\partial h}{\partial t} d\Omega , \tag{A.2.1}$$

où $q$ est le débit spécifique ($m^2\ s^{-1}$), $h$ est le niveau d'eau (m) et $t$ est le temps (s).

En appliquant le théorème de divergence de Gauss, on peut transformer l'intégrale de surface Ω en intégrale de contour $\Gamma$ :

$$\oint_{\Gamma} \vec{q} \cdot \vec{n} d\Gamma = -\int_{\Omega} \frac{\partial h}{\partial t} d\Omega . \tag{A.2.2}$$

Appliqué à un volume de contrôle en rivière, l'intégrale de contour est égale à la somme des débits entrants et sortants à travers les frontières du système :

$$\sum_i Q_i = -\int_{\Omega} \frac{\partial h}{\partial t} d\Omega . \tag{A.2.3}$$

Les débits entrants et sortants $Q_i$ peuvent être divisés en deux parties : les débits des tributaires $Q_r$ et le débit tidal $Q_t$ (inconnu) :

$$\sum_i Q_i = Q_t - \sum_r Q_r . \tag{A.2.4}$$

Pour résoudre l'intégrale de l'Éq. (A.2.3), une discrétisation en 2D par éléments finis du domaine est utilisée, où la dérivée temporelle de $h$ est exprimée par une fonction d'approximation $N$ multipliée par les valeurs nodales de $\partial h/\partial t$ :

$$\frac{\partial h}{\partial t} = \langle N \rangle \left\{ \frac{\partial h_n}{\partial t} \right\}. \tag{A.2.5}$$

Le débit élémentaire, calculé sur un élément du maillage, est défini comme l'intégrale de surface suivante :

$$Q^e = -\int_{\Omega^e} \langle N \rangle \left\{ \frac{\partial h_n}{\partial t} \right\} d\Omega^e , \tag{A.2.6}$$

où les dérivées temporelles au temps $i$ sont calculées à chaque nœud du maillage, pour un pas de temps $\Delta t$ donné, à l'aide de différences finies centrées :

$$\left.\frac{\partial h_n}{\partial t}\right|_i = \frac{h_{i+1} - h_{i-1}}{2\Delta t}. \tag{A.2.7}$$

La somme des débits élémentaires du maillage mène au résultat de l'intégrale de l'Éq. (A.2.3). Ainsi, la forme finale de l'équation de continuité est :

$$Q_t = \sum_r Q_r + \sum_e Q^e. \tag{A.2.8}$$

Les différentes étapes de la méthode peuvent se résumer comme suit :

1. Générer le maillage sur lequel sont basés les calculs et extraire la topographie associée;
2. Définir les conditions limites, qui consistent en tous les débits $Q_r$ entrants dans le système de l'amont et des tributaires;
3. À chaque pas de temps :
    a. Projeter les niveaux d'eau sur le maillage;
    b. Identifier les nœuds inondés et exondés;
    c. Calculer les dérivées temporelles aux nœuds;
    d. Calculer les débits élémentaires (boucle sur les éléments);
    e. Calculer le débit tidal à partir de l'Éq. (A.2.8).

Le domaine d'intégration Ω est représenté par la surface mouillée, laquelle change dans le temps en fonction des zones inondées et exondées par la marée. Le calcul doit donc se faire en ne considérant que les nœuds qui composent cette surface. Pour ce faire, une condition de couvre-ment-découvrement est posée aux nœuds, basée sur la différence entre le niveau d'eau et la topographie, où les nœuds secs sont ramenés à une profondeur nulle. Enfin, pour connaître le débit à une section donnée, le calcul est effectué sur la portion du maillage allant de la section en question jusqu'à la limite la plus en amont du système, là où l'influence de la marée semi-diurne devient imperceptible, tel que schématisé à la Figure A.2.3.

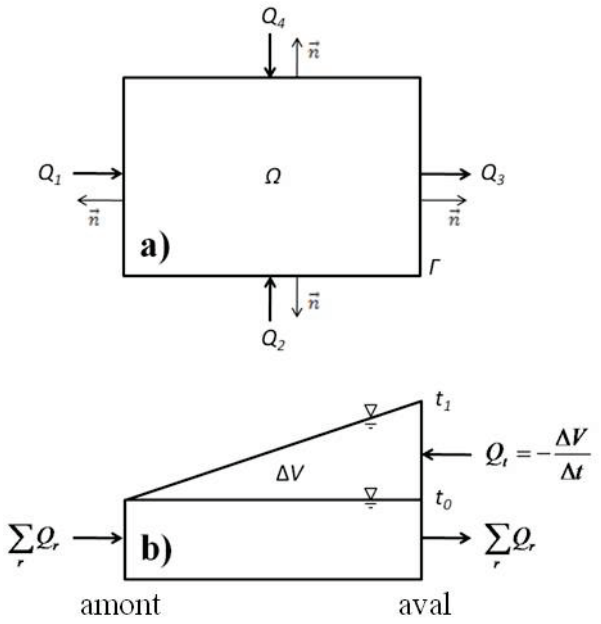


**Figure A.2.3 Représentation schématisée du calcul du débit tidal basé sur l'équation de continuité : a) vue en plan du domaine d'intégration, incluant les débits entrants et sortants à travers la frontière du domaine ($Q_r$); b) vue en coupe illustrant la portion du domaine allant de la limite amont, où l'influence de la marée disparaît, jusqu'à la section aval pour laquelle est calculé le débit.**

### *A.2.3.2 Application à l'estuaire fluvial du Saint-Laurent*

#### A.2.3.2.1 Maillage 2D aux éléments finis

La méthode de cubature présentée est appliquée à l'estuaire fluvial du Saint-Laurent. Le maillage 2D utilisé est en partie repris du modèle hydrodynamique développé à l'objectif 3 de cette thèse pour le secteur de l'estuaire fluvial (Trois-Rivières – Île-aux-Coudres, tronqué à Québec) et en partie tiré du modèle opérationnel du tronçon Montréal – Trois-Rivières du fleuve (tronqué à Lanoraie), développé à Environnement Canada (Morin & Champoux, 2006). Des éléments de type T3 sont utilisés pour les calculs de cubature. La Figure A.2.4 présente les limites du maillage pour l'ensemble du secteur Lanoraie – Québec.

#### A.2.3.2.2 Topographie

Pour que le modèle reproduise bien les volumes d'eau emmagasinés et évacués cycliquement par la marée, une bonne description de la géométrie de la rivière, et plus particulièrement de la topographie des estrans, est nécessaire. La topographie utilisée pour le secteur Trois-Rivières –

Québec est issue du modèle hydrodynamique développé à l'objectif 3 de cette thèse. Elle se base sur des données bathymétriques du Service Hydrographique du Canada (SHC) et sur un jeu de données LIDAR couvrant l'ensemble des estrans de l'estuaire fluvial du Saint-Laurent. La topographie des embouchures des principaux tributaires (c.-à-d. des rivières Saint-Maurice, Batiscan, Sainte-Anne, Jacques-Cartier et Chaudière) est également incluse de façon à tenir compte des volumes emmagasinés en fonction de la marée. En raison d'un manque de données, la bathymétrie des tributaires a été approximée par un chenal régulier de profondeur et largeur variables. Pour le lac Saint-Pierre, les données de terrain tirées du modèle d'Environnement Canada (Morin & Champoux, 2006) ont été utilisées. La topographie pour le secteur Lanoraie – Québec est présentée à la Figure A.2.5.

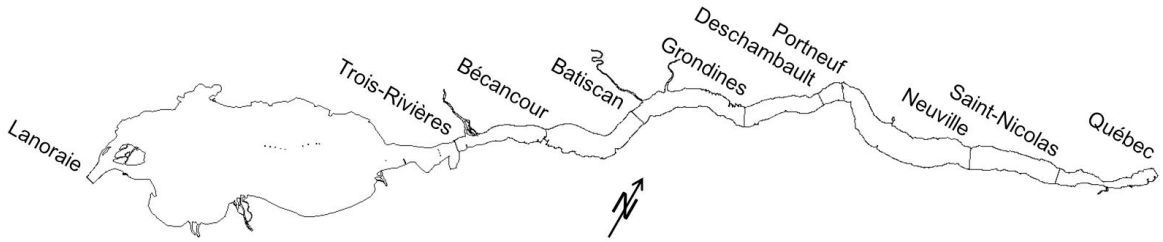


**Figure A.2.4 Limites du maillage 2D aux éléments finis pour le secteur Lanoraie – Québec, incluant la liste des stations de validation.**

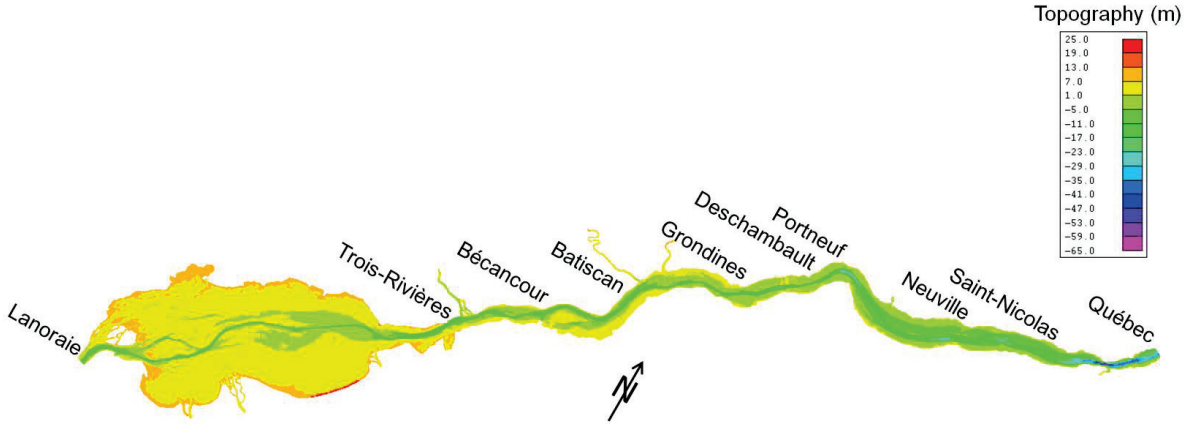


**Figure A.2.5 Topographie pour le secteur Lanoraie – Québec.**

#### A.2.3.2.3 Conditions limites en débit

Les débits imposés aux limites, c.-à-d. la somme des $Q_r$ [cf. Éq. (A.2.4)], sont obtenus de la reconstruction des débits moyens journaliers de Bouchard & Morin (2000) dans le fleuve et ses tributaires, qui tient compte des apports latéraux et des aires drainées. Les variations du débit à la limite amont du domaine, située à Lanoraie, sont supposées indépendantes de la marée. Les calculs sont réalisés en utilisant un pas de temps $\Delta t$ de 6 minutes qui permet de bien capter les extrema de la marée.

#### A.2.3.2.4 Interpolation des niveaux d'eau

Le passage des niveaux mesurés aux stations de l'estuaire fluvial du Saint-Laurent vers le maillage 2D doit se faire par interpolation. Les niveaux d'eau interpolés sont obtenus du modèle 1D de propagation de la marée décrit dans Matte *et al.* (2014c). Ce dernier permet de générer une prédiction du niveau d'eau en tout point le long d'un profil longitudinal (1D) du fleuve Saint-Laurent, centré sur le chenal de navigation. Les niveaux prédits le long de ce profil sont ensuite projetés (extrapolés) sur le maillage 2D, les valeurs attribuées aux nœuds correspondant aux plus proches valeurs interpolées du profil 1D.

Le modèle de propagation de la marée (Matte *et al.*, 2014c), utilisé comme interpolateur des niveaux d'eau, est basé sur une représentation harmonique de la marée dans laquelle les niveaux d'eau sont exprimés sous la forme d'une somme de termes harmoniques :

$$h(t) = b_{0,0} + \sum_{k=1}^{n} [b_{1,k} \cos(\sigma_k t) + b_{2,k} \sin(\sigma_k t)], \tag{A.2.9}$$

où $\sigma_k$ sont les fréquences connues, $n$ est le nombre de composantes, et $b_{0,0}$, $b_{1,k}$ et $b_{2,k}$ sont des coefficients définis par :

$$b_{l,k}(t) = a_{0,l,k} + a_{1,l,k} Q^{p_l}(t) + a_{2,l,k} \frac{R^{q_l}(t)}{Q^{r_l}(t)}, \tag{A.2.10}$$

où $Q$ est le débit fluvial ($m^3s^{-1}$), $R$ est le marnage océanique (m), $p$, $q$, $r$ sont les exposants du modèle, et $a_{0,l,k}$, $a_{1,l,k}$, $a_{2,l,k}$ sont les coefficients du modèle déterminés par régression linéaire.

Le logiciel NS_TIDE (Matte *et al.*, 2013) a été utilisé pour l'analyse des séries de niveaux d'eau aux stations. L'interpolation spatiale (1D) entre les stations est effectuée sur les coefficients du modèle, plutôt que sur les niveaux eux-mêmes, à l'aide de fonctions cubiques d'Hermite par morceaux (Fritsch & Carlson, 1980). Cela permet une reconstruction en tout point des niveaux, composante par composante, et ainsi de conserver l'information sur le contenu fréquentiel de la marée sur l'ensemble du domaine. De même, la reconstruction des débits tidaux peut également se faire composante par composante afin d'évaluer leur contribution respective au débit total. De plus, puisque le modèle permet de prédire la marée pour différentes conditions de débit fluvial $Q$ et de marnage océanique $R$, cette capacité prédictive est transmise à la méthode de cubature, de sorte que des prédictions de débits tidaux peuvent être générées pour ces mêmes conditions.

A.2.3.2.5 Validation

La méthode est testée et validée sur une période couvrant l'été 2009, afin de comparer les débits reconstruits par cubature avec ceux mesurés lors d'une campagne de mesure réalisée pour la même période. Les données de vitesses (à l'ADCP) et de niveaux d'eau (au RTK GPS) issues de cette campagne ont été utilisées pour calculer les débits sur 13 sections de l'estuaire fluvial du Saint-Laurent, dont 9 sont utilisées pour la validation de la méthode (cf. Figure A.2.4). Le détail de la campagne et des analyses effectuées est présenté dans Matte *et al.* (2014a).

## A.2.4 Résultats

### *A.2.4.1 Surface totale mouillée*

La superficie du domaine d'intégration change en fonction du temps dû à la marée. L'utilisation d'un maillage 2D et d'une topographie précise permet de prendre en compte l'évolution des surfaces inondées et exondées dans le calcul des volumes. Les variations de la surface mouillée sont un indicateur de l'étendue des estrans, bien que ces derniers ne soient pas inondés de façon synchrone sur tout le domaine en raison des temps de propagation de la marée. Les fluctuations de la surface totale mouillée en fonction de la marée sont illustrées à la Figure A.2.6.

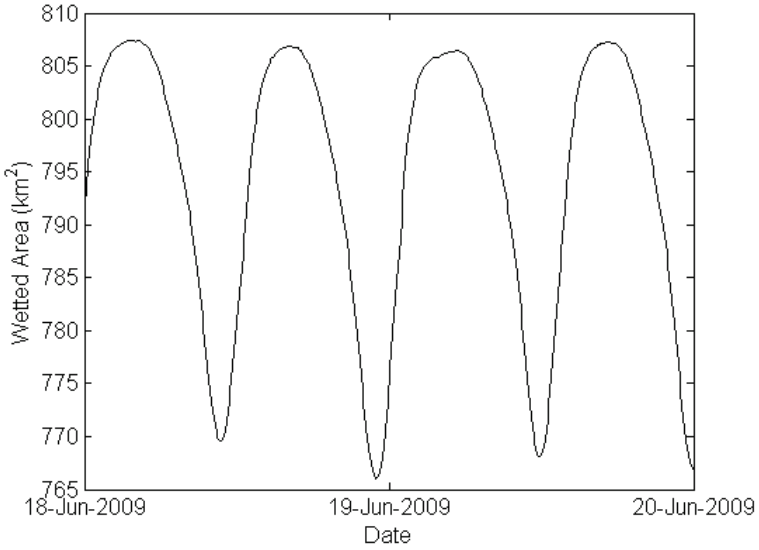


**Figure A.2.6 Évolution de la surface totale mouillée en fonction de la marée sur l'ensemble du domaine d'intégration (Lanoraie – Québec), calculée par la méthode de cubature.**

### *A.2.4.2 Débits aux transects*

Les résultats du calcul des débits tidaux pour les sections en aval de Lanoraie (cf. Figure A.2.4) sont présentés aux Figure A.2.7 à Figure A.2.15. Sur chacune des figures apparaissent les surfaces mouillées en amont de la limite, les niveaux d'eau mesurés et prédits au transect, les débits mesurés lors de la campagne de 2009 et les débits calculés par la méthode de cubature. Les étales de courant sont également identifiées par une ligne continue de débit nul, marquant la séparation entre le jusant (débits positifs) et le flot (débits négatifs). À noter que les débits positifs sont dirigés vers l'aval, alors que les débits négatifs sont dirigés vers l'amont. Les erreurs moyennes et maximales sont présentées à la Table A.2.1. La Figure A.2.16, quant à elle, présente pour la période du 18 au 19 juin 2009 les débits tidaux calculés par la méthode de cubature pour l'ensemble des transects.

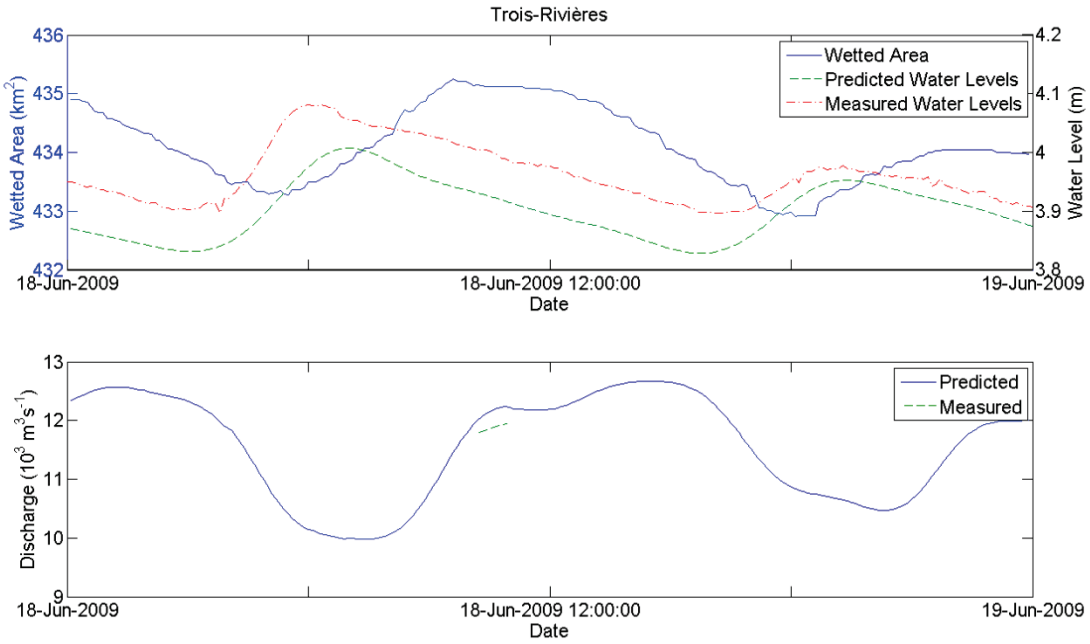


**Figure A.2.7** **Transect de Trois-Rivières : (haut) surface totale mouillée en amont et niveaux mesurés au transect; (bas) débits mesurés et calculés.**

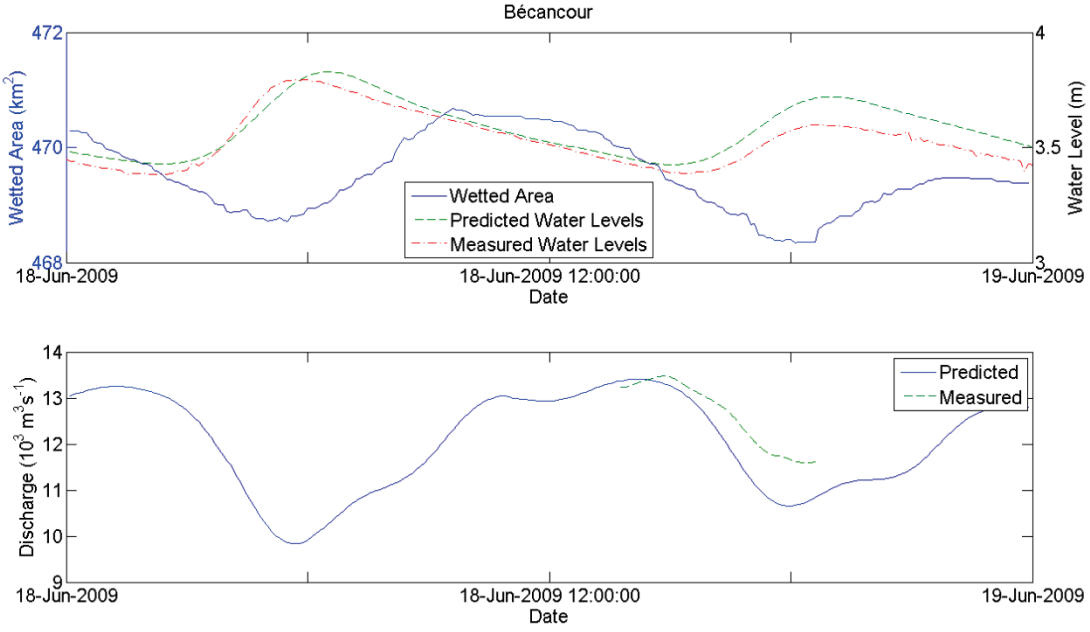


**Figure A.2.8** **Transect de Bécancour : (haut) surface totale mouillée en amont et niveaux mesurés au transect; (bas) débits mesurés et calculés.**

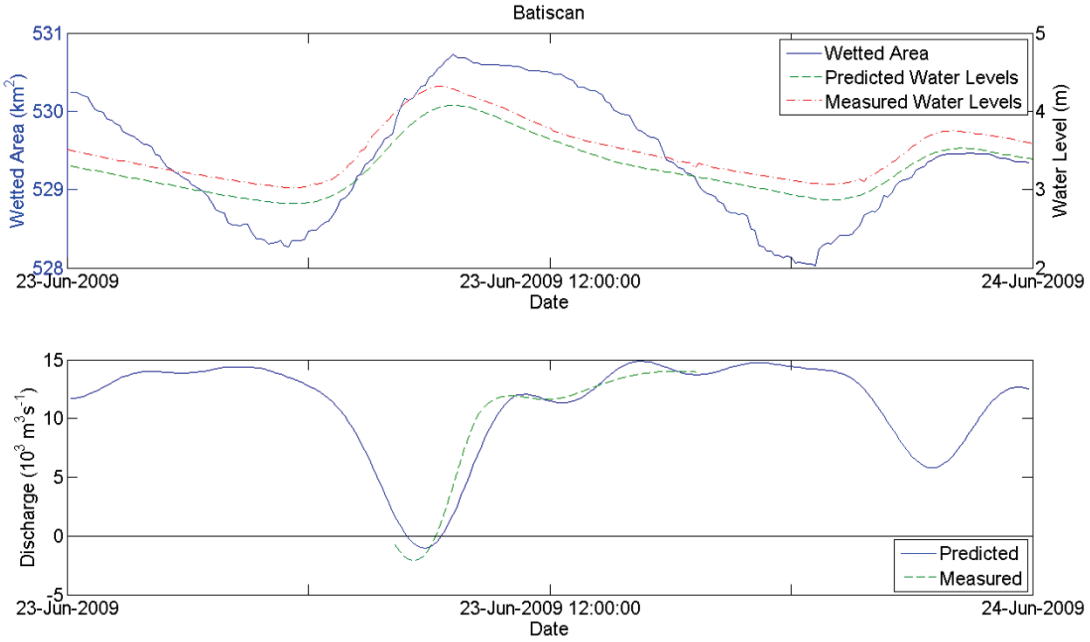


**Figure A.2.9** **Transect de Batiscan : (haut) surface totale mouillée en amont et niveaux mesurés au transect; (bas) débits mesurés et calculés.**

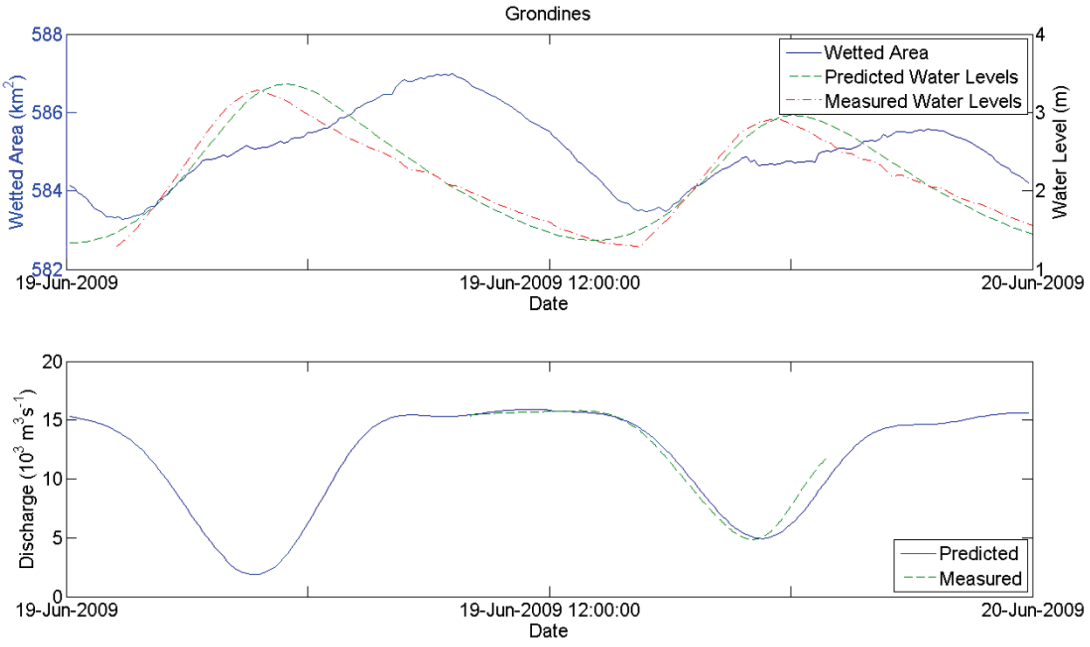


**Figure A.2.10** **Transect de Grondines : (haut) surface totale mouillée en amont et niveaux mesurés au transect; (bas) débits mesurés et calculés.**

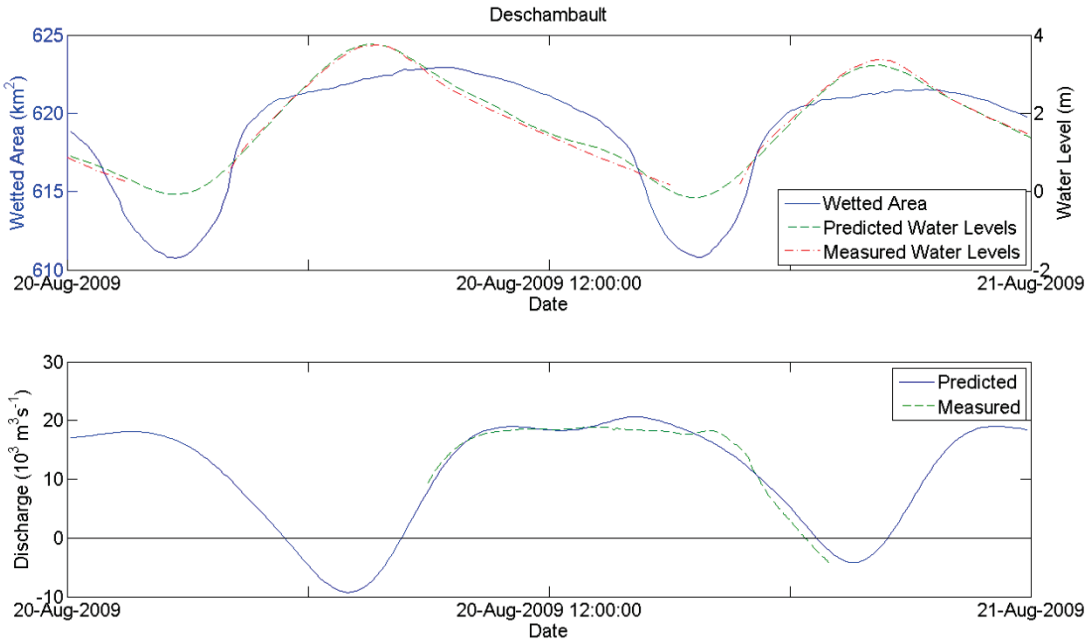


**Figure A.2.11 Transect de Deschambault : (haut) surface totale mouillée en amont et niveaux mesurés au transect; (bas) débits mesurés et calculés.**

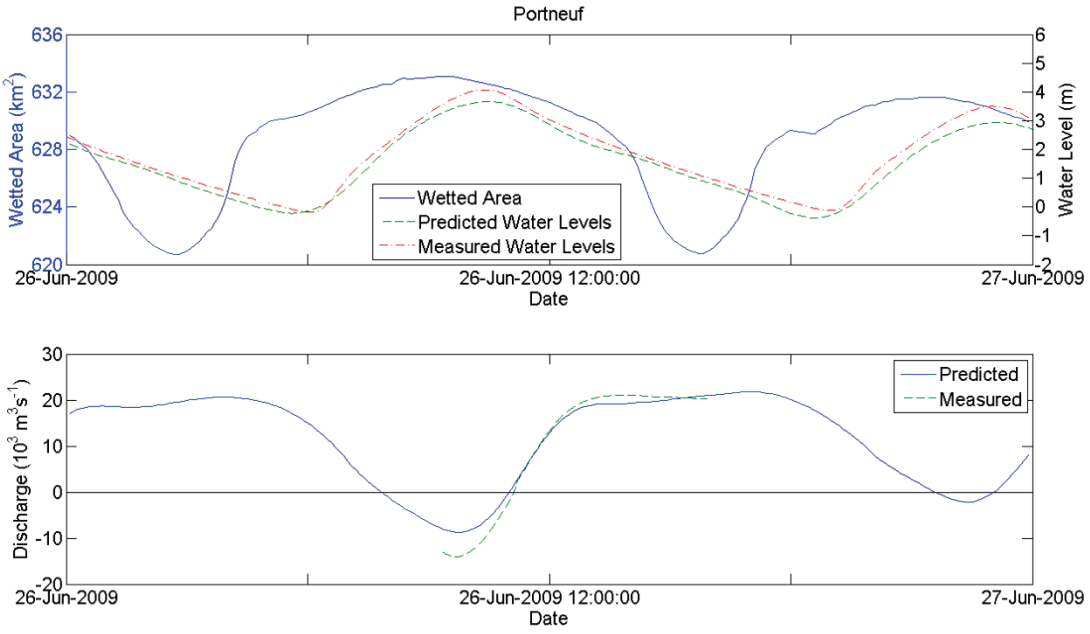


**Figure A.2.12 Transect de Portneuf : (haut) surface totale mouillée en amont et niveaux mesurés au transect; (bas) débits mesurés et calculés.**

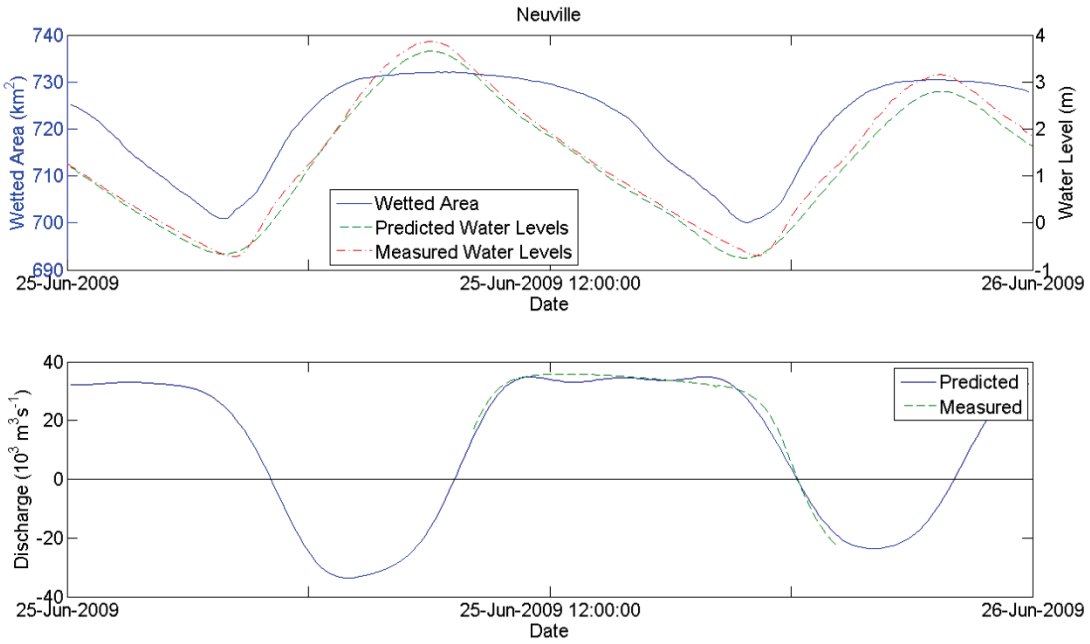


**Figure A.2.13 Transect de Neuville : (haut) surface totale mouillée en amont et niveaux mesurés au transect; (bas) débits mesurés et calculés.**

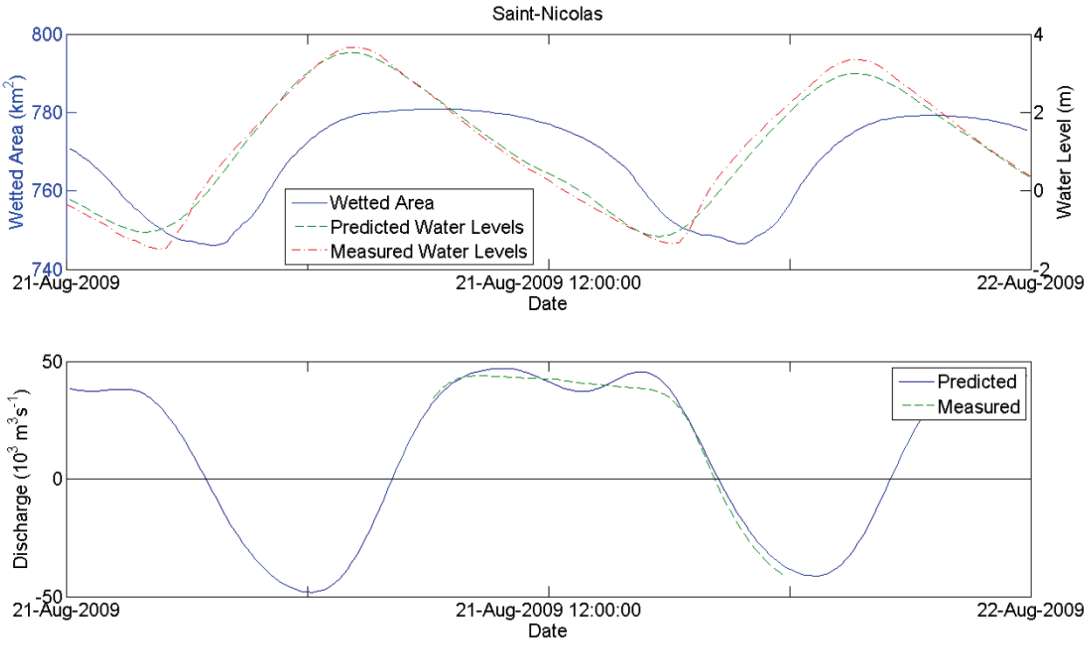


**Figure A.2.14 Transect de Saint-Nicolas : (haut) surface totale mouillée en amont et niveaux mesurés au transect; (bas) débits mesurés et calculés.**

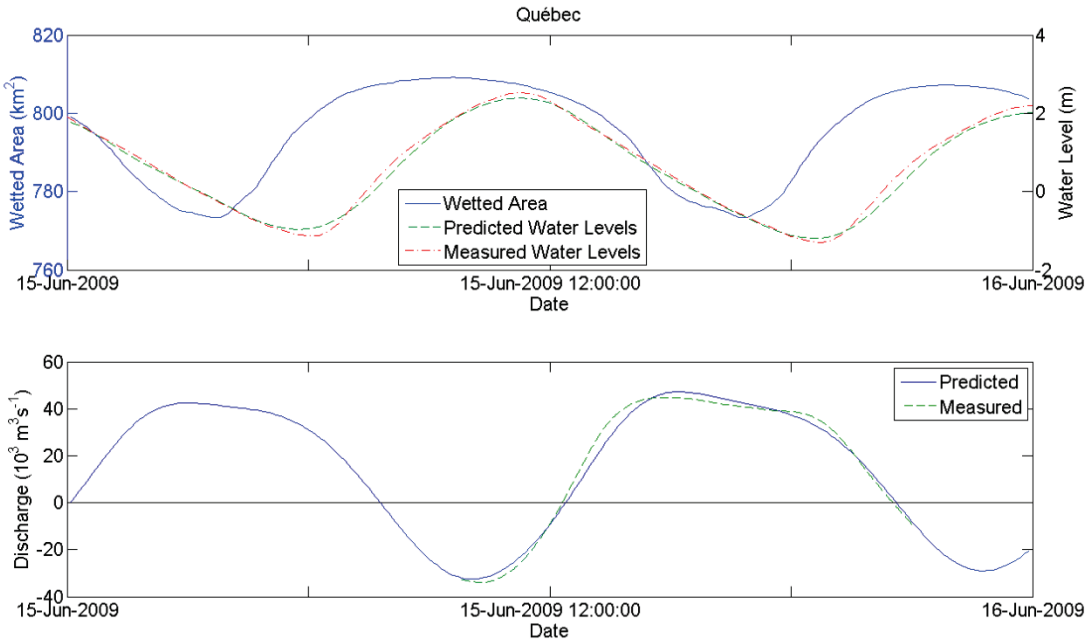


**Figure A.2.15 Transect de Québec : (haut) surface totale mouillée en amont et niveaux mesurés au transect; (bas) débits mesurés et calculés.**

De façon générale, en observant les Figure A.2.7 à Figure A.2.15, les marées basses mesurées à chaque transect ne sont pas systématiquement synchronisées avec les minimums de superficies inondées. Cela s'explique par les temps de propagation de la marée basse de l'aval vers l'amont et par la distribution spatiale des estrans. Les minimums de l'aire mouillée apparaissent donc au moment où la marée basse rejoint les zones composées d'une plus large proportion de zones peu profondes.

Les débits calculés, pour leur part, présentent certaines oscillations notamment liées à l'interpolation spatiale des composantes quart-diurnes (ex.: Figure A.2.14). Ces composantes sont responsables de l'asymétrie du signal de marée et du retard dans l'arrivée des marées basses. Leur interpolation spatiale dans le modèle 1D présente certaines oscillations liées à la distance séparant les stations de mesure, lorsque cette dernière approche la longueur d'onde des composantes de marée (Matte *et al.*, 2014c). Néanmoins, dans l'ensemble, les prédictions de débit suivent assez bien les variations mesurées lors de la campagne de 2009. Les temps d'occurrence des étales de courant et des débits minimums et maximums sont très bien reproduits pour les stations en aval de Deschambault (Figure A.2.11 à Figure A.2.15). Les durées du jusant et du flot peuvent facilement être identifiées en comparant les périodes de débits positifs et négatifs,

respectivement. L'amplitude des variations sur un cycle de marée est toutefois légèrement sous-estimée par la méthode. En amont de Deschambault (Figure A.2.7 à Figure A.2.10), les cycles de débit se trouvent légèrement déphasés par rapport aux débits mesurés. Les niveaux extraits du modèle de propagation de la marée, utilisés lors du calcul, sont entachés d'une plus grande erreur aux stations en amont du système, lorsque mis en relation avec leur marnage (Matte *et al.*, 2014c); les différences entre les niveaux prédits et mesurés en témoignent. Les marées sont en effet très non-linéaires et difficiles à prédire dans cette portion du fleuve, particulièrement les temps d'arrivée des marées basses et l'asymétrie de la marée, tous deux dictés en majeure partie par les composantes quart-diurnes. Ces erreurs se répercutent donc sur les débits calculés.

**Table A.2.1 Erreurs moyennes et maximales (en $m^3s^{-1}$) entre les débits mesurés et prédits par la méthode de cubature.**

| Station | Erreur moyenne | Erreur maximale |
|---|---|---|
| Trois-Rivières | 282 | 306 |
| Bécancour | 661 | 1050 |
| Batiscan | 1385 | 3465 |
| Grondines | 746 | 2134 |
| Deschambault | 1395 | 2333 |
| Portneuf | 2360 | 5368 |
| Neuville | 2253 | 5387 |
| Saint-Nicolas | 3464 | 7044 |
| Québec | 2856 | 7266 |

La Table A.2.1 met en chiffres les différences entre les débits mesurés et calculés par la méthode de cubature. L'erreur instantanée augmente vers l'aval, puisque les superficies d'intégration augmentent et l'erreur se cumule, les calculs étant toujours faits depuis la limite amont (Lanoraie). Mises en relation avec l'amplitude des signaux, ces erreurs sont inférieures à 10 % à chaque station. Une grande partie de l'erreur est attribuable aux erreurs du modèle de propagation de la marée utilisé pour l'interpolation spatiale des niveaux d'eau. La précision des prédictions obtenues de ce modèle est de l'ordre de 30 cm (Matte *et al.*, 2014c). Un aperçu de cette erreur apparait aux Figure A.2.7 à Figure A.2.15 en comparant les niveaux mesurés aux niveaux prédits. À ces erreurs s'ajoutent le transfert des niveaux du modèle 1D vers un maillage 2D, les erreurs de topographie des berges servant à définir le domaine d'intégration, de même que les variations latérales des niveaux d'eau dans les régions où des gradients latéraux sont attendus (ex.: estrans, zones de forte courbure du chenal).

En dépit des erreurs observées, la méthode permet de reconstruire avec succès les débits tidaux en n'importe quelle section du domaine, pour n'importe quelle période passée ou future. Par exemple, la Figure A.2.16 superpose pour l'ensemble des stations l'évolution des débits tidaux sur une période de deux jours, issue des résultats de reconstruction. On constate qu'en aval de Portneuf, le système est clairement dominé par la marée, alors qu'en amont de Portneuf, le signal est fortement atténué par la friction et l'influence grandissante du débit fluvial. Les rapides Richelieu sont responsables de cette diminution marquée du débit tidal et marquent la transition du régime tidal vers le régime fluvio-tidal.

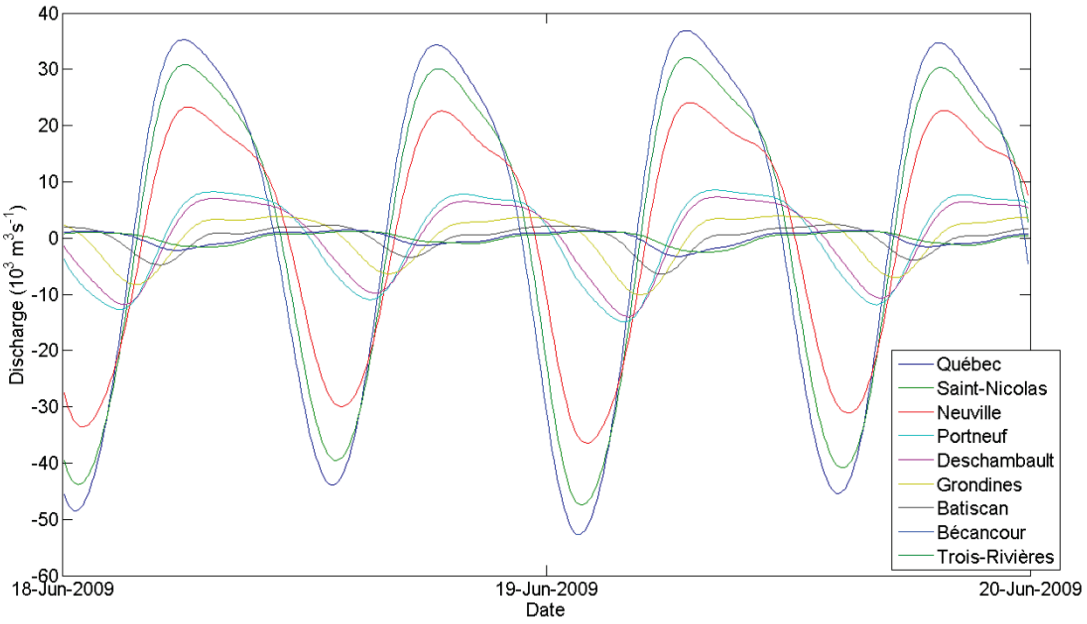


**Figure A.2.16 Débits tidaux calculés par la méthode de cubature pour l'ensemble des stations, pour la période du 18 au 19 juin 2009.**

### A.2.5 Conclusion

Une méthode de reconstruction des débits tidaux basée sur la résolution de l'équation de continuité a été présentée et appliquée à l'estuaire fluvial du Saint-Laurent. La méthode prend en compte la nature bidimensionnelle du terrain par le biais de données topographiques détaillées et d'une discrétisation 2D aux éléments finis, accompagnée d'une condition de couvrant-

découvrant. En entrée au modèle, aucune connaissance des vitesses n'est nécessaire *a priori*; seuls les débits fluviaux en amont de la zone à marée et les variations des niveaux d'eau sont nécessaires. Ces dernières sont obtenues à partir d'un modèle 1D non-stationnaire de propagation de la marée qui tient compte de l'influence des débits fluviaux et du marnage océanique sur les amplitudes et les phases de la marée. Les résultats du modèle ont été validés à partir de mesures réalisées en 2009. La méthode parvient à reproduire les signaux attendus avec une bonne précision (erreurs instantanées inférieures à 10% de l'amplitude du cycle de débit).

La capacité prédictive du modèle rend possible non seulement la reconstruction de séries historiques de débit, mais également la prévision des débits tidaux attendus pour différents scénarios de débit fluvial et de marée. Les reconstructions historiques doivent néanmoins être faites en portant une attention particulière aux modifications anthropiques ayant pu être apportées au système historiquement, particulièrement au niveau des estrans et de la délimitation des berges. De plus, en conditions hivernales, les glaces en berge peuvent limiter la surface mouillée et introduire un biais systématique dans le calcul des débits.

Une reconstruction des débits tidaux basée sur une représentation harmonique de la marée ouvre la voie à des analyses du débit par composantes (ex.: Forrester, 1972), en exprimant le signal comme une somme d'harmoniques. Les modèles numériques 1D traditionnels ne permettent généralement pas une telle analyse, en plus de nécessiter une phase d'étalonnage des paramètres de frottement. Une nouvelle compréhension des processus physiques en jeu peut ainsi être obtenue.

## A.3 Suppléments à la validation du modèle hydrodynamique 2D de l'estuaire fluvial du Saint-Laurent

Cette section rassemble une série de figures servant de supplément à la validation du modèle hydrodynamique 2D de l'estuaire fluvial du Saint-Laurent. Pour chacune des sections de mesures, une comparaison des niveaux d'eau, des vitesses (composantes *u* et *v*) et des débits observés et simulés est réalisée sur approximativement un cycle semi-diurne de marée. La bathymétrie mesurée à chaque section est également comparée avec celle du modèle, laquelle est issue des données de sondages bathymétriques du Service Hydrographique du Canada (SHC), directement incorporées au MNT. Les statistiques (RMSE et critère de compétence, ou « skill ») apparaissent dans les légendes pour chacune des variables présentées.

### A.3.1 Saint-Jean

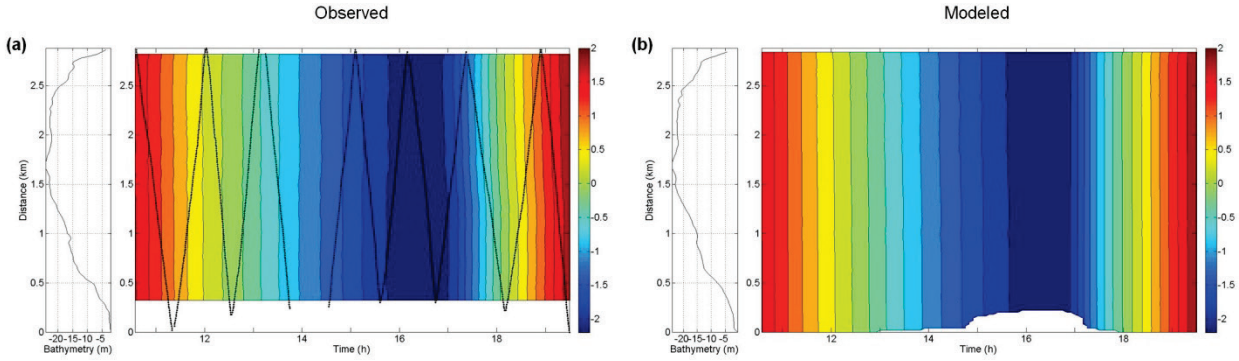


**Figure A.3.1** **(a) Niveaux d'eau observés et (b) simulés (en m) à Saint-Jean le 24 août 2009, en fonction du temps et de la distance le long de la section (RMSE = 0.092 m, Skill = 0.999).**

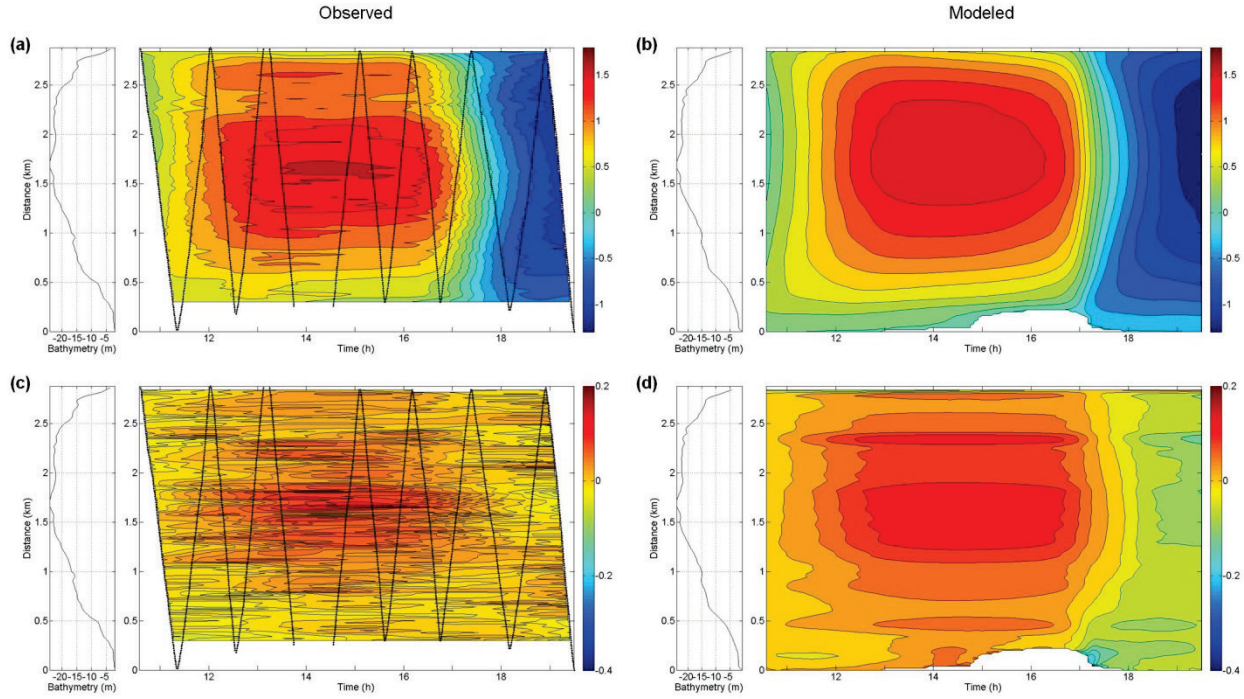


**Figure A.3.2** **(a) Vitesses u observées et (b) simulées (en m $s^{-1}$) à Saint-Jean le 24 août 2009, en fonction du temps et de la distance le long de la section (RMSE = 0.142 m $s^{-1}$, Skill = 0.992). (c) Vitesses v observées et (d) simulées (RMSE = 0.053 m $s^{-1}$, Skill = 0.640).**

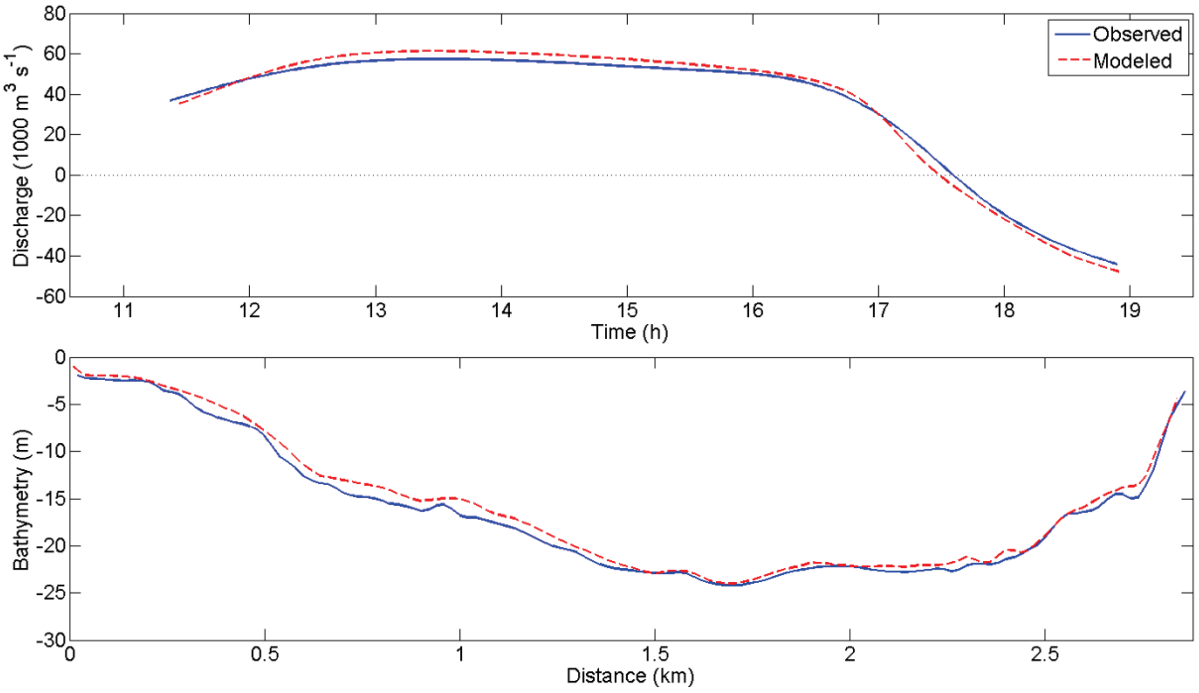


**Figure A.3.3** **(haut) Débits observés et simulés à Saint-Jean le 24 août 2009, en fonction du temps (RMSE = 3256.9 $m^3$ $s^{-1}$, Skill = 0.997). (bas) Bathymétrie mesurée le long de la section (bleu) et issue des données du SHC (rouge) (RMSE = 0.800 m, Skill = 0.997).**

## A.3.2 Château-Richer

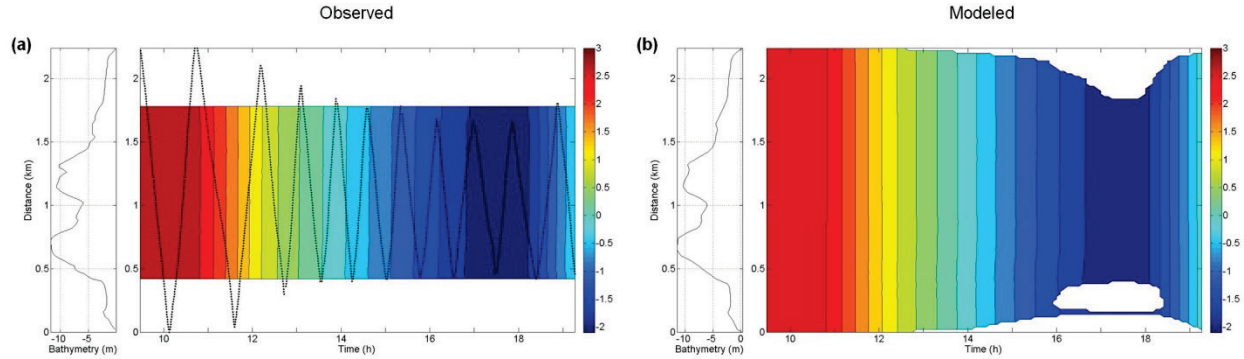


**Figure A.3.4** **(a) Niveaux d'eau observés et (b) simulés (en m) à Château-Richer le 25 août 2009, en fonction du temps et de la distance le long de la section (RMSE = 0.111 m, Skill = 0.999).**

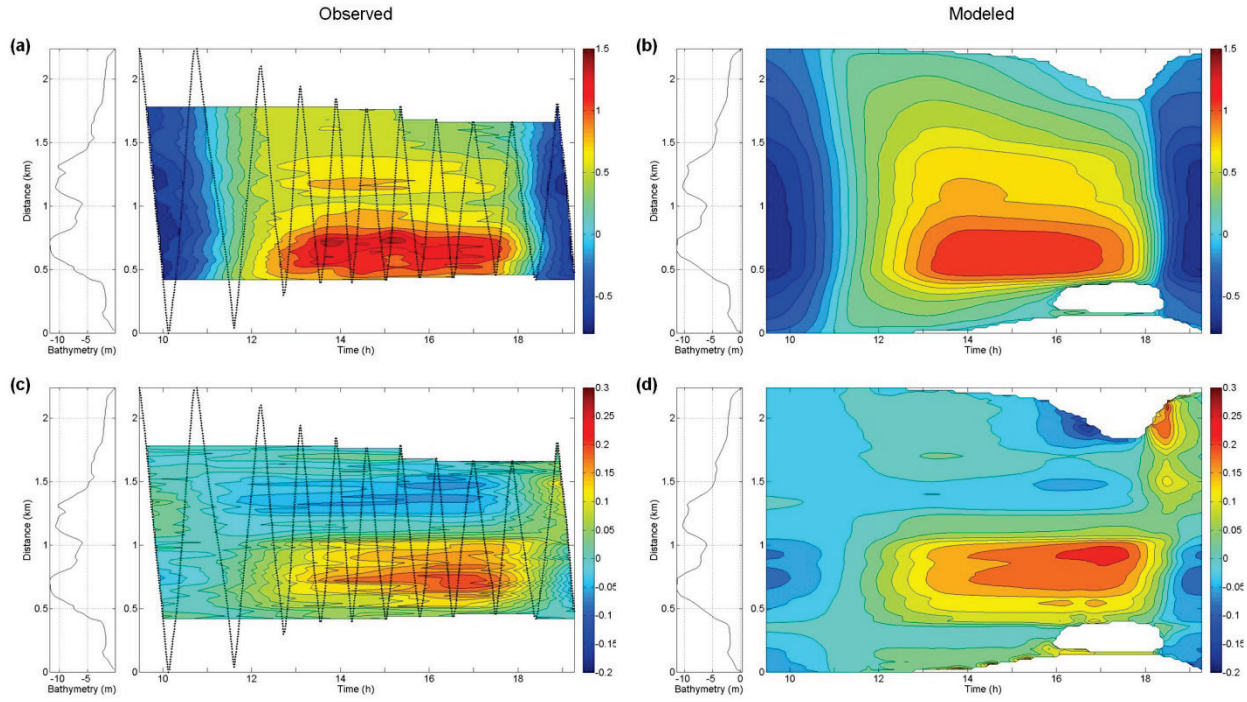


**Figure A.3.5** **(a) Vitesses u observées et (b) simulées (en m $s^{-1}$) à Château-Richer le 25 août 2009, en fonction du temps et de la distance le long de la section (RMSE = 0.096 m $s^{-1}$, Skill = 0.991). (c) Vitesses v observées et (d) simulées (RMSE = 0.032 m $s^{-1}$, Skill = 0.944).**

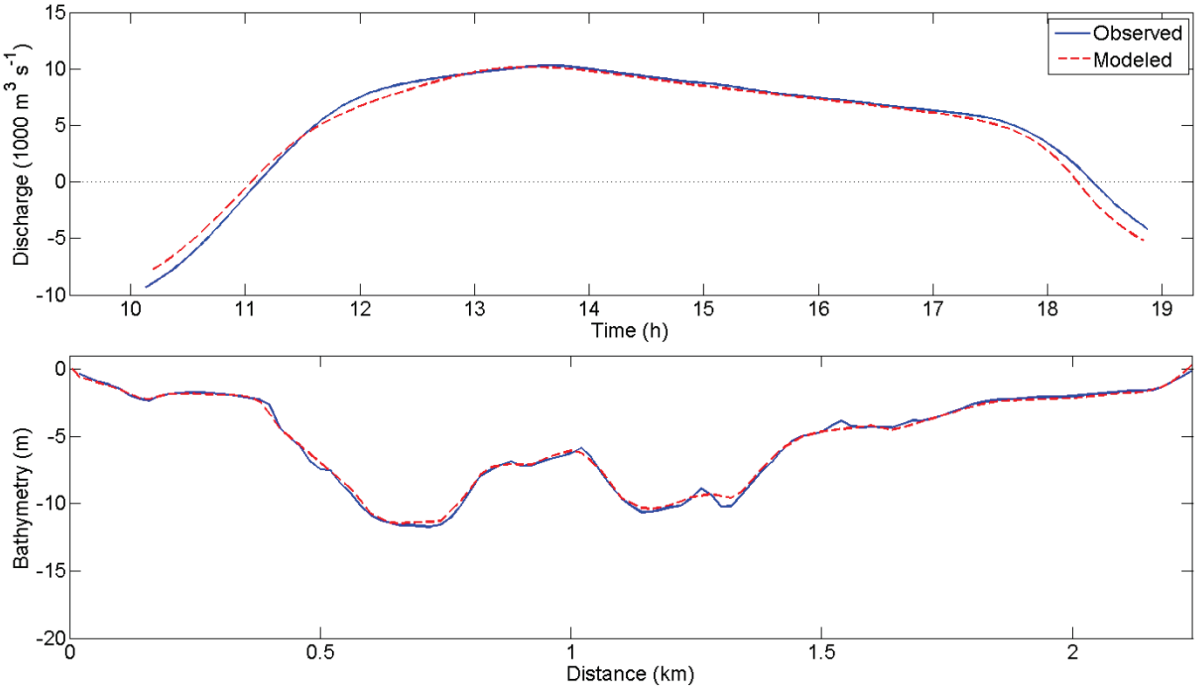


**Figure A.3.6** **(haut) Débits observés et simulés à Château-Richer le 25 août 2009, en fonction du temps (RMSE = 628.7 $m^3 s^{-1}$, Skill = 0.996). (bas) Bathymétrie mesurée le long de la section (bleu) et issue des données du SHC (rouge) (RMSE = 0.236 m, Skill = 0.999).**

## A.3.3 Beauport

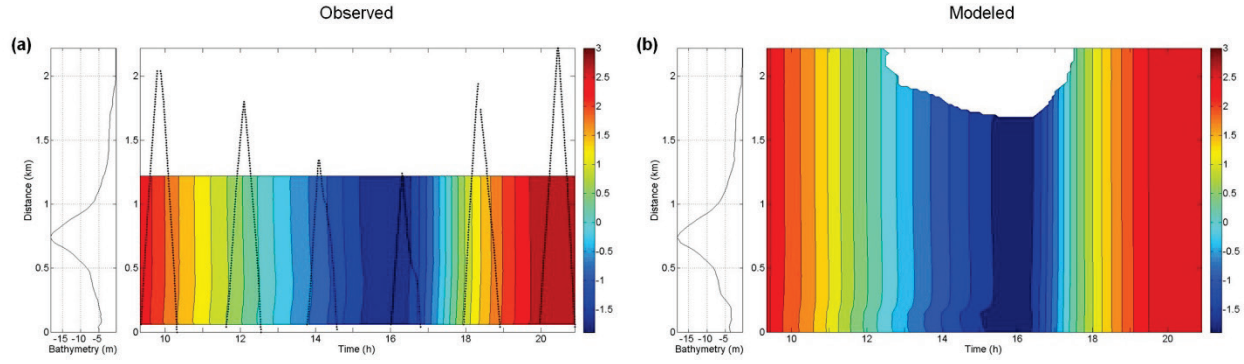


**Figure A.3.7** **(a) Niveaux d'eau observés et (b) simulés (en m) à Beauport le 24 juin 2009, en fonction du temps et de la distance le long de la section (RMSE = 0.144 m, Skill = 0.998).**

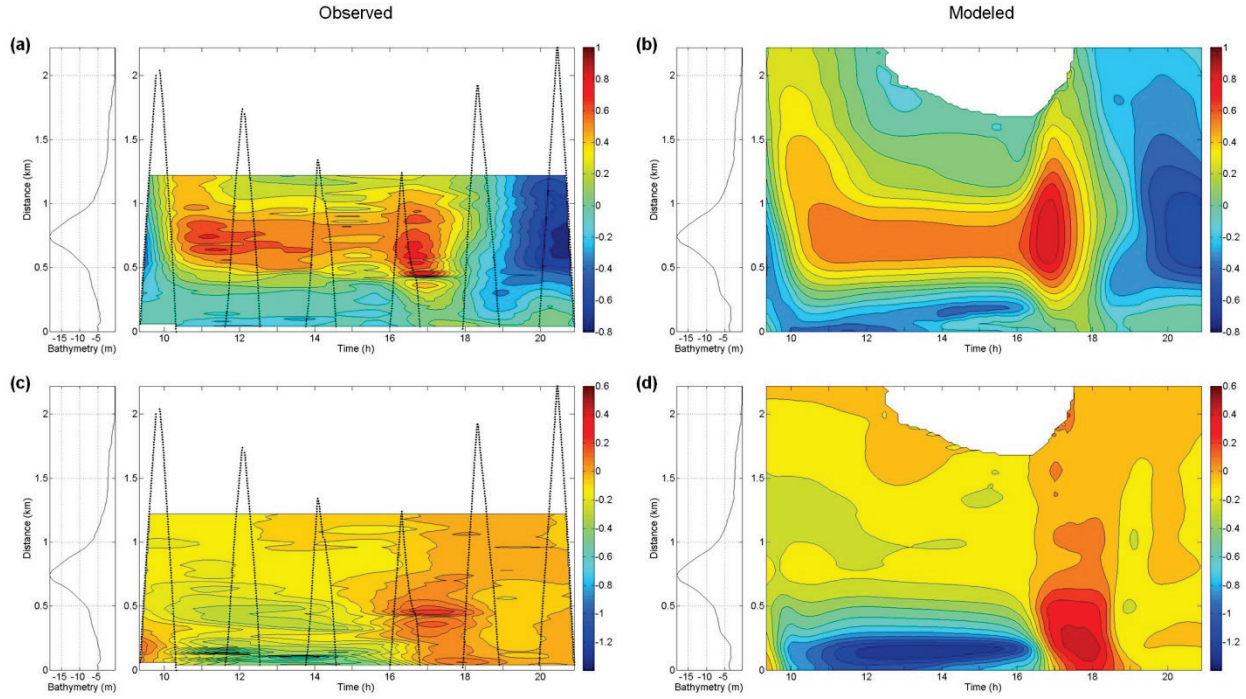


**Figure A.3.8** **(a) Vitesses u observées et (b) simulées (en m $s^{-1}$) à Beauport le 24 juin 2009, en fonction du temps et de la distance le long de la section (RMSE = 0.101 m $s^{-1}$, Skill = 0.978). (c) Vitesses v observées et (d) simulées (RMSE = 0.306 m $s^{-1}$, Skill = 0.585).**

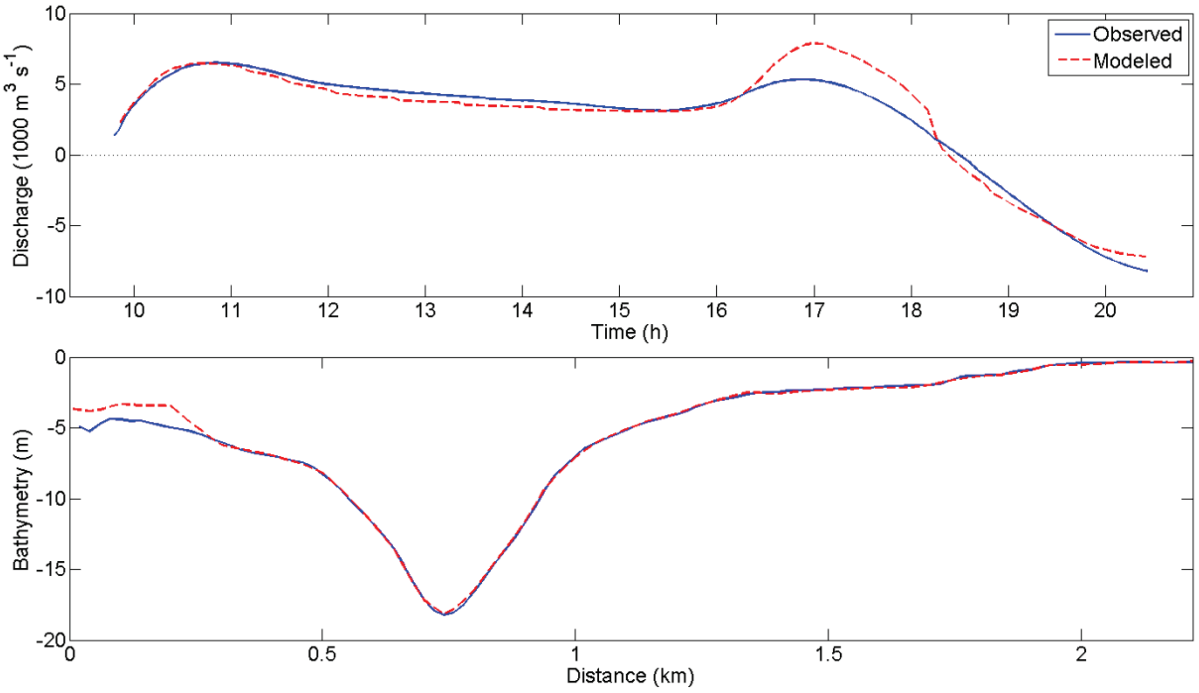


**Figure A.3.9** **(haut) Débits observés et simulés à Beauport le 24 juin 2009, en fonction du temps (RMSE = 942.9 $m^3$ $s^{-1}$, Skill = 0.985). (bas) Bathymétrie mesurée le long de la section (bleu) et issue des données du SHC (rouge) (RMSE = 0.392 m, Skill = 0.998).**

## A.3.4 Lauzon

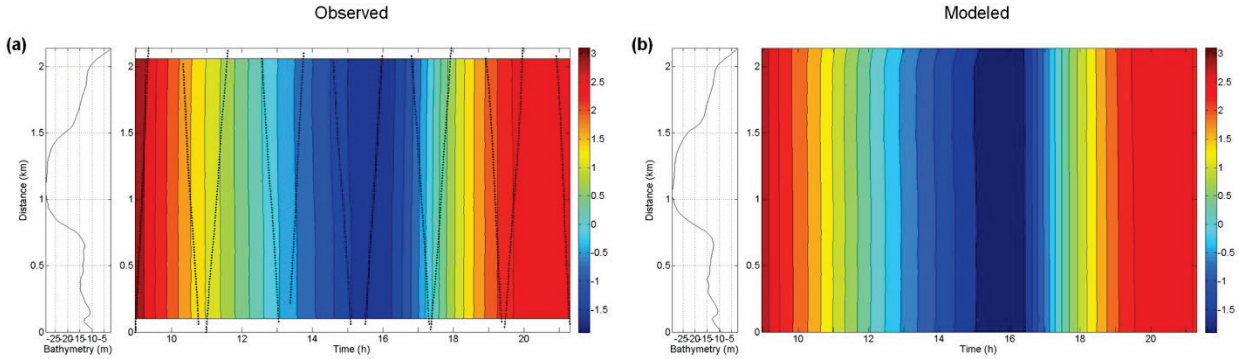


**Figure A.3.10** **(a) Niveaux d'eau observés et (b) simulés (en m) à Lauzon le 24 juin 2009, en fonction du temps et de la distance le long de la section (RMSE = 0.167 m, Skill = 0.997).**

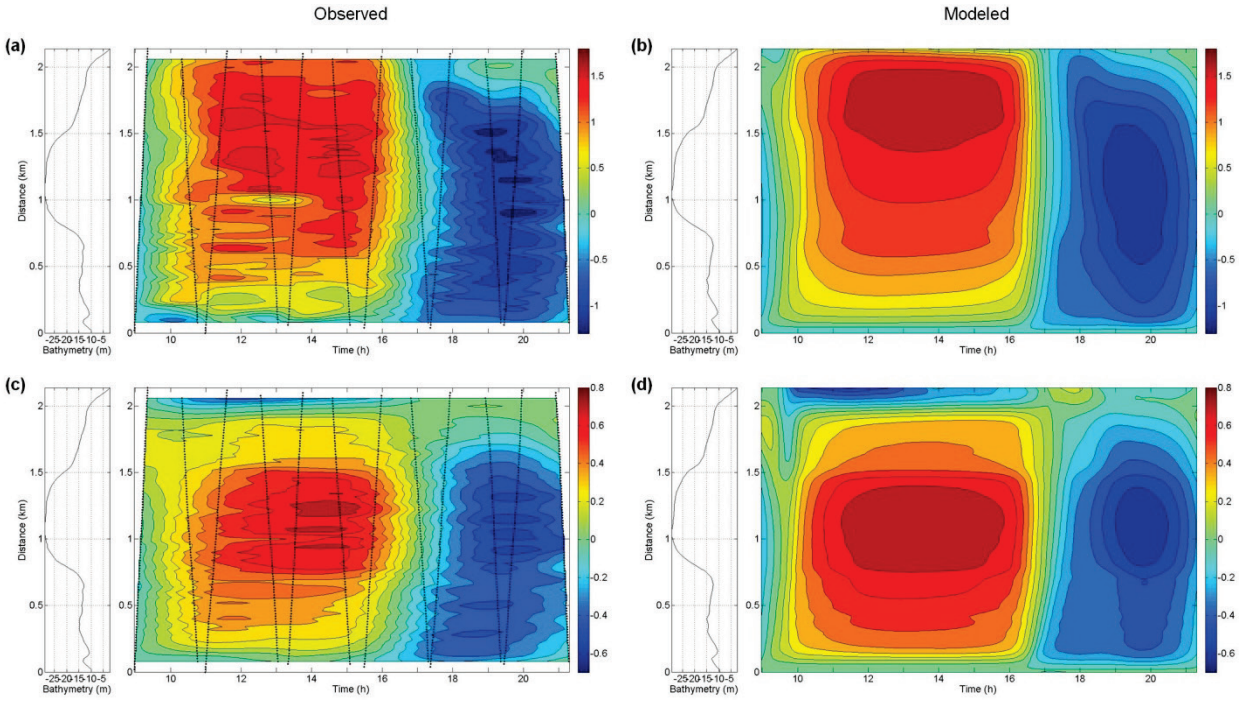


**Figure A.3.11** **(a) Vitesses u observées et (b) simulées (en m $s^{-1}$) à Lauzon le 24 juin 2009, en fonction du temps et de la distance le long de la section (RMSE = 0.205 m $s^{-1}$, Skill = 0.986). (c) Vitesses v observées et (d) simulées (RMSE = 0.132 m $s^{-1}$, Skill = 0.968).**

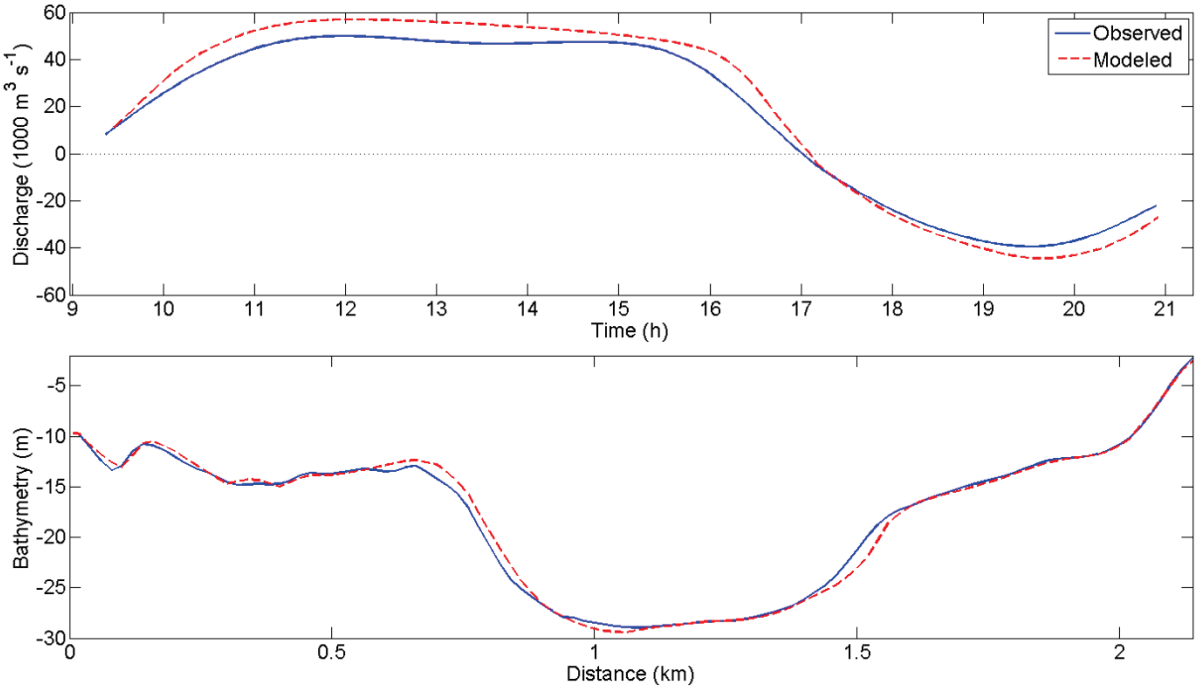


**Figure A.3.12** **(haut) Débits observés et simulés à Lauzon le 24 juin 2009, en fonction du temps (RMSE = 6198.6 $m^3 s^{-1}$, Skill = 0.993). (bas) Bathymétrie mesurée le long de la section (bleu) et issue des données du SHC (rouge) (RMSE = 0.596 m, Skill = 0.998).**

## A.3.5 Québec

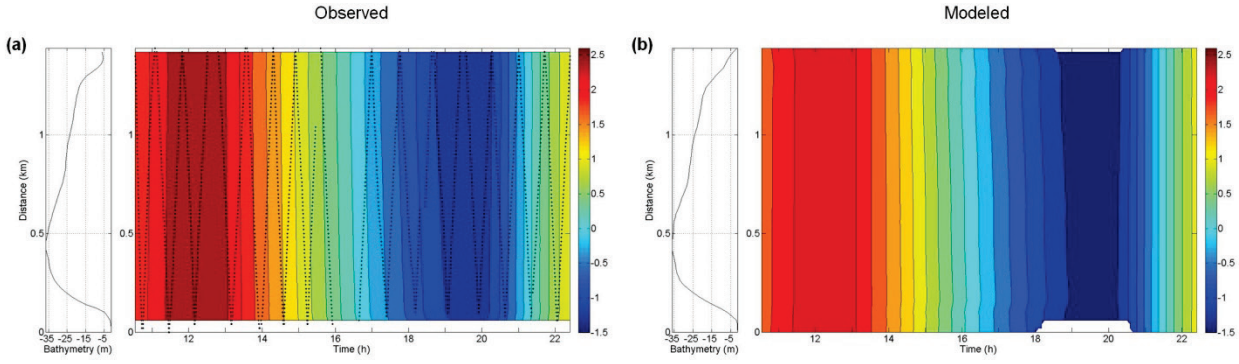


**Figure A.3.13** **(a) Niveaux d'eau observés et (b) simulés (en m) à Québec le 15 juin 2009, en fonction du temps et de la distance le long de la section (RMSE = 0.183 m, Skill = 0.995).**

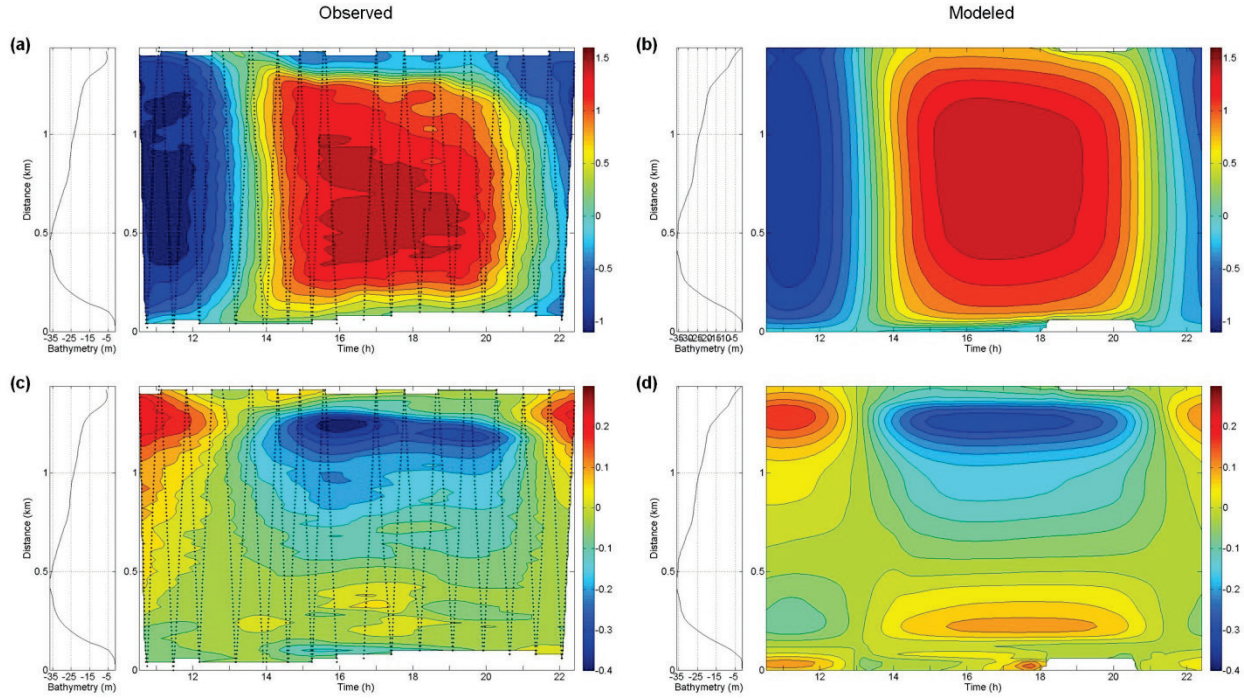


**Figure A.3.14** **(a) Vitesses u observées et (b) simulées (en m $s^{-1}$) à Québec le 15 juin 2009, en fonction du temps et de la distance le long de la section (RMSE = 0.294 m $s^{-1}$, Skill = 0.968). (c) Vitesses v observées et (d) simulées (RMSE = 0.055 m $s^{-1}$, Skill = 0.912).**

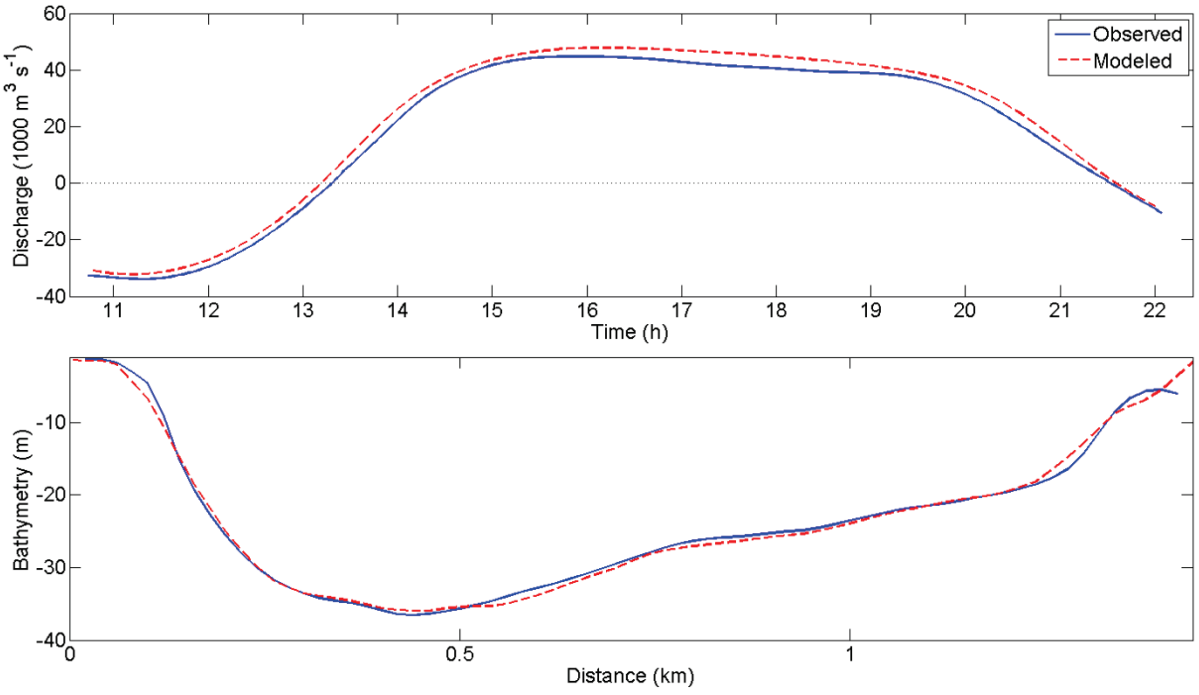


**Figure A.3.15** **(haut) Débits observés et simulés à Québec le 15 juin 2009, en fonction du temps (RMSE = 3133.5 $m^3$ $s^{-1}$, Skill = 0.997). (bas) Bathymétrie mesurée le long de la section (bleu) et issue des données du SHC (rouge) (RMSE = 0.736 m, Skill = 0.999).**

## A.3.6 Saint-Nicolas

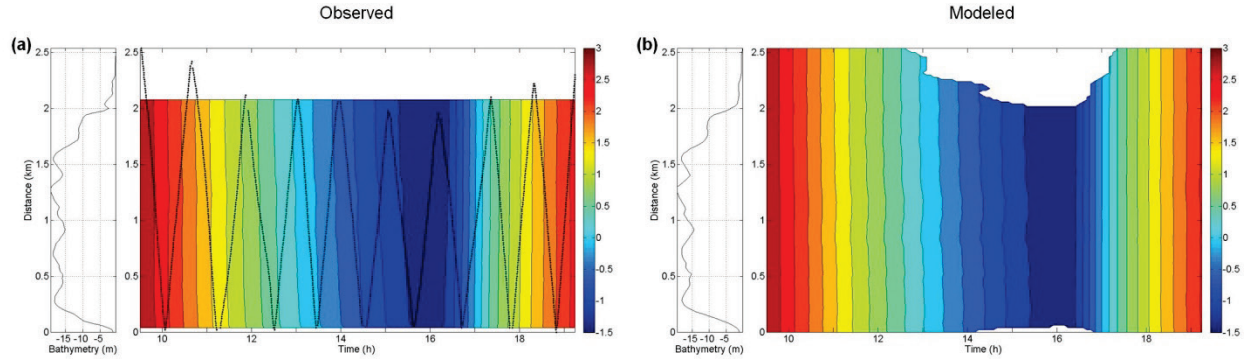


**Figure A.3.16** **(a) Niveaux d'eau observés et (b) simulés (en m) à Saint-Nicolas le 21 août 2009, en fonction du temps et de la distance le long de la section (RMSE = 0.036 m $s^{-1}$, Skill = 1.000).**

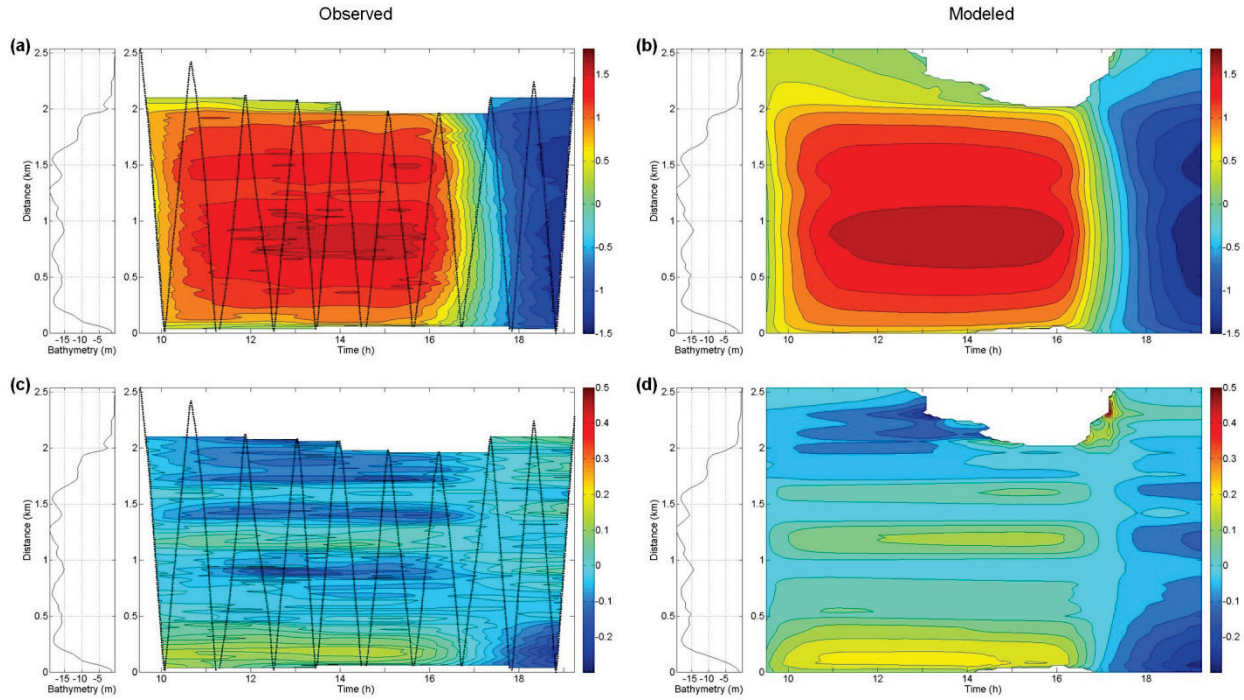


**Figure A.3.17** **(a) Vitesses u observées et (b) simulées (en m $s^{-1}$) à Saint-Nicolas le 21 août 2009, en fonction du temps et de la distance le long de la section (RMSE = 0.103 m $s^{-1}$, Skill = 0.997). (c) Vitesses v observées et (d) simulées (RMSE = 0.070 m $s^{-1}$, Skill = 0.761).**

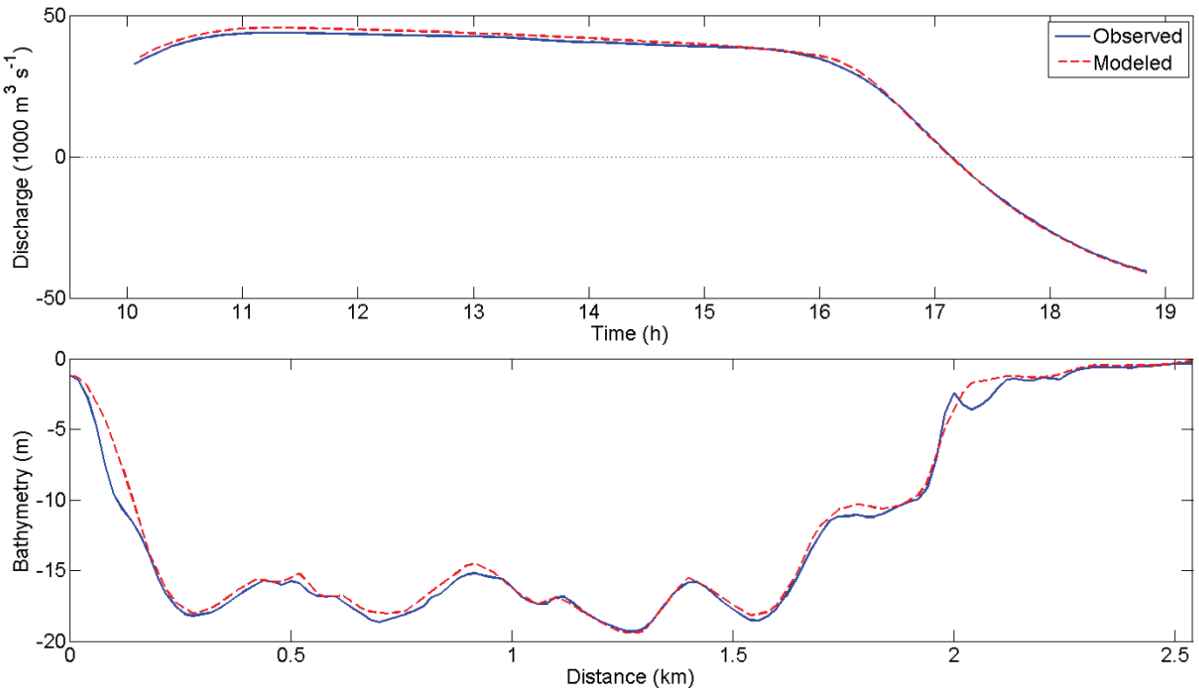


**Figure A.3.18** **(haut) Débits observés et simulés à Saint-Nicolas le 21 août 2009, en fonction du temps (RMSE = 1192.2 $m^3 s^{-1}$, Skill = 1.000). (bas) Bathymétrie mesurée le long de la section (bleu) et issue des données du SHC (rouge) (RMSE = 0.710 m, Skill = 0.997).**

## A.3.7 Neuville

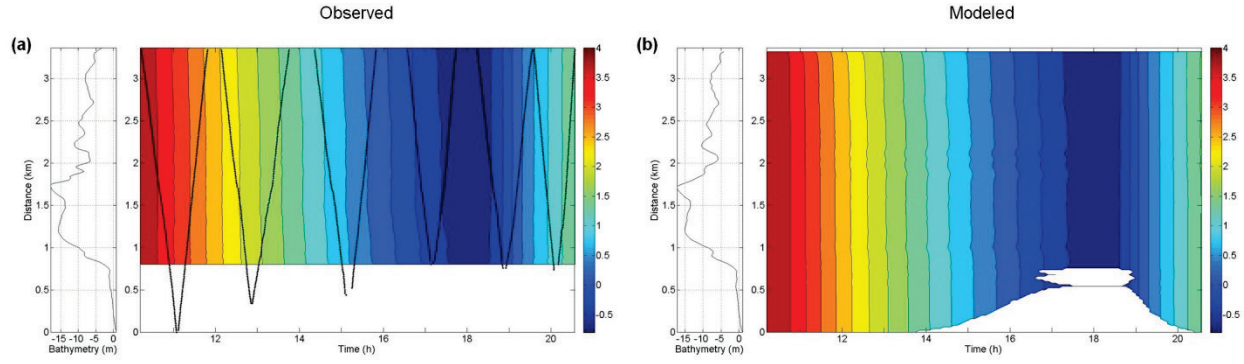


**Figure A.3.19** **(a) Niveaux d'eau observés et (b) simulés (en m) à Neuville le 25 juin 2009, en fonction du temps et de la distance le long de la section (RMSE = 0.045 m, Skill = 1.000).**

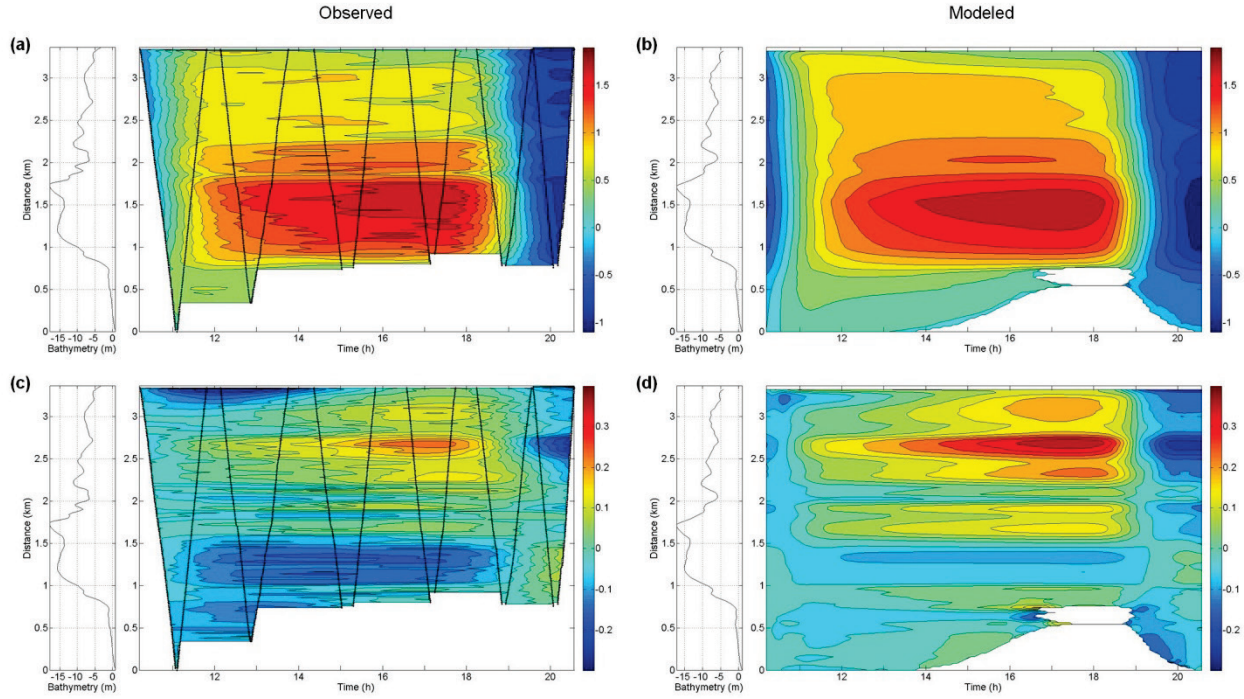


**Figure A.3.20** **(a) Vitesses u observées et (b) simulées (en m $s^{-1}$) à Neuville le 25 juin 2009, en fonction du temps et de la distance le long de la section (RMSE = 0.124 m $s^{-1}$, Skill = 0.991). (c) Vitesses v observées et (d) simulées (RMSE = 0.078 m $s^{-1}$, Skill = 0.830).**

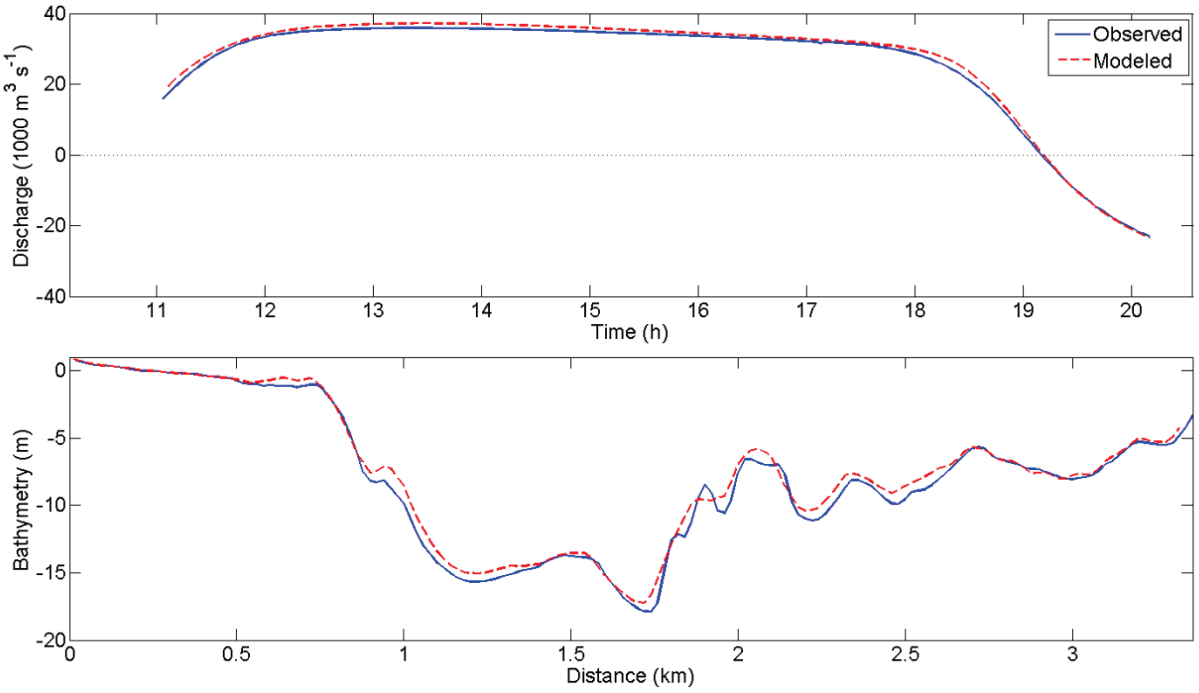


**Figure A.3.21** **(haut) Débits observés et simulés à Neuville le 25 juin 2009, en fonction du temps (RMSE = 1137.3 $m^3$ $s^{-1}$, Skill = 0.999). (bas) Bathymétrie mesurée le long de la section (bleu) et issue des données du SHC (rouge) (RMSE = 0.588 m, Skill = 0.997).**

## A.3.8 Portneuf

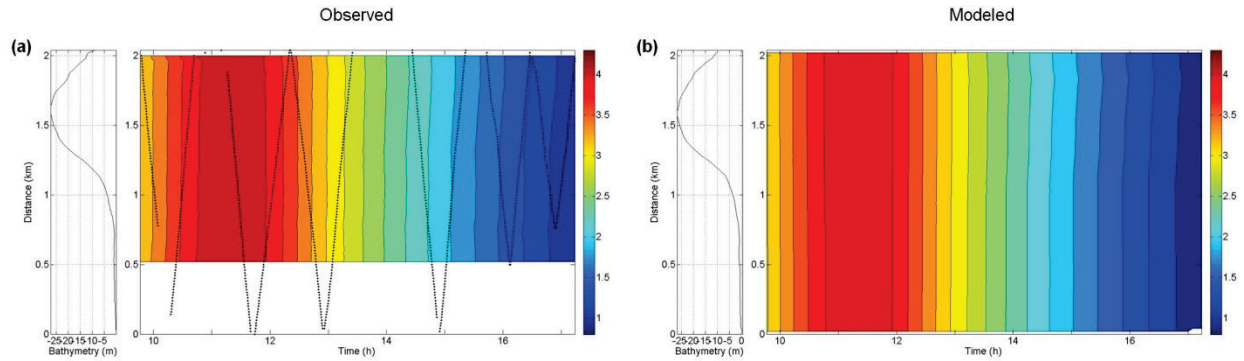


**Figure A.3.22** **(a) Niveaux d'eau observés et (b) simulés (en m) à Portneuf le 26 juin 2009, en fonction du temps et de la distance le long de la section (RMSE = 0.089 m, Skill = 0.998).**

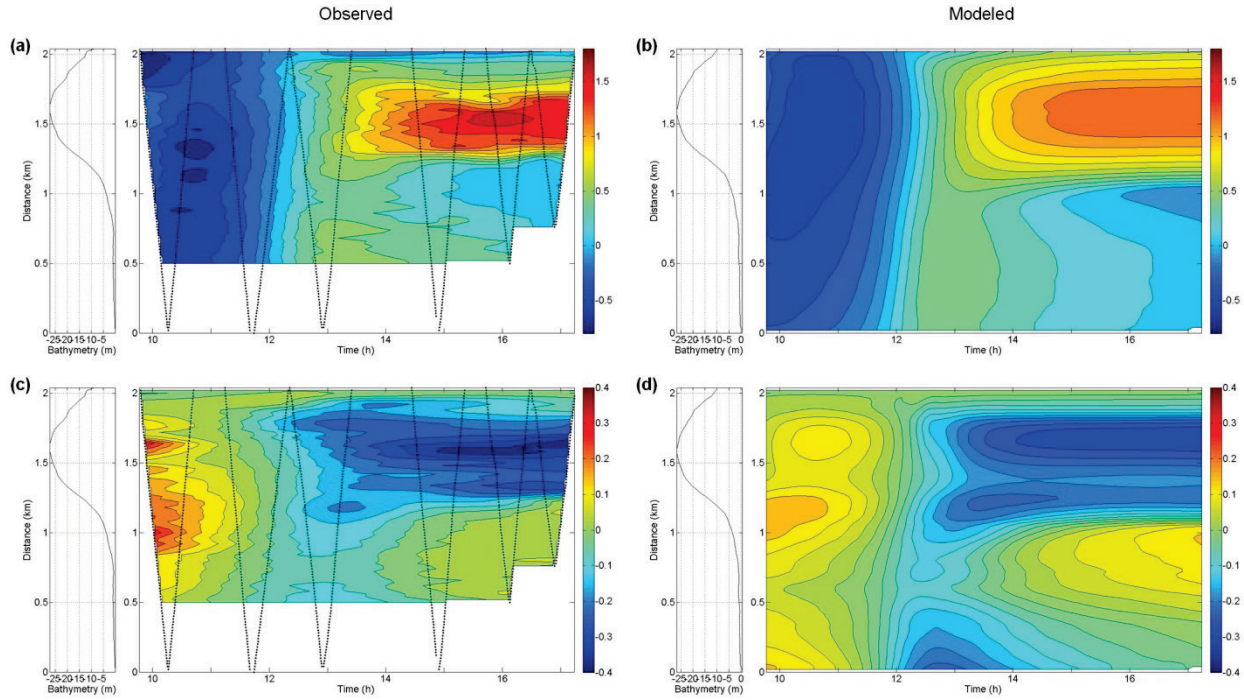


**Figure A.3.23** **(a) Vitesses u observées et (b) simulées (en m $s^{-1}$) à Portneuf le 26 juin 2009, en fonction du temps et de la distance le long de la section (RMSE = 0.212 m $s^{-1}$, Skill = 0.963). (c) Vitesses v observées et (d) simulées (RMSE = 0.048 m $s^{-1}$, Skill = 0.960).**

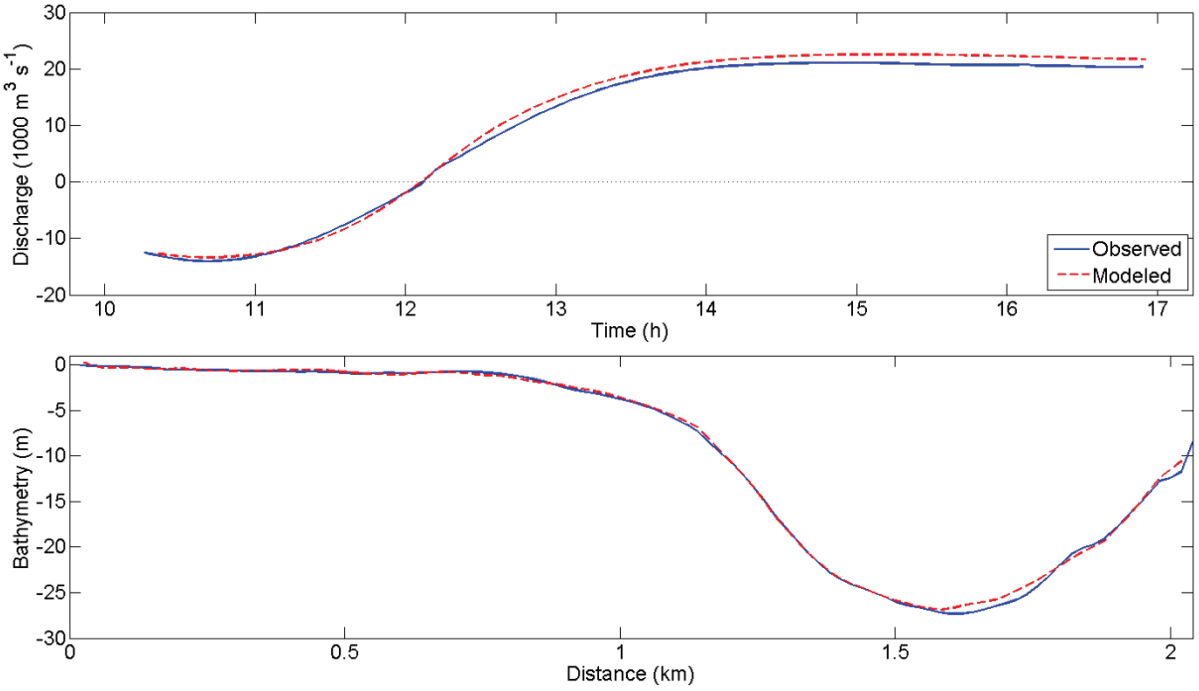


**Figure A.3.24** **(haut) Débits observés et simulés à Portneuf le 26 juin 2009, en fonction du temps (RMSE = 1215.1 $m^3 s^{-1}$, Skill = 0.998). (bas) Bathymétrie mesurée le long de la section (bleu) et issue des données du SHC (rouge) (RMSE = 0.342 m, Skill = 1.000).**

## A.3.9 Deschambault

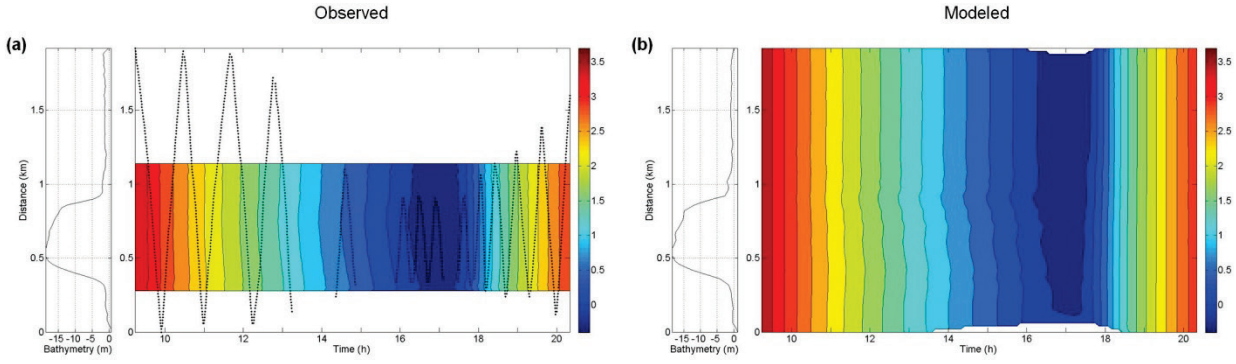


**Figure A.3.25** **(a) Niveaux d'eau observés et (b) simulés (en m) à Deschambault le 20 août 2009, en fonction du temps et de la distance le long de la section (RMSE = 0.050 m, Skill = 1.000).**

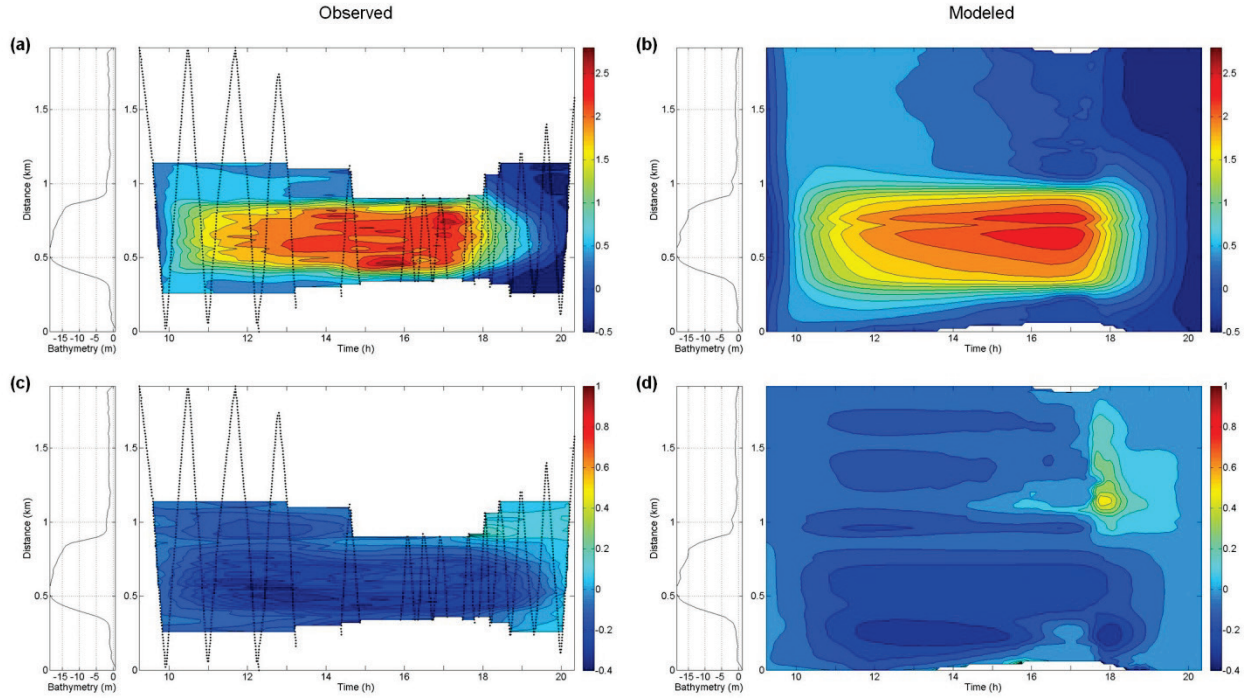


**Figure A.3.26** **(a) Vitesses u observées et (b) simulées (en m $s^{-1}$) à Deschambault le 20 août 2009, en fonction du temps et de la distance le long de la section (RMSE = 0.416 m $s^{-1}$, Skill = 0.933). (c) Vitesses v observées et (d) simulées (RMSE = 0.058 m $s^{-1}$, Skill = 0.912).**

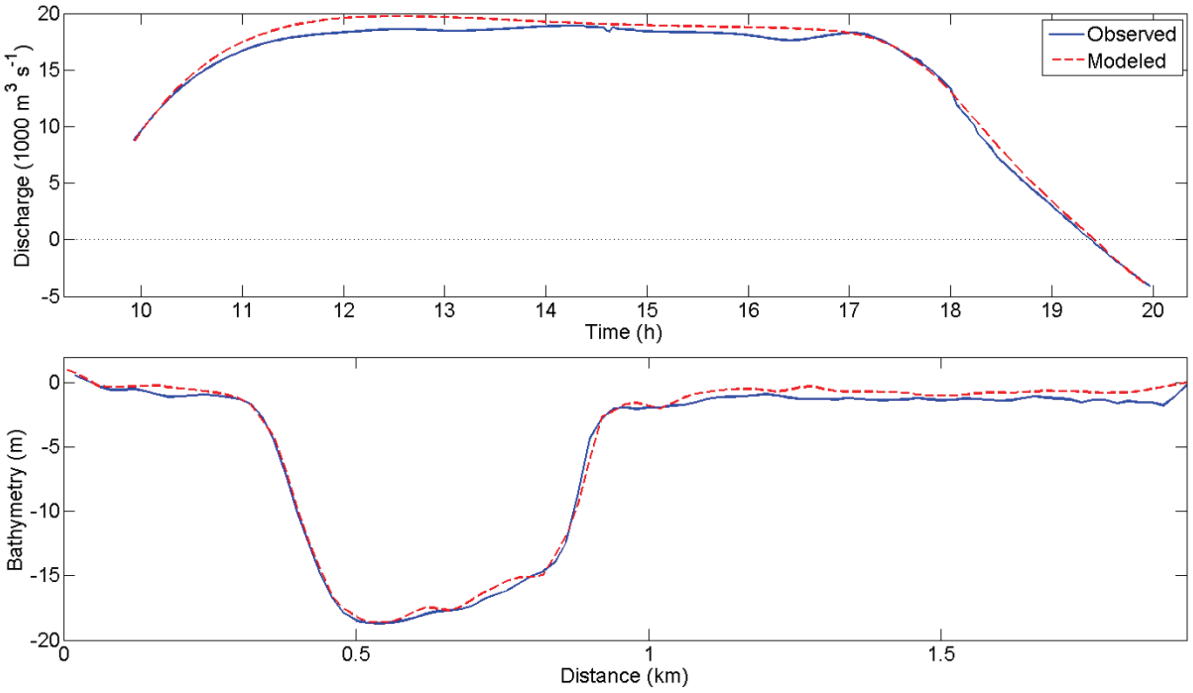


**Figure A.3.27** **(haut) Débits observés et simulés à Deschambault le 20 août 2009, en fonction du temps (RMSE = 726.4 $m^3$ $s^{-1}$, Skill = 0.997). (bas) Bathymétrie mesurée le long de la section (bleu) et issue des données du SHC (rouge) (RMSE = 0.541 m, Skill = 0.998).**

## A.3.10 Grondines

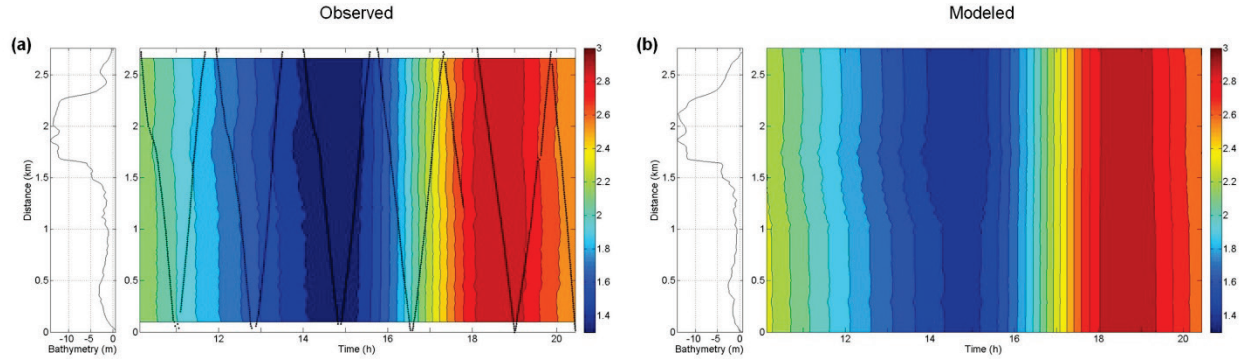


**Figure A.3.28** **(a) Niveaux d'eau observés et (b) simulés (en m) à Grondines le 19 juin 2009, en fonction du temps et de la distance le long de la section (RMSE = 0.067 m, Skill = 0.996).**

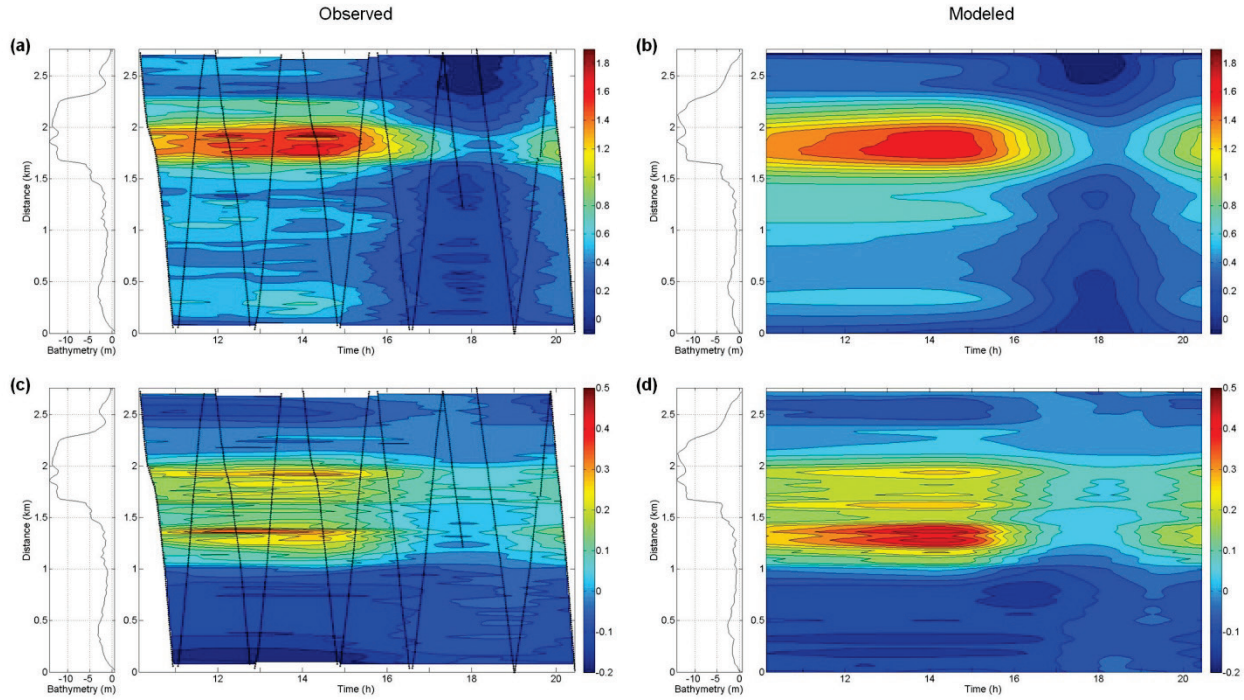


**Figure A.3.29** **(a) Vitesses u observées et (b) simulées (en m $s^{-1}$) à Grondines le 19 juin 2009, en fonction du temps et de la distance le long de la section (RMSE = 0.128 m $s^{-1}$, Skill = 0.968). (c) Vitesses v observées et (d) simulées (RMSE = 0.046 m $s^{-1}$, Skill = 0.963).**

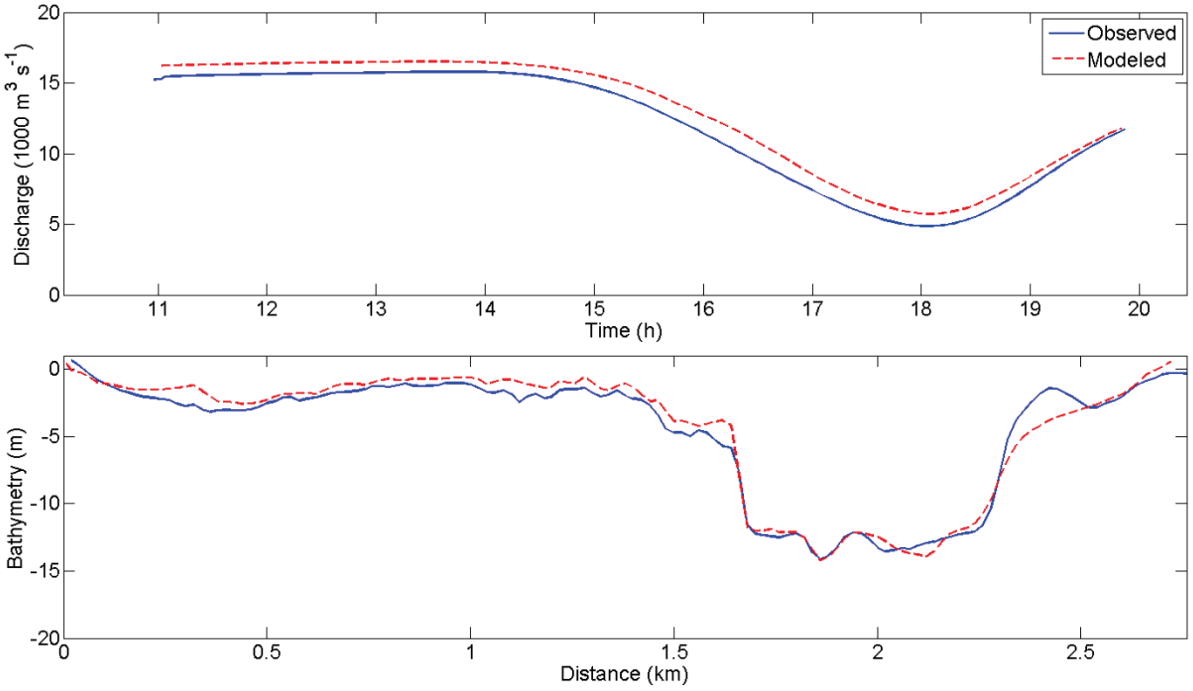


**Figure A.3.30** **(haut) Débits observés et simulés à Grondines le 19 juin 2009, en fonction du temps (RMSE = 898.4 $m^3 s^{-1}$, Skill = 0.988). (bas) Bathymétrie mesurée le long de la section (bleu) et issue des données du SHC (rouge) (RMSE = 0.797 m, Skill = 0.993).**

## A.3.11 Batiscan

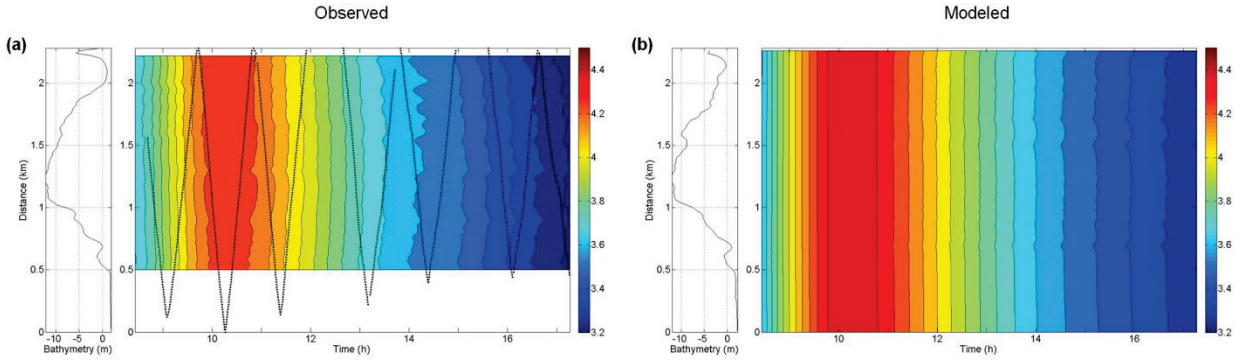


**Figure A.3.31** **(a) Niveaux d'eau observés et (b) simulés (en m) à Batiscan le 23 juin 2009, en fonction du temps et de la distance le long de la section (RMSE = 0.081 m, Skill = 0.987).**

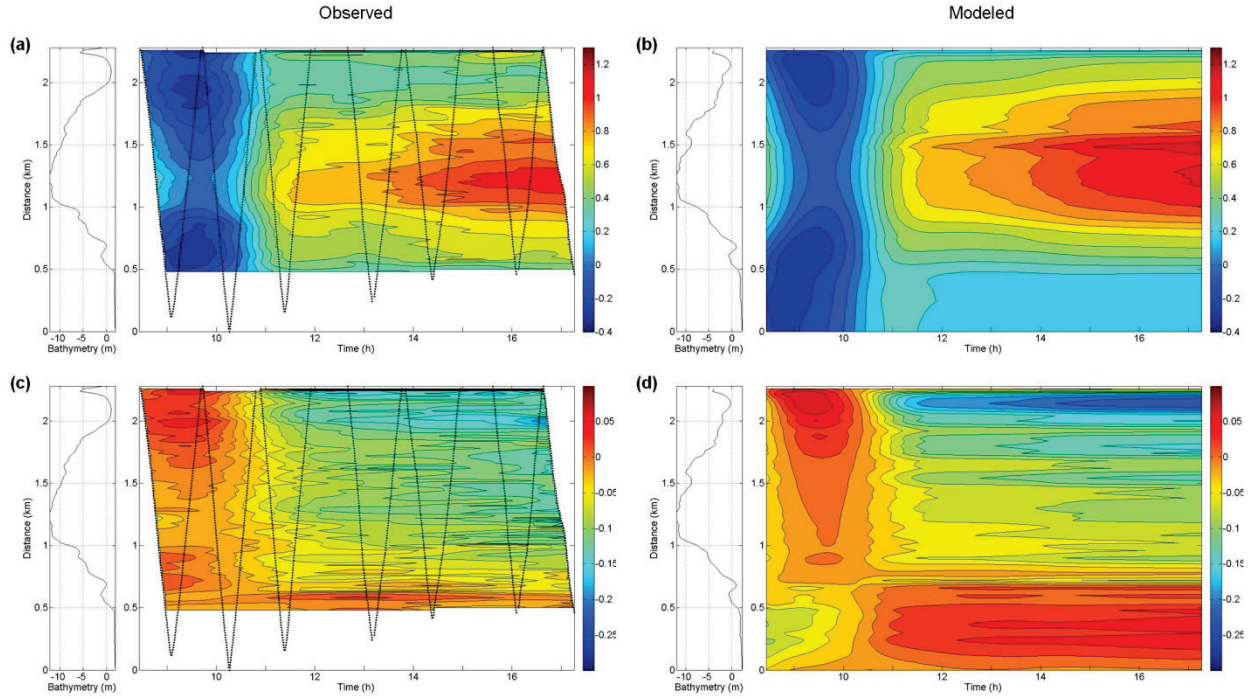


**Figure A.3.32** **(a) Vitesses u observées et (b) simulées (en m $s^{-1}$) à Batiscan le 23 juin 2009, en fonction du temps et de la distance le long de la section (RMSE = 0.113 m $s^{-1}$, Skill = 0.975). (c) Vitesses v observées et (d) simulées (RMSE = 0.028 m $s^{-1}$, Skill = 0.922).**

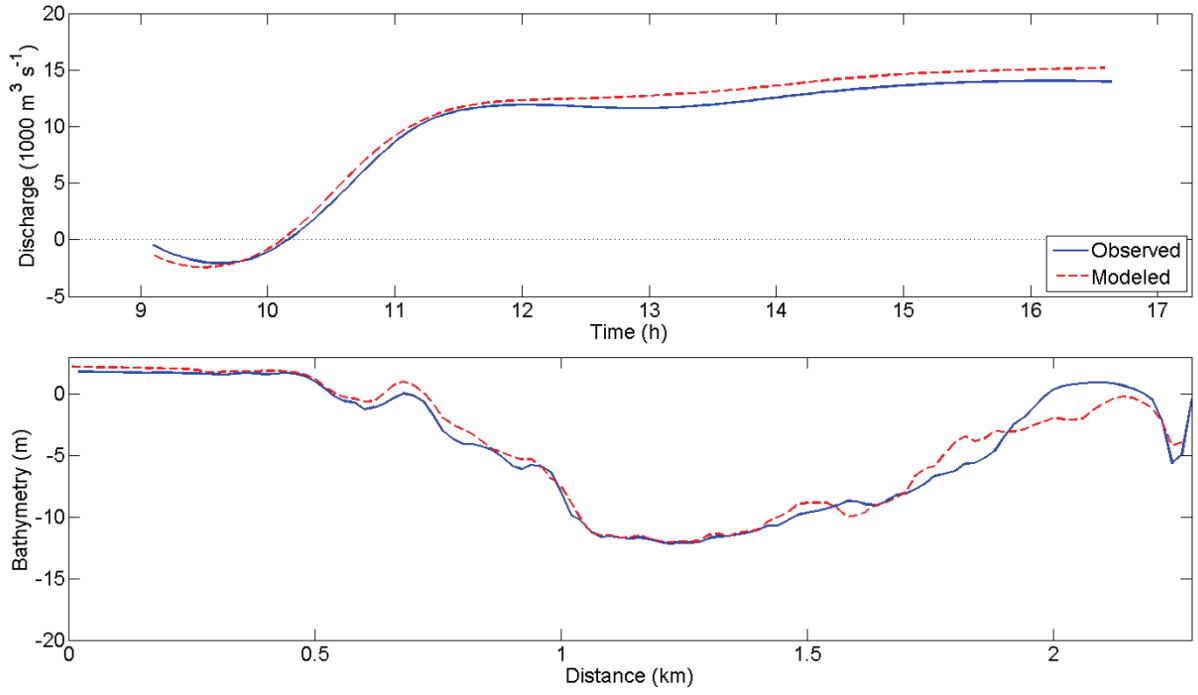


**Figure A.3.33** **(haut) Débits observés et simulés à Batiscan le 23 juin 2009, en fonction du temps (RMSE = 847.9 $m^3$ $s^{-1}$, Skill = 0.994). (bas) Bathymétrie mesurée le long de la section (bleu) et issue des données du SHC (rouge) (RMSE = 0.938 m, Skill = 0.991).**

## A.3.12 Bécancour

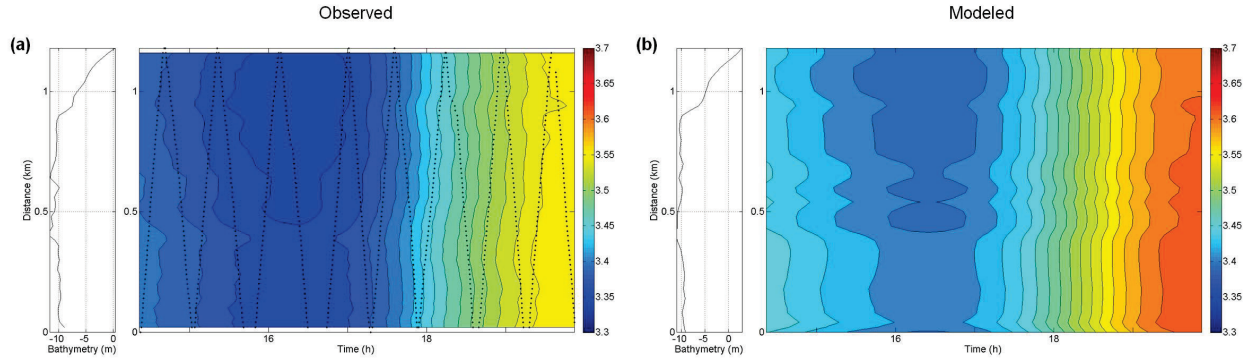


**Figure A.3.34** **(a) Niveaux d'eau observés et (b) simulés (en m) à Bécancour le 18 juin 2009, en fonction du temps et de la distance le long de la section (RMSE = 0.049 m, Skill = 0.901).**

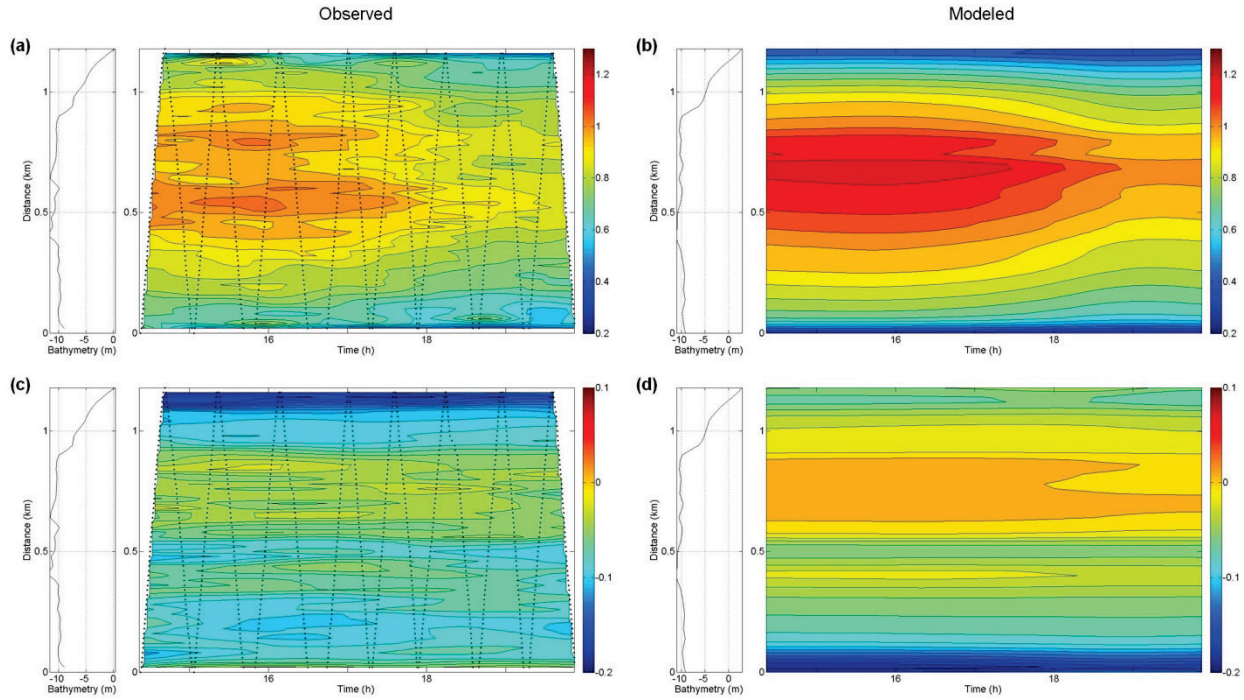


**Figure A.3.35** **(a) Vitesses u observées et (b) simulées (en m $s^{-1}$) à Bécancour le 18 juin 2009, en fonction du temps et de la distance le long de la section (RMSE = 0.121 m $s^{-1}$, Skill = 0.858). (c) Vitesses v observées et (d) simulées (RMSE = 0.055 m $s^{-1}$, Skill = 0.501).**

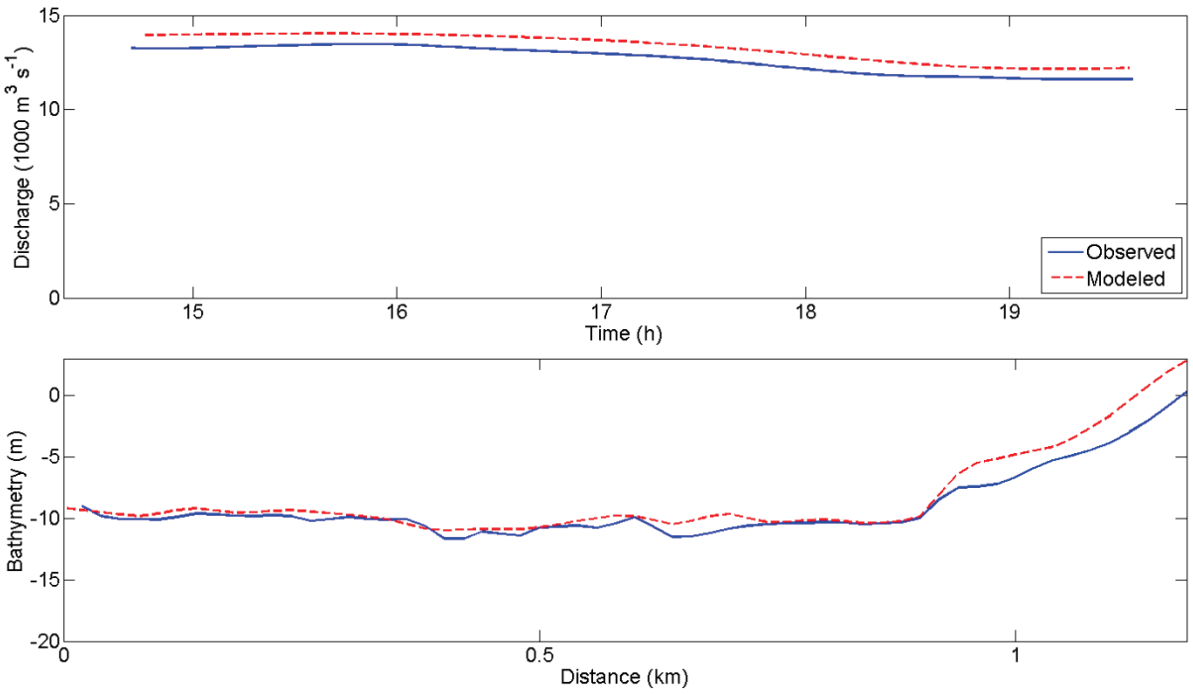


**Figure A.3.36** **(haut) Débits observés et simulés à Bécancour le 18 juin 2009, en fonction du temps (RMSE = 658.2 $m^3s^{-1}$, Skill = 0.826). (bas) Bathymétrie mesurée le long de la section (bleu) et issue des données du SHC (rouge) (RMSE = 1.067 m, Skill = 0.970).**

## A.3.13 Trois-Rivières

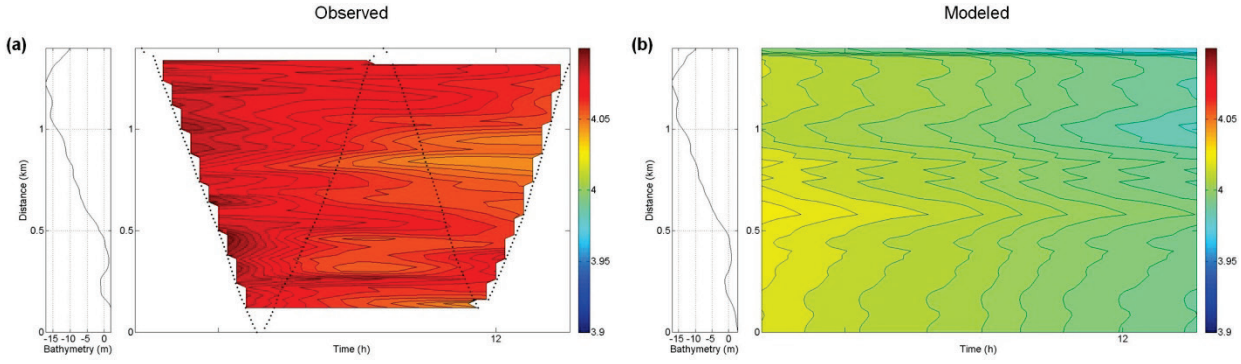


**Figure A.3.37** **(a) Niveaux d'eau observés et (b) simulés (en m) à Trois-Rivières le 18 juin 2009, en fonction du temps et de la distance le long de la section (RMSE = 0.066 m, Skill = 0.199).**

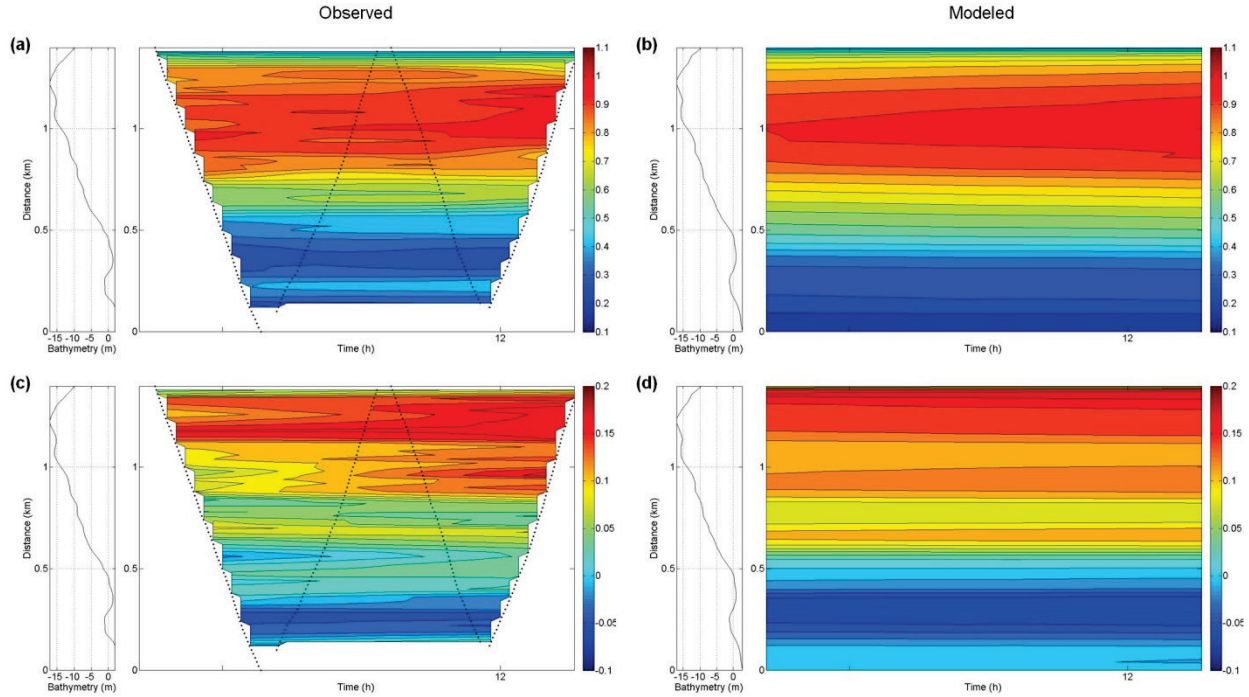


**Figure A.3.38** **(a) Vitesses u observées et (b) simulées (en m $s^{-1}$) à Trois-Rivières le 18 juin 2009, en fonction du temps et de la distance le long de la section (RMSE = 0.099 m $s^{-1}$, Skill = 0.957). (c) Vitesses v observées et (d) simulées (RMSE = 0.033 m $s^{-1}$, Skill = 0.936).**

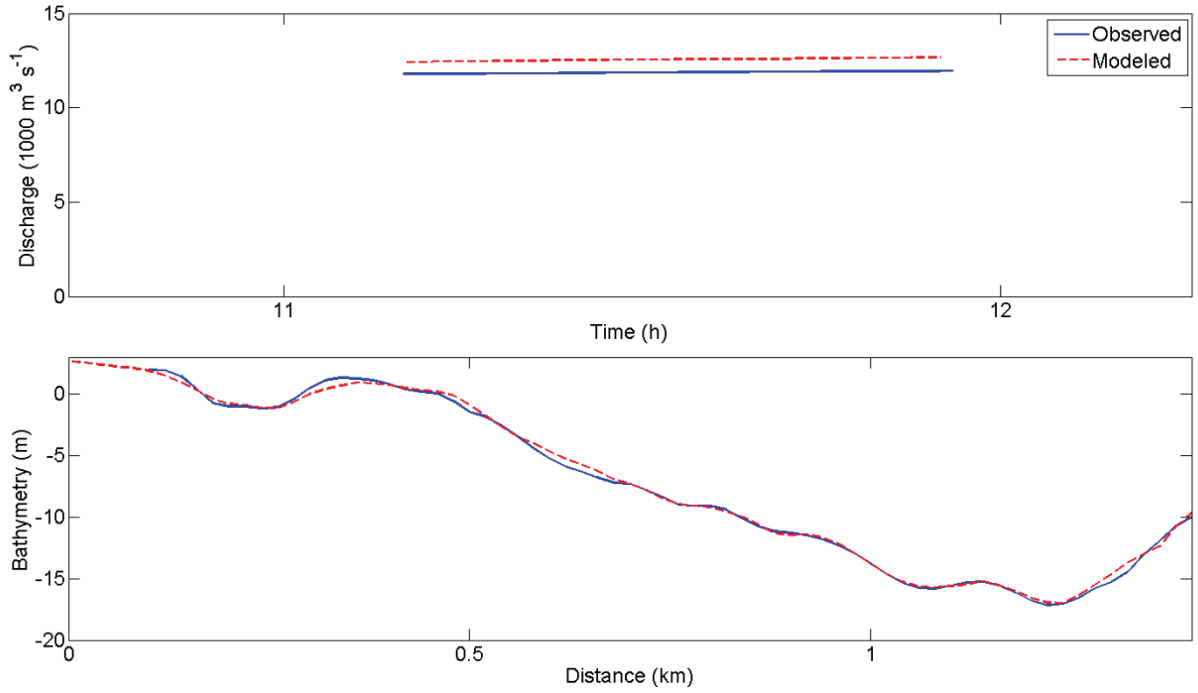


**Figure A.3.39** **(haut) Débits observés et simulés à Trois-Rivières le 18 juin 2009, en fonction du temps (RMSE = 680.1 $m^3s^{-1}$, Skill = 0.124). (bas) Bathymétrie mesurée le long de la section (bleu) et issue des données du SHC (rouge) (RMSE = 0.299 m, Skill = 1.000).**